TESIS DOCTORAL

Coordination Compounds of Organosulfur Ligands as Precursors of Nanostructured Materials.

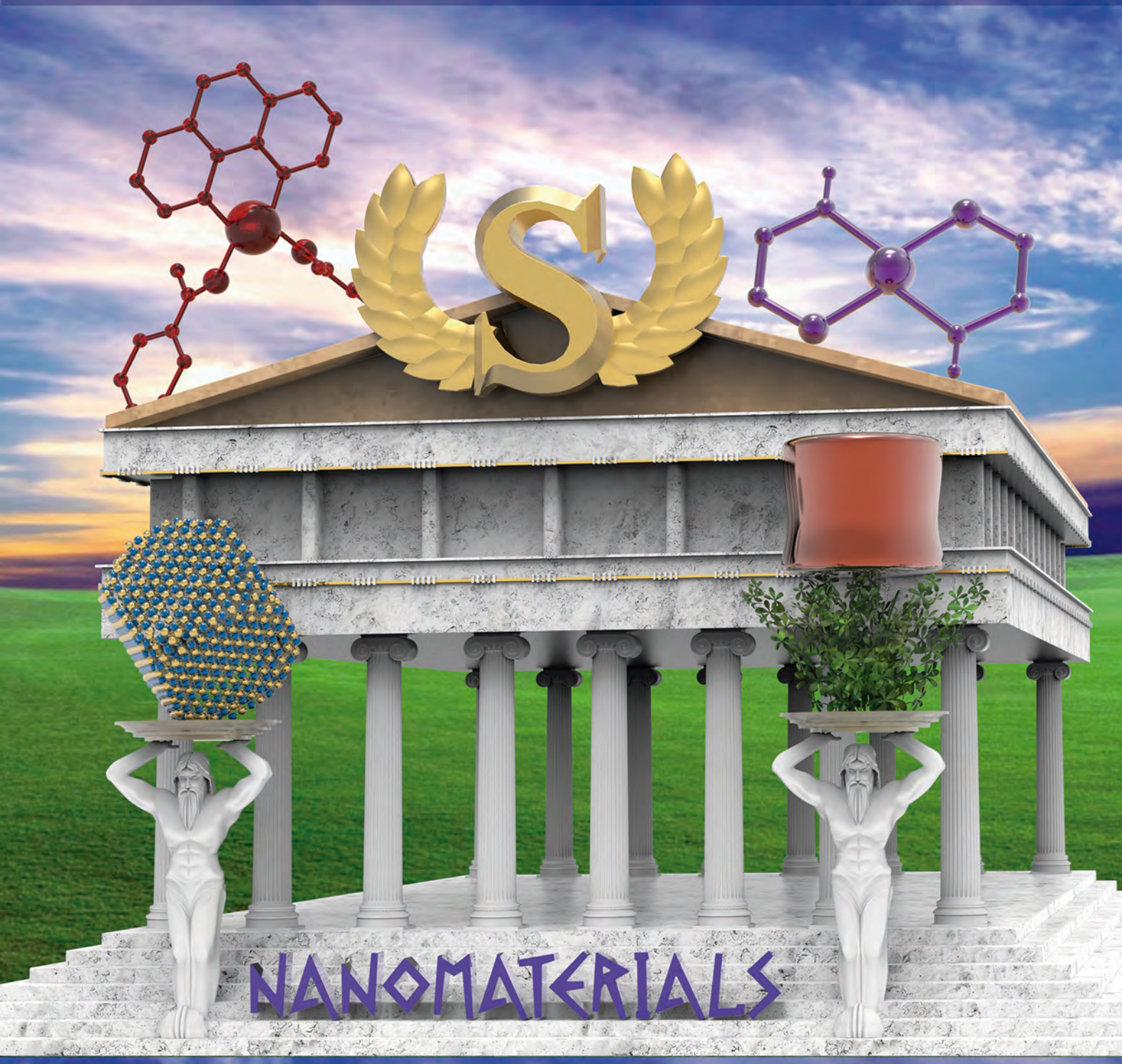

Daniel Vallejo Sánchez

Leioa, mayo de 2017

COORDINATION COMPOUNDS OF ORGANOSULFUR LIGANDS AS PRECURSORS OF NANOSTRUCTURED MATERIALS

PhD Thesis

Daniel Vallejo Sánchez

Leioa, May 2017

AGRADECIMIENTOS

Realizar una Tesis Doctoral es una tarea ardua y compleja que requiere de mucho sacrificio y motivación. El camino se vuelve más tortuoso, si cabe, cuando te ves obligado eventualmente a compaginar los estudios con otros oficios para subsistir por falta de un apoyo económico. En la culminación del trabajo, ha sido de vital importancia el haber tenido a mi alrededor personas positivas que han confiado en mis capacidades. A continuación, nombraré a todas esas personas a las que debo mi gratitud.

A mis directores de tesis, el Dr. Oscar Castillo García y el Dr. Garikoitz Beobide Pacheco, ambos profesores del Departamento de Química Inorgánica de la Facultad de Ciencia y Tecnología de la UPV/EHU, por ser las personas más influyentes de mi vida profesional. Como buenos pregoneros de sabiduría, prácticamente todo lo que he aprendido se lo debo a ellos. Todavía recuerdo con emoción el primer día que Oscar me propuso entrar en su laboratorio. Desde aquel día me quedé prendado por el abanico de posibilidades que ofrecían los compuestos de coordinación. No satisfechos de ser cada cual más talentoso, también son generosos y atentos con su grupo, a los que dedican todo el tiempo que disponen. Me dirijo a ellos como directores por protocolo y respeto, pero el vínculo que he forjado con ellos es más bien de hermandad.

A Pascual Román, Catedrático y Director del Departamento de Química Inorgánica, por inculcarme valores y aconsejarme con mucho acierto en distintas cuestiones tanto científicas como personales. Admiro su entrega y dedicación para divulgar al público la historia que hay detrás de los científicos más relevantes y las curiosidades que esconde la tabla periódica. Agradecimientos al Catedrático y ferviente madridista el Prof. Antonio Luque Arrebola por todas las charlas informales que hemos tenido y por el conocimiento que me ha transmitido durante mi época predoctoral.

A todos los miembros del grupo de investigación al cual pertenezco (*Metal-Organic Materials Research Group*). Investigadores con sobradas aptitudes para el estudio de los materiales siempre predispuestos a ayudar a un compañero. Más que un grupo lo consideraría una colonia o un enjambre. El Dr. Javier Cepeda, la Dra. Sonia Pérez, la Dra. Mónica Lanchas, Rubén Pérez, Markel Sánchez, Jon Pascual, el Dr. Juan Pablo Terán, la Dra. Jintha Thomas, Fabio Scé, Sandra Arcediano y Asier Bárbara han compartido laboratorio conmigo y por ello guardaré gratos recuerdos en mi memoria. Una especial mención merece la Dra. Mónica por mi parte. Una amiga incombustible, cariñosa y sincera que ha permanecido a mi lado desde mis comienzos en la universidad. Asimismo, me gustaría recordar a Urko García, otro compañero brillante que desgraciadamente falleció hace algunos años y que casualmente este año se cumple el décimo aniversario de la defensa de su Tesis Doctoral.

Al Dr. Pedro Castaños del Departamento de Ingeniería Química de la Facultad de Ciencia y Tecnología de la UPV/EHU por prestarse a hacerme medidas experimentales puntuales de fisisorción y termogravimétricas. Al Dr. Jonathan Albo de la Universidad de Cantabria por la excelente labor que ha realizado en el estudio de la actividad catalítica de los compuestos metal-orgánicos porosos. A la Dra. Prof. Pilar Amo y la Catedrática Prof. Pilar Ocón de la Universidad Complutense de Madrid por su colaboración y asesoramiento en las medidas de conductividad DC y AC, respectivamente. Al Catedrático Michael Fröba y al Dr. Frank Hoffmann por las medidas adsorptivas que realizaron antes de que dispusiésemos de un equipo propio de adsorción.

A todos los integrantes de la compañia *BeAble Capital* por la fantástica idea empresarial que han desarrollado; novedosa en el ámbito europeo y que apoya la salida efectiva de know-how al sector tecnológico. A Gorka Artola, Director de Innovación y Transferencia de la UPV/EHU, y a

Juan Arrue, profesor de MBAe3 y responsable de BEAZ S.A. en las incubadoras de UPV/EHU, por facilitarme el tránsito del ámbito académico al empresarial.

A todos los investigadores y profesores que conforman el Departamento de Química Inorgánica de la Facultad de Ciencia y Tecnología de la UPV/EHU por su amable y agradable compañía durante todos estos años.

A la unidad de servicios generales de investigación de la UPV/EHU (SGIker) por su dedicación y profesionalidad. En especial al Dr. Aitor Larrañaga, al Dr. Javier Sangüesa y a la Dra. Leire San Felices por las medidas de difracción de rayos X, a la Dra. Ana Martínez y al Dr. Sergio Fernández por las medidas de microscopía electrónica, a la Dra. Loli Martín por los ensayos de compresión realizados y finalmente, a la Dra. Maria Belén Sánchez por los análisis de espectroscopia fotoelectrónica de rayos X.

A toda mi cuadrilla del barrio bilbaíno de Zorroza; tanto a los miembros de la peña *Z.G.* como a otros amigos/as que he conocido durante todos estos años. Javi, Gorka, Piti, Pozo, Txamo, Cerezo, Truji, Txema, Kepa y Miguel son sólo algunos de ellos. Frente al resto de amistades destaco la que comparto con Rafa; una persona afable, impetuosa y honesta con la que he vivido infinidad de experiencias. A mi buen amigo Roberto Carlos de Getafe, que a pesar de vernos de ciento al viento seguimos manteniendo una amistad muy estrecha.

A todos los allegados parentales. En especial a mis padres Mari Carmen y Francisco Javier por haber aguantado mis impertinencias y haberme ayudado en los momentos personales más delicados. A mi hermana Mónica por reírme las gracias y estar dispuesta a todo por mi bienestar. A mi abuelo José María y mis abuelas Asunción y Juliana por la comprensión y ternura que me han obsequiado. A mi difunto abuelo Aurelio por haber sido el primero en mostrarme la naturaleza en su plenitud y enseñarme a entenderla. A mis tíos (Juan, Herminia, Javi, Mari, Pedro, Chema y Cristina) y a mis primos (Joan, David, Leire, Josune, Laura e Iván) por el afecto incondicional que me han ofrecido. A mis tres recientes sobrinos/as Andrea, Arenne e Izaro con los que quiero compartir muchos años venideros.

A Oddy, mi querida mascota, por la compañía que me aporta y por la tranquilidad y sosiego que me transmite. Es sin duda alguna el perro aristócrata más adorable del mundo.

A mis suegros Carlos y Mayte por la aceptación que he tenido por su parte desde el principio de nuestra relación y el trato cálido que me dan. A todos los familiares y amigos/as de mi pareja que ahora también constituyen parte de mi vida. Y por supuesto, no puedo dejar sin mención a sus tres perros Crispy, Dalí y Lino.

Finalmente, quisiera dedicar mis últimas palabras a mi pareja Mayte Arratia; una bruma que se opone al viento de poniente, un oasis de conciliación en un mundo comburente. Apareció del mismo modo que un haz se cuela por la rendija de una persiana; un instante le bastó para transmutar un escenario incierto en una novela de pasión interurbana. Ayer puede que estuviera en estado estacionario con el alma constreñida, hoy sólo pienso en ser un principio activo en su ajetreada vida. Siento como si fuese mi enantiomero; su personalidad no llega a superponerse a la mía pero define hasta mi último anhelo. Le doy las gracias por mostrarse comprensiva ante mi incoherencia y por mirar a otro lado cada vez que intimo con la ciencia. Por regalarme su alegría y amor; pero sobretodo, por diseñar una portada con tanto detalle y rigor ;).

A mis padres y hermana

A Mayte

"Study hard what interests you the most in the most undisciplined, irreverent and original manner possible."

Richard Phillips Feynman

"Estudia duro lo que sea de interés para ti y hazlo de la forma más indisciplinada, irreverente y original posible."

AcCN	Acetonitrile
AcOH	Acetic acid
Ade	Adenine
AES	Atomic Emission Spectroscopy
AFM	Atomic Force Microscopy
ATR	Attenuated Total Reflectance
BET	Brunauer-Emmett-Teller
BJH	Barret-Joyner-Halenda
Bpe or BPE	1,2-Bis(4-pyridil)ethylene
Bpy or BPY	2,2'-Bipyridine
CdOAc	Cadmium(II) acetate dihydrate
COF	Covalent-Organic Framework
CSD	Cambridge Structural Database
CShM	Continuous Shape Measurements
CVD	Chemical Vapor Deposition
DCPDTA	*N,N'*-Dicyclopentyldithiooxamidato
DEA	*N,N'*-Diethylacetamide
DEAM	Diethanolamine
DET	Diethylenetriamine
DMA	*N,N'*-Dimethylacetamide
DMF	*N,N'*-Dimethylformamide
DMSO	Dimethylsulfoxide
DTA	Differential Thermoanalysis
DTA	Dithiooxamidato
DTG	Differential Thermogravimetry
EDTA	Ethylenediaminetetraacetic acid
EDX or EDXS	Energy-Dispersive X-Ray Spectroscopy
Et_3N	Triethylamine
EtOH	Ethanol
Et_2O	Diethyl ether
FE	Faradaic Efficiency
FWHM	Full Width at Half Maximum
FID	Flame Ionization Detector
FTIR	Fourier Transform Infrared Spectroscopy
GC	Gas Chromatography
GDE	Gas Diffusion Electrode
H_2DTA	Dithiooxamide
$H_2GLYDTA$	*N,N'*-bis(carboxymethyl)dithiooxamide
HTAc	Thioacetic acid
HTBn	Thiobenzoic acid
ICP	Inductively Coupled Plasma

IR	Infrared
IUPAC	International Union of Pure and Applied Chemistry
JCPDS	Joint Committee on Powder Diffraction Standards
MeOH	Methanol
MOA	Metal-Organic Aerogel
MOCVD	Metal-Organic Chemical Vapor Deposition
MOF	Metal-Organic Framework
MOG	Metal-Organic Gel
MOPM	Metal-Organic Porous Materials
MS	Mass Spectrometry
MOX	Metal-Organic Xerogel
Neo or NEO	Neocuproine
NP	Nanoparticle
PdOAc	Palladium(II) acetate dihydrate
PE	Polyethylene
Phen or PHEN	1,10'-Phenanthroline
PPh_3	Triphenylphosphine
PPh_4	Tetraphenylphosphonium
PS	Polystyrene
Ptu	6-*n*-propylthiouracil
PU	Polyurethane
PVC	Polyvinyl chloride
QD	Quantum Dot
RF	Resorcinol-Formaldehyde
SDTA	Scanning Differential Thermoanalysis
SBU	Secondary Building Unit
SEM	Scanning Electron Microscopy
SS	Stainless Steel
TAc	Thioacetato
TBn	Thiobenzoato
TEM	Transmission Electron Microscopy
TG	Thermogravimetry
TMED	*N,N,N',N'*-Tetramethylethylenediamine
TOPO	Trioctylphosphine oxide
Tu	Thiouracil
UV-Vis	Ultraviolet-Visible
XPS	X-Ray Photoelectron Spectroscopy
XRD	X-Ray Diffraction
XRPD	X-Ray Powder Diffraction
ZnOAc	Zinc(II) acetate dihydrate

1. GENERAL INTRODUCTION

1. GENERAL INTRODUCTION

1.1. CONTEXT OF THE THESIS

The current work involves the use of metal complexes based on ligands containing sulfur donor atoms to prepare nanostructured materials built from metal-sulfur bonds. Precisely, the research has focused on obtaining two classes of nanomaterials with different dimensionality and chemical nature. On the one hand, metal-thiocarboxylato complexes have been used as direct precursors of metal(II) sulfide nanoparticles through a route known as dry thermolysis. On the other hand, metal-dithiooxamidato gels and aerogels (three-dimensional nanoarchitectures) have been synthesized by controlling polymerization kinetics and performing the supercritical drying of the parent gels, respectively.

Keeping all this in mind, the introductory section describes first the coordination chemistry of metal complexes based on organosulfur ligands, also known as S-ligands. Thereafter, it deals with the relevance of compounds built from metal-sulfur bonds in the field of nanoscience, to finish up with an introduction to gels, aerogels and porous coordination polymers.

1.2. COORDINATION CHEMISTRY OF METAL COMPLEXES BASED ON ORGANOSULFUR LIGANDS

The sulfur donor atom is able to coordinate relatively strong to soft metal ions such as silver, cadmium, gold, mercury, lead, etc.[1] Besides, the highly diffuse orbitals of the sulfur atoms provide a good overlap with metal d orbitals giving rise to extended molecular orbitals in which electrons are delocalized, and as a result, electrical properties are notoriously improved with respect to less polarizable M–O and M–N bonds.

The strength of the M–S bond in metal-organosulfur compounds lies between 100–250 $KJ \cdot mol^{-1}$,[2] a value that is far greater than that of the supramolecular

interactions (hydrogen-bonds, aromatic π-π stacking, dipole-dipole interactions and other dispersive forces) and it is close to the lower edge of the covalent bonds (Figure 1.1).

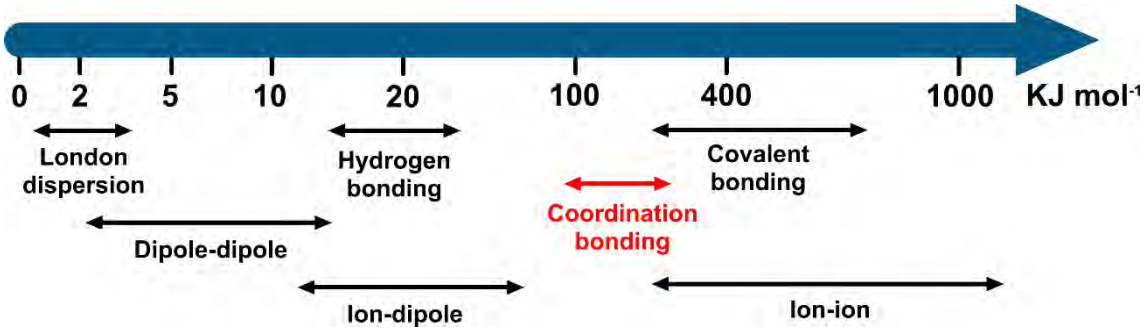

Figure 1.1 Energy intervals for each force type. [2, 3]

In nature, there are many examples of sulfur-containing biomolecules such as cysteine, cystine, and methionine amino acids; and biotin and thiamine vitamins. Many cofactors also contain sulfur including glutathione, thioredoxin and iron–sulfur proteins. On the other hand, disulfides (S–S bonds) confer mechanical strength and insolubility to protein structures as keratin, which is found in outer skin, hair, and feathers. In Figure 1.2 there are depicted some of these molecules.

These sulfur-biomolecules have also been employed as ligands towards different metal centers to provide model systems for a wide number of active catalytic sites of enzymes and also to developed new drugs for medical applications. For instance, some thiouracil-containing complexes have been found to be effective antitumor, anti-thyroid and anti-arthritic compounds *in vitro* and *in vivo* (Figure 1.3).[5]

Organosulfur ligands also stand out for providing materials with interesting physicochemical properties such as luminescence, chemical sensing, catalysis, conductivity, and magnetism.[6] Among the most resourced organosulfur ligands we have thiols, thiocarboxylic acids, dithiocarboxylic acids, thioamides, thiocarbamates, dithiocarbamates, thioureas and sulfur donor heterocycles like thiophenes, tetrahydrothiophenes, dithianes, dithiepanes as well as sulfur-containing nucleobases such as 6-mercaptopurine and thioguanine (Figure 1.4).[7]

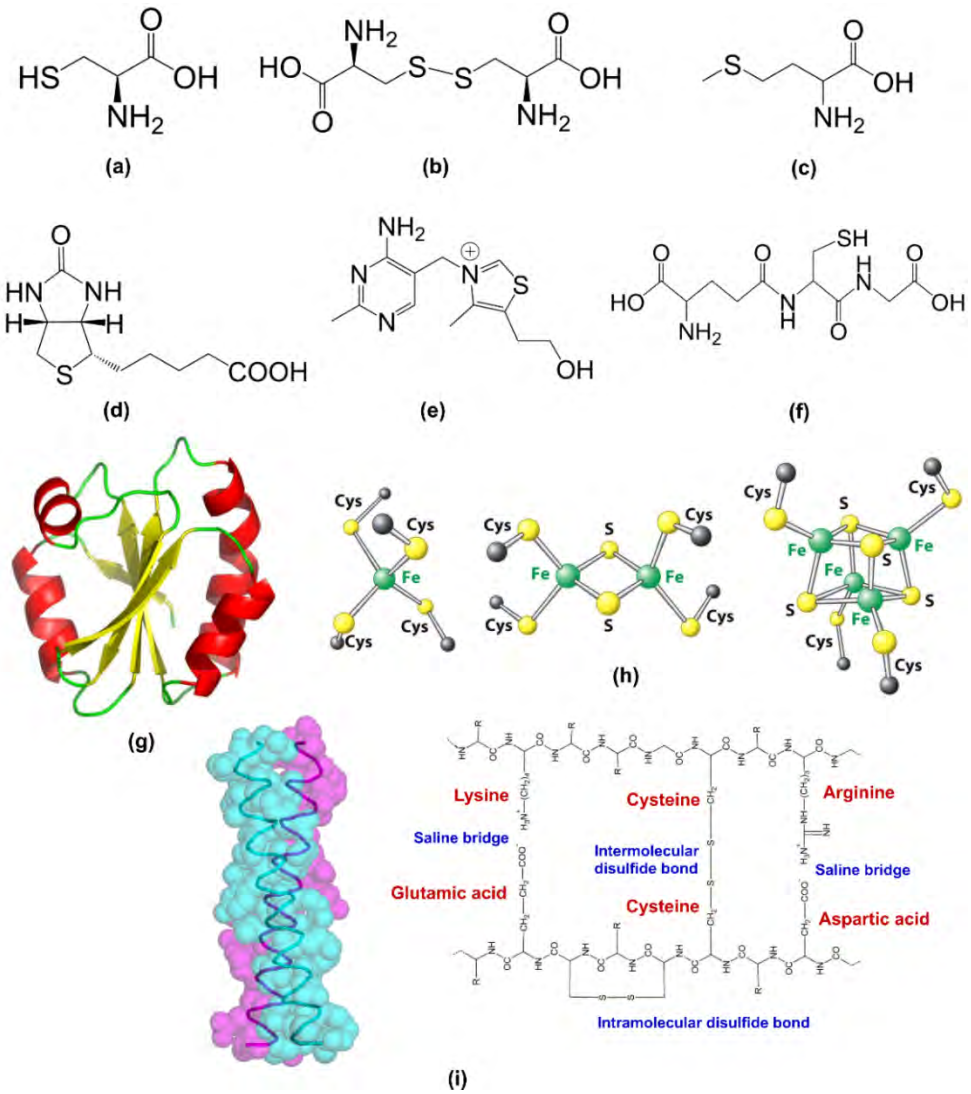

Figure 1.2 Molecular structures of (a) L-cysteine, (b) L-cystine, (c) methionine, (d) biotin, (e) thiamine and (f) glutathione. (g) Tertiary structure of thioredoxin protein. (h) Iron-sulfur structures found in different proteins. (i) Tertiary structure (left) and molecular scheme (right) of α-keratin and types of crosslinks that can form.[4]

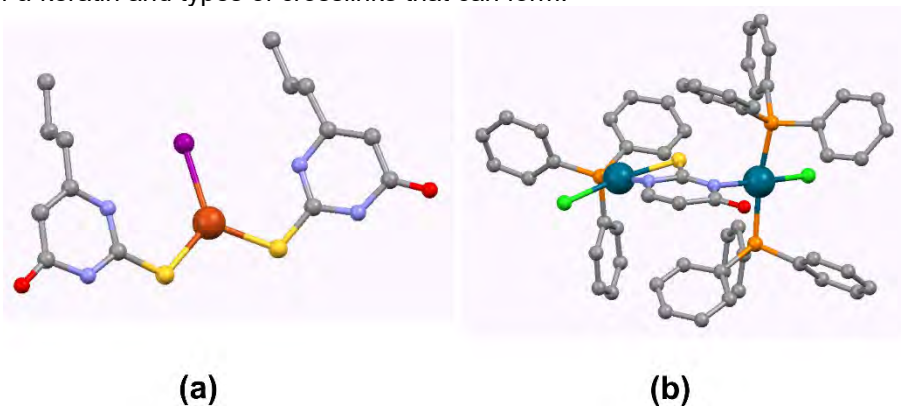

Figure 1.3 (a) Complex unit of $[CuI(ptu)_2]$ (ptu: 6-*n*-propylthiouracil), a compound which has in its structure a thiouracil derivative with anti-thyroid activity and which catalyzes the cycloaddition of benzo[*b*]furans, organic precursors of a large number of drugs. (b) Dinuclear unit of $[Pd_2(Tu)(PPh_3)_3Cl_2]$ (Tu: thiouracil, PPh_3: triphenylphosphine) complex, a compound that has been screened against human tumor cell lines and has shown promising *in vitro* cytotoxicity. Hydrogen atoms were omitted for clarity.

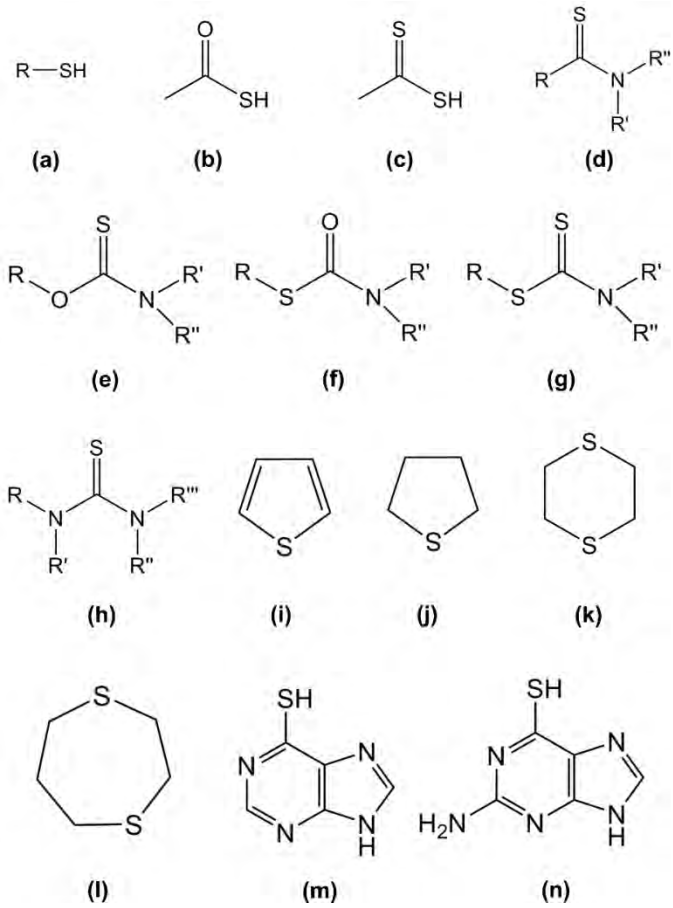

Figure 1.4 Molecular structures of some sulfur ligands: (a) thiols, (b) thiocarboxylic acids, (c) dithiocarboxylic acids, (d) thioamides, (e) S-thiocarbamates, (f) O-thiocarbamates, (g) dithiocarbamates, (h) thioureas, (i) thiophene, (j) tetrahydrothiophene, (k) 1,4-dithiane, (l) 1,4-dithiepane, (m) 6-thiopurine, and (n) 6-thioguanine.

In order to clearly show the feasibility of these organosulfur molecules to act as ligands a perusal in the Cambridge Structural Database (CSD)[8] has been performed (Figure 1.5). It provides a total amount of 14,146 hits with the greater ratio of results belonging to thiolato (76.9%) based coordination compounds. It can be also observed that the functional groups relevant for the current work (thioacids and thioamides) represent a 4% of the total hits. The compounds that have emerged in the above-mentioned perusal range from monomeric and polynuclear discrete entities to 1D, 2D and 3D coordination polymers.

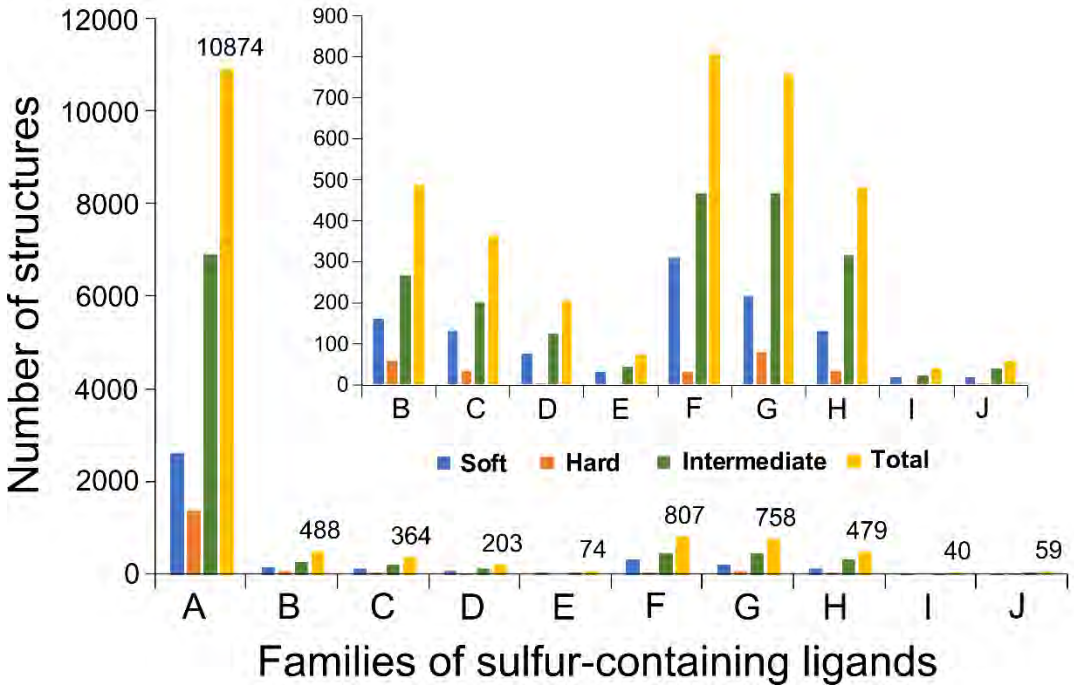

Figure 1.5 Number of crystal structures found in the CSD for each family of sulfur-containing ligands. A: thiols, B: thiocarboxylic acids, C: dithiocarboxylic acids, D: thioamides, E: thiocarbamates, F: thioureas, G: 5-membered heterocycles; H: 6-membered heterocycles, I: 7-membered heterocycles, J: sulfur-containing nucleobases. The inset graphic shows the enhanced area of the minor components. The different columns appearing for each coordination mode correspond to the soft, hard, and intermediate nature of the metal center according to Pearson's Hard-Soft Acid-Base classification.[1]

1.2.1. Thiocarboxylato ligands

Thiocarboxylates[9] have donor atoms of different Pearson hardness (S is soft and O hard) which extends the type of target metal center at which they can be coordinated. The CSD database provides again an insight into the coordination modes of this ligand (Figure 1.6). The more usual coordination mode involves the sulfur donor atom in a monodentate mode (A mode). The second more frequent coordination mode implies the bridging of two metal centers through S and O donor atoms (D mode). The structural search has also revealed that softest metal centers do mostly coordinate only to the sulfur donor atom, the medium hardness ones trend to coordinate simultaneously to the sulfur and oxygen donor atoms, and finally the harder ones do preferentially coordinate the oxygen atom.

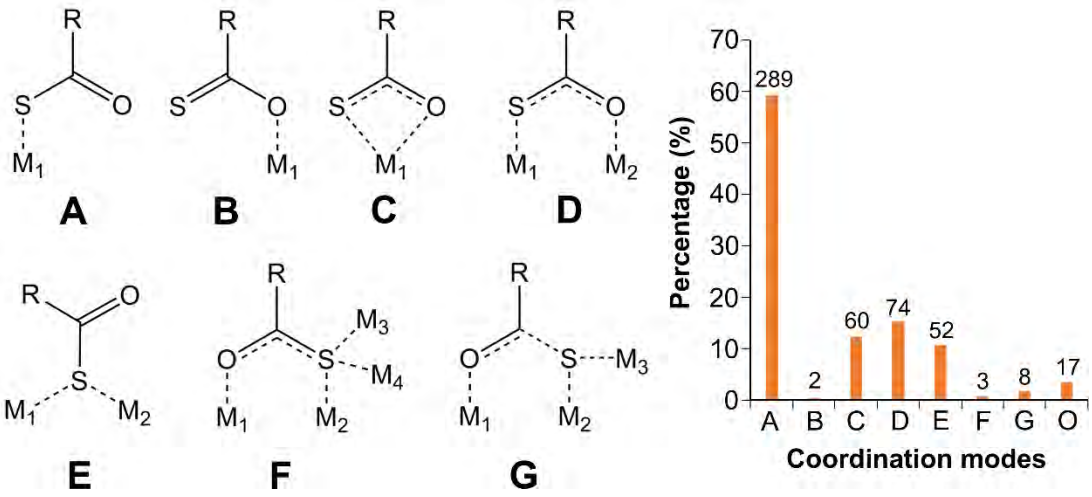

Figure 1.6 Coordination modes of thiocarboxylates (left) and CSD data with the number of structures published for each mode of coordination as well as the percentage they represent (right). O: Structures containing two or more different coordination modes.

These coordination modes give rise to a great diversity of crystal structures. However, most cases correspond to monomeric entities. As an example, the monomeric compound $(PPh_4)[Cd(TAc)_3]$ (TAc: thioacetato) synthesized by Sampanthar and coworkers presents three thioacetates chelating the cadmium(II) ion in a bidentate fashion to provide a distorted CdO_3S_3 octahedral geometry (Figure 1.7a).[10] The three sulfur atoms are strongly bound to Cd giving a pyramidal CdS_3 kernel.

Dinuclear, trinuclear and tetranuclear complexes can be also found in which thiocarboxylato-κO:κS bridges two adjacent metal center to usually provide a paddle-wheel arrangement (Figure 1.7b-c), analogous to that reported for carboxylates. We have selected as an illustrative example of this kind of complexes, a Rh(II)-thiobenzoato dimers capped by pyridine ligands $[Rh_2(TBn)_4(C_5H_5N)_2]$ (TBn: thiobenzoato) in which the $[Rh_2(TBn)_4]$ core is centrosymmetric with each metal ion coordinated by two oxygen and two sulfur donor atoms acquiring a paddle-wheel configuration (Figure 1.7b).[11] An example of a more extended oligomer was reported by D. K. Joshi and S. Bhattacharya, who succeeded in synthesizing a dimeric assembly of dinuclear Ni entities giving rise to a complex of the formula $[Ni_4(TBn)_8(AcCN)_2]$.[12] The two dinuclear units are joined to each other by bridging through S atoms. Two

molecules of acetonitrile are coordinated to the two outer Ni(II) centers of the complex assembly. Each dinuclear unit has a four bladed paddle wheel structure and the coordinated acetonitrile appears like a shaft. Interestingly, the paddle-wheel structure is not symmetric (Figure 1.7c), leading to rather different coordination environments (O_4N and S_5 for outer and inner Ni atoms, respectively).

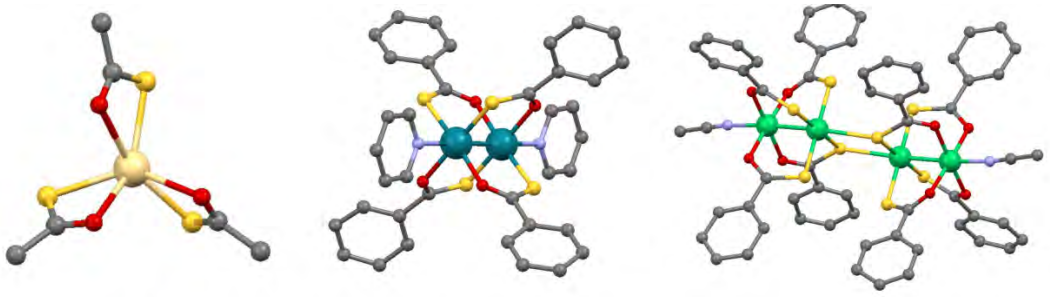

Figure 1.7 Examples of thiocarboxylato discrete complexes: (a) $(PPh_4)[Cd(TAc)_3]$, (b) $[Rh_2(TBn)_4(C_5H_5N)_2]$, (c) $[Ni_4(TBn)_8(AcCN)_2]$.

In addition, the different nature of the donor atoms promotes the isolation of heteronuclear complexes. M. Gennari *et al.* have prepared discrete bimetallic (Pt/Ni) compounds of formula $[(H_2O)Ni(\mu\text{-}TBn)_4PtCl]$ with interesting redox properties (Figure 1.8a).[13] F. G. Baddour and colleagues have studied the magnetic behavior of bimetallic paddle-wheel complexes of platinum, with formula $[PtM(TAc)_4(OH_2)]$ (where M: Co and Ni), in which an antiferromagnetic coupling has been observed between *d* metal ions through non-covalent metallophilic interactions (Figure 1.8b).[14]

Among the polymeric structures, J. Troyano and coauthors have synthesized a silver two-dimensional coordination polymer $[Ag(TBn)]_n$ which shows semiconductivity and an intense luminescent emission that undergoes a thermochromic effect when the crystals are cooled (Figure 1.8c).[15]

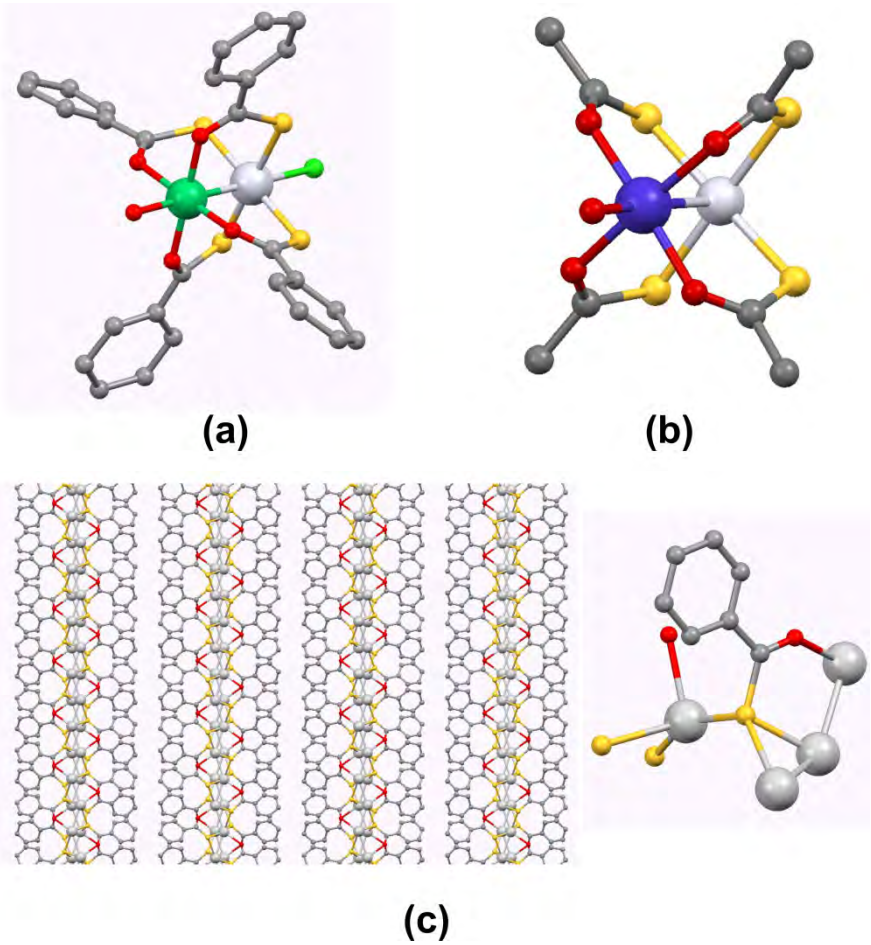

Figure 1.8 Examples of thiobenzoato complexes: (a) [(H_2O)Ni(μ-TBn)$_4$PtCl], (b) [PtCo(TAc)$_4$(OH_2)], and (c) [Ag(TBn)]$_n$.

1.2.2. Dithiooxamidato ligand

Dithiooxamidato (DTA) or rubeanato ligand is similar to oxalato but with oxygens replaced by two nitrogens and two sulfur atoms. It is a planar molecule in which two thioamide groups are fused. The presence of both nitrogen and sulfur donor atoms enables dithiooxamidato to bind to a metal in different ways, and can in principle, give rise to a variety of structural motifs. The dibasic-acid character and the proton-coupled redox properties of the ligand favor the proton conduction of dithiooxamidato based transition metal compounds.[16]

There are relatively few examples of crystalline structures based on the dithiooxamidato ligand because it is a molecule that prompt the polymerization of metal complexes very easily, being difficult to slow down enough the nucleation to obtain crystals suitable for structural elucidation. Dithiooxamide (H_2DTA) is a complexing

agent that is generally used in the spectrometric determination of certain metals in solution, including copper, iron, nickel, and cobalt, among others.[18] Dithiooxamidato ligand has a simple C–C bond that allows it to rotate to adopt a *cis* or *trans* conformation upon coordination. There are very few examples gathered in CSD in which dithiooxamidato act as bis(bidentate) ligand, and in most cases, the ligand is disordered in two positions making difficult to subtract a statistic on the *cis*/*trans* coordination modes. Even so, two clear crystal structures of *trans* coordination can be observed. H. C. Hofmans *et al.* have successfully isolated a monomer of Pd(II) with a DTA derivative in *cis* conformation of formula $[Pd(DCPDTA)_2]$ (DCPDTA: *N,N'*-dicyclopentyldithiooxamidato) by adding a Pd^{+2} solution to the ligand dissolved in a mixture of acetone and water, buffered at pH 7 (Figure 1.9a).[18] An example of a discrete polynuclear entity is presented by P. Kopel and coauthors; a Cu/Ni trimer bridged by dithiooxamidato ligands in *cis* fashion (Figure 1.9b) with Cu(II) ends capped by two triphenylphosphine terminal ligands.[19]

Despite most of the reported crystal structures correspond to discrete complexes in which capping ligands have been employed to prevent the polymerization, there are some few cases of polymeric structures. For instance, A. Mosset and coworkers have been able to crystallize the coordination compound $\{[CuCl(H_2DTA)_{1.5}]\cdot 0.45H_2O\}_n$ which consists of a 2D-coordination network in which neutral dithiooxamide ligand links together three Cu(I) ions through sulfur atoms in a *syn*,*syn*,*anti*-mode (Figure 1.9c).[20] Furthermore, A. Castiñeiras and coauthors have prepared a 3D porous structure of formula $[Mn(H_2GLYDTA)(H_2O)_2]_n$ with *N,N'*-bis(carboxymethyl)dithiooxamide ($H_2GLYDTA$), a substituted dithiooxamide.[21] Each Mn(II) ion is six-coordinated to four carboxylate oxygen atoms from four different $H_2GLYDTA$ ligands and two symmetrically related water oxygen atoms (Figure 1.9d). The carboxylate groups link the neighboring manganese centers to form infinite one-dimensional helical chains that run along the crystallographic *b*-axis. These Mn atoms

are shared by neighboring helical chains that are alternately left- and right-handed. In addition, these channels are interconnected by the $O_2C–C–N–C–C–N–C–CO_2$ groups of H_2GLYDTA to form a three-dimensional framework.

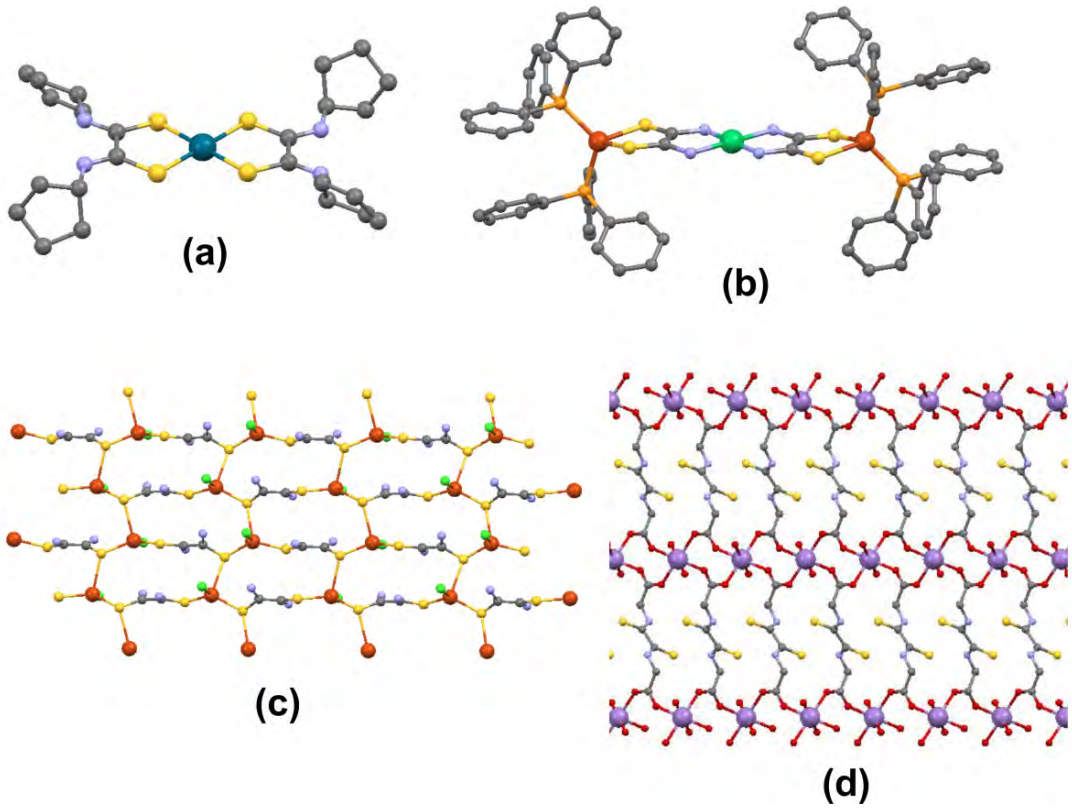

Figure 1.9 Examples of dithiooxamidato based complexes: (a) $[Pd(DCPDTA)_2]$, (b) $[(PPh_3)_2Cu(DTA)Ni(DTA)Cu(PPh_3)_2]$, (c) $\{[CuCl(H_2DTA)_{1.5}]\cdot 0.45H_2O\}_n$, and (d) $[Mn(H_2GLYDTA)(H_2O)_2]_n$.

1.3. NANOSCIENCE

Nanoscience studies the physicochemical behavior of substances with at least one dimension ranging from 1 to 100 nm. At nanoscale, the laws of physics operate in an unfamiliar way because of two important reasons: high surface-to-volume ratio and quantum effect. Precisely, the properties of the material become strongly dependent on the surface of the material since the amount of surface is now at the same level as the amount of bulk. Therefore, the surface derived quantum mechanical properties can dominate over bulk properties, providing a completely new method to tune the properties of materials.

Scientists have made great progress in constructing numerous nanoobjects with dimensionalities that range from discrete (zero-dimensional, 0D) to extended (1D, 2D, and 3D) systems based on very different materials: from inorganic to pure organic components, from amorphous to ordered materials, and from nonporous to porous networks (Figure 1.10a-k).[23]

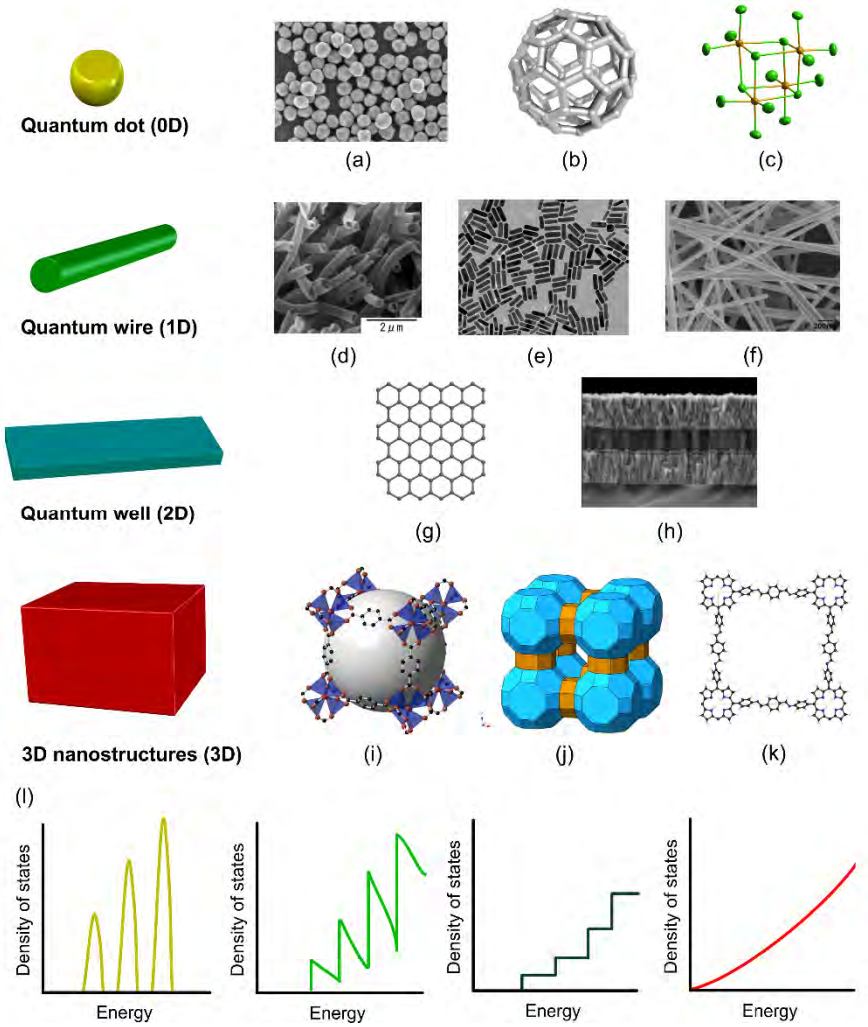

Figure 1.10 Schematic classification of nanostructures in terms of their dimensionality (a: nanoparticles, b: fullerene, c: metal cluster, d: carbon nanotubes, e: nanorods, f: nanowires, g: graphene, h: thin film, i: metal-organic framework, j: zeolite, and k: covalent organic framework). (l) Graphical representation of the quantum confinement according to the dimensionality of the nanostructure (0D, 1D, 2D and 3D).[24]

Among the 0D nanoobjects the best well known materials comprise quantum dots,[25] single molecular magnets,[26] superparamagnetic and metal nanoparticles,[27] and fullerenes.[28] They present a wide range of applications in areas such as optics, medicine, quantum computation, hyperthermia, and catalysis.[29] The most representative example of 1D nanoobjects are carbon nanotubes[30] but there are also

some other examples of linear nanostructures such as nanowires, nanotubes, nanobelts, or nanorods that can be generated from metals, semiconductors, organic and coordination polymers.[31] Thin films[32] and graphene[33] are the best known 2D nanomaterials which are being subjected to an intense research due to their potential application in electronic and solar cell technologies, among others.

Finally, the most conceptually striking nanomaterials are the 3D ones, in which the confined dimension does not correspond to the material but to the pores present within it. Based on the pore size, IUPAC classifies porous materials into ultramicroporous (< 0.7 nm), supermicroporous (0.7–2 nm), mesoporous (2–50 nm) and macroporous (> 50 nm).[34] Materials with nanometer-scale pores (basically micro- and mesoporous materials) exhibit specific properties and functions that would be impossible to attain in non-porous materials. Progress in chemistry and materials science has given rise to several distinct classes of porous materials, which are characterized by general trends in structural evolution: from inorganic to organic components; from small to large pores; from rigid frameworks to soft dynamic skeletons. The behavior and performance of such materials can be determined by many characteristics such as surface area, porosity, and pore size distribution. Porous materials, such as zeolites,[35] activated carbons,[36] pillared clays,[37] metal-organic frameworks (MOFs),[38] covalent organic frameworks (COFs),[39] gels,[40] aerogels,[41] and foams[42] have a broad range of applications that include catalysis, thermal insulation, electrode materials, environmental filters and membranes as well as controlled release of drugs.[43]

Attending to the many synthesis methods that have been reported to afford nanomaterials (0D−3D), they can be classified as bottom-up or top-down approaches. Top-down approaches[44] (*i.e.* milling, mechanochemical route, sputtering, laser ablation, nanolithography, etc) start with a bulk material and then break it into smaller pieces using mechanical, chemical, or any other form of energy. On the other hand, the

bottom-up approach (*i.e.* sol-gel method, chemical reduction, chemical vapor deposition, solvothermal synthesis, etc),[45] synthesizes nanomaterials from atomic or molecular species via chemical reaction or self-assembly.

In order to provide the necessary background to fully understand the following chapters, we will get a deeper insight into nanosystems based on materials containing metal-sulfur bonds and also into gels and aerogels.

1.3.1. Metal sulfide quantum dots, quantum wires and quantum wells

Metal sulfides are a group of highly valued materials mainly due to their catalytic and optoelectronic characteristics.[46] In particular, 12 group transition metal sulfides are compounds appreciated by properties derived from their direct and wide-bandgap semiconduction.[47] Photodetection, photocatalysis and cathodoluminiscence are their best-known applications.[48] However, thanks to the development of nanostructuring, its range of applicability has been extended to the field of medicine (biolabeling and contrast agents), energy (solar cells and fuel cells) as well as other more exotic applications (diluted semiconductor magnets).[49] Currently, both quantum dots and quantum wires of ZnS and CdS are prepared through wet routes starting from precursors with metal-sulfur bonds available in their structure.[50] They are usually accompanied by coordinating agents that limit the excessive growth of the particle and its agglomeration. To provoke decomposition of the precursor, the synthesis is performed in the presence of a heat source or irradiation (commonly under closed conditions).[51] For the formation of quantum wells or thin layers it is preferred to work with Chemical Vapor Deposition (CVD), using gaseous reagents or aerosols as starting materials.[52]

To date, a large number of metal-organic precursors have been tested for the production of cadmium and zinc chalcogenides, among them stand out xanthates,

dithiocarbamates and thiocarboxylates.[53] Metal-thiocarboxylates undergo facile thiocarboxylic anhydride elimination, and hence they can be used as single molecular precursors for metal sulfide materials.[54] Anionic thiocarboxylate complexes[55] have been exploited as metalloligands and a good number of bimetallic complexes have been prepared during recent years which have also been used as precursors for ternary chalcogenides.[56]

In this work, we are focused on the synthesis of quantum dots of cadmium and zinc sulfides. Thus, we will provide some additional details on the characteristics and theoretical background of these nanoobjects.

Quantum dots (QDs) are crystalline semiconductor nanoparticles with sizes ranging from 1 to 30 nm. Due to their small size, electrons in quantum dots are confined in a small space (quantum box), and when the radii of the semiconductor nanocrystal is smaller than the exciton Bohr radius,[57] there is quantization of the energy levels according to Pauli's exclusion principle.

Generally, as the size of the crystal decreases, the difference in energy between the highest valence band and the lowest conduction band increases. More energy is then needed to excite the dot, and concurrently, more energy is released when the crystal returns to its ground state, resulting in a color shift from red to blue in the emitted light (Figure 1.11a-c). Additionally, it is possible to control over the bandgap of the nanocrystals by changing the composition of semiconductors; therefore, emission color of quantum dots can also be tuned by changing dopant during synthesis.[58]

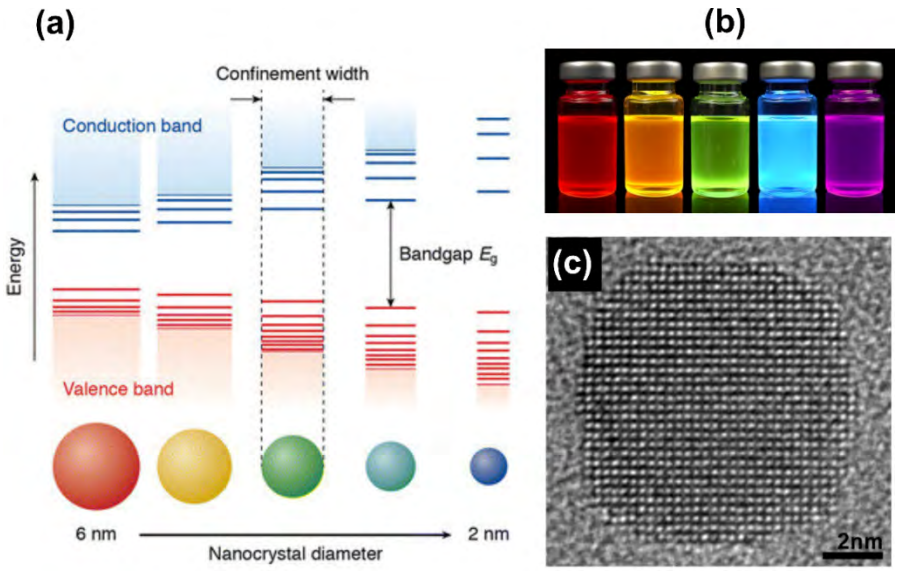

Figure 1.11 (a) Schematic representation of bandgap variation with nanoparticle size; (b) photograph of quantum dots dispersions irradiated by UV light; (c) TEM image of a cubic quantum dot.[59]

The main method of preparation of semiconductor nanoparticles was, until recently, classical colloid chemistry, involving controlled arrested precipitation from colloidal solutions.[60] However, it could be problematic due to air sensitivity and/or poor crystallinity of the material. Another approach for preparing semiconductor nanoparticles is to decompose organometallic and/or metal-organic compounds under anaerobic conditions (known as single-source precursor route).[61] In this case, the precursor is injected into a hot solution (150–350ºC) of trioctylphosphine oxide (TOPO) or a similar solvent in the presence of a surfactant (especially long chain amines, thiols or carboxylic acids). Varying the temperature and time of the reaction one can control the particle size of the resulting nanoparticle.

A less widespread alternative is the thermal decomposition of a metal-organic or organometallic precursor under solvent-free conditions and in absence of surfactants. This route is called dry thermolysis and it is performed under an inert atmosphere.[62] If temperatures are moderate and exposure times are brief, it is possible to obtain non-sintered nanoparticles. The organic substituents on the precursor migrate upon thermolysis and act as capping agents on the surface of the nanoparticle. Usually, nanoparticles produced through dry thermolysis present a good crystallinity

degree and low polydispersion. A negative aspect is that the resulting products are prone to show high impurity contents from poor combustion of the precursor.

There are some other few examples of nanosized porous materials but due to their relevance to this work, they would be described separately in the next section.

1.3.2. Metal-sulfide based porous materials

3D porous structures based on metal-sulfide bonds constitute an important part of the current thesis. Despite we will focus on those built from organosulfur ligands, at this point, it deserves to note that there exist some appealing cases of metal-sulfide based nanoporous materials with structure dimensionality ranging from 0D to 3D. For instance, recently ZnS porous nanospheres have been prepared by hydrothermal and colloidal routes (Figure 1.12a).[63] ZnS hollow nanotubes prepared from the reaction of ZnO nanorods with Na_2S or thioamide constitute an example of one-dimensional metal-sulfide porous materials (Figure 1.12b).[64] Likewise, it has been possible to obtain porous CdS nanofibers using a cholesterol-derived organogel as a template (Figure 1.12c).[65] In the case of two-dimensional sulfides, quantum-size CdS porous membranes have been reported by L. Spanhel and M. A. Anderson.[66] Regarding to 3D architectures, in 2004, J. L. Mohanan and S. L. Brock published a completely different type of metal-sulfur based porous materials based on sol-gel chemistry.[67] The sol-gel process can shortly be defined as the conversion of a precursor solution (sol) into a three-dimensional (3D) open network structure (gel) via polymerization reactions (commonly in water).[68] The reported aerogel is constituted by interconnected networks of CdS building blocks and have been prepared from controlled aggregation of discrete nanoparticles to create a gel which is later supercritically dried (Figure 1.12d).[69] The nature and structural features of gels and aerogels will be thoroughly discussed in the following section.

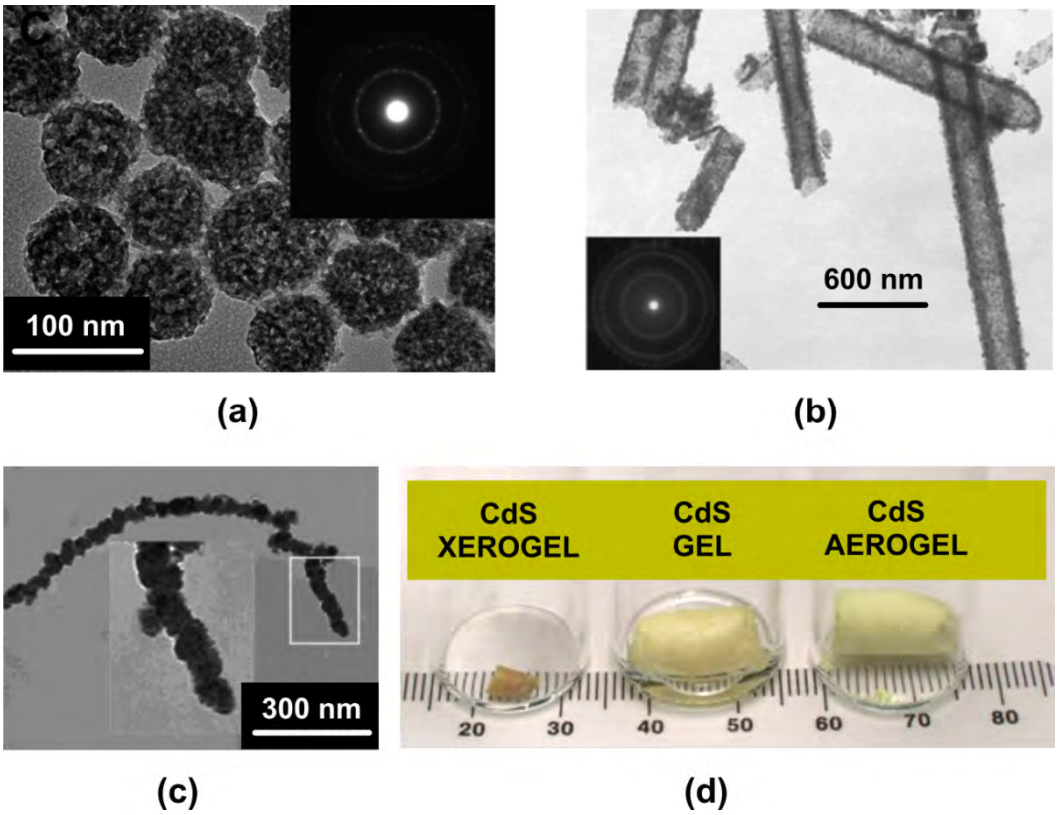

Figure 1.12 Electron microscopy images of porous metal sulfides with different dimensionality: (a) ZnS nanospheres, (b) ZnS nanotubes, and (c) CdS nanofibers. (d) Optical image of a CdS xerogel (left), gel (center) and aerogel (right).

1.3.3. Nanoporous coordination materials: gels, aerogels and metal-organic frameworks

In the current work, we will pursue an alternative way to generate 3D nanostructures provided with metal-sulfur bonds, precisely, nanoporous architectures will be built based on metal-organosulfur coordination complex entities. In this sense, there are two way to prepare porous coordination materials. The first way, the most conventional and popular one, is based in crystal engineering principles to synthesize open coordination networks known as metal-organic frameworks (MOFs), whose porosity is related to the crystal structure. The second option for achieving nanoporous metal-organic structures is the gelation of a coordination complex and its processing as aerogel, whose porosity is ascribed to the microstructural features. It must be emphasized that, metal-organic gels and aerogels constitute an emerging area within the coordination chemistry and materials science.

Herein, to define well the limits between two types of porous materials, a brief introduction to MOFs precedes to a section dealing with gels, aerogels and metal-organic examples of these materials.

1.3.3.1. Metal-organic frameworks

MOFs represent a class of hybrid organic-inorganic materials comprised of ordered networks formed from organic electron donor linkers and metal cations.[70] The self-assembly of these components creates rigid pores that do not collapse upon removal of solvent. The presence of inorganic and organic components enables the pore size and chemical environment to be tailored to achieve specific properties.[71] The topology of MOFs is intimately related to both the coordination environment favored by the metal ion and to the geometry of the organic "linker" groups, which together form so-called secondary building units (SBUs) that establish the network symmetry (Figure 1.13).[72]

MOFs have properties that extend their potential range of use far beyond traditional microporous materials. These include: extremely high surface areas (> 3000 $m^2 \cdot g^{-1}$),[73] luminosity resulting from conjugated organic linkers;[74] structural flexibility in response to molecular adsorption or changing environmental conditions;[75] charge transfer (ligand-to-metal or metal-to-ligand);[76] high thermal stability relative to many organic polymers;[77] conducting properties;[78] and pH-sensitive stability.[79]

Since first examples of MOFs at mid-90s of last century,[80] they have experienced an extensive exploration, with applications in gas capture[81] and separation,[82] catalysis,[83] drug delivery,[84] optical, magnetic and electronic applications,[85] and sensing.[86]

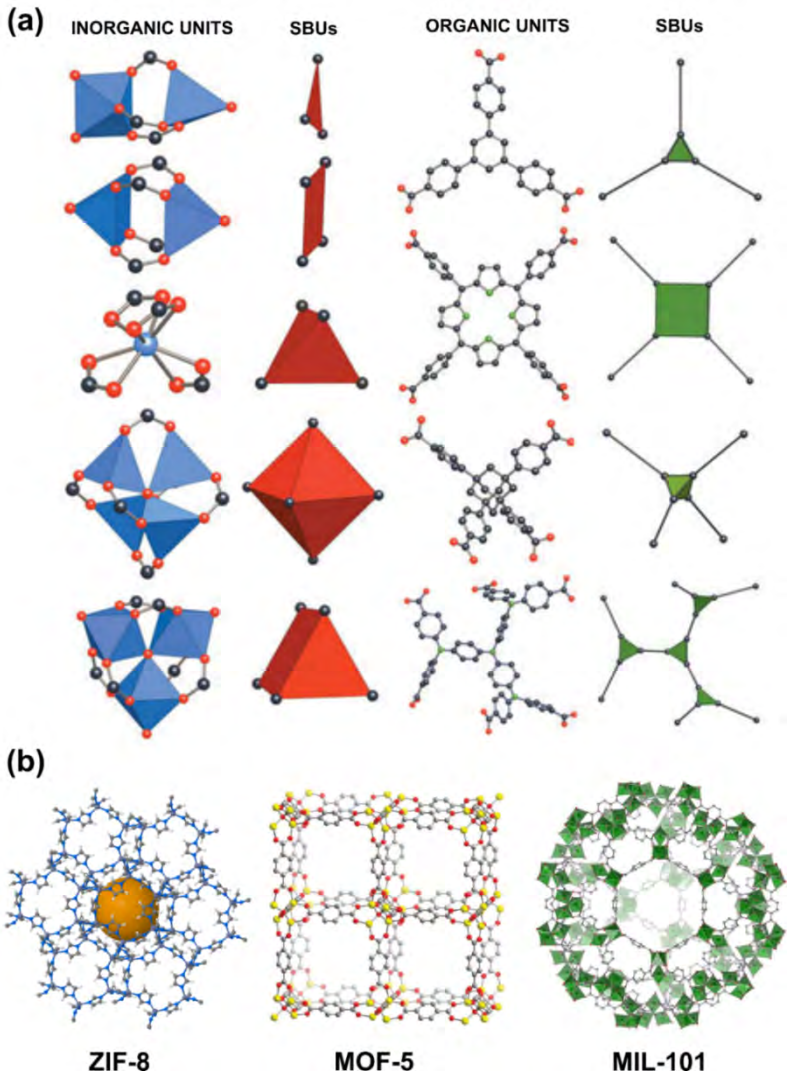

Figure 1.13. (a) Some secondary building units (SBUs) commonly employed in crystal engineering; (b) three examples of MOFs.[88]

1.3.3.2. Gels and aerogels

Gels are three-dimensional polymeric structures with a high degree of crosslinking that expands during polymerization to entrap the solvent within. As a result, gels behave as viscoelastic substances that can acquire the size and shape of the recipient that contains it.

Gels can be classified according to the chemical nature of the polymer formed in organic,[89] inorganic[90] (Figure 1.14a) or metal-organic (MOGs).[91] Likewise, gels are classified as either physical or chemical gels according to the nature of the interactions involved in their formation. Supramolecular gels formed by weak non-covalent

interactions such as hydrogen bonding, π–π stacking and hydrophobic interactions are physical gels, and their formation is generally reversible[92] whereas chemical gels are formed by strong covalent bonds; these ones cannot be re-dissolved and are thermally irreversible.[93] Gels are also termed either colloidal (particulate structure) or polymeric (fibrillar structure) depending on the nature of the building blocks of the network (Figure 1.14b-c).

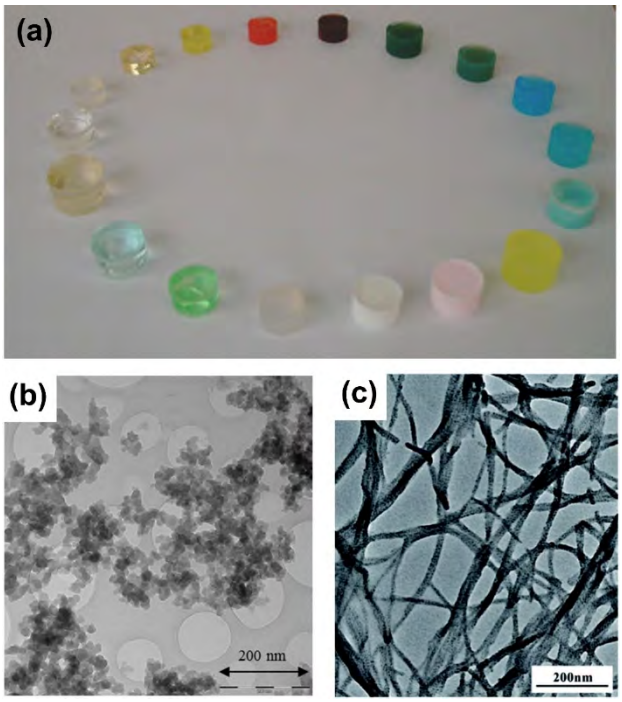

Figure 1.14 (a) Silica gels doped with transition metals; (b) TEM image of a gel showing a particulated microstructure; (c) TEM image of a gel with nanofibrillar microstructure.[94]

At the forefront of gel research are metallogels (metal-organic gels: MOGs), which are gels formed from gelators containing complexed metals or clusters.[95] Gels based on coordination polymer complexes can be endowed with other physicochemical properties of metals, such as magnetism,[96] color change and luminescence,[97] stimuli-tunable rheological properties,[98] sorption capability,[99] self-healing properties,[100] catalytic activity,[101] and redox behavior.[102] Therefore metal-containing gels react to a broader range of chemical and physical stimuli compared to inorganic or organic gels. Furthermore, the strength of metal–ligand coordination interaction lies between that of strong covalent bonding interaction and that of other non-covalent interactions. Thus, MOGs may display properties of either physical or chemical gels in different situations.

If a gel is dried by evaporation, then capillary forces provoke the shrinkage of the gel, the solid network collapses and a material of reduced porosity named as xerogel is formed (Figure 1.15).[103]

If a gel is dried supercritically, ideally, the solvent is replaced by air without affecting the microstructure resulting in a highly porous material called aerogel (Figure 1.15). However, in most cases, the structure tends to suffer a certain degree of contraction until it is fully consolidated. Other drying methods have been satisfactorily tested in the preparation of aerogels, including solvent-replaced ambient drying, surface-modified ambient drying, freezing drying (criogel), etc.[104] However, latter methods are less efficient and/or more time consuming than the supercritical drying process.

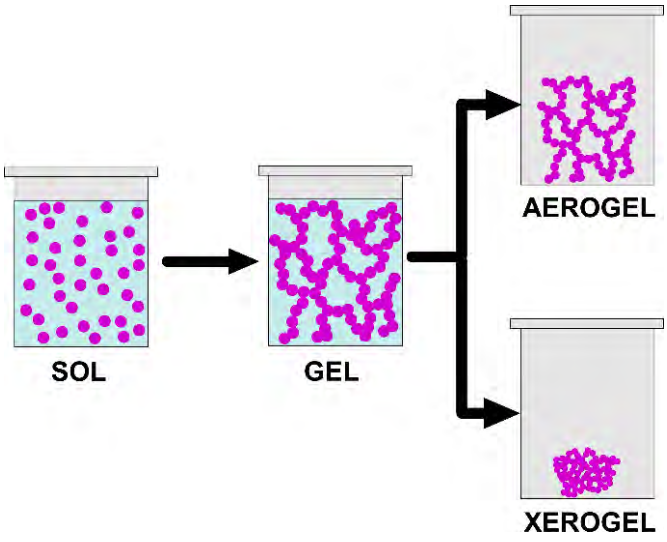

Figure 1.15 Graphic diagram of sol-gel process showing products that can be obtained from the gel.

Aerogels are low-density solid materials (Figure 1.16) with a fine open-pore structure. An aerogel is composed of individual primary particles or fibers only a few nanometers in size which are linked in a three-dimensional structure. This microstructure causes characteristic properties of aerogel materials: meso- and macroporosity (5–100 nm), high surface areas (200–2400 $m^2 \cdot g^{-1}$)[105] and ultralow densities (0.003–0.15 $g \cdot cm^{-3}$).[106]

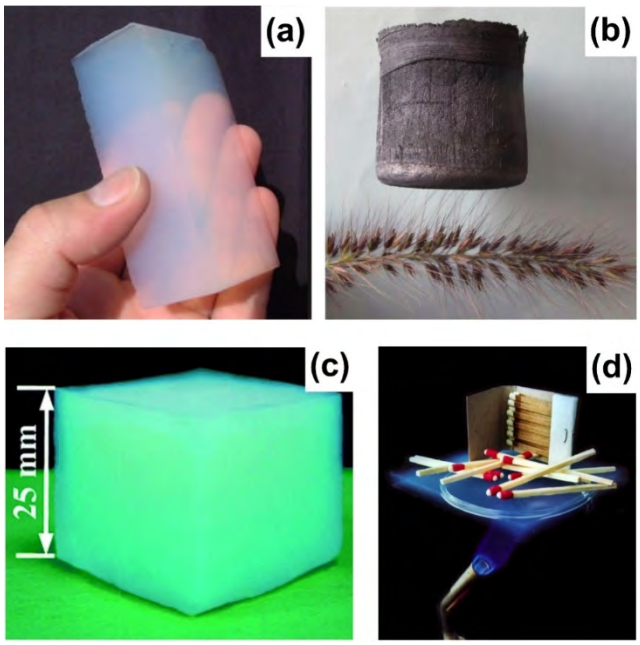

Figure 1.16 (a) Silica aerogel; (b) graphene aerogel; (c) lanthanide doped aerogel exhibiting luminescence; (d) visual demonstration of the low thermal conductivity exhibited by a silica aerogel.[107]

An aerogel should possess the below described characteristics:

- Structure characteristics: gel-like structure, normally with nanoscale coherent skeletons and pores; hierarchical and fractal microstructure (primary structure coexists and is related with larger-scale structure); able to form macroscopic monolith; randomly cross-linked network, normally composed of non-crystalline matter.

- Property characteristics: unique bulk properties different from solid matter, gas matter or normal foam, such as ultralow thermal conductivity, ultralow elastic modulus, ultralow refractive index, etc.

In this way, aerogels of different chemical nature have been synthesized: inorganic,[108] organic and polymeric,[109] peptidic,[110] metallic,[111] carbon based,[112] hybrid[113] and metal-organic (metal-organic aerogels: MOAs).[114]

Thanks to the attractive properties presented by aerogels today, their exploitation is being investigated as thermal and sound insulation materials,[115] supercapacitors,[116] ultralight structures for the aerospace industry,[117] desiccants or

absorbents for environmental remediation,[118] and Cherenkov counters,[119] among others.

As a concluding remark, synthesis of metal-organic gels (MOGs) and aerogels (MOAs) constitute a route that allows preparing porous materials from coordination compounds not being subjected to their crystal structure. This feature markedly enhances the possibility of obtaining multifunctional porous materials when compared to conventional MOFs, which need to meet reticular chemistry principles to provide an open framework. Furthermore, processing and shaping of MOFs implies still nowadays a challenge that requires facing some problems (post-processing optimization, binder removal, loss of porosity and pore blocking). In this regard, MOGs and MOAs can be shaped as desired during the synthesis process by simple molding, not requiring post-processing neither use of binders. Besides, the greater pore-size of MOGs and MOAs improves the molecular diffusion processes and allow dealing with big-sized guest molecules (i.e. macromolecules, nanoparticle, etc).

1.4. OBJECTIVES AND STRUCTURE OF THE WORK

The present work is encompassed within one of the research lines of the Department of Inorganic Chemistry of the Science and Technology Faculty (Leioa Campus) of the University of the Basque Country (UPV/EHU). The thesis is mainly focused on the synthesis and chemical and structural characterization of metal-organosulfur coordination compounds for their subsequent use as precursors of zero- and three-dimensional nanostructures.

Accordingly, the work is divided into two parts. The first one (chapter 2 and 3) emphasizes on the use of metal-thiocarboxylato complexes for the production of metallic sulfide nanoparticles of scientific and technological interest such as ZnS and CdS.[120] The selected thiocarboxylic acids (acetic and thiobenzoic acids) will be responsible for providing a sulfur source to the system. Although this class of

organosulfur molecules sometimes show the ability to bridge metal centers, given the chemical nature of the elements of 12 group, it is expected that the ligands will be coordinated in a terminal manner through the sulfur atom. In order to complete the coordination sphere of the metal, heterocycles with two or more donor nitrogen atoms will be employed as secondary ligands or co-ligands. Some of these co-ligands have a high predisposition to chelate the metal (2,2'-bipyridine, 1,10-phenanthroline, neocuproine) producing monomeric entities while others have the ability to bridge metals (1,2-di(4-pyridil)ethylene and adenine). It has been decide to use nitrogenous co-ligands because in their decomposition they do not leave behind fragments that may hinder the formation of the corresponding sulfide (*i.e.* the formation of oxides or sulfates). Likewise, the selected heterocycles have the robustness necessary to obtain chemically stable precursors and direct the decomposition of the precursor towards a specific polymorph.

The synthetic procedure that will follow to obtain this kind of nanoparticles is a variation of the single-source precursor route. Metal-organic precursors will be decomposed in solid state without the addition of solvents or surfactants, at relative moderate temperatures (300−500°C) and in air atmosphere. The influence of ligands on the distribution of nanoparticle sizes will be analyzed. Also, we will try to find a possible correlation between the average particle diameter and the structural variability of the compounds (*i.e.* effect of distance M···M, dimensionality of the complex, etc.). On the other hand, experiments will be made to understand which operational parameters related to the decomposition (temperature, time, heating rate, etc) are the most critical.

The second part of the work (chapter 4 and 5) will pursue the synthesis of nanoporous metal-organic gels (MOGs) and their processing as aerogels (MOAs) and xerogels (MOXs) based on metal-dithiooxamidato complexes. The linear coordination geometry of dithiooxamidato and the possibility of forming hydrogen bonds are two propitious characteristics for the creation of anisotropic coordination structures.

Additionally, the presence of sulfur atoms in the structure, a more voluminous element than oxygen or nitrogen with a greater capacity of overlapping, can confer a significant electrical conductivity to the material.

In chapter 4 a screening will be performed to understand the influence of the synthetic parameters on the gelation of the metal-dithioxamidato compounds. The process of preparing their respective aerogels will be optimized in order to obtain well defined monoliths. Metal-organic aerogels will be chemically characterized by infrared spectroscopy, elemental analysis and thermogravimetric analysis. Additionally, microstructure of the aerogels will be studied by electron microscopy and porosity through gas physisorption. Finally, the electrical properties of these materials will be analyzed through DC and AC conductivity measurements as well as the variation of conductivity in response to an external chemical stimulus.

In last chapter (chapter 5) we will discuss the applicability of the obtained metal-organosulfur gels among other metal-organic materials (basically MOFs) into the methanol synthesis by carbon dioxide electroreduction. It must be emphasized that methanol synthesis from CO_2 and H_2O can be considered in line with the policy of the future of the chemical industry.[121] This process could be an option for attenuating the greenhouse effect by transforming CO_2 into valuable chemicals and fuels, such as alcohols. Note that methanol is a potential alternative energy source to fossil fuels and a medium for the transport of hydrogen.

Potentiostatic techniques will be used to verify the catalytic activity of the metal-organic porous materials (MOPMs) deposited on carbon electrodes. On the other hand, the evolution of the catalytic activity will be assessed as a function of the time of use. The stability of the materials after the electroreduction of carbon dioxide to alcohols will be checked by means of X-ray diffraction and vibrational analysis.

Chapters 2−5 have been edited in article format, following the text structure of the journal in which each one has been published. The instrumental techniques have

been detailed in the experimental section of each chapter. The bibliography cited can be found at the end of each chapter. The bibliographic style used is that of the corresponding journal while the introduction of the thesis obeys to the style of the WILEY-VCH editorial which includes journals representative for the scope of this doctoral thesis (*European Journal of Inorganic Chemistry*, *Angewandte Chemie International Edition*, *Advanced Materials*, among others.). Accordingly, in this section references to articles have been arranged by authors, journal name, publication date, volume and pages. The cited books have been referenced following this scheme: authors, title of the book, year of publication and editorial. Internet links have been abbreviated for the reader's convenience and they have been last reviewed on May 20 of 2017.

1.5. REFERENCES

[1] R. G. Pearson, *J. Am. Chem. Soc.* **1963**, *85*, 3533−3539.

[2] a) A. G. de Souza, J. H. de Souza, C. Airoldi, *J. Chem. Soc., Dalton Trans.***1991**, 1751–1754; b) K. J. Cavell, J. O. Hill, R. J. Magee, *J. Chem. Soc., Dalton Trans.***1980**, 1638–1640; c) K. J. Cavell, J. O. Hill, R. J. Magee, *J. Chem. Soc., Dalton Trans.***1980**, 763–766; d) R. J. Irving, T. N. Lockyer, *J. Chem. Soc., Dalton Trans.* **1976**, 2140–2143; e) S. J. Ashcroft, *J. Chem. Soc. A* **1970**, 1020–1024.

[3] https://goo.gl/q0255H.

[4] a) https://goo.gl/Uf9GNN; b) https://goo.gl/K8PgxI; https://goo.gl/zSLHfd.

[5] a) K. Paizanos, D. Charalampou, N. Kourkoumelis, D. Kapogiannaki, L. Hadjiarapoglou, A. Spanopoulou, K. Lazarou, M. J. Manos, A. J. Tasiopoulos, M. Kubicki, S. K. Hadjikakou, *Inorg. Chem.* **2012**, *51*, 12248–12259; b) F. Shaheen, A. Badashah, M. Gielen, L. Marchio, D. de Vos, M. K. Khosa, *Appl. Organomet. Chem.* **2007**, *21*, 626–632; c) E. R. T. Tiekink, P. D. Cookson, B. M. Linahan, L. K. Webster, *Met. Based Drugs* **1994**, 299–304; d) D. L. Geffner, M. Azukizawa, J. M. Heisman, *J. Clin. Invest.* **1975**, *55*, 224–229.

[6] a) J. Troyano, O. Castillo, P. Amo-Ochoa, V. Fernández-Moreira, C. J. Gómez-García, F. Zamora, S. Delgado, *J. Mater. Chem. C* **2016**, *4*, 8545–8551; b) K. N. Sharma, H. Joshi, V. V. Singh, P. Singh, A. K. Singh, *Dalton Trans.* **2013**, *42*, 3908–3918; c) M. O. Odago, A. E. Hoffman, R. L. Carpenter, D. C. T. Tse, S. -S. Sun, A. J. Lees, *Inorg. Chim. Acta* **2011**, *374*, 558–565; d) K. Kubo, M. Nakano, S. Hamaguchi, G. Matsubayashi, *Inor. Chim. Acta* **2003**, *346*, 43–48; e) N. Robertson, L. Cronin, *Coord. Chem. Rev.* **2002**, *227*, 93–127; f) V. W. -W. Yam, E. C. -C. Cheng, *Gold Bull.* **2001**, *34*, 20–23; g) J. C. Bayón, C. Claver, A. M. Masdeu-Bultó, *Coord. Chem. Rev.* **1999**, *193–195*, 73–145.

[7] a) S. Poirier, F. Rahmani, C. Reber, *Dalton. Trans.* **2017**, *46*, 5279–5287; b) J. S. Ovens, P. R. Christensen, D. B. Leznoff, *Chem. Eur. J.* **2016**, *22*, 8234–8239; c) N. Khadir, D. M. Boghaei, A. Assoud, O. R. Nascimento, A. Nicotina, L. Ghivelder, R. Calvo, *Dalton Trans.* **2015**, *44*, 2431–2438; d) K. M. Henline, C. Wang, R. D. Pike, J. C. Ahern, B. Sousa, H. H. Patterson, A. T. Kerr, C .L. Cahill, *Cryst. Growth Des.* **2014**, *14*, 1449–1458; e) M. Rittmeier, S. Demeshko, S. Dechert, F. Meyer; *Z. Anorg. Allg. Chem.* **2013**, *639*, 1445–1454; f) S. Singh, J. Chaturvedi, S. Bhattacharya, *Inorg. Chim. Acta* **2012**, *385*, 112–118; g) H. -Y. Chao, L. Wu, C. -L. Li, W. Lu, L. Liu, X. -L. Feng, *Z. Anorg. Allg. Chem.* **2011**, *637*, 1533–1538; h) K. A. McGee, K. R. Mann, *Inorg. Chem.* **2007**, *46*, 7800–7809; i) S. Ahrland, B. Noren, A. Oskarsson, *Inorg. Chem.* **1985**, *24*, 1330–1333; j) C. Bellitto, G. Dessy, V. Fares, *Inorg. Chem*. **1985**, *24*, 2815–2820.

[8] a) https://goo.gl/zjZbmB; b) C. R. Groom, F. H. Allen*, Angew. Chem. Int. Ed.* **2014**, *53*, 662−671.

[9] a) A. Kreider-Mueller, P. J. Quinlivan, J. S. Owen, G. Parkin, *Inorg. Chem.* **2015**, *54*, 3835–3850; b) S. Singh, J. Chaturvedi, S. Bhattacharya, *Inorg. Chim. Acta* **2013**, *407*, 31–36; c) M. El-khateeb, T. M. A. Jazzazi, H. Görls, T. M. A. Al-Shboul, M. Westerhausen, *Transit. Metal. Chem*. **2011**, *36*, 29–33; d) C. V. Amburose, T. C.

Deivaraj, G. X. Lai, J. T. Sampanthar, J. J. Vittal, *Inorg. Chim. Acta* **2002**, *332*, 160–166.

[10] J. T. Sampanthar, T. C. Deivaraj, J. J. Vittal, P. A. W. Dean, *J. Chem. Soc., Dalton Trans.* **1999**, 4419−4423.

[11] N. Mehmet, D. A. Tocher, *Inorg. Chim. Acta* **1991**, *188*, 71–77.

[12] S. Bhattacharya, D. K. Joshi, *Inorg. Chim. Acta* **2014**, *411*, 119–127.

[13] M. Gennari, G. Givaja, O. Castillo, L. Hermosilla, C. J. Gómez-García, C. Duboc, A. Lledós, R. Mas-Ballesté, F. Zamora, *Inorg. Chem.* **2014**, *53*, 10553–10562.

[14] F. G. Baddour, S. R. Fiedler, M. P. Shores, J. A. Golen, A. L. Rheingold, L. H. Doerrer, *Inorg. Chem.* **2013**, *52*, 4926–4933.

[15] J. Troyano, O. Castillo, P. Amo-Ochoa, V. Fernández-Moreira, C. J. Gómez-García, F. Zamora, S. Delgado, *J. Mater. Chem. C* **2016**, *4*, 8545–8551.

[16] a) Y. Nagao, T. Kubo, K. Nakasuji, R. Ikeda, T. Kojima, H. Kitagawa, *Synthetic Met.* **2005**, *154*, 89–92; b) H. Kitagawa, Y. Nagao, M. Fujishima, R. Ikeda, S. Kanda, *Inorg. Chem. Commun.* **2003**, *6*, 346–348.

[17] a) S. Abbasi, A. Bahiraei, *Food Chem.* **2012**, *133*, 1075–1080; b) M. B. Saha, A. K. Chakraburtty, *J. Indian Chem. Soc.* **1983**, *60*, 176–177; c) P. Agnes, *Anal. Chem.* **1963**, *35*, 2119–2121.

[18] H. C. Hofmans, H. O. Desseyn, R. A. Dommisse, *Transition Met. Chem.* **1984**, *9*, 213–217.

[19] P. Kopel, F. Březina, Z. Trávníček, Z. Šindelář, J. Lasovský, *Polyhedron* **1995**, *14*, 991–996.

[21] A. Mosset, M. Abboudi, J. Galy, *Z. Kristallogr.* **1983**, *164*, 171–181.

[22] A. Castiñeiras, I. García-Santos, J. M. Varela, *Polyhedron* **2009**, *28*, 860–864.

[23] J. N. Tiwari, R. N. Tiwari, K. S. Kim, *Prog. Mater. Sci.* **2012**, *57*, 724–803.

[24] a) https://goo.gl/2pxv7e; b) https://goo.gl/G5MXG6; c) https://goo.gl/UnaxOM; d) https://goo.gl/XbmTYF; e) https://goo.gl/pqCA8S; f) https://goo.gl/QT7IQ8; g) https://goo.gl/IODtpP; h) https://goo.gl/e9JGsX; i) https://goo.gl/BcNEPu.

[25] a) D. Bera, L. Qian, T. -K. Tseng, P. H. Holloway, *Materials* **2010**, *3*, 2260–2345; b) V. Biju, T. Itoh, A. Anas, A. Sujith, M. Ishikawa, *Anal. Bioanal. Chem.* **2008**, *391*, 2469–2495; c) T. Trindade, P. O'Brien, N. L. Pickett, *Chem. Mater.* **2001**, *13*, 3843–3858; d) A. P. Alivisatos, *Science* **1996**, *271*, 933–937.

[26] a) L. Bogani, W. Wernsdorfer, *Nat. Mater.* **2008**, *7*, 179–186; b) R. H. Laye, E. J. L. McInnes, *Eur. J. Inorg. Chem.* **2004**, 2811–2818; c) D. Gatteschi, A. Caneschi, L. Pardi, R. Sessoli, *Science* **1994**, *265*, 1054–1058.

[27] a) T. K. Sau, A. L. Rogach, *Adv. Mater.* **2010**, *22*, 1781–1804; b) W. Cai, J. Wan, *J. Colloid Interf. Sci.* **2007**, *305*, 366–370; c) K. L. Kelly, E. Coronado, L. L. Zhao, G. C. Schatz, *J. Phys. Chem. B* **2003**, *107*, 668–677.

[28] a) M. A. Petrukhina, L. T. Scott, H. W. Kroto, *Fragments of Fullerenes and Carbon Nanotubes: Designed Synthesis, Unusual Reactions, and Coordination Chemistry*, Wiley-VCH, John Wiley & Sons, Hoboken, USA, **2011**, p. 41; b) K. E. Geckeler, S. Samal, *Polym. Int.* **1999**, *48*, 743–757; c) S. V. Kozyrev, V. V. Rotkin, *Semiconductors* **1993**, *27*, 777–791.

[29] a) S. Zeng, K. -T. Yong, I. Roy, X. -Q. Dinh, X. Yu, F. Luan, *Plasmonics* **2011**, *6*, 491–506; b) C. -A. J. Lin, T. Liedl, R. A. Sperling, M. T. Fernández-Argüelles, J. M. Costa-Fernández, R. Pereiro, A. Sanz-Medel, W. H. Chang, W. J. Parak, *J. Mater. Chem.* **2007**, *17*, 1343–1346; c) D. Astruc, F. Lu, J. R. Aranzaes, *Angew. Chem. Int. Ed.* **2005**, *44*, 7852–7872; d) R. Hergt, R. Hiergeist, I. Hilger, W. A. Kaiser, Y. Lapatnikov, S. Margel, U. Richter, *J. Magn. Magn. Mater.* **2004**, *270*, 3, 345–357; e) V. I. Klimov, A. A. Mikhailovsky, S. Xu, A. Malko, J. A. Hollingworth, C. A. Leatherdale, H. -J. Eisler, M. G. Bawendi, *Science* **2000**, *290*, 314–317; f) D. Loss, D. P. DiVincenzo, *Phys. Rev. A* **1998**, *57*, 120–126.

[30] a) S. J. Tans, M. H. Devoret, H. Dai, A. Thess, R. E. Smalley, L. J. Geerligs, C. Dekker, *Nature* **1997**, *386*, 474–477; b) S. Iijima, T. Ichihashi, *Nature* **1993**, *363*, 603–605.

[31] a) S. Weon, J. Choi, T. Park, W. Choi, *Appl. Catal. B-Environ.* **2017**, *205*, 386–392; b) T. Wang, Y. Xu, Z. He, H. Zhang, L. Xiong, M. Zhou, W. Yu, B. Shi, K. Huang, *Macromol. Chem. Phys.* **2017**, *218*, 1600431; c) J. Wu, H. Chen, L. Zhao, X. He, W. Fang, W. Li, X. Du, *Ceram. Int.* **2017**, *43*, 5145–5149; d) A. Knöller, T. Runĉevski, R. E. Dinnebier, J. Bill, Z. Burghard, *Sci. Rep-UK* **2017**, *7*, 42951; e) J. Zhong, X. Yang, S. Lou, S. Zhou, *Mater. Lett.* **2017**, *191*, 26–29; f) A. Morsali, L. Hashemi, *Main Group Metal Coordination Polymers: Structures and Nanostructures*, John Wiley & Sons, Hoboken, USA, **2017**; g) C. Luo, J. Wang, X. Fan, Y. Zhu, F. Han, L. Suo, C. Wang, *Nano Energy* **2015**, *13*, 537–545; h) A. Datar, K. Balakrishnan, X. Yang, X. Zuo, J. Huang, R. Oitker, M. Yen, J. Zhao, D. M. Tiede, L. Zang, *J. Phys. Chem. B* **2006**, *110*, 12327–12332; i) S. Virji, J. Huang, R. B. Kaner, B. H. Weiller, *Nano Lett.* **2004**, *4*, 491–496; j) K. -S. Kim, H. W. Kim, *Physica B* **2003**, *328*, 368–371.

[32] a) E. Fortunato, P. Barquinha, R. Martins, *Adv. Mater.* **2012**, *24*, 2945–2986; b) A. R. Murphy, J. M. J. Fréchet, *Chem. Rev.* **2007**, *107*, 1066−1096; c) R. S. Mane, C. D. Lokhande, *Mater. Chem. Phys.* **2000**, *65*, 1–31.

[33] a) Y. Shao, J. Wang, H. Wu, J. Liu, I. A. Aksay, Y. Lin, *Electroanal.* **2010**, *22*, 1027–1036; b) M. J. Allen, V. C. Tung, R. B. Kaner, *Chem. Rev.* **2010**, *110*, 132–145.

[34] M. Thommes, K. Kaneko, A. V. Neimark, J. P. Olivier, F. Rodriguez-Reinoso, J. Rouquerol, K. S. W. Sing, *Pure Appl. Chem.* **2015**, *87*, 1051–1069.

[35] a) M. Niwa, N. Katada, K. Ukumura, *Characterization and Design of Zeolite Catalysts*, Springer Series in Materials Science, Vol. 141, Heidelberg, Germany, **2010**,; b) S. M. Auerbach, K. A. Carrado, P. K. Dutta, *Handbook of Zeolite Science and Technology*, CRC Press, New York, USA, **2003**.

[36] J. F. Kwiatkowski, *Activated Carbon: Classifications, Properties and Applications*, Nova Science, Chemical Engineering Methods and Technology, New York, USA, **2012**.

[37] A. Gil, L. M. Gandía, M. A. Vicente, *Catal. Rev. Sci. Eng.* **2000**, *42*, 145–212.

[38] a) S. T. Meek, J. A. Greathouse, M. D. Allendorf, *Adv. Mater.* **2011**, *23*, 249–267; b) J. L. C. Rowsell, O. M. Yaghi, Micropor. Mesopor. Mat. **2004**, *73*, 3–14; c) S. L. James, *Chem. Soc. Rev.* **2003**, *32*, 276–288.

[39] a) X. Feng, X. Ding, D. Jiang, *Chem. Soc. Rev*. **2012**, *41*, 6010–6022; b) A. P. Côté, A. I. Benin, N. W. Ockwig, M. O'Keeffe, A. J. Matzger, O. M. Yaghi, *Science* **2005**, *310*, 1166–1170.

[40] a) M. Vázquez, B. Paul, *Anal. Chim. Acta* **2010**, *668*, 100–113.

[41] a) https://goo.gl/kTRRO2; b) M. Aegerter, N. Leventis, M. M. Koebel, *Aerogels Handbook*, Springer Science, New York, USA, **2011**.

[42] a) L. -P. Lefebvre, J. Banhart, D. C. Dunand, *Adv. Eng. Mater.* **2008**, *10*, 775–787; b) B. Krause, K. Diekmann, N. F. A. van der Vegt, M. Wessling, *Macromolecules* **2002**, *35,* 1738–1745.

[43] P. S. Liu, G. F. Chen, *Porous Materials: Processing and Applications*, Elsevier, Waltham, USA, **2014**.

[44] a) B. Ameri, S. S. H. Davarani, R. Roshani, H. R. Moazami, A. Tadjarodi, *J. Alloy. Compd.* **2017**, *695*, 114–123; b) G. -X. Liang, X. -H. Zhang, H. -L. Ma, J. -G. Hu, B. Fan, Z. -K. Luo, Z. -H. Zheng, J. -T. Luo, P. Fan, *Sol. Energy Mat. Sol. C* **2017**, *160*, 257–262; c) V. M. Chakka, B. Altuncevahir, Z. Q. Jin, Y. Li, J. P. Liu, *J. Appl. Phys.* **2006**, *99*, 08E912.

[45] a) H. S. Mund, B. L. Ahuja, *Mater. Res. Bull.* **2017**, *85*, 228–233; b) P. R. Somani, S. P. Somani, M. Umeno, *Chem. Phys. Lett.* **2006**, *430*, 56–59; c) M. Wen, M. Zhong, K. E. J. Wu, L. Li, H. Qi, S. Cao, T. Zhang, *J. Alloy. Compd.* **2005**, *417*, 245–249.

[46] a) S. Shen, Q. Wang, *Chem. Mater.* **2013**, *25*, 1166–1178; b) C. -H. Lai, M. -Y. Lu, L. -J. Chen, *J. Mater. Chem.* **2012**, *22*, 19–30; c) R. R. Chianelli, G. Berhault, B. Torres, *Catal. Today* **2009**, *147*, 275–286; d) S. Eijsbouts, S. W. Mayo, K. Fujita, *Appl. Catal. A-Gen.* **2007**, *322*, 58–66.

[47] a) S. Chellammal, S. Sankar, S. Selvakumar, E. Viswanathan, R. Murugaraj, K. Sivaji, *J. Mater. Sci.* **2010**, *45*, 1242–1247; b) S. S. Nair, M. A. Khadar, *Sci. Technol. Adv. Mater.* **2008**, *9*, 035004–035010; c) J. -O. Joswig, M. Springborg, G. Seifert, *J. Phys. Chem. B* **2000**, *104*, 2617–2622.

[48] a) P. D. Rack, P. H. Holloway, *Mater. Sci. Eng. R-Rep.* **1998**, *21*, 171–219; b) M. Kanemoto, T. Shiragami, C. Pac, S. Yanagida, *J. Phys. Chem.* **1992**, *96*, 3521–3526; c) A. P. Davis, C. P. Huang, *Water Res.* **1991**, *25*, 1273–1278; d) R. H. Bube, *Phys. Rev.* **1953**, *90*, 70–80.

[49] a) O. Yehezkeli, N. M. Bedford, E. Park, K. Ma, J. N. Cha, *ChemSusChem* **2016**, *9*, 3188–3195; b) H. Ang, M. Bosman, R. Thamankar, M. F. B. Zulkifli, S. K. Yen, A. Hariharan, T. Sudhaharan, S. T. Selvan, *ChemPhysChem* **2016**, *17*, 2489–2495; c) J. Aswathy, N. V. Seethalekshmy, K. R. Hiran, M. R. Bindhu, K. Manzoor, V. N. Shantikumar, M. Deepthy, *Nanotechnology* **2014**, *25*, 445102; d) M. A. Halim, *Nanomaterials* **2013**, *3*, 22–47; e) T. P. Brennan, P. Ardalan, H. -B. -R. Lee, J. R. Bakke, I. -K. Ding, M. D. McGehee, S. F. Bent, *Adv. Energy Mater.* **2011**, *1*, 1169–1175.

[50] a) G. B. Shombe, E. B. Mubofu, S. Mlowe, N. Revaprasadu, *Mat. Sci. Semicon. Proc.* **2016**, *43*, 230–237; b) D. C. Onwudiwe, C. A. Strydom, O. S. Oluwafemi, E. Hosten, A. Jordaan, *Dalton Trans.* **2014**, *43*, 8703–8712; c) A. A. Memon, M. Afzaal, M. A. Malik, C. Q. Nguyen, P. O'Brien, J. Raftery, *Dalton Trans.* **2006**, 4499–4505.

[51] a) A. Aboulaich, D. Billaud, M. Abyan, L. Balan, J. -J. Gaumet, G. Medjadhi, J. Ghanbaja, R. Schneider, *ACS Appl. Mater. Inter.* **2012**, *4*, 2561–2569; b) M. Salavati-Niasari, F. Davar, M. Mazaheri, *J. Alloy. Compd.* **2009**, *470*, 502–506; b) Y. C. Zhang, G. Y. Wang, X. Y. Hu, Q. F. Shi, T. Qiao, Y. Tang, *J. Cryst. Growth* **2005**, *284*, 554–560.

[52] a) M. A. Buckingham, A. L. Catherall, M. S. Hill, A. L. Johnson, J. D. Parish, *Cryst. Growth Des.* **2017**, *17*, 907−912; b) S. Mlowe, L. D. Nyamen, P. T. Ndifon, M. A. Malik, J. Raftery, P. O'Brien, N. Revaprasadu, *Inorg. Chim. Acta* **2015**, *434*, 181–187; c) M. Lazell, P. O'Brien, D. J. Otway, J. -H. Park, *J. Chem. Soc., Dalton Trans.* **2000**, 4479–4486; d) T. L. Chu, S. S. Chu, *Solid State Electron.* **1995**, *38*, 533–549.

[53] a) N. M. Hosny, A. Dahshan, *J. Mol. Struct.* **2015**, *1085*, 78–83 b) S. K. Maji, N. Mukherjee, A. Mondal, B. Adhikary, B. Karmakar, S. Dutta, *Inorg. Chim. Acta* **2011**, *371*, 20–26; c) Q. Han, F. Qiang, M. Wang, J. Zhu, L. Lu, X. Wang, *Mater. Res. Bull.* **2010**, *45*, 813–817.

[54] a) M. Nayak, S. Bhattacharya, *Inorg. Chim. Acta* **2014**, *410*, 54–59; b) J. J. Vittal, M. T. Ng, *Acc. Chem. Res.* **2006**, *39*, 869–877.

[55] a) S. Singh, J. Chaturvedi, A. S. Aditya, N. R. Reddy, S. Bhattacharya, *Inorg. Chim. Acta* **2013**, *396*, 6–9; b) J. T. Sampanthar, J. J. Vittal, P. A. W. Dean, *J. Chem. Soc., Dalton Trans.***1999**, 3153–3156.

[56] a) J. Chaturvedi, S. Singh, S. Bhattacharya, H. Nöth, *Inorg. Chem.* **2011**, *50*, 10056–10069; b) T. C. Deivaraj, J. -H. Park, M. Afzaal, P. O'Brien, J. J. Vittal, *Chem. Mater.* **2003**, *15*, 2383–2391.

[57] Y. Zhang, Y. Liu, C. Li, X. Chen, Q. Wang, *J. Phys. Chem. C* **2014**, *118*, 4918−4923.

[58] a) A. Le Donne, S. K. Jana, S. Banerjee, S. Basu, *J. Appl. Phys.* **2013**, *113*, 014903; b) S. E. Irvine, T. Staudt, E. Rittweger, J. Engelhardt, S. W. Hell, *Angew. Chem. Int. Ed.* **2008**, *47*, 2685–2688.

[59] a) https://goo.gl/Eighl4; b) https://goo.gl/JJ4EvI, c) X. Lim, *Nature* **2016**, *531*, 26–28.

[60] a) J. Lang, X. Li, J. Yang, L. Yang, Y. Zhang, Y. Yan, Q. Han, M. Wei, M. Gao, X. Liu, R. Wang, *Appl. Surf. Sci.* **2011**, *257*, 9574–9577; b) S. K. Mishra, R. K. Srivastava, S. G. Prakash, R. S. Yadav, A. C. Panday, *Electron. Mater. Lett.* **2011**, *7*, 31–38.

[61] a) Y. Du, B. Xu, T. Fu, M. Cai, F. Li, Y. Zhang, Q. Wang, *J. Am. Chem. Soc.* **2010**, *132*, 1470–1471; b) N. L. Pickett, P. O'Brien, *Chem. Rec.* **2001**, *1*, 467–479.

[62] a) D. Jose, B. R. Jagirdar, *J. Solid State Chem.* **2010**, *183,* 2059–2067; b) H. G. Cha, D. K. Lee, Y. H. Kim, C. W. Kim, C. S. Lee, Y. S. Kang, *Inorg. Chem.* **2008**, *47*, 121−127; c) T. H. Larsen, M. Sigman, A. Ghezelbash, R. C. Doty, B. A. Korgel, *J. Am. Chem. Soc.* **2003**, *125*, 5638–5639.

[63] a) M. S. Akhtar, S. Riaz, R. F. Mehmood, K. S. Ahmad, Y. Alghamdi, M. A. Malik, S. Naseem, *Mater. Chem. Phys.* **2017**, *189*, 28–34; b) S. Li, Z. Wu, W. Li, Y. Liu, R. Zhuo, D. Yan, W. Jun, P. Yan, *CrystEngComm* **2013**, *15*, 1571–1577.

[64] D. Wu, B. Xiao, N. Liu, K. Jiang, *Mater. Sci. Eng. B* **2010**, *175*, 195–200; R. Yi, G. Qiu, X. Liu, *J. Solid State Chem.* **2009**, *182*, 2791–2795.

[65] P. Xue, R. Lu, Y. Huang, M. Jin, C. Tan, C. Bao, Z. Wang, Y. Zhao, *Langmuir* **2004**, *20*, 6470−6475.

[66] L. Spanhel, M. A. Anderson, *J. Am. Chem. Soc.* **1990**, *112*, 2278−2284.

[67] J. L. Mohanan, S. L. Brock, *J. Non-Cryst. Solids*, **2004**, *350*, 1−8.

[68] a) D. P. Debecker, V. Hulea, P. H. Mutin, *Appl. Catal. A-Gen.* **2013**, *451*, 192–206; b) L. L. Hench, J. K. West, *Chem. Rev.* **1990**, *90*, 33–72.

[69] a) Y. Kong, X. Shen, S. Cui, M. Fan, *Green Chem.* **2015**, *17*, 3436–3445; b) V. Štengl, S. Bakardjieva, J. Šubrt, L. Szatmary, *Micropor. Mesopor. Mat.* **2006**, *91*, 1–6; c) Y. Wan, J. Ma, W. Zhou, Y. Zhu, X. Song, H. Li, *Appl. Catal. A-Gen.* **2004**, *277*, 55–59; d) K. Tajiri, K. Igarashi, T. Nishio, *J. Non-Cryst. Solids* **1995**, *186*, 83–87.

[70] a) S. T. Meek, J. A. Greathouse, M. D. Allendorf, *Adv. Mater.* **2011**, *23*, 249–267; b) J. L. C. Rowsell, O. M. Yaghi, Micropor. Mesopor. Mat. **2004**, *73*, 3–14; c) S. L. James, *Chem. Soc. Rev.* **2003**, *32*, 276–288.

[71] a) T. K. Kim, J. H. Lee, D. Moon, H. R. Moon, *Inorg. Chem.* **2013**, *52*, 589−595; b) Y. -Q. Lan, S. -L. Li, H. -L. Jiang, Q. Xu, *Chem. Eur. J.* **2012**, *18*, 8076–8083.

[72] a) D. J. Tranchemontagne, J. L. Mendoza, M. O´Keeffe, O. M. Yaghi, *Chem. Soc. Rev.* **2009**, *38*, 1257–1283; b) A. J. Blake, N. R. Champness, P. Hubberstey, W. -S. Li, M. A. Withersby, M. Schröder, *Coord. Chem. Rev.* **1999**, *183*, 117–138; c) D. Braga, F. Grepioni, G. R. Desiraju, *Chem. Rev.* **1998**, *98*, 1375–1405.

[73] a) O. K. Farha, I. Eryazici, N. C. Jeong, B. G. Hauser, C. E. Wilmer, A. A. Sarjeant, R. Q. Snurr, S. T. Nguyen, A. Ö. Yazaydin, J. T. Hupp, *J. Am. Chem. Soc.* **2012**, *134*, 15016−15021; b) H. Furukawa, N. Ko, Y. B. Go, N. Aratani, S. B. Choi, E. Choi, A. Ö. Yazaydin, R. Q. Snurr, M. O'Keeffe, J. Kim, O. M. Yaghi, *Science* **2010**, *329*, 424–428.

[74] a) J. Heine, K. Müller-Buschbaum, *Chem. Soc. Rev.* **2013**, *42*, 9232–9242; b) C. A. Bauer, T. V. Timofeeva, T. B. Settersten, B. D. Patterson, V. H. Liu, B. A. Simmons, M. D. Allendorf, *J. Am. Chem. Soc.* **2007**, *129*, 7136–7144.

[75] a) A. J. Fletcher, K. M. Thomas, M. J. Rosseinsky, *J. Solid State Chem.* **2005**, *178*, 2491–2510; b) M. J. Rosseinsky, *Micropor. Mesopor. Mat.* **2004**, *73*, 15–30.

[76] a) K. Leong, M. E. Foster, B. M. Wong, E. D. Spoerke, D. V. Gough, J. C. Deaton, M. D. Allendorf, *J. Mater. Chem. A* **2014**, *2*, 3389–3398; b) H. Miyasaka, *Accounts Chem. Res.* **2013**, *46*, 248–257.

[77] a) C. -T. Yeh, W. -C. Lin, S. -H. Lo, C. -C. Kao, C. -H. Lin, C. -C. Yang, *CrystEngComm* **2012**, *14*, 1219–1222; b) V. Colombo, S. Galli, H. J. Choi, G. D. Han, A. Maspero, G. Palmisano, N. Masciocchi, J. R. Long, *Chem. Sci.* **2011**, *2*, 1311–1319; c) X. Guo, G. Zhu, Z. Li, F. Sun, Z. Yang, S. Qiu, *Chem. Commun.* **2006**, 3172–3174.

[78] a) A. A. Talin, A. Centrone, A. C. Ford, M. E. Foster, V. Stavila, P. Haney, R. A. Kinney, V. Szalai, F. El Gabaly, H. P. Yoon, F. Léonard, M. D. Allendorf, *Science* **2014**, *343*, 66–69; b) S. Horike, D. Umeyama, S. Kitagawa, *Accounts Chem. Res.* **2013**, *46*, 2376–2384.

[79] a) X. Y. Xu, B. Yan, *Dalton Trans.* **2016**, *45*, 7078–7084; b) W. J. Phang, W. R. Lee, K. Yoo, D. W. Ryu, B. Kim, C. S. Hong, *Angew. Chem. Int. Ed.* **2014**, *53*, 8383–8387.

[80] O. M. Yaghi, H. Li, *J. Am. Chem. Soc.* **1995**, *117*, 10401–10402.

[81] a) K. Sumida, D. L. Rogow, J. A. Mason, T. M. McDonald, E. D. Bloch, Z. R. Herm, T. -H. Bae, J. R. Long, *Chem. Rev.* **2012**, *112*, 724–781; b) L. J. Murray, M. Dincă, J. R. Long, *Chem. Soc. Rev.* **2009**, *38*, 1294–1314.

[82] a) M. Maes, L. Alaerts, F. Vermoortele, R. Ameloot, S. Couck, V. Finsy, J. F. M. Denayer, D. E. De Vos, *J. Am. Chem. Soc.* **2010**, *132*, 2284–2292; b) M. P. M. Nicolau, P. S. Barcia, J. M. Gallegos, J. A. C. Silva, A. E. Rodrigues, B. L. Chen, *J. Phys. Chem. C* **2009**, *113*, 13173–13179; c) H. L. Guo, G. S. Zhu, I. J. Hewitt, S. L. Qiu, *J. Am. Chem. Soc.* **2009**, *131*, 1646–1647; d) R. W. Baker, *Ind. Eng. Chem. Res.* **2002**, *41*, 1393–1411.

[83] a) A. Corma, H. García, F. X. Llabrés i Xamena, *Chem. Rev.* **2010**, *110*, 4606–4655; b) C. -D. Wu, W. Lin, *Angew. Chem. Int. Ed.* **2007**, *46*, 1075–1078.

[84] a) P. Horcajada, C. Serre, G. Maurin, N. A. Ramsahye, F. Balas, M. Vallet-Regí, M.Sebban, F. Taulelle, G. Férey, *J. Am. Chem. Soc.* **2008**, *130*, 6774–6780; b) P. Horcajada, C. Serre, M. Vallet-Regí, M. Sebban, F. Tautelle, G. Férey, *Angew. Chem. Int. Ed.* **2006**, *45*, 5974–5978.

[85] a) M. D. Allendorf, A. Schwartzberg, V. Stavila, A. A. Talin, *Chem. Eur. J.* **2011**, *17*, 11372–11388; b) M. Kurmoo, *Chem. Soc. Rev.* **2009**, *38*, 1353–1379.

[86] a) L. E. Kreno, K. Leong, O. K. Farha, M. Allendorf, R. P. V. Duyne, J. T. Hupp, *Chem. Rev.* **2012**, *112*, 1105–1125; b) B. Chen, S. Xiang, G. Qian, Accounts Chem. Res. **2010**, *43*, 1115–1124.

[88] a) O. M. Yaghi, M. O'Keeffe, N. W. Ockwig, H. K. Chae, M. Eddaoudi, J. Kim, *Nature* **2003**, *423*, 705–714; b) https://goo.gl/yjAH7D; c) https://goo.gl/tMhUqy; d) https://goo.gl/f8rLqV.

[89] a) X. Gu, B. Bai, H. Wang, M. Li, *RSC Adv.* **2017**, *7*, 218–223; b) M. Zhang, R. G. Weiss, *Chem. Eur. J.* **2016**, *22*, 8262–8272; c) M. George, R. G. Weiss, *Accounts Chem. Res.* **2006**, *39*, 489–497; d) K. Sugiyasu, N. Fujita, S. Shinkai, *Angew. Chem. Int. Ed.* **2004**, *43*, 1229–1233; e) R. Wang, C. Geiger, L. Chen, B. Swanson, D. G. Whitten, *J. Am. Chem. Soc.* **2000**, *122*, 2399–2400.

[90] a) S. K. Samantha, A. Gomathi, S. Bhattacharya, C. N. R. Rao, *Langmuir* **2010**, *26*, 12230–12236; b) S. Bag, P. N. Trikalitis, P. J. Chupas, G. S. Armatas, M. G. Kanatzidis, *Science* **2007**, *317*, 490–493; c) A. E. Gash, T. M. Tillotson, J. H. Satcher Jr, L. W. Hrubesh, R. L. Simpson, *J. Non-Cryst. Solids* **2001**, *285*, 22–28.

[91] a) P. Sutar, T. K. Maji, *Chem. Commun.* **2016**, *52*, 8055–8074; b) J. Zhang, C. -Y. Su, *Coord. Chem. Rev.* **2013**, *257*, 1373–1408; c) Q. Wei, S. L. James, *Chem. Commun.* **2005**, 1555–1556.

[92] a) W. -T. Yeh, P. -D. Hong, *J. Polym. Res.* **2016**, *23*, 193–203; b) S. S. Halacheva, T. J. Freemont, B. R. Saunders, *J. Mater. Chem. B* **2013**, *1*, 4065–4078; c) T. Kato, Y. Hirai, S. Nakaso, M. Moriyama, *Chem. Soc. Rev.* **2007**, *36*, 1857–1867; d) N. M. Sangeetha, U. Maitra, *Chem. Soc. Rev.* **2005**, *34*, 821–836.

[93] a) M. Asai, T. Katashima, T. Sakai, M. Shibayama, *Soft Matter* **2015**, *11*, 7101–7108; b) Y. Hirokawa, T. Okamoto, K. Kimishima, H. Jinnai, S. Koizumi, K. Aizawa, T. Hashimoto, *Macromolecules* **2008**, *41*, 8210–8219; c) J. E. Martin, D. Adolf, *Annu. Rev. Phys. Chem.* **1991**, *42*, 311–339; d) D. DeRossi, K. Kajiwara, Y. Osada, A. Yamaguchi, *Polymer Gel*, Plenum Press, New York, USA, **1991**.

[94] a) https://goo.gl/o49ULa; b) A. Lazaro, G. Quercia, H. J. H. Brouwers, J. W. Geus, *WJNSE*, **2013**, 3, 41–51; c) X. Wen, L. Tang, L. Qiang, *Soft Matter* **2014**, *10*, 3960–3969.

[95] M. -O. M. Piepenbrock, N. Clarke, J. W. Steed, *Langmuir* **2009**, *25*, 8451–8456.

[96] a) J. Park, J. H. Lee, J. Jaworski, S. Shinkai, J. H. Jung, *Inorg. Chem.* **2014**, *53*, 7181−7187; b) O. Roubeau, A. Colin, V. Schmitt, R. Clerac, *Angew. Chem. Int. Ed.*, **2004**, *43*, 3283–3286.

[97] K. Liu, L. Meng, S. Mo, M. Zhang, Y. Mao, X. Cao, C. Huang, T. Yi, *J. Mater. Chem. C* **2013**, *1*, 1753–1762.

[98] M. -O. M. Piepenbrock, N. Clarke, J. W. Steed, *Soft Matter* **2010**, *6*, 3541–3547.

[99] a) S. Sarkar, S. Dutta, P. Bairi, T. Pal, *Langmuir* **2014**, *30*, 7833−7841; b) B. Xing, M. -F. Choi, Z. Zhou, B. Xu, *Langmuir* **2002**, *18*, 9654–9658.

[100] T. Feldner, M. Häring, S. Saha, J. Esquena, R. Banerjee, D. D. Díaz, *Chem. Mater.* **2016**, *28*, 3210−3217.

[101] a) F. Rodriguez, J. F. Miravet, B. Escuder, *Chem. Commun.* **2009**, 7303–7305; b) T. Tu, W. Assenmacher, H. Peterlik, R. Weisbarth, M. Nieger, K. H. Dötz, *Angew. Chem. Int. Ed.* **2007**, *46*, 6368–6371.

[102] a) K. Mitsumoto, J. M. Cameron, R. -J. Wei, H. Nishikawa, T. Shiga, M. Nihei, G. N. Newton, H. Oshio, *Chem. Eur. J.* **2017**, *23*, 1502–1506; b) S. Kawano, N. Fujita, S. Shinkai, *J. Am. Chem. Soc.* **2004**, *126*, 8592–8593.

[103] a) N. Job, S. D. Lambert, A. Zubiaur, C. Cao, J. -P. Pirard, *Catalysts* **2015**, *5*, 40–57 b) S. M. Fields, *Anal. Chem.* **1996**, *68*, 2709–2712; c) V. R. Kaufman, D. Avnir, *Langmuir* **1986**, *2*, 717–722.

[104] a) A. Freytag, S. Sánchez-Paradinas, S. Naskar, N. Wendt, M. Colombo, G. Pugliese, J. Poppe, C. Demirci, I. Kretschmer, D. W. Bahnemann, P. Behrens, N. C. Bigall, *Angew. Chem. Int. Ed.* **2016**, *55*, 1200–1203; b) L. Wu, Y. Huang, Z. Wang, L. Liu, H. Xu, *Appl. Surf. Sci.* **2010**, *256*, 5973–5977; c) C. J. Lee, G. S. Kim, S. H. Hyun, *J. Mater. Sci.* **2002**, *37*, 2237–2241.

[105] a) H. Long, A. Harley-Trochimczyk, T. Pham, Z. Tang, T. Shi, A. Zettl, C. Carraro, M. A. Worsley, R. Maboudian, *Adv. Funct. Mater.* **2016**, *26*, 5158–5165; b) F. Rechberger, F. J. Heiligtag, M. J. Süess, M. Niederberger, *Angew. Chem. Int. Ed.* **2014**, *53*, 6823–6826; c) T. F. Baumann, M. A. Worsley, T. Y. -J. Han, J. H. Satcher Jr., *J. Non-Cryst. Solids* **2008**, *354*, 3513–3515.

[106] M. Tabata, H. Kawai, H. Yano, E. Imai, H. Hashimoto, S.-I Yokobori, A. Yamagishi, *J. Sol-Gel Sci. Technol.* **2016**, *77*, 325–334; b) D. J. Boday, R. J. Stover, B. Muriithi, D. A. Loy, *J. Mater. Sci.* **2011**, *46*, 6371–6377; c) R. Pool, *Science* **1990**, *247*, 807–807.

[107] a) https://goo.gl/AoKo5Z; b) https://goo.gl/R8KVg7; c) L. S. White, M. F. Bertino, G. Kitchen, J. Young, C. Newton, R. Al-Soubaihi, S. Saeed, K. Saoud, *J. Mater. Chem. A* **2015**, *3*, 762–772; d) https://goo.gl/0Ym4Yc.

[108] a) Y. Kong, X. Shen, S. Cui, M. Fan, *Ceram. Int.* **2014**, *40*, 8265–8271; b) Y. Tokudome, K. Nakanishi, K. Kanamori, K. Fujita, H. Akamatsu, T. Hanada, *J. Colloid Interf. Sci.* **2009**, *338*, 506–513; c) P. Jeevanandam, K. J. Klabunde, *Langmuir* **2002**, *18*, 5309–5313.

[109] a) H. Cai, S. Sharma, W. Liu, W. Mu, W. Liu, X. Zhang, Y. Deng, *Biomacromolecules* **2014**, *15*, 2540−2547; b) T. Horikawa, J. Hayashi, K. Muroyama, *Carbon* **2004**, *42*, 1625–1633; c) F. Placin, J. -P. Desvergne, F. Cansell, *J. Mater. Chem.* **2000**, *10*, 2147–2149.

[110] M. Betz, C. A. García-González, R. P. Subrahmanyam, I. Smirnova, U. Kulozik, *J. of Supercritical Fluids* **2012**, *72*, 111–119.

[111] a) S. Henning, L. Kühn, J. Herranz, M. Nachtegaal, R. Hübner, M. Werheid, A. Eychmüller, T. J. Schmidt, *Electrochim. Acta* **2017**, *233*, 210–217; b) M. K. Kundu, T. Bhowmik, S. Barman, *J. Mater. Chem. A* **2015**, *3*, 23120–23135.

[112] a) H. Sun, Z. Xu, C. Gao, *Adv. Mater.* **2013**, *25*, 2554–2560; b) M. A. Worsley, P. J. Pauzauskie, T. Y. Olson, J. Biener, J. H. Satcher, Jr., T. F. Baumann, *J. Am. Chem. Soc.* **2010**, *132*, 14067–14069; c) S. A. Al-Muhtaseb, J. A. Ritter, *Adv. Mater.* **2003**, *15*, 101–114.

[113] a) Y. -J. Wan, P. -L. Zhu, S. -H. Yu, R. Sun, C. -P. Wong, W. -H. Liao, *Carbon* **2017**, *115*, 629–639; b) H. Yin, C. Zhang, F. Liu, Y. Hou, *Adv. Funct. Mater.* **2014**, *24*, 2930–2937; c) H. Hu, Z. Zhao, W. Wan, Y. Gogotsi, J. Qiu, *ACS Appl. Mater. Inter.* **2014**, *6*, 3242−3249.

[114] a) A. Angulo-Ibáñez, G. Beobide, O. Castillo, A. Luque, S. Pérez-Yáñez, D. Vallejo-Sánchez, *Polymers* **2016**, *8*, 16–28; b) A. Ahmed, M. Foster, R. Clowes, P. Myers, H. Zhang, *Chem. Commun.* **2014**, *50*, 14314–14316.

[115] a) E. Cuce, P. M. Cuce, C. J. Wood, S. B. Riffat, *Renew. Sust. Energ. Rev.* **2014**, *34*, 273–299; b) R. Baetens, B. P. Jelle, A. Gustavsen, *Energ. Buildings* **2011**, *43*, 761–769.

[116] a) P. Hao, Z. Zhao, J. Tian, H. Li, Y. Sang, G. Yu, H. Cai, H. Liu, C. P. Wong, A. Umar, *Nanoscale* **2014**, *6*, 12120–12129; b) S. J. Kim, S. W. Hwang, S. H. Hyun, *J. Mater. Sci.* **2005**, *40*, 725–731.

[117] a) Y. -J. Wan, P. -L. Zhu, S. -H. Yu, R. Sun, C. -P. Wong, W. -H. Liao, *Carbon* **2017**, *115*, 629–639; b) N. Bheekhun, A. R. A. Talib, M. R. Hassan, *Adv. Mater. Sci. Eng.* **2013**, *2013*, 1–18.

[118] a) H. Maleki, *Chem. Eng. J.* **2016**, *300*, 98–118; b) Z. Wang, P. Jin, M. Wang, G. Wu, C. Dong, A. Wu, *ACS Appl. Mater. Inter.* **2016**, *8*, 32862–32868.

[119] M. Tabata, I. Adachi, Y. Hatakeyama, H. Kawai, T. Morita, T. Sumiyoshi, *J. of Supercritical Fluids* **2016**, *110*, 183–192.

[120] a) J. Kaur, M. Sharma, O. P. Pandey, *Superlattices Microst.* **2015**, *77*, 35–53; b) N. V. Hullavarad, S. S. Hullavarad, P. C. Karulkar, *J. Nanosci. Nanotechno.* **2008**, *8*, 3272–3299.

[121] a) K. P. Kuhl, T. Hatsukade, E. R. Cave, D. N. Abram, J. Kibsgaard, T. F. Jaramillo, *J. Am. Chem. Soc.* **2014**, *136*, 14107–14113; b) I. Ganesh, *Renew. Sust. Energ. Rev.* **2014**, *31*, 221–257.

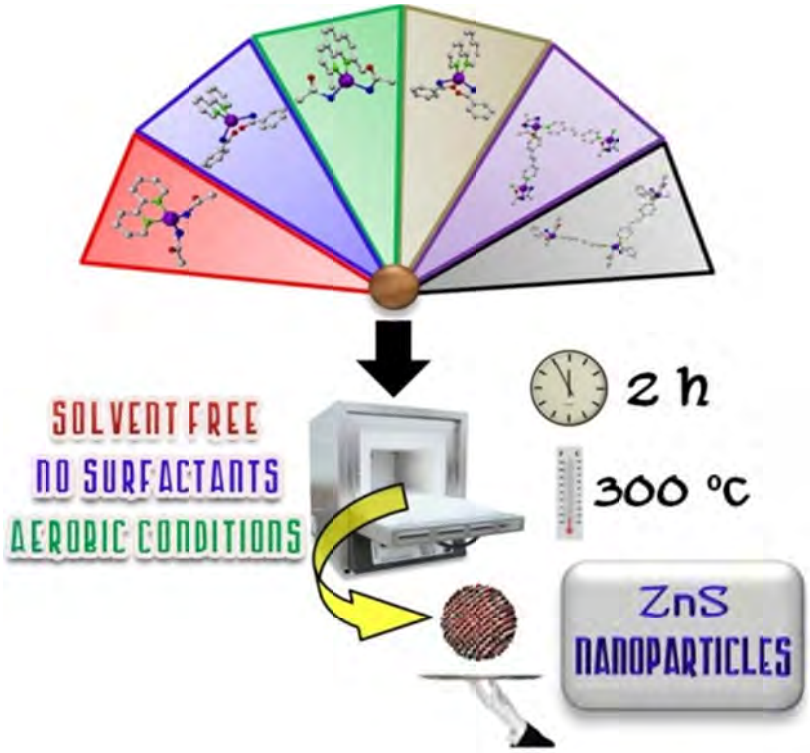

2. ZINC-THIOCARBOXYLATE COMPLEXES AS PRECURSORS FOR ZINC SULFIDE NANOPARTICLES UNDER AEROBIC CONDITIONS

2.1. SUMMARY

As detailed in section 1.4 of the general introduction, chapter two describes the first approach to obtain metal sulfide nanoparticles from the aerobic combustion of zinc-thiocarboxylato complexes with *N,N'*-heterocycles as secondary ligands. The first part is devoted to the synthesis, chemical and structural characterization of six new compounds with the formula $[Zn(SCOR)_2(N–N)]$ [R = $–CH_3$ (TAc), $–C_6H_5$ (TBn); N–N = 2,2'-bipyridine (BPY), 1,10-phenanthroline (PHEN), 1,2-bis(4-pyridyl)ethylene (BPE), neocuproine (NEO)] obtained by the reaction of $Zn(CH_3COO)_2{\cdot}2H_2O$ with the corresponding pyridine derivative and thiocarboxylate in methanol in the ratio Zn/SCOR/N–N = 1:2:1. In all compounds, the metal atom is bonded to sulfur atoms of two thiocarboxylato ligands and to two nitrogen atoms from one pyridine derivative imposing a distorted-tetrahedral ZnS_2N_2 coordination sphere. The use of chelating dipyridine ligands leads to discrete monomeric entities in compounds $[Zn(TAc)_2(BPY)]$ (1), $[Zn(TBn)_2(BPY)]$ (2), $[Zn(TAc)_2(NEO)]$ (3), and $[Zn(TBn)_2(PHEN)]$ (4). On the contrary, the bridging capability of the dipyridine BPE ligand gives rise to the polymeric chains observed in compounds $[Zn(TAc)_2(\mu\text{-BPE})]_n$ (5) and $[Zn(TBn)_2(\mu\text{-BPE})]_n$ (6).

Numerous complexes of organosulfur ligands have been studied as precursors for the deposition of II/VI type semiconductor materials. In this sense, the presence of direct zinc–sulfur bonds is a key factor to use these compounds as single-source precursors for the synthesis of nanometric metal sulfide particles. Thiocarboxylates fulfill the above mentioned requirement and have demonstrated an enormous potential as single-source precursors. However, despite works reported to date requiring an inert gas to prepare the metal–chalcogenide NPs from single-source precursors, we make use of dry thermolysis under aerobic conditions to achieve ZnS nanoparticles. The second part of this chapter deals with these decomposition studies under different atmospheres and the subsequent analysis of

the produced ZnS nanoparticles (purity, average size, crystalline phase, degree of agglomeration, etc.). These studies have demonstrated the feasibility of soft thermolysis treatment (300ºC) under air atmosphere conditions to achieve ZnS nanoparticles. The crystallite size measurements indicate the suitability of this method to obtain particles with a diameter below 10 nm. Semiconductor nanoparticles with a diameter of 1–20 nm are of particular interest since they represent the transition regime between solid-state and molecular or cluster physics.

On the other hand, the nature of the starting zinc(II)-thiocarboxylato precursor seems to exert a crucial influence on the final blende or wurtzite crystalline phase of the resulting ZnS nanoparticles, as compounds with π-extended systems such as phenanthroline or neocuproine give rise to a wurtzite phase, whereas the less extended 2,2'-bipyridine provides the blende phase. The 1,2-bis(4-pyridyl)ethylene ligand seems to be midway, since depending on the thiocarboxylate it provides blende (for thioacetate) or wurtzite (for thiobenzoate).

The results, which demonstrate the feasibility of the soft thermolysis under aerobic conditions to afford metal sulfide nanoparticles, were published in the *European Journal of Inorganic Chemistry* (year 2013, pp. 5592–5602). The corresponding article and its supporting material are gathered below. They also provide the basis for a further study in chapter 3.

2.2. PUBLICATION

EurJIC European Journal of Inorganic Chemistry
ChemPubSoc Europe
FULL PAPER

DOI:10.1002/ejic.201300649

Zinc Thiocarboxylate Complexes as Precursors for Zinc Sulfide Nanoparticles under Aerobic Conditions

Daniel Vallejo-Sánchez,[a] Garikoitz Beobide,*[a] Oscar Castillo,*[a] and Mónica Lanchas[a]

Keywords: Zinc / Thiocarboxylates / Nanoparticles / Dry thermolysis / Heterocycles

Six new compounds with the formula $[Zn(SCOR)_2(N–N)]$ [R = $–CH_3$ (TAc), $–C_6H_5$ (TBn); N–N = 2,2′-bipyridine (BPY), 1,10-phenanthroline (PHEN), 1,2-bis(4-pyridyl)ethylene (BPE), neocuproine (NEO)] have been obtained by the reaction of $Zn(CH_3COO)_2·2H_2O$ with the corresponding pyridine derivative and thiocarboxylate in methanol in the ratio Zn/SCOR/N–N = 1:2:1. In all compounds, the metal atom is bonded to sulfur atoms of two thiocarboxylato ligands and to two nitrogen atoms from one pyridine derivative imposing a distorted-tetrahedral geometry. The use of chelating dipyridine ligands leads to discrete monomeric entities in compounds $[Zn(TAc)_2(BPY)]$ (**1**), $[Zn(TBn)_2(BPY)]$ (**2**), $[Zn(TAc)_2(NEO)]$ (**3**), and $[Zn(TBn)_2(PHEN)]$ (**4**). On the contrary, the bridging capability of the dipyridine BPE ligand gives rise to the polymeric chains observed in compounds $[Zn(TAc)_2(\mu\text{-BPE})]$ (**5**) and $[Zn(TBn)_2(\mu\text{-BPE})]$ (**6**). The occurrence of Zn···O weak interactions is rationalized on the basis of the $\nu_{C=O}$ shift and continuous shape measurements. Additionally, the present work demonstrates how ZnS nanoparticles can be obtained by dry thermolysis of the prepared thiocarboxylate complexes under aerobic conditions and moderate temperatures (300 °C). The analysis of the X-ray diffraction pattern and SEM/TEM images reveals the presence of ZnS crystallites below 10 nm. The influence of the N-heterocycle and thiocarboxylato ligands on the crystalline phase (blende or wurtzite), size, and purity of the resulting zinc sulfide nanoparticles is discussed.

Introduction

Thiocarboxylates are an interesting class of ligands that exhibit a large variety of coordination modes due to the presence of both soft sulfur and hard oxygen donor sites (Figure 1).[1] Thus, with group XII metals, as they are relatively soft ions, the sulfur atom is typically joined in a monodentate fashion to the metal center. Despite the zinc(II) ion being a borderline case and possessing an intermediate hardness, given its small size it generally binds through the bulkier sulfur atom.[2]

Nanocrystalline semiconductors with a particle size below 20 nm, also referred to as quantum dots (QDs), have gained considerable interest over the last decades due to their countless technological applications in different fields of chemistry and physics.[3] The small size of quantum dots results in the three-dimensional confinement of the charge carriers and the corresponding transformation of the bulk energy bands into discrete energy states.[4] This bulk-to-molecule transition is continuous, such that the band gap of the nanocrystalline material can be tuned to a desired energy controlling the particle size, and, thus, materials with customized optoelectronic properties can be created.[5] An important class of QDs are metal sulfides. Nanosized ZnS

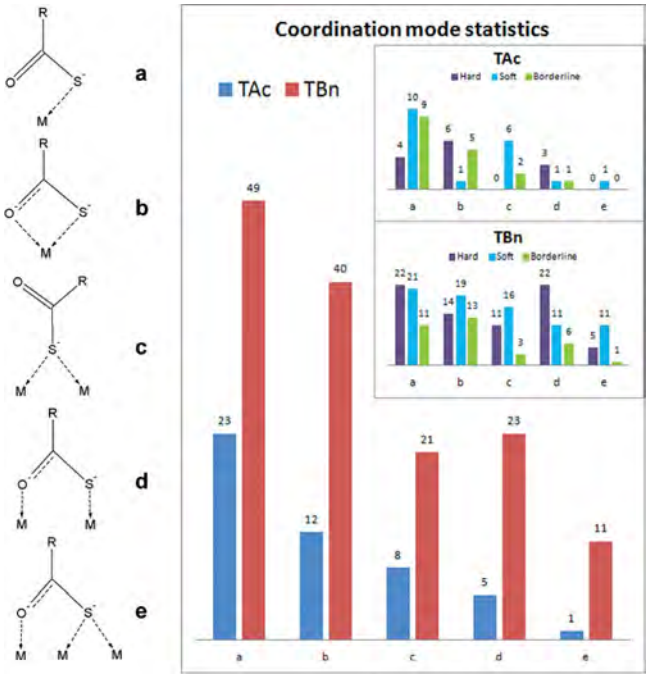

Figure 1. CSD database[8] coordination mode statistics for thiocarboxylato ligands coordinated to metals classified according to Pearson's hardness.[9]

[a] Departamento de Química Inorgánica, Facultad de Ciencia y Tecnología, Universidad del País Vasco (UPV/EHU), Apartado 644, 48080 Bilbao, Spain
E-mail: oscar.castillo@ehu.es
http://www.ehu.es/

Supporting information for this article is available on the WWW under http://dx.doi.org/10.1002/ejic.201300649.

particles, especially, exhibit a wide band gap and excellent optical properties.[6] These attributes make ZnS nanoparticles an excellent candidate for a wide range of applications in sensors, displays, electronic devices, laser devices, nonlinear optical devices, etc.[7]

To date, many techniques for preparing transition-metal sulfide nanoparticles (NPs) have been developed. Among them those that stand out are solvothermal processes,[10] metal–organic chemical vapor deposition (MOCVD),[11] microemulsions,[12] sol–gel methods,[13] spray pyrolysis,[14] and single-source precursor routes.[15] The last technique consists of employing coordination compounds as starting material with metal–chalcogenide bonds already available in the structure. The starting material is dispersed in a coordinating solvent (usually amines or amides) for later injection onto a hot solution containing a surfactant.[16] The role of the surfactant is to stabilize these nanoparticles and control their growth. This synthetic route has the advantage of being simple and allows nanoparticles with narrow size distributions to be obtained. However, several studies have shown that it can go further using a dry thermolysis under an inert gas to obtain NPs and avoiding, in this way, the use of surfactant molecules. The use of moderate temperatures during the decomposition of the precursor prevents the sintering of the NPs.[17] This solvent-free synthesis has a relatively low cost and precludes the use of toxic and environmentally unfriendly organic solvents and/or surfactant molecules. During the dry thermolysis, it was found that in the heating process the ligands passivate the surface of the particle limiting its growth and – as a consequence – determining its size.[18] The kind of ligand also influences the final phase and crystallinity of the achieved metal chalcogenide.[19] However, when working at relatively low temperatures the percentage of impurities is generally quite high because of the lack of sufficient energy to complete the elimination of the ligands.

Numerous complexes of chalcogenide-containing ligands have been studied as precursors for the deposition of II/VI-type semiconductor materials.[20] These include thiocarboxylates, which have demonstrated an enormous potential as single-source precursors because of their high volatility at moderate temperatures and their ability to establish direct metal–chalcogenide bonds.[21]

In the present work we have synthesized and structurally characterized six new Zn^{II} compounds based on thiocarboxylato ligands and pyridine derivatives with a ZnS_2N_2 coordination sphere. Despite works reported to date requiring an inert gas to prepare the metal–chalcogenide NPs from single-source precursors, we make use of dry thermolysis under aerobic conditions to achieve the ZnS nanoparticles.

Results and Discussion

Mononuclear Zn^{II} complexes are obtained when thiocarboxylate is used in the presence of chelating N-heterocycles, while polymeric complexes are grown when bridging N-heterocycles are employed. A common feature of all the complexes is the N_2S_2 coordination environment that resembles a distorted tetrahedron (Table 1). However, there are also weaker interactions between the metal center and the oxygen atom of the thiocarboxylato groups, with Zn···O distances (2.74–3.26 Å) close, and in some cases shorter than the sum of the van der Waals radii (2.91 Å). Further evidence of this interaction is that compounds with shorter Zn···O contacts also present the more elongated C=O bond length, an effect that is also reflected in the IR spectra by a displacement of ν(C=O) towards longer wavelengths (Table 2). This interaction also affects the coordination geometry as compounds with closer Zn···O contacts present

Table 1. Selected bond lengths [Å] for compounds **1**–**6**.

Compound	**1**	**2**	**3**	**5**	**6**
Zn(1)–N(1)	2.078(1)	2.095(2)	2.076(2)	2.057(2)	2.064(1)
Zn(1)–S(1)	2.2970(4)	2.2959(5)	2.2859(5)	2.072(2)	2.052(2)
Zn(1)–N(2)		2.098(2)	2.052(2)	2.2932(8)	2.2780(5)
Zn(1)–S(2)		2.2989(5)	2.2937(5)	2.3024(8)	2.3136(5)
Compound **4**[a]		D_{max}	D_{min}	D_{mean}	
Zn(1)–N(1)		2.109(3)	2.104(3)	2.106(3)	
Zn(1)–S(1)		2.297(5)	2.291(5)	2.294(5)	

[a] Compound **4** presents an incommensurate crystal structure (see Experimental Section).

Table 2. Correlation between the Zn···O distance [Å], the C=O tension vibration wavenumber [cm^{-1}], and deviations from the ideal geometries.

Compound	Zn···O [Å]	$\nu_{C=O}$ [cm^{-1}]	S_{TET}[a]	S_{OC}[a]
Thioacetato-based compounds				
1	2.880(1)	1615	3.5	16.7
3	3.122(1)/3.156(1)	1624/1635	2.9	27.6
5	3.066(3)/3.257(3)	1612/1627	1.3	17.5
Thiobenzoato-based compounds				
2	2.792(1)	1605	3.8	13.9
4	2.740(2)	1620	4.1	12.5
6	3.035(2)	1612	1.3	18.3

[a] Deviations from ideal tetrahedral (T_d) and octahedral (O_h) geometries calculated from continuous shape measurements.[22]

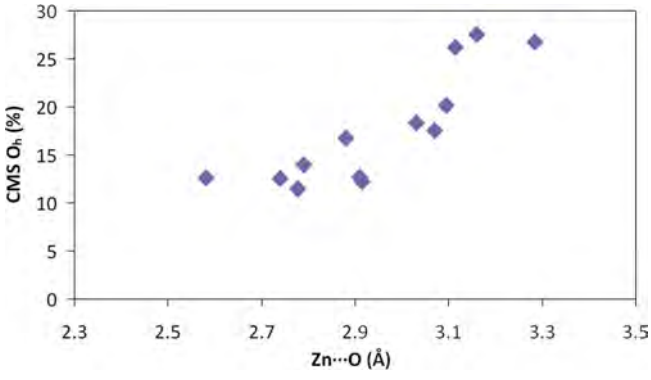

Figure 2. Correlation between the Zn···O distance and the deviation from the octahedral geometry determined from continuous shape measurements for zinc thiocarboxylate complexes with a $ZnS_2N_2(O_2)$ coordination sphere.

larger deviations with regard to the ideal tetrahedral geometry, while the trend is inverted for an octahedral geometry when a hexacoordination is assumed. In fact, a perusal of the CSD database for other thioacetate/thiobenzoate complexes with aromatic diazines that present a $ZnS_2N_2(O_2)$ coordination environment corroborates this trend as can be observed in Figure 2.

Structures of Compounds 1–3

Compounds **1**–**3** contain monomeric entities in which the metal center is tetrahedrally coordinated to two sulfur atoms belonging to two thiocarboxylato ligands and to two N atoms of the chelating pyridine derivative (Figure 3). The main difference of the coordination environment of the Zn^{II} center is the semicoordination distance with the oxygen atom of the thiocarboxylate. The steric hindrance of the chelating diimine ligand clearly affects the resulting Zn···O approach. The methyl groups of the neocuproine ligand weaken this interaction giving rise to a weaker contact for compound **3** (3.12 Å) than for compounds containing the nonsubstituted 2,2′-bipyridine ligand (2.88 and 2.79 Å for compounds **1** and **2**, respectively). In any case, the bond length values found here are similar to those observed for analogous compounds.

Obviously, the different nature of the N-heterocyclic and thiocarboxylato ligands leads to supramolecular crystal structures that differ considerably. The cohesiveness of the crystal structure of compound **1** is sustained by a combination of weak hydrogen-bonding interactions involving the aromatic C–H groups as donors and the oxygen and sulfur atoms of the thiocarboxylate as acceptors. The symmetrically related double hydrogen bond between the C(6) –H groups and the sulfur atoms of an adjacent entity generates a supramolecular chain of monomers running along the *b* axis. These chains are further connected by means of C(4)–H···O hydrogen bonds. There is no evidence of π–π interactions between pyridine rings of the 2,2′-bipyridine molecules. In compound **2**, non-classic C–H···S and C–H···O hydrogen-bonding interactions appear along with the π–π interactions. The hydrogen-bonding interactions lead to supramolecular sheets spreading along the *ac* plane. These layers pile up one above the other interacting by means of edge-to-face π–π interactions involving the aromatic rings of the thiobenzoato and 2,2′-bipyridine ligands. In compound **3**, the steric hindrance of the neocuproine ligand avoids the presence of C–H···S hydrogen-bonding interactions. The overall cohesiveness of the compound is therefore achieved through C(9)–H···O1 and C(12)–H···O2 hydrogen bonds that give rise to sheets parallel to the *bc* plane. Surprisingly, although the sulfur atoms of the thioacetato ligand are pointing outwards of the sheets, these are held together only by means of weak van der Waals interactions.

Structure of Compound 4

Given the incommensurable nature of compound **4**, we proceed to describe its average structure, for subsequently, analyze the structural fluctuations induced by the modulation vector. The compound consists of monomeric axiosymmetric entities, where the metal center shows a slightly distorted tetrahedral coordination environment formed by the two nitrogen atoms of a PHEN ligand and two sulfur atoms from two thiobenzoato ligands (Figure 4). The values of the coordination bond lengths are within the range observed in complexes **1**–**3**. The crystal structure is stabilized by π–π interactions between pyridine rings from PHEN ligands of adjoining monomeric entities (shorter distances: ca. 3.50 Å) and through C–H···O-type hydrogen bonds between the aromatic carbon atoms of PHEN (C6) and the oxygen atoms of the thiobenzoato ligands (O1).

Induced modulation incommensurability translates into a change in relative position and orientation of the monomers, as shown in Figures 4a, b, and c, which, moreover, also affects the bond lengths and angles. This variation is most pronounced in the case of the semi-coordinating oxygen atom (2.74–2.85 Å). Figure 3e shows the modulation of the electron density in the vicinity of the metal center.

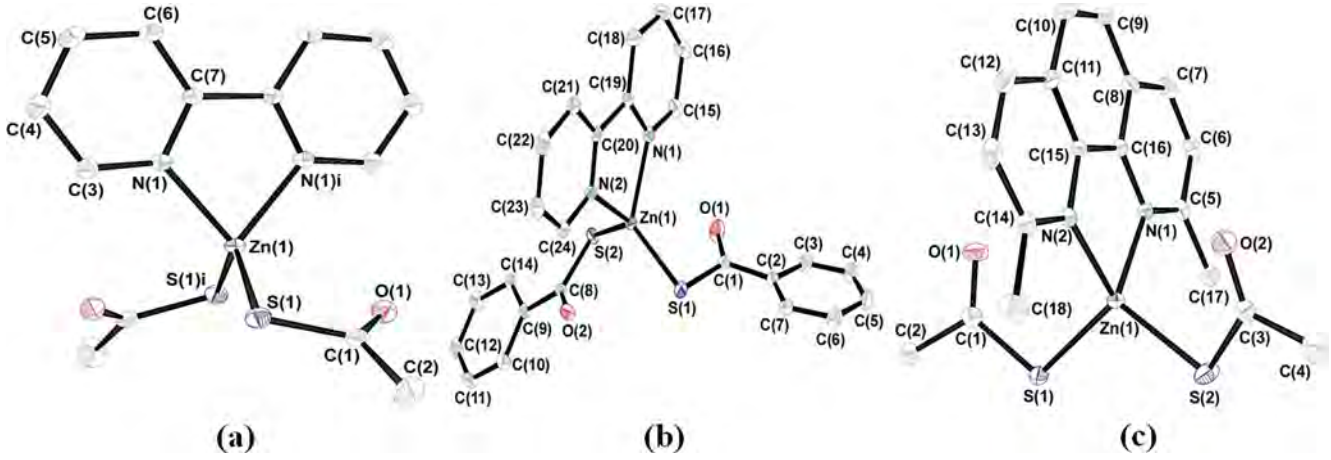

Figure 3. ORTEP diagrams of compounds **1** (a), **2** (b), and **3** (c); hydrogen atoms are omitted for clarity.

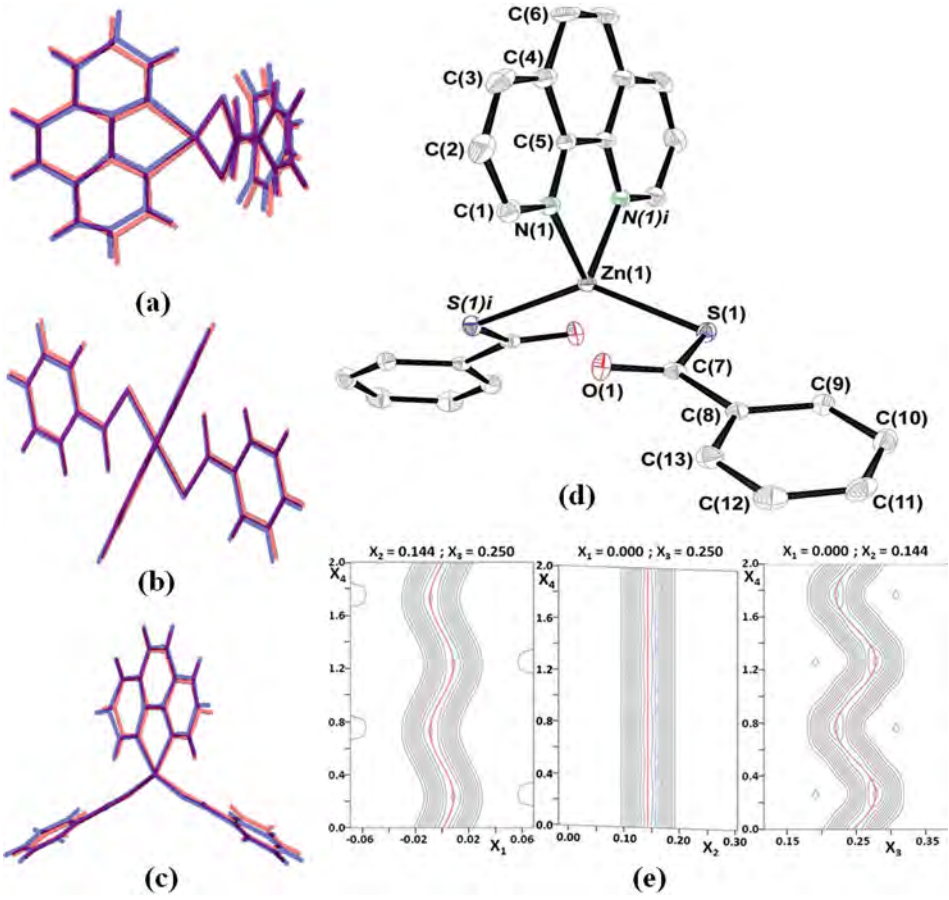

Figure 4. Maximum discrepancy between the two boundary orientations of the mononuclear entity projected along the crystallographic axes *a* (a), *b* (b), and *c* (c). (d) Monomeric complex of compound **4**. (e) Electron density cuts around the Zn atom in compound **4**.

Structures of Compounds 5 and 6

Compounds **5** and **6** present a polymeric structure where neutral units [Zn(RCOS)$_2$] (R: methyl and phenyl, respectively) are joined through BPE ligands forming zigzag chains (Figure 5). The N_2S_2 distorted tetrahedral coordination environment of Zn^{II} is composed of the sulfur atoms of two thiocarboxylate ligands and the nitrogen atoms of two symmetrically equivalent BPE ligands. As is the case for monomeric complexes, despite the fact that the $RCOS^-$ anion is bonded in a monodentate manner through its sulfur atom, a weak semi-coordination of its oxygen atoms with Zn···O distances ranging from 3.03 to 3.26 Å is present. In compound **5** the Zn atom is displaced by 0.54 and 0.79 Å from the mean plane of the thioacetato ligand due to the steric hindrance between its methyl group and the pyridine group of the BPE ligand. On the other hand, the rotation of the phenyl group of the thiobenzoato ligand overcomes the cited steric hindrance, and the Zn^{II} atom only deviates slightly from the ligand plane (0.22 and 0.50 Å). With regard to the intramolecular Zn···Zn distance, both compounds show a similar value (13.458 and 13.454 Å, respectively).

Polymeric chains of compound **5** run along the [11$\bar{1}$] and [011] crystallographic directions with an intersecting angle of 71.73°, while in compound **6** they spread along the [$\bar{1}$11] and [111] directions with an almost perpendicular crossing angle (86.09°). In addition, whenever chains intersect they establish two C–H···O hydrogen bonds involving a pyridine C–H group and the ethylene group as hydrogen donors and the oxygen atom of the thiocarboxylate as the acceptor of both hydrogen bonds. Likewise, π–π interactions are present between the ethylene group and pyridine ring of adjacent chains (closest contacts: 3.36–3.48 Å). All these supramolecular interactions provide the necessary cohesion to the crystal structure.

Dry Thermolysis Experiments

The thermal degradation in a synthetic air environment shows (Figure 6) that all the compounds start their decomposition at relatively low temperatures (**1**: 157 °C; **2**: 177 °C; **3**: 200 °C; **4**: 175 °C; **5**: 140 °C; **6**: 175 °C). The two lower values correspond to those containing the thioacetato ligand, all with BPY or BPE (compounds **1** and **5**). This

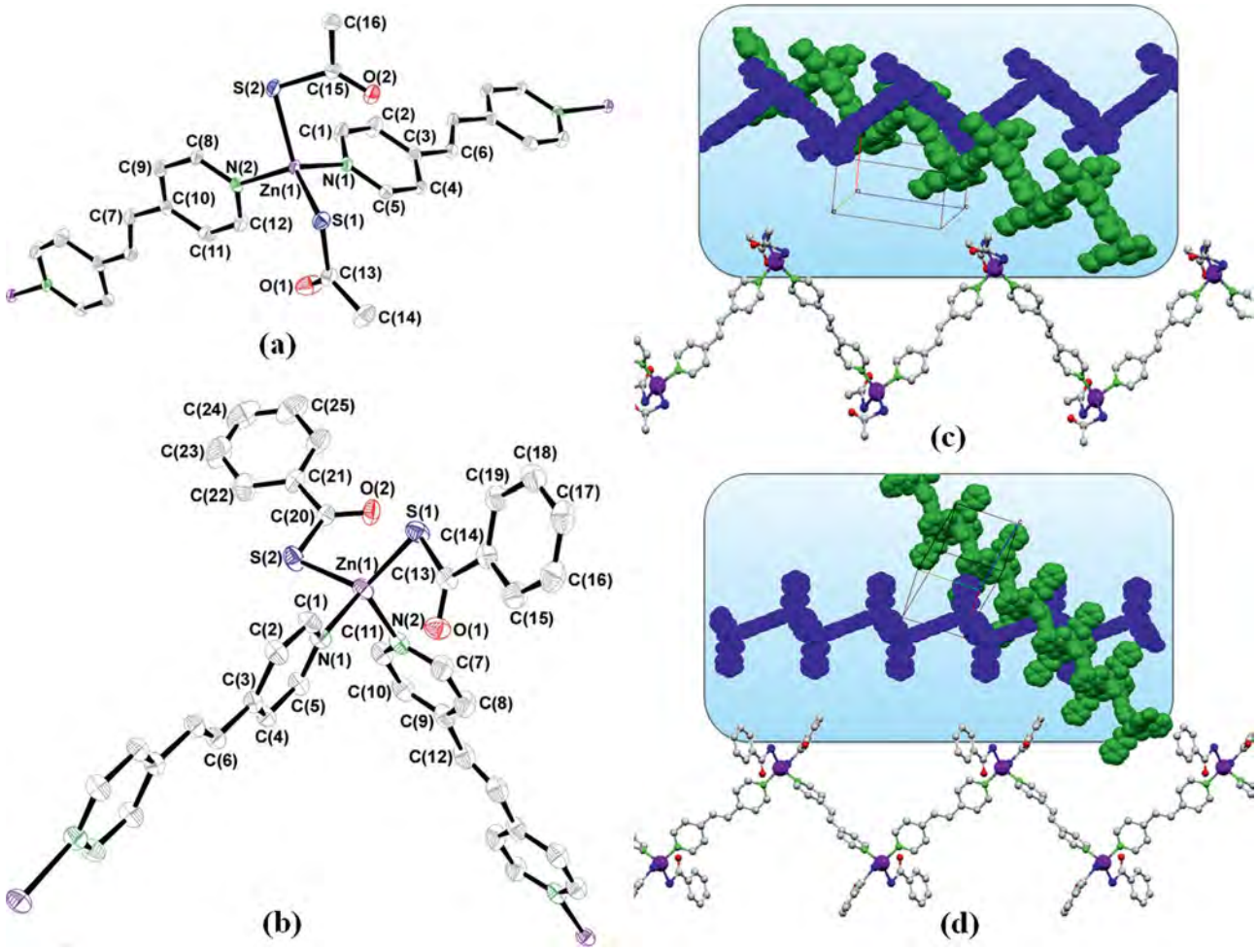

Figure 5. ORTEP diagrams of the asymmetric units of compounds **5** (a) and **6** (b). Cross-linking chain fragments in compounds **5** (c) and **6** (d).

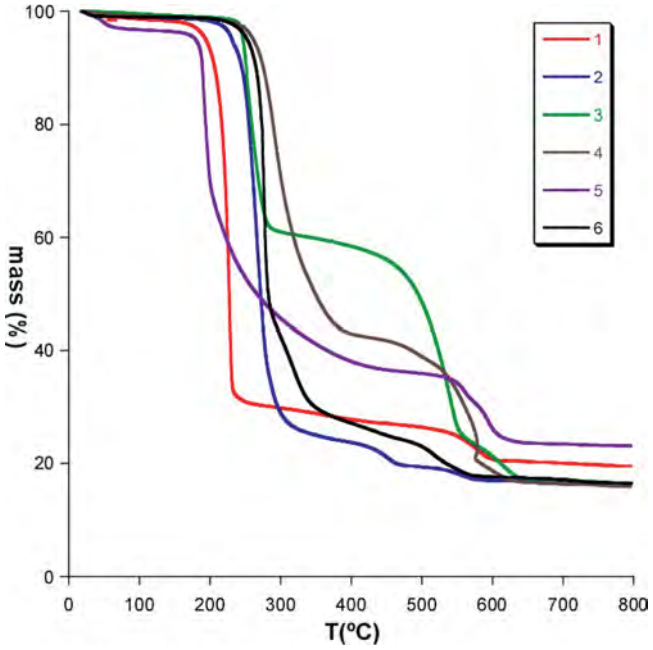

Figure 6. Thermogravimetric analysis of zinc thiocarboxylate compounds under a synthetic air environment.

observation is relatively common, because the thioacetate salts are usually less stable than the thiobenzoate ones.[23] However, it is worth noting that for compound **3** the use of neocuproine, a bulkier chelating ligand with methyl groups adjacent to the nitrogen donor atoms, protects the thiocarboxylate functional group increasing its thermal stability to temperatures higher than those found for the thiobenzoate ones (compounds **2**, **4**, and **6**). After the first mass loss all compounds achieve a more or less stable plateau that corresponds to a variable mixture of ZnS and amorphous carbon. The amount of carbon accompanying the ZnS, ranging from 5 to 32%, depends on the starting material. Compounds **3** and **4**, containing the ligands with the most extended π-systems, neocuproine and phenanthroline, respectively, are notorious for needing a larger amount of carbon. At temperatures between 450 and 650 °C these intermediates are further oxidized to give ZnO (JCPDS No. 89-0511) as the final product. Additional thermoanalytical data are available in the Supporting Information.

Therefore, these thermogravimetric (TG) measurements show that by controlling the decomposition process it is possible to obtain ZnS even under aerobic conditions. It is worth noting that, as far as we are concerned, all the dry

thermolysis processes reported to date make use of an inert gas in order to isolate the corresponding metal chalcogenide and to avoid the presence of undesired oxide compounds. Taking into account the results of the TG analyses, the ZnS samples were prepared by heating at a rate of 5 °C min^{-1} up to 300 °C and maintaining this temperature for 2 h, with the exception of compound **4** for which the temperature plateau was extended up to 24 h. The X-ray diffraction profiles, with very broad peaks, clearly reveal the nanometric nature of the crystalline domains (Figure 7). The resulting ZnS obtained from compounds **1**, **2**, and **6** correspond to blende (JCPDS: 80-0020; $F\bar{4}3m$; a = 5.420 Å), whereas those obtained from compounds **3** and **4** correspond to the wurtzite polymorph (JCPDS: 80-0007; $P6_3mc$; a = 3.82 Å and c = 6.26 Å). For the thermolysis product of compound **5** the shape and asymmetry of the diffraction peaks suggest a wurtzite main contribution, although the minor presence of a blende phase cannot be disregarded.

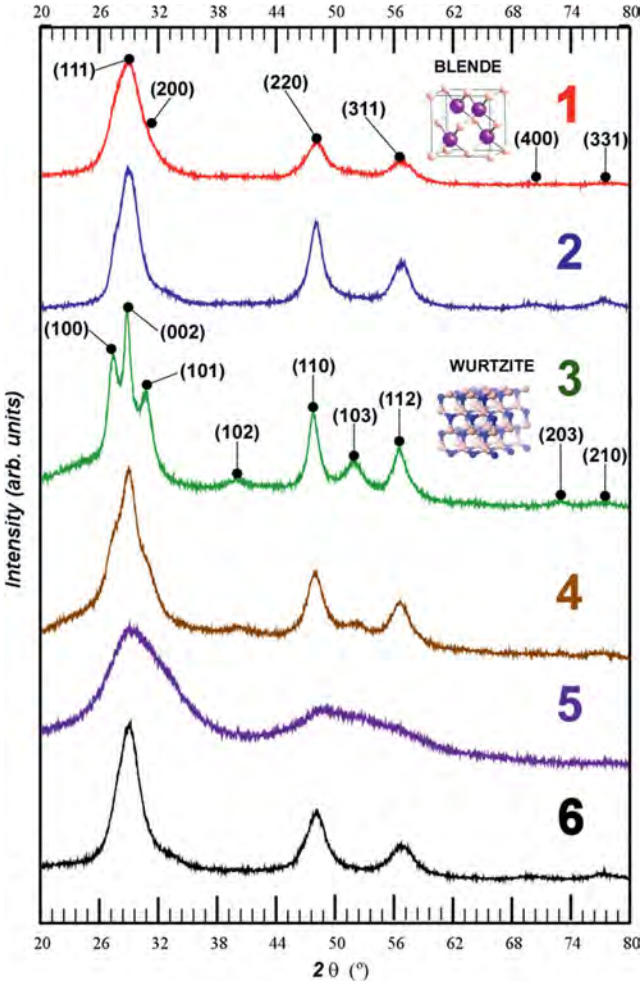

Figure 7. X-ray diffraction patterns of dry thermolysis products obtained at 300 °C under aerobic conditions. Blende (cubes); wurtzite (hexagons).

At 298 K and 1 atm, bulk ZnS polymorphs of wurtzite and blende have a Gibbs free-energy difference of 10.25 kJ mol^{-1},[24] which reflects the higher stability of blende compared with wurtzite. The transformation from the blende to the wurtzite phase occurs at 1020 °C.[25] However, with decreasing particle size, surface energy starts to

Table 3. Scherrer expression-based crystallite size analysis.[a]

Precursor	Phase/JDPS	Reflection (*hkl*)	β [rad]	L_v [nm]	D_v [nm]
1	B/80-0020	(111)	0.0787	1.7	**2.3**
2	B/80-0020	(111)	0.0513	2.6	**3.4**
3	W/80-0007	(110)	0.0234	5.3	**7.1**
4	W/80-0007	(110)	0.0563	2.5	**3.3**
6	B/80-0020	(111)	0.0861	1.6	**2.1**

[a] $L_V = K{\cdot}\lambda/\beta{\cdot}\cos\theta$, where L_V is the volume-weighted average crystallite size measured in a direction perpendicular to the surface of the specimen, λ is the average wavelength, in nanometers, of the K_α radiation of Cu (0.154252 nm), θ is the Bragg angle in radians, β (2θ) is the integral width of the diffraction peak in radians discounting the instrumental contribution, and K is the Scherrer constant, considered as 0.89 for spherical particles with cubic symmetry. The average diameter of particles (D_v) has been calculated from the $D_v = (4/3){\cdot}L_v$ expression. The crystallite size for compound **5** could not be estimated because of the great overlap of the (110) reflection with the neighboring peaks; however, the width of the diffraction peaks clearly indicates the presence of very small nanoparticles.

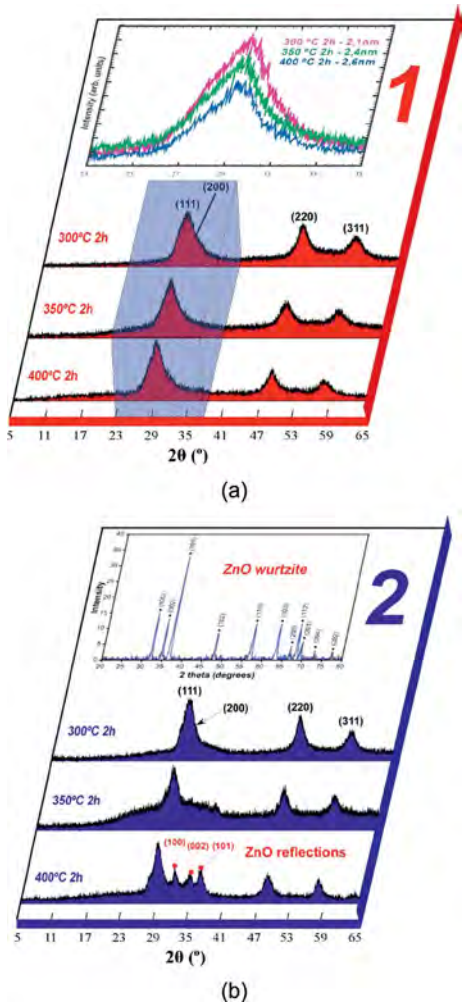

Figure 8. Diffractograms of ZnS nanoparticles obtained at different temperatures for compounds **1** (a) and **2** (b).

play an increasingly dominant role in determining structural stability. Therefore, the synthesis of the wurtzite phase nanoparticles at mild temperatures (far below its bulk transition temperature) becomes feasible as evidenced from the dry thermolysis of compounds **3**–**5** and by the examples reported by other research groups.[26]

The average crystal domain size of the as-synthesized nanoparticles was estimated from the Scherrer formula,[27] using the integral breadth[28] of the (111) reflection for the blende phase and (110) for the wurtzite one (Table 3). The results show average crystallite sizes in the range 1–7 nm.

In order to explore the influence of the dry thermolysis conditions in the nanoparticle, the size, time, and temperature parameters were modified. While the lengthening of the thermal-treatment time has no noticeable effect on the particle size, it allowed for purer metal chalcogenide samples to be obtained. On the other hand, higher temperatures promote a slight increase of the particle size and purity, but care must be taken, because some of the compounds show the presence of zinc oxide when higher temperatures are applied (Figure 8).

SEM images performed over the ZnS samples show nanometric conglomerates (below 100 nm) with a nanotexture that indicates the presence of extremely small crystallites (Figure 9a). TEM was employed to obtain a better insight into the conglomerates (Figure 9b, c, and d). Transmission micrographs show very tiny crystallites well below 10 nm embedded into an amorphous carbonaceous matrix. Statistical analysis of the TEM images provides the following ZnS particle sizes: 5.3 ± 1.1 (**1**), 3.2 ± 0.5 (**2**), 5.1 ± 1.3 (**3**), 5.2 ± 1.1 (**4**), 3.1 ± 0.5 (**5**), and 3.9 ± 0.9 nm (**6**). The measured interplanar distances match those expected for the blende and wurtzite structures, respectively. EDX analyses indicate the equimolar presence of zinc and sulfur atoms in addition to a relevant carbon contribution (ranging from 5 to 28% depending on the examined area; zones near nanoparticles present lower carbon content than those on the amorphous matrix).

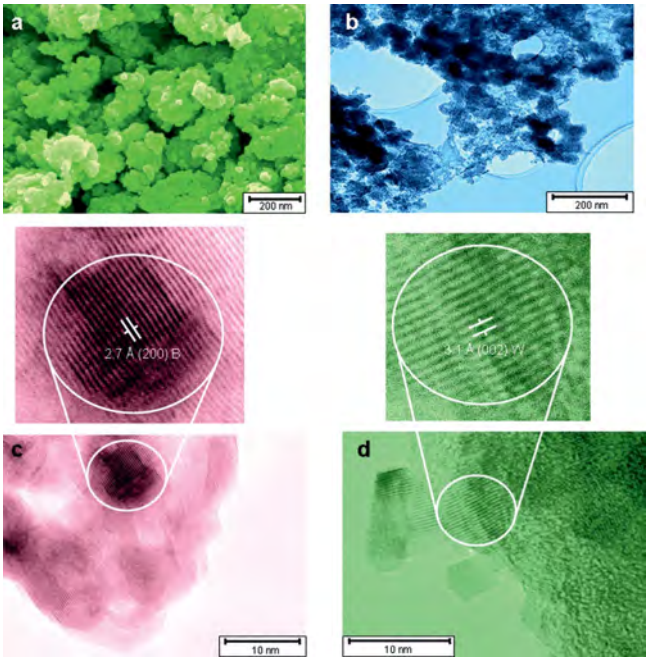

Figure 9. Thermolysis residues of compound **1** [SEM (a) and TEM (b,c)] and of compound **3** [TEM (d)].

Conclusions

We have obtained six different air-stable compounds based on thiocarboxylato ligands all with N-heterocycles to complete the coordination sphere of the Zn^{II} ion. The presence of direct zinc–sulfur bonds is a key factor to use these compounds as single-source precursors for the synthesis of nanometric chalcogenide particles. We have also demonstrated the feasibility of soft thermolysis treatment under open atmosphere conditions to achieve ZnS nanoparticles. Semiconductor nanoparticles with a diameter of 1–20 nm are of particular interest since they represent the transition regime between solid-state and molecular or cluster physics. The crystallite size measurements indicate the suitability of this method to obtain particles with a diameter below 10 nm.

On the other hand, the nature of the starting zinc thiocarboxylate precursor seems to exert a crucial influence on the final blende or wurtzite crystalline phase of the resulting ZnS nanoparticles, as compounds with π-extended systems such as phenanthroline or neocuproine give rise to a wurtzite phase, whereas the less extended 2,2′-bipyridine provides the blende phase. The 1,2-bis(4-pyridyl)ethylene ligand seems to be midway, since depending on the thiocarboxylate it provides blende (for thioacetate) or wurtzite (for thiobenzoate).

Experimental Section

General Information: Commercially available thioacetic acid (HTAc), thiobenzoic acid (HTBn), zinc acetate dihydrate, 2,2-bipyridine (BPY), 1,10-phenanthroline (PHEN), neocuproine (NEO), 1,2-bis(4-pyridyl)ethylene (BPE), and all the solvents were used as received. The new compounds are stable in air at room temperature. The yields calculated are based on the metal salt.

[$Zn(TAc)_2$(BPY)] (1): BPY (0.0937 g, 0.6 mmol) dissolved in MeOH (10 mL) was added slowly to a methanol solution (15 mL) containing zinc acetate (0.1317 g, 0.6 mmol). HTAc (84.4 μL, 1.2 mmol) was added to the reaction mixture to give a clear pale-yellow solution. Several minutes later, a whitish precipitate was obtained. The mixture was stirred for 2 h. The product was filtered in vacuo and washed with MeOH. The mother liquors were allowed to concentrate at room temperature to obtain colorless single crystals. Yield: 0.07454 g (33%). Main IR features of compound **1** (KBr pellet): $\tilde{\nu}$ = 3435 (sh), 3108 (m), 3057 (m), 3036 (m), 1718 (w), 1616 (vs), 1597 (sh), 1567 (w), 1492 (w), 1478 (m), 1444 (s), 1400 (sh), 1384 (vs), 1344 (w), 1323 (m), 1248 (w), 1179 (w), 1160 (m), 1119 (s), 1059 (w), 1041 (w), 1027 (m), 1016 (sh), 1004 (w), 995 (m), 976 (sh), 956 (w), 766 (s), 735 (m), 658 (s), 634 (w), 562 (w), 535 (w), 500 (w), 436 (w), 417 (m) cm^{-1}. $C_{14}H_{14}N_2O_2S_2Zn$ (371.78): calcd. C 45.23, H 3.80, N 7.53, S 17.25, Zn 17.59; found

C 45.07, H 3.82, N 7.37, S 17.10, Zn 17.51. The compound is soluble in acetone, DMF, DMSO, CH_2Cl_2, and warm water.

[Zn(TBn)$_2$(BPY)] (2): The synthetic procedure was similar to that of **1**, except that HTBn (141.1 μL, 1.2 mmol) was used instead of HTAc. The polycrystalline product was washed with MeOH and acetone. The filtrate was left undisturbed at room temperature to obtain pale-yellow single crystals. Yield: 0.22843 g (77%). Main IR features of compound **2** (KBr pellet): $\tilde{\nu}$ = 3435 (sh), 3107 (m), 3056 (m), 3033 (sh), 1715 (w), 1605 (s), 1597 (sh), 1589 (s), 1576 (m), 1565 (s), 1489 (w), 1474 (m), 1442 (s), 1400 (m), 1385 (s), 1322 (m), 1249 (w), 1208 (vs), 1169 (s), 1159 (sh), 1120 (w), 1103 (w), 1078 (w), 1058 (w), 1040 (w), 1024 (m), 1015 (sh), 1002 (w), 994 (w), 975 (w), 940 (sh), 932 (vs), 903 (sh), 778 (sh), 770 (s), 735 (m), 702 (sh), 693 (s), 654 (s), 632 (w), 617 (w), 550 (w), 533 (w), 424 (sh), 415 (w) cm^{-1}. $C_{24}H_{18}N_2O_2S_2Zn$ (495.92): calcd. C 58.12, H 3.66, N 5.65, S 12.93, Zn 13.18; found C 58.05, H 3.59, N 5.67, S 12.99, Zn 13.19. The compound is soluble in DMF, DMSO, and CH_2Cl_2.

[Zn(TAc)$_2$(NEO)] (3): The synthetic procedure was similar to that of **1**, except that NEO (0.1250 g, 0.6 mmol) was used instead of BPY, and the polycrystalline product was additionally washed with acetone. The filtrate was left undisturbed at room temperature to obtain colorless single crystals. Yield: 0.08482 g (33%). Main IR features of compound **3** (KBr pellet): $\tilde{\nu}$ = 3434 (w), 3139 (w), 3068 (sh), 3019 (sh), 1721 (w), 1636 (s), 1625 (sh), 1594 (m), 1571 (w), 1509 (m), 1424 (sh), 1400 (sh), 1385 (s), 1349 (w), 1295 (w), 1222 (w), 1149 (m), 1117 (m), 1033 (w), 1003 (w), 953 (m), 858 (m), 813 (w), 783 (w), 730 (w), 680 (w), 653 (m), 623 (sh), 550 (w), 538 (sh), 494 (w), 449 (w), 436 (w), 417 (w) cm^{-1}. $C_{18}H_{18}N_2O_2S_2Zn$ (423.85): calcd. C 51.00, H 4.28, N 6.61, S 15.13, Zn 15.43; found C 51.07, H 4.30, N 6.75, S 15.21, Zn 15.35. The compound is soluble in DMF, DMSO, and CH_2Cl_2.

[Zn(TBn)$_2$(PHEN)] (4): The synthetic procedure was similar to that of **2**, except that PHEN (0.1081 g, 0.6 mmol) was used instead of BPY. Yield: 0.25283 g (80%). Main IR features of compound **4** (KBr pellet): $\tilde{\nu}$ = 3435 (m), 3133 (m), 3063 (sh), 3027 (sh), 1620 (m), 1589 (vs), 1579 (sh), 1567 (vs), 1516 (m), 1492 (w), 1446 (m), 1429 (s), 1420 (s), 1400 (s), 1385 (vs), 1348 (w), 1207 (vs), 1171 (w), 1151 (w), 1140 (w), 1101 (w), 1076 (w), 1028 (w), 1003 (w), 993 (w), 932 (vs), 868 (w), 854 (s), 777 (m), 729 (s), 704 (m), 694 (s), 669 (w), 654 (m), 644 (w), 619 (w), 562 (w), 552 (w), 424 (w) cm^{-1}. $C_{26}H_{18}N_2O_2S_2Zn$ (519.94): calcd. C 60.05, H 3.49, N 5.39, S 12.33, Zn 12.58; found C 59.97, H 3.54, N 5.42, S 12.42, Zn 12.64. The compound is soluble in DMF, DMSO, and CH_2Cl_2.

[Zn(TAc)$_2$(μ-BPE)] (5): HTAc (141.1 μL, 1.2 mmol) was added to a solution of zinc acetate (0.1317 g, 0.6 mmol) in MeOH (15 mL) to obtain a clear yellow solution. A methanol solution (10 mL) of BPE (0.1093 g, 0.6 mmol) was added dropwise, and the mixture was stirred for 2 h. The light yellowish precipitate was filtered, washed with MeOH and acetone and dried in vacuo. In order to obtain single crystals, the synthesis was carried out by using DMF, a more coordinating solvent that prevents the immediate precipitation of the complex. Several days later, yellow crystals of compound **5**, mixed with a polycrystalline powder, were observed. Yield: 0.20022 g (84%). Main IR features of compound **5** (KBr pellet): $\tilde{\nu}$ = 3435 (m), 3133 (m), 3017 (sh), 1627 (vs), 1612 (vs), 1506 (w), 1430 (sh), 1401 (sh), 1385 (s), 1354 (w), 1300 (w), 1260 (w), 1212 (w), 1148 (m), 1110 (m), 1070 (m), 1023 (m), 1003 (m), 988 (m), 952 (m), 845 (m), 832 (m), 652 (m), 624 (sh), 565 (m), 552 (m), 492 (w) cm^{-1}. $C_{16}H_{16}N_2O_2S_2Zn$ (397.81): calcd. C 48.30, H 4.05, N 7.04, S 16.12, Zn 16.44; found C 48.22, H 4.12, N 7.04, S 16.07, Zn 16.15. The compound is soluble in DMF, DMSO, and hot water.

[Zn(TBn)$_2$(μ-BPE)] (6): The synthetic procedure for the preparation of the polycrystalline sample was similar to that of **5**, except that HTBn (141.1 μL, 1.2 mmol) was used instead of HTAc. Yellowish single crystals were obtained by slow diffusion of a methanol solution containing zinc acetate and HTBn into a solution of BPE in DMF. Yield: 0.28488 g (90%). Main IR features of compound **6** (KBr pellet): $\tilde{\nu}$ = 3446 (m), 3129 (m), 3090 (sh), 3057 (sh), 1612 (vs), 1604 (sh), 1574 (s), 1505 (w), 1484 (sh), 1446 (m), 1432 (m), 1400 (sh), 1385 (vs), 1352 (sh), 1303 (w), 1250 (w), 1222 (sh), 1204 (s), 1171 (m), 1158 (m), 1068 (m), 1026 (m), 1003 (m), 994 (w), 979 (w), 962 (w), 923 (s), 873 (w), 838 (m), 782 (m), 692 (s), 673 (w), 652 (m), 618 (w), 570 (m), 553 (m) cm^{-1}. $C_{26}H_{20}N_2O_2S_2Zn$ (521.96): calcd. C 59.83, H 3.86, N 5.37, S 12.29, Zn 12.53; found C 59.76, H 3.94, N 5.32, S 12.35, Zn 12.48. The compound is soluble in DMF and DMSO and sparingly soluble in hot CH_2Cl_2 and water.

Physical Measurements: Elemental analyses (C, H, N, S) were performed with a Euro EA Elemental Analyzer, whereas the metal content, determined by inductively coupled plasma (ICP-AES), was obtained with a Horiba Yobin Yvon Activa spectrometer. Infrared spectra were recorded with a Nicolet 740 FTIR spectrometer as KBr disks. Thermal analysis (TG/DTG/DTA) was performed with a TA Instruments SDT 2960 thermal analyzer in a synthetic air environment (79% N_2, 21% O_2) with a heating rate of 5 °C min^{-1} and a sample size of about 10–20 mg per run. The X-ray powder diffraction patterns (XRPD) were collected with an X-Pert PRO, PAN analytical machine by employing a Cu-K_α radiation source at a scanning rate of 0.026 ° s^{-1}. The morphology of the zinc sulfide NPs was examined by using a JEOL JSM-7000F scanning electron microscope (SEM) and a Philips CM200 transmission electron microscope (TEM) equipped with an EDXS collection unit. The samples for SEM were prepared by deposition of the product onto a carbon tape, while those for TEM were dispersed on ethanol and placed on a carbon-coated copper grid followed by drying under vacuum.

X-ray Structure Determination: The single crystals were mounted at the end of a glass fiber by using epoxy glue. Diffraction experiments were carried out with an Xcalibur diffractometer equipped with graphite-monochromated Mo-K_α radiation (λ = 0.71073 Å) at 100(2) K. Data were processed and corrected for Lorentz and polarization effects with the CrysAlis RED program.[29] The structures of all compounds except **4** were solved by direct methods using the SIR92 program.[30] Full-matrix least-squares refinements were performed on F^2 by using SHELXL97.[31] All non-hydrogen atoms were refined anisotropically. All calculations for these structures were performed by using the WINGX crystallographic software package.[32] In the case of compound **4**, careful examination of the positions of the peaks extracted from the CCD images obtained at 100 K showed that in addition to the main reflections the diffraction pattern also contained strong satellite reflections that could be indexed with four integers as $H = ha^* + kb^* + lc^* + mq$ with q = (0 0 0.296820). Thus, this structure was solved directly in superspace with the charge-flipping algorithm, while the initial structure models were refined by full-matrix least squares on F by using the JANA2006 program.[33] After averaging the electron density according to the superspace symmetry, we obtained a good estimate of both the basic positions of the atoms and their modulation functions. Crystallographic details are listed in Tables 4 and 5.

Supporting Information (see footnote on the first page of this article): TG, XRPD, FTIR spectra, SEM/TEM images, UV/Vis spectra, TG-MS results, tables of hydrogen-bonding interactions, figures of crystal packing, and thermolysis optimization experiments.

Table 4. Crystal data and structure refinement of the compounds **1**–**3**, **5**, and **6**.

Compound	**1**	**2**	**3**	**5**	**6**
Empirical formula	$C_{14}H_{14}N_2O_2S_2Zn$	$C_{24}H_{18}N_2O_2S_2Zn$	$C_{18}H_{18}N_2O_2S_2Zn$	$C_{16}H_{16}N_2O_2S_2Zn$	$C_{26}H_{20}N_2O_2S_2Zn$
M_r [g mol^{-1}]	371.76	495.89	423.83	397.80	521.97
T [K]	100(2)	100(2)	100(2)	100(2)	100(2)
Crystal system	monoclinic	triclinic	monoclinic	orthorhombic	monoclinic
Space group	$C2/c$ (No.15)	$P\bar{1}$ (No.2)	$P2_1/c$ (No.14)	$Pna2_1$ (No.33)	$P2_1/c$ (No.14)
a [Å]	15.5829(3)	8.4262(5)	10.5150(2)	9.9015(3)	11.6106(2)
b [Å]	8.1768(2)	11.6138(8)	11.0576(2)	11.4738(4)	13.0890(2)
c [Å]	12.4330(3)	11.6237(6)	15.6367(3)	15.8722(6)	19.7024(4)
α [°]	90	77.704(5)	90	90	90
β [°]	98.223(2)	84.897(4)	92.402(2)	90	123.209(2)
γ [°]	90	76.201(5)	90	90	90
V [Å^3]	1567.90(6)	1078.45(11)	1816.48(6)	1803.21(11)	2505.18(10)
Z	4	2	4	4	4
$D_{calcd.}$ [g cm^{-3}]	1.575	1.527	1.550	1.465	1.384
μ [mm^{-1}]	1.836	1.357	1.596	1.602	1.172
$F(000)$	760	508	872	816	1072
θ range [°]	2.82–29.00	1.79–26.60	2.26–27.99	2.72–28.96	2.92–30.00
Reflections collected	12870	7524	14949	14421	24110
Independent reflections	2080 [R_{int} = 0.0362]	4510 [R_{int} = 0.0227]	4240[R_{int} = 0.0352]	4157 [R_{int} = 0.042]	7311[R_{int} = 0.030]
Parameters/restraints	97/0	280/0	247/0	208/1	298/0
R [$I > 2\sigma(I)$][a]	R_1 = 0.0243	R_1 = 0.0288	R_1 = 0.0302	R_1 = 0.0333	R_1 = 0.0403
	wR_2 = 0.0616	wR_2 = 0.0607	wR_2 = 0.0717	wR_2 = 0.0767	wR_2 = 0.0969
R (all data)	R_1 = 0.0271	R_1 = 0.0325	R_1 = 0.0357	R_1 = 0.0372	R_1 = 0.0588
	wR_2 = 0.0623	wR_2 = 0.0637	wR_2 = 0.0749	wR_2 = 0.0787	wR_2 = 0.1014
GOF on F^2 (S)[b]	1.022	1.056	1.064	1.079	0.962
Weighting scheme[c]	SHELX	SHELX	SHELX	SHELX	SHELX

[a] $R_1 = \Sigma(|F_o| - |F_c|)/\Sigma|F_o|$; $wR_2 = \{\Sigma[w(F_o^2 - F_c^2)^2]/\Sigma[w|F_o|^2]\}^{1/2}$. [b] $S = [\Sigma w(|F_o| - |F_c|)^2/(N_{obs} - N_{param})]^{1/2}$. [c] Scheme = $1/[\sigma^2(F_o^2) + (aP)^2 + bP]$ where $P = (F_o^2 + 2F_c^2)/3$; compound (a, b): **1** (0.0420, 0), **2** (0.0196, 0.3497), **3** (0.0360, 0.8273), **5** (0.0417, 0.4334), and **6** (0.0650, 0).

Table 5. Crystallographic data and refinement conditions for compound **4**.

Empirical formula	$C_{26}H_{18}N_2O_2S_2Zn$
M_r [g mol^{-1}]	519.96
Crystal system	monoclinic
Superspace group	$C2/c$ (0\b0)s0
a [Å]	21.72(4)
b [Å]	9.32(5)
c [Å]	11.34(5)
β [°]	101.5(3)
V [Å^3]	2251(17)
Q vector	00.29682 0
Z	4
$D_{calcd.}$ [g cm^{-3}]	1.534
$F(000)$	1064
μ [mm^{-1}]	1.304
R_{int}	0.0404
Independent reflections	12873
Observed reflections [I ≥ 3/σ(I)]	6177
θ range [°]	2.97–29.09
Parameters	250
GOF (all)	1.33
GOF [$I > 3/\sigma(I)$]	1.86
R_1/wR_2 [$I \geq 3/\sigma(I)$]	0.0378/0.0426
Main reflections m = 0	0.0337/0.0421
Satellites m = 1	0.0381/0.0406
Satellites m = 2	0.0542/0.0585
R_1/wR_2 (all)	0.0783/0.0444
Main reflections m = 0	0.0458/0.0428
Satellites m = 1	0.0668/0.0421
Satellites m = 2	0.1949/0.0684
Weighting scheme	$1/[\sigma^2(F_o) + 0.0001F_o^2]$

Acknowledgments

Financial support from the Gobierno Vasco (IT477-10, SAIOTEK S-PE12UN004) and the Universidad del País Vasco/Euskal Herriko Unibertsitatea (UPV/EHU) (UFI 11/53, predoctoral fellowship) is gratefully acknowledged. Technical and human support provided by Servicios Generales de Investigación de la UPV/EHU (SGIker) [Universidad del País Vasco/Euskal Herriko Unibertsitatea (UPV/EHU), Ministerio de Ciencia e Innovació (MICINN), Gobierno Vasco/Eusko Jaurlaritza (GV/EJ), European Social Fund (ESF)] is also acknowledged.

[1] a) E. W. Dahl, F. G. Baddour, S. R. Fiedler, W. A. Hoffert, M. P. Shones, G. T. Yee, J.-P. Djukic, J. W. Bacon, A. L. Rheingold, L. H. Doerrer, *Chem. Sci.* **2012**, *3*, 602–609; b) F. Maratini, L. Pandolfo, S. Rizzato, A. Albinati, A. Venzo, E. Tondello, S. Gross, *Eur. J. Inorg. Chem.* **2011**, 3281–3283; c) J. Chaturvedi, S. Singh, S. Bhattacharya, H. North, *Inorg. Chem.* **2011**, *50*, 10056–10069; d) J. Chaturvedi, S. Bhattacharya, R. Prasad, *Dalton Trans.* **2010**, *39*, 8725–8732; e) L. Tian, W. H. Lye, T. C. Deivaraj, J. J. Vittal, *Inorg. Chem.* **2006**, *45*, 8258–8263; f) T. C. Deivaraj, J.-H. Park, M. Afzaal, P. O'Brien, J. J. Vittal, *Chem. Mater.* **2003**, *15*, 2383–2391; g) T. C. Deivaraj, W. H. Lye, J. J. Vittal, *Inorg. Chem.* **2002**, *41*, 3755–3760; h) T. C. Deivaraj, P. A. W. Dean, J. J. Vittal, *Inorg. Chem.* **2000**, *39*, 3071–3074; i) J. J. Vittal, P. A. W. Dean, *Inorg. Chem.* **1993**, *32*, 791–794.

[2] a) J. J. Vittal, J. T. Sampanthar, Z. Lu, *Inorg. Chim. Acta* **2003**, *343*, 224–230; b) M. Rombach, H. Brombacher, H. Vahrenkamp, *Eur. J. Inorg. Chem.* **2002**, 153–159; c) C. V. Amburose, T. C. Deivaraj, G. X. Lai, J. T. Sampanthar, J. J. Vittal, *Inorg. Chim. Acta* **2002**, *332*, 160–166; d) J. T. Sampanthar, T. C. De-

ivaraj, J. J. Vittal, P. A. W. Dean, *J. Chem. Soc., Dalton Trans.* **1999**, 4419–4423; e) M. D. Nyman, M. J. Hampden-Smith, E. N. Duesler, *Inorg. Chem.* **1997**, *36*, 2218–2224; f) M. Ruf, H. Vahrenkamp, *Inorg. Chem.* **1996**, *35*, 6571–6578; g) M. Hofbauer, M. Mobius, F. Knoch, R. Benedix, *Inorg. Chim. Acta* **1996**, *247*, 147–154; h) L. Golic, N. Bulc, W. Dietzsch, *Acta Crystallogr., Sect. C* **1986**, *42*, 811–814; i) M. Bonamico, G. Dessy, V. Fares, L. Scaramuzza, *J. Chem. Soc., Dalton Trans.* **1976**, 67–70.

[3] a) D. V. Talapin, J. S. Lee, M. V. Kovalenko, E. V. Shevchenko, *Chem. Rev.* **2010**, *110*, 389–458; b) A. P. Alivisatos, *Science* **1996**, *271*, 933–937.

[4] a) L. Z. Zhang, W. Sun, P. Cheng, *Molecules* **2003**, *8*, 211–218; b) C. F. Landes, S. Link, M. B. Mohamed, B. Nikoobakht, M. A. El-Sayed, *Pure Appl. Chem.* **2002**, *74*, 1675–1692.

[5] a) I. Matsui, *J. Chem. Eng. Jpn.* **2005**, *38*, 535–546; b) T. Trindade, P. O'Brien, N. L. Pickett, *Chem. Mater.* **2001**, *13*, 3843–3858; c) J. H. Fendler, F. C. Meldrum, *Adv. Mater.* **1995**, *7*, 607–632; d) A. Hagfeldt, M. Grätzel, *Chem. Rev.* **1995**, *95*, 49–88; e) H. Weller, *Adv. Mater.* **1993**, *5*, 88–95; f) M. L. Steigerwald, L. E. Brus, *Acc. Chem. Res.* **1990**, *23*, 183–188.

[6] a) S.-D. Han, K. C. Singh, H.-S. Lee, T.-Y. Cho, J. P. Hulme, C.-H. Han, I.-S. Chun, J. Gwak, *Mater. Chem. Phys.* **2008**, *112*, 1083–1087; b) A. Chatterjee, A. Priyam, S. C. Bhattacharya, A. Saha, *Colloids Surf. A* **2007**, *297*, 258–266; c) B. C. Cheng, Z. G. Wang, *Adv. Funct. Mater.* **2005**, *15*, 1883–1890; d) S. Wageh, Z. S. Ling, X. Xu-Rong, *J. Cryst. Growth* **2003**, *255*, 332–337; e) W. Park, J. S. King, C. W. Neff, C. Liddell, C. Summers, *Phys. Status Solidi B* **2002**, *229*, 949–960; f) M. Oshikiri, F. Aryasetiawan, *Phys. Rev. B* **1999**, *60*, 10754.

[7] a) H. Pang, Y. Yuan, Y. Zhou, J. Lian, L. Cao, J. Zhang, X. Zhou, *J. Lumin.* **2007**, *122–123*, 587–589; b) M. Bär, A. Ennaoui, J. Klaer, R. Sáez-Araoz, T. Kropp, L. Weinhardt, C. Heske, H.-W. Schock, Ch.-H. Fischer, M. C. Lux-Steiner, *Chem. Phys. Lett.* **2006**, *433*, 71–74; c) O. A. Korotchenkov, A. Cantarero, A. P. Schpak, Y. A. Kunitskii, A. I. Senkevich, M. O. Borovoy, A. B. Nadtochii, *Nanotechnology* **2005**, *16*, 2033–2038; d) I. Gur, N. A. Fromer, M. L. Geier, A. P. Alivisatos, *Science* **2005**, *310*, 462–465; e) U. Gangopadhyay, K. Kim, D. Mangalaraj, J. Yi, *Appl. Surf. Sci.* **2004**, *230*, 364–370; f) H. Chandler, V. Shanker, D. Haranath, S. Dudeja, P. Sharma, *Mater. Res. Bull.* **2003**, *38*, 279–288; g) A. P. Greef, H. C. Swart, *Surf. Interface Anal.* **2002**, *34*, 593–596; h) I. K. Sou, Z. H. Ma, Z. Q. Zhang, G. K. L. Wong, *Appl. Phys. Lett.* **2000**, *76*, 1098–1100.

[8] F. H. Allen, *Acta Crystallogr., Sect. B* **2002**, *58*, 380–388.

[9] R. G. Pearson, *Inorg. Chem.* **1988**, *27*, 734–740.

[10] a) J. Liu, J. Ma, Y. Liu, Z. Song, Y. Sun, J. Fang, Z. Liu, *J. Alloys Compd.* **2009**, *486*, L40–L43; b) J. Zou, J. Zhang, B. Zhang, P. Zhao, K. Huang, *Mater. Lett.* **2007**, *61*, 5029–5032; c) J. P. Li, Y. Xu, D. Wu, Y. H. Sun, *Solid State Commun.* **2004**, *130*, 619–622; d) H. Zhang, D. Yang, S. Li, Y. Ji, X. Ma, D. Que, *Nanotechnology* **2004**, *15*, 1122–1125; e) S. H. Yu, M. Yoshimura, *Adv. Mater.* **2002**, *14*, 296–300.

[11] a) D. Barreca, A. Gasparotto, C. Maragno, E. Tondello, C. Sada, *Chem. Vapor Depos.* **2004**, *10*, 229–236; b) C. Heyn, C. Dumat, *J. Cryst. Growth* **2001**, *227*, 990–994; c) A. N. Gleizes, *Chem. Vapor Depos.* **2000**, *6*, 155–173; d) S. Fafard, Z. R. Wasilewski, C. N. Allen, D. Picard, M. Spanner, J. P. McCaffrey, P. G. Piva, *Phys. Rev. B* **1999**, *59*, 15368–15373; e) L. Landin, M. S. Miller, M. E. Pistol, C. E. Pryor, L. Samuelson, *Science* **1998**, *280*, 262–264; f) P. O'Brien, R. Nomura, *J. Mater. Chem.* **1995**, *5*, 1761–1773.

[12] a) R. T. Lv, C. B. Cao, Y. J. Guo, H. S. Zhao, *J. Mater. Sci.* **2004**, *39*, 1575–1578; b) W. S. Chae, J. H. Yoon, H. Yu, D. J. Jang, Y. R. Kim, *J. Phys. Chem. B* **2004**, *108*, 11509–11513; c) J. Cizeron, M. P. Pileni, *Nanostruct. Mater.* **1997**, *8*, 419–434; d) M. P. Pileni, I. Motte, C. Petit, *Chem. Mater.* **1992**, *4*, 338–345; e) R. R. Chandler, J. L. Coffer, *J. Phys. Chem.* **1991**, *95*, 4–6; f) A. R. Kortan, E. R. Hull, R. L. Opila, M. G. Bawendi, M. L. Steigerwald, P. J. Carroll, L. E. Brus, *J. Am. Ceram. Soc.* **1990**, *112*, 1327–1332.

[13] a) N. I. Kovtyukhova, E. U. Buzaneva, C. C. Waraksa, N. R. Martin, T. E. Mallouk, *Chem. Mater.* **2000**, *12*, 383–389; b) D. U. Saenger, G. Jung, *J. Sol-Gel Sci. Technol.* **1998**, *13*, 635–639; c) K. Osakada, A. Taniguchi, E. Kubota, S. Dev, K. Tanaka, K. Kubota, T. Yamamoto, *Chem. Mater.* **1992**, *4*, 562–570.

[14] a) M. A. Fenollosa, M. C. López, V. Donderis, M. González, B. Mari, J. R. Ramos-Barrado, *Thin Solid Films* **2008**, *516*, 1622–1625; b) M. Nyman, M. J. Hampden-Smith, E. N. Duesler, *Chem. Vapor Depos.* **1996**, *2*, 171–174; c) C. Falcony, M. Garcia, A. Ortiz, J. C. Alonso, *J. Appl. Phys.* **1992**, *72*, 1525–1527.

[15] a) I. J.-L. Plante, T. W. Zeit, P. Yang, T. Mokari, *J. Mater. Chem.* **2010**, *20*, 6612–6617; b) J. J. Vittal, M. T. Ng, *Acc. Chem. Res.* **2006**, *39*, 869; c) T. Mirkovic, M. A. Hines, P. S. Nair, G. D. Scholes, *Chem. Mater.* **2005**, *17*, 3451–3456; d) N. Pradhan, S. J. Efrima, *J. Am. Chem. Soc.* **2003**, *125*, 2050–2051; e) S. L. Cumberland, K. M. Hanif, A. Javier, G. A. Khitrov, G. F. Strouse, S. M. Woessner, C. S. Yun, *Chem. Mater.* **2002**, *14*, 1576–1584; f) T. Trindade, P. J. O'Brien, *J. Mater. Chem.* **1996**, *6*, 343–347; g) D. M. Frigo, O. F. Z. Khan, P. J. O'Brien, *J. Cryst. Growth* **1989**, *96*, 989–992.

[16] a) P. S. Nair, T. Radhakrishnan, N. Revaprasadu, G. A. Kolawole, P. O'Brien, *Chem. Commun.* **2002**, 564–565; b) X. G. Peng, *Chem. Eur. J.* **2002**, *8*, 335–339; c) M. Lazell, S. J. Norager, P. O'Brien, N. Revaprasadu, *Mater. Sci. Eng.* **2001**, *C16*, 129–133; d) J. Hambrock, A. Birkner, R. A. Fischer, *J. Mater. Chem.* **2001**, *11*, 3197–3201; e) C. B. Murray, D. J. Norris, M. G. Bawendi, *J. Am. Chem. Soc.* **1993**, *115*, 8706–8715.

[17] a) J. Chen, L. Chen, L.-M. Wu, *Inorg. Chem.* **2007**, *46*, 8038–8043; b) L. Cademartiri, J. Bertolotti, R. Sapienza, D. S. Wiersma, G. V. Freymann, G. A. Ozin, *J. Phys. Chem. B* **2006**, *110*, 671–673; c) M. B. Sigman, B. A. Korgel, *Chem. Mater.* **2005**, *17*, 1655–1660; d) A. Ghezelbash, M. B. Sigman, B. A. Korgel, *Nano Lett.* **2004**, *4*, 537–542; e) M. B. Sigman, A. Ghezelbash, T. Hanrath, A. E. Saunders, F. Lee, B. A. Korgel, *J. Am. Chem. Soc.* **2003**, *125*, 16050–16057.

[18] S. V. Voitekhovich, D. V. Talapin, C. Klinke, A. Kornowski, H. Weller, *Chem. Mater.* **2008**, *20*, 4545–4547.

[19] a) S. Song, Q. Gao, *J. Appl. Phys.* **2006**, *99*, 106107; b) G. T. Zhou, X. C. Wang, J. C. Yu, *Cryst. Growth Des.* **2005**, *5*, 1761–1765; c) Y. C. Li, X. H. Li, C. H. Yang, Y. F. Li, *J. Phys. Chem. B* **2004**, *108*, 16002–16011; d) X. J. Chen, H. F. Xu, N. S. Xu, M. M. Wu, *Inorg. Chem.* **2003**, *42*, 3100–3106.

[20] a) J. R. Dethlefsen, A. Døssing, *Nano Lett.* **2011**, *11*, 1964–1969; b) W. D. Marty, K. M. Atkins, A. Borecki, H. Rösner, J. F. Corrigan, *J. Mater. Chem.* **2008**, *18*, 1123–1130; c) A. A. Memon, M. Afzaal, M. A. Malik, C. Q. Nguyen, P. O'Brien, J. Raftery, *Dalton Trans.* **2006**, 4499–4505; d) H. Wang, H. Nakamura, M. Uehara, Y. Yamaguchi, M. Miyazaki, H. Maeda, *Adv. Funct. Mater.* **2005**, *15*, 603–608; e) A. V. Naumov, Y. V. Meteleva, N. L. Sermakasheva, V. N. Semenov, G. F. Novikov, *J. Appl. Spectrosc.* **2002**, *69*, 120–125; f) N. L. Pickett, P. O'Brien, *Chem. Rec.* **2001**, *1*, 467–479; g) L. Ou, Z. A. Peng, X. Peng, *Nano Lett.* **2001**, *1*, 333–337; h) L. Manna, E. C. Scher, A. P. Alivisatos, *J. Am. Chem. Soc.* **2000**, *122*, 12700–12706; i) X. Peng, J. Wickham, A. P. Alivisatos, *J. Am. Chem. Soc.* **1998**, *120*, 5343–5344; j) P. Boudjouk, B. R. Jarabek, D. L. Simonson, D. J. Seidler, D. G. Grier, G. J. McCarthy, L. P. Keller, *Chem. Mater.* **1998**, *10*, 2358–2364; k) J. E. B. Katari, V. L. Colvin, A. P. Alivisatos, *J. Phys. Chem.* **1994**, *98*, 4109–4117.

[21] a) S. K. Maji, N. Mukherjee, A. Mondal, B. Adhikary, B. Karmakar, S. Dutta, *Inorg. Chim. Acta* **2011**, *371*, 20–26; b) Z. H. Zhang, W. S. Chin, J. J. Vittal, *J. Phys. Chem. B* **2004**, *108*, 18569–18574; c) M. D. Nyman, K. Jenkins, M. J. Hampden-Smith, T. T. Kodas, E. N. Duesler, A. L. Rheingold, M. L. Liable-Sands, *Chem. Mater.* **1998**, *10*, 914–921; d) M. D. Nyman, M. J. Hampden-Smith, E. N. Duesler, *Inorg. Chem.* **1997**, *36*,

2218–2224; e) T. Ouhadi, A. J. Hubert, P. Teyssie, E. G. Derouane, *J. Am. Chem. Soc.* **1973**, *95*, 449–453.

[22] a) A. Ruiz-Martínez, D. Casanova, S. Alvarez, *Chem. Eur. J.* **2008**, *14*, 1291–1303; b) M. Llunel, D. Casanova, J. Cirera, J. M. Bofill, P. Alemany, S. Alvarez, M. Pinsky, D. Avnir, *SHAPE* (1.7), University of Barcelona, Barcelona, **2010**.

[23] J. J. Vittal, T. J. Sampanthar, Z. Lu, *Inorg. Chim. Acta* **2003**, *343*, 224–230.

[24] I. Barin, O. Knacke, O. Kubschewski, *Thermochemical Properties of Inorganic Substances*, Springer, Berlin, **1977**, pp. 827–828.

[25] Z. Wang, L. L. Daemen, Y. Zhao, C. S. Zha, R. T. Downs, X. Wang, Z. L. Wang, R. J. Hemley, *Nat. Mater.* **2005**, *4*, 922–927.

[26] a) A. M. Palve, S. S. Garje, *Bull. Mater. Sci.* **2011**, *4*, 667–671; b) A. M. Palve, S. S. Garje, *J. Cryst. Growth* **2011**, *326*, 157–162; c) G.-T. Zhou, X. Wang, J. C. Yu, *Cryst. Growth Des.* **2005**, *5*, 1761–1765; d) J.-S. Hu, L.-L. Ren, Y.-G. Guo, H.-P. Liang, A.-M. Cao, L.-J. Wan, C.-L. Bai, *Angew. Chem.* **2005**, *117*, 1295; *Angew. Chem. Int. Ed.* **2005**, *44*, 1269–1273.

[27] a) C. Suryanarayana, M. G. Norton, *X-ray Diffraction, A Practical Approach*, Plenum Press, New York, **1998**, pp. 207–221; b) J. I. Langford, A. J. C. Wilson, *J. Appl. Crystallogr.* **1978**, *11*, 102–113; c) P. Scherrer, *Nachr. Ges. Wiss. Goettingen Math.-Phys. Kl.* **1918**, *26*, 98–100.

[28] P. Escardi, N. Leoni, R. Delhez, *J. Appl. Crystallogr.* **2004**, *37*, 381–390.

[29] *CrysAlis RED*, version 1.171.33.55, Oxford Diffraction, Wroclaw, Poland, **2010**.

[30] A. Altomare, M. Cascarano, C. Giacovazzo, A. Guagliardi, *J. Appl. Crystallogr.* **1993**, *26*, 343–350.

[31] G. M. Sheldrick, *SHELX-97, Program for X-ray Crystal Structure Refinement*, University of Göttingen, Göttingen, Germany, **1997**.

[32] L. J. Farrugia, *J. Appl. Crystallogr.* **1999**, *32*, 837–838.

[33] V. Petricek, M. Dusek, L. Palatinus, *Jana2006, The crystallographic computing system*, Institute of Physics, Praha, Czech Republic, **2006**.

Received: May 22, 2013
Published Online: September 19, 2013

2.3. SUPPORTING INFORMATION

Eur. J. Inorg. Chem. **2013** · © WILEY-VCH Verlag GmbH & Co. KGaA, 69451 Weinheim, 2013 · ISSN 1099–0682

SUPPORTING INFORMATION

DOI: 10.1002/ejic.201300649
Title: Zinc Thiocarboxylate Complexes as Precursors for Zinc Sulfide Nanoparticles under Aerobic Conditions
Author(s): Daniel Vallejo-Sánchez, Garikoitz Beobide,* Oscar Castillo,* Mónica Lanchas

S1. Thermogravimetric measurements

S2. X-ray powder diffraction patterns

S3. FTIR spectra

S4. Hydrogen bonding and coordination angles

S5. Thermolysis optimization under aerobic conditions

S6. TG-MS of compound **1** in synthetic air atmosphere

S7. UV-Vis spectra of the thermolysis products at 300ºC of compounds **1**-**6** obtained sonicating with an ultrasonic tip and filtrating the suspension to remove the bulkier aggregates.

S8. FTIR spectra of the thermolysis products at 300ºC of compounds **1**-**6**.

S9. SEM images of the thermolysis products at 300ºC of compounds **1**-**6**.

S10. TEM images of the thermolysis products at 300ºC of compounds **1**-**6**.

S11. ZnS particle size distribution from TEM images of the thermolysis products at 300ºC.

S1. Thermogravimetric measurements

Table S1. Thermogravimetric measurements for the compounds **1**–**6** in synthetic air.

Compound	T_i[a]	T_f	T_{peak}	Δm (%)	ΔH	ΣΔm (%)	$\Sigma\Delta m_{theor}$ (%)	Residue [b] (JCPDS-No)
1	157	268	229	67.7	ENDO	69.6	73.8	ZnS, B (80-0020)
	502	615	584	5.9	EXO	79.5	78.1	ZnO,W (89-0511)
2	177	585	234/ 256/ 302/ 465/ 561		ENDO/ EXO/ EXO/ EXO/ EXO		80.3	ZnS, B (80-0020)
				81.6		83.0	83.6	ZnO,W (89-0511)
3	200	655	218/ 248/ 278/ 341/ 531/ 624.5		ENDO/ EXO/ EXO/ EXO/ EXO/ EXO		77.0	ZnS, W (80-0007)
				81.7		82.8	80.8	ZnO,W (89-0511)
4	175	650	223/ 249/ 280/ 315/ 340/ 390/ 489/ 578/ 636	82.1	ENDO/ ENDO/ EXO/ EXO/ EXO/ EXO/ EXO/ EXO/ ENDO		81.3	ZnS, W (80-0007)
						83.4	84.3	ZnO,W (89-0511)
5	140	455	191/ 199.5/ 226/ 390/ 420	59.9	ENDO/ EXO/ EXO/ EXO/ EXO	63.5	75.5	ZnS, B (80-0020)
	498	645	560/ 591.5	12.4	EXO/ EXO/	76.4	79.5	ZnO,W (89-0511)
6	175	375	262/ 274.5/ 276.5/ 316		ENDO/ EXO/ EXO/ EXO/		81.3	ZnS, B (80-0020)
	380	605	450/ 513.5/ 561.5	81.2	EXO/ EXO/ EXO	82.4	84.4	ZnO,W (89-0511)

[a] T_i: Initial temperature (ºC), T_f: Final temperature (ºC), T_{peak}: DTA peak temperature (ºC); Δm(%): Weight loss percent in each process; ΔH: Type process according to ATD; ΣΔm(%): percentage of total weight loss after each process; $\Sigma\Delta m_{theor}$(%).: Theoretically calculated weight loss percent.

[b] Crystalline phases found in the residues. W: Wurtzite $(F\bar{4}3m)$, B: Blende ($P6_3mc$).

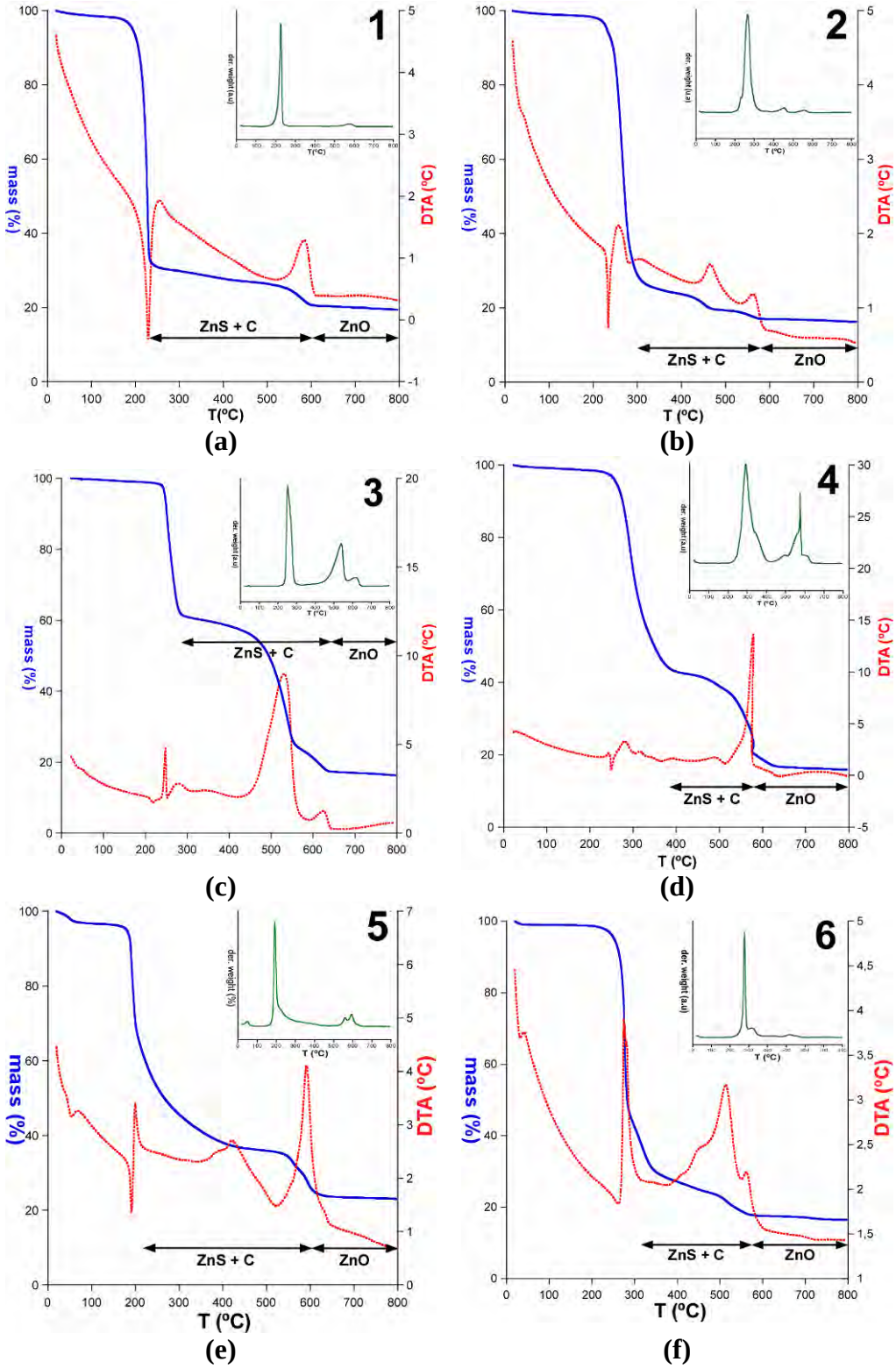

Figure S1. Thermoanalysis of compounds **1**–**6**: TG curve (blue), differential thermal analysis (red) and derivative weight (green).

S2. X-ray powder diffraction patterns

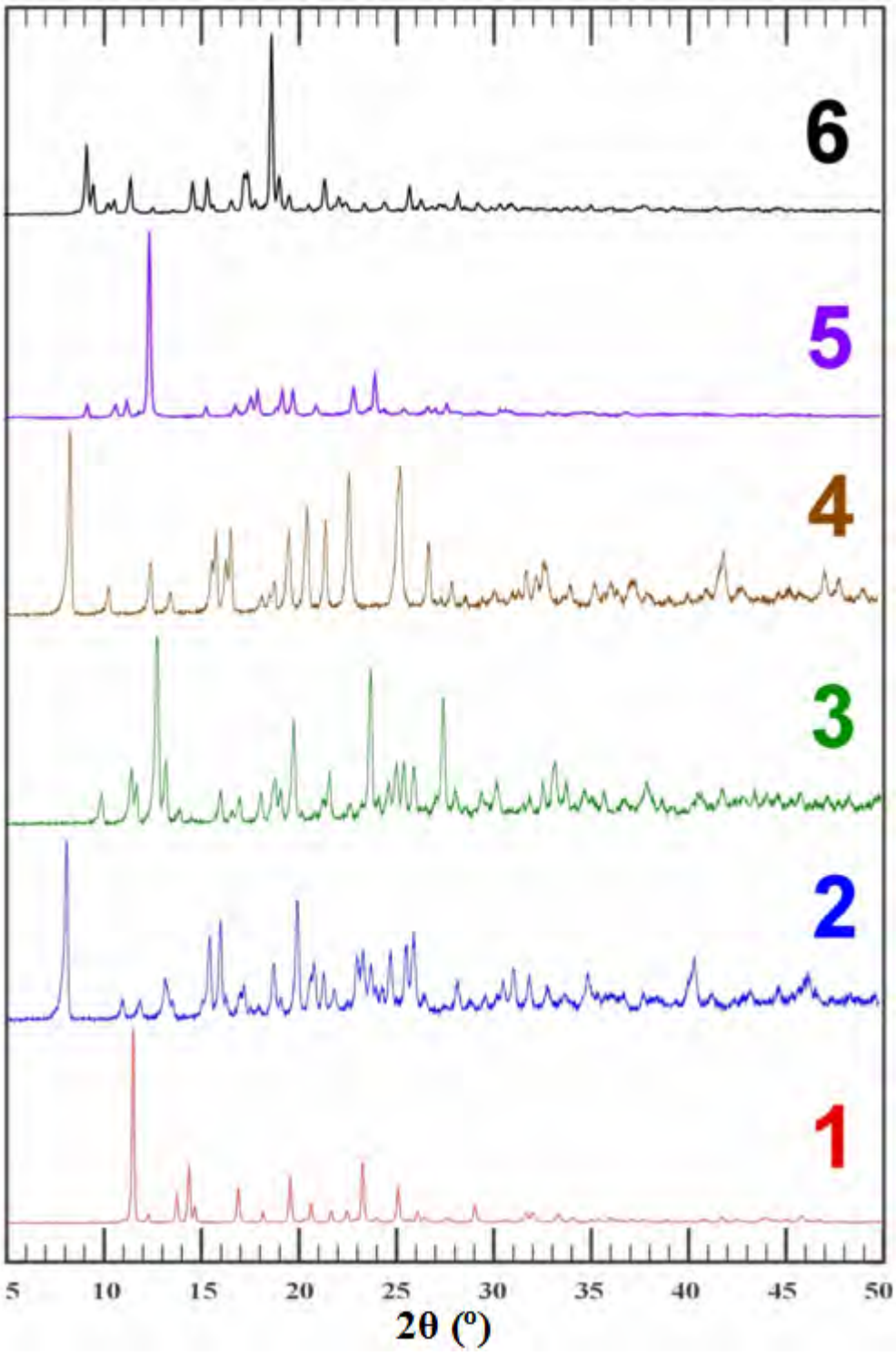

Figure S2. X-ray powder diffraction patterns of compounds **1**–**6**.

S3. FTIR spectra

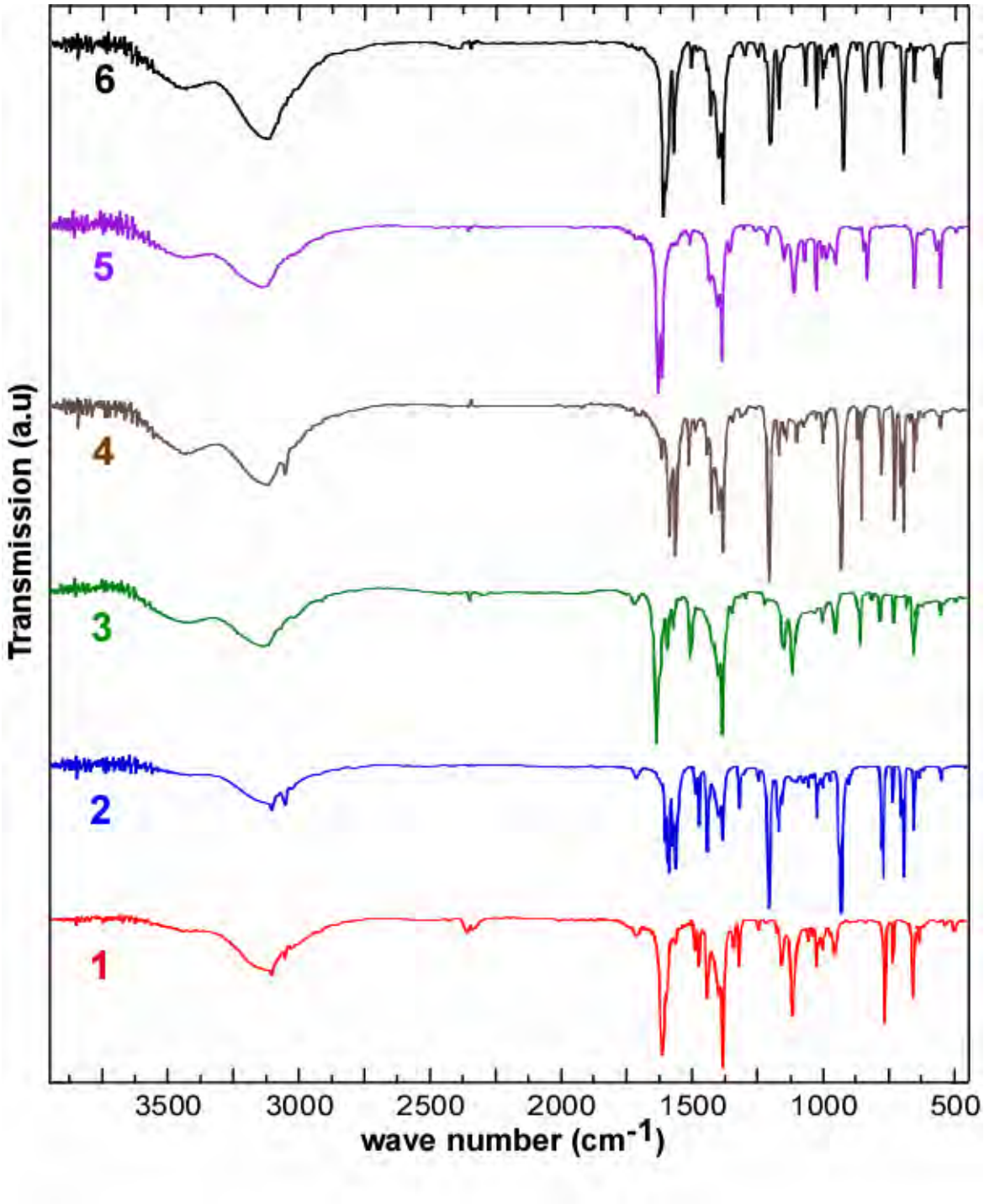

Figure S3. FTIR spectra of compounds **1**–**6**.

S4. Hydrogen bonding and coordination angles**.**

Table S4.1 Hydrogen bonding in compounds **1**–**6**.

1			
D–*H*···*A*	*H*···*A*	*D*···*A*	*D*–*H*···*A*
C(4)–H(4)···O(1) [a]	2.72	3.487(2)	140.2
C(6)–H(6)···S(1) [b]	3.03	3.796(2)	141.0
2			
D–*H*···*A*	*H*···*A*	*D*···*A*	*D*–*H*···*A*
C(21)–H(21)···O(1) [c]	2.58	3.349	140
C(3)–H(3)···O(2) [d]	2.47	3.341	155
3			
D–*H*···*A*	*H*···*A*	*D*···*A*	*D*–*H*···*A*
C(9)–H(9)···O(1) [e]	2.45	3.284	148
C(12)–H(12)···O(2) [f]	2.41	3.213	154
4			
D–*H*···*A*	*H*···*A*	*D*···*A*	*D*–*H*···*A*
C(6)–H(6)···O(1) [h]	2.53	3.370	146.0
5			
D–*H*···*A*	*H*···*A*	*D*···*A*	*D*–*H*···*A*
C(4)–H(4)···O(2) [i]	2.63	3.483(4)	153.6
C(6)–H(6)···O(2) [i]	2.57	3.444(4)	156.6
6			
D–*H*···*A*	*H*···*A*	*D*···*A*	*D*–*H*···*A*
C(4)–H(4)···O(2) [j]	2.52	3.327(2)	144.8
C(6)–H(6)···O(2) [j]	2.44	3.246(2)	145.5
C(7)–H(7)···O(1)	2.34	3.143(2)	143.7
C(8)–H(8)···S(2) [k]	2.85	3.549(2)	132.6
C(24)–H(24)···S(1) [l]	2.91	3.695(3)	143.5

Symmetry codes: (a) –x+3/2, –y+1/2, –z+1; (b) –x+1, y–1, –z+1/2; (c) 1–x, 1–y, 1–z; (d) 1–x, y–1/2, 3/2–z; (e) –x, y–1/2, 3/2–z; (f) 1+x, y, z; (g) 1–x, –y, 2–z; (h) x, y+1, z; (i) x+1/2, –y+1/2, z; (j) –x+2, y+1/2, –z+1/2; (k) –x+2, y–1/2, –z+1/2; (l) –x+1, y+1/2, –z+1/2.

Table S4.2 Coordination bond angles in compounds **1**–**6**.

	2	**3**	**5**	**6**
N(1)–Zn(1)–S(2)	116.72(5)	115.11(5)	111.11(7)	96.40(4)
N(1)–Zn(1)–N(2)	78.32(6)	81.68(6)	96.61(9) [a]	101.77(6)
N(1)–Zn(1)–S(1)	107.53(4)	118.11(4)	109.18(7)	111.02(4)
N(2)–Zn(1)–S(1)	114.16(4)	111.68(4)	121.24(7) [a]	115.09(4)
N(2)–Zn(1)–S(2)	102.80(4)	119.49(4)	103.05(7) [a]	107.57(5)
S(1)–Zn(1)–S(2)	126.76(2)	108.95(2)	114.22(3)	121.69(2)
	1		**4**	
		$Angle_{max}$	$Angle_{min}$	$Angle_{mean}$
N(1)–Zn(1)–S(1)	118.37(3)	114.8(2)	112.8(2)	113.8(2)
N(1)–Zn(1)–S(1)	106.63(3) [b]	101.9(3) [c]	101.2(3) [c]	101.5(3) [c]
S(1)–Zn(1)–S(1)	120.70(2) [b]	133.8(3) [c]	133.8(3) [c]	133.8(3) [c]
N(1)–Zn(1)–N(1)	79.37(6) [b]	79.6(4) [c]	79.6(4) [c]	79.6(4) [c]

Symmetry codes: [a] –x+5/2, y+1/2, z+1/2, [b] 1–x, y, 1/2 – z, [c] –x1, x2, –x3+1/2, x4+1/2

Figure S4. Hydrogen bonding in compounds **1**–**6**.

1

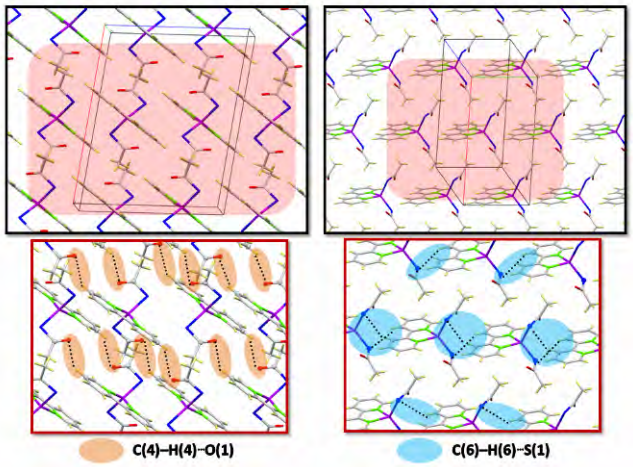

2

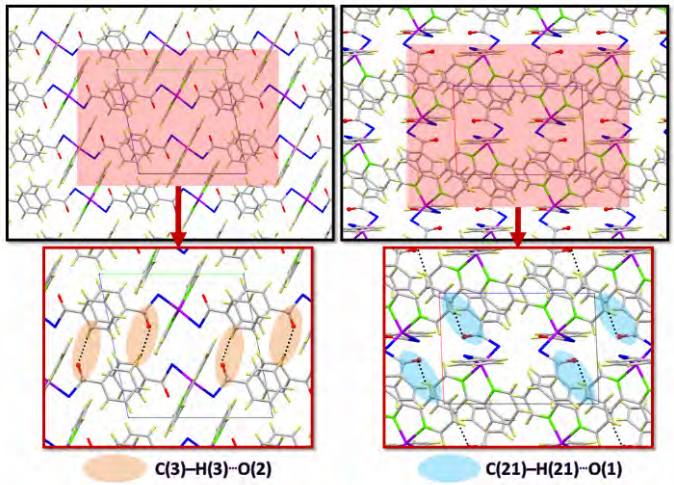

3

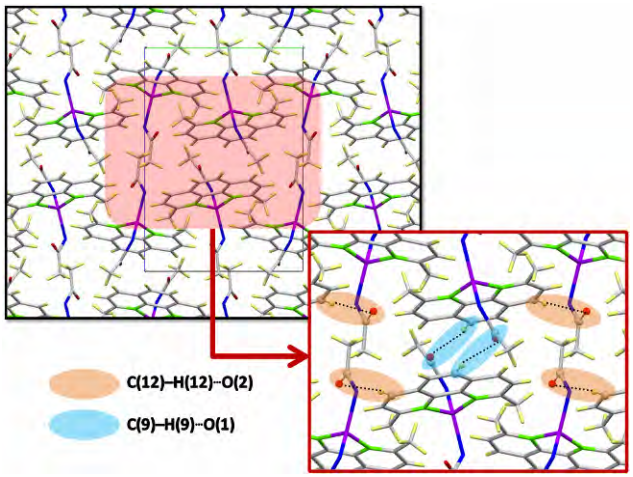

4

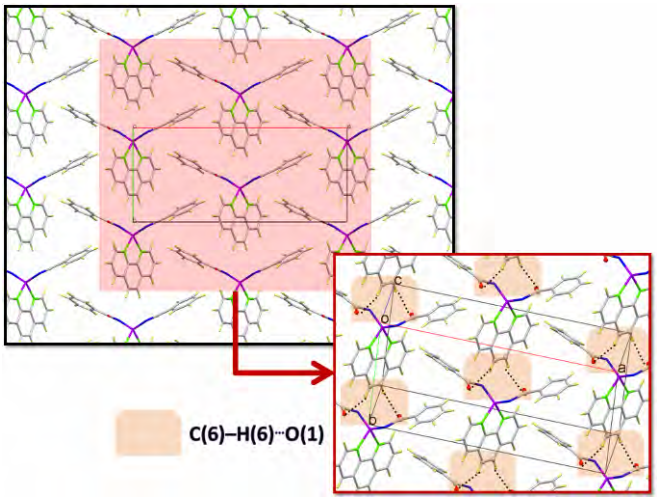

6

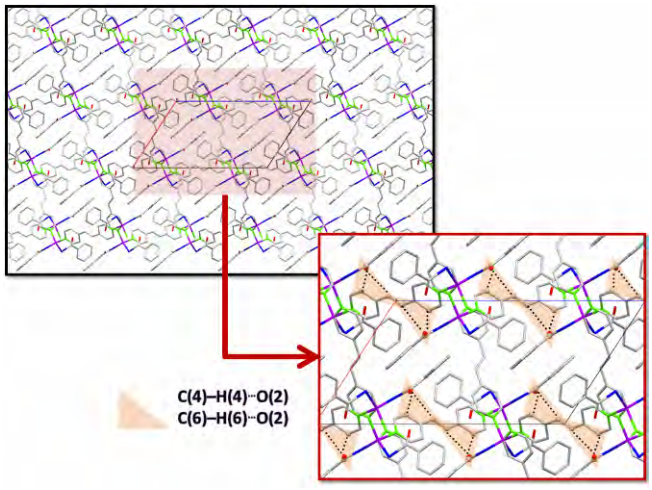

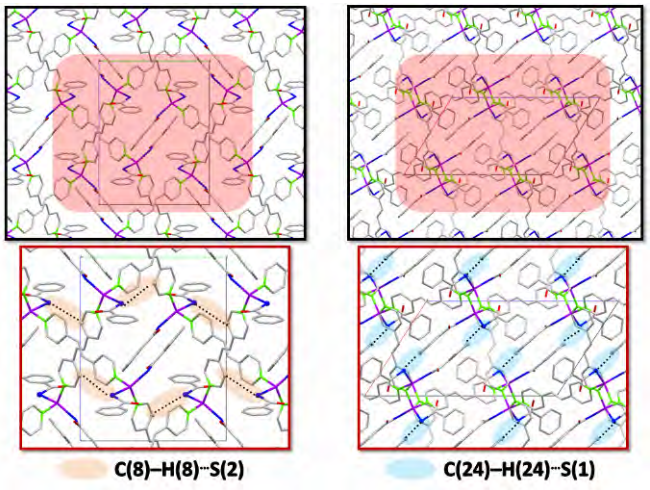

S5. Thermolysis optimization under aerobic conditions.

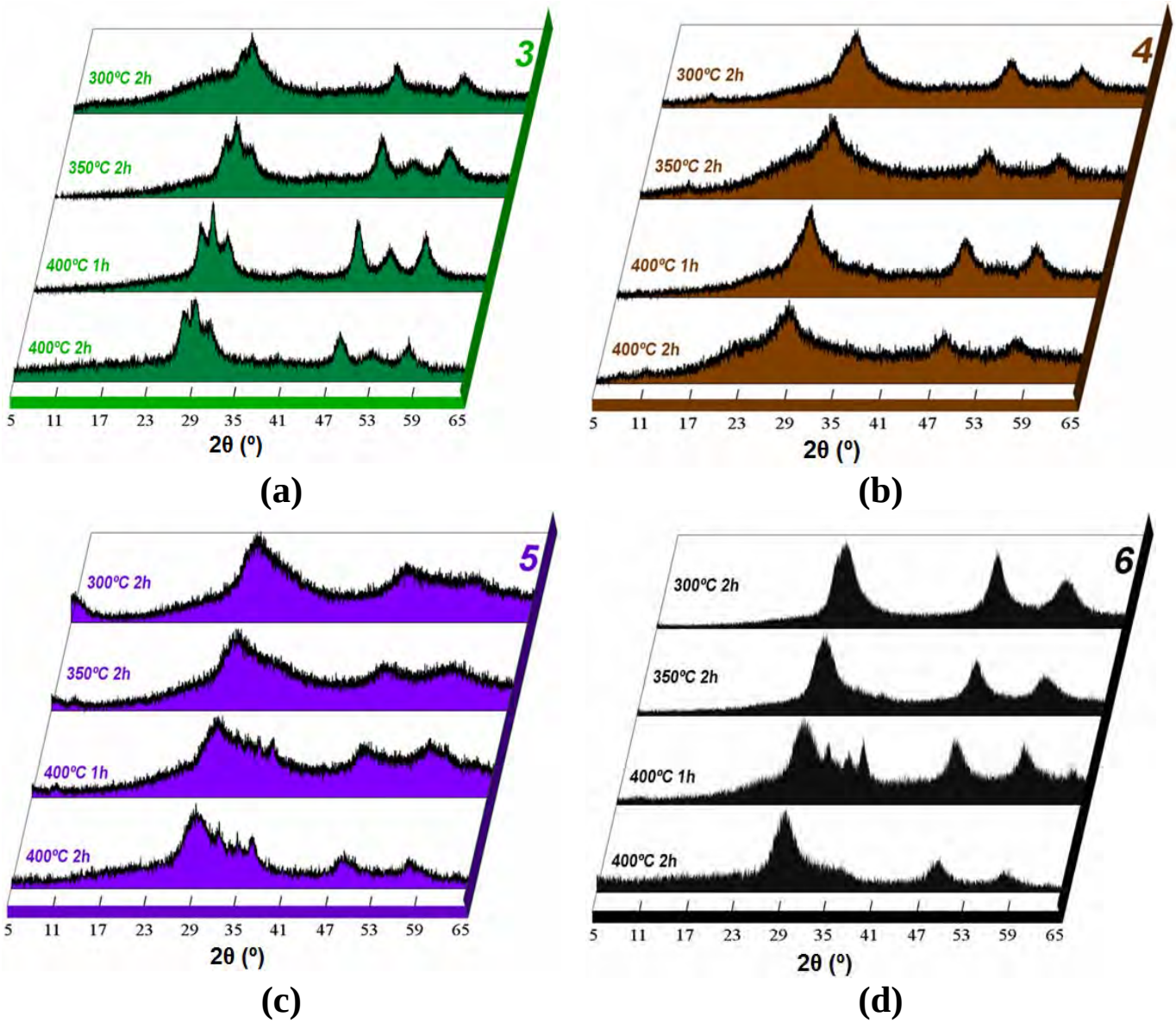

Figure S5.1 PXRD patterns of compounds **3**–**6** after the pyrolysis at different temperatures and times.

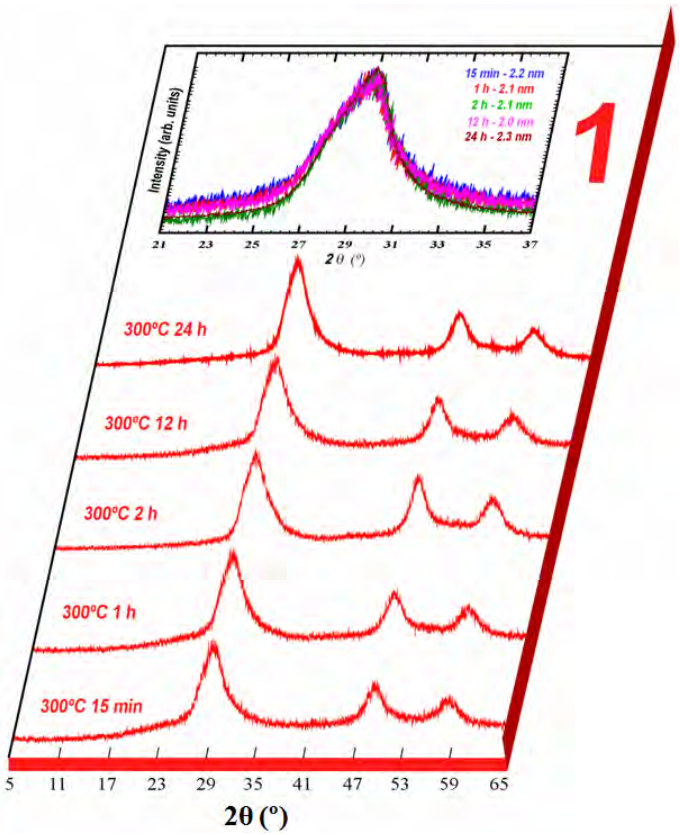

Figure S5.2 PXRD patterns of compound **1** after the pyrolysis at 300ºC using different times.

S6. TG-MS of compound **1** in synthetic air atmosphere.

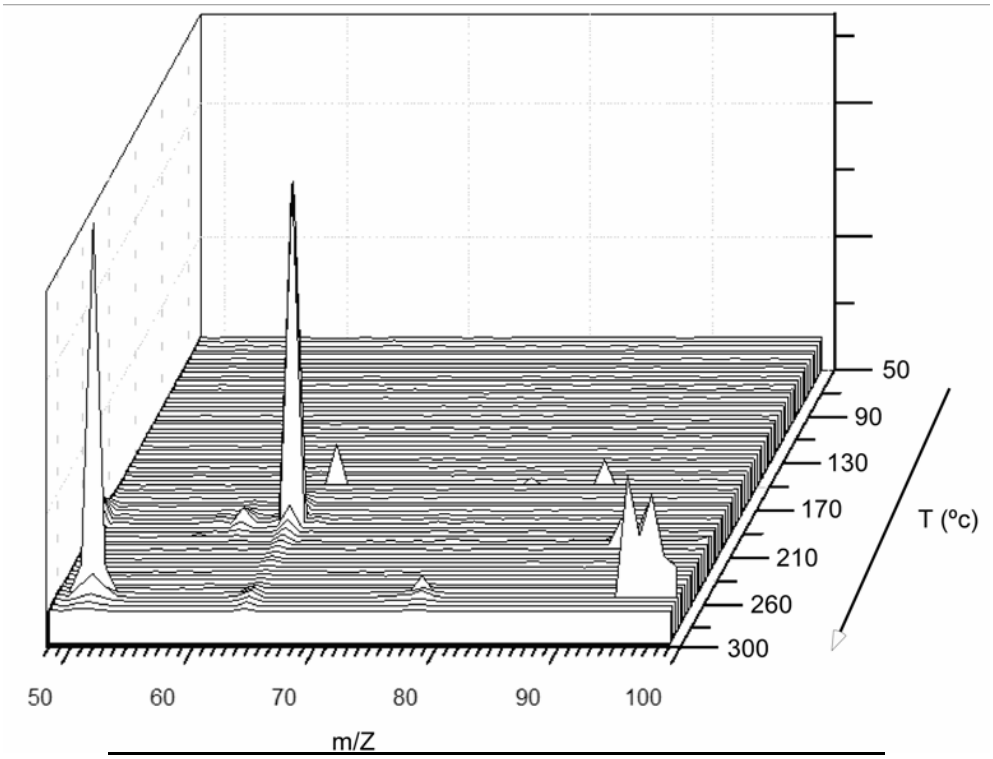

Compound **1**	2,2´-bipyridine	Thioacetic anhydride	S_2
50	50		
51	**51**		
52	52		
57		57	
58		58	
59		59	
60		60	
61		61	
64			**64**
66			66
74	74		
75	75		
76	76	76	
77	77		
78	**78**		
79	79		
82			
88			
91			
92			
94			
95			
96			
97			
98			
99			

S7. UV-Vis spectra of the thermolysis products at 300ºC of compounds **1**-**6** obtained sonicating with an ultrasonic tip and filtrating the suspension to remove the bulkier aggregates.

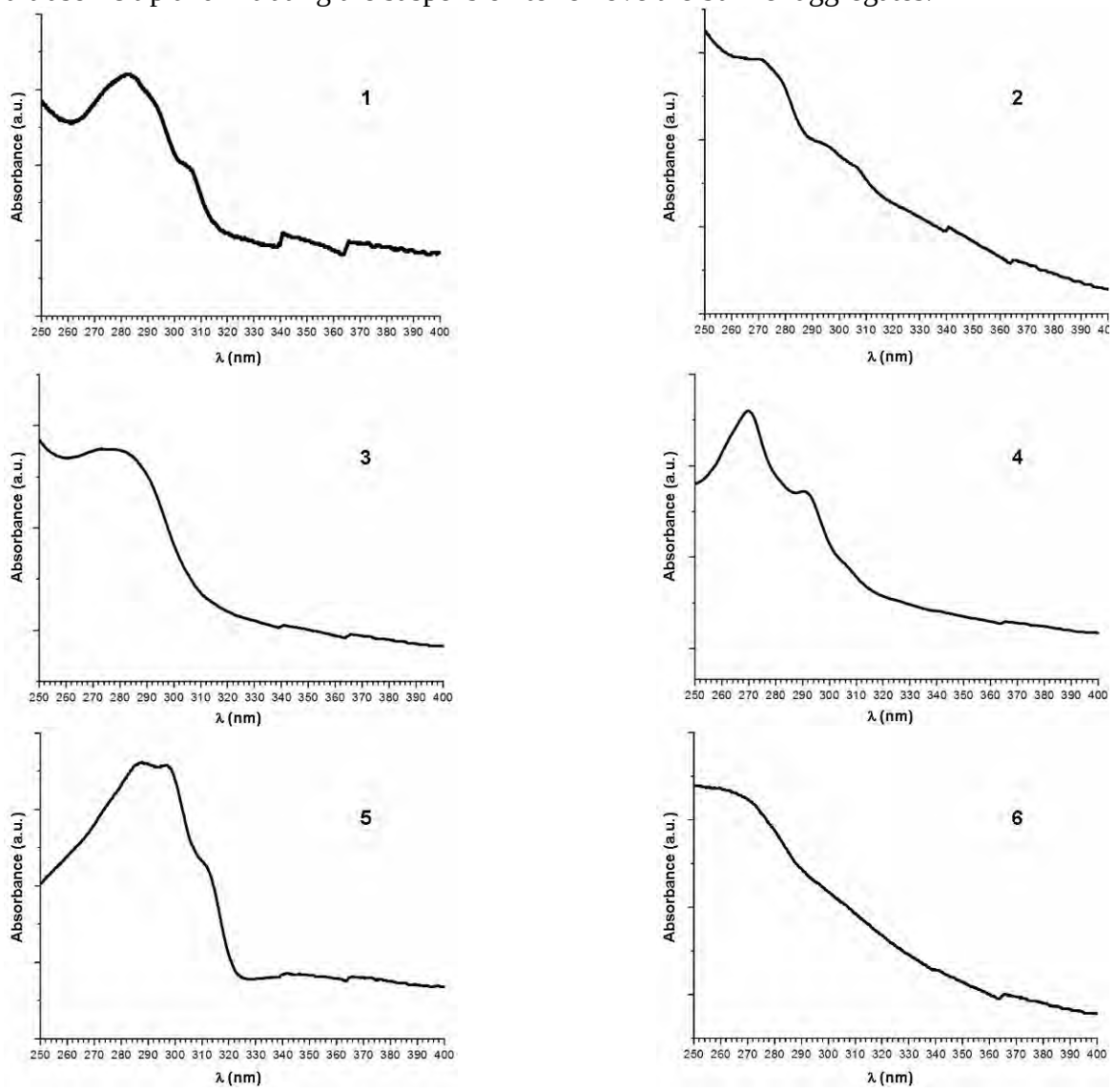

Table S7.1 Particle size estimated from the effective mass approximation (Brus equation).

Precursor	***λ_{onset} (nm)***	***E_g (eV)***	***Diameter (nm)***
1	282	4.39	9.0
2	271	4.58	8.1
3	282	4.40	10.1
4	270	4.60	8.9
5	287	4.32	9.4
6	269	4.61	8.0

Brus equation:

$$E_{NP} = E_g + \frac{\hbar^2 \pi^2}{2r^2}\left[\frac{1}{m_e^*} + \frac{1}{m_h^*}\right] - \frac{1.786e^2}{4\pi\varepsilon\varepsilon_0 r}$$ from reference: L. E. Brus, *Appl. Phys. A*, **1991**, *53*, 465.

where E_g = 3.68 eV for blende and 3.73 eV for wurtzite from reference: S.M. Sze, *Physics of Semiconductor Devices*, 2nd ed.; John Wiley & Sons: New York, **1981**; p. 492.]
and $m_e^* = 0.42\ m_e$; $m_h^* = 0.61\ m_e$; $\varepsilon = 8.3\ \varepsilon_0$ from reference: P. E. Lippens, M. Lanoo, *Phys. Rev. B*, **1989**, *39*, 10935.

Note: The particle size estimated from the Brus equation indicate very small particle sizes, below 10 nm although slightly greater than those estimated from Scherrer formula and TEM images. Probably because absorption peaks of the carbonaceous matrix are also present in the UV-Vis spectra. Therefore, these results must be taken with care.

S8. FTIR spectra of the thermolysis products at 300ºC of compounds **1**-**6**.

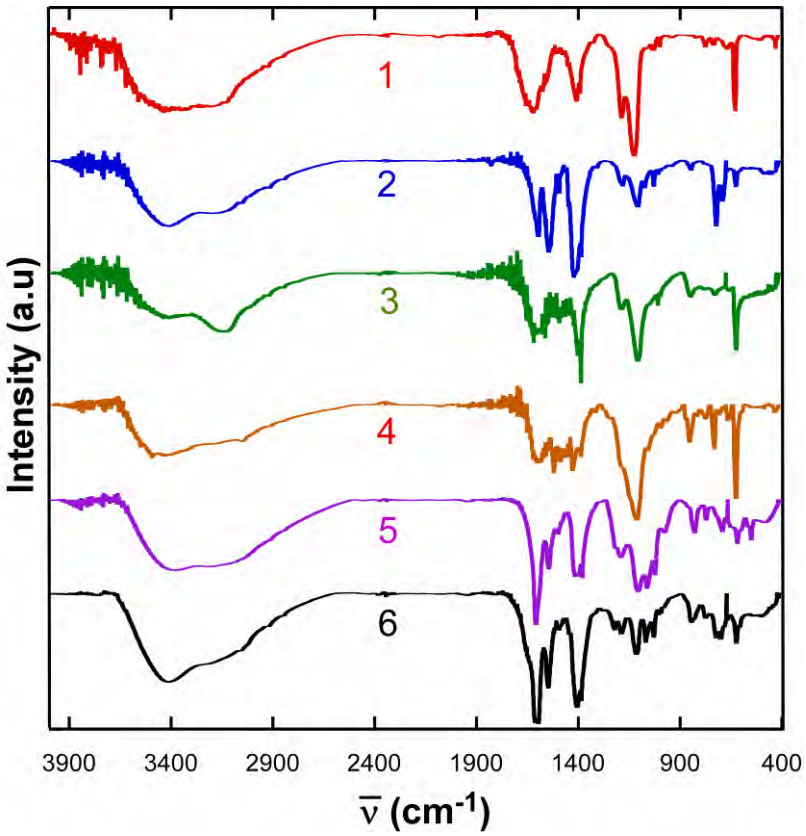
Intensity (a.u)
1
2
3
4
5
6
3900
3400
2900
2400
1900
1400
900
400
$\overline{\nu}$ (cm^{-1})

S9. SEM images of the thermolysis products at 300ºC of compounds **1**-**6**.

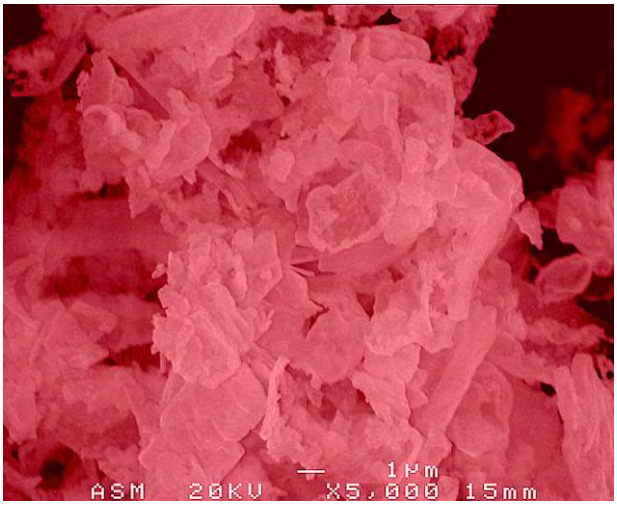

1

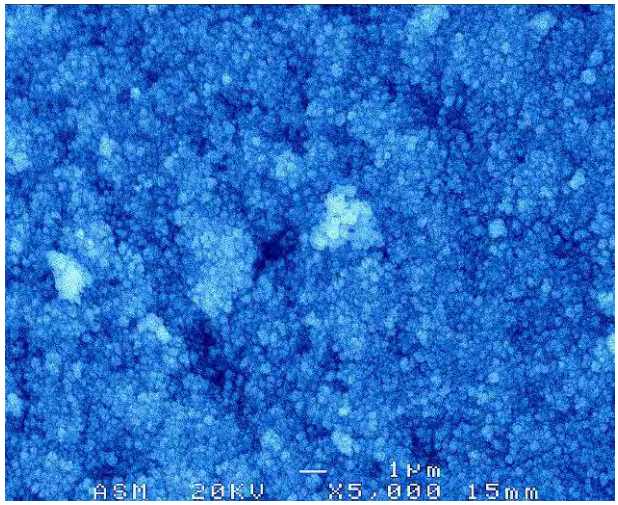

2

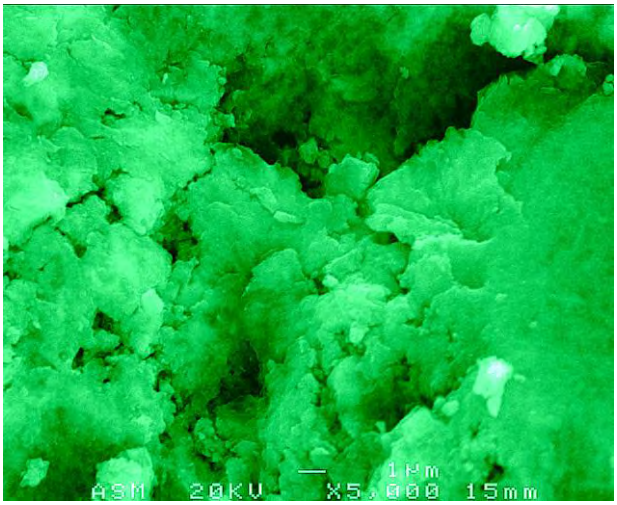

3

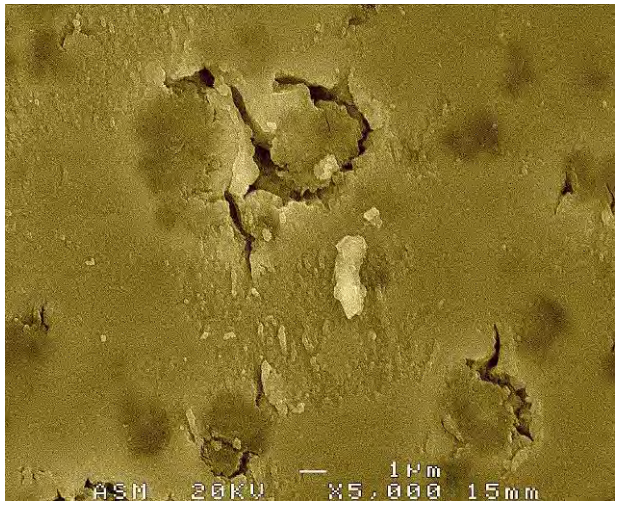

4

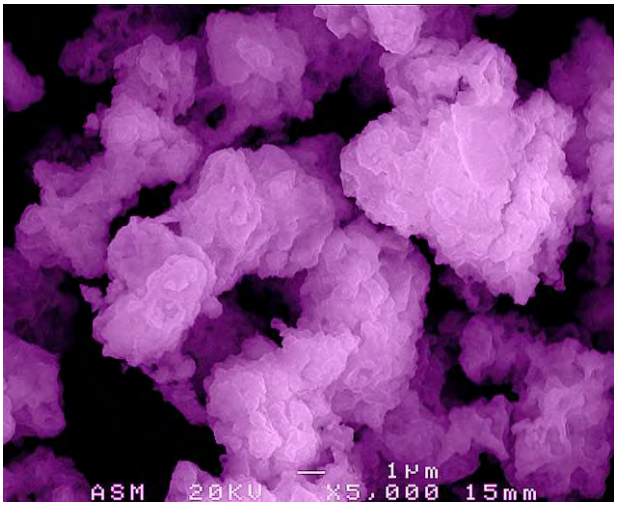

5

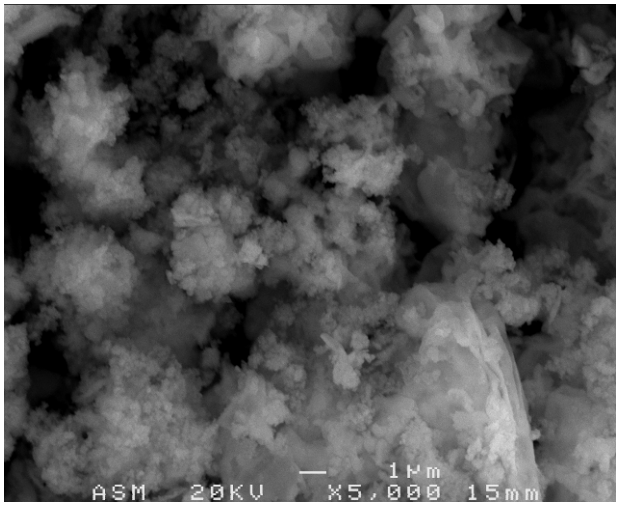

6

S10. TEM images of the thermolysis products at 300ºC of compounds **1**-**6**.

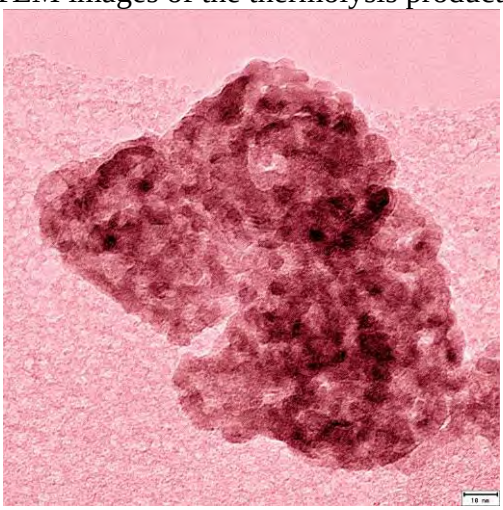

1

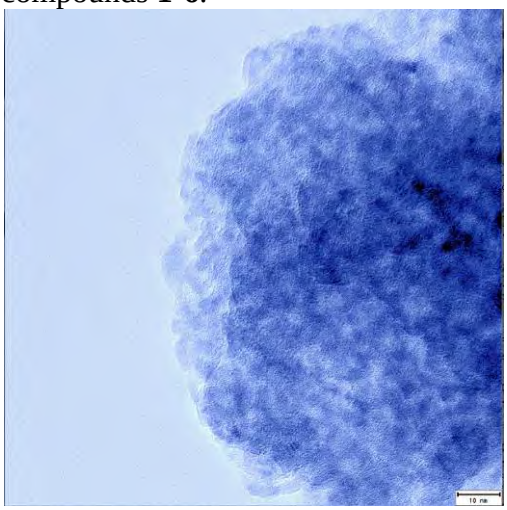

2

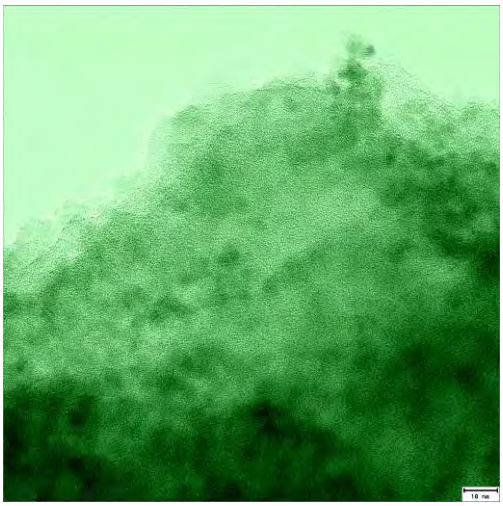

3

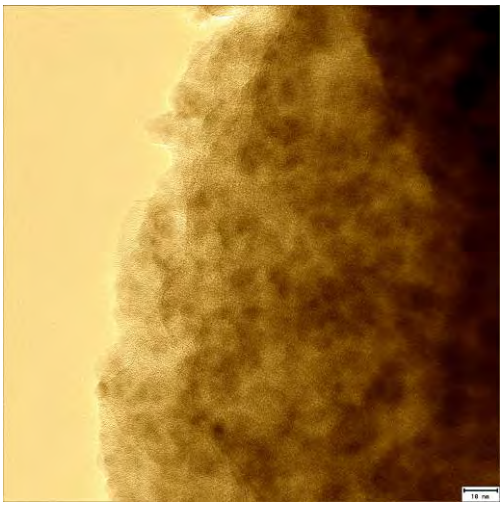

4

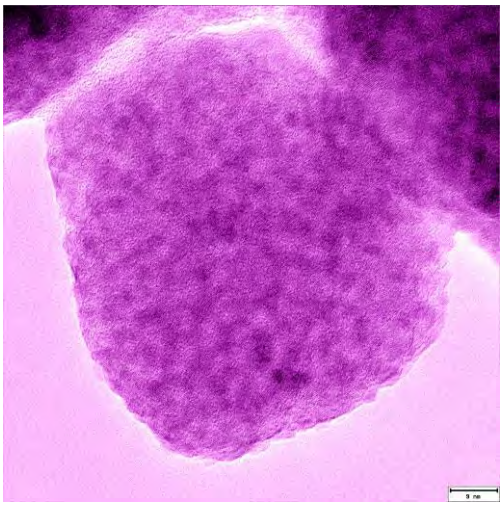

5

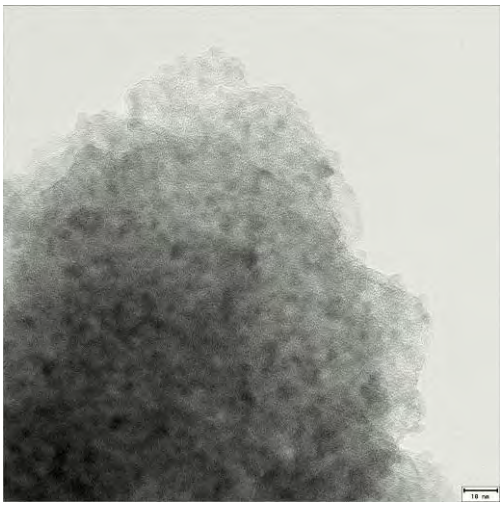

6

S11. ZnS particle size distribution from TEM images of the thermolysis products at 300ºC.

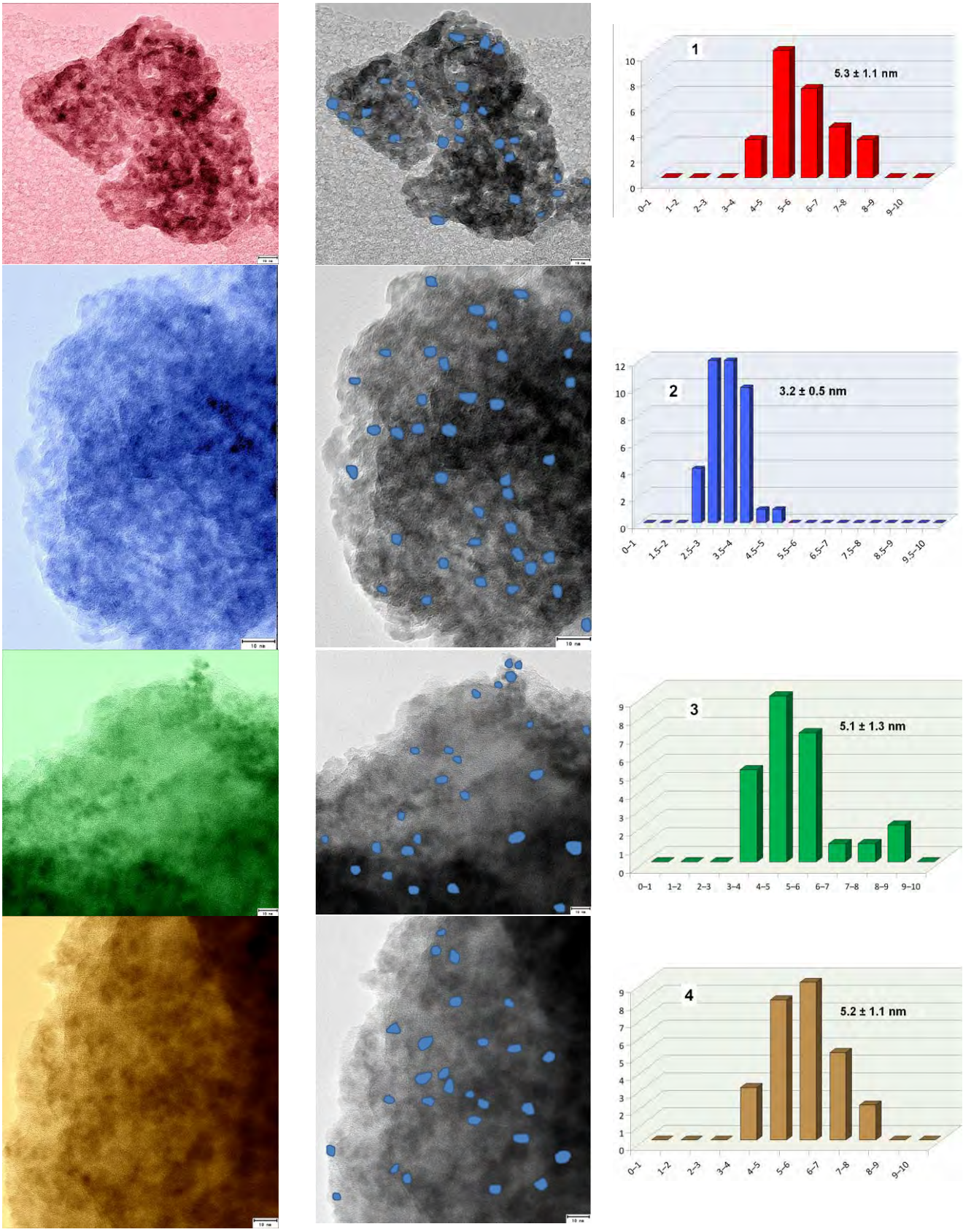

S11 (cont.). ZnS particle size distribution from TEM images of the thermolysis products at 300ºC.

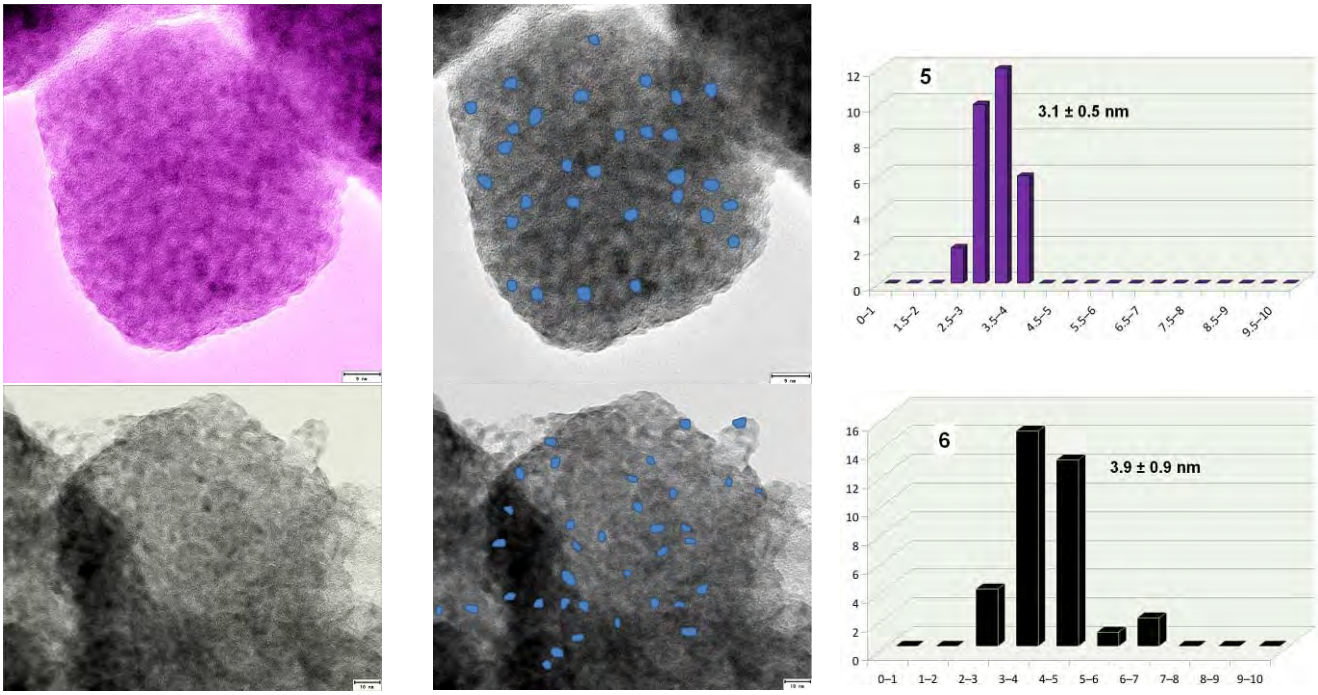

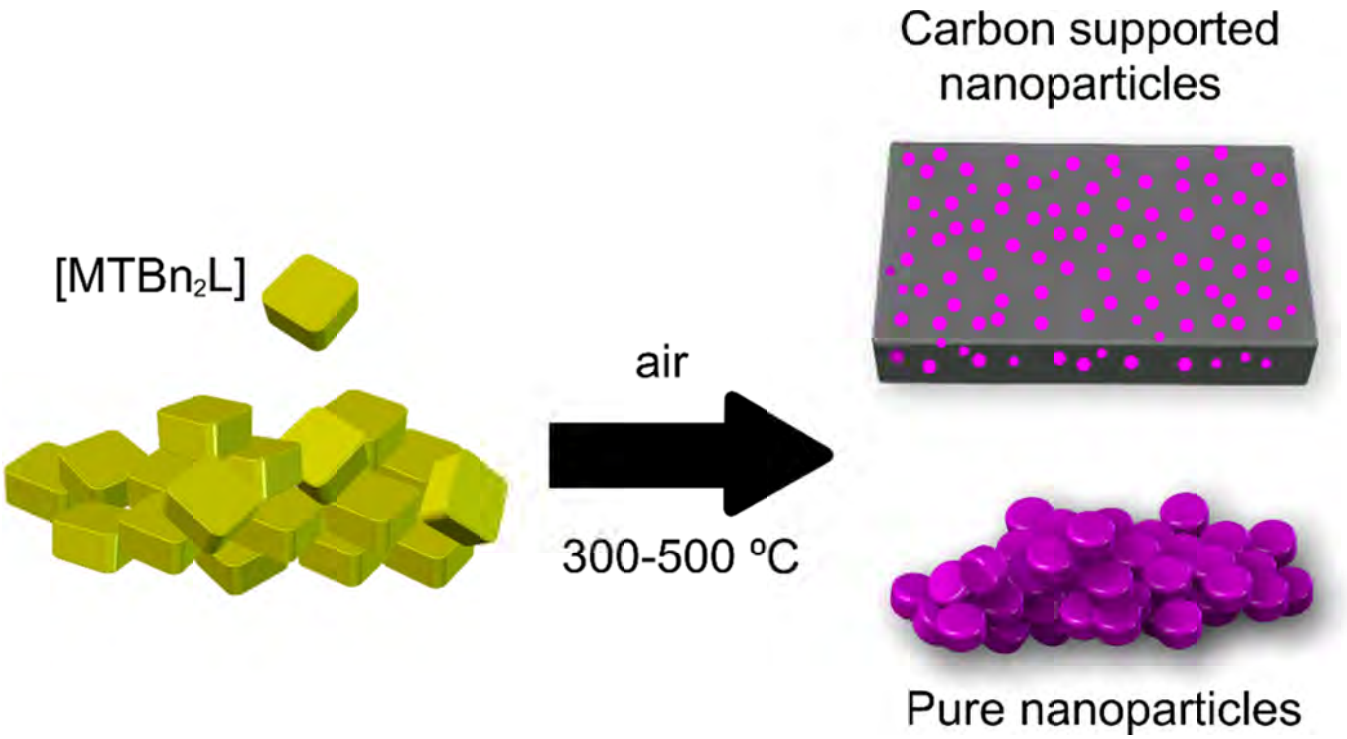

3. METAL-THIOBENZOATO COMPLEXES: SYNTHESIS, STRUCTURE AND PROCESSING AS CARBON SUPPORTED NANOPARTICLES

3.1. SUMMARY

The third chapter can be considered as a continuation of the research carried out in the previous chapter, extending the studies to other metallic systems (palladium and cadmium).

The first part of the chapter accounts for the synthesis, chemical and structural characterization of six new compounds of formula $[M(TBn)_2L]$ [TBn: thiobenzoate; M: Cd(II), Pd(II), Zn(II); L: 2,2'-bipyridine (bpy), 1,10-phenantroline (phen), 1,2-di-(4-pyridil)-ethylene (bpe), neocuproine (neo), adenine (ade)] that have been obtained by the reaction of $M(CH_3COO)_2{\cdot}2H_2O$ with the corresponding N-heterocyclic ligand and thiobenzoate (TBn) in methanol or *N,N'*-dimethylformamide (DMF). The use of chelating ligands leads to discrete monomeric entities in compounds $[Pd(TBn)_2(bpy)]$ (PdBPY), $[Pd(TBn)_2(phen)]$ (PdPHEN), $[Zn(TBn)_2(neo)]$ (ZnNEO) and $[Cd(TBn)_2(neo)]$ (CdNEO). In these compounds the metal is bonded to sulfur atoms of two thiobenzoate ligands and to two nitrogen atoms from one pyridine derivative. On the contrary, the bridging capability of the bipyridinic ligand gives rise to the polymeric chains observed in compound $[Cd(TBn)_2(\mu\text{–}bpe)]_n$ (CdBPE). The synthesis of compound $[Cd(TBn)_2(ade)(CH_3OH)]$ (CdADE) gives rise to a monomer in which cadmium is bound to two sulfur atoms from TBn, to one nitrogen atom from Hoogsteen face of ade and to an oxygen from a molecule of methanol.

The second part of the chapter is devoted to the use of these metal-thiobenzoate complexes as precursors for the synthesis of metallic (Pd) and metal sulfide (ZnS and CdS) nanoparticles. It is achieved through a thermal treatment that consist again on a solventless decomposition under aerobic conditions using moderate temperatures (300–500ºC) and short exposure times (less than an hour). During the heating process ligands passivate the surface of the particle limiting its growth, and the resulting crystalline phase. SEM/TEM images reveal the presence of these nanoparticles (ZnS: 8–9 nm; CdS: 8–19 nm; Pd: 32–70 nm) embedded in a

carbonaceous matrix. In general, during the thermolysis of the precursors, moderate temperatures are used to prevent the sintering of the NPs, but it also implies a generally quite high percentage of non-volatile carbonaceous residues impurities because of the lack of sufficient energy to complete the elimination of the ligands. However, it has been observed that the amount of carbon correlates with carbon content of the co-ligands employed to stabilize the metal-thiobenzoates in such a way that it is possible to obtain from almost carbon free nanoparticles to a homogeneous dispersion of them in a thick carbonaceous matrix.

Although in a first instance the non-volatilized carbonaceous part could be considered a disadvantage, numerous studies prove that heterostructures based on semiconducting nanoparticles embedded in carbon materials show promising features for its implementation in batteries, electrocatalysis and photocatalysis. The dispersion of metal nanoparticles on carbon matrix is a common practice in industry since this class of hybrid materials are widely employed as electrochemical electrodes for fuel cell and battery applications, as well as heterogeneous catalyst for organic synthesis, hydrodesulphurization, wastewater treatment, etc. The carbon matrix further prevents the agglomeration and sintering of the nanoparticles and in the same way it serves as continuous, porous and conductive support. The controlled decomposition of metal-organic precursors in solid state opens a new synthetic single-stage route for the production of carbon-based nanocomposites implying benefits related to solvent use, technical simplicity, and lower manufacturing cost.

The results of this chapter (article plus supporting information) have been submitted to *European Journal of Inorganic Chemistry* scientific journal.

3.2. PUBLICATION

EurJIC European Journal of Inorganic Chemistry
ChemPubSoc Europe
FULL PAPER

DOI: 10.1002/ejic.201((will be filled in by the editorial staff))

Metal-Thiobenzoato Complexes: Synthesis, Structure and Processing as Carbon Supported Nanoparticles

Daniel Vallejo-Sánchez,[a] Garikoitz Beobide,*[a] Oscar Castillo,*[a] Mónica Lanchas,[a] Antonio Luque,[a] Sonia Pérez-Yáñez,[a, b] Pascual Román[a]

Keywords: thiobenzoato / thiocarboxylato / single-source precursors / carbon supported nanoparticles / dry thermolysis

Six new compounds of formula $[M(TBn)_2L]$ [TBn: thiobenzoato; M: Pd(II), Zn(II), Cd(II); L: 2,2'-bipyridine (bpy), 1,10-phenantroline (phen), 1,2-di-(4-pyridil)-ethylene (bpe), neocuproine (neo), adenine (ade)] have been obtained by the reaction of $M(CH_3COO)_2{\cdot}2H_2O$ with the corresponding *N*-heterocyclic ligand and thiobenzoato (TBn) in methanol or *N,N'*-dimethylformamide (DMF). The use of chelating ligands leads to discrete monomeric entities in compounds $[Pd(TBn)_2(bpy)]$ (PdBPY), $[Pd(TBn)_2(phen)]$ (PdPHEN), $[Zn(TBn)_2(neo)]$ (ZnNEO) and $[Cd(TBn)_2(neo)]$ (CdNEO). In these compounds the metal is bonded to sulfur atoms of two thiobenzoate ligands and to two nitrogen atoms from one pyridine derivative. On the contrary, the bridging capability of the bpe bipyridinic ligand gives rise to the polymeric chains observed in compound $[Cd(TBn)_2(\mu\text{–}bpe)]_n$ (CdBPE). The use of adenine as co-ligand gives rise to the monomeric compound $[Cd(TBn)_2(ade)(CH_3OH)]$ (CdADE) in which cadmium is bound to two sulfur atoms from TBn, to one nitrogen atom from Hoogsteen face of ade and to an oxygen from a methanol molecule.

The presence of sulfur donor atoms and carbon rich co-ligands enables these complexes yielding a set of metallic and metal sulfide nanoparticles embedded into a carbonaceous support. Precisely, the thermal treatment process to produce the latter materials consist of a solventless decomposition under aerobic conditions using moderate temperatures (300–500ºC) and short exposure times (less than an hour). The analysis of the X-ray diffraction pattern and SEM/TEM images reveal that the carbonaceous matrix hosts well dispersed nanocrystallites. The influence of metal(II) ion and the *N*-heterocycle ligand on the crystalline phase, size and purity of the resulting carbon supported nanoparticles is discussed.

[a] Departamento de Química Inorgánica, Facultad de Ciencia y Tecnología, Universidad del País Vasco (UPV/EHU), Apartado 644, E–48080 Bilbao, Spain
Fax: 34-94601-3500
E-mail: garikoitz.beobide@ehu.eus
[b] Departamento de Química Inorgánica, Facultad de Farmacia, Universidad del País Vasco (UPV/EHU), E–01006 Vitoria-Gasteiz, Spain

Introduction

Thiocarboxylato ligands provide a valuable tool to design and synthesise metal-complexes as the presence of both soft sulfur and hard oxygen donor sites implies not only the ability to bind metals of rather different nature,[1] but it also endorses appealing electronic properties such as luminescence and conductivity.[2] Apart from that, complexes of chalcogenide have been studied as precursors for the deposition of II/VI type semiconductor nanoparticles through single-source precursor routes,[3] which makes this kind of coordination compounds of particular interest due to the increasing demand of quantum dots (QDs) for technological applications.[4] Precisely, the single-source precursor routes employ sulfur containing coordination compounds as starting material since metal-chalcogenide bonds are already present in the structure. In this approach, the metal-organic precursor is dispersed in a coordinating solvent (usually amines or amides) and injected into a hot solution containing a surfactant in order to stabilize the chalcogenide particles and to limit their growth. Thus, nanoparticles (NPs) with narrow size distributions are achievable. More recently, an alternative procedure called solventless thermolysis have been the focus of several research works,[5] as it allows to prepare nanostructures by using solely metal-organic precursors. In comparison to solvent assisted single-source precursor route, dry thermolysis implies lower costs as diminishes the use of toxic and environmentally unfriendly organic solvents and hardly extractable surfactants. In this solventless approach, during the heating process the ligands passivate the surface of the particle limiting its growth, and as consequence, determine its size. The nature of the ligand influences also on the final phase and crystallinity of the achieved metal chalcogenide.[6] In general, during the thermolysis of the precursor, moderate temperatures are used to prevent the sintering of the NPs, but it also implies a generally quite high percentage of carbon impurities because of the lack of sufficient energy to complete the elimination of the ligands.[7]

Although in a first instance the non-volatilized carbonaceous part could be considered a disadvantage, numerous studies prove that heterostructures based on semiconducting nanoparticles embedded in carbon materials show promising features for its implementation in batteries, electrocatalysis and photocatalysis.[8] In fact, the dispersion of metal nanoparticles on carbon matrix is a

common practice in industry since this class of hybrid materials are widely employed as electrochemical electrodes for fuel cell[9] and battery applications,[10] as well as heterogeneous catalyst for organic synthesis,[11] hydrodesulfurization,[12] wastewater treatment,[13] etc. Furthermore, the carbon matrix prevents the agglomeration and sintering of the nanoparticles and in the same way it serves as continuous, porous and conductive support. Conventional methods for the preparation of heterogeneous catalysts focus on impregnation or dip-coating techniques that require long optimization times to achieve reproducible and homogeneous results.[14] The controlled decomposition of metal-organic precursors in solid state opens a new synthetic single-stage route for the production of carbon-based nanocomposites implying benefits related to solvent dispensal, technical simplicity, and lower manufacturing cost.

In a previous work[15] we demonstrated that thiocarboxylato complexes can be employed as single-source precursors for the synthesis of zinc sulfide nanoparticles. It was concluded that dry thermolysis, under aerobic conditions, of thioacetato complexes favoured the formation of highly pure sulfides. In this work we are focused on replacing the thioacetato ligand by the more stable thiobenzoato ligand in combination with *N*-heterocycle ligands of different C/N ratio and aromaticity degree to provide a carbonaceous matrix for the resulting nanoparticles. In particular, six new M^{II} (Pd, Cd, and Zn) thiobenzoate compounds containing additional bidentated nitrogen ligands (phen, neo, bpy, bpe and ade) were prepared and structuraly characterized, after which they were subjected to dry thermolysis under aerobic conditions and moderate temperatures to provide Pd@C, ZnS@C and CdS@C composites.

Results and Discussion

This section describes first the chemical and crystal structures of metal-organic precursors, as these data will support the discussion regarding the formation of carbonaceous composites of metal and metal sulfide nanoparticles (M@C and MS@C, respectively). Prior to the dry thermolysis experiments, a sub-section devoted to preliminary thermogravimetric analyses is presented in which decomposition mechanistics and optimum treatment temperature ranges will be set. Thereafter, results on the dry thermolysis experiments are thoroughly discussed, detailing microstructures and particle sizes obtained in each case, to end up with the influence of the thermal treatment parameters.

Crystal structures of precursors. At first glance, the coordination sphere of these complexes (Figures 1 and 2) involves two sulfur bonded thiobenzoate ligands and the remaining coordination positions are occupied by two nitrogen donor atoms from a chelating *N*,*N*´-heterocyclic ligand in compounds PdBPY, PdPHEN, ZnNEO and CdNEO and from two *N*,*N*´-pillared bridging ligands in compound CdBPE. In the case of CdADE, apart from the two S atoms, the coordination sphere is completed by a nitrogen atom from an adenine molecule and the oxygen atom of a methanol molecule. At deeper insight, coordination sphere and corresponding polyhedron can be affected by the semicoordination of thiocarboxylate O atoms which is dependent of the ion type and size as well as the bulkiness of the co-ligands of each compound. As expected from its electronic configuration Pd^{II} (d^8) does not present such semicoordination (Pd···O: 3.32–3.39 Å; distances larger than the sum of the van der Waals radii) and it sets in all cases a square planar coordination geometry [S(sp)=0.70–0.81] (Table 1). On the contrary, the semicoordination of O atoms in Zn^{II} and Cd^{II} (d^{10}) complexes leads to coordination numbers that range from 4 to 6. Initially, ruling out the semicoordination of oxygen atoms, the coordination polyhedron (MN_2S_2) of ZnNEO, CdBPE, CdNEO and CdADE can be described as a distorted tetrahedron. When considering higher coordination numbers, the small ionic radii of Zn^{II} imposes great steric hindrances that implies long Zn···O contacts (3.06 Å) and results into a coordination environment closer to the ideal tetrahedral geometry. On the other hand, the bigger Cd^{II} size allows to set shorter Cd···O contacts (2.55–2.85 Å) and it leads to a smaller deviation respect to polyhedrons of higher coordination number.

Table 1. Continuous shape measures (CShM) calculation results.[16]

Compound	**Geometries** [a]					
	C.N. = 4		C.N. = 5		C.N. = 6	
	SP	T	TBPY	SPY	OC	TPR
PdBPY	0.70	30.73	—	—	—	—
PdPHEN	0.81	28.56	—	—	—	—
ZnNEO	29.12	2.80	8.05	8.09	25.62	13.78
CdBPE	26.14	2.67	2.86	7.32	6.61	11.26
CdNEO	29.12	5.46	3.41	6.27	8.40	12.10
CdADE	28.23	2.06	3.29	3.89	11.78	4.53

[a] SP: square-planar, T: tetrahedron, TBPY: trigonal bipyramid, SPY: spherical square pyramid, OC: octahedron, TPR: trigonal prism.

All compounds, except CdBPE, consist of discrete monomeric entities in which the supramolecular assembly is strongly determined by the interactions ocurring between TBn and the N-donor co-ligand, as described below. Bpy and phen ligands in compounds PdBPY and PdPHEN are able to link complex entities through T-shaped aromatic interactions and weak C–H···O and C–H···S hydrogen bonds. On the contrary, the more extended neo ligand in compound ZnNEO establishes π-π parallel stacking interactions that assisted by C–H···O hydrogen bonds assemble the monomeric entities into 1D supramolecular chains. The neo ligand in compound CdNEO, establishes again π-π parallel stacking interactions between them to arrange monomeric entities into supramolecular dimers that are held together by means of T-shaped aromatic interactions and weak C–H···O and C–H···S hydrogen bonds. The presence of the bridging bpe ligand in compound CdBPE, affords a zig-zag 1D polymeric complex entity with Cd···Cd distances of 14.057 and 13.851 Å. These chains are held together by means of T-shaped aromatic interactions among the benzene aromatic rings and weak C–H···O and C–H···S hydrogen bonds.

In compound CdADE, the adenine molecule is coordinated to the cadmium atom through its N7 donor position. This coordination mode is reinforced by an additional intramolecular hydrogen bond between the N6–H amino group and the oxygen atom of the coordinated methanol molecule. Consequently, the Watson-Crick and sugar edges of the adenine are ready to prompt the self-assembly of the complex entities by means of further supramolecular interactions. Sugar edges of two adjacent adenines assemble together by complementary hydrogen bonding, but the Watson-Crick edge also selectively recognise the thiol and methanol oxygen atoms from an adjacent monomeric entity. Both interactions generate a supramolecular 2D arrangement of the monomeric entities in which the aromatic ring of the thiobenzoate ligands establishes π-π parallel stacking interactions that held together the sheets among them. Further details on the crystal

structures, including packing views and bond distances, are gathered in the supporting information.

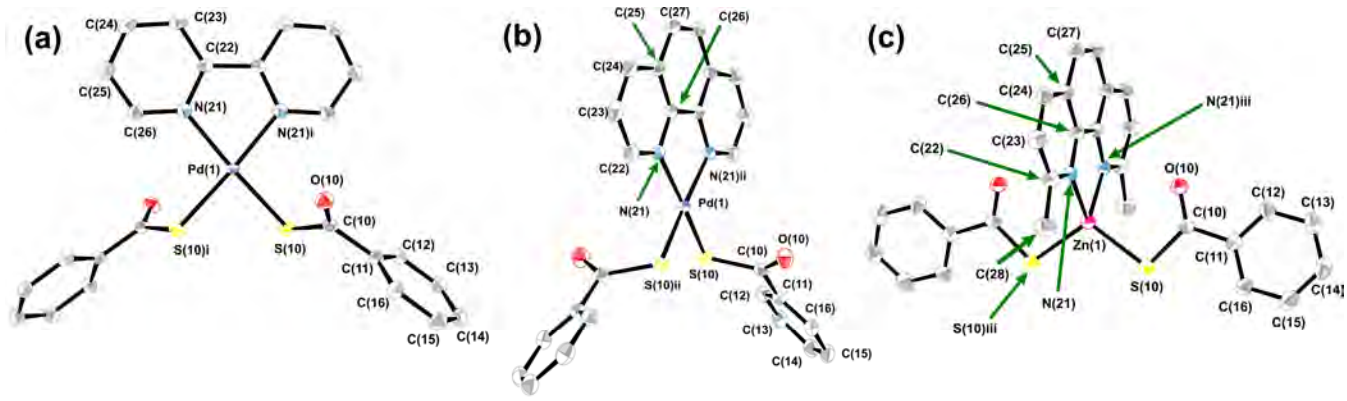

Figure 1. ORTEP diagrams of compounds (a) PdBPY, (b) PdPHEN, and (c) ZnNEO showing the labelling scheme. Hydrogen atoms are omitted for clarity. Symmetry codes: (i) -x+1, y, -z+1/2; (ii) -x+3/2, y, -z+1; (iii) -x+1, y, -z+3/2.

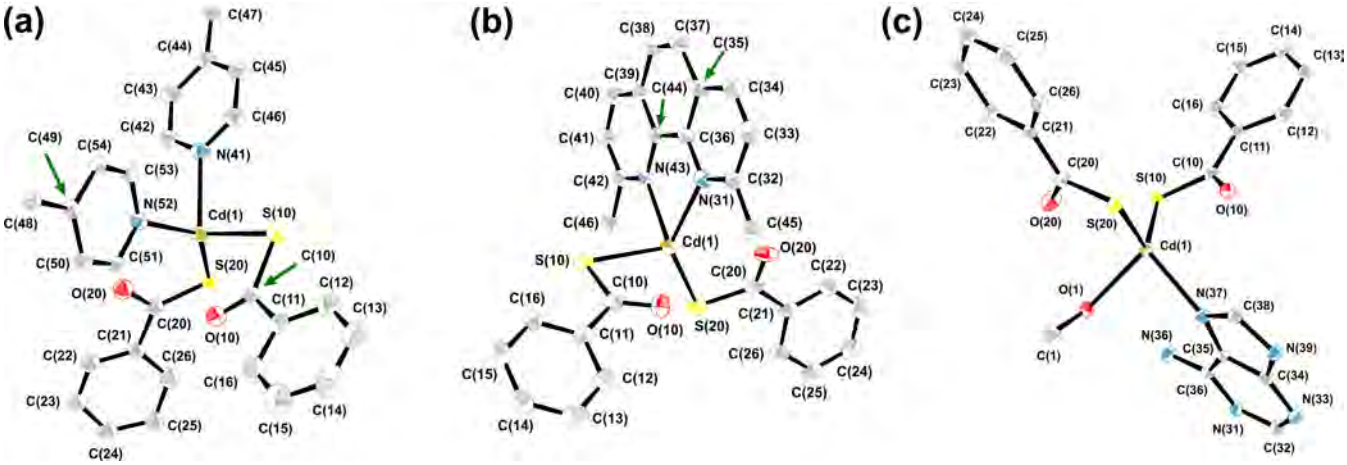

Figure 2. ORTEP diagrams of compounds (a) CdBPE, (b) CdNEO, and (c) CdADE showing the labelling scheme. Hydrogen atoms are omitted for clarity.

Decomposition mechanism and optimum treatment temperature. The evaluation of synthesized compounds as single-source precursors for carbon supported nanomaterials was initially checked by thermogravimetric measurements in order to define an optimum range to afford desired products. The thermal degradation under synthetic air atmosphere shows (Figure 3a) that all the compounds start their decomposition at relatively low temperatures (PdBPY: 198ºC; PdPHEN: 230ºC; ZnNEO: 239ºC; CdBPE: 220ºC; CdNEO: 237ºC; CdADE: 151ºC). Apparently, the decomposition temperatures are more dependent on the nature of the co-ligands than on the type of the metal centers. In fact, compounds containing a chelating ligand with three fused aromatic hexagonal rings (phen and neo), provide thermally more robust products (230–240ºC) whereas the remaining compounds are notoriously less stable. The analysis of DTA curves (Figure 3b) indicates the occurrence of an endothermic event possibly related to a pyrolytic partial fragmentation of the ligands. After this first mass loss all compounds achieve a more or less stable plateau that corresponds to a variable mixture of $PdSO_4$ or $M^{II}S$ (M^{II}: Zn, Cd) nanoparticles and amorphous carbon, as confirmed by PXRD and microanalysis of these intermediates (see Table S3.1 in the supporting information). On the other hand, precursors provided with non-fused pyridine ligands such as bpe and bpy generate samples with low carbon content (2–4 %) as the fragments formed during the thermolysis (*i.e.* pyridine, methylamine, H_2CN, H_2O, NH_3) are more volatile in nature.[17] In precursors PdBPY and PdPHEN, the previously formed $PdSO_4$ decomposes around 330–350 °C to form elemental palladium. Prior to the pyrolytic stage, the methanol molecule of compound CdADE is released without providing any stable product as successive decomposition processes take place.

At greater temperatures, between 295 and 485 ºC, there is a second weight drop consisting of an overlapped set of exothermic stages related to the oxidation of the carbonaceous phase. Amorphous carbon typically burns at temperatures ranging from 550 to 610°C under aerobic conditions.[18] Nevertheless, in certain precursors (PdBPY, PdPHEN) a substantial lowering in the combustion temperature is noticed implying a decrease of *ca.* 300ºC respect to the typical onset temperature. This fact is explained by the catalytic activity of palladium prompting the oxidation of soot.[19] In group 12 transition metal precursors, the metal sulfide is further oxidized to give ZnO (JPDS: 01-075-0576; *P6$_3$mc*; a= 3.243 Å and c= 5.1948 Å) in the case of ZnNEO or a mixture of CdO (JPDS: 00-001-1049; *Fm-3m*; a= 4.689 Å) and

cadmium oxysulfate (JPDS: 00-032-0140; *Cm2a*; a= 6.976 Å, b= 23.343 Å, c= 6.853 Å) for CdBPE, CdNEO and CdADE. In PdBPY and PdPHEN, at this temperature range, the previously formed elemental palladium undergoes a passivation with the consequent formation of a thin layer of PdO (JCPDS: 01-075-0584; *P-4n2*; a= 3.036 Å and c= 5.327 Å). Additional thermoanalytic data are available in the supporting information.

Dry thermolysis experiments. The aforementioned results indicate that by controlling the decomposition process it is possible to access metal and metal sulfides even under aerobic conditions. It deserves to note that, as far as we are concerned, all the dry thermolysis processes reported up to date, except our previous work,[15] make use of an inert atmosphere in order to yield the corresponding metal chalcogenide. Taking into account the results of the thermogravimetric analyses, precursor powders were introduced for 15 minutes in a tubular oven open to air and preheated to a temperature at which intermediate sulfides or metal are expected to be formed (see Table 2).

The X-ray diffraction profiles taken on thermolysis products prove their crystalline nature (Figure 4) and confirm the achievement of the pursued phase. In the residues of compounds PdBPY and PdPHEN the cubic phase of elemental palladium is found (JCPDS: 01-087-0638; *Fm*-3*m*; a= 3.879 Å). Additionally, in compound PdPHEN a small peak corresponding to the plane (110) of tetragonal PdO is glimpsed. The resulting ZnS obtained from compound ZnNEO corresponds to the wurtzite phase (JCPDS: 00-036-1450; $P6_3mc$; a= 3.821 Å and c= 6.257 Å). This polymorph is metastable at standard conditions in bulk state (the transformation from blende to wurtzite occurs at 1020 ºC)[20] and it is more interesting than the blende cubic phase in terms of optoelectronic properties.[21] CdS obtained from compound CdBPE corresponds to a mixture of wurtzite (JCPDS: 01-077-2306; $P6_3mc$; a= 4.136 Å and c= 6.713 Å) and blende (JCPDS: 00-042-1411; *F*-43*m*; a= 5.818 Å) polymorphs, but CdNEO and CdADE precursors render the pure CdS wurtzite and blende phases, respectively. Thus, it can be concluded that the correct choice of the N-donor co-ligand allows stabilizing a specific crystalline phase.

The amount of carbon accompanying nanoparticles, ranging from 2 to 43 %wt (see Table 2), depends on the starting material, being notorious the presence of a greater percentage of carbon in compounds containing molecules with fused aromatic rings as ancillary ligand (PdPHEN, ZnNEO, CdADE and CdNEO).

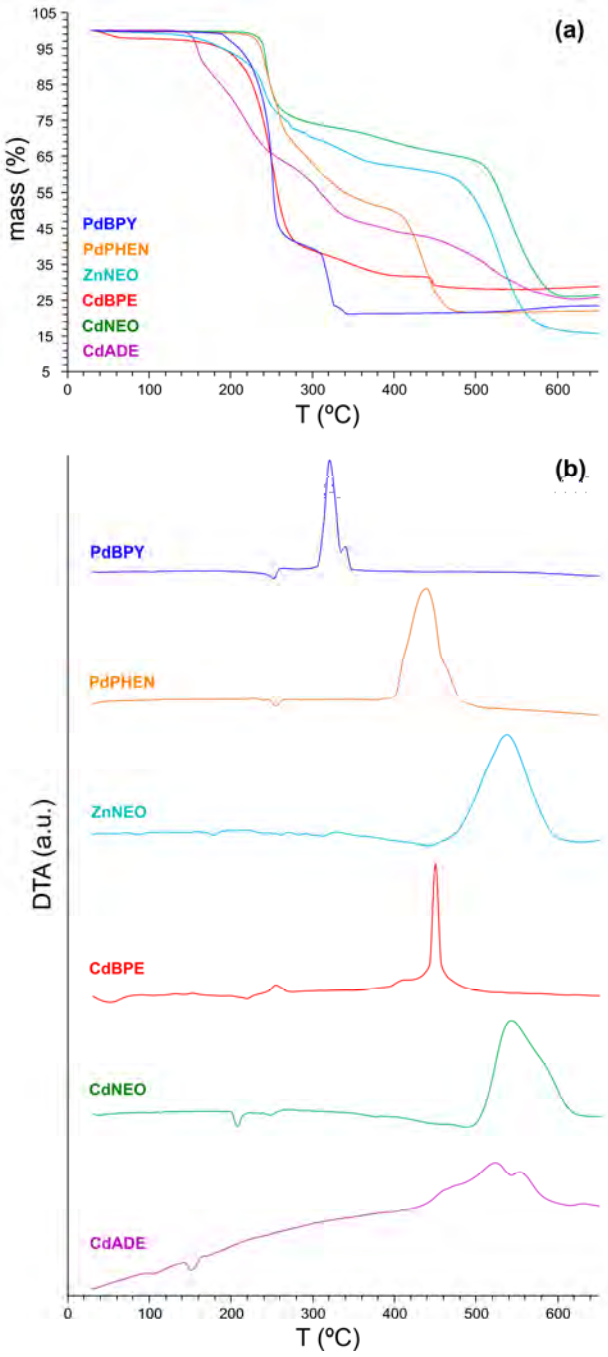

Figure 3. (a) Thermogravimetric analysis of metal(II)-thiobenzoate compounds under synthetic air atmosphere and (b) their corresponding DTA curves.

Table 2. Main characteristics of the dry thermolysis products obtained under aerobic conditions.

Precursor	T (ºC)	Products (JPDS Card) [a]	D_{XRD} (nm) [b]	D_{TEM} (nm) [c]	C.V. (%) [d]	C (% wt) [e]
PdBPY	345	Pd (01-087-0638)	60	3±1 / 119±52	33.3 / 43.7	1.6
PdPHEN	480	Pd (01-087-0638) PdO (01-075-0584)	70	21±6 / 78±26	28.6 / 33.3	38.4
ZnNEO	400	w-ZnS (00-036-1450)	9	8±2	25.0	41.8
CdBPE	400	c-CdS (00-042-1411) w-CdS (01-077-2306)	13 (blende) 8 (wurtzite)	28±8	28.6	3.9
CdNEO	480	w-CdS (01-077-2306)	19 (wurtzite)	35±9	25.7	42.7
CdADE	400	c-CdS (00-042-1411)	11 (blende)	16±4	25.0	22.2

[a] JPDS card number. [b] Mean particle size estimated from Debye-Scherrer equation. Diffraction peaks chosen for each crystalline phase: (111) for Pd, (110) for w-ZnS, (110) for w-CdS and (200) for c-CdS. [c] Mean particle size along with its standard deviation calculated from the statistical analysis of TEM images. [d] C.V.: coefficient of variation. [e] Carbon mass percentage range calculated by gravimetry.

The average crystallite size of the as-synthesized nanoparticles was estimated from Debye-Scherrer[22] equation (Table 2). The great widening of diffraction peaks observed in ZnS and CdS samples reveals the nanometric nature of the crystalline domains for which size estimate ranges from 8 to 19 nm. In contrast, full widths at half maximum (FWHM) of the measured signals for metal palladium samples are markedly thinner, and lead to crystallite size of 60–70 nm. Note that particle size obtained from XRD analyses corresponds to the statistic of the bulk sample, and the contribution of the smallest particles is masked. This fact will be further discussed in TEM (transmission electron microscopy) analyses.

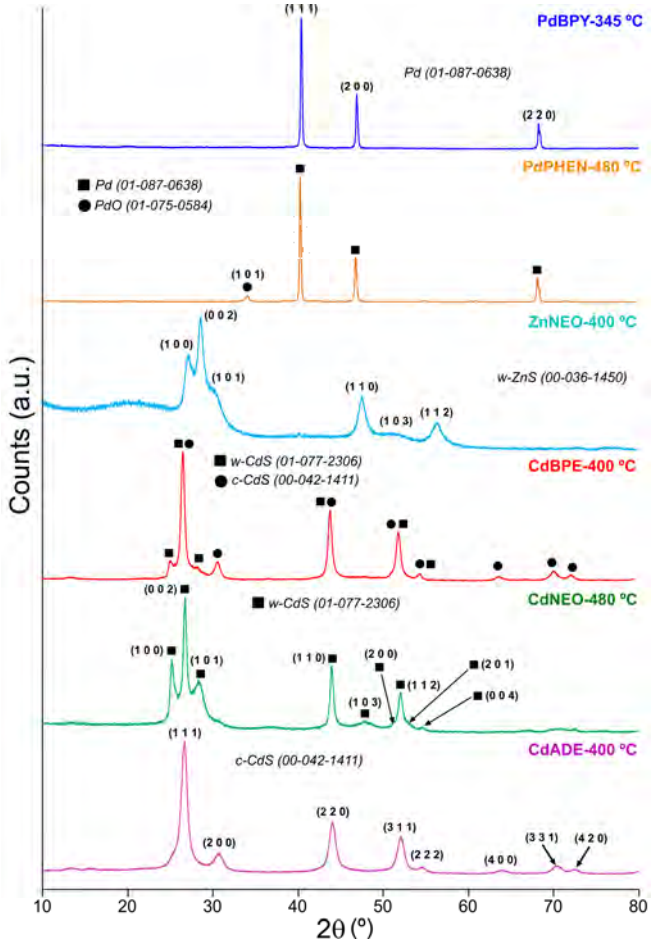

Figure 4. X-ray diffraction patterns of dry thermolysis products obtained under aerobic conditions after having been subjected to 345–480°C for 15 minutes.

SEM images were performed over combustion samples in order to inquire into their microstructural characteristics (Figure 5). Thermolysis products of PdBPY and PdPHEN consist of compact microsized aggregates with smooth surfaces. At high magnifications, the nanoparticles embedded in the carbon matrix are hardly discerned, despite they will become clear in below described TEM analysis. In the case of ZnNEO, the obtained product shows greater compositional heterogeneities at nanometric scale since ZnS nanoparticles tend to aggregate forming clusters of approximately 1–3 micron size. Thermolysis of CdBPE generates an agglomerated granular nanotexture indicative of the presence of partially sintered nanocrystallites. CdS@C nanocomposite prepared from compound CdNEO presents a higher surface rugosity in comparison to the product of ZnNEO (despite both precursors contain neocuproine ligand). The dispersed CdS nanoparticles exhibit a well-defined spherical shape and are better distributed along the carbon matrix at nanoscale. Like carbon-rich precursors (PdPHEN, ZnNEO and CdNEO), compound CdADE degrades creating completely compact and glassy surfaces. However, the compositional arrangement of the material is just the reverse: carbon is grouped forming microparticles and these are surrounded by a matrix composed of CdS nanoparticles linked to each other through a thin carbon coating (Figure 6a-d). This unexpected phenomenon will be discussed later when analyzing the TEM images of samples.

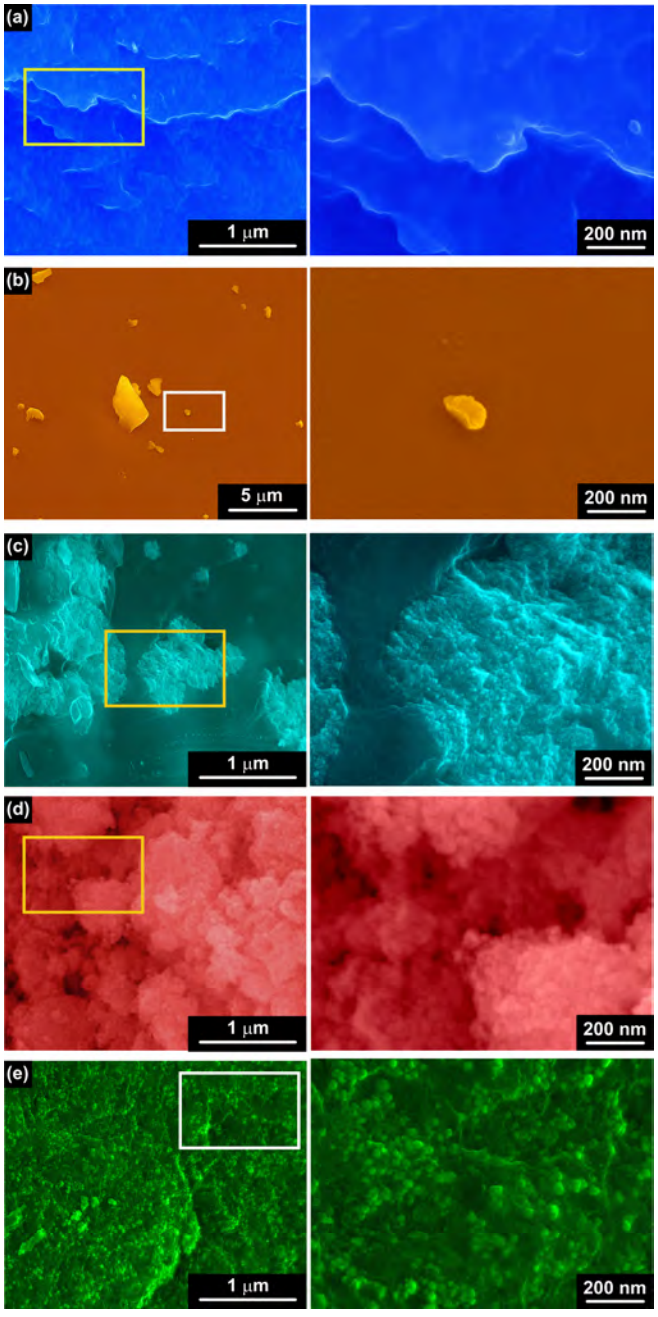

Figure 5. SEM images (10 kX of magnification on the left and 100 kX rightwards) of decomposition products synthetized from (a) PdBPY, (b) PdPHEN, (c) ZnNEO, (d) CdBPE and (e) CdNEO after having been subjected to 345–480°C for 15 minutes.

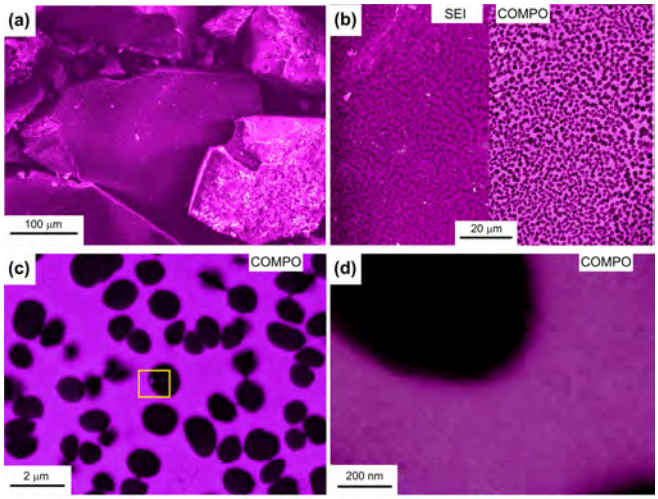

Figure 6. SEM images at different magnifications obtained for thermolysis product of compound CdADE (400ºC for 15 min).

TEM was employed to get a better insight into the generated nanocomposites (Figure 7). Transmission micrographs confirm the existence of nanoparticles dispersed into an amorphous carbonaceous matrix. Data on statistical particle size analysis of the TEM images are provided in Table 2. Accordingly, elemental palladium nanoparticles display a bimodal size distribution in which fine particles (3–21 nm) (Figure 7a-b) and coarse particles (>40 nm) (Figure S4.8) can be distinguished. With regard to particle morphology, spherical particles and low aspect ratio nanorods are obtained for PdBPY and PdPHEN, respectively. This clue suggests that the heterocyclic co-ligand plays a key role in both size and morphology of the resulting Pd nanoparticles.

On the contrary, the sizes found for metal sulfide nanoparticles show smaller polydispersion (coefficients of variation less than 29 %) and generally, smaller than 60 nm (Figure 8). The resulting sizes are comparable to those obtained by wet routes in which surfactants are employed to control particle growth kinetics.[23] All them have monomodal curves except CdS nanoparticles prepared from CdNEO which describe a bimodal behavior with maxima around 25–30 nm and 35–40 nm. The effect of the metal center on particle size also becomes evident by observing the size distributions of sulfide obtained from ZnNEO and CdNEO; ZnS obtained from ZnNEO is composed of nanoparticles lower than 15 nm whereas all CdS nanoparticles generated from CdNEO exceed this limit.

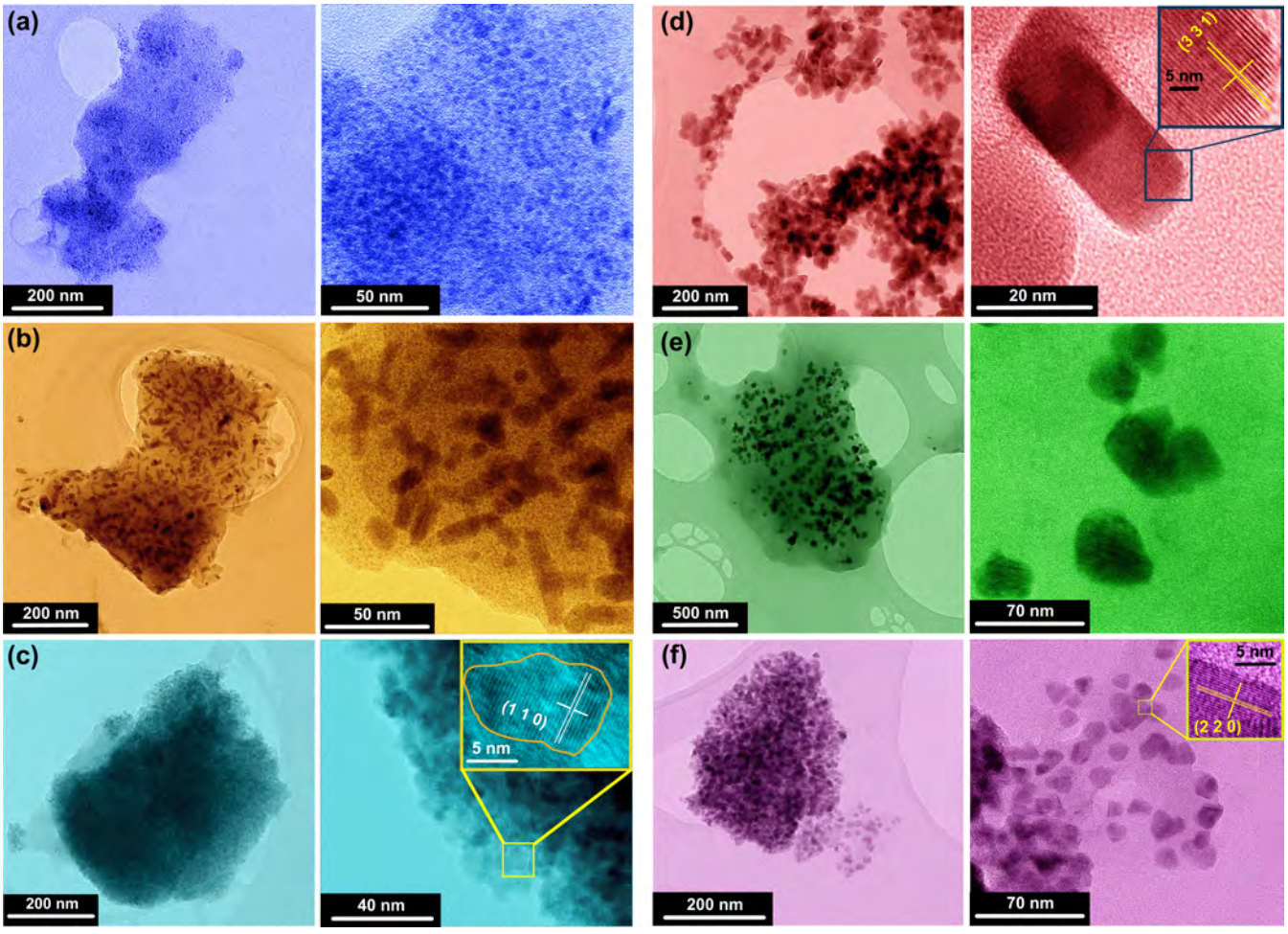

Figure 7. TEM images of thermolysis products: (a) PdBPY, (b) PdPHEN, (c) ZnNEO, (d) CdBPE, (e) CdNEO and (f) CdADE.

TEM images taken on thermolysis product of CdADE will serve to enlighten about the mechanism of formation of the aforementioned micrometric carbon clusters (Figure 6). During dry thermolysis, the first nucleation points appear at the surface of the precursor grains and they grow by incorporating the newly formed cadmium and sulfur atoms that diffuse from inner core of the grain. As semiconducting nanoparticles are formed, they tend to diffuse towards grain boundaries and accumulate therein creating a species of halos for greater carbonaceous agglomerates (Figure S4.10) but a more homogeneus dispersion is obtained for smaller ones. When the grain size is relatively small (< 1 μm) this phenomenon is not observable because nanoparticles do not have enough space to move and well dispersed agglomerates are generated.

On the other hand, decomposition products show a low degree of agglomeration of nanoparticles within the carbon matrix, being appreciable the individual morphology of themselves along the solid. In MS@C samples, it has even been possible to identify certain crystallographic orientations (Figure S4.9) in contrast to Pd@C nanocomposites. The interplanar distances measured match those expected for each decomposition product: 0.1977 nm for sample ZnNEO which corresponds to the plane (110) of ZnS wurtzite phase, 0.1743 nm for sample CdBPE which coincides with the plane (331*)* of the CdS cubic phase, 0.2474 nm for sample CdNEO which adjusts to (102) reflection of CdS wurtzite phase and 0.2086 nm for sample CdADE which is consistent with (220) index of CdS cubic polymorph. Each decomposition product has been subjected to qualitative compositional measurements using EDX analysis (Figure S4.11). In zones with lower contrast (*i.e.* matrix rich zone) the carbon ratio is substantially higher, being this increment more abrupt in carbon rich products obtained from PdPHEN, ZnNEO, CdNEO and CdADE. In the case of Pd@C nanocomposites, spectra realized over these brighter areas also show an additional peak corresponding to S element with a Pd/S ratio close to the unity. Thus, the carbonaceous matrix in palladium products contains also amorphous phase of sulfide or palladium sulphate which has not yet been reduced to metal (note, that according to thermogravimetric analysis $PdSO_4$ precedes to the formation of elemental Pd). This sulfur impurities together with the small particle size in PdBPY and high carbon content in PdPHEN seems to hinder the recognition of crystallographic planes.

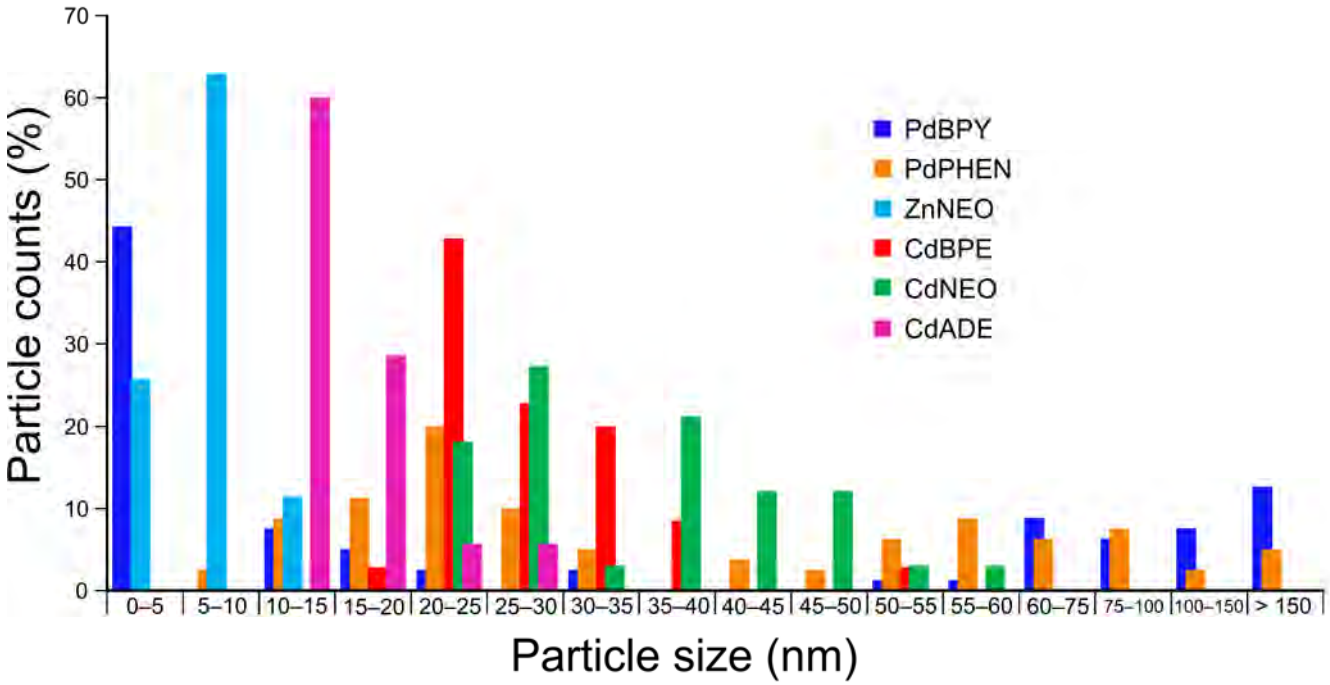

Figure 8. Particle size histograms estimated from TEM images acquired for different decomposition products.

Influence of thermal treatment parameters. In order to understand the degree of influence of the main thermolysis variables on the particle size, crystallinity and the final carbon content of the product, different thermogravimetric tests were performed on the precursor PdBPY. Despite particle size polydispersion found in elemental Pd samples, Debye-Scherrer analysis and TEM images will allow to monitor how coarse and fine particles evolve, respectively. When fixing the onset temperature at 345ºC, TEM images (Figure 9) show how finest particles trend to grow progressively from 3–5 nm at five minutes of treatment time to 80–200 nm after sixty minutes. Considering that the carbon matrix prevents the particle sintering, its elimination as the exposure time increases, prompts the nuclei grow by following Ostwald's maturation but also their aggregation into bigger sized cumules (500–1000 nm). Accordingly, the flattening of PXRD profiles (Figure S1.14) as the treatment time increased is also consistent with the decrease of the amorphous carbon amount. Similarly carbonaceous matrix is also reduced when increasing the onset temperature (at fixed exposure time and heating rate; Figure S1.15) and lowering heating rate (at fixed exposure time and onset temperature; Figure S1.16). Again, Debye-Scherrer analysis (Table 3) does not allow to follow the evolution of finest particles, but it indicates that after fifteen minutes the sintering of small particles into coarse crystallites reaches a limit close to 60 nm. Regarding influence of thermal treatment parameters on the formation of metal sulfides, ZnNEO and CdNEO have been selected as representaive cases. Unlike Pd particles, the size of ZnS and CdS particles is not affected by the exposure temperature and time within the analysed range (400–480ºC; < 60 min).

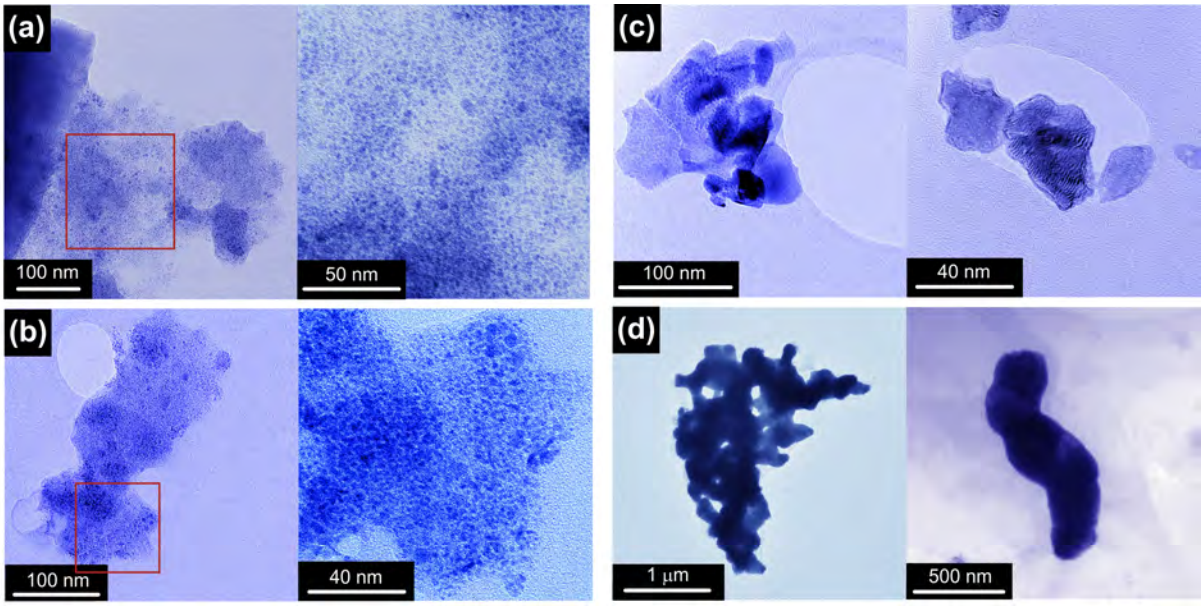

Figure 9. TEM images of the products obtained from compound PdBPY at different combustion times: (a) 5 min, (b) 15 min, (c) 30 min, and (b) 60 min.

Table 3. Debye-Scherrer expression based crystallite size analysis of cadmium and zinc based compounds.

Precursor	T (ºC) [a]	r_H (ºC·min^{-1}) [b]	t (min)	(hkl)	D_v (nm)
PdBPY	345	5	5	(111)	41
	345	5	15	(111)	60
	345	5	30	(111)	66
	345	5	60	(111)	57
	345	15	5	(111)	32
	345	15	15	(111)	69
	345	30	5	(111)	[c]
	360	15	5	(111)	67
ZnNEO	400	[d]	15	(110)-w	9
	480	[d]	15	(110)-w	9
	480	[d]	60	(110)-w	8
CdNEO	400	[d]	15	(110)-w	15
	480	[d]	15	(110)-w	19
	480	[d]	60	(110)-w	17

[a] Combustion temperature. [b] Heating rate. [c] The crystallite size could not be estimated due to the large background level exhibited that partially obscures the diffraction peaks. [d] The precursor was introduced into a preheated oven.

Conclusions

We have obtained 6 different air-stable metal-thiobenzoato compounds (M: Pd, Zn, Cd) altogether with *N*-heterocycles (bpy, phen, neo, bpe and ade) to complete the coordination sphere of the metal(II) ion. The presence of direct metal-sulfur bonds is a key factor to use these compounds as single-source precursors for the synthesis of nanometric chalcogenide particles. Despite thiocarboxylate based compounds are characterized by experiencing clean decompositions at relatively low temperatures,[24] the use of ligands containing aromatic rings make feasible to afford through a mild thermolysis treatment in air atmosphere carbon supported metal and metal sulfide nanocrystallites. The nature of the starting metal-thiobenzoato precursor seems to exert a crucial influence on the final blende/sphalerite or wurtzite crystalline phase of the resulting metal(II) sulfide nanoparticles, as neocuproine based compounds with π-extended systems give rise to wurtzite phase, adenine favors blende phase whereas less extended 1,2-di-(4-pyridil)-ethylene ligand provides a mixture of both polymorphic phases. The carbon content in each sample is also strongly influenced by the nature of the co-ligand. Phen, neo and ade form non-volatile byproducts during pyrolysis resulting in carbonaceous matrices, whereas less fused ligands such as bpy and bpe practically generate pure samples.

Zn(II) and Cd(II) metal-organic precursors render metal(II) sulfides nanoparticles with a fine size distributions and mean size values ranging from 8 to 19 nm. On the contrary, Pd(II) complexes lead to metal nanoparticles with a significant polydispersion, where fine particles (3–20 nm) and coarser ones (< 40 nm) can be distinguished. Accordingly, the analysis of thermal treatment parameters shows that the formation of Pd nanoparticles is highly sensitive to exposure time, heating rates and onset temperature, in such a way that sintering and nuclei growth can be notably affected. On the other hand, size of the formed metal(II) sulfide nanoparticles is not notably influenced by aforementioned parameters, which makes them more reliable product for a hypothetic upscaling. Thus, the single-step method for obtaining nanostructures does not require expensive equipment and production times are brief. Furthermore, the possibility of working under aerobic conditions reduces costs substantially. All these reasons make dry thermolysis an interesting synthetic method in order to satisfy the industrial demand of this new class of materials.

Experimental Section

General information. Commercially available zinc acetate dihydrate (ZnOAc), cadmium acetate dihydrate (CdOAc), palladium acetate dihydrate (PdOAc), thiobenzoic acid (HTBn), 2,2'-bipyridine (bpy), 1,10-phenantroline (phen), neocuproine (neo), 1,2-di-(4-pyridil)-ethylene (bpe), adenine (ade) and all the solvents were of analytical grade and they were used without further purification. The new compounds are stable in air at room temperature. The yields calculated are based on metal salt.

[Pd(TBn)$_2$(bpy)] (PdBPY): 2.5 mmol of PdOAc was dissolved in 45 mL of *N*,*N'*-dimethylformamide (DMF). In another beaker, 2.5 mmol of bpy and 5 mmol of HTBn were dissolved in 5 mL DMF. The resulting solution was added over the solution containing the metal salt while it was subjected to magnetic stirring. In few seconds the dark reddish solution became opaque

by the appearance of a yellowish polycrystalline powder of PdBPY. One hour later the obtained product was filtered and then washed several times with methanol (MeOH) to finally be dried at room temperature for one day. The filtrate was left undisturbed at room temperature to obtain yellow single crystals of PdBPY suitable for X-ray diffraction analysis. Yield (based on metal salt): 0.8993 g (67%). Main IR features of compound PdBPY (cm^{-1}): 3163(vw), 3104(w), 3093(vw), 3078(w), 3058(w), 3029(vw), 2995(vw), 1671(w), 1609(vs), 1595(vs), 1573(s), 1491(w), 1483(w), 1464(w), 1441(s), 1415(w), 1387(vw), 1318(w), 1313(w), 1303(m), 1290(w), 1277(vw), 1263(vw), 1257(vw), 1245(w), 1201(s), 1175(m), 1119(vw), 1104(w), 1096(vw), 1080(w), 1066(w), 1044(vw), 1030(w), 1020(w), 1005(vw), 992(vw), 972(vw), 931(m), 907(s), 846(vw), 800(vw), 775(m), 763(s), 725(m), 702(m), 695(s), 660(m). Anal. Found (%): C, 53.79; H, 3.45; N, 5.42; O, 5.91; Pd, 19.55; S, 11.88. Calc. for $C_{24}H_{18}N_2O_2PdS_2$ (%): C, 53.68; H, 3.38; N, 5.22; O, 5.96; Pd, 19.82; S, 11.94.

[Pd(TBn)$_2$(phen)] (PdPHEN): The synthetic procedure was similar to that of PdBPY, except that phen (2.5 mmol) was used instead of bpy. In this case ligands were added sequentially onto the solution containing the dissolved metal salt (first HTBn and then phen). The polycrystalline product of PdPHEN was washed with MeOH. The mother liquors were left undisturbed at room temperature to obtain yellow single crystals. Yield: 1.1503 g (82%). Main IR features of compound PdPHEN (cm^{-1}): 3158(vw), 3143(vw), 3067(w), 3024(w), 2992(w), 2926(vw), 2856(vw), 1674(m), 1608(vs), 1595(vs), 1570(vs), 1513(m), 1496(w), 1481(w), 1449(sh), 1444(m), 1421(s), 1413(w), 1403(w), 1387(w), 1338(m), 1318(w), 1309(w), 1290(w), 1253(vw), 1218(vw), 1193(s), 1167(s), 1143(w), 1106(m), 1093(w), 1076(w), 1056(vw), 1036(vw), 1024(vw), 1000(vw), 987(vw), 931(m), 908(vs), 875(w), 847(s), 813(vw), 797(vw), 776(s), 739(w), 723(vw), 718(s), 691(s).

Anal. Found (%): C, 55.58; H, 3.16; N, 5.04; O, 5.76; Pd, 19.09; S, 11.37. Calc. for $C_{26}H_{18}N_2O_2PdS_2$ (%): C, 55.67; H, 3.23; N, 4.99; O, 5.70; Pd, 18.97; S, 11.43.

[Zn(TBn)$_2$(neo)] (ZnNEO): The procedure is similar to that of compound PdBPY. ZnOAc (2.5 mmol) was used instead of PdOAc and bpy was replaced by neo (2.5 mmol). The solvent selected for the reaction was MeOH. In few seconds the colorless solution became opaque by the appearance of a whitish polycrystalline powder of ZnNEO. One hour later the obtained product was filtered and then washed several times with methanol (MeOH) to finally be dried at room temperature for one day. The filtrate was left undisturbed at room temperature to obtain colourless single crystals. Yield: 1.2052 g (88 %). Main IR features of compound ZnNEO (cm^{-1}): 3065(w), 3022(w), 1619(w), 1596(vs), 1567(vs), 1500(m), 1481(w), 1441(m), 1426(w), 1375(w), 1337(vw), 1325(vw), 1299(w), 1245(vw), 1220(w), 1194(vs), 1164(s), 1151(sh), 1130(sh), 1098(vw), 1071(vw), 1054(vw), 1026(w), 1001(vw), 987(vw), 970(vw), 920(vs), 853(m), 843(w), 813(vw), 791(sh), 781(sh), 774(m), 729(w), 691(s), 683(m), 663(vw). Anal. Found (%): C, 61.45; H, 3.92; N, 5.08; O, 5.86; S, 11.75; Zn: 11.94. Calc. for $C_{28}H_{22}N_2O_2S_2Zn$ (%): C, 61.37; H, 4.05; N, 5.11; O, 5.84; S, 11.70; Zn, 11.93.

[Cd(TBn)$_2$(μ-bpe)] (CdBPE): The synthetic procedure was similar to that of ZnNEO, except that CdOAc was used as metal source, bpe (2.5 mmol) was used instead of neo and HTBn was added firstly onto metal solution. After one hour of reaction a yellowish powder of CdBPE was recovered. The filtrate was left undisturbed at room temperature to obtain yellow single crystals. Yield: 1.1239 g (79 %). Main IR features of compound CdBPE (cm^{-1}): 3068(vw), 3050(vw), 3024(vw), 1601(vs), 1555(s), 1537(s), 1501(m), 1483(w), 1445(w), 1426(s), 1351(w), 1304(w), 1259(vw), 1247(vw), 1204(vs), 1168(s), 1155(sh), 1115(vw), 1097(vw), 1068(m), 1019(w), 1011(m), 1001(w), 982(m), 961(w), 938(s), 923(s), 866(w), 845(sh), 833(s), 799(sh), 775(s), 742(vw), 721(vw), 689(vs), 675(sh), 652(w). Anal. Found (%): C, 54.92; H, 3.57; Cd, 19.70; N, 4.87; O, 5.73; S, 11.21. Calc. for $C_{26}H_{20}CdN_2O_2S_2$ (%): C, 54.88; H, 3.54; Cd, 19.76; N, 4.92; O, 5.62; S, 11.27.

[Cd(TBn)$_2$(neo)] (CdNEO): The synthetic procedure was similar to that of CdBPE, except that neo (2.5 mmol) was used instead of bpe. The polycrystalline product of CdNEO was washed with MeOH. The mother liquors were left undisturbed at room temperature to obtain pale-yellow single crystals. Yield: 1.3831 g (93 %). Main IR features of compound CdNEO (cm^{-1}): 3053(w), 3022(w), 2999(vw), 2966(vw), 2922(vw), 1616(w), 1590(m), 1539(s), 1502(s), 1441(m), 1410(w), 1376(w), 1364(w), 1305(w), 1291(w), 1251(vw), 1207(vs), 1172(m), 1152(m), 1118(sh), 1102(vw), 1075(w), 1025(w), 994(vw), 931(vs), 858(m), 844(w), 810(vw), 793(vw), 773(m), 728(w), 691(vs), 654(w). Anal. Found (%): C, 56.50; H, 3.62; Cd, 18.78; N, 4.80; O, 5.44; S: 10.86. Calc. for $C_{28}H_{22}CdN_2O_2S_2$ (%): C, 56.52; H, 3.72; Cd, 18.89; N, 4.71; O, 5.38; S, 10.79.

[Cd(TBn)$_2$(ade)] (CdADE): 2.5 mmol of CdOAc was dissolved in 40 mL MeOH and allowed to stirrer at room temperature. In another beaker, 2.5 mmol of ade and 5 mmol of HTBn were mixed in 8 mL of hot MeOH. Immediately, the mixture becomes clear and after one hour of stirring at room temperature the yellow solution is kept in a refrigerator at about 5 ºC. Several days after CdADE appeared as colourless single-crystals mixed with a whitish polycrystalline powder. Yield: 0.7614 g (55 %). Main IR features of compound CdADE (cm^{-1}): 3240(m), 3154(m), 3053(s), 2963(m), 2814(m), 2714(w), 2668(w), 1678(vs), 1647(w), 1599(w), 1585(m), 1545(sh), 1524(s), 1512(s), 1445(s), 1427(m), 1414(m), 1337(m), 1308(w), 1230(sh), 1204(vs), 1167(s), 1119(w), 1101(w), 1076(w), 1059(sh), 1026(vw), 999(vw), 937(s), 916(s), 895(m), 843(w), 824(w), 775(m), 716(vw), 690(s), 656(w). Anal. Found (%): C, 43.33; H, 3.49; Cd, 20.31; N, 12.67; O, 8.58; S: 11.62. Calc. for $C_{20}H_{19}CdN_5O_3S_2$ (%): C, 43.36; H, 3.46; Cd, 20.29; N, 12.64; O, 8.66; S, 11.58.

Physical measurements. Elemental analyses (C, H, N, S) were performed on a Euro EA Elemental Analyzer, whereas the metal content, determined by inductively coupled plasma (ICP-AES), was quantified using a Horiba Yobin Yvon Activa spectrometer Infrared spectra (ATR mode) were recorded at a resolution of 4 cm^{-1} on a FTIR 8400S Shimadzu spectrophotometer for a total of 40 scans in the 4000–650 cm^{-1} spectral region by using a horizontal single-reflection ATR ZnSe prism. Thermal analysis (TG/DTG/DTA) were carried out on a Mettler Toledo TGA/SDTA 851e thermal analyser employing a synthetic air (79% N_2, 21% O_2) flux of 150 $cm^3 \cdot min^{-1}$ with heating rates of 5–30 ºC·min^{-1} and a sample size of about 10–25 mg per run. Combustions of precursors were performed under aerobic conditions within a Carbolite 3216 tubular furnace.

The X-ray powder diffraction patterns (XRPD) were collected on a X-Pert PRO PAN analytical machine employing a Cu Kα radiation source at a scanning rate of 0.026°·s^{-1}. The average diameter of particles (D_v) has been calculated from $D_v = (4/3) \cdot L_v$ expression. $L_V = K \cdot \lambda / \beta \cdot \cos\theta$, where L_V is the volume-weighted average crystallite size measured in a direction perpendicular to surface of the specimen, λ is the average wavelength, in nanometers, of the Kα radiation of Cu (0.154252 nm), θ is the Bragg angle in radians, β (2θ) is the Full Width at Half Maximum (FWHM) of the diffraction peak in radians discounting instrumental contribution [FWHM(º) = 0.0755 + 4 x $10^{-4} \cdot 2\theta$] and K is the shape factor constant, considered as 0.9.

The morphology of carbon supported nanoparticles was examined using a JEOL JSM-7000F scanning electron microscope (SEM) and a Philips CM200 transmission electron microscope (TEM) equipped with an EDXS collection unit. The samples for SEM were prepared just by deposition of the product on a carbon tape while those for TEM were dispersed on ethanol solution containing 5 %wt of *n*-decylamine and placed on a carbon-coated copper grid followed by drying under vacuum.

X-ray structure determination. Diffraction experiments were carried out on an Agilent Technologies SuperNova diffractometers ($\lambda_{Cu-K\alpha}$ = 1.54184 Å for PdBPY, PdPHEN and CdNEO; $\lambda_{Mo-K\alpha}$ = 0.71073 Å for ZnNEO, CdBPE and CdADE). Data were processed and corrected for Lorentz and polarization effects with the CrysAlisPro program.[25] The structures of all compounds were solved by direct methods using the SIR92 program (Table 4 and 5).[26] Full matrix least-squares refinements were performed on F^2 using SHELXL97.[27] All non-hydrogen atoms were refined anisotropically. All calculations for these structures were performed using the WINGX crystallographic software package.[28] During the data reduction process of PdPHEN, CdNEO and CdADE, it became clear that the crystal specimens were twinned with twin laws: (-0.9999 0.0002 -0.0000 / -0.0002 -1.0002 -0.0002 / 0.3008 -0.0007 0.9996) for PdPHEN; (-1.0000 -0.0005 0.0001 / 0.0159 0.0828 -0.9106 / -0.0160 -1.0899 -0.0850) for CdNEO; (-0.4089 0.0003 -0.5927 / -0.0003 -1.0000 -0.0001 / -1.4040 0.0010 0.4094) for CdADE. The final result showed a percentage for minor component of 45.9% (PdPHEN), 36.7% (CdNEO), 41.6% (CdADE). In compound CdBPE, one of the crystallographically independent thiobenzoate ligands is disordered over two almost coplanar arrangements with 50% occupation factors. The internal carboxylate bond distances in the disordered thiocarboxylate were imposed to be nearly equal using SADI command.

Table 4. Crystal data and structure refinement of the compounds PdBPY, PdPHEN and ZnNEO.

Compound	**PdBPY**	**PdPHEN**	**ZnNEO**
Empirical formula	$C_{24}H_{18}N_2O_2PdS_2$	$C_{26}H_{18}N_2O_2PdS_2$	$C_{28}H_{22}N_2O_2S_2Zn$
Mr [g mol^{-1}]	536.92	560.94	547.96
T [K]	100(2)	100(2)	293(2)
Crystal system	monoclinic	monoclinic	Orthorhombic
Space group	*C2/c* (*No.15*)	*I2/a* (*No.15*)	*Pbcn* (*No.60*)
a [Å]	23.9837(14)	10.1891(3)	20.8924(6)
b [Å]	9.4545(3)	10.4666(3)	13.3194(6)
c [Å]	9.8614(6)	20.3093(6)	9.1806(3)
α [°]	90	90	90
β [°]	112.358(7)	94.328(3)	90
γ [°]	90	90	90
V [Å^3]	2068.0(2)	2159.71(11)	2554.72(16)
Z	4	4	4
ρ_{calcd} [g cm^{-3}]	1.725	1.725	1.425
μ [mm^{-1}]	9.335	8.972	1.153
F(000)	1080	1128	1128
θ range [°]	3.99–73.98	4.37–73.97	2.87–26.00
Reflections collected	2074	5464	2508
Independent reflections	2021	5159	1550
Parameters/restraints	141/0	151/0	160/0
R[I > 2σ(I)][a]	R_1 = 0.0363	R_1 = 0.0428	R_1 = 0.0478
	wR_2 = 0.1015	wR_2 = 0.1190	wR_2 = 0.1164
R (all data)	R_1 = 0.0370	R_1 = 0.0443	R_1 = 0.0802
	wR_2 = 0.1019	wR_2 = 0.1200	wR_2 = 0.1317
GOF on F^2 (S)[b]	1.178	1.024	0.905
Weighting scheme[c]	SHELX	SHELX	SHELX

[a] $R_1 = \Sigma(|F_0| - |F_c|)/\Sigma|F_0|$; $wR_2 = \{\Sigma[w(F_0^2 - F_c^2)^2]/\Sigma[w|F_0|^2]\}1/2$. [b] $S = [\Sigma w(|F_0| - |F_c|)^2/(N_{obs} - N_{param})]^{1/2}$. [c] Scheme = $I/[\sigma^2(F_0^2) + (aP)^2 + bP]$ where $P = (F_0^2 + 2F_c^2)/3$; compound (a,b): PdBPY (0.0426, 16.6867), PdPHEN (0.1028, 0), and ZnNEO (0.0543, 0).

Table 5. Crystal data and structure refinement of the compounds CdBPE, CdNEO and CdADE.

Compound	**CdBPE**	**CdNEO**	**CdADE**
Empirical formula	$C_{26}H_{20}CdN_2O_2S_2$	$C_{28}H_{22}CdN_2O_2S_2$	$C_{20}H_{19}CdN_5O_3S_2$
Mr [g mol^{-1}]	568.96	594.99	553.92
T [K]	100(2)	100(2)	100(2)
Crystal system	monoclinic	triclinic	monoclinic
Space group	*C2/c* (*No.15*)	*P*-1 (*No.2*)	$P2_1/n$ (*No.14*)
a [Å]	25.0653(5)	9.0970(7)	11.2499(5)
b [Å]	12.3273(2)	11.1808(10)	10.7383(5)
c [Å]	16.1337(3)	12.4222(9)	18.2771(7)
α [°]	90	81.599(7)	90
β [°]	105.714(2)	83.998(6)	96.992(4)
γ [°]	90	85.110(7)	90
V [Å^3]	4798.79(16)	1239.93(17)	2191.54(17)
Z	8	2	4
ρ_{calcd} [g cm^{-3}]	1.575	1.594	1.679
μ [mm^{-1}]	1.110	8.859	1.219
F(000)	2288	600	1112
θ range [°]	1.69–28.30	3.61–74.00	2.02–28.35
Reflections collected	5488	8573	8763
Independent reflections	4917	6970	7085
Parameters/restraints	289/5	317/0	286/0
R[I > 2σ(I)][a]	R_1 = 0.0425	R_1 = 0.0476	R_1 = 0.0285
	wR_2 = 0.1000	wR_2 = 0.1181	wR_2 = 0.0718
R (all data)	R_1 = 0.0482	R_1 = 0.0578	R_1 = 0.0359
	wR_2 = 0.1044	wR_2 = 0.1214	wR_2 = 0.0733
GOF on F^2 (S)[b]	1.039	0.959	0.975
Weighting scheme[c]	SHELX	SHELX	SHELX

[a] $R_1 = \Sigma(|F_0| - |F_c|)/\Sigma|F_0|$; $wR_2 = \{\Sigma[w(F_0^2 - F_c^2)^2]/\Sigma[w|F_0|^2]\}^{1/2}$. [b] $S = [\Sigma w(|F_0| - |F_c|)^2/(N_{obs} - N_{param})]^{1/2}$. [c] Scheme = $I/[\sigma^2(F_0^2) + (aP)^2 + bP]$ where $P = (F_0^2 + 2F_c^2)/3$; compound (a,b): CdBPE (0.0390, 33.3626), CdNEO (0.0819, 0) and CdADE (0.0472, 0).

Supporting Information (see footnote on the first page of this article): Thermoanalytic data, PXRD patterns, FTIR spectra, SEM/TEM images, bond distances and angles, figures of crystal packings and thermolysis optimization experiments.

Acknowledgments

This work has been funded by Universidad del País Vasco/Euskal Herriko Unibertsitatea (PPG17/37 and UFI 11/53) and Ministerio de Economía y Competitividad (MAT2016-75883-C2-1-P). Technical and human support provided by SGIker (UPV/EHU, MICINN, GV/EJ, ESF) is also acknowledged.

References

[1] a) A. Kreider-Mueller, P. J. Quinlivan, J. S. Owen, G. Parkin, *Inorg. Chem.* **2015**, *54*, 3835–3850; b) S. Singh, S. Bhattacharya, *RSC Adv.* **2014**, *4*, 49491–49500; c) S. Singh, J. Chaturvedi, S. Bhattacharya, *Inorg. Chim. Acta* **2013**, *407*, 31–36; d) H. -Y. Chao, L. Wu, C. -L. Li, W. Lu, L. Liu, X. -L. Feng, *Z. Anorg. Allg. Chem.* **2011**, *637*, 1533–1538; e) M. El-khateeb, T. M. A. Jazzazi, H. Görls, T. M. A. Al-Shboul, M. Westerhausen, *Transition Met. Chem.* **2011**, *36*, 29–33; f) J. Chaturvedi, S. Singh, S. Bhattacharya, H. Nöth, *Inorg. Chem.* **2011**, *50*, 10056–10069; g) J. T. Sampanthar, J. J. Vittal, P. A. W. Dean, *J. Chem. Soc., Dalton Trans.* **1999**, 3153–3156.

[2] a) J. Troyano, O. Castillo, P. Amo-Ochoa, V. Fernández-Moreira, C. J. Gómez-García, F. Zamora, S. Delgado, *J. Mater. Chem. C* **2016**, *4*, 8545–8551; b) B. M. Amoli, S. Gumfekar, A. Hu, Y. N. Zhou, B. Zhao, *J. Mater. Chem.* **2012**, *22*, 20048–20056; c) H. -Y. Chao, L. Wu, C. -L. Li, W. Lu, L. Liu, X. -L. Feng, *Z. Anorg. Allg. Chem.* **2011**, *637*, 1533–1538.

[3] a) M. A. Buckingham, A. L. Catherall, M. S. Hill, A. L. Johnson, J. D. Parish, *Cryst. Growth Des.* **2017**, *17*, 907–912; b) D. C. Onwudiwe, C. A. Strydom, O. S. Oluwafemi, E. Hosten, A. Jordaan, *Dalton Trans.* **2014**, *43*, 8703–8712; c) S. L. Cumberland, K. M. Hanif, A. Javier, G. A. Khitrov, G. F. Strouse, S. M. Woessner, C. S. Yun, *Chem. Mater.* **2002**, *14*, 1576–1584; d) M. A. Malik, N. Revaprasadu, P. O'Brien, *Chem. Mater.* **2001**, *13*, 913–920.

[4] a) X. Wang, G. Sun, N. Li, P. Chen, *Chem. Soc. Rev.* **2016**, *45*, 2239–2262; b) M. Kouhnavard, S. Ikeda, N. A. Ludin, N. B. A. Khairudin, B. V. Ghaffari, M. A. Mat-Teridi, M. A. Ibrahim, S. Sepeai, K. Sopian, *Renew. Sustainable Energy Rev.* **2014**, *37*, 397–407; c) C. Frigerio, D. S. M. Ribeiro, S. S. M. Rodrigues, V. L. R. G. Abreu, J. A. C. Barbosa, J. A. V. Prior, K. L. Marques, J. L. M. Santos, *Anal. Chim. Acta* **2012**, *735*, 9–22; d) T. –H. Kim, K. –S. Cho, E. K. Lee, S. J. Lee, J. Chae, J. W. Kim, D. H. Kim, J. –Y. Kwon, G. Amaratunga, S. Y. Lee, B. L. Choi, Y. Kuk, J. M. Kim, K. Kim, *Nat. Photonics* **2011**, *5*, 176–182; e) P. Xue, *Phys. Lett. A* **2010**, *374*, 2601–2604.

[5] a) M. Hashemi, F. Mohandes, M. Salavati-Niasari, A. S. Esmaeily, *J. Mater. Sci.-Mater. Elec.* **2016**, *9*, 6860–6867; b) C. Zhang, S. Zhang, L. Yu, Z. Zhang, P. Zhang, Z. Wu, *Mater. Lett.* **2012**, *85*, 77–80; c) D. Jose, B. R. Jagirdar, *J. Solid State Chem.* **2010**, *183*, 2059–2067; d) H. G. Cha, D. K. Lee, Y. H. Kim, C. W. Kim, C. S. Lee, Y. S. Kang, *Inorg. Chem.* **2008**, *47*, 121–127.

[6] a) S. H. Lu, T. F. Chen, A. J. Wang, D. Zheng, Y. L. Li, Y. S. Wang, *Mater. Sci. Eng. B* **2016**, *203*, 19–26; b) R. Gaur, P. Jeevanandam, *J. Nanopart. Res.* **2015**, *17*, 156–169; c) A. Ghezelbash, B. A. Korgel, *Langmuir* **2005**, *21*, 9451–9456.

[7] a) A. Tiwari, A. K. Mishra, H. Kobayashi, A. P. F. Turner, *Intelligent Nanomaterials*, 1st ed., Wiley, New Jersey, **2012**, pp. 251–316; b) H. S. Park, S. D. Waezsada, A. H. Cowley, H. W. Roesky, *Chem. Mater.* **1998**, *10*, 2251–2257.

[8] a) X. Du, H. Zhao, Z. Zhang, Y. Lu, C. Gao, Z. Li, Y. Teng, L. Zhao, K. Swierczek, *Electrochim. Acta* **2017**, *225*, 129–136; b) J. Chen, F. Zhang, Y. –L. Zhao, Y. –C. Guo, P. Gong, Z. –Q. Li, H. –S. Qian, *Appl. Surf. Sci.* **2016**, *362*, 126–131; c) B. K. Barman, K. K. Nanda, *Dalton Trans.* **2016**, *45*, 6352–6356; d) Y. Hu, X. Gao, L. Yu, Y. Wang, J. Ning, S. Xu, X. W. Lou, *Angew. Chem. Int. Ed.* **2013**, *52*, 5636–5639; e) H. Ma, J. Han, Y. Fu, Y. Song, C. Yu, X. Dong, *Appl. Catal. B-Environ.* **2011**, *102*, 417–423.

[9] a) D. Duan, X. You, J. Liang, S. Liu, Y. Wang, *Electrochim. Acta* **2015**, *176*, 1126–1135; b) A. Sáez, J. Solla-Gullón, E. Expósito, A. Aldaz, V. Montiel, *Int. J. Electrochem. Sci.* **2013**, *8*, 7030–7043; c) G. F. Álvarez, M. Mamlouk, S. M. S. Kumar, K. Scott, *J. Appl. Electrochem.* **2011**, *41*, 925–937; d) S. Rojas, F. J. García-García, S. Järas, M. V. Martínez-Huerta, J. L. G. Fierro, M. Boutonnet, *Appl. Catal. A-Gen.* **2005**, *285*, 24–35.

[10] a) A. Zahoor, M. Christy, Y. Kim, A. Arul, Y. S. Lee, K. S. Nahm, *J. Solid State Electrochem.* **2016**, *20*, 1397–1404; b) R. D. McKerracher, C. Alegre, V. Baglio, A. S. Arico, C. Ponce de León, E. Mornaghini, M. Rodlert, F. C. Walsh, *Electrochim. Acta* **2015**, *174*, 508–515; c) F. Li, Y. Chen, D. -M. Tang, Z. Jian, C. Liu, D. Golberg, A. Yamada, H. Zhou, *Energy Environ. Sci.* **2014**, *7*, 1648–1652.

[11] a) K. D. Collins, R. Honeker, S. Vázquez-Céspedes, D. -T. D. Tang, F. Glorius, *Chem. Sci.* **2015**, *6*, 1816–1824; b) S. Hayashi, Y. Kojima, T. Koizumi, *Polym. Chem.* **2015**, *6*, 881–885; c) F. -X. Felpin, T. Ayad, S. Mitra, *Eur. J. Org. Chem.* **2006**, 2679–2690; d) A. Perosa, P. Tundo, M. Selva, S. Zinovyev, A. Testa, *Org. Biomol. Chem.* **2004**, *2*, 2249–2252; e) N. Nakamichi, Y. Kawashita, M. Hayashi, *Org. Lett.* **2002**, *4*, 3955–3957.

[12] a) F. Cui, G. Li, X. Li, M. Lu, M. Li, *Catal. Sci. Technol.* **2015**, *5*, 549–555; b) E. J. M. Hensen, H. J. A. Brans, G. M. H. J. Lardinois, V. H. J. De Beer, J. A. R. Van Veen, R. A. Van Santen, *J. Catal.* **2000**, *192*, 98–107; c) G. M. K. Abotsi, A. W. Scaroni, *Fuel Process. Technol.* **1989**, *2*, 107–133.

[13] a) S. Karthikeyan, R. Boopathy, G. Sekaran, *J. Colloid Interf. Sci.* **2015**, *448*, 163–174; b) A. Rodríguez, G. Ovejero, M. D. Romero, C. Díaz, M. Barreiro, J. García, *J. of Supercritical Fluids* **2008**, *46*, 163–172; c) S. Cao, G. Chen, X. Hu, P. L. Yue, *Catal. Today* **2003**, *88*, 37–47.

[14] a) M. Sterrer, H. -J. Freund, *Catal. Lett.* **2013**, *143*, 375–385; a) X. Liu, J. G. Khinast, B. J. Glasser, *Chem. Eng. Sci.* **2008**, *63*, 4517–4530; b) G. Li, L. Hu, J. M. Hill, *Appl.Catal. A-Gen.* **2006**, *301*, 16–24; c) A. J. Van Dillen, R. J. A. M. Terörde, D. J. Lensveld, J. W. Geus, K. P. De Jong, *J. Catal.* **2003**, *216*, 257–264; d) M. Campanati, G. Fornasari, A. Vaccari, *Catal. Today* **2003**, *77*, 299–314.

[15] a) D. Vallejo-Sánchez, G. Beobide, O. Castillo, M. Lanchas, *Eur. J. Inorg. Chem.* **2013**, 5592–5602.

[16] a) M. Pinsky, D. Avnir, *Inorg. Chem.* **1998**, *37*, 5575–5582. b) D. Casanova, J. Cirera, M. Llunell, P. Alemany, D. Avnir, S. Alvarez. *J. Am. Chem. Soc.* **2004**, *126*, 1755–1763.

[17] a) http://sdbs.db.aist.go.jp; b) http://webbook.nist.gov/chemistry/ (last accessed on 2017/05/17).

[18] a) B. R. Stanmore, J. F. Brilhac, P. Gilot, *Carbon* **2001**, *39*, 2247–2268; b) I. M. Kennedy, *Prog. Energy Combust. Sci.* **1997**, *23*, 95–132.

[19] a) H. F. M. Dacosta, J. J. Driscoll, T. E. Paulson, W. J. Robel, S. M. Zemskova, US2009056320-A1; b) H. S. Han, J. H. Bae, KR2007005406-A.

[20] a) F. A. La Porta, J. Andrés, M. S. Li, J. R. Sambrano, J. A. Varela, E. Longo, *Phys. Chem. Chem. Phys.* **2014**, *16*, 20127–20137.

[21] a) S. Biswas, S. Kar, *Nanotechnology* **2008**, *19*, 045710; b) H. Zhang, L. Qi, *Nanotechnology* **2006**, *17*, 3984–3988.

[22] a) C. Suryanarayana, M. G. Norton, *X-Ray Diffraction, A Practical Approach*, Plenum Press, New York, **1998**, pp. 207–221; b) J. I. Langford, A. J. C. Wilson, *J. Appl. Cryst.* **1978**, *11*, 102–113; c) P. Scherrer, *Nachr. Ges. Wiss. Göttingen* **1918**, *26*, 98–100.

[23] a) S. Muruganandam, G. Anbalagan, G. Murugadoss, *Optik* **2017**, *131*, 826–837; b) G. B. Shombe, E. B. Mubofu, S. Mlowe, N. Revaprasadu, *Mat. Sci. Semicon. Proc.* **2016**, *43*, 230–237; c) V. Singh, P. Chauhan, *J. Phys. Chem. Solids* **2009**, *70*, 1074–1079.

[24] a) S. K. Maji, N. Mukherjee, A. Mondal, B. Adhikary, B. Karmakar, S. Dutta, *Inorg. Chim. Acta* **2011**, *371*, 20–26; b) T. C. Deivaraj, J. -

H. Park, M. Afzaal, P. O'Brien, J. J. Vittal, *Chem. Mater*. **2003**, *15*, 2383–2391.

[25] *CrysAlisPro*, version 1.171.35.15; Agilent Technologies: Yarnton, U. K., **2011**.

[26] A. Altomare, M. Cascarano, C. Giacovazzo, A. Guagliardi, *J. Appl. Crystallogr*. **1993**, *26*, 343–350.

[27] G. M. Sheldrick, *Acta Crystallogr., Sect. A: Found. Crystallogr*. **2008**, *A64*, 112–122.

[28] L. J. Farrugia, *J. Appl. Crystallogr*. **1999**, *32*, 837–838.

Received: ((will be filled in by the editorial staff))
Published online: ((will be filled in by the editorial staff))

Received: ((will be filled in by the editorial staff))
Published online: ((will be filled in by the editorial staff))

Entry for the Table of Contents

FULL PAPER

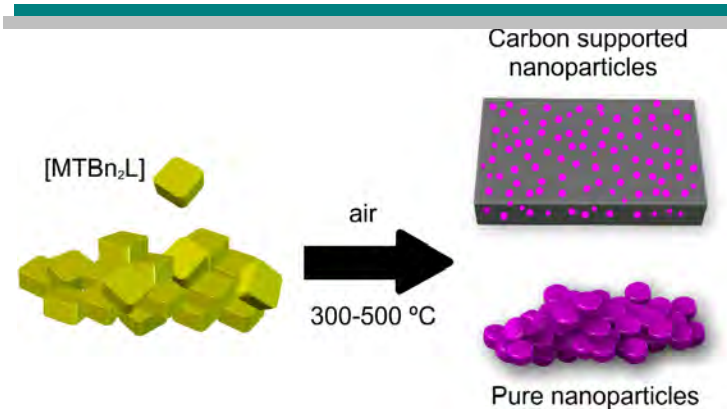

Dry-thermolsysis / Carbon supported nanoparticles *

Daniel Vallejo-Sánchez, Garikoitz Beobide, Oscar Castillo,* Mónica Lanchas, Antonio Luque, Sonia Pérez-Yáñez, Pascual Román*

Page No. – Page No.

Metal-thiobenzoato complexes: synthesis, structure and processing as carbon supported nanoparticles

Six new air-stable metal-thiobenzoato compounds with *N*-heterocycles have been synthesized and structurally characterized. Their solventless thermolysis under aerobic conditions and at relatively mild temperature (350–480ºC) provides in a single step carbon supported metal and metal sulfide nanoparticles with high crystallinity.

3.3. SUPPORTING INFORMATION

Metal-Thiobenzoato Complexes: Synthesis, Structure and Processing as Carbon Supported Nanoparticles

Daniel Vallejo-Sánchez,[a] Garikoitz Beobide,*[a] Oscar Castillo,*[a] Mónica Lanchas,[a] Antonio Luque,[a] Sonia Pérez-Yáñez,[a, b] and Pascual Román[a]

[a] Departamento de Química Inorgánica, Facultad de Ciencia y Tecnología, Universidad del País Vasco (UPV/EHU), Apartado 644, E–48080 Bilbao, Spain.
E-mail: garikoitz.beobide@ehu.eus

[b] Departamento de Química Inorgánica, Facultad de Farmacia, Universidad del País Vasco (UPV/EHU), E–01006 Vitoria-Gasteiz, Spain.

S1: X-RAY DIFFRACTION MEASUREMENTS

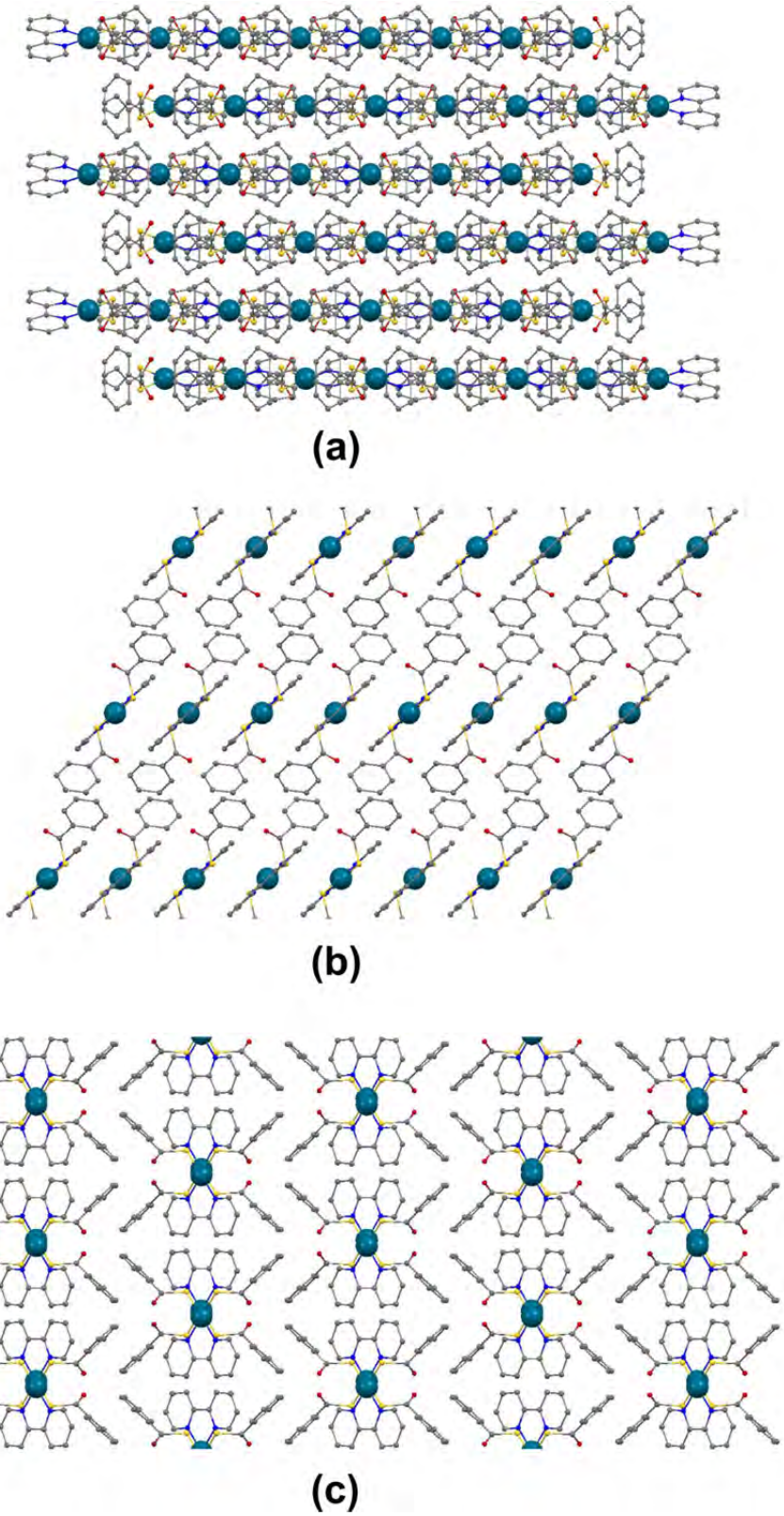

Figure S1.1 Crystallographic views of compound PdBPY along (a) *a* axis, (b) *b* axis and (c) *c* axis.

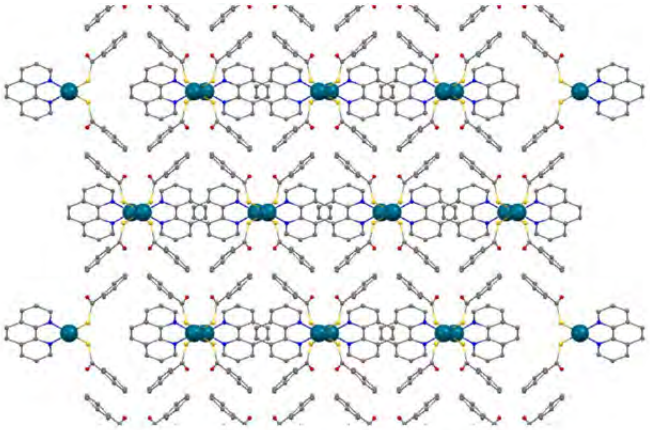

(a)

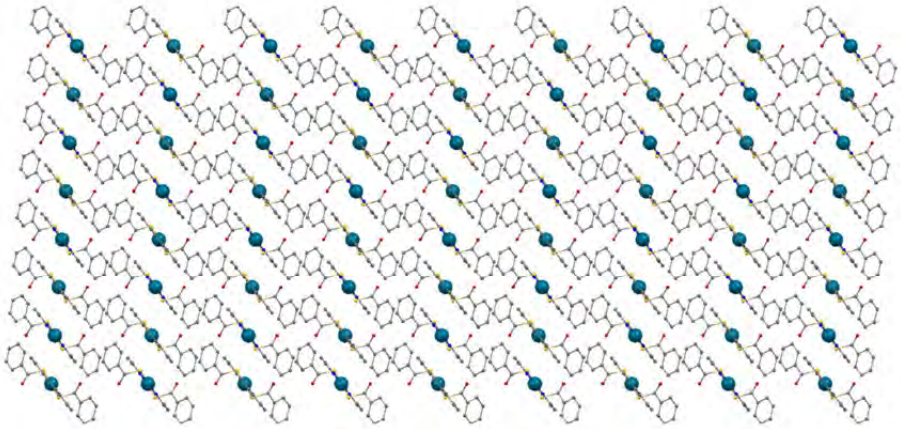

(b)

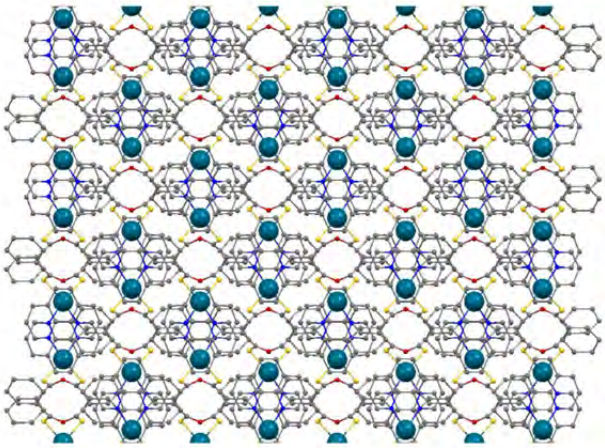

(c)

Figure S1.2 Crystallographic views of compound PdPHEN along (a) *a* axis, (b) *b* axis and (c) *c* axis.

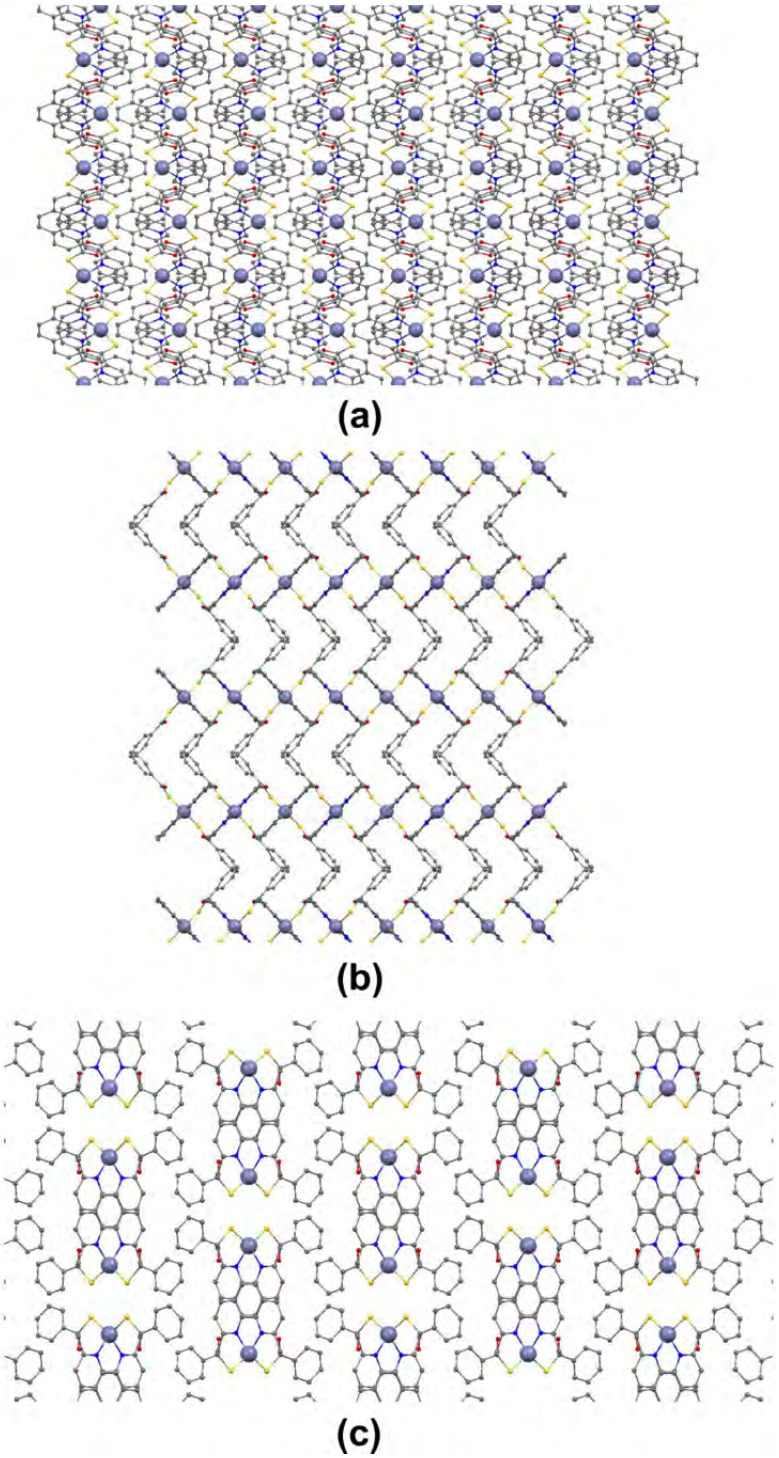

Figure S1.3 Crystallographic views of compound ZnNEO along (a) *a* axis, (b) *b* axis and (c) *c* axis.

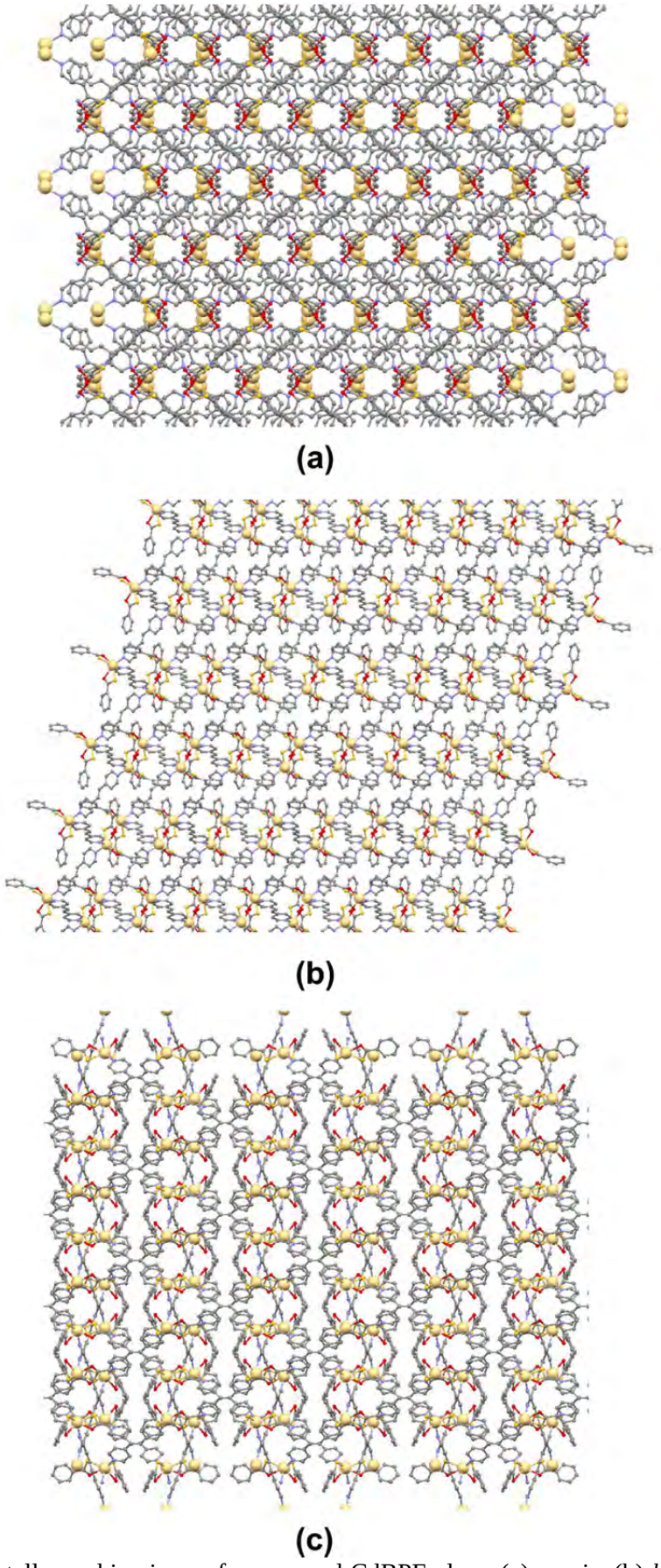

Figure S1.4 Crystallographic views of compound CdBPE along (a) *a* axis, (b) *b* axis and (c) *c* axis.

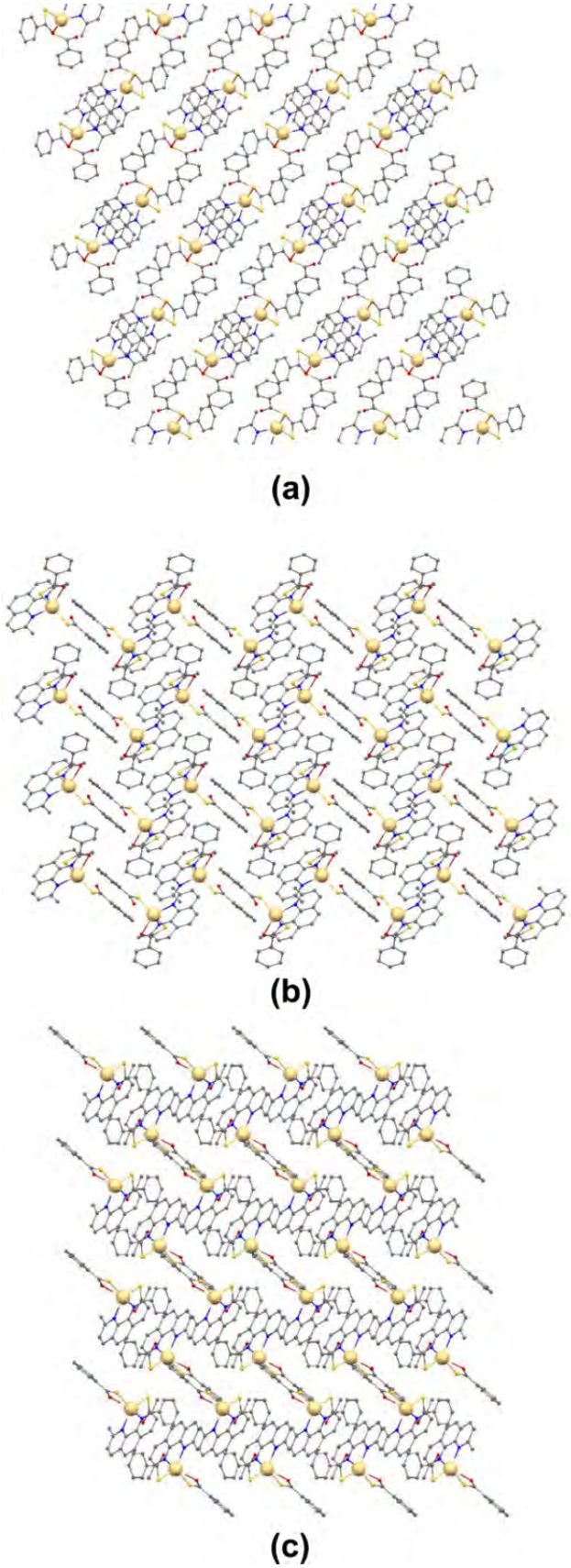

Figure S1.5 Crystallographic views of compound CdNEO along (a) *a* axis, (b) *b* axis and (c) *c* axis.

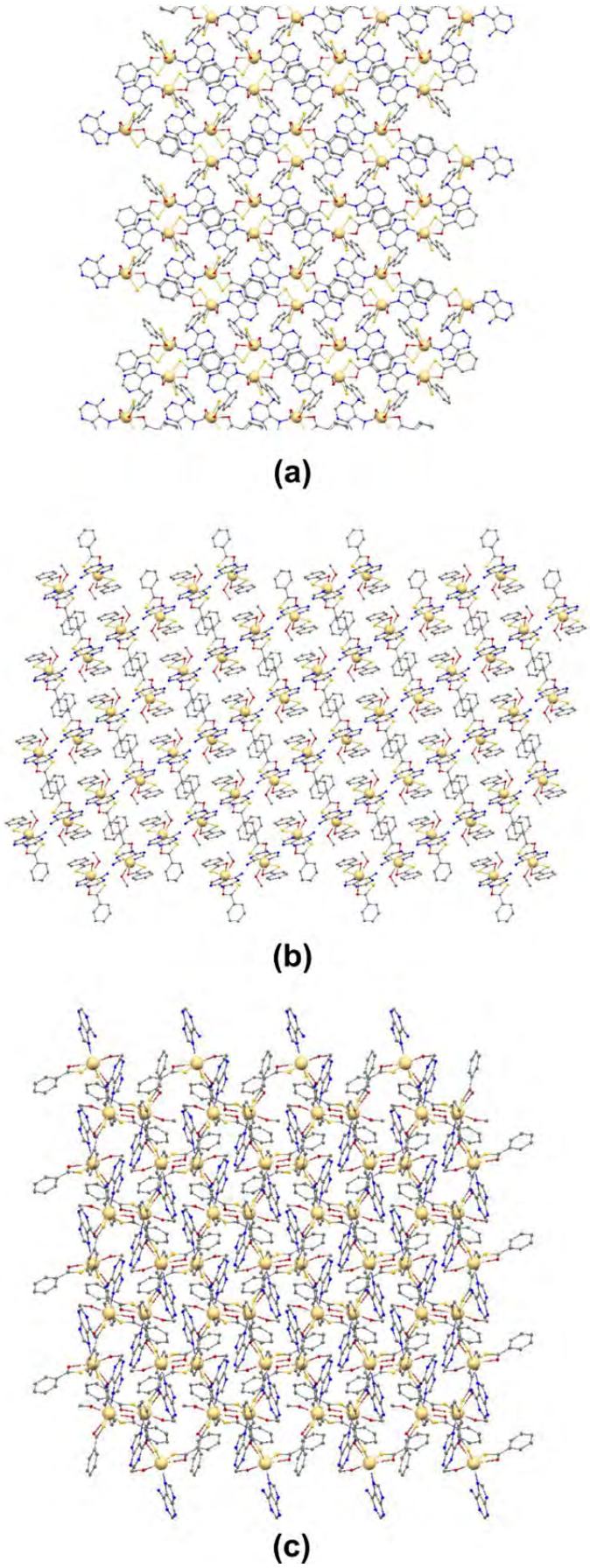

Figure S1.6 Crystallographic views of compound CdADE along (a) *a* axis, (b) *b* axis and (c) *c* axis.

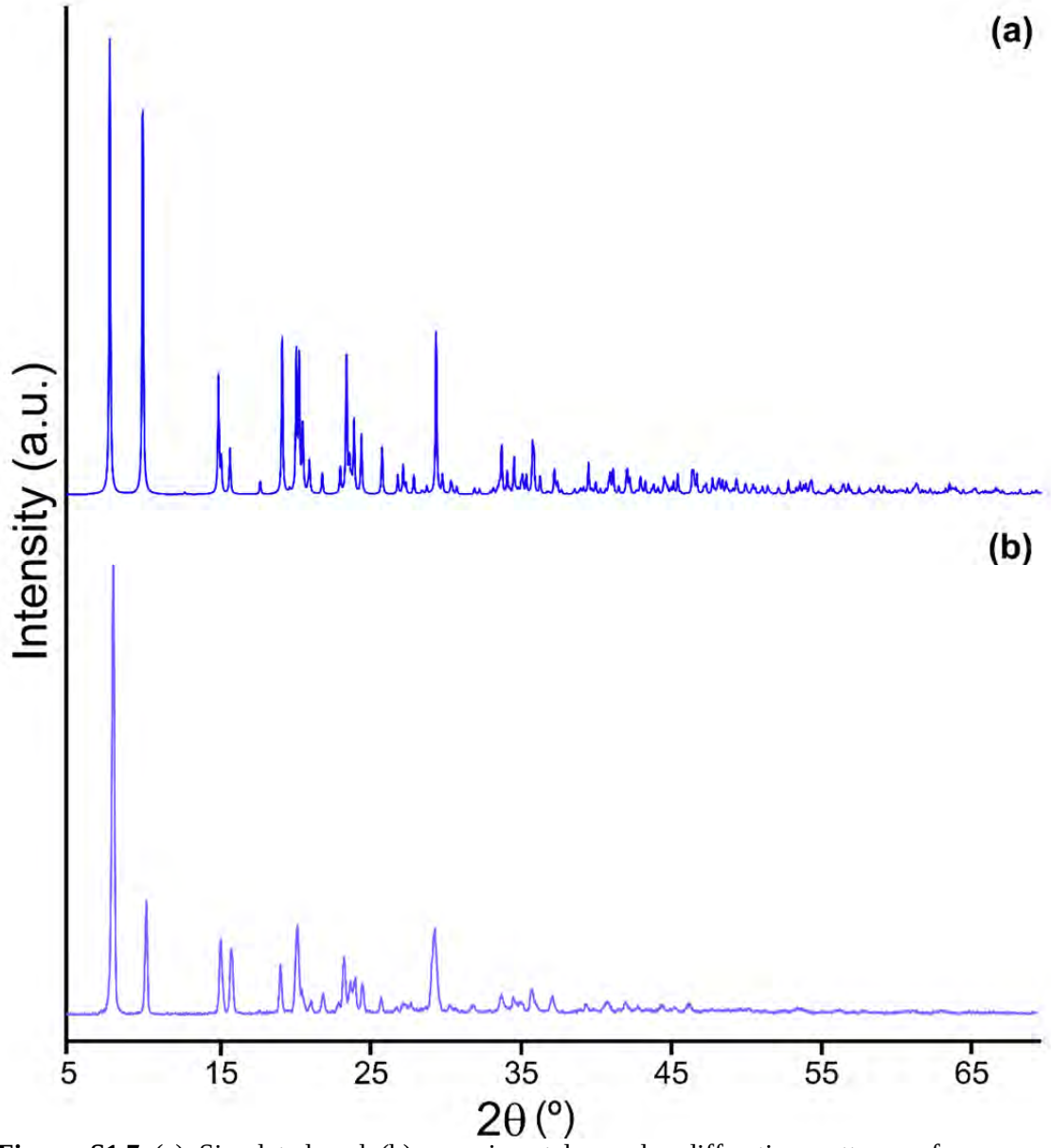

Figure S1.7 (a) Simulated and (b) experimental powder diffraction patterns of compound PdBPY.

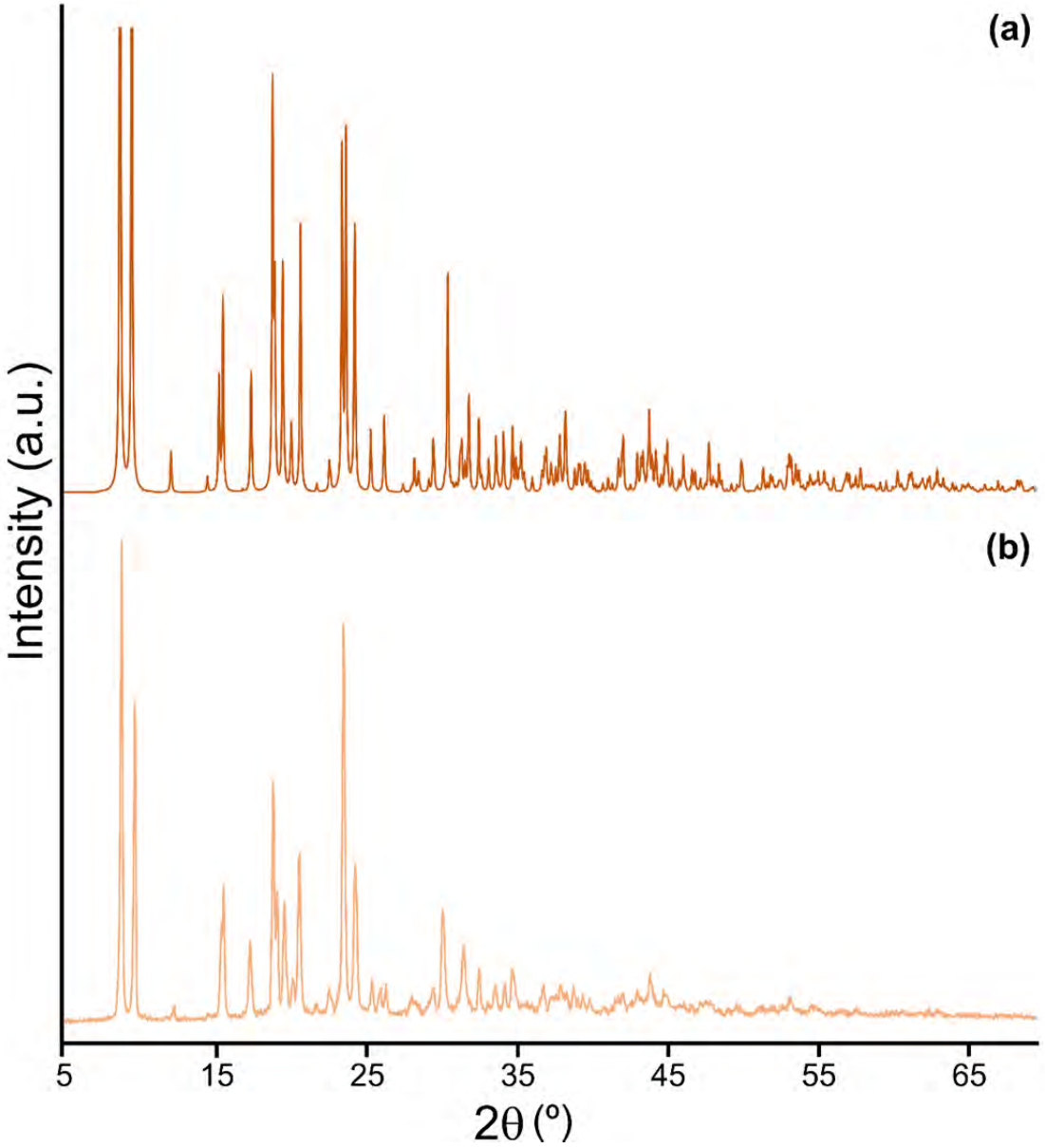

Figure S1.8 (a) Simulated and (b) experimental powder diffraction patterns of compound PdPHEN.

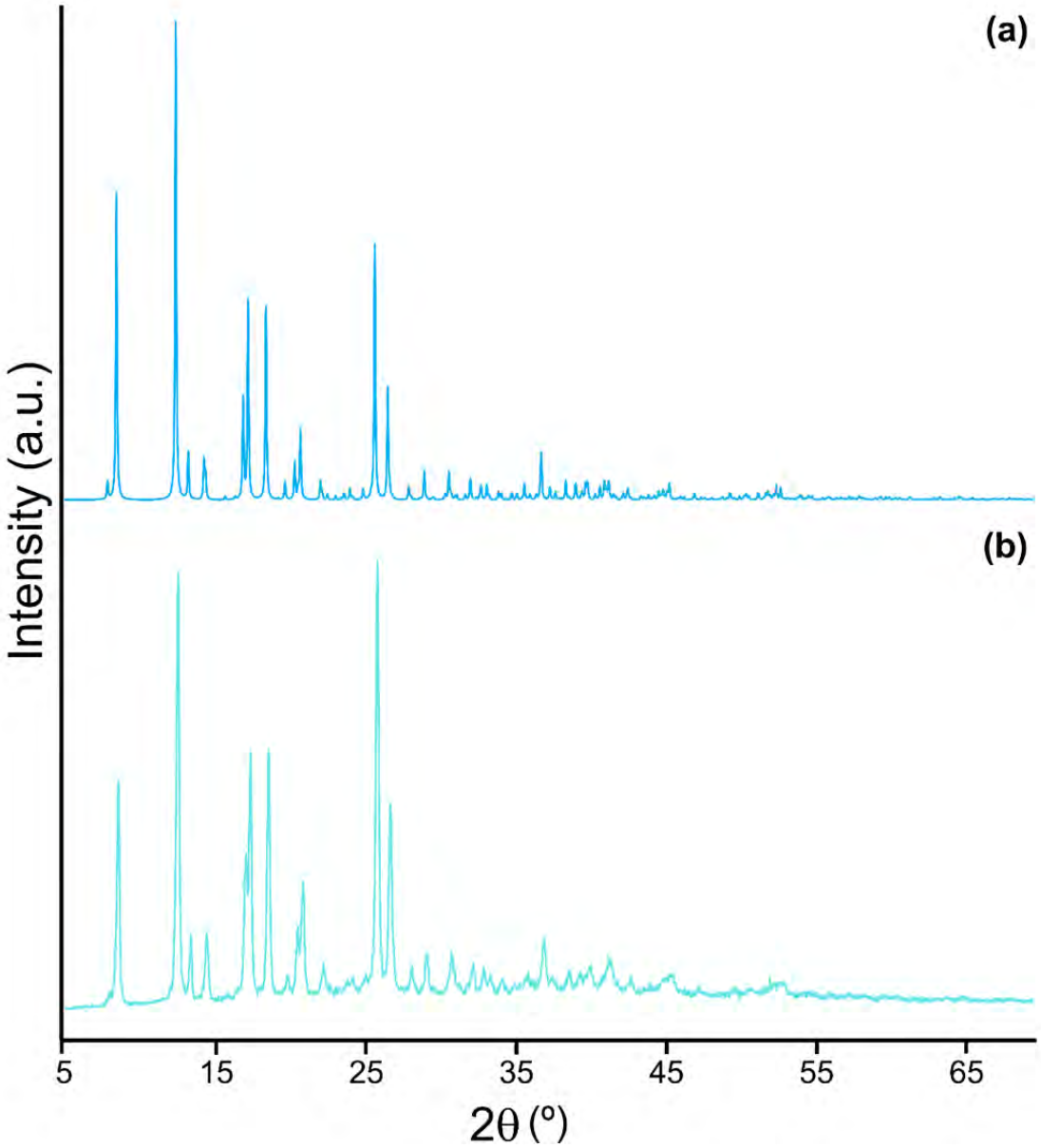

Figure S1.9 (a) Simulated and (b) experimental powder diffraction patterns of compound ZnNEO.

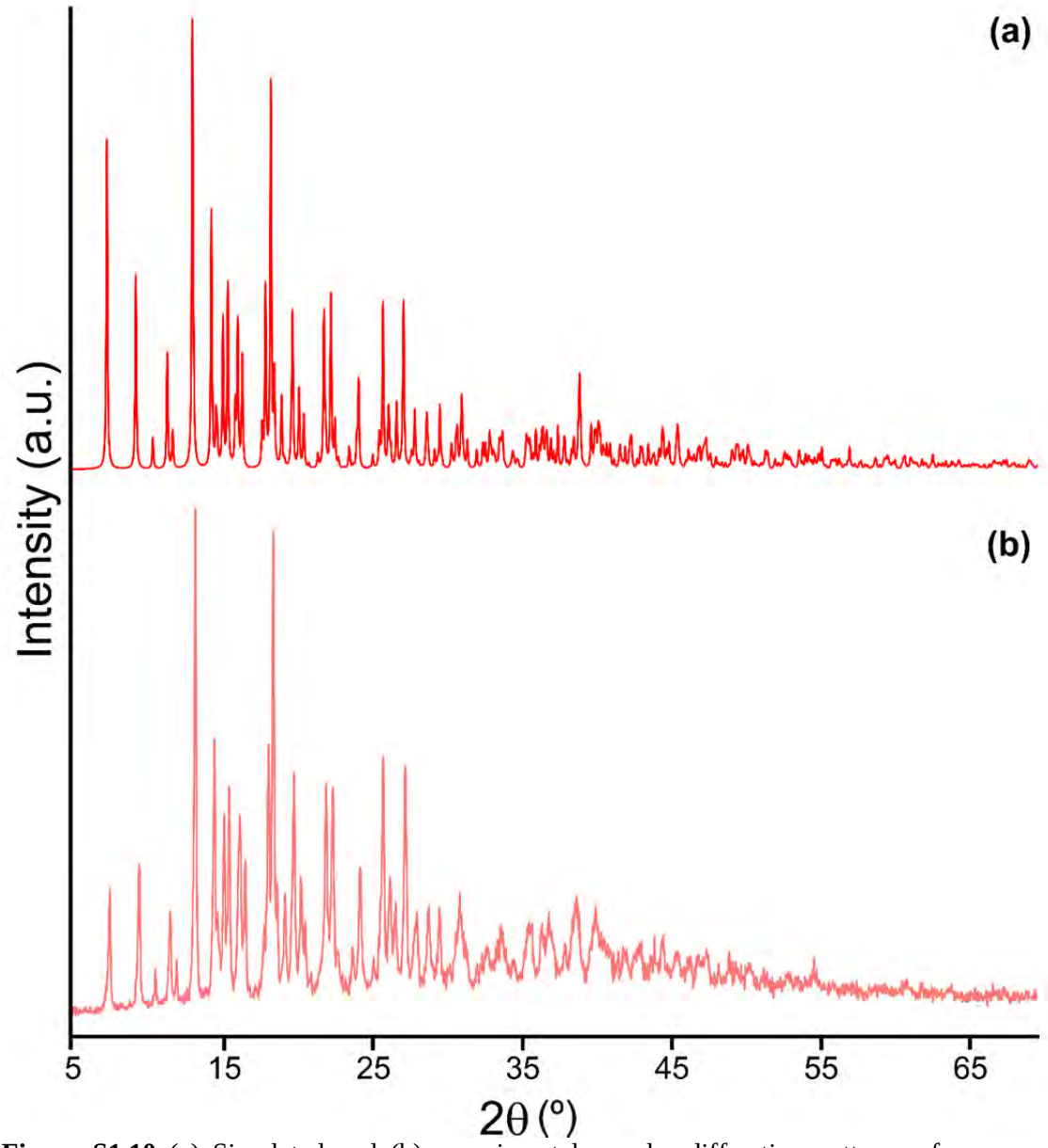

Figure S1.10 (a) Simulated and (b) experimental powder diffraction patterns of compound CdBPE.

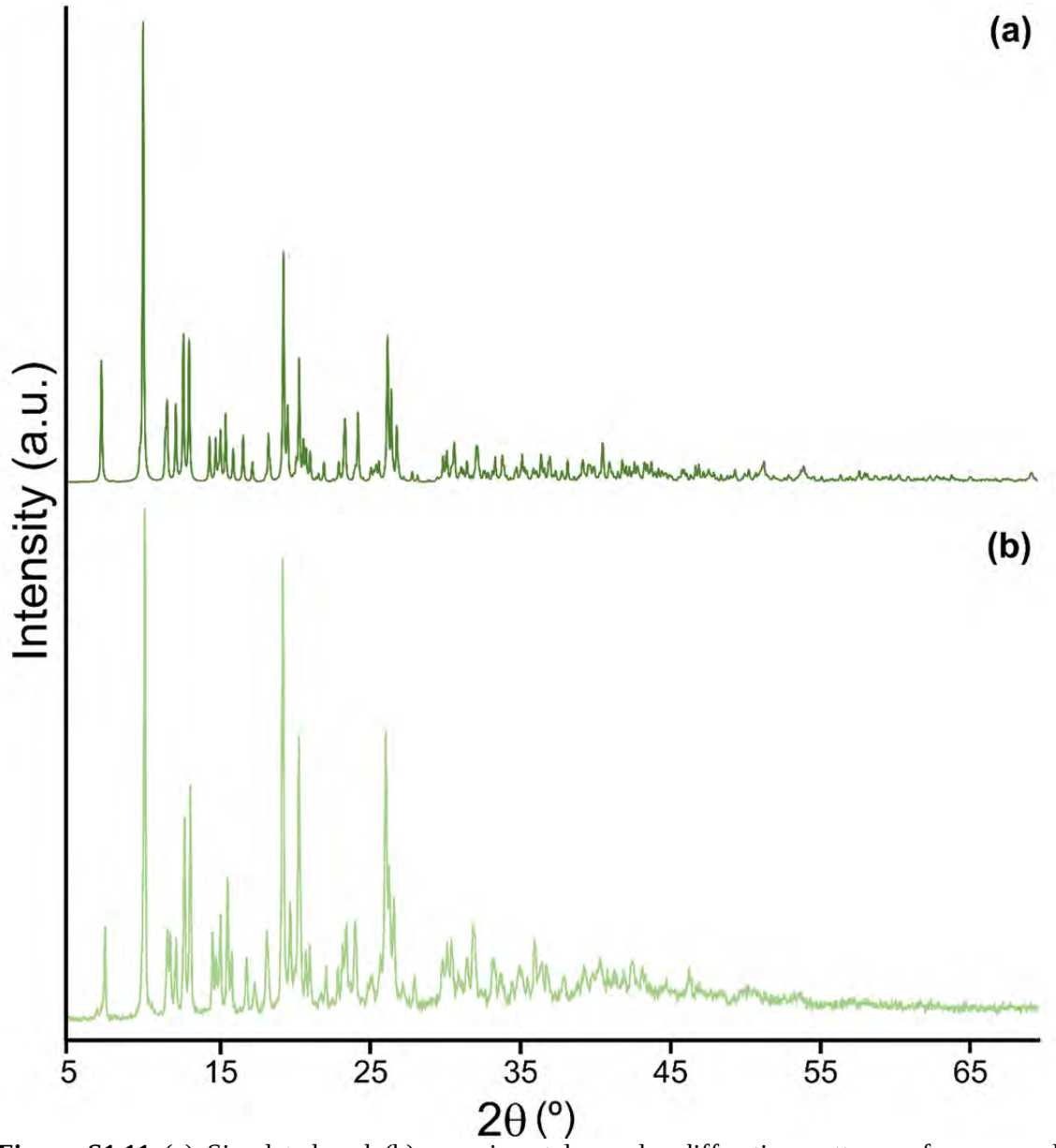

Figure S1.11 (a) Simulated and (b) experimental powder diffraction patterns of compound CdNEO.

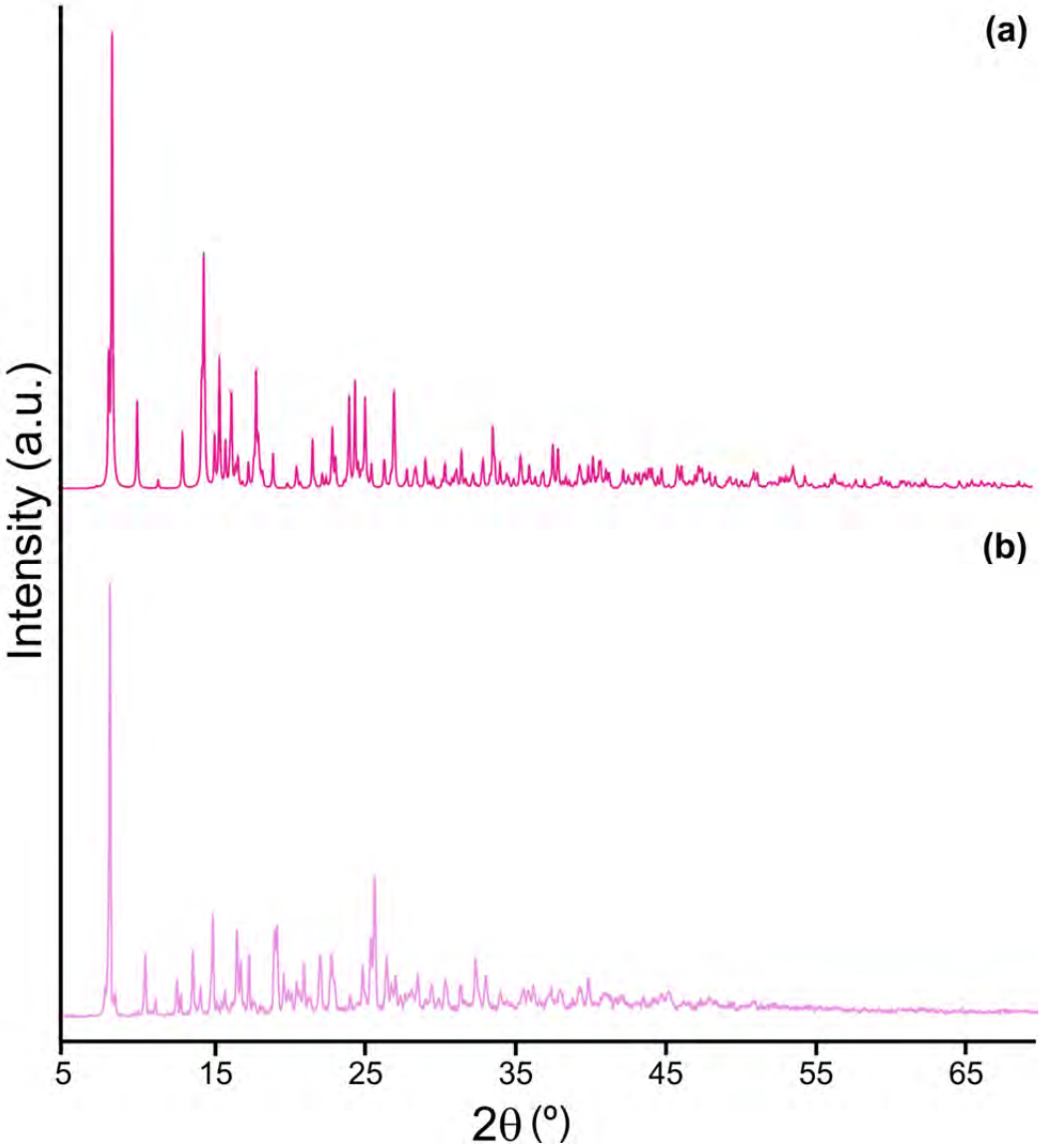

Figure S1.12 (a) Simulated and (b) experimental powder diffraction patterns of compound CdADE.

Table S1.1 Bond distances and angles of precursors.

PdBPY

Distances		*Angles*	
Pd(1)–N(21)	2.082(3)[a]	N(21)–Pd(1)–N(21)^{i}	79.79(19)[a]
Pd(1)–S(10)	2.2797(10)[a]	N(21)^{i}–Pd(1)–S(10)	96.51(10)[a]
S(10)–C(10)	1.751(4)	N(21)^{i}–Pd(1)–S(10)^{i}	174.86(9)[a]
O(10)–C(10)	1.223(5)	S(10)–Pd(1)–S(10)^{i}	87.40(5)[a]

PdPHEN

Distances		*Angles*	
Pd(1)–N(21)	2.085(3)[b]	N(21)–Pd(1)–N(21)^{i}	80.49(17)[b]
Pd(1)–S(10)	2.2773(10)[b]	N(21)^{i}–Pd(1)–S(10)	94.88(9)[b]
S(10)–C(10)	1.748(4)	N(21)^{i}–Pd(1)–S(10)^{i}	172.13(9)[b]
O(10)–C(10)	1.214(5)	S(10)–Pd(1)–S(10)^{i}	90.41(6)[b]

ZnNEO

Distances		*Angles*	
Zn(1)–N(21)	2.069(3)[c]	N(21)–Zn(1)–N(21)^{i}	81.32(15)[c]
Zn(1)–S(10)	2.2951(11)[c]	N(21)^{i}–Zn(1)–S(10)	115.54(8)[c]
S(10)–C(10)	1.743(4)	N(21)^{i}–Zn(1)–S(10)^{i}	115.36(8)[c]
O(10)–C(10)	1.212(4)	S(10)–Zn(1)–S(10)^{i}	111.00(6)[c]

CdBPE

Distances		*Angles*	
Cd(1)–N(41)	2.346(3)		
Cd(1)–N(52)	2.271(3)	N(52)–Cd(1)–N(41)	96.01(10)
Cd(1)–S(10)	2.5302(11)	N(52)–Cd(1)–S(20)	138.56(9)
Cd(1)–S(20)	2.473(2)	N(41)–Cd(1)–S(20)	102.99(9)
S(10)–C(10)	1.740(4)	N(52)–Cd(1)–S(10)	95.11(8)
O(10)–C(10)	1.215(4)	N(41)–Cd(1)–S(10)	101.16(8)
S(20)–C(20)	1.689(6)	S(20)–Cd(1)–S(10)	116.34(6)
O(20)–C(20)	1.297(6)		

CdNEO

Distances		*Angles*	
Cd(1)–N(31)	2.307(4)		
Cd(1)–N(43)	2.350(4)	N(31)–Cd(1)–N(43)	72.72(15)
Cd(1)–S(10)	2.5638(13)	N(31)–Cd(1)–S(20)	136.18(11)
Cd(1)–S(20)	2.4711(13)	N(43)–Cd(1)–S(20)	109.67(11)
S(10)–C(10)	1.736(5)	N(31)–Cd(1)–S(10)	107.00(11)
O(10)–C(10)	1.236(7)	N(43)–Cd(1)–S(10)	93.82(11)
S(20)–C(20)	1.723(6)	S(20)–Cd(1)–S(10)	116.25(5)
O(20)–C(20)	1.237(7)		

CdADE

Distances		*Angles*	
Cd(1)–N(37)	2.276(2)		
Cd(1)–O(1)	2.3568(19)	N(37)–Cd(1)–O(1)	89.27(7)
Cd(1)–S(10)	2.5252(7)	N(37)–Cd(1)–S(20)	110.92(5)
Cd(1)–S(20)	2.5001(7)	O(1)–Cd(1)–S(20)	112.49(5)
S(10)–C(10)	1.743(3)	N(37)–Cd(1)–S(10)	117.70(6)
O(10)–C(10)	1.234(3)	O(1)–Cd(1)–S(10)	98.98(5)
S(20)–C(20)	1.740(3)	S(20)–Cd(1)–S(10)	121.51(2)
O(20)–C(20)	1.234(3)		

[a] –x+1, y, -z+1/2. [b] –x+3/2, y, -z+1. [c]-x+1, y, -z+3/2.

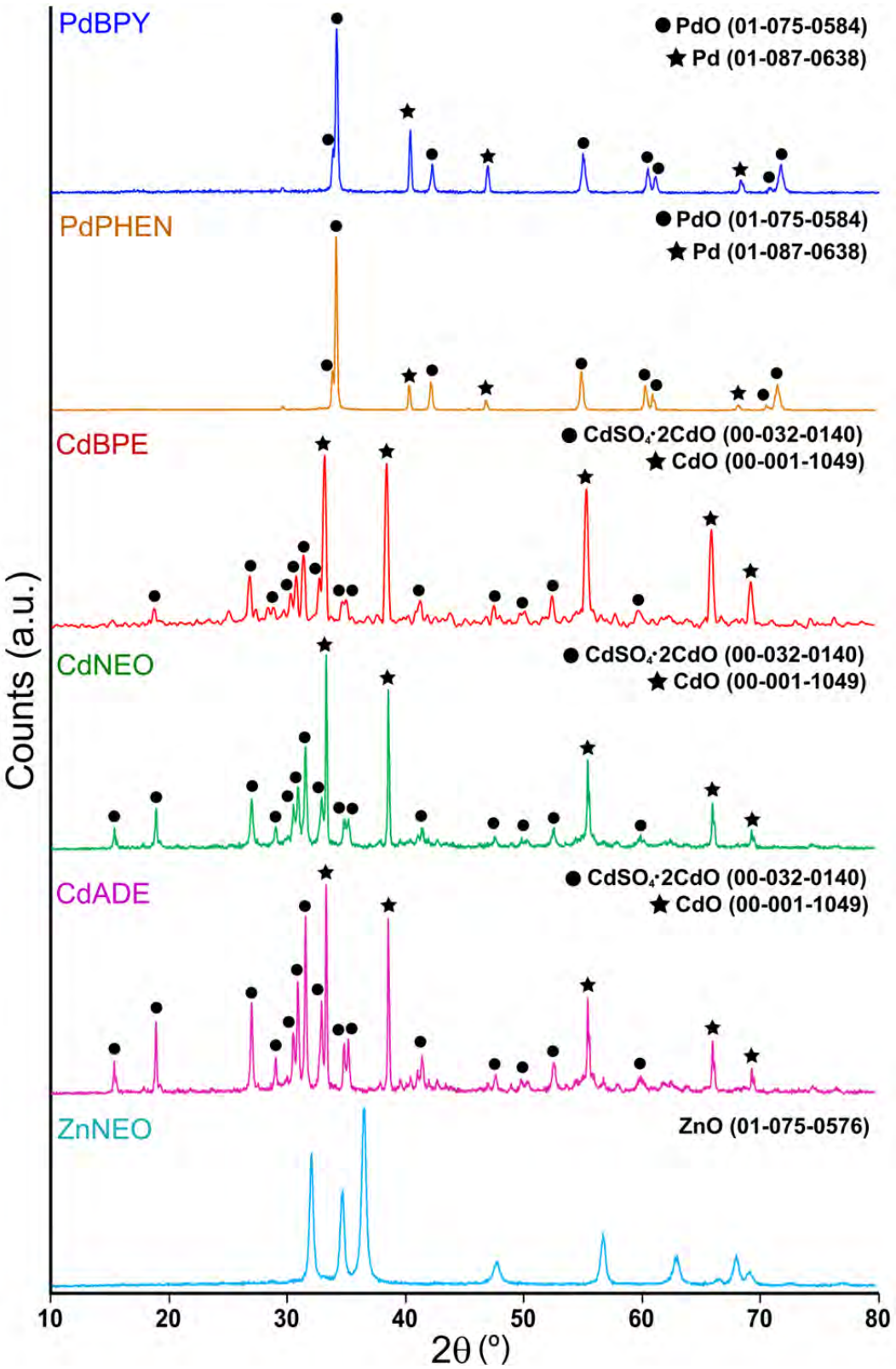

Figure S1.13 PXRD patterns of thermogravimetric residues in synthetic air atmosphere at 700ºC with a heating rate of 5 ºC·min^{-1}.

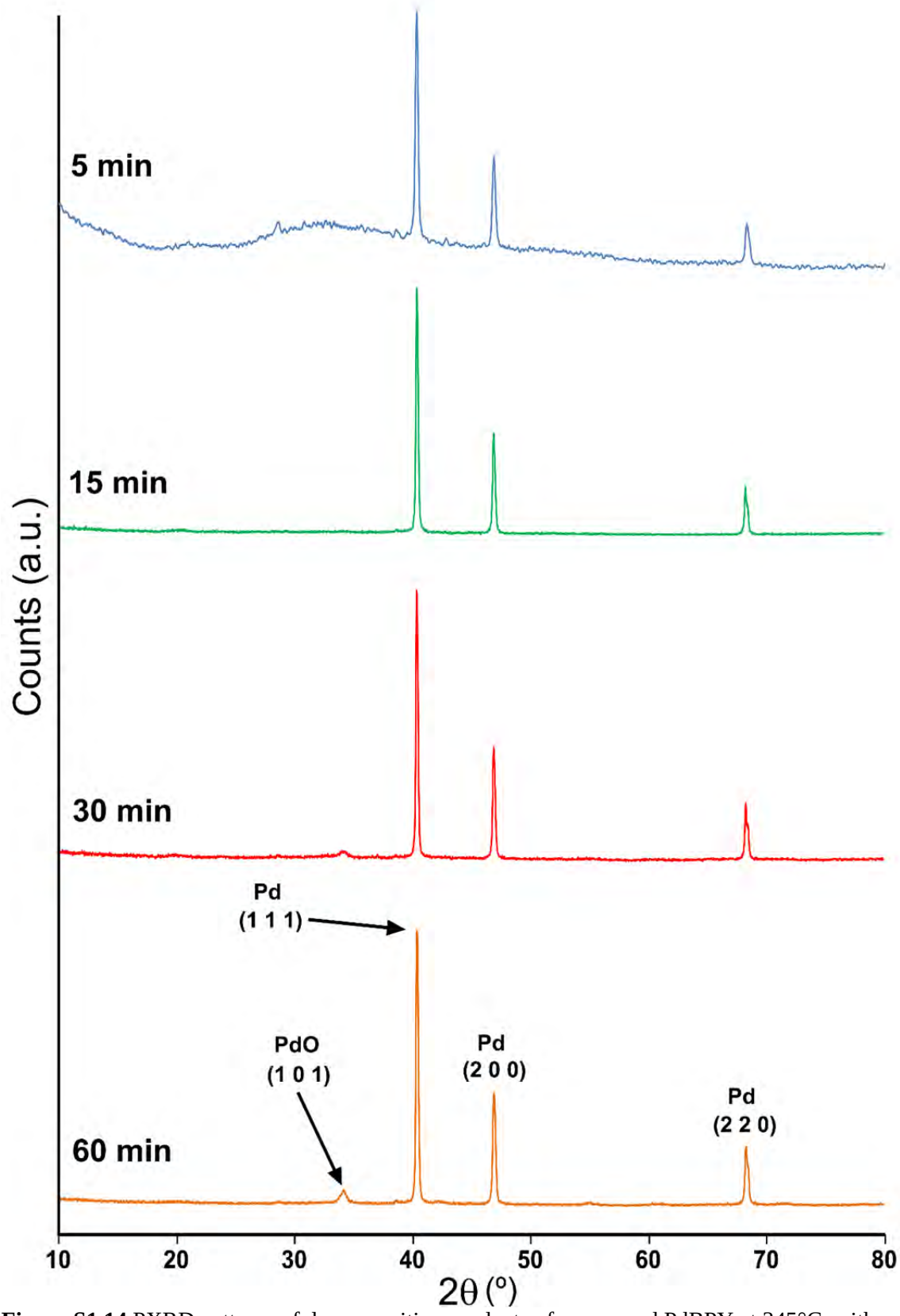

Figure S1.14 PXRD patterns of decomposition products of compound PdBPY at 345°C, with a heating rate of 5 ºC·min^{-1}and varying the time of the isothermal step.

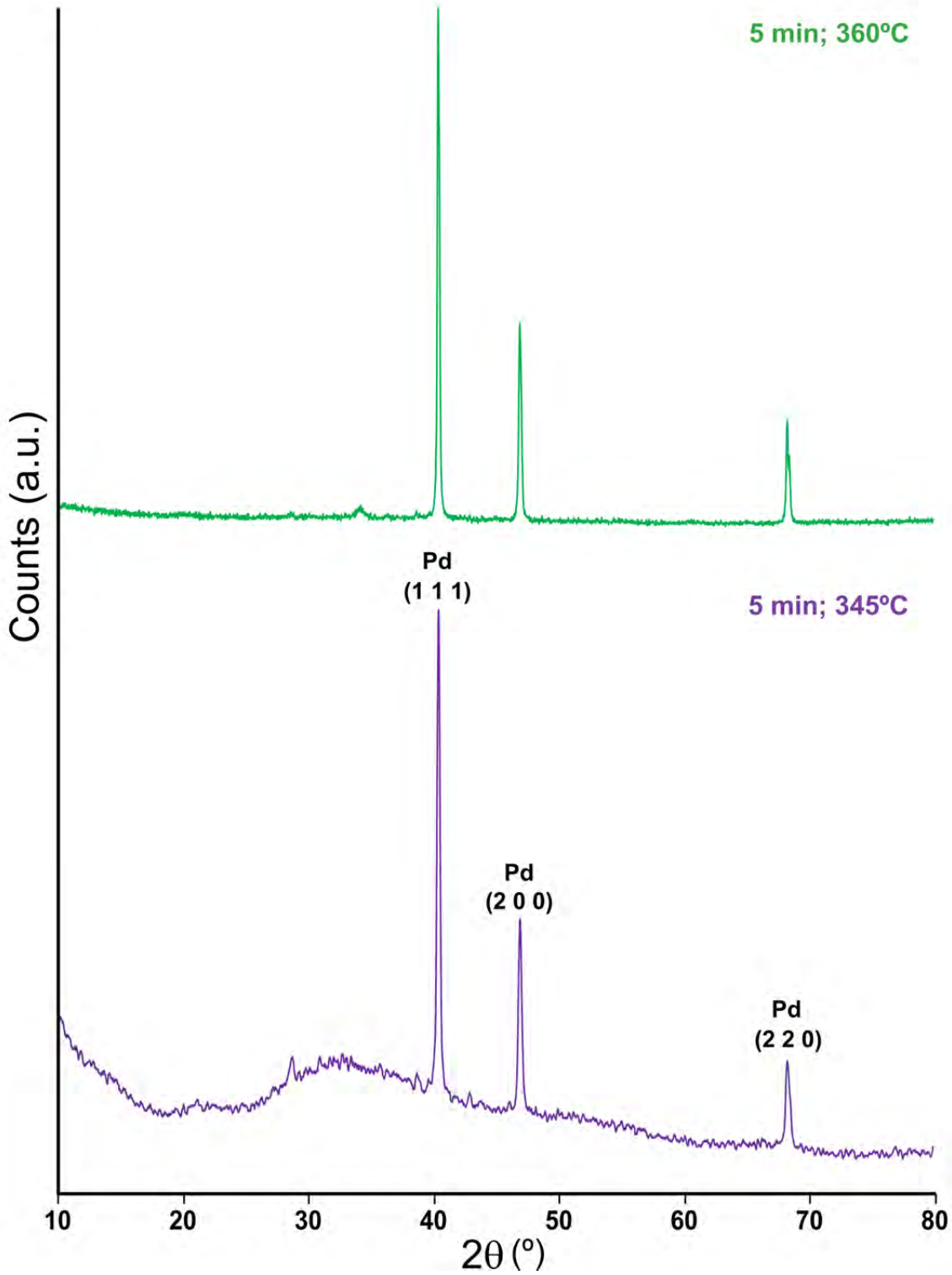

Figure S1.15 PXRD patterns of decomposition products of compound PdBPY at different combustion temperatures and a heating rate of 5 ºC·min^{-1}.

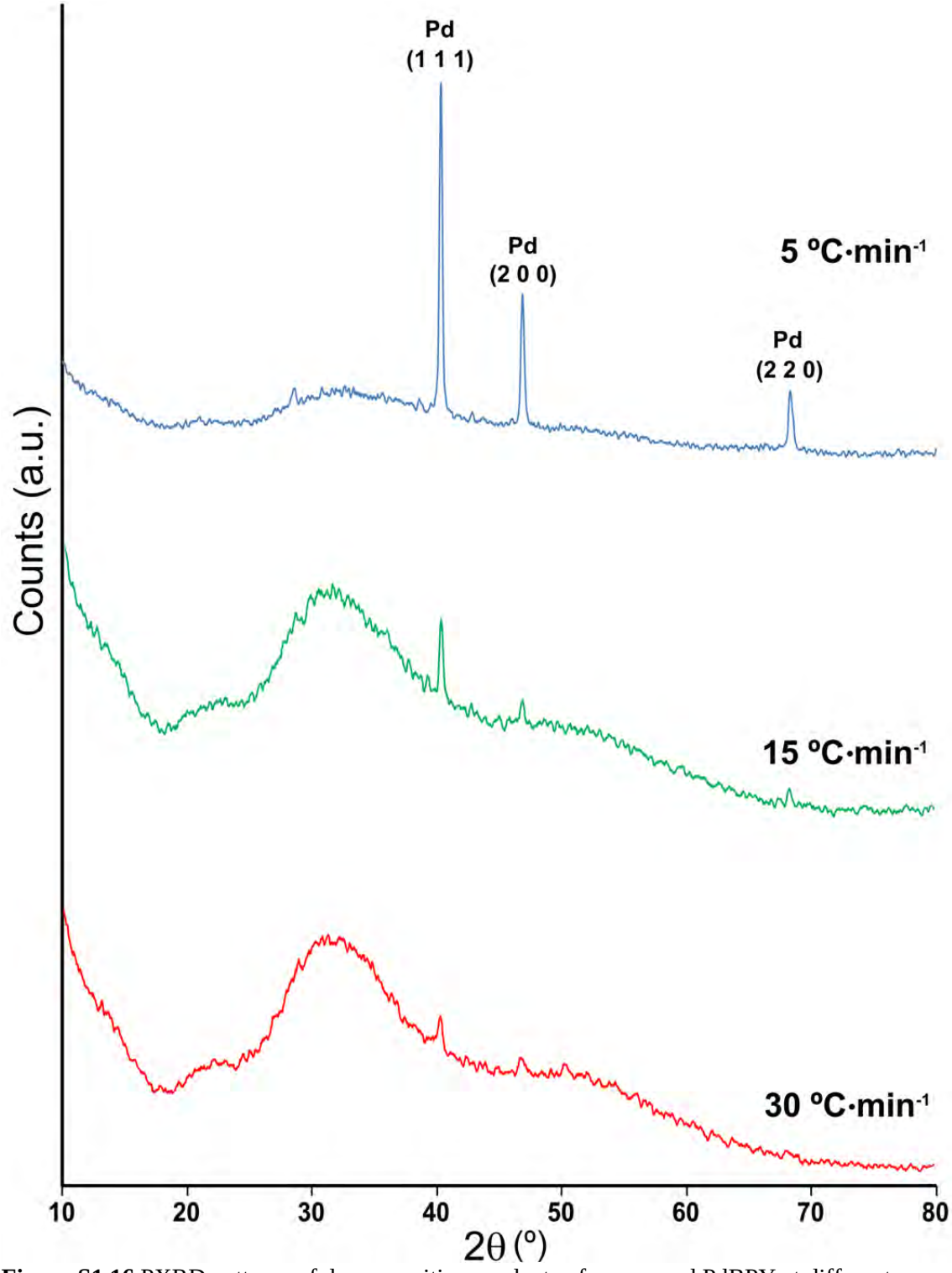

Figure S1.16 PXRD patterns of decomposition products of compound PdBPY at different heating rates (5 minutes at 345ºC).

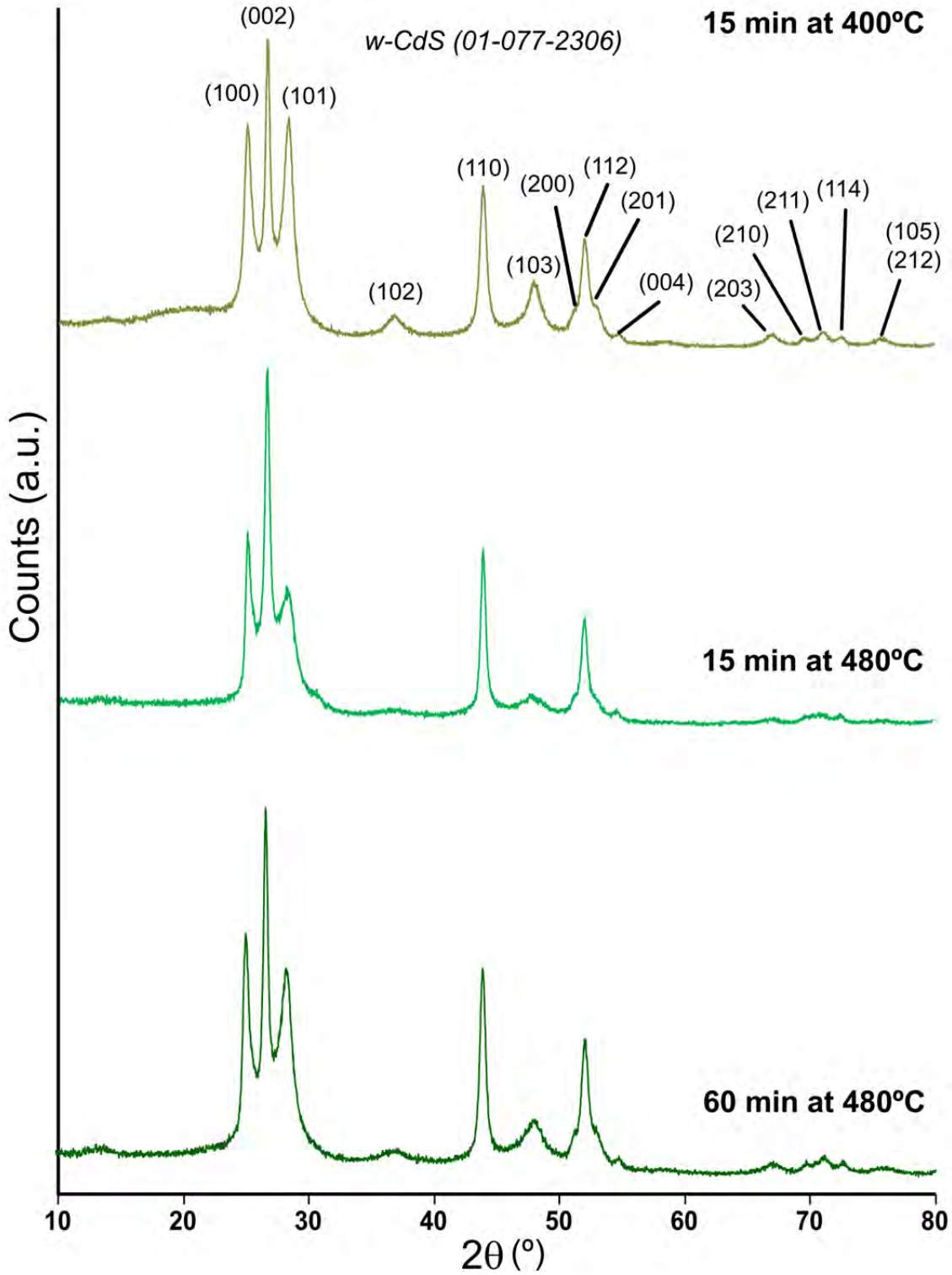

Figure S1.17 PXRD patterns of dry thermolysis products of compound CdNEO at different combustion conditions.

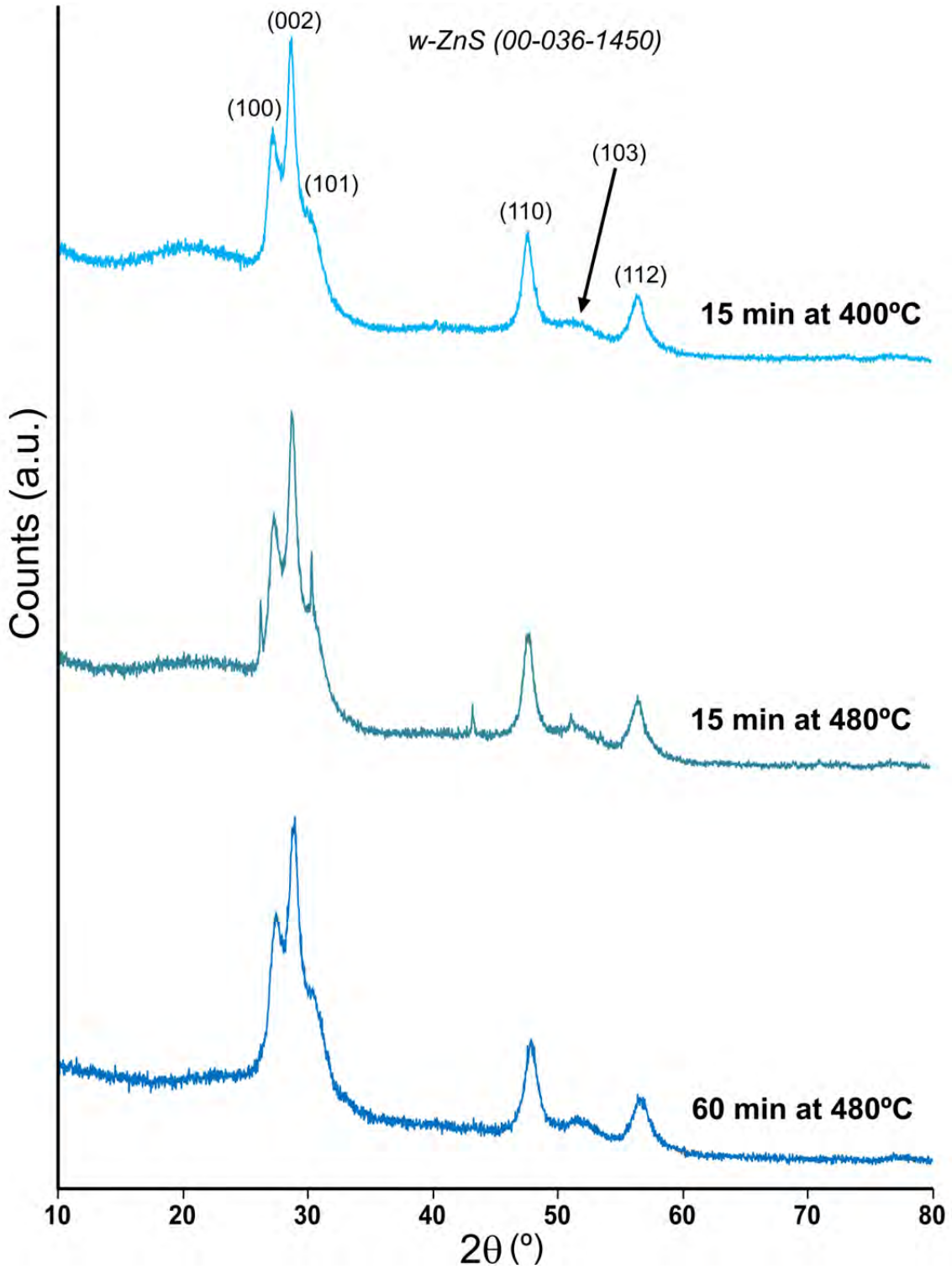

Figure S1.18 PXRD patterns of dry thermolysis products of compound ZnNEO at different combustion conditions.

S2: VIBRATIONAL SPECTROSCOPY

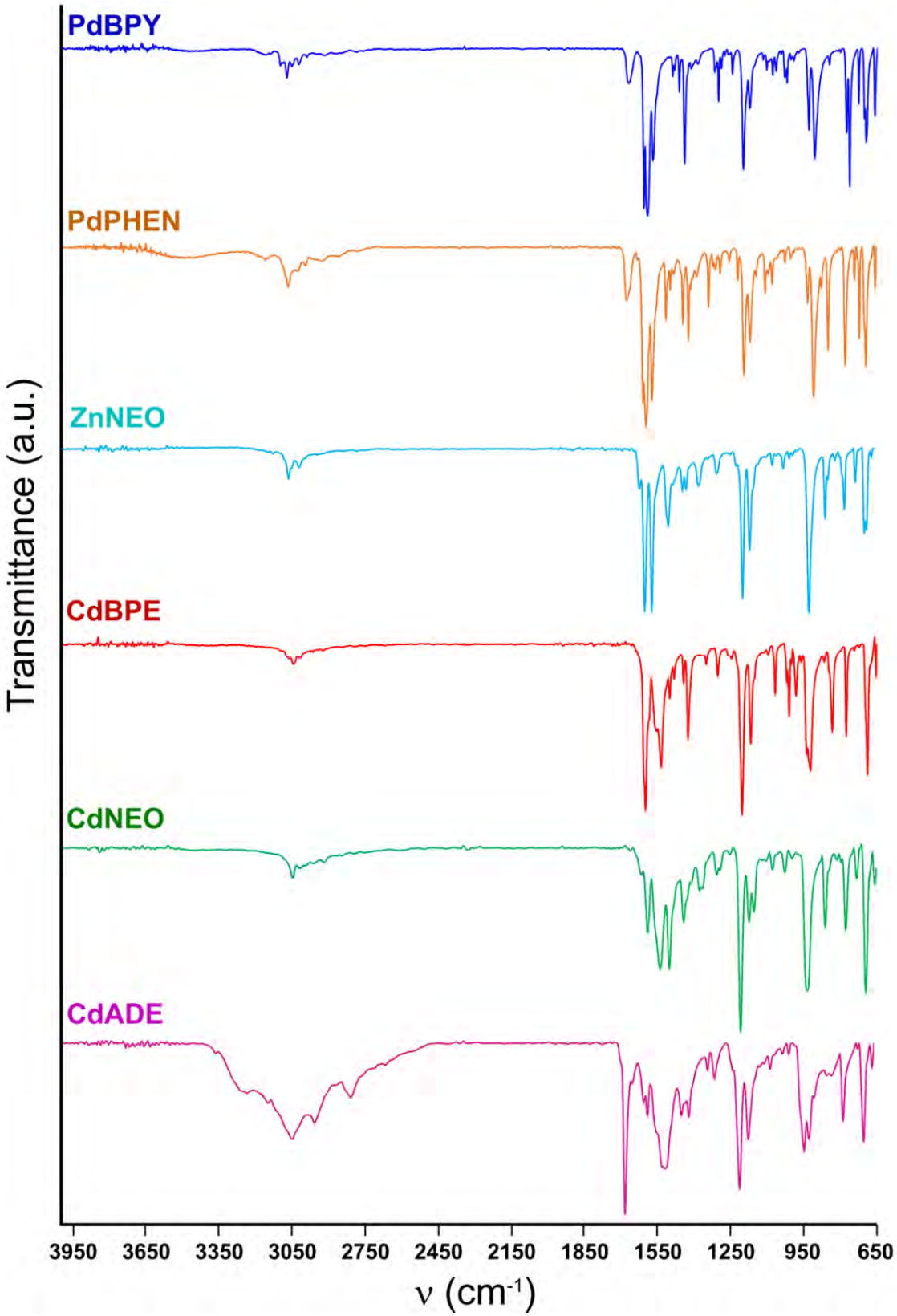

Figure S2.1 FTIR spectra of MTBnL precursors.

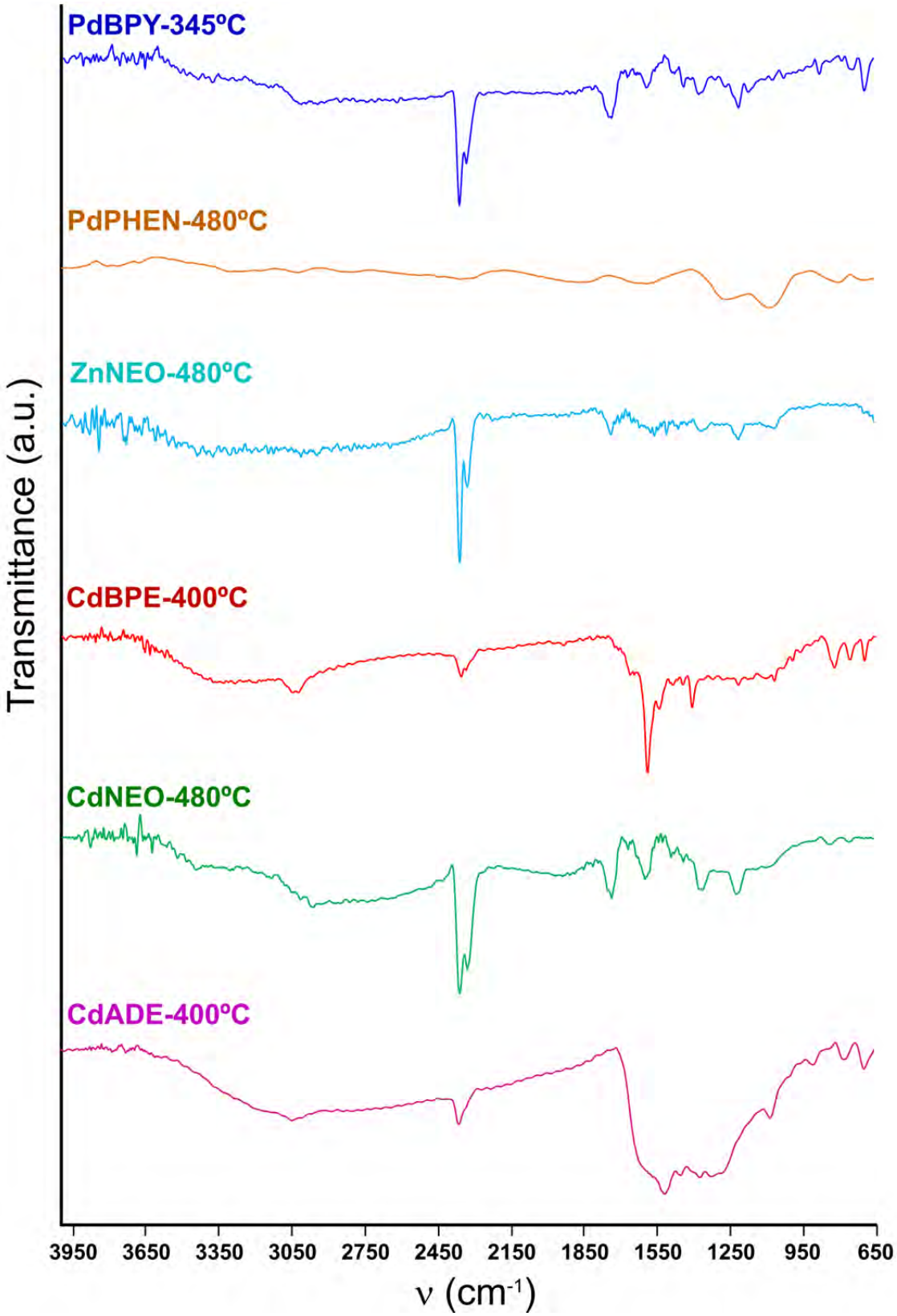

Figure S2.2 FTIR spectra of thermolysis products.

S3: THERMAL ANALYSIS

Table S3.1 Thermoanalytic data for precursors in synthetic air.

Compound	Stages	T_{peak} (ΔH)[a]	Δm[b]	Σ Δm[c]	Product [d]
PdBPY	I) RT–280 °C II) 280–351 °C III) 351–700 °C	I) 251(+) II) 324(–), 339(–)	I) 59.0 II) 20.1 III) -2.3	II) 59.0 III) 79.1 IV) 76.8	$PdSO_4$ + C (3.3 %wt) Pd + C (1.1 %wt) Pd + PdO
PdPHEN	I) RT–379 °C II) 379–506 °C III) 506–700 °C	I) 241(+), 255(+) II) 439(–), 458 (–), 461(–)	I) 48.7 II) 30.2 III) -0.8	I) 48.7 II) 78.9 III) 78.1	$PdSO_4$ + C (32.3 %wt) Pd + C (2.1 % wt) Pd + PdO
ZnNEO	I) RT–70 °C II) 70–411 °C III) 411–700 °C	I) 53 (+) II) 128 (+), 187 (+), 211 (+), 261 (+), 289 (+), 303 (+), 310 (+), 332 (+) III) 535(–)	I) 10.7 II) 33.5 III) 41.7	I) 10.7 II) 44.2 III) 85.9	-2 CH_3OH ZnS + C (38 %wt) ZnO
CdBPE	I) RT–137 °C II) 137–403 °C III) 403–452 °C IV) 452–700 °C	I) 50 (+) II) 210(+), 220(+), 254(–) III) 408(–), 448(–)	I) 2.6 II) 65.7 III) 2.8 IV) -0.4	I) 2.6 II) 68.3 III) 71.1 IV) 70.7	- 0.5 CH_3OH CdS + C (6.3 %wt) CdO + $CdSO_4$·2CdO CdO + $CdSO_4$·2CdO
CdNEO	I) RT–208 °C II) 208–483 °C III) 483–607 °C IV) 607–700 °C	I) 206 (+) II) 246 (+) III) 539 (+)	I) 0.5 II) 33.7 III) 38.5 IV) -0.9	I) 0.5 II) 34.2 III) 72.7 IV) 71.8	Phase transformation CdS + C (41.5 %wt) CdO + $CdSO_4$·2CdO CdO + $CdSO_4$·2CdO
CdADE	I) RT–413 °C II) 413–615 °C III) 615–700 °C	I) 106 (+), 154 (+) II) 465 (–), 524 (–), 555 (–)	I) 56.4 II) 18.3 III) -0.6	I) 56.4 II) 74.7 III) 74.1	CdS + C (17.5 %wt) CdO + $CdSO_4$·2CdO CdO + $CdSO_4$·2CdO

[a] T_{peak} (ΔH) = DTA peak temperature (energy process type in the basis of DTA: + or endothermic and – or exothermic); [b] mass loss percentage for each stage; [c] total mass loss percentage; [d] crystalline phases detected by PXRD.

S4: MICROSTRUCTURAL ANALYSIS

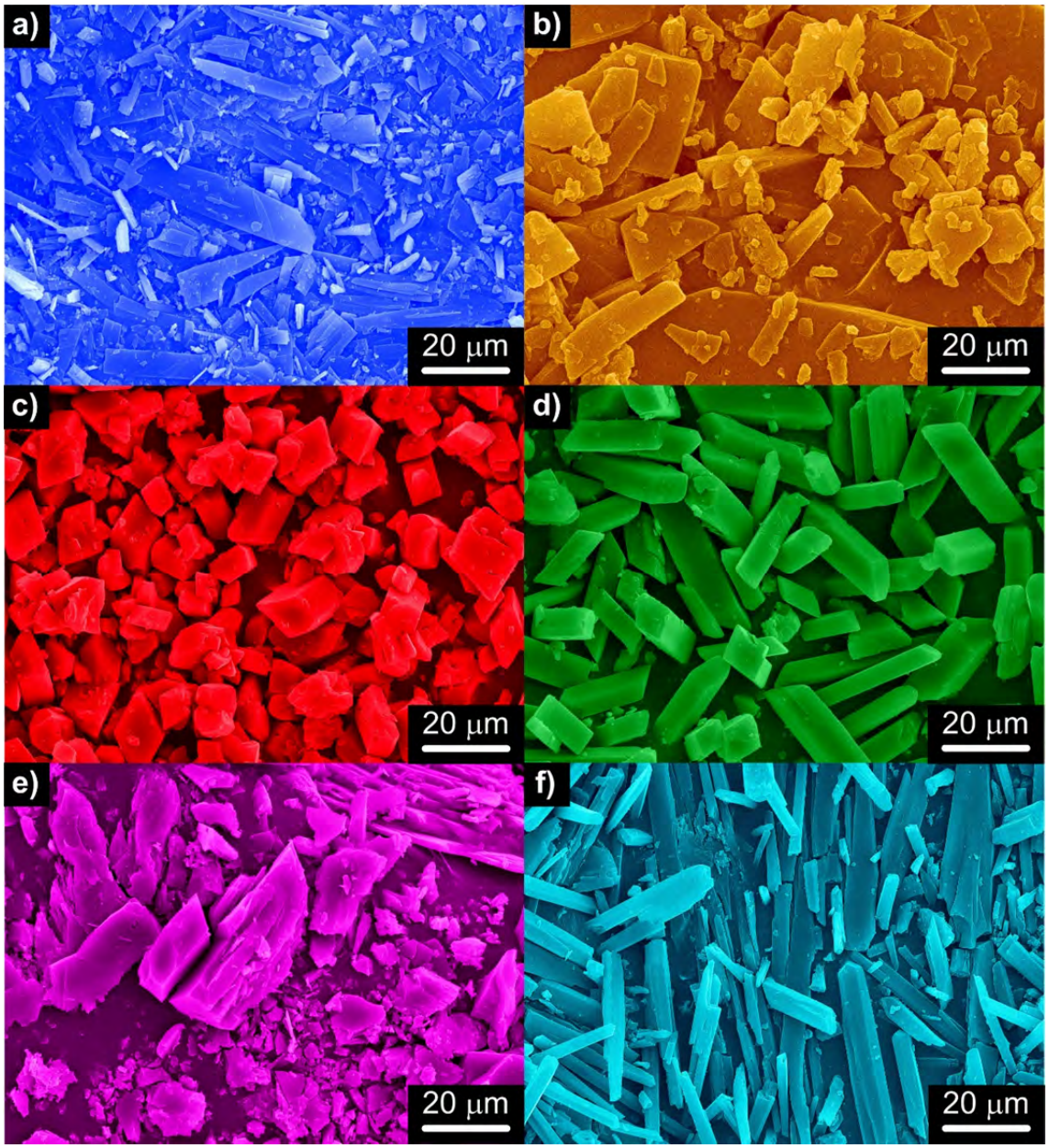

Figure S4.1 SEM images of powder precursors: (a) PdBPY, (b) PdPHEN, (c) CdBPE, (d) CdNEO, (e) CdADE, and (f) ZnNEO.

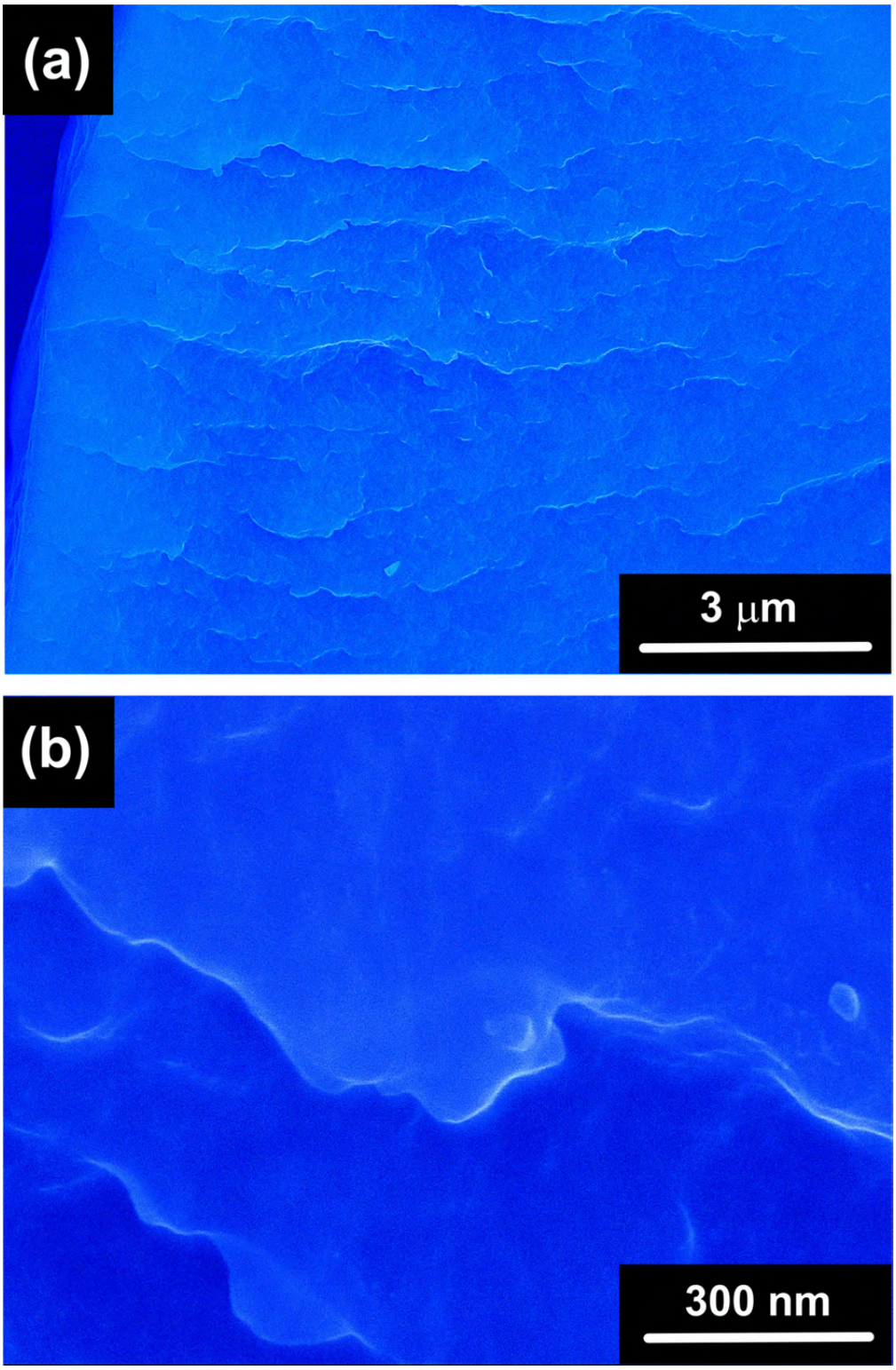

Figure S4.2 SEM images of PdBPY: (a) 10 kX, and (b) 100 kX.

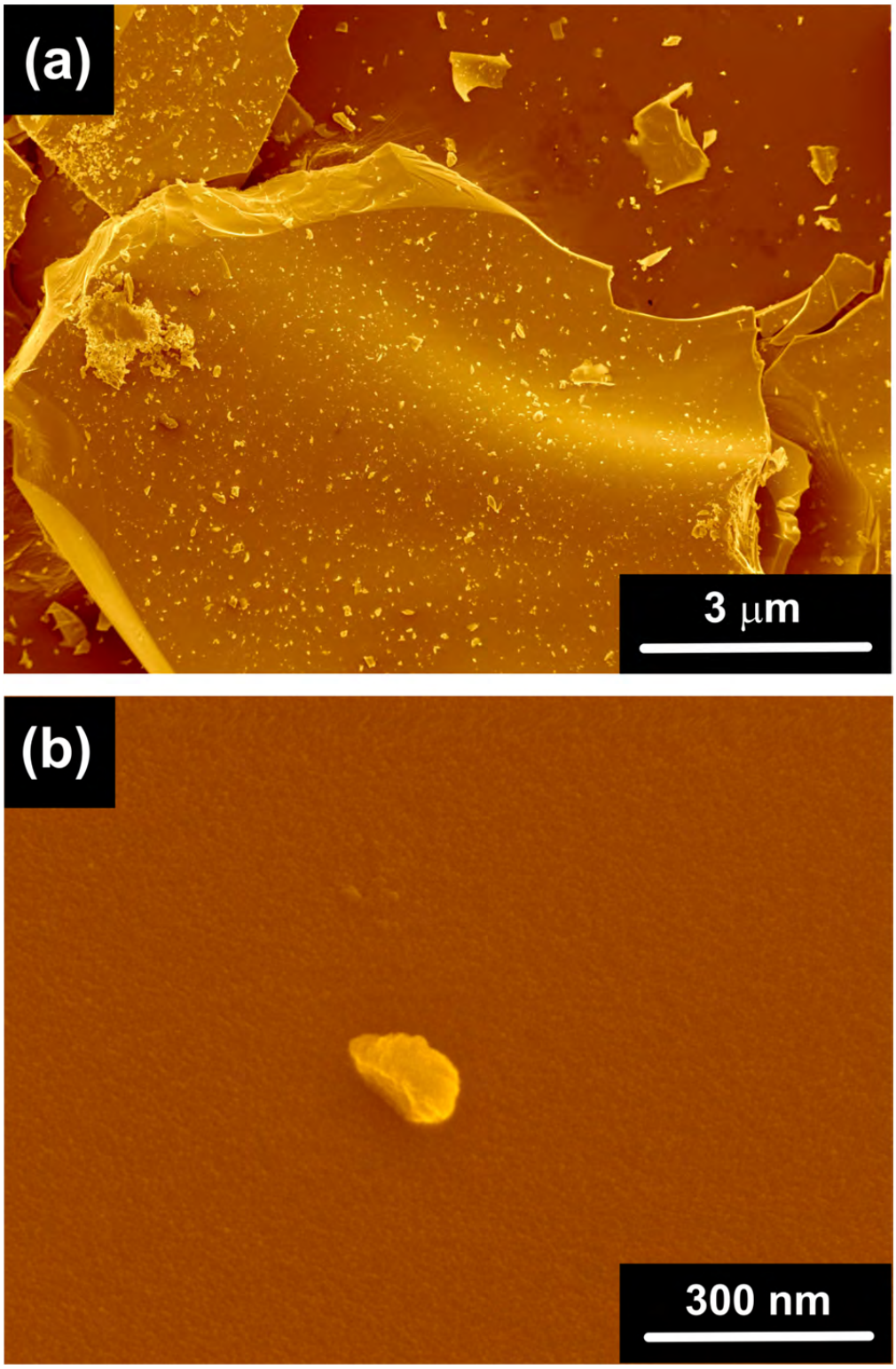

Figure S4.3 SEM images of PdPHEN: (a) 10 kX, and (b) 100 kX.

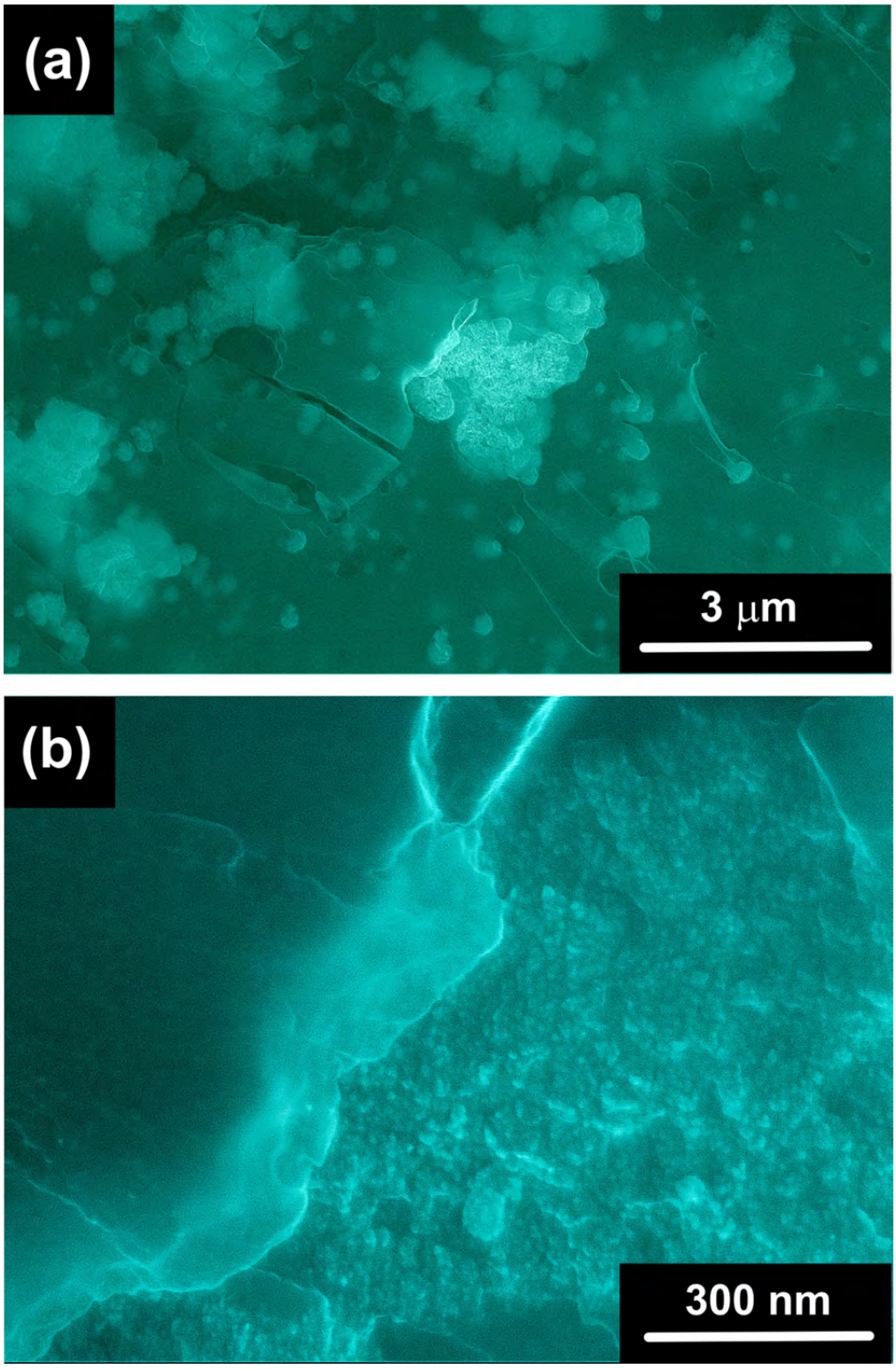

Figure S4.4 SEM images of ZnNEO: (a) 10 kX, and (b) 100 kX.

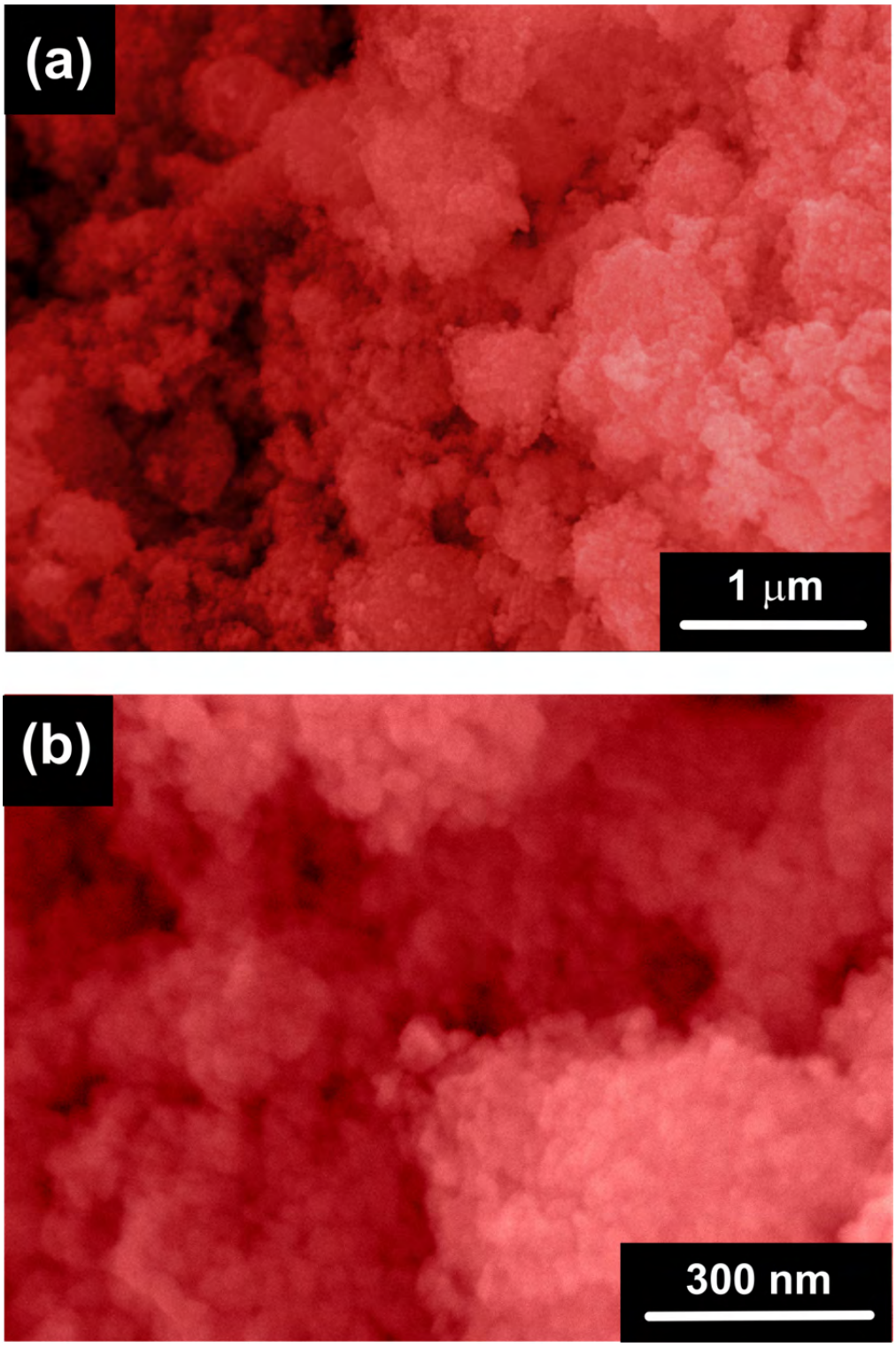

Figure S4.5 SEM images of CdBPE: (a) 10 kX, and (b) 100 kX.

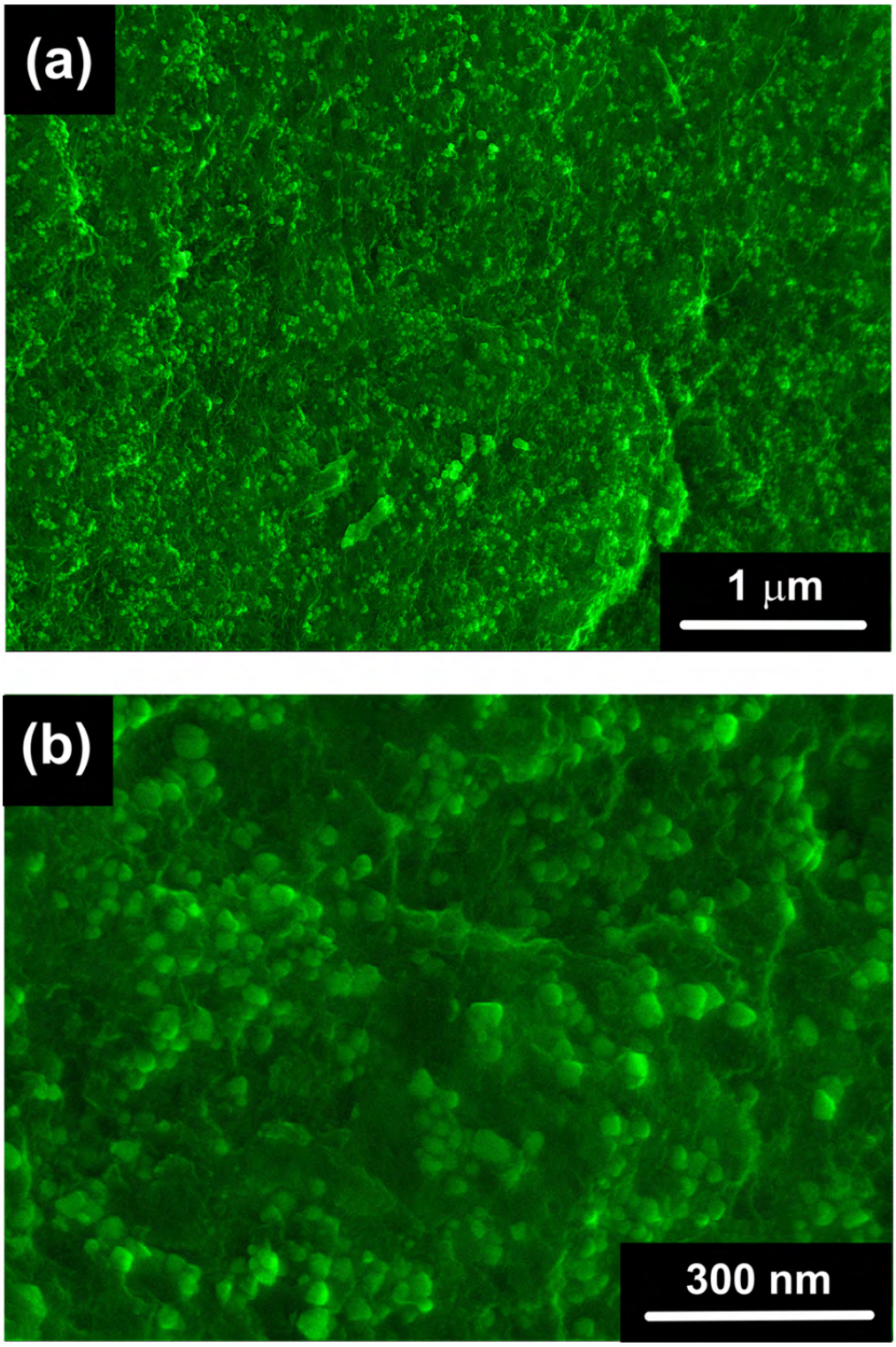

Figure S4.6 SEM images of CdNEO: (a) 25 kX, and (b) 100 kX.

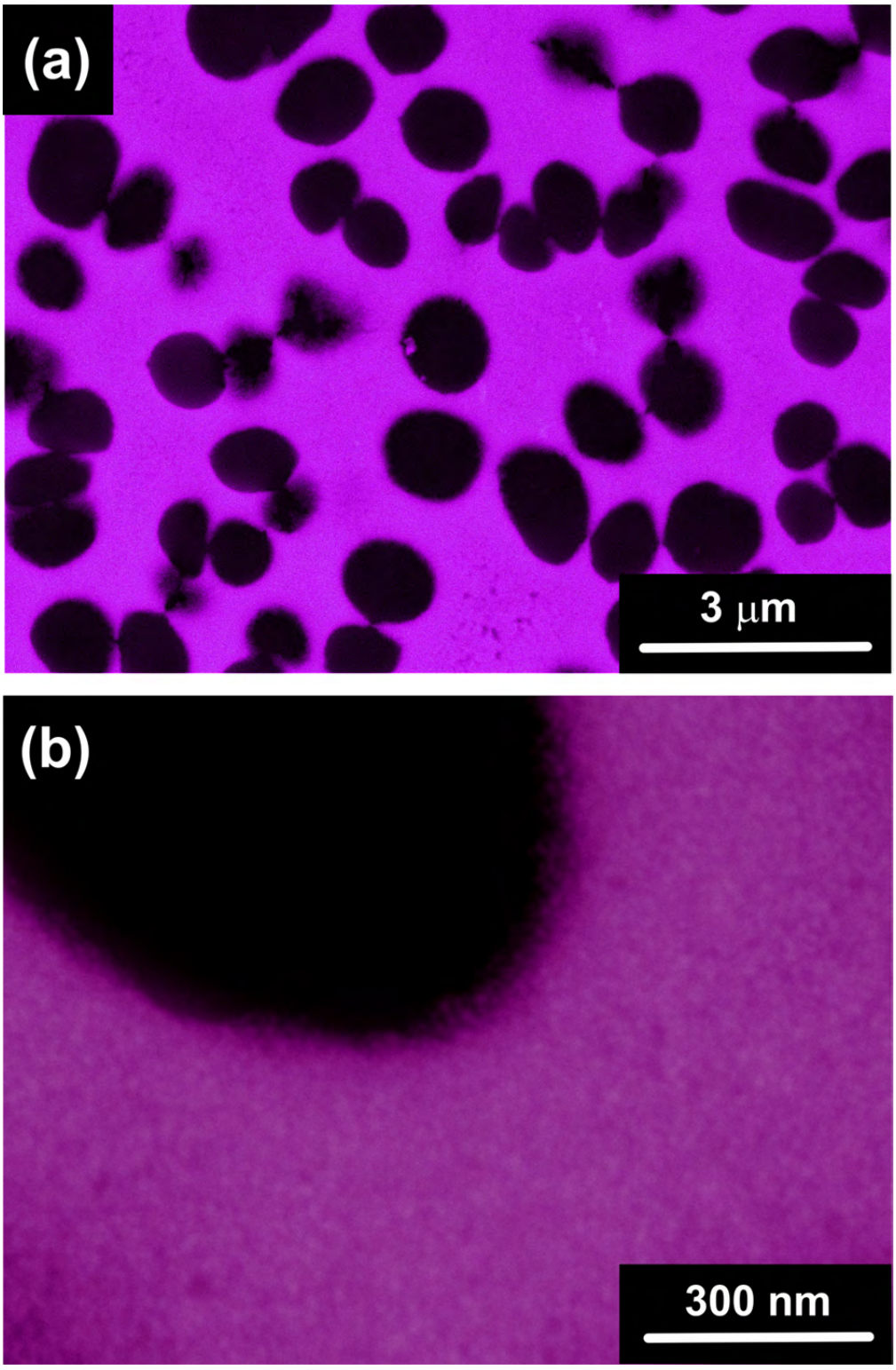

Figure S4.7 SEM images of CdADE: (a) 10 kX, and (b) 100 kX.

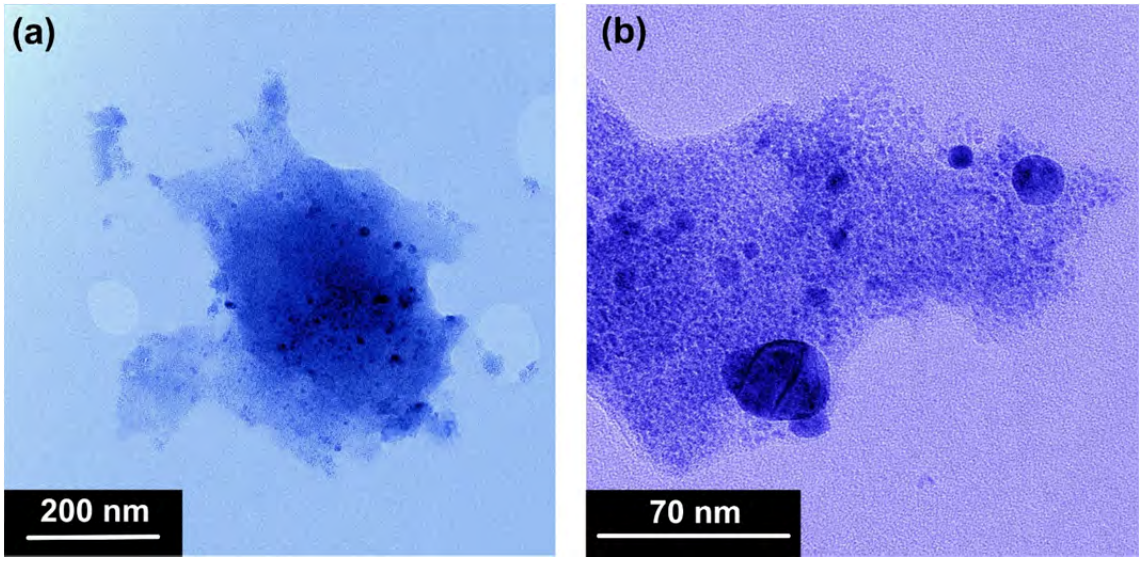

Figure S4.8 TEM images of some particles obtained from the decomposition of PdBPY at 345°C for 15 min. It is noticed that some nuclei have grown much more than the rest.

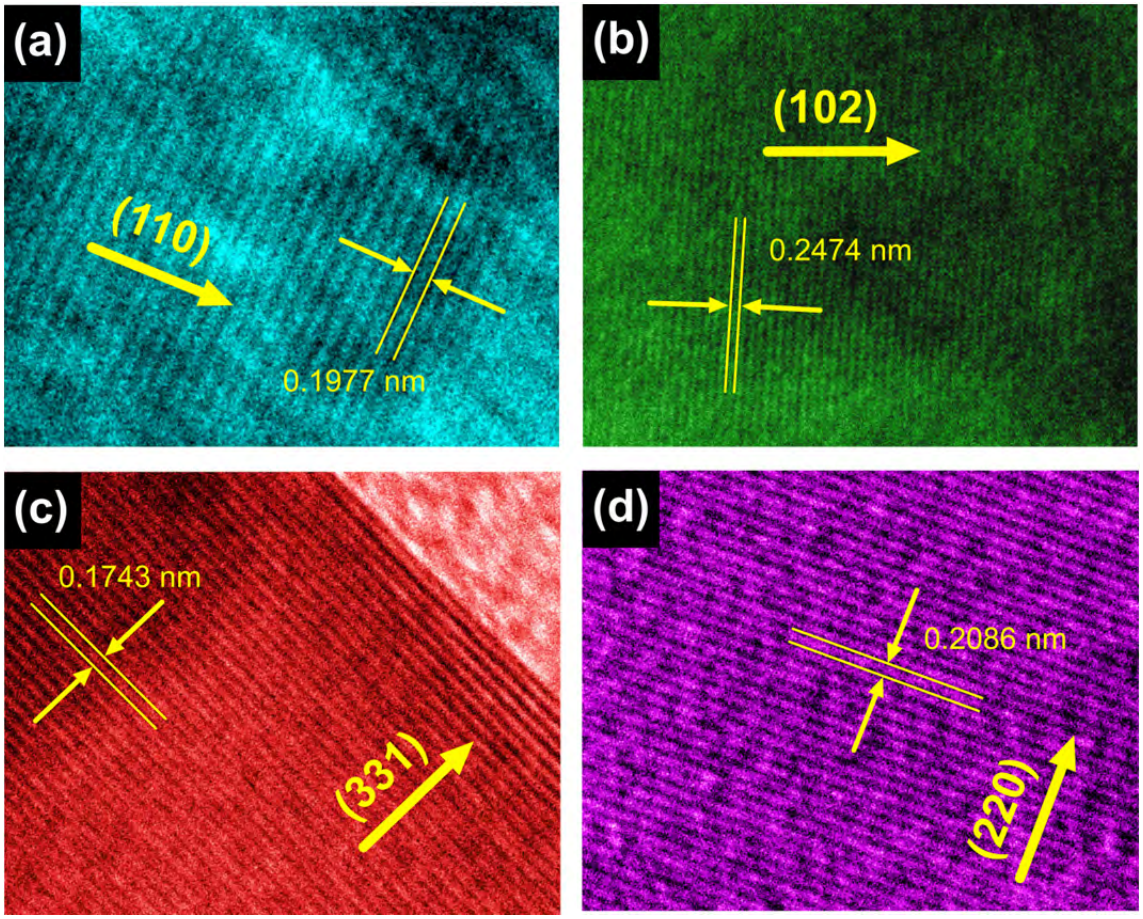

Figure S4.9 Determination of the interplanar distance and crystallographic direction of the decomposition products: (a) ZnNEO, (b) CdNEO, (c) CdBPE, and (d) CdADE.

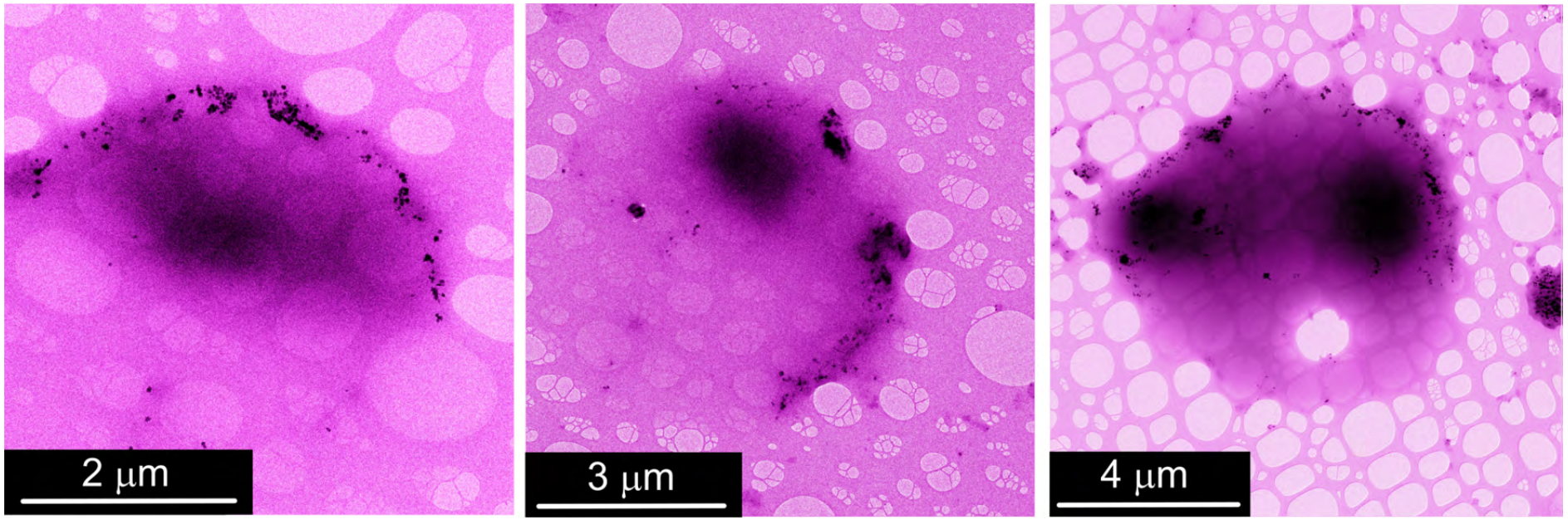

Figure S4.10 TEM images of some partially combusted fragments of CdADE precursor (15 min at 400°C). It can be seen that in the internal part of the microparticles there are dark and diffused areas corresponding to nanoscale nuclei (< 2 nm) of CdS that have begun to form. The thermal effect causes the nuclei to migrate towards the boundary of the microparticle where they agglomerate giving rise to nanoparticles of larger size (10–30 nm).

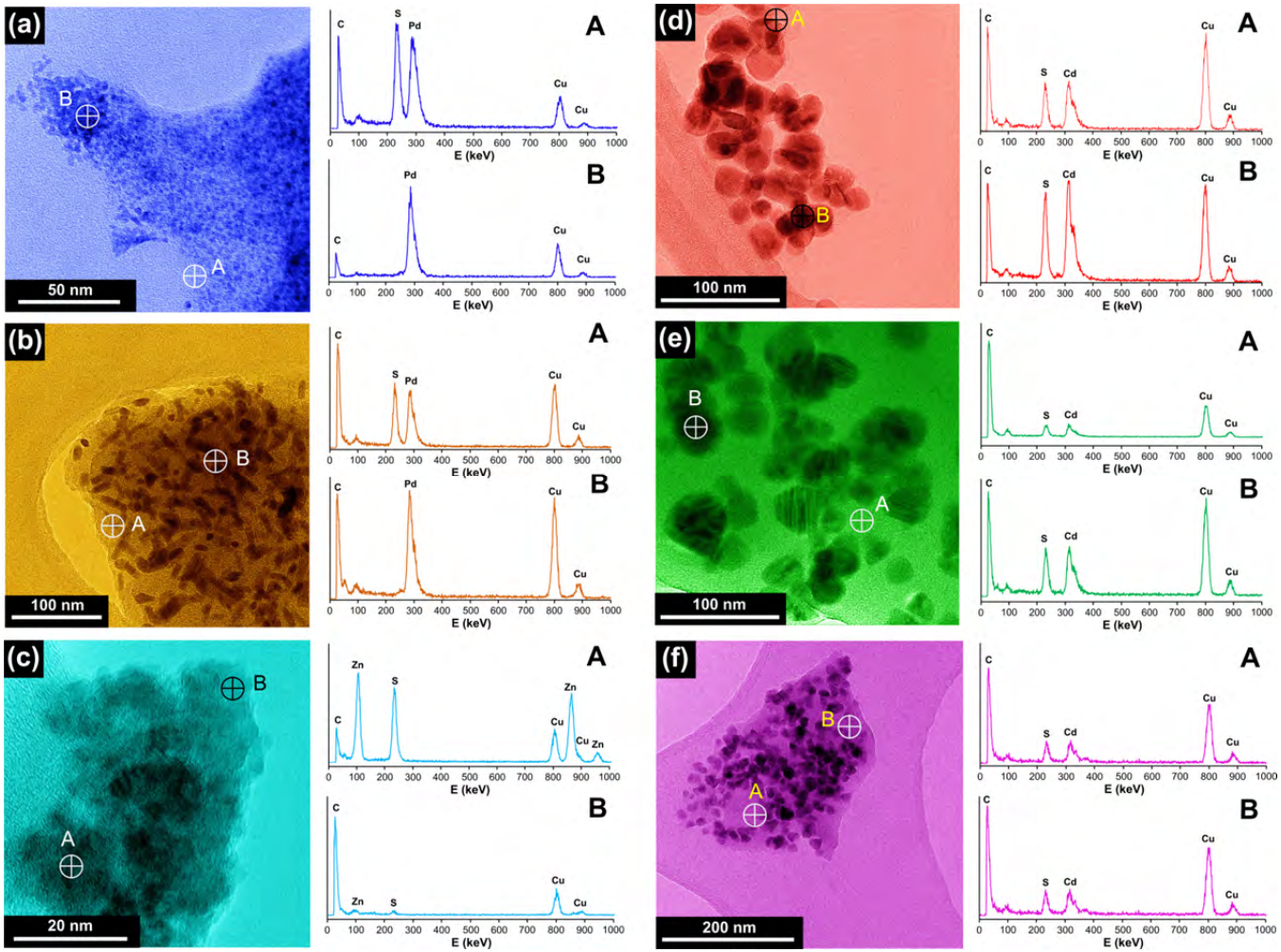

Figure S4.11 TEM images of dry thermolysis products and their respective EDX spectra in two distinct areas of the sample: (a) PdBPY, (b) PdPHEN, (c) ZnNEO, (d) CdBPE, (e) CdNEO, and (f) CdADE.

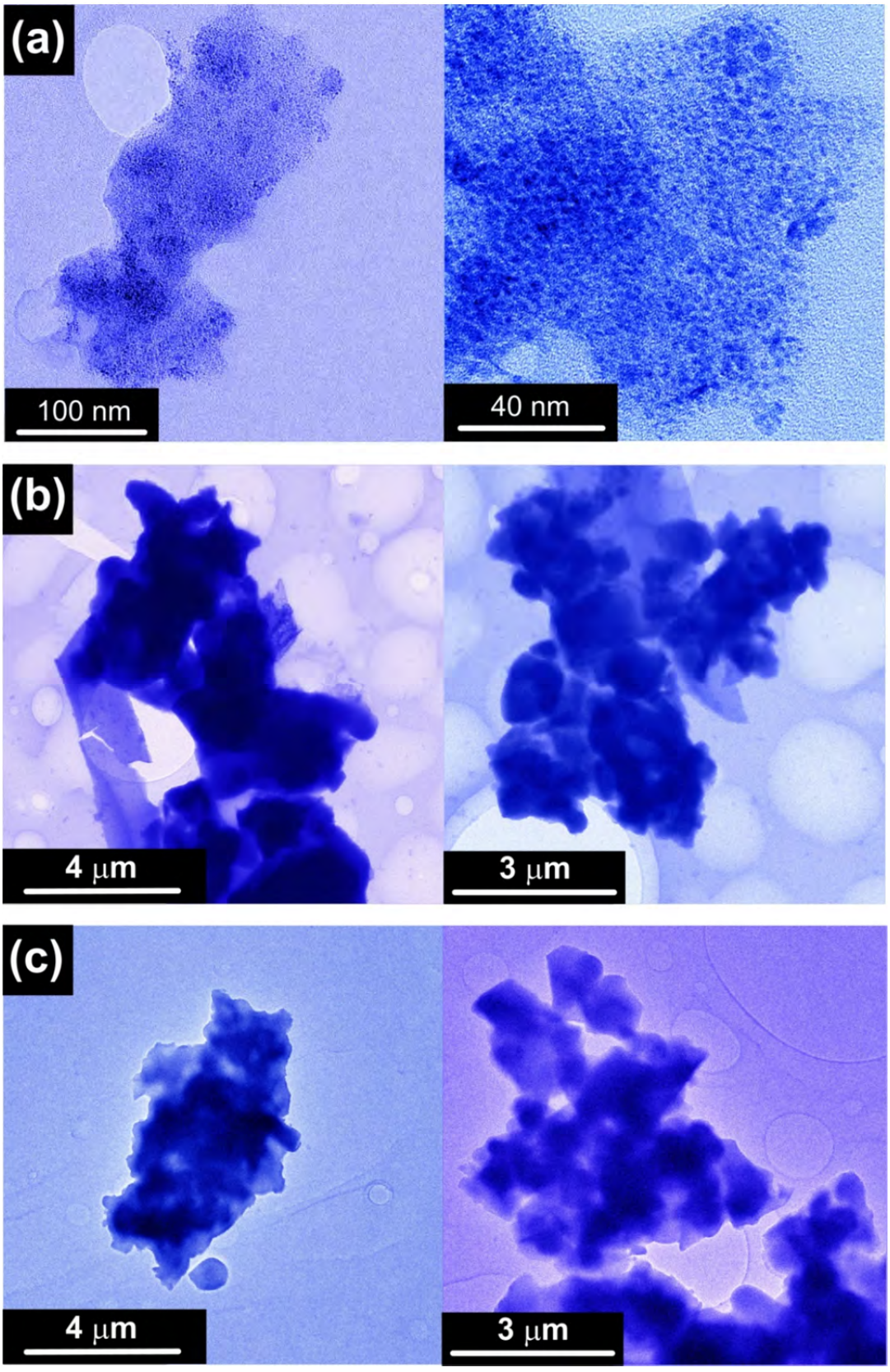

Figure S4.12 TEM images of PdBPY thermolysis products obtained by varying the heating rate: (a) 5 ºC·min^{-1}, (b) 15 ºC·min^{-}1, and (c) 30 ºC·min^{-1}.

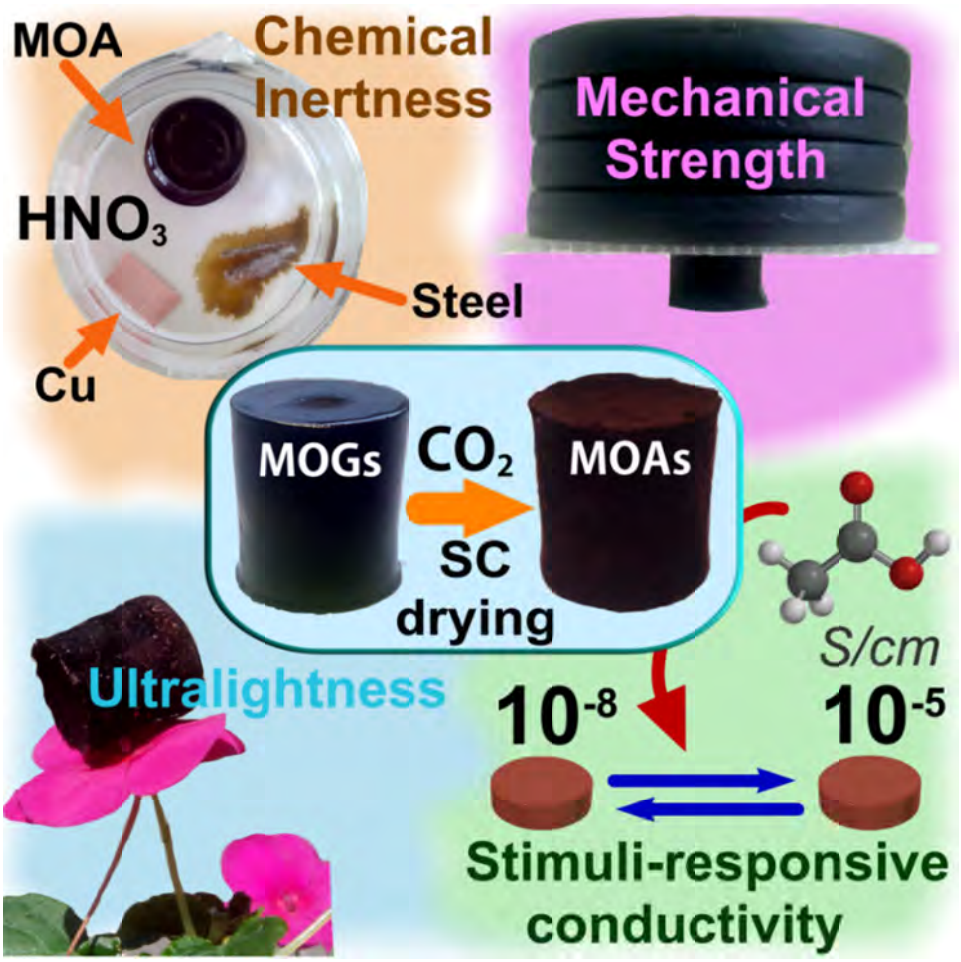

4. CHEMICALLY RESISTANT, SHAPEABLE AND CONDUCTING METAL-ORGANIC GELS AND AEROGELS BUILT FROM DITHIOOXAMIDATO LIGAND

4.1. SUMMARY

Chapters 2 and 3 conclude the first part of the PhD thesis that was focused on the synthesis of pure or carbon supported nanoparticles through the thermal decomposition of coordination complexes under air atmosphere. The next two chapters address another very different class of nanomaterials: metal-organic gels and aerogels (MOGs and MOAs, respectively).

Metal-organic gels (MOGs) appear as a blooming alternative to well-known metal-organic frameworks (MOFs). MOFs are 3D periodic porous structures based on the assembly of metal centers or clusters through multidentate ligands, with cavities generally located in the microporous regime (< 2 nm). Their hybrid nature allows combining porous characteristics with prominent physicochemical properties (magnetism, luminescence, conductivity, catalysis, etc.). However, the industrial presence of MOFs currently remains scarce due largely to problems associated with low chemical stability and poor shaping and processability. Coordination bond strength of a common organic linker containing carboxylate and/or σ-donor nitrogen groups is not sufficient in most cases to withstand the exposure to acid pHs or coordinating solvents, and even some of them are moisture sensitive. Moreover, MOFs are generally obtained as powder but applications such as catalysis, separation, or adsorption often require molding into monoliths or pellets which involve the addition of binders that reduce the surface area of the material.

In the last few years, metal-organic gels (MOGs), also called metallogels, have emerged as an alternative material to MOFs. Ideally, during the gel formation, the coordination polymer grows as nanoscopic primary particles that crosslink stochastically into the reaction media, creating a 3D solid network that entraps all synthesis solvent within. Gel drying by evaporation of the solvent induces a severe shrinkage of the microstructure and leads to a material called xerogel (MOX, metal-

organic xerogel) with reduced porosity. Contrarily, supercritical drying of MOGs removes the solvent without collapsing their microstructure, and it leads to metal-organic aerogels (MOAs) that are hundreds of times lighter than MOFs. Therefore, porosity in MOGs and MOAs has a microstructural origin and not a strictly crystallographic one like in MOFs. Thus, the gelation approach enables the preparation of porous materials from metal-organic systems that do not necessarily render an open framework. Keeping in mind that the examples of MOGs and MOAs are still relatively rare, there is an exciting chance to prepare metal-organic porous materials from coordination polymers that lack crystalline origin porosity but gather striking electrical, magnetic, and optical properties.

The stochastic nature of the gelling process generates open voids of random shape and size with distribution modes usually located in the mesopore range (2–50 nm). Larger pores facilitate migration and diffusion of chemical species and allow even the passage of macromolecules. The augmentation of MOF channel sizes to the mesoporous range still poses a great challenge. Ligand extension is an apparent option, but MOFs built from large ligands tend to collapse upon guest removal and often are accompanied by framework interpenetration. Last but not least, MOGs solve the aforementioned shaping drawbacks of MOFs because they are viscoelastic fluids that adopt the geometry of mold without requiring a post-synthetic processing and/or the use of any binder or additive.

However, MOGs described to date are based on easily reversible metal-ligand bonds which make them unsuitable to be used in extreme environments. Moreover, none of the reported MOGs encompass notable electrical conductivity; a property that combined with porosity provides the opportunity to build chemical sensors. In this chapter, a series of MOGs based on the assembly of 1D-coordination polymer nanofibers of formula $[M(DTA)]_n$ (MII: Ni, Cu, Pd; DTA:

dithiooxamidato) are reported, in which properties such as porosity, chemical inertness, mechanical robustness, and stimuli-responsive electrical conductivity are brought together into an unprecedented material.

The selection of DTA ligand and cited metal(II) centers is due to three main reasons: (1) the affinity of N,S-moiety toward medium/soft metal ions render strong covalent bonds; (2) the trend of the selected M(II) centers to adopt a square-planar geometry, in combination with a bis-chelating coordination mode of the ligand, can promote an anisotropic growth of the colloidal particles favoring their entangling and gelation; and (3) the presence of S-donor atoms with diffuse orbitals can promote electron delocalization and electrical conductivity through the polymeric chain.

The 1D nature of the $[M(DTA)]_n$ coordination system is the key to promote the fibrillar growth of the particles, but only under well-selected synthesis conditions the gelation succeeded, being remarkable the role that the metal salt and solvent play. Supercritical drying of the gels renders ultralight MOAs (ρ: 0.03–0.06 $g \cdot cm^{-3}$; porosity: 98–99% for NiDTA and CuDTA) that preserve the intertwined nanofibrillar structure (diameter: 8–20 nm). Microstructural parameters, such as the aspect ratio of the nanofibers and their spatial concentration, govern the surface area, pore diameter, and mechanical properties. Accordingly, the highest surface area and pore diameter values correspond to MOAs presenting highest aspect ratios (NiDTA, NiCuDTA). Despite the surface area of MDTA, MOAs is far away from most outstanding MOFs; it is comparable to many MOFs and zeolites with moderate surface area values and to organic and inorganic aerogels. On the contrary, pore size can be considered as relatively high (7−23 nm). In fact, almost all mean, median, and mode pore diameters far exceed the maximum value reported for MOFs up to date (< 10 nm). Moreover, it should be stressed that the maximum pore volume values obtained for MDTA MOAs (4.25 $cm^3 \cdot g^{-1}$) are comparable to the record values

reported for MOFs (up to 4.40 $cm^3 \cdot g^{-1}$). Regarding the mechanical properties, Pd(II) MOAs, with the lowest aspect ratio fibers, exhibit a brittle behavior, and Ni(II) MOAs, containing highest aspect ratio fibers, behave as a plastic material. Such plastic behavior has not been previously reported for a material based on a coordination polymer and it allows processing them as films by simply applying pressure. Room-temperature conductivity measurements yielded values ranging from 10^{-7} to 10^{-12} S cm^{-1} that, combined with its fibrillar porous network, results in a stimuli-response material that shows reversible conductivity increase (up to 10^{-5} S cm^{-1}) when subjected to acetic acid vapors. Considering all the above, to the best of our knowledge the reported material implies an unprecedented case within the area of coordination polymers (including MOFs), since it successfully brings together porosity with outstanding chemical inertness, mechanical robustness, and stimuli-responsive electrical conductivity.

The results have been published in *Advanced Functional Materials* journal (year 2017, vol. 27, pp. 1605448). It has been also selected to illustrate the back cover of the corresponding issue. A copy of the corresponding article and its supporting material are gathered below.

4.2. FRONT INSIDE COVER

Vol. 27 • No. 15 • April 18 • 2017

www.afm-journal.de

ADVANCED FUNCTIONAL MATERIALS

WILEY-VCH

4.3. PUBLICATION

Chemically Resistant, Shapeable, and Conducting Metal-Organic Gels and Aerogels Built from Dithiooxamidato Ligand

Daniel Vallejo-Sánchez, Pilar Amo-Ochoa, Garikoitz Beobide, Oscar Castillo,* Michael Fröba, Frank Hoffmann, Antonio Luque, Pilar Ocón, and Sonia Pérez-Yáñez*

Metal-organic gels (MOGs) appear as a blooming alternative to well-known metal-organic frameworks (MOFs). Porosity of MOGs has a microstructural origin and not strictly crystalline like in MOFs; therefore, gelation may provide porosity to any metal-organic system, including those with interesting properties but without a porous crystalline structure. The easy and straightforward shaping of MOGs contrasts with the need of binders for MOFs. In this contribution, a series of MOGs based on the assembly of 1D-coordination polymer nanofibers of formula $[M(DTA)]_n$ (M^{II}: Ni, Cu, Pd; DTA: dithiooxamidato) are reported, in which properties such as porosity, chemical inertness, mechanical robustness, and stimuli-responsive electrical conductivity are brought together. The strength of the M—S bond confers an unusual chemical resistance, withstanding exposure to acids, alkalis, and mild oxidizing/reducing chemicals. Supercritical drying of MOGs provides ultralight metal-organic aerogels (MOAs) with densities as low as 0.03 g cm^{-3} and plastic/brittle behavior depending on the nanofiber aspect ratio. Conductivity measurements reveal a semiconducting behavior (10^{-12} to 10^{-7} S cm^{-1} at 298 K) that can be improved by doping (10^{-5} S cm^{-1}). Moreover, it must be stressed that conductivity of MOAs reversibly increases (up to 10^{-5} S cm^{-1}) under the presence of acetic acid.

1. Introduction

In the field of porous materials science, metal-organic frameworks (MOFs)[1–3] are recognized to exhibit elevated specific surface areas (up to 7000 m^2 g^{-1}) and a higher chemical versatility than other porous materials such as zeolites,[4] covalent-organic frameworks (COFs),[5,6] or activated carbons.[7] MOFs are 3D periodic porous structures based on the assembly of metal centers or clusters through multidentate ligands, with cavities generally located in the microporous regime (<2 nm). Their hybrid nature allows combining porous characteristics with prominent physicochemical properties (magnetism, luminescence, conductivity, catalysis, etc.).[8–13] However, the industrial presence of MOFs currently remains scarce due largely to problems associated with low chemical stability and poor shaping and processability.[14–16] Coordination bond strength of a common organic linker containing carboxylate and/or σ-donor nitrogen groups is not sufficient in most cases to withstand the exposure to acid pHs or coordinating solvents, and even some of them are moisture sensitive. Moreover, MOFs are generally obtained as powder but applications such as catalysis, separation, or adsorption often require molding into monoliths or pellets which involve the addition of binders that reduce the surface area of the material.[17,18]

In the last few years, metal-organic gels (MOGs),[19,20] also called metallogels, have emerged as an alternative material to MOFs. Ideally, during the gel formation, the coordination polymer grows as nanoscopic primary particles that crosslink stochastically into the reaction media, creating a 3D solid network that entraps all synthesis solvent within. Gel drying by evaporation of the solvent induces a severe shrinkage of the microstructure and leads to a material called xerogel (MOX, metal-organic xerogel) with reduced porosity. Contrarily, supercritical drying of MOGs removes the solvent without collapsing their microstructure, and it leads to metal-organic aerogels (MOAs)[21,22] that are hundred of times lighter than MOFs. Therefore, porosity in MOGs and MOAs has a microstructural origin and not a strictly crystallographic one like in MOFs. Thus, the gelation approach enables the preparation of porous materials from metal-organic systems that do not necessarily render an open framework. Keeping in mind that the examples of MOGs and MOAs are still relatively rare, there is an exciting chance to prepare metal-organic porous materials from

D. Vallejo-Sánchez, Dr. G. Beobide, Dr. O. Castillo, Prof. A. Luque, Dr. S. Pérez-Yáñez
Departamento de Química Inorgánica
Facultad de Ciencia y Tecnología
Universidad del País Vasco
UPV/EHU, Apartado 644 48080, Bilbao, Spain
E-mail: garikoitz.beobide@ehu.eus; oscar.castillo@ehu.es

Dr. P. Amo-Ochoa, Prof. P. Ocón
Departamento de Química Inorgánica y Química Física
Universidad Autónoma de Madrid
Madrid 28049, Spain

Prof. M. Fröba, Dr. F. Hoffmann
Institute of Inorganic and Applied Chemistry
University of Hamburg
Martin-Luther-King Platz 6, Hamburg 20146, Germany

DOI: 10.1002/adfm.201605448

coordination polymers that lack crystalline origin porosity but gather striking electrical, magnetic, and optical properties.[23–25]

The stochastic nature of the gelling process generates open voids of random shape and size with distribution modes usually located in the mesopore range (2–50 nm). Larger pores facilitate migration and diffusion of chemical species and allow even the passage of macromolecules.[26–28] The augmentation of MOF channel sizes to the mesoporous range still poses a great challenge. Ligand extension is an apparent option, but MOFs built from large ligands tend to collapse upon guest removal and often are accompanied by framework interpenetration.[29] Last but not least, MOGs solve the aforementioned shaping drawbacks of MOFs because they are viscoelastic fluids that adopt the geometry of mold without requiring a postsynthetic processing and/or the use of any binder or additive.

However, MOGs described to date are based on easily reversible metal–ligand bonds which make them unsuitable to be used in extreme environments.[30,31] Moreover, none of the reported MOGs encompass notable electrical conductivity, a property that combined with porosity provides the opportunity to build chemical sensors. In this paper, a series of MOGs based on the assembly of 1D-coordination polymer nanofibers of formula $[M(DTA)]_n$ (M^{II}: Ni, Cu, Pd; DTA: dithiooxamidato) are reported, in which properties such as porosity, chemical inertness, mechanical robustness, and stimuli-responsive electrical conductivity are brought together into an unprecedented material. The selection of DTA ligand and cited metal(II) centers is due to three main reasons: (1) the affinity of N,S-moiety toward medium/soft metal ions render strong covalent bonds; (2) the trend of the selected M(II) centers to adopt a square-planar geometry, in combination with a bis-chelating coordination mode of the ligand, can promote an anisotropic growth of the colloidal particles favoring their entangling and gelation; and (3) the presence of S-donor atoms with diffuse orbitals can promote electron delocalization and electrical conductivity through the polymeric chain.[32,33]

2. Results and Discussion

2.1. Gelation Studies

Conditions required for gel formation demand a fine control of the kinetics of the process to scrutinize several physicochemical factors: solvent, basifying agent, metal salt type, reagent ratio, addition order, concentration, and temperature. A detailed description of the screening is gathered in the Supporting Information (Table S1.1 and Figures S1.1 and S1.2, Supporting Information), while optimum conditions are defined in the Experimental Section. The most relevant parameters to gel the system were solvent and metal salt type, despite other factors' influence in the final stiffness of the gel. Among all the tested solvents, only those with greater coordinative capacity and sterically hindered were able to promote the gelation, specifically *N,N*-dimethylformamide (DMF), *N,N*-dimethylacetamide (DMA), DMSO (dimethylsulfoxide), and DEA (*N,N*-diethylacetamide). Regarding the explored metal salts (bromides, hydroxides, nitrates, perchlorates, etc.) only acetates promote the gelation. The gelation process seems to involve an initial stage in which a sudden and massive nucleation event occurs in the entire reaction volume which depletes at the same time the concentration of dissociated M(II) ions. However, the relatively low dissociation value of the acetate salt provides a reservoir of additional M(II) ions that are slowly released. It allows nuclei growth to create a branching in such a way that a semicoherent 3D solid lattice is formed. As a result, the entrapped solvent represents about 88%–99% of the total mass. Regarding gel shaping, it must be noted that monoliths of different volumes and shapes are easily achievable (**Figure 1**).

Moreover, supercritical drying shrinks gel volume around 50%–82%, being more pronounced in compounds based on Pd(II), but retaining their shape. Ambient pressure gel drying produced MOXs with greater shrinkages (95%–98%) and deformation (Figure 1b).

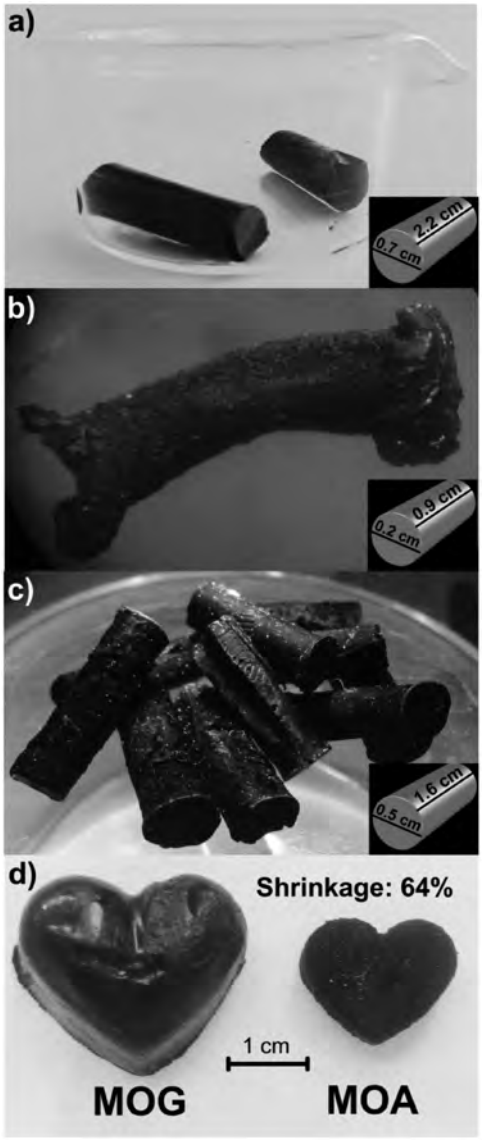

Figure 1. Cylinders made of NiDTA in different solid states: a) gel, b) xerogel, and c) aerogel. d) The system allows creating complex geometries by molding.

2.2. Structural and Microstructural Characterization

The oxalato ligand and its derivatives (oxamidato, dithiooxalato, and dithiooxamidato) are expected to sequentially bridge transition metal ions in a bis-bidentate coordination mode, and as a result, to yield 1D-coordination polymers when combined with metal centers with square-planar coordination geometry.[34] The synthesis of the dithiooxamidato polymeric species provides scarcely crystalline products[35] that preclude the elucidation of their structure based on X-ray diffraction data. However, their powder X-ray diffraction (PXRD) patterns exhibit two weak and broad signals sited at 2θ values of 15.5°–16.1° and 25.1°–27.2° (see Figure S2.5 in the Supporting Information). The former corresponds to *d*-spacings of 5.5–5.7 Å, which fit fairly well the M—M distances found in the Cambridge Structural Database for bis-bidentate dithiooxamidato discrete complexes (5.7–5.9 Å).[36] Additionally, Fourier transform infrared (FTIR) and Raman spectroscopy studies support a structure consisting of a 1D polymeric chain (**Scheme 1**) in which the metal centers are sequentially bridged by dithiooxamidato ligands in a μ_2-κ^2N,S:κ^2N',S' coordination mode (see Section S.2 of the Supporting Information).

Transmission electron microscopy (TEM) analysis of MOGs shows extended fibrillar networks of intertwined strands with mean diameters in the range of 8–20 nm that give rise to cobweb-like structures (**Figure 2**). These results agree quite well with the fiber-height values measured by atomic force microscopy (see Figure S3.7 in the Supporting Information).

Scanning electron microscopy (SEM) images of MOAs (**Figure 3**) show fibers with similar average diameters (3–8 nm) that differ widely in length (30–800 nm). SEM observations over xerogels indicate that fibers collapse, creating surfaces lacking porosity (Figures S3.4–3.6). Returning to aerogel samples, it is possible to make a classification based on textural similarities (Figures S3.8–3.16): PdDTA and NiPdDTA possess the lowest aspect ratios, PdCuDTA and CuDTA exhibit intermediate values, while NiCuDTA and NiDTA hold the highest ratios.

Thus, in comparison to Pd(II), the presence of Cu(II) or Ni(II) in the compound seems to encourage the growth of the chain. The differences in mean fiber size can be explained on the basis of the interaction that the solvent establishes with the polymeric chains and how this interaction governs kinetics of lateral and longitudinal growth. (1) Coordination of the solvent to the end of the chain influences the 1D growth rate in such a way that the length of the fibers is inversely proportional to the coordination strength of the amidic solvent (Pd > Cu ≈ Ni). (2) Side interactions of the chain with the solvent (coordination to the apical positions of the M(II) and noncovalent interactions) determine the chain packing: the weaker the interaction

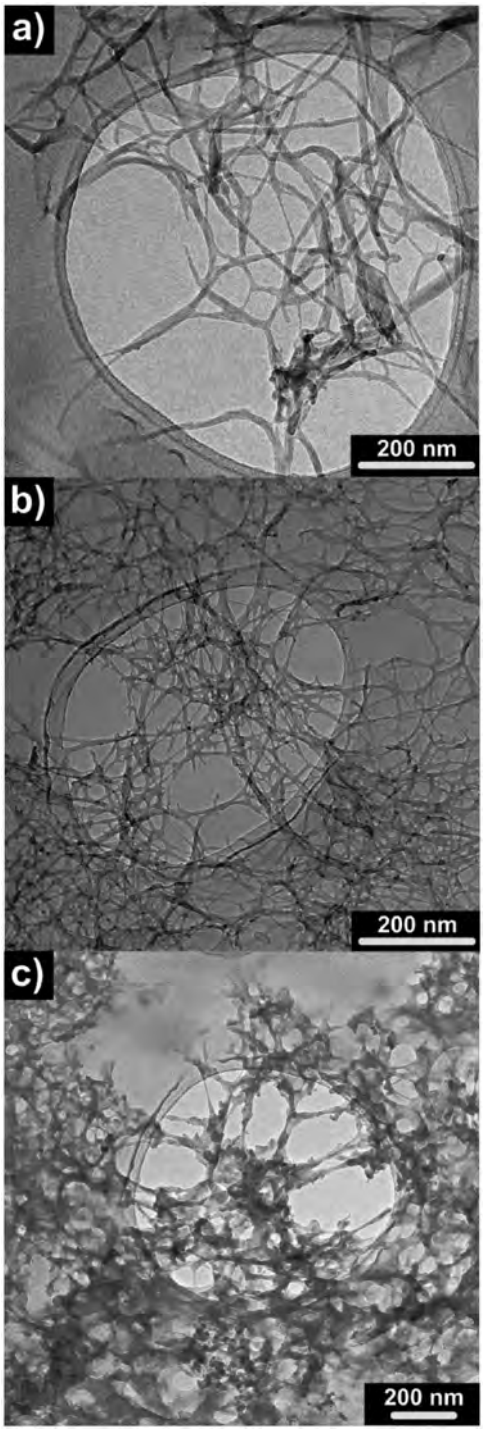

Figure 2. TEM images of a) NiDTA, b) NiPdDTA, and c) PdDTA MOGs dispersed in ethanol in the presence of *n*-decylamine.

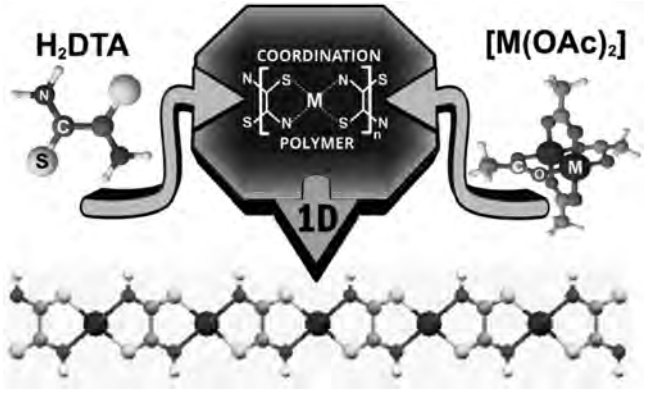

Scheme 1. Scheme of the polymerization process and a fragment of the MDTA polymer chain.

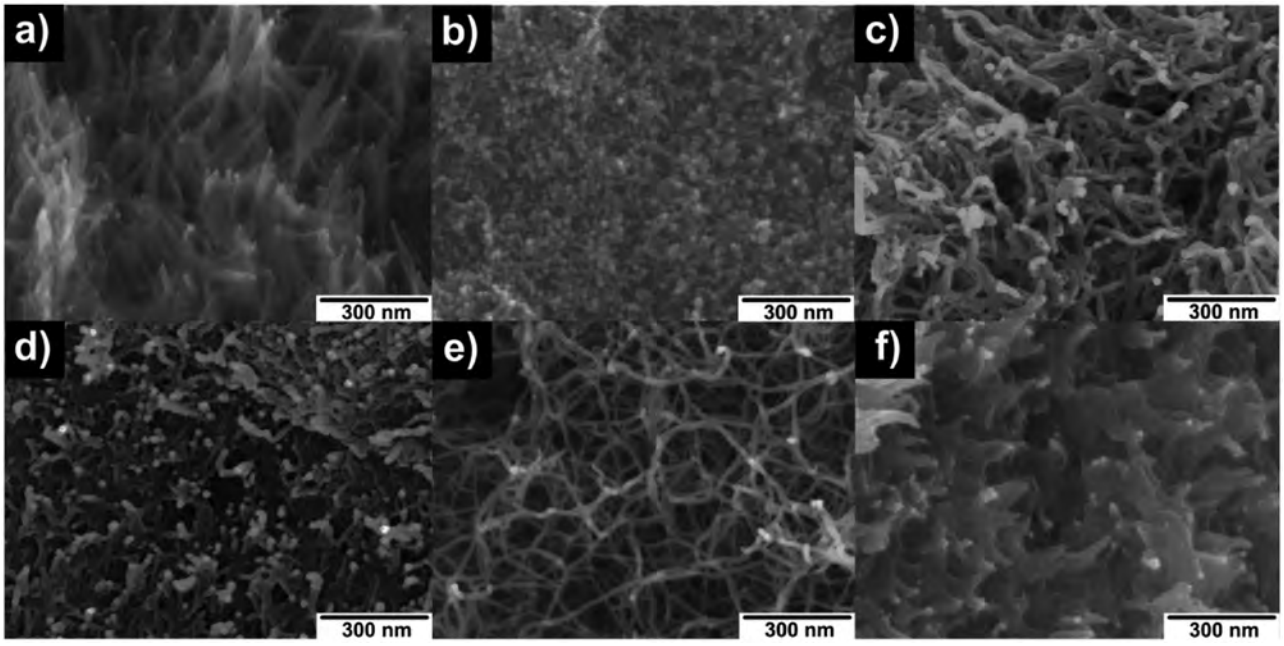

Figure 3. SEM images of MDTA MOAs with a magnification of 100 kX: a) NiDTA, b) PdDTA, c) CuDTA, d) NiPdDTA, e) NiCuDTA, and f) PdCuDTA.

with the solvent the thicker the fiber. Although the strength of the noncovalent contacts is difficult to guess, it can be stated that the apical coordinative interaction of the solvent is disfavored for Pd(II) due to its marked trend to adopt square-planar geometry, which is in good agreement with the smaller aspect ratio values found for Pd-containing compounds. On the other hand, Ni(II) and Cu(II) are likely to display higher coordination numbers, but the Jahn–Teller effect of Cu(II) imposes longer distances through the apical position (semicoordination) and weakens the interactions with the solvent, which would favor the thickening of the chains resulting in a slightly smaller aspect ratio for Cu(II)- than for Ni(II)-based materials. In any case, considering all the above stated, the nature of the solvent is crucial to prompt the fibrillary growth and the gelation (see Section S.1 of the Supporting Information); only coordinating solvents such as DMF or DMSO with hydrogen bonding acceptor capability worked.

SEM images were also used to estimate the density of the fibrillar network (Table S3.1, Supporting Information). The number of fibers per unit area of MOAs oscillates between 100 and 800 fibers μm^{-2} except for PdDTA, which shows a surface density higher than 1400 fibers μm^{-2}. It is deserving of note that aspect ratio as well as fibrillar density play a key role in the below-described porosity and mechanical behavior.

2.3. Density and Porosity in MOAs

Apparent density of aerogels (**Table 1**) ranged between 0.03 and 0.11 g cm^{-3}, except for the PdDTA sample whose higher density value (0.49 g cm^{-3}) is in concordance with the textural observations (Figure 3f; Figure S3.12, Supporting Information). Density of lighter monoliths obtained for NiDTA system (see Video S.1 in the Supporting Information) is comparable to many metal-free aerogels[37–39] and slightly lower than typical organic polymeric foams.[40–42] The final density of NiDTA aerogels seems to be quite insensitive to the initial reagent concentration, at least at high values (50×10^{-3}–100×10^{-3} M), providing densities around 0.05–0.06 g cm^{-3}. Framework densities estimated by helium pycnometric measurements ranged around 2.4–3.0 g cm^{-3}. Curiously, Pd(II)-constituted MOAs present the lowest framework density value, probably due to differences in the molecular packing. The degree of porosity exceeds 95% in all MOAs except for PdDTA, which shows a more moderate value of 79%.

The porosity of the aerogels was further analyzed by adsorption isotherms of N_2 measured at 77 K (Figures S4.1–4.4, Supporting Information). Subtracted porosity data is gathered in **Table 2**. Specific surface areas obtained by fitting the adsorption

Table 1. Density and porosity values of MOAs.

Sample[a)]	ρ_A[b)] [g cm^{-3}]	ρ_F[c)] [g cm^{-3}]	P[d)] [%]
NiDTA-25	0.03(1)	2.99(31)	99.0
NiDTA-50	0.06(1)	–	98.0
NiDTA-75	0.06(1)	–	98.0
NiDTA-100	0.05(1)	–	98.3
PdDTA	0.49(8)	2.42(10)	79.7
CuDTA	0.05(2)	3.02(30)	98.3
NiPdDTA	0.08(1)	2.57(9)	96.9
NiCuDTA	0.04(2)	2.38(7)	97.9
PdCuDTA	0.11(1)	2.54(7)	95.7

[a)]Sample code indicates compound name and, for NiDTA, synthesis concentration ($\times 10^{-3}$ M); [b)]Apparent density; [c)]Framework density measured by helium; [d)]Porosity percentage of MOAs calculated from true and apparent density.

Table 2. Most relevant adsorption parameters of MOAs.

Sample	S_{BET} [$m^2\ g^{-1}$][a)]	V_P [$cm^3\ g^{-1}$][b)]	D [nm][c)]	D_{mode} [nm]	C.V.[d)]
NiDTA-25	407	1.406	8.6	11.1	20.6
NiDTA-50	427	4.250	11.0	23.2	43.2
NiDTA-75	406	3.002	18.6	18.2	37.8
NiDTA-100	418	2.192	9.1	9.0	39.1
PdDTA	189	0.441	6.8	6.8	38.3
CuDTA	211	2.243	21.0	22.6	110.9
NiPdDTA	307	3.917	23.4	23.0	38.9
NiCuDTA	372	2.508	16.0	18.0	97.7
PdCuDTA	248	1.742	13.4	15.0	108.4

[a)]BET specific surface; [b)]Total pore volume calculated from N_2 isotherm at 77 K at relative pressures of ≈0.99; [c)]Mean pore diameter; [d)]Variation coefficient [%].

data to the Brunauer–Emmett–Teller (BET) equation ranged from 189 to 427 $m^2\ g^{-1}$. Pore volumes varied between 0.44 and 4.25 $cm^3\ g^{-1}$ in agreement with the trend observed for apparent density. All of them have isotherms of type II/IV according to the IUPAC classification,[43] with a hysteresis loop that anticipates a significant meso/macroporous contribution, except for PdDTA, which fits better to a pure type IV isotherm, indicating the predominance of mesopores. In most of them, capillary condensation implies a sharp increase of the isotherm above 0.80 P P_0^{-1}. In PdDTA this phenomenon begins at lower relative pressures, which is in concordance with the smaller pore size revealed by the Barret-Joyner-Halenda (BJH) distribution (Table 2).

All of them show a wide monomodal pore size distribution centered at the mesoporous region with a tail that in most cases extends into the macroporous regime. Note that despite the fact that the fibrillar network is formed in a stochastic process, the degree of pore size polydispersity in most MOAs is relatively moderate, achieving at best a coefficient of variation of ≈20%.

2.4. Chemical and Mechanical Resistance

NiDTA MOG was expressly subjected to chemical inertness tests based on the immersion of 1–2 g of gel for a week in a series of solutions covering the most problematic scenes (see Table S5.1 in the Supporting Information). The samples were filtered, thoroughly washed, dried at room temperature, and analyzed by attenuated total reflection FTIR to check the possible existence of chemical modifications. In contrast to metallogels reported in the literature that are primarily of supramolecular nature,[44–46] NiDTA MOG showed unusual stability to be based on a coordination polymer. It is due to the strength of the metal–sulfur bond and to the presence of the double chelating coordination mode of the DTA ligand. The affinity of the N,S-moiety toward medium/soft metal ions renders strong covalent bonds. At room temperature its structure remains unchanged upon acid and base aqueous solutions (pH = 0–14) (**Figure 4**; Video S.1, Supporting Information). The gel was also stable under hydrothermal conditions, pH = 2–12, at least up to 373 K for 24 h. Apart from that, the gel is stable when subjected to mechanical agitation, surfactants, and saline solutions, which points to a chemical gel with irreversible crosslinks. Nevertheless, concentrated inorganic acids (H_2SO_4, HNO_3, HCl) and strong oxidizing agents (H_2O_2, $KMnO_4$) cause the breakdown of the polymer network. However, it is remarkable that the gel is stable under the oxidant conditions exerted by HNO_3 at moderate concentrations (0.5 M), where elemental copper and some stainless steels are easily oxidized. In the case of coordinating agents, such as trimesic acid, bipyridines, and ethylenediamine tetraacetic acid, the infrared spectra collected on the recovered solids indicate that the overall gel structure is retained, but the presence of some extra peaks points to the coordination of the test chemicals to a significant fraction of exposed Ni(II) ions (i.e., those located at the surface of the fiber). This observation suggests the feasibility of performing postsynthetic functionalization while retaining the overall porous framework.[47–49] To complete the chemical stability studies, thermogravimetric analyses were conducted on MOAs under synthetic air conditions (Figure S5.10, Supporting Information). The samples were stable up to 538, 603, and 648 K for Cu, Ni, and Pd, respectively.

Stiffness of Ni/Pd-based gels and aerogels was suitable to accomplish with uniaxial quasistatic compression tests. First, measurements were performed over NiDTA gels and aerogels obtained at different concentrations (25×10^{-3}, 50×10^{-3}, 75×10^{-3}, and 100×10^{-3} M) in order to relate the mechanical properties with their microstructural parameters (**Table 3**). Gels behave elastically below 2.5% of strain and can be plastically compressed to values around 19%–35%, after which fractures propagate and the material yields further. An increased concentration gives rise to materials with a greater rigidity and brittleness with an increase in Young modulus, although the maximum compressive strength is reached for the sample prepared at 50×10^{-3} M (**Figure 5**a). In regard to MOAs, their compression–strain curves follow the basic form of classical rigid cellular foams:[50,51] a linear elastic deformation in a first stage, then a nonlinear region until reaching

Figure 4. Gel fragments subjected to different pH solutions.

Table 3. Most relevant mechanical parameters of MDTA gels and aerogels.

Sample	ρ[a]	l/D[b]	E[c]	σ_{10}[d]	σ_{break}[e]	σ_{TS}[f]	ε_{break}[g]	U_T[h]
				MOGs				
NiDTA-25	–	1.05	0.3	6.6	10.6	49.0	21.9	0.01
NiDTA-50	–	0.93	1.0	25.8	48.8	123.6	18.0	0.04
NiDTA-75	–	1.06	1.7	22.3	31.1	148.2	18.7	0.04
NiDTA-100	–	1.13	2.3	28.3	26.1	138.0	42.1	0.09
				MOAs				
NiDTA-25	0.078	1.83	1.4	15.5	–	186.1	–	0.56
NiDTA-50	0.063	0.96	2.4	89.5	–	1100.1	–	4.65
NiDTA-75	0.057	1.13	3.1	104.7	–	813.4	–	3.73
NiDTA-100	0.059	1.01	74.6	750.8	–	8152.6	–	84.22
NiPdDTA	0.062	1.18	3.7	24.1	–	455.0	–	1.42
PdDTA	0.386	1.09	11.5	88.3	99.5	99.5	10.7	0.03

[a]Apparent density in g cm^{-3}; [b]Aspect ratio of the specimens; [c]Compressive Young modulus in kPa; [d]Compressive strength at 10% of deformation in kPa; [e]Crushing strength in kPa; [f]Ultimate compressive strength in kPa; [g]Fracture strain in %; [h]Specific energy absorption in J g^{-1}.

the yield point, and finally a densification regime beyond the yield point as the void space collapses. Aerogels exhibit significantly higher modulus of elasticity than their respective MOGs due to the shrinkage of the fibrillar network taking place during supercritical treatment (maximum Young's modulus being 74.6 kPa for samples prepared at 100×10^{-3} M). The marked difference between NiDTA-100 and other aerogels can be attributed to a greater crosslinking of the fibers in the former (see Figures S3.8.–S3.11 in the Supporting Information). In any case, these values are far below those reported for inorganic aerogels of particulate nature like SiO_2 or Al_2O_3.[52,53] Noticeably, after the elastic regime (ε < 5%), NiDTA aerogels exhibit a plastic behavior all along the compression test, which enables this material to be malleable and processable, for example, as films by simply applying pressure. To the best of our knowledge, none of the porous coordination polymers (including MOFs and MOAs) reported to date exhibits such behavior.

On the other hand, the comparison of aerogels based on different metals (NiDTA, PdDTA, and NiPdDTA) shows that fiber aspect ratio is an influencing factor on the mechanical properties of the material. MOA with the shortest fibers (PdDTA) present more points of contact (related to a higher fiber concentration; see Table S3.1 in the Supporting Information) for cracks to propagate, resulting in a brittle and friable solid. On the contrary, MOAs with long aspect ratio fibers render a larger amount of empty areas, thus preventing breakage and conferring plasticity upon material. Specific compressive strength measured for the toughest MOAs (NiDTA-100: 12725 J kg^{-1}; NiDTA-50: 1662 J kg^{-1}; and PdDTA: 258 J kg^{-1}) is far higher than that found for the unique MOF-aerogel mechanically characterized,[54] and somewhat higher than many carbon,[55] organic,[56,57] ceramic,[58] and metal[59] aerogels, and comparable to some conventional polymeric foams[40,60–64] like polystyrene, polyurethane, etc. (Figure 5b).

Finally, as a proof of concept (**Figure 6**a,b), NiDTA-50 MOG (44 g) and MOA (0.37 g) monoliths were allowed to hold up 2 kg of dumbbell weights (i.e., around 45 and 5550 times their weight). After removing the dumbbell weights, the exhibited strain values were 2.3% and 5.0%, respectively, which fit rather well with the values expected from the compression–strain test curves.

2.5. Conductivity Measurements

Considering the 1D molecular structure of the polymer, it may be assumed that the electronic conduction of these systems, possessing a conjugated organic molecule with sulfur and nitrogen atoms as donors of electrons, is determined by the transition of the electrons over the metal bridges.[65] Previously reported ab initio calculations propose that the lowest unoccupied and highest occupied (nd_{x2-y2} from metal transition and ligand pσ) molecular orbitals contribute to the electrical conduction.[65,66] Herein, DC electrical conductivity measurements were initially made at 298 K by the two probe techniques, using pressed disks of each MOA, including the heterometallic samples to assess the influence of combining different metal ions. The results show conductivity values between 10^{-7} and 10^{-12} S cm^{-1} (**Table 4**), with CuDTA and NiCuDTA samples being the most conductive ones. The homometallic Cu(II) sample renders conductivity values three orders of magnitude higher than the Ni(II) and Pd(II) counterparts. Moreover, the inclusion of a second metal ion (i.e., heterometallic samples) does not have a synergetic effect, but worsens in all cases the conductivity with respect to the homometallic counterpart with the maximum value. The lower conductivity presented by the Ni, PdDTA, and heterometallic polymers may be rationalized by a lower charge density as a result of replacement of d^9 Cu(II) with the d^8 Ni(II) or Pd(II). In fact, it has been reported that Ni(II) centers do not provide high energy electrons as effective charge carriers.[67]

Conductivity measurements at variable temperature (298–373 K) carried out for the compounds with the best performance, NiCuDTA and CuDTA, allowed calculating their activation energies (0.16 eV and 0.37 meV, respectively; Figure S6.3,

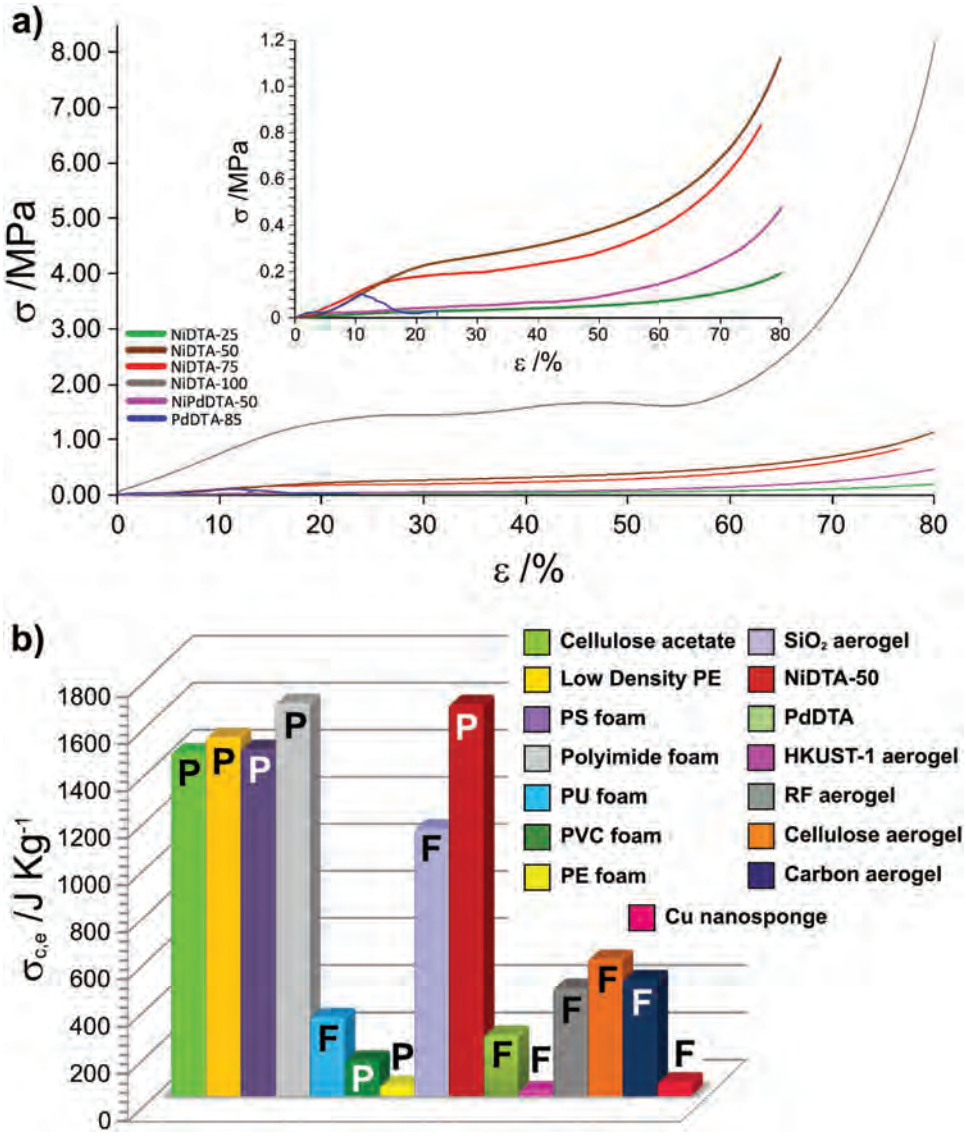

Figure 5. a) Experimental compression–strain curves of Pd/Ni system MOAs. b) Comparison of NiDTA-50 and PdDTA specific compressive strengths with others aerogels, polymeric materials, and foams found in the literature. F: fracturable material; P: plastic material; PE: polyethylene; PS: polystyrene; PU: polyurethane; PVC: polyvinyl chloride; RF: resorcinol–formaldehyde. Crushing compressive strength had been used for brittle materials, while for plastic ones, compressive strength has been defined at 10% of deformation.

Supporting Information). These measurements showed in both cases that the conductivity increases with the temperature and decreases on cooling, in agreement with semiconducting behavior (see Section S6 in the Supporting Information).

Doping experiments with I_2 vapor were also carried out on the most conductive CuDTA and NiCuDTA samples (before doping: 3.0×10^{-7} and 2.8×10^{-8} S cm^{-1}, respectively). The conductivity values of the doped samples increase by two and three orders of magnitude (Table 4). I_2 is usually employed as a mild oxidizing agent to seize electrons from the valence band of the semiconducting materials, in order to enhance their conductivity.[68] In the current case, it can be assumed that the conductivity enhancement takes place through a similar mechanism involving an electronic charge transfer from the ligand to the oxidant.

The stimuli-response electrical conductivity of CuDTA and NiCuDTA MOAs was studied at room temperature by subjecting the samples to the chemical stimuli of acetic acid (AcOH) vapor. Conductivity values were determined from the Nyquist plot by arc extrapolation to the *Z*′-axis. The obtained impedance measurements were analyzed by means of the equivalent circuit method, which simulates the behavior of metal-organic materials in an electronic circuit. The Nyquist plot for compound CuDTA after 8 h of exposure to AcOH vapor in the frequency range of 1 Hz to 1 MHz (**Figure 7**a) shows the presence of a depressed semicircular arc at high frequencies (1 kHz to 1 MHz), which is attributed to the bulk properties of the compound. In the low-frequency region, another arc/line is observed which is typical of materials with capacitive behavior between the mobile ions (that

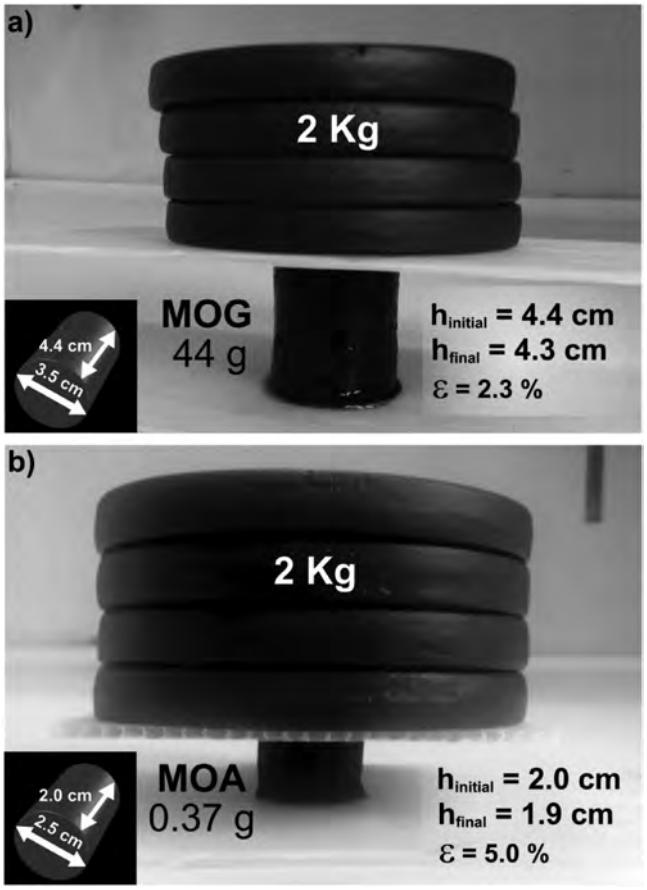

Figure 6. a) MOG (44 g) and b) MOA (0.37 g) monoliths holding up 2 kg of dumbbell weights.

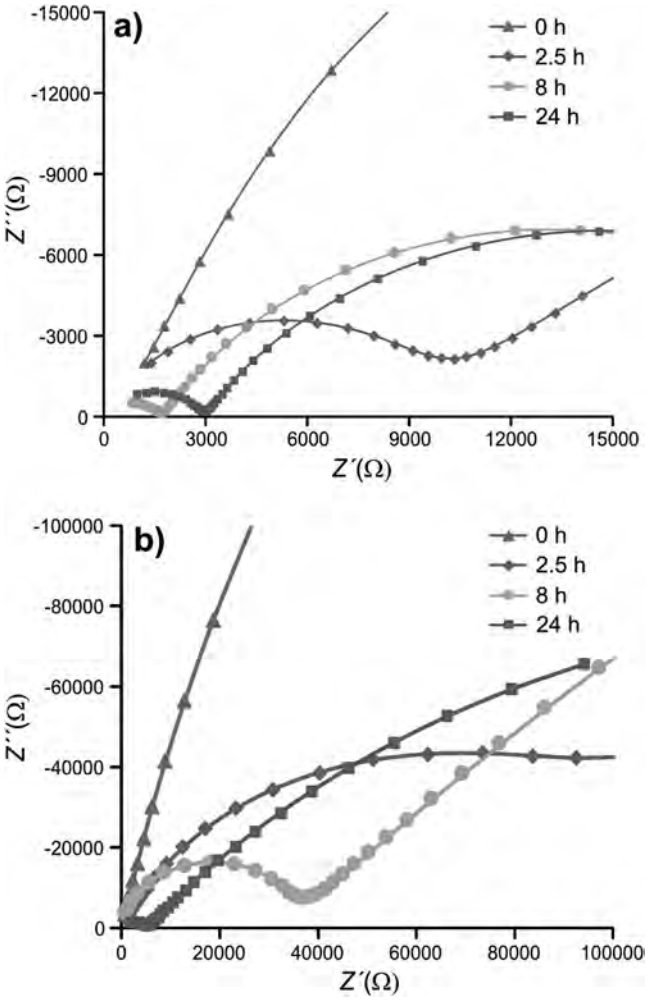

Figure 7. Nyquist plots at 298 K of a) CuDTA and b) NiCuDTA at representative exposure times (0, 2.5, 8, and 24 h) to AcOH vapor (experimental values (■), fitting values (–)).

are blocked by the electrode–electrolyte interphase). The Nyquist plots recorded for CuDTA after different exposure times (0, 1, 2.5, 24, and 48 h) are similar to those obtained at 8 h of exposure; however, the intercept of the semicircle with the *Z*′-axis shifts toward higher values. Nyquist plots for NiCuDTA sample shows a comparable behavior, however, the intercept of the semicircle with the Z′-axis shifts toward a low value with increased exposure time (Figure 7b). At low exposure times, the conductivity increases sharply for both samples (Figure S6.4, Supporting Information), reaching values almost 2 orders of magnitude higher than the t = 0 h. Thereafter, in the case of CuDTA sample, the electrical conductivity reaches a plateau ($\approx 10^{-5}$ S cm^{-1}) at 8 h, while the NiCuDTA sample, after the initial acute step, exhibits a monotonic enhancement of conductivity up to 3.8×10^{-5} S cm^{-1} after 48 h of exposure.

Table 4. Conductivity values obtained for MOA samples at 298 K, using two contact method and pressed pellets.

Sample	Conductivity [S cm^{-1}] at 298 K	
	As-prepared samples	I_2-doped samples
NiDTA	4.4×10^{-10}	–
PdDTA	7.1×10^{-10}	–
CuDTA	3.0×10^{-7}	1.0×10^{-5}
NiCuDTA	2.8×10^{-8}	2.4×10^{-5}
NiPdDTA	3.4×10^{-12}	–
PdCuDTA	1.4×10^{-11}	–

The remarkable change in the specific conductivity of CuDTA and NiCuDTA, could be related to the establishment of a favorable pathway for proton transportation provided by the interaction between guest AcOH molecules and probably the grain boundary of the hosting fibrillar porous network. When saturated acetic acid pellets were exposed to ambient conditions, the Nyquist plot and the conductivity ($\approx 10^{-7}$ S cm^{-1}) retrieve the shape and the values of the corresponding pristine material, ratifying the reversibility of the AcOH capture/release process. Cycling data experiments have been performed on CuDTA at 4 h intervals and NiCuDTA at 12 h intervals (**Figure 8**). NiCuDTA was subjected to longer cycling time to obtain comparable conductivity change to that of CuDTA. The cycling provides reproducible changes in conductivity upon exposure to acetic acid, which endows these materials of sensing capability.

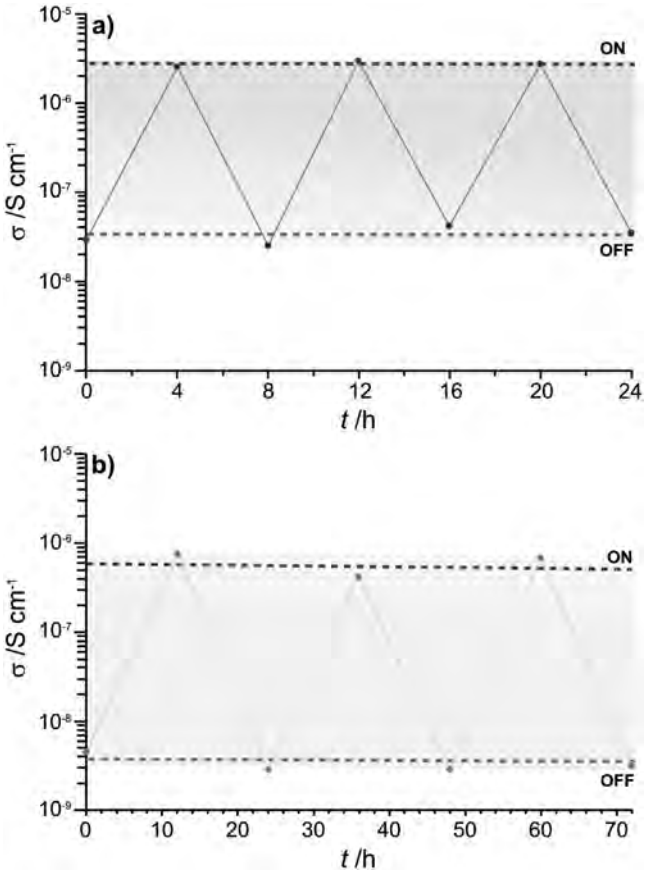

Figure 8. Cycling data at 18 °C of a) CuDTA at 4 h intervals and b) NiCuDTA at 12 h intervals.

3. Conclusion

The 1D nature of the $[M(DTA)]_n$ coordination system is the key to promote the fibrillar growth of the particles, but only under well-selected synthesis conditions the gelation succeeded, being remarkable the role that the metal salt and solvent play. Supercritical drying of the gels renders ultralight MOAs (ρ: 0.03–0.06 g cm^{-3}; porosity: 98%–99% for NiDTA and CuDTA) that preserve the intertwined nanofibrillar structure (diameter: 8–20 nm). Microstructural parameters, such as the aspect ratio of the nanofibers and their spatial concentration, govern the surface area, pore diameter, and mechanical properties. Accordingly, the highest surface area and pore diameter values correspond to MOAs presenting highest aspect ratios (NiDTA, NiCuDTA). Despite the surface area of MDTA, MOAs is far away from most outstanding MOFs; it is comparable to many MOFs and zeolites with moderate surface area values[69] and to organic and inorganic aerogels.[70] On the contrary, pore size can be considered as relatively high (7–23 nm), in fact, almost all mean, median, and mode pore diameters far exceed the maximum value reported for MOFs up to date (<10 nm). Moreover, it should be stressed that the maximum pore volume values obtained for MDTA MOAs (4.25 cm^3 g^{-1}) are comparable to the record values reported for MOFs (up to 4.40 cm^3 g^{-1}). Regarding the mechanical properties, Pd(II) MOAs, with the lowest aspect ratio fibers, exhibit a brittle behavior, and Ni(II) MOAs, containing highest aspect ratio fibers, behave as a plastic material. Such plastic behavior has not been previously reported for a material based on a coordination polymer and it allows processing them as films by simply applying pressure. Room-temperature conductivity measurements yielded values ranging from 10^{-7} to 10^{-12} S cm^{-1} that, combined with its fibrillar porous network, results in a stimuli-response material that shows reversible conductivity increase (up to 10^{-5} S cm^{-1}) when subjected to acetic acid vapors. Considering all the above, to the best of our knowledge the reported material implies an unprecedented case within the area of coordination polymers (including MOFs), since it successfully brings together porosity with outstanding chemical inertness, mechanical robustness, and stimuli-responsive electrical conductivity.

4. Experimental Section

Physical Measurements: Details are provided in Section S8 of the Supporting Information.

Chemicals: All the chemicals were of reagent grade and were used as commercially obtained.

Synthesis of MOGs: In a general procedure, the corresponding metal acetate was dissolved in a mixture of DMA and DMF of 60:40 volumetric ratio, aided by an ultrasonic tip (Vibra-Cell VCX130 20 kHz and 130 W, Sonics) working at 80% of its power for 2 min. Then, an equimolar amount of dithiooxamide (H_2DTA) ligand basified with triethylamine and dissolved in the same DMF/DMA solvent mixture was added all at once on the aforementioned metal salt solution (or in some cases, dispersion) while it was maintained in an ultrasound bath (ULTRASONS-H, Selecta) at a temperature of 288 K until a change of viscosity took place (depending on the metal and the concentration, the process lasts from few seconds to several minutes). Once the metallogel had reached certain consistency, it was allowed to age at room temperature for one day. Thereafter, successive solvent exchanges were performed to replace the synthesis solvent by ethanol. Optimum metal salts and dithiooxamide concentrations used on the synthesis for obtaining metallogels were set at 85×10^{-3} M for PdDTA, 25×10^{-3} M for CuDTA, 75×10^{-3} M for NiDTA, and 50×10^{-3} M for heteronuclear NiPdDTA, NiCuDTA, and PdCuDTA. For comparative purposes, NiDTA samples were also prepared at 25×10^{-3}, 50×10^{-3}, and 100×10^{-3} M. Stiffest gels were obtained for NiDTA, PdDTA, and NiPdDTA, which well-retained the shape of the molds and/or were easily processed by cutting into regular geometries. All the MOGs were found to be stable for several months at room temperature. The absolute amounts can be scaled to fit shape and volume of the mold or flask, specifically; herein, samples with volumes ranging from 5 to 200 mL were prepared.

Synthesis of MOXs and MOAs: Metal-organic xerogels were prepared subjecting the metallogels to open-atmosphere drying. To prepare the metal-organic aerogels, an E3100 critical point dryer from Quorum Technologies equipped with gas inlet, vent, and purge valves, and with a thermal bath was employed. First, the metallogel was immersed in liquid CO_2 at 293 K and 50 bar for one hour. Then, the exchanged ethanol was removed through the purge valve. This process was repeated five times. Subsequently, the sample was dried under supercritical conditions, increasing the temperature and pressure to 313 K and 85–95 bar. Finally, under constant temperature (313 K), the chamber was slowly vented up to atmospheric pressure.

We have also tested the freeze-drying of gels. However, the results are quite discouraging (see Section S7 of the Supporting Information). The monoliths retain their shape and the shrinkage is comparable to that of supercritical drying, but the growth of the water crystals during the cooling with N_2(l) promotes the fusing of the nanofibers into a lamellar structure. As a result, the solid is mainly macroporous with an almost negligible surface area (10 m^2 g^{-1}) and extremely brittle.

Supporting Information

Supporting Information is available from the Wiley Online Library or from the author.

Acknowledgements

This work was funded by Eusko Jaurlaritza/Gobierno Vasco (Grant No. IT477-10), Universidad del País Vasco/Euskal Herriko Unibertsitatea (Grant No. UFI 11/53), and Ministerio de Economía y Competitividad (Grant Nos. MAT2013-46502-C2-1-P and MAT2016-75883-C2-1-P). Technical and human support provided by SGIker (UPV/EHU, MICINN, GV/EJ, ESF) and by Mrs. Sandra König and Mrs. Uta Sazama (University of Hamburg) is also acknowledged.

Received: October 18, 2016
Revised: January 13, 2017
Published online: March 10, 2017

[1] J. L. C. Rowsell, O. M. Yaghi, *Microporous Mesoporous Mater.* **2004**, *73*, 3.
[2] S. T. Meek, J. A. Greathouse, M. D. Allendorf, *Adv. Mater.* **2011**, *23*, 249.
[3] O. M. Farha, I. Eryazici, N. C. Jeong, B. G. Hauser, C. E. Wilmer, A. A. Sarjeant, R. Q. Snurr, S. T. Nguyen, A. Ö. Yazaydin, J. T. Hupp, *J. Am. Chem. Soc.* **2012**, *134*, 15016.
[4] A. K. Cheetham, G. Férey, T. Loiseau, *Angew. Chem., Int. Ed.* **1999**, *38*, 3268.
[5] A. P. Côté, A. I. Benin, N. W. Ockwig, M. O'Keeffe, A. J. Matzger, O. M. Yaghi, *Science* **2005**, *310*, 1166.
[6] X. Feng, X. Dinga, D. Jiang, *Chem. Soc. Rev.* **2012**, *41*, 6010.
[7] J. Lee, J. Kim, T. Hyeon, *Adv. Mater.* **2006**, *18*, 2073.
[8] L. Sun, M. G. Campbell, M. Dincă, *Angew. Chem., Int. Ed.* **2016**, *55*, 3566.
[9] A. Corma, H. García, I. Llabrés, F. X. Xamena, *Chem. Rev.* **2010**, *110*, 4606.
[10] M. D. Allendorf, C. A. Bauer, R. K. Bhaktaa, R. J. T. Houka, *Chem. Soc. Rev.* **2009**, *38*, 1330.
[11] R. J. Kuppler, D. J. Timmons, Q.-R. Fang, J.-R. Li, T. A. Makal, M. D. Young, D. Yuan, D. Zhao, W. Zhuang, H.-C. Zhou, *Coord. Chem. Rev.* **2009**, *253*, 3042.
[12] A. U. Czaja, N. Trukhanb, U. Müeller, *Chem. Soc. Rev.* **2009**, *38*, 1284.
[13] P. Silva, S. M. F. Vilela, J. P. C. Tomé, F. A. A. Paz, *Chem. Soc. Rev.* **2015**, *44*, 6774.
[14] Y. Chen, X. Huang, S. Zhang, S. Li, S. Cao, X. Pei, J. Zhou, X. Feng, B. Wang, *J. Am. Chem. Soc.* **2016**, *138*, 10810.
[15] H. Zhu, X. Yang, E. D. Cranston, S. Zhu, *Adv. Mater.* **2016**, *28*, 7652.
[16] C. Liu, J. Zhang, L. Zheng, J. Zhang, X. Sang, X. Kang, B. Zhang, T. Luo, X. Tan, B. Han, *Angew. Chem., Int. Ed.* **2016**, *55*, 11372.
[17] D. Bazer-Bachi, L. Assié, V. Lecocq, B. Harbuzarua, V. Falk, *Powder Technol.* **2014**, *255*, 52.
[18] F. Akhtar, L. Andersson, S. Ogunwumi, N. Hedin, L. Bergström, *J. Eur. Ceram. Soc.* **2014**, *34*, 1643.
[19] J. Zhang, C.-Y. Su, *Coord. Chem. Rev.* **2013**, *257*, 1373.
[20] A. Y.-Y. Tam, V. W.-W. Yam, *Chem. Soc. Rev.* **2013**, *42*, 1540.
[21] L. Li, S. Xiang, S. Cao, J. Zhang, G. Ouyang, L. Chen, C.-Y. Su, *Nat. Commun.* **2013**, *4*, 1.
[22] M. R. Lohe, M. Rose, S. Kaskel, *Chem. Commun.* **2009**, 6056.
[23] S.-C. Wei, M. Pan, K. Li, S. Wang, J. Zhang, C.-Y. Su, *Adv. Mater.* **2014**, *26*, 2072.
[24] S. Samai, K. Biradha, *Chem. Mater.* **2012**, *24*, 1165.
[25] J. H. Jung, J. H. Lee, J. R. Silverman, G. John, *Chem. Soc. Rev.* **2013**, *42*, 924.
[26] F. Chejne, D. Camargo-Trillos, E. Pabón, F. Carrasco-Marín, *Heat Mass Transfer* **2015**, *51*, 1141.
[27] J. C. Groen, W. Zhu, S. Brouwer, S. J. Huynink, F. Kapteijn, J. A. Moulijn, J. Pérez-Ramírez, *J. Am. Chem. Soc.* **2007**, *129*, 355.
[28] S. A. El-Safty, M. A. Shenashen, M. Khairy, *Colloids Surf., B* **2013**, *103*, 288.
[29] H.-L. Jiang, T. A. Makal, H.-C. Zhou, *Coord. Chem. Rev.* **2013**, *257*, 2232.
[30] M. O. M. Piepenbrock, G. O. Lloyd, N. Clarke, J. W. Steed, *Chem. Rev.* **2010**, *110*, 1960.
[31] F. Fages, *Angew. Chem.* **2006**, *118*, 1710.
[32] X. Huang, P. Sheng, Z. Tu, F. Zhang, J. Wang, H. Geng, Y. Zou, C. Di, Y. Yi, Y. Sun, W. Xu, D. Zhu, *Nat. Commun.* **2015**, *6*, 7408.
[33] L. Sun, M. G. Campbell, M. Dinca, *Angew. Chem., Int. Ed.* **2015**, *55*, 3566.
[34] W. L. Leong, J. J. Vittal, *Chem. Rev.* **2011**, *111*, 688.
[35] M. Ghaedi, F. Ahmadi, M. J. Soylak, *Hazard. Mater.* **2007**, *147*, 226.
[36] F. H. Allen, *Acta Crystallogr.* **2002**, *B58*, 380.
[37] J. Zou, J. Liu, A. S. Karakoti, A. Kumar, D. Joung, Q. Li, S. I. Khondaker, S. Seal, L. Zhai, *ACS Nano* **2010**, *4*, 7293.
[38] A. Salam, R. A. Venditti, J. J. Pawlak, K. El-Tahlawy, *Carbohydr. Polym.* **2011**, *84*, 1221.
[39] J. Yang, E. Zhang, X. Li, Y. Zhang, J. Qu, Z.-Z. Yu, *Carbon* **2016**, *98*, 50.
[40] J. Andersons, M. Kirpluks, L. Stiebra, U. Cabulis, *Mater. Des.* **2016**, *92*, 836.
[41] D. D. Luong, D. Pinisetty, N. Gupta, *Composites, Part B* **2013**, *44*, 403.
[42] K. L. Calvert, K. P. Trumble, T. J. Webster, L. A. Kirkpatrick, *J. Mater. Sci: Mater. Med.* **2010**, *21*, 1453.
[43] M. Thommes, K. Kaneko, A. V. Neimark, J. P. Olivier, F. Rodriguez-Reinoso, J. Rouquerol, K. S. W. Sing, *Pure Appl. Chem.* **2015**, *87*, 1051.
[44] T. Feldner, M. Häring, S. Saha, J. Esquena, R. Banerjee, D. D. Díaz, *Chem. Mater.* **2016**, *28*, 3210.
[45] H. Xing, H. Wang, X. Yan, X. Ji, *Dalton Trans.* **2015**, *44*, 11264.
[46] Q. Lin, B. Sun, Q.-P. Yang, Y.-P. Fu, X. Zhu, T.-B. Wei, Y.-M. Zhang, *Chem. – Eur. J.* **2014**, *20*, 11457.
[47] S. M. Cohen, *Chem. Rev.* **2012**, *112*, 970.
[48] G. Zhan, H. C. Zheng, *Adv. Funct. Mater.* **2016**, *26*, 3268.
[49] S. Wang, W. Morris, Y. Liu, C. M. McGuirk, Y. Zhou, J. T. Hupp, O. K. Farha, C. A. Mirkin, *Angew. Chem., Int. Ed.* **2015**, *54*, 14738.
[50] D. S. Cronin, S. Ouellet, *Polym. Test.* **2016**, *53*, 40.
[51] S. Ouellet, D. Cronin, M. Worswick, *Polym. Test.* **2006**, *25*, 731.
[52] K. E. Parmenter, F. Milstein, *J. Non-Cryst. Solids* **1998**, *223*, 179.
[53] Y. Zhu, X. Zhang, Z. Lan, H. Li, X. Zhang, Q. Li, *Mater. Des.* **2016**, *93*, 503.
[54] B. Zhang, J. Zhang, C. Liu, L. Peng, X. Sang, B. Han, X. Ma, T. Luo, X. Tan, G. Yang, *Sci. Rep.* **2016**, *6*, 21401.
[55] J. Zhong, J. Meng, X. Gui, T. Hu, N. Xie, X. Lu, Z. Yang, N. Koratkar, *Carbon* **2014**, *77*, 637.
[56] J. Liu, F. Cheng, H. Grénman, S. Spoljaric, J. Seppälä, J. E. Eriksson, S. Willför, C. Xu, *Carbohydr. Polym.* **2016**, *148*, 259.
[57] M. Schwan, M. Naikade, D. Raabe, L. Ratke, *J. Mater. Sci.* **2015**, *50*, 5482.
[58] S. O. Kucheyev, M. Stadermann, S. J. Shin, J. H. Satcher, S. A. Gammon, S. A. Letts, T. van Buuren, A. V. Hamza, *Adv. Mater.* **2012**, *24*, 776.
[59] S. M. Jung, D. J. Preston, H. Y. Jung, Z. Deng, E. V. Wang, J. Kong, *Adv. Mater.* **2016**, *28*, 1413.
[60] K. Tateyama, H. Yamada, N. Ogasawara, *Polym. Test.* **2016**, *52*, 54.

[61] S. Kurosawa, A. S. Teja, J. Kowalik, L. Tolbert, *Polymer* **2006**, *47*, 2997.
[62] H. Demir, M. Sipahioğlu, D. Balköse, S. Úlkü, *J. Mater. Process. Technol.* **2008**, *195*, 144.
[63] R. Gu, *J. Am. Oil Chem. Soc.* **2012**, *89*, 2103.
[64] A. Yoshimoto, H. Kobayashi, K. Horikawa, K. Tanigaki, *EPJ Web Conf.* **2015**, *94*, 01047.
[65] A. El-Shekeil, M. A. Khalid, H. Al-Maydama, A. Al-Karbooly, *Eur. Polym. J.* **2001**, *37*, 575.
[66] P. Nagels, R. Mertens, H. O. Desseyn, *Synth. Met.* **2002**, *128*, 1.
[67] M. Fujishima, R. Ikeda, T. Kawamura, H. Kitagawa, *Synth. Met.* **2003**, *411*, 135.
[68] G. Givaja, P. Amo-Ochoa, C. J. Gomez-Garcia, F. Zamora, *Chem. Soc. Rev.* **2012**, *41*, 115.
[69] B. Sels, L. Kustov, *Zeolites and Zeolites-like Materials* (Eds: B. Sels, L. Kustov), Elsevier B.V., Amsterdam **2016**.
[70] M. A. Aegerter, N. Leventis, M. M. Koebel, *Aerogels Handbook*, Springer, New York **2011**.

4.4. FIGURES OF THE ARTICLE IN HIGH QUALITY AND WITH COLOR

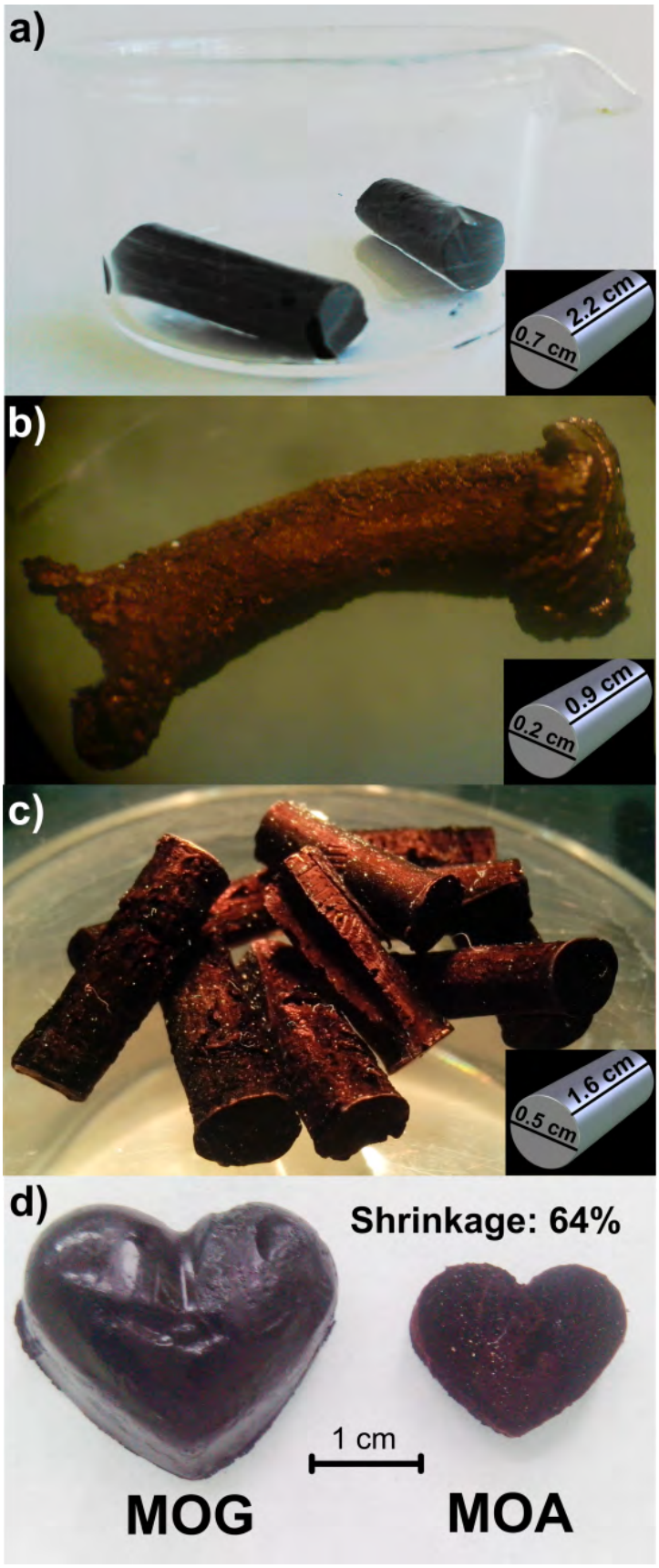

Figure 1. Cylinders made of NiDTA in different solid states: a) gel, b) xerogel and c) aerogel. d) The system allows creating complex geometries by molding.

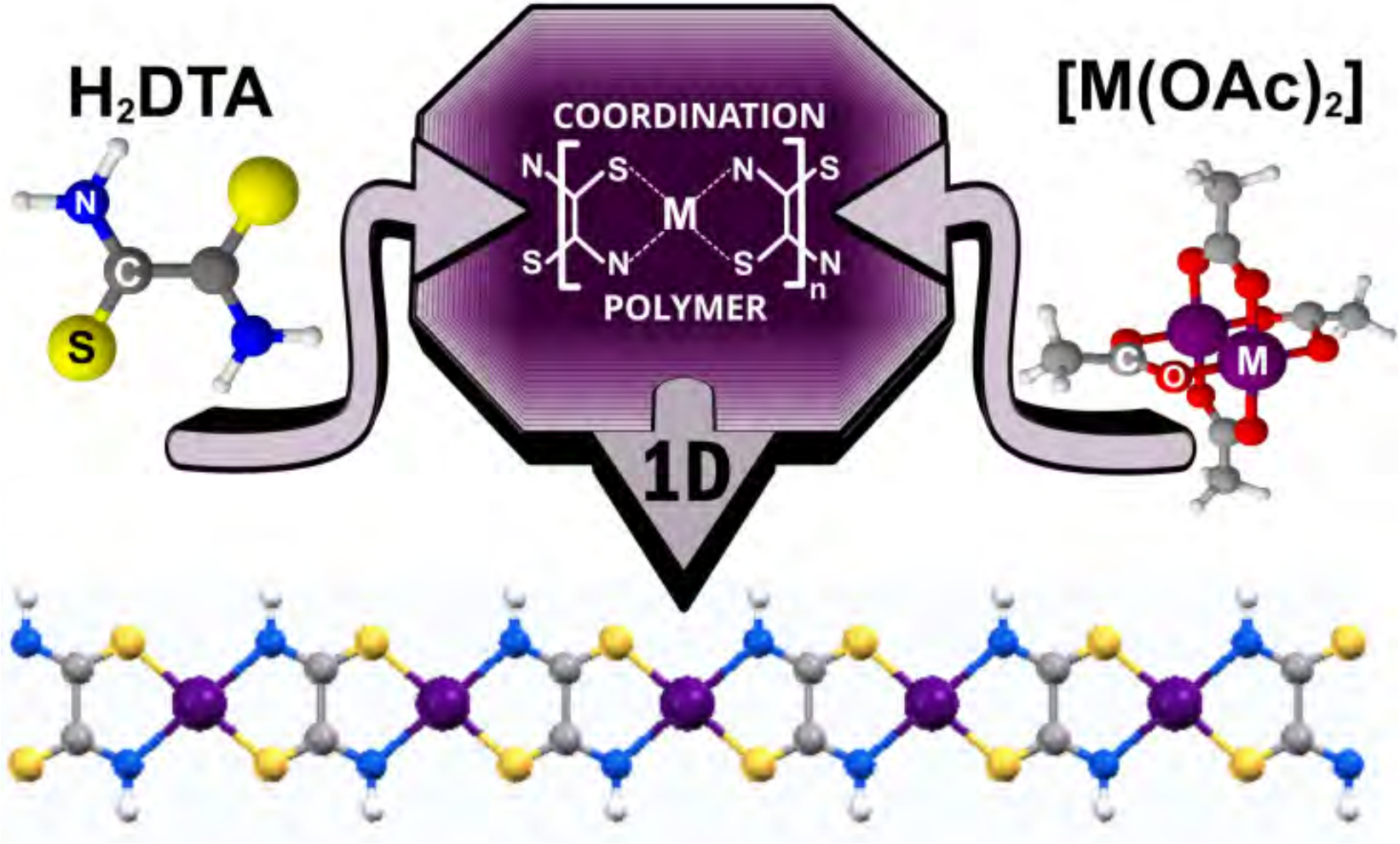

Scheme 1. Scheme of the polymerization process and a fragment of the MDTA polymer chain.

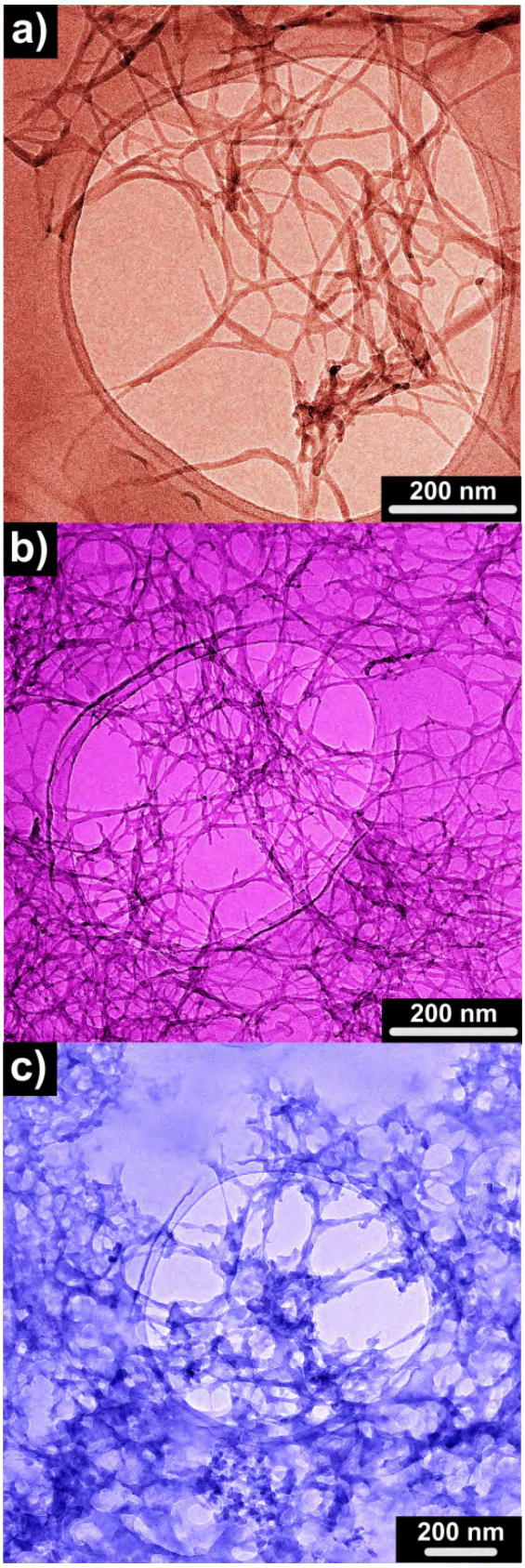

Figure 2. TEM micrographs of a) NiDTA, b) NiPdDTA and c) PdDTA MOGs dispersed in ethanol in the presence of *n*-decylamine.

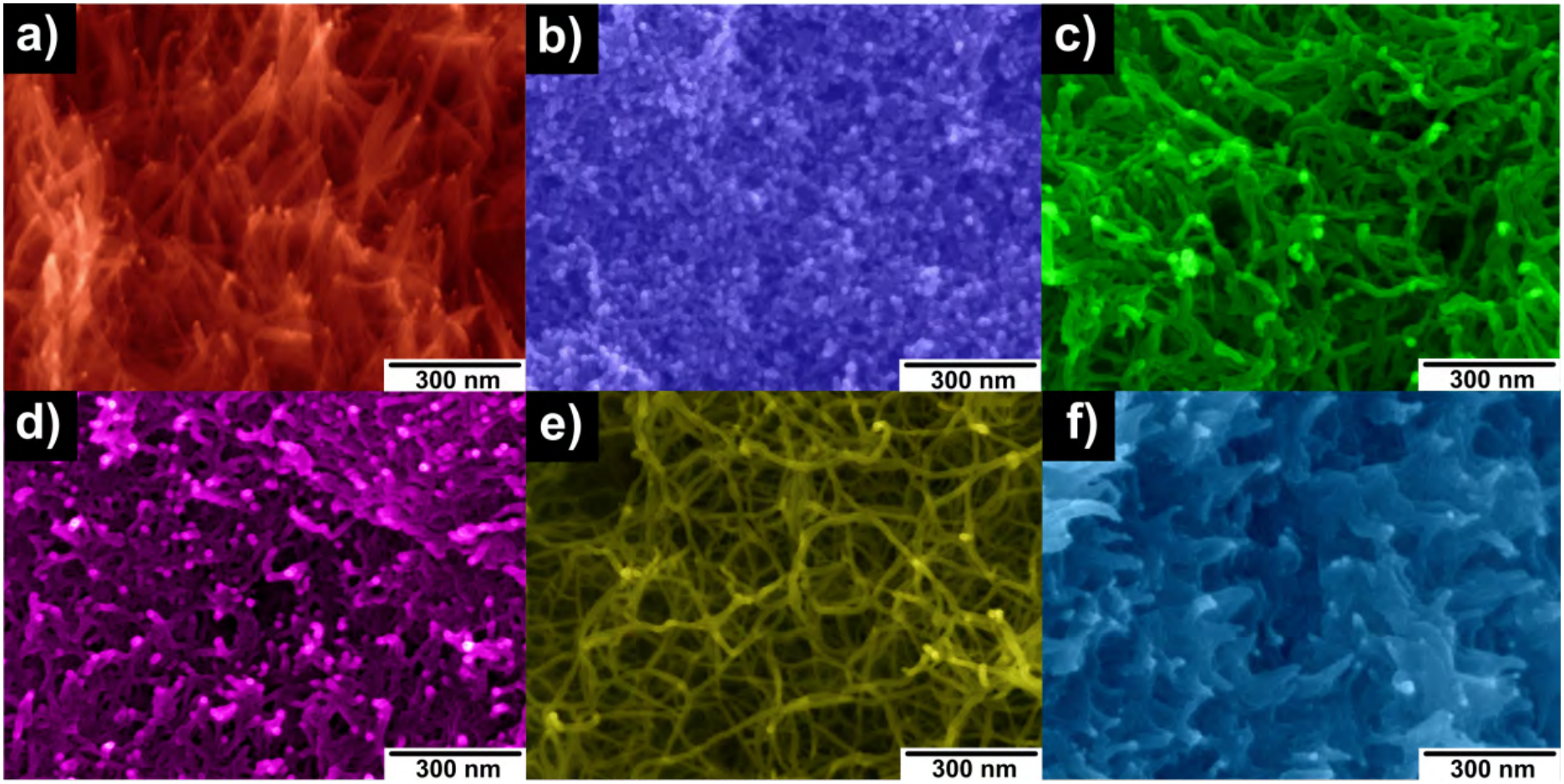

Figure 3. SEM images of MDTA MOAs with a magnification of 100 kX: a) NiDTA; b) PdDTA; c) CuDTA; d) NiPdDTA; e) NiCuDTA and f) PdCuDTA.

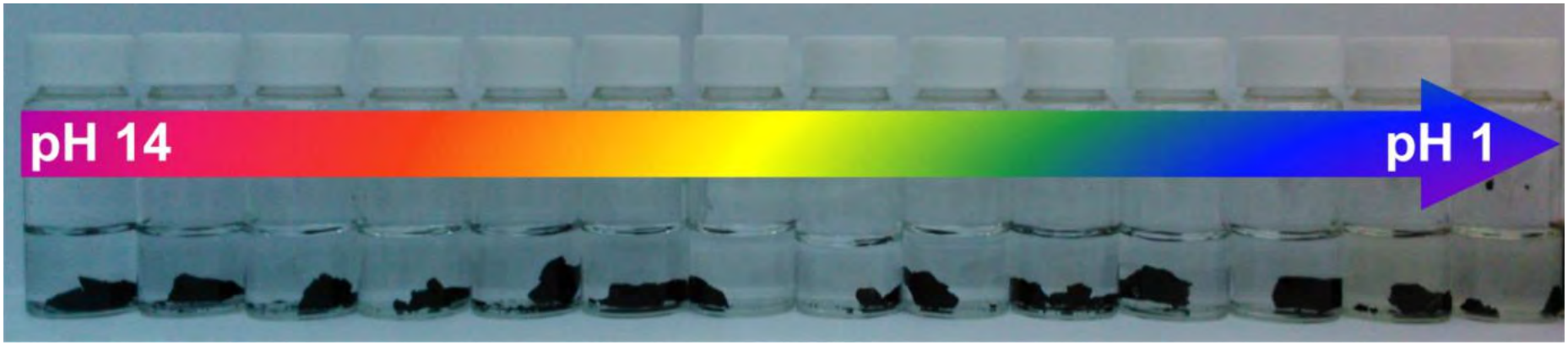

Figure 4. Gel fragments subjected to different pH solutions.

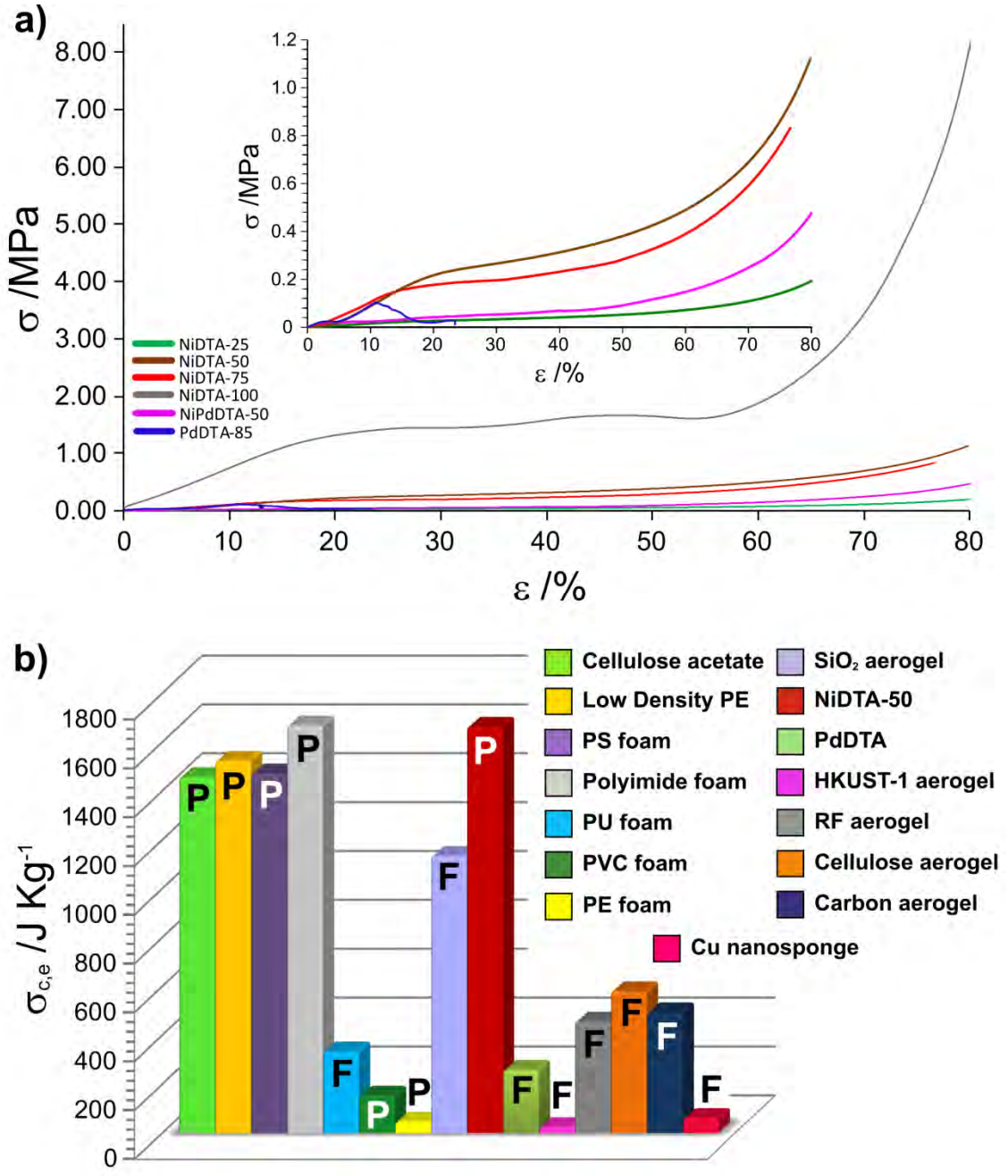

Figure 5. a) Experimental compression-strain curves of Pd/Ni system MOAs. b) Comparison of NiDTA-50 and PdDTA specific compressive strengths with others aerogels, polymeric materials and foams found in the literature. F: fracturable material, P: plastic material. PE: polyethylene, PS: polystyrene, PU: polyurethane, PVC: polyvinyl chloride, and RF: resorcinol-formaldehyde. Crushing compressive strength had been used for brittle materials, while for plastic ones, compressive strength has been defined at 10 % of deformation.

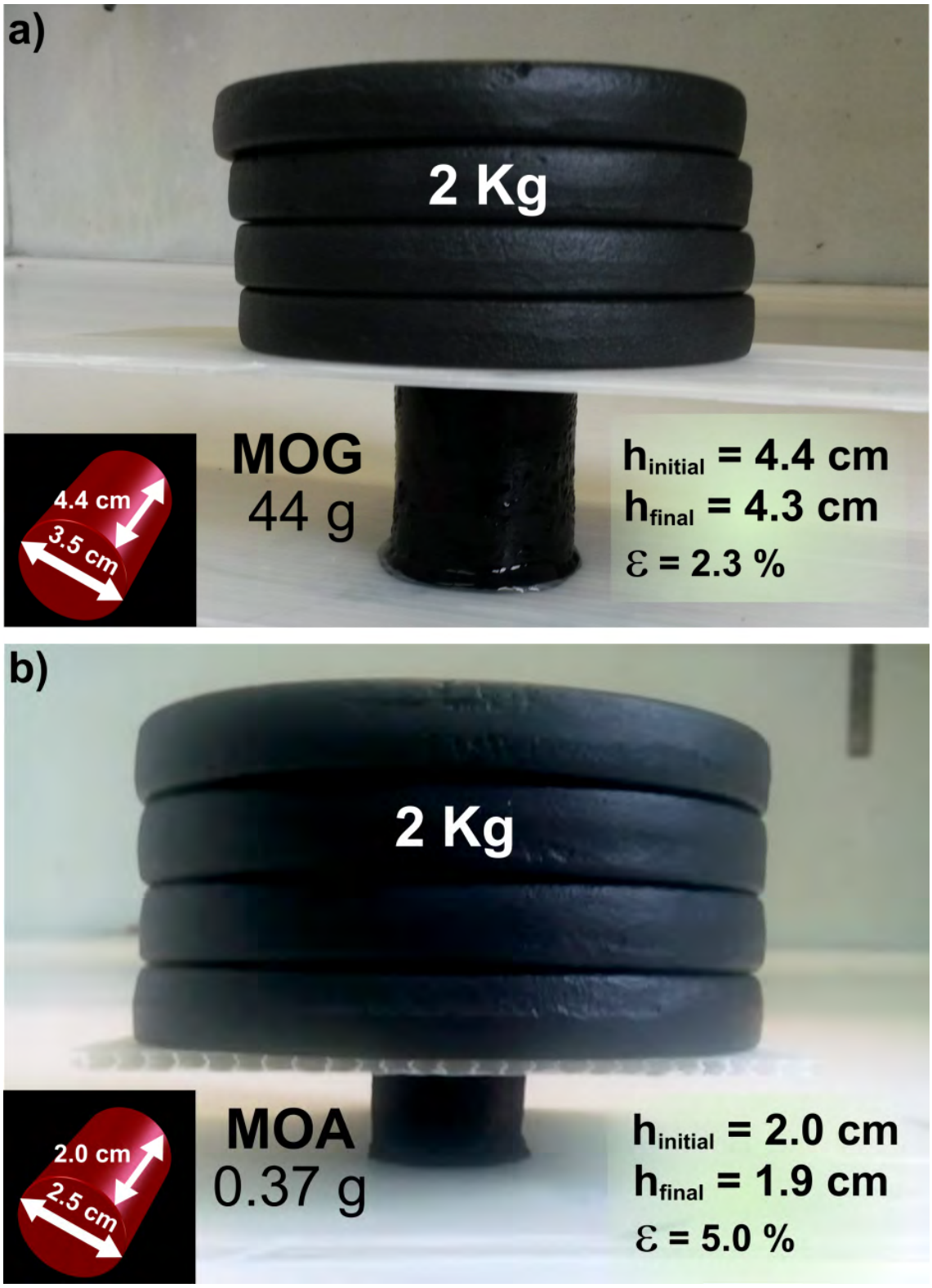

Figure 6. a) MOG (44 g) and b) MOA (0.37 g) monoliths holding up 2 kg of dumbbell weights.

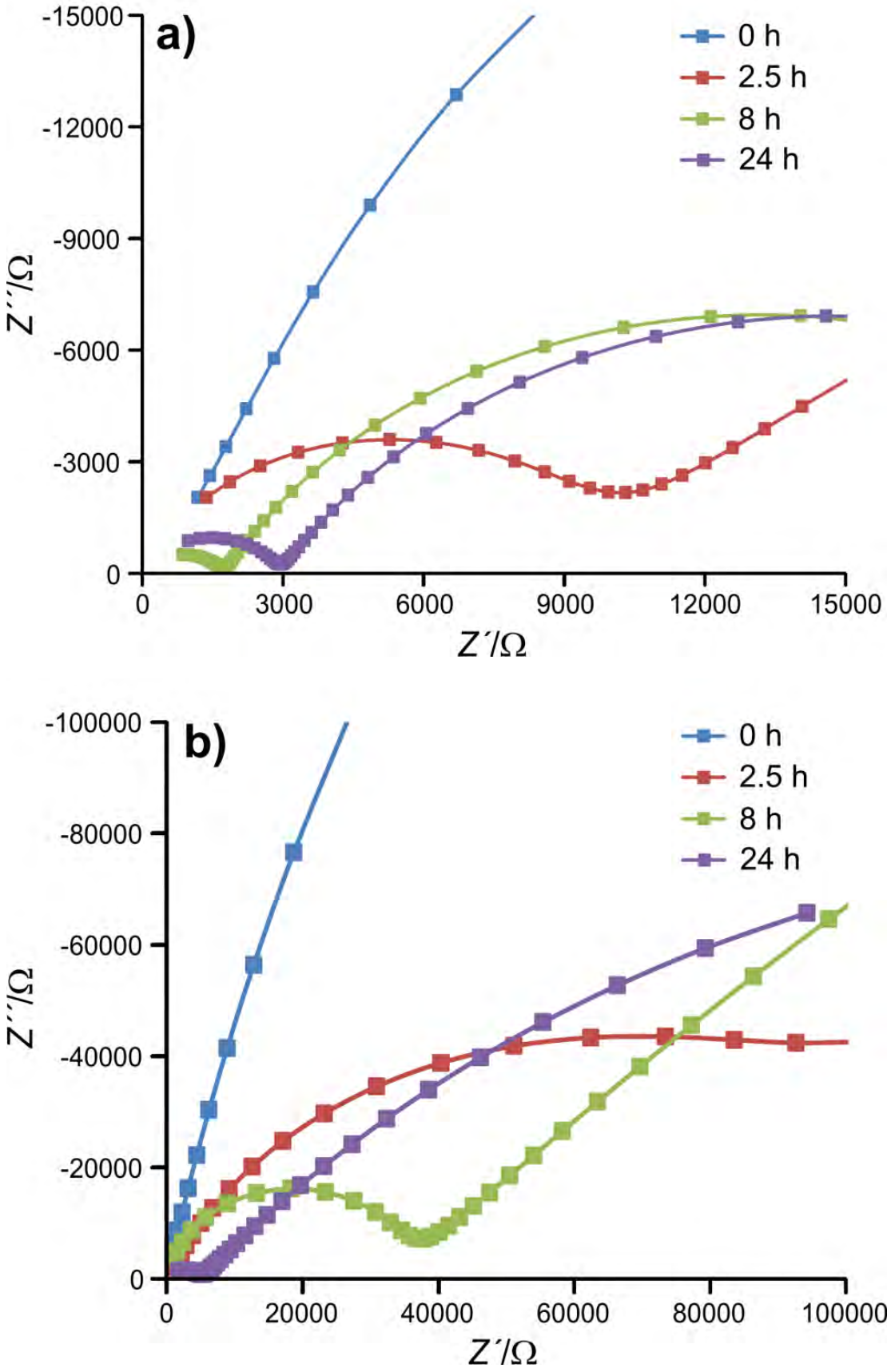

Figure 7. Nyquist plots at 298 K of a) CuDTA and b) NiCuDTA at representative exposure times (0, 2.5, 8 and 24 h) to AcOH vapor (experimental values (■), fitting values (−).).

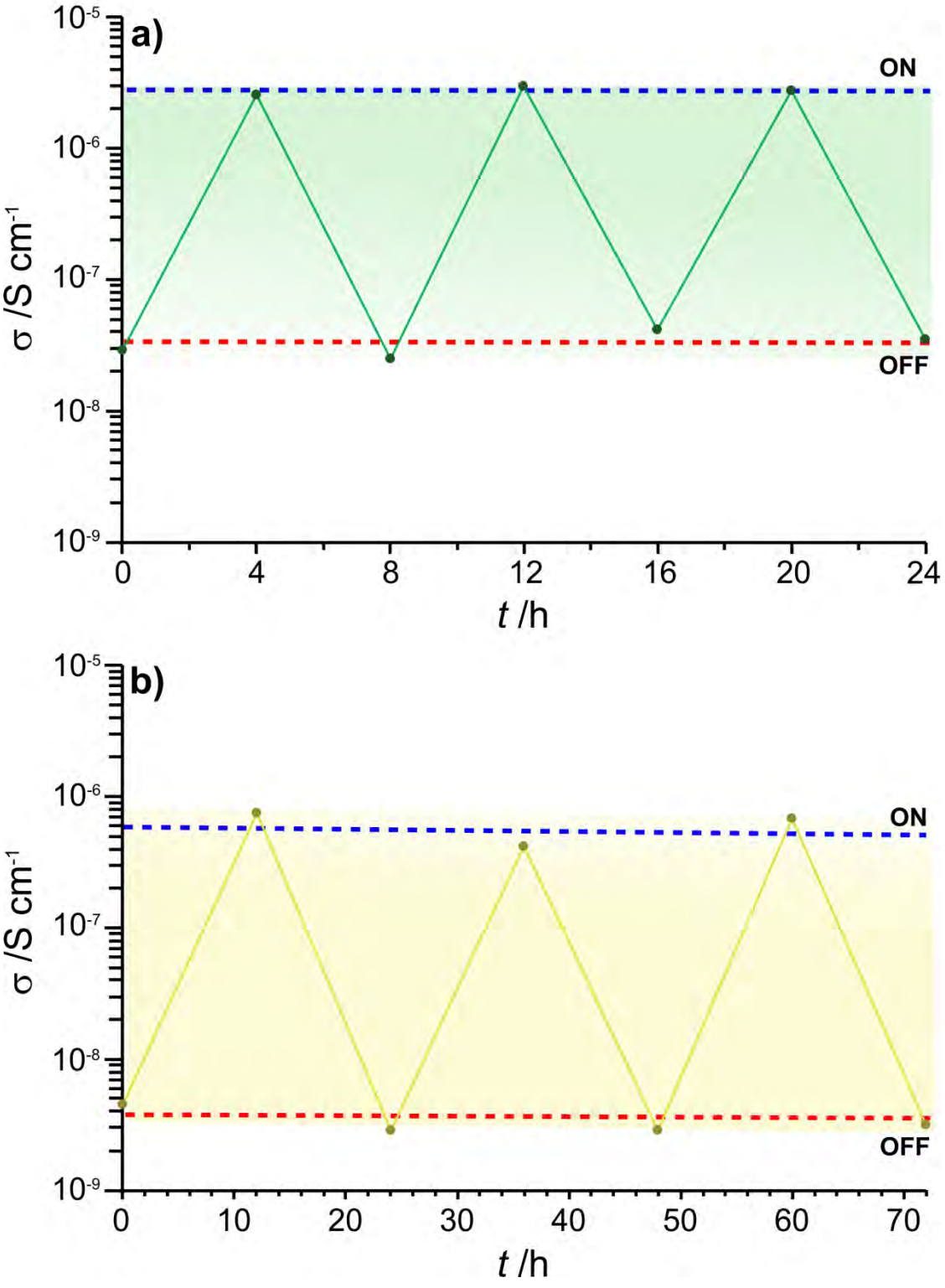

Figure 8. Cycling data at 18ºC of a) CuDTA at 4 h intervals and b) NiCuDTA at 12 h intervals.

4.5. SUPPORTING INFORMATION

Supplementary Information for

Chemically Resistant, Shapeable and Conducting Metal-Organic Gels and Aerogels Built from Dithiooxamidato Ligand

Daniel Vallejo-Sánchez,[†] Pilar Amo-Ochoa,[§] Garikoitz Beobide,[,†], Oscar Castillo,*[,†] Michael Fröba,[‖] Frank Hoffmann,[‖] Antonio Luque,[†] Pilar Ocón,[‡] and Sonia Pérez-Yáñez[†]*

[†]Departamento de Química Inorgánica, Facultad de Ciencia y Tecnología, Universidad del País Vasco, UPV/EHU, Apartado 644, 48080 Bilbao, Spain.

[§]Departamento de Química Inorgánica, Universidad Autónoma de Madrid, Madrid 28049, Spain.

[‡]Departamento de Química Física Aplicada, Universidad Autónoma de Madrid, Madrid 28049, Spain.

[‖]Institute of Inorganic and Applied Chemistry, University of Hamburg, Martin-Luther-King Platz 6, Hamburg 20146, Germany.

S1. GELATION STUDIES

The gelation was checked by the test-tube inversion method in which a material is considered a gel if it does not suffer deformity after inverting the vial where it is contained.

In first instance, 11 common solvents were checked by using the stoichiometric ligand-to-metal ratio of 1:1 and by adding triethylamine as basifying agent. Among all the solvents tested, only those with greater coordinative capacity (DMF: N,N'-dimethylformamide, DMA: N,N'-dimethylacetamide, DMSO: dimethylsulfoxide, DEA: N,N'-diethylacetamide) showed tendency to gel. However, such gels lacked the necessary mechanical consistency to be manipulated. After conducting a screening with different binary mixtures of these solvents, we were able to obtain optimum gels in a mixture of DMF/DMA in 40:60 ratio. Once chosen a suitable solvent mixture, the order of addition of the reactants was varied. Deprotonated ligand addition onto metal salt resulted in stiffer gel compared with the product formed following the opposite sequence, whereas the addition of base to a solution containing both ligand and metal salt produced a viscous granular solid. On the other hand, it was found that a ligand excess (> 4 ligand to metal ratio) precludes the gelation, probably due to the formation of soluble complexes of higher stoichiometry. Conversely, an increase of metal ratio results in an improvement in rigidity and a depletion at the rate of polymerization. Base promotes the creation of intermolecular crosslinks through the deprotonation of amino groups of the ligand since both its absence and the presence of acetic acid give rise to particulate precipitate or slimy samples, respectively. Likewise, gelation occurs even without adding the stoichiometric amount of base while an excess of triethylamine accelerates the process.

Furthermore, various nickel(II) salts were tested in order to study the influence of the counter-anion. Interestingly, this system also displayed a marked anion-specific

behavior, because no gelation was observed when other nickel(II) salts were employed instead of $Ni(OAc)_2$. The remaining salts ($Ni(OH)_2$, $NiBr_2$, $Ni(NO_3)_2$, and $Ni(ClO_4)_2$) precipitate or are soluble, suggesting that the chelating effect of acetate ion is key when it comes to slowing down polymerization. Apparently, a low dissociation constant prevents the number of nuclei to be high, giving the system enough time to create semi-organized branching. In addition, it was noted that the higher concentration of the system the greater the stiffness of the gels, as long as no threshold concentration was exceeded, which in the case of NiDTA was of 0.1 M. As for external physical factors are concerned, working at low temperatures improves the stiffness of gels and equally, the application of ultrasound during ligand addition helps to consolidate the final structure.

These results suggest that the control of nucleation kinetics is crucial for producing these gels. The polymerization must be sufficiently slow to promote a crosslinking of the nucleous in such a way that a semi-coherent three-dimensional lattice is formed and not a precipitate, but at the same time the crosslinkage needs to be speedy enough to retain inside solvent molecules and to prevent the coordination polymer from organizing itself, thus forming a polycrystalline powder.

Table S1.1. Gelation study results for NiDTA system. Ø: solution, P: precipitate, C: colloidal suspension, S: slurry, UC: unconsolidated gel, O: optimum gel. The rest of acronyms are DMF: *N,N*-dimethylformamide, DMSO: dimethylsulfoxide, DEA: *N,N*-diethylacetamide, DMA: *N,N*-dimethylacetamide, M: nickel(II) acetate, L: dithiooxamide and B: triethylamine.

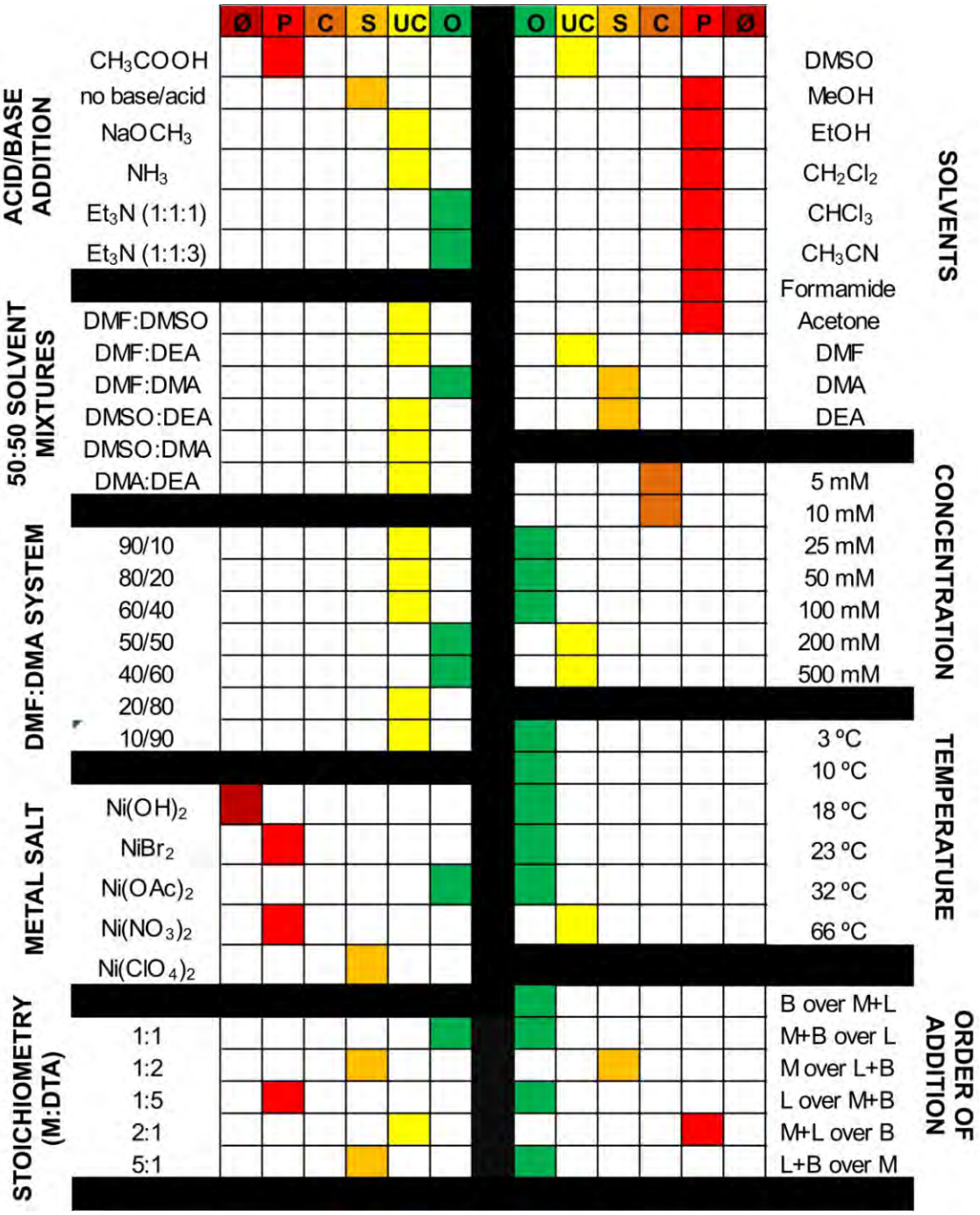

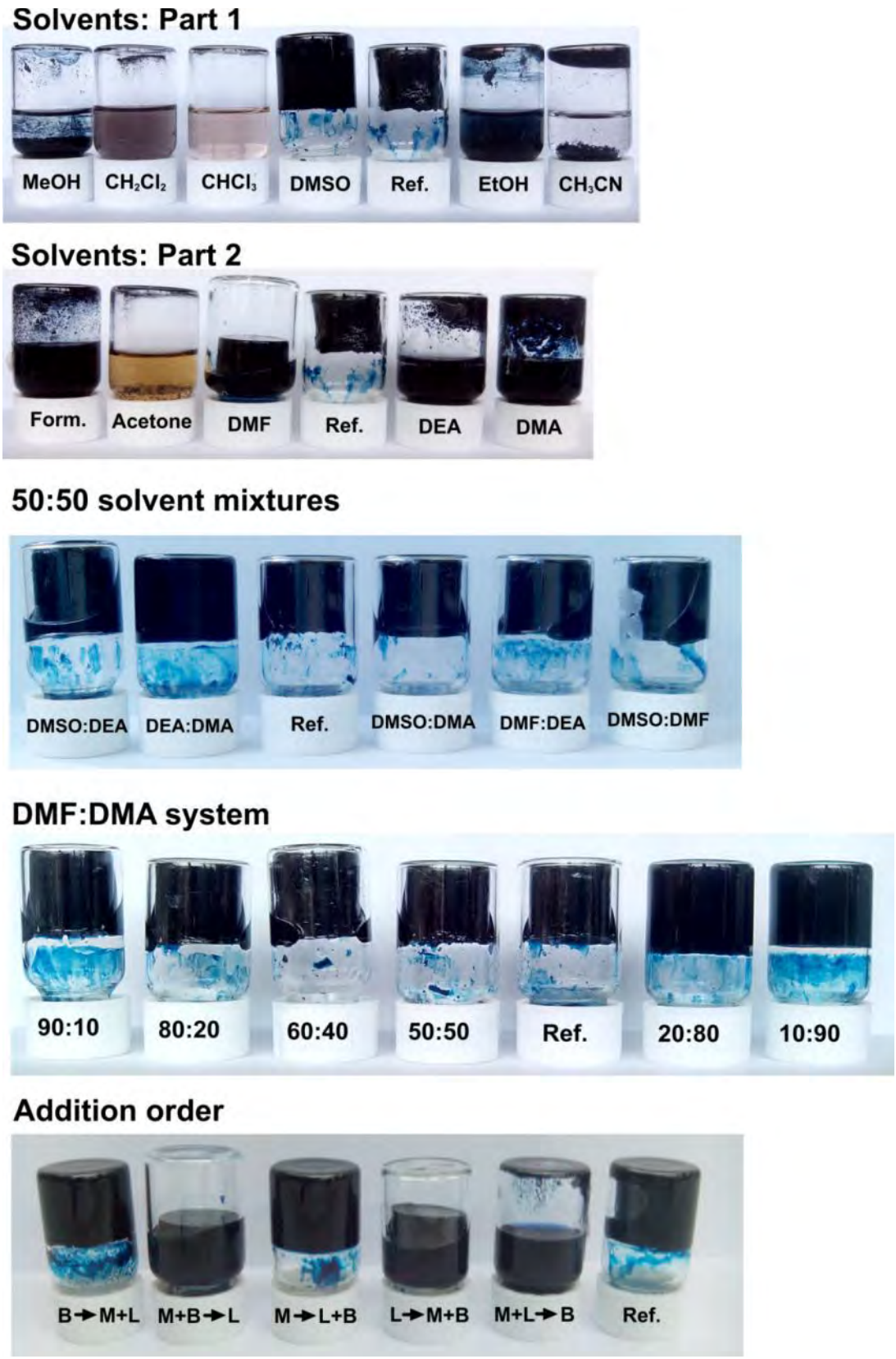

Figure S1.1. Photographs of the results obtained in gelation studies (part 1). It is considered as reference the synthetic procedure described in the experimental section for MOGs. Form: formamide, DMF: *N,N*-dimethylformamide, DMSO: dimethylsulfoxide, DEA: *N,N*-diethylacetamide, DMA: *N,N*-dimethylacetamide, M: nickel(II) acetate, L: dithiooxamide and B: triethylamine.

Figure S1.2. Photographs of the results obtained in gelation studies (part 2). It is considered as reference the synthetic procedure described in the experimental section for MOGs. M: nickel(II) acetate, H_2DTA: dithiooxamide, B: base and A: acid.

S2. STRUCTURAL ANALYSIS

Table S2.1. Vibrational and elemental analysis of MDTA compounds.

Compound	MW [g/mol]	Formula	Elemental analysis [%]	FT–IR [cm^{-1}]	Raman [cm^{-1}]
NiDTA	176.88	$C_2H_2N_2S_2Ni$	*Theo:* C, 13.64; H, 1.15; N, 15.92; S, 36.35; Ni, 32.9. *Found:* C, 13.58; H, 1.17; N, 15.80; S, 36.26; Ni, 33.18.	773(w), 856(s), 1047(vw), 1107(w), 1285(m), 1347(w), 1371(vw), 1497(vs), 1618(vw), 1652(vw), 2925(vw), 2972(vw), 3261(m), 3398(sh).	164(vw), 244(vw), 397(vw), 600(vw), 711(vw), 783(sh), 875(vw), 1107(m), 1359(sh), 1398(vs), 1521(vs), 1764(sh), 1811(vw), 1917(vw), 1994(vw), 2117(w), 2269(sh), 2400(sh), 2503(w), 2627(w), 2793(w), 2917(m), 3037(w), 3283(w).
PdDTA	224.60	$C_2H_2N_2S_2Pd$	*Theo:* C, 10.72; H, 0.90; N, 12.51; S, 28.56; Pd, 47.30. *Found:* C, 10.77; H, 1.04; N, 12.60; S, 28.69; Pd, 46.90.	757(w), 859(vw), 974(sh), 1046(sh), 1088(m), 1283(w), 1338(m), 1481(vs), 1610(vw), 2926(sh), 2977(vw), 3257(m), 3455(sh).	207(vw), 353(vw), 376(sh), 574(vw), 654(vw), 704(sh), 774(vw), 862(vw), 965(vw), 1107(m), 1352(m), 1372(vs), 2217(m), 2463(m), 2600(m), 2860(m), 2976(m).
CuDTA	181.73	$C_2H_2N_2S_2Cu$	*Theo:* C, 13.27; H, 1.11; N, 15.48; S, 35.35; Cu, 34.79. *Found:* C, 13.17; H, 1.19; N, 15.41; S, 35.26; Cu, 34.97.	780(w), 861(w), 960(vw), 1052(vw), 1128(vw), 1270(w), 1310(m), 1489(vs), 1610(vw), 3257(w).	296(sh), 316(vs), 354(vs), 565(vs), 624(m), 689(w), 719(sh), 789(w), 864(s), 953(vw), 1058(m), 1144(vw), 1225(vw), 1275(vw), 1316(m), 1351(w), 1374(sh), 1513(vs), 1662(vw), 1787(vw), 1873(vw).
NiPdDTA	200.74	$C_2H_2N_2S_2Ni_{0.5}Pd_{0.5}$	*Theo:* C, 12.00; H, 1.01; N, 14.01; S, 31.99; Ni, 14.49; Pd, 26.49. *Found:* C, 12.03; H, 1.06; N, 14.05; S, 32.08; Ni, 14.57; Pd 26.21.	683(sh), 765(w), 855(w), 1044(w), 1099(m), 1317(sh), 1338(s), 1477(vs), 1605(vw), 2894(sh), 2932(sh), 3264(m), 3420(sh).	193(vw), 275(vw), 343(vw), 386(vw), 594(vw), 642(vw), 683(sh), 702(sh),1097(sh), 1117(m), 1360(m), 1381(s), 1494(vs), 1713(vw), 1763(vw), 2003(sh), 2140(w), 2227(w), 2490(w), 2613(m), 2758(sh), 2872(s), 2986(s), 3260(m).
NiCuDTA	179.30	$C_2H_2N_2S_2Cu_{0.5}Ni_{0.5}$	*Theo:* C, 13.45; H, 1.13; N, 15.70; S, 35.84; Cu 17.64; Ni, 16.24. *Found:* C, 13.35; H, 1.06; N, 15.67; S, 35.75; Cu 17.56; Ni, 16.61.	778(w), 858(m), 973(sh), 1093(w), 1280(w), 1347(vw), 1371(vw), 1503(vs), 1600(vw), 1652(vw), 2913(sh), 2990(sh), 3250(m), 3453(sh).	
PdCuDTA	203.17	$C_2H_2N_2S_2Cu_{0.5}Pd_{0.5}$	*Theo:* C, 11.86; H, 0.99; N, 13.84; S, 31.60; Cu, 15.55; Pd 26.16. *Found:* C, 11.93; H, 1.07; N, 13.82; S, 31.67; Cu, 15.48; Pd 26.03.	681(sh), 783(w), 860(vw), 954(vw), 1066(w), 1281(sh), 1318(vs), 1362(w), 1483(vs), 1589(sh), 1621(sh), 1660(sh), 2974(vw), 3264(s), 3447(sh).	

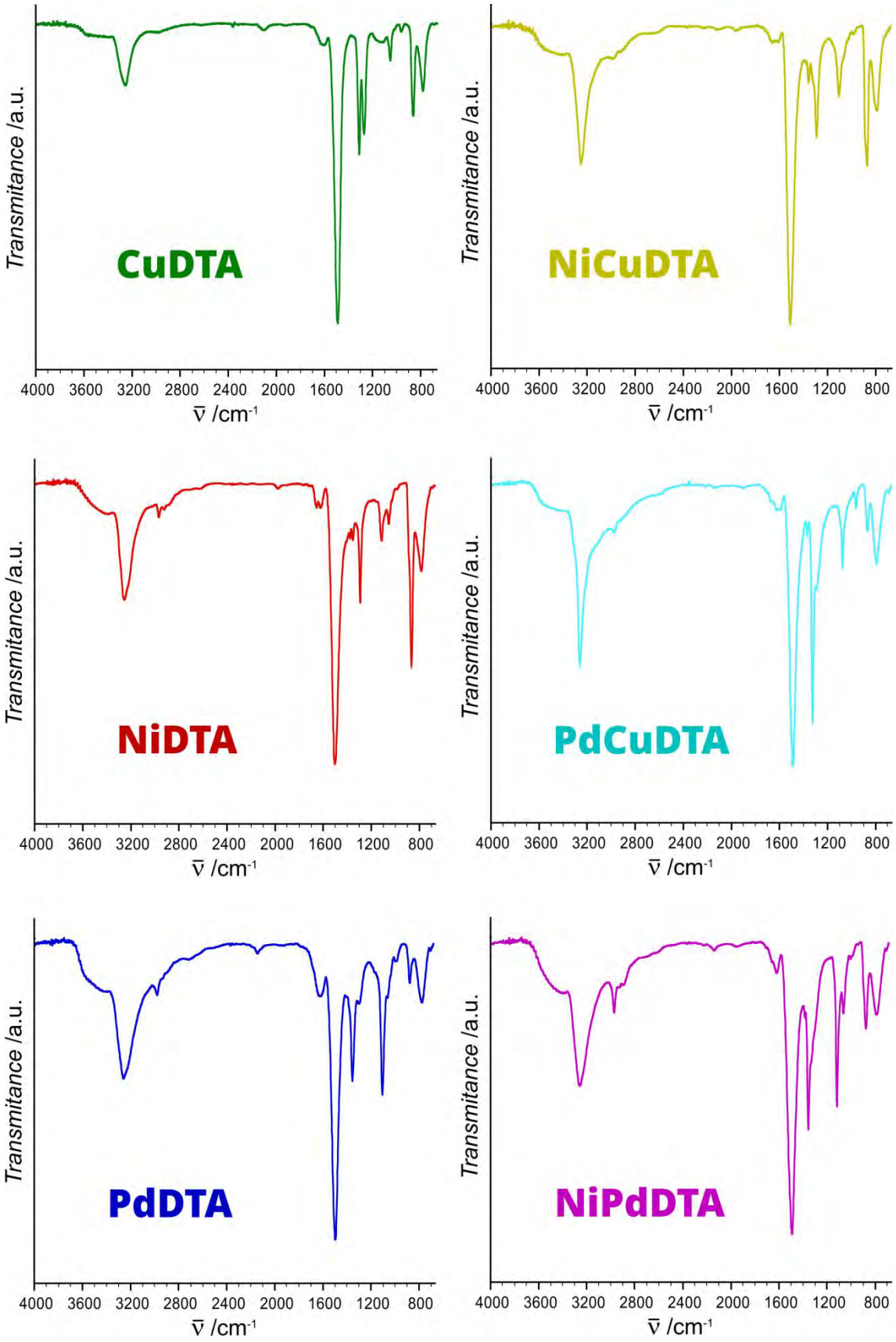

Figure S2.1. FTIR spectra of MOAs recorded on ATR mode**.**

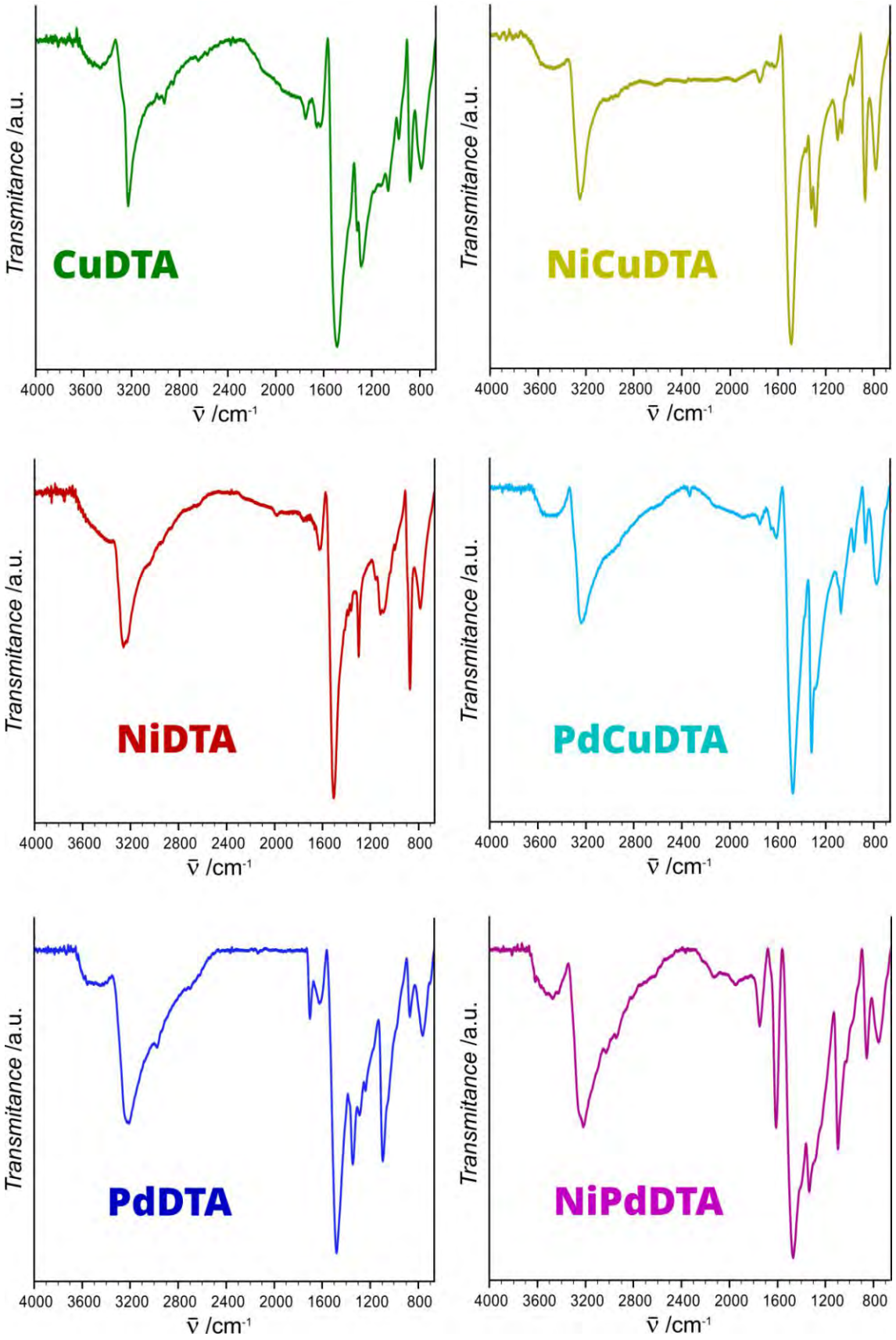

Figure S2.2. FTIR spectra of MOXs recorded on ATR mode**.**

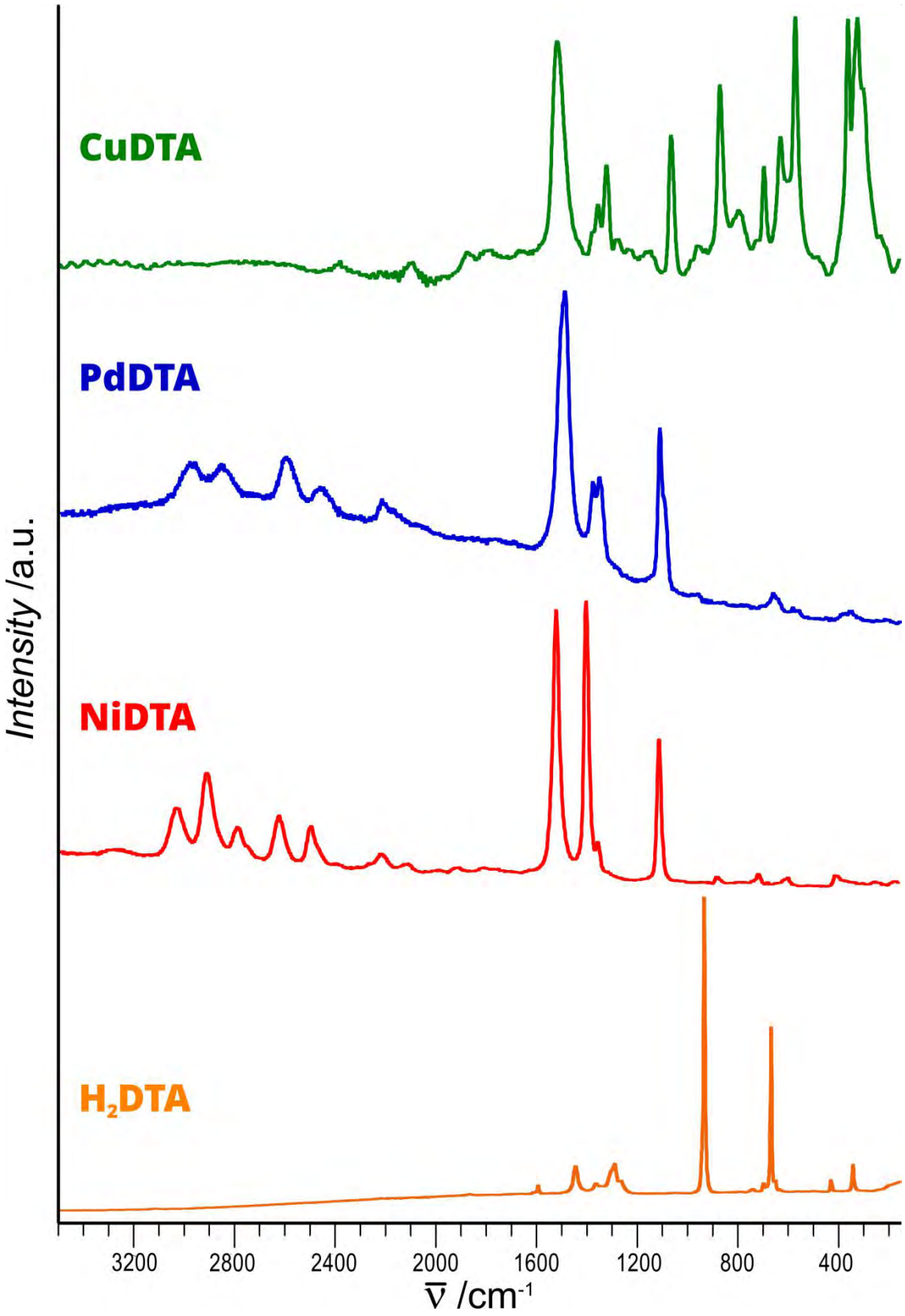

Figure S2.3. Raman spectra of homonuclear MOXs and H_2DTA.

Table S2.2. Experimental and simulated vibrational signals of NiDTA for *cis* and *trans* dispositions.

NiDTA		Simulation *trans*-DTA		Simulation *cis*-DTA		Mode	Character
IR [cm^{-1}]	Raman [cm^{-1}]	IR [cm^{-1}]	Raman [cm^{-1}]	IR [cm^{-1}]	Raman [cm^{-1}]		*trans /cis* [a)]
		3555		3357	3354	ν_{as} (N–H)	
			3347	3341	3342	ν_{s} (N–H)	
	1515		1520	1549	1548	ν_{s} (C–N)	A_g / A_1
1496		1502		1504	1503	ν_{as} (C–N)	B_u / B_2
	1393		1405	1381	1380	$\delta_{ip\text{-}s}$ (N–H)	
1284		1334		1346	1346	$\delta_{ip\text{-}as}$ (N–H)	
	1104		977		1000		
	872		927	883	882	$\delta_{op\text{-}s}$ (N–H)	
857		880		865	866	$\delta_{op\text{-}as}$ (N–H)	
773		753		814	815	ν_{as} (C–S)	A_g / A_1
	705		736	721	720	ν_{s} (C–S)	B_u / B_2

[a)] Characters were estimated for *trans* and *cis* dispositions in ideal C_{2h} and C_{2v} symmetries respectively. ν_s: symmetric tension mode, ν_{as}: asymmetric tension mode, δ_{ip}: in-plane bending mode, δ_{op}: out of plane bending mode.

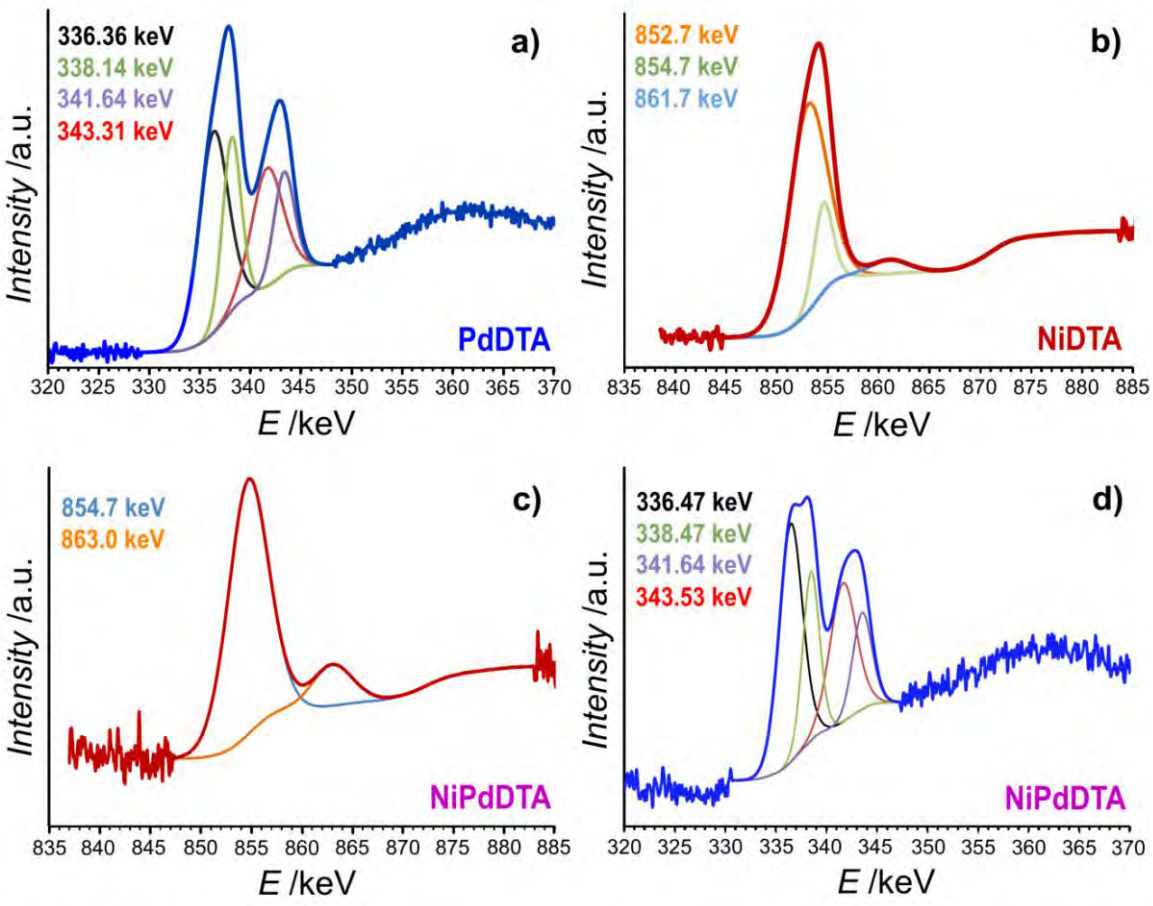

Figure S2.4. XPS spectra of MOXs based on Ni/Pd system.

Table S2.3. Summary of results obtained from XPS measurements for Ni/Pd system:

Sample	C	N	S	Ni	Pd	M:S	C:N	N:S	M_1:M_2
NiDTA-A	38.37[a)] 21.29[b)]	19.57[a)] 12.67[b)]	21.60[a)] 32.04[b)]	9.55[a)] 25.92[b)]	–	0.44	1.96	0.91	–
NiDTA-X	34.73[a)] 18.07[b)]	23.99[a)] 14.56[b)]	24.60[a)] 33.87[b)]	11.75[a)] 29.91[b)]	–	0.48	1.45	0.99	–
NiPdDTA-X	48.51[a)] 25.40[b)]	16.29[a)] 9.95[b)]	16.79[a)] 23.49[b)]	4.44[a)] 11.37[b)]	5.08[a)] 3.58[b)]	0.57	2.98	0.97	0.88
PdDTA-X	52.83[a)] 23.73[b)]	14.74[a)] 7.73[b)]	18.77[a)] 22.53[b)]	–	11.18[a)] 44.53[b)]	0.60	3.58	0.78	–

[a)] Atomic percentage. [b)] Mass percentage.

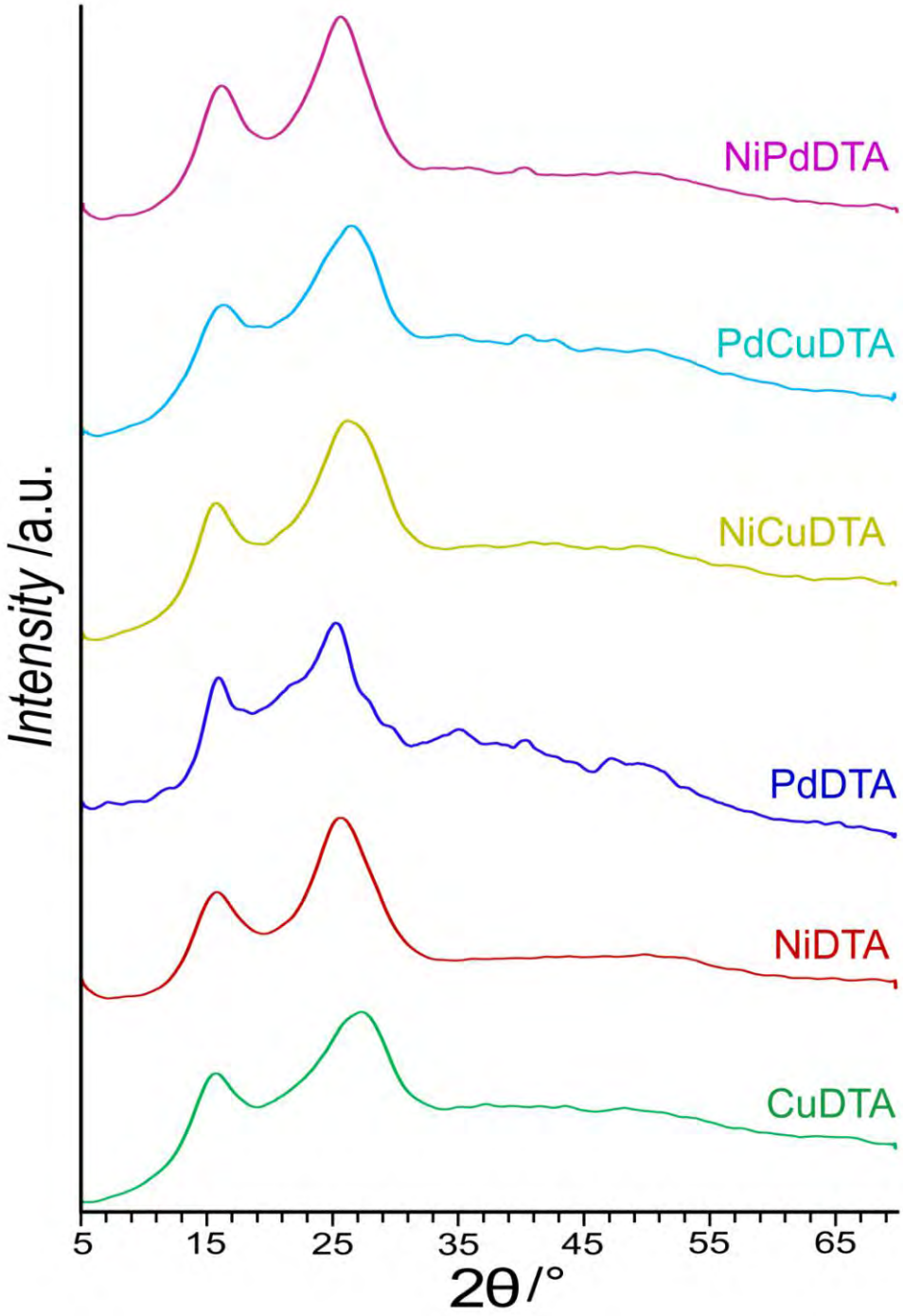

Figure S2.5. XRD patterns of pelletized MOXs.

Computational details and discussion

Computational analysis of the vibrational modes and IR/Raman spectra simulation was performed using density-functional theory (DFT) calculations were performed using the code DMOL3 included in the Accelrys "Materials Studio" package (Materials Studio, v. 5.5; Accelrys Inc., 2011.). Prior to the vibrational analysis DFT geometry optimization was performed on molecular models for DTA ligand on cis and trans conformations using B3LYP exchange-correlation functional and DNP type (double numerical plus polarization) atomic basis set.

Coordination mode of dithiooxamidato ligand

Additionally, the Cambridge structural database survey also indicates that the majority of complexes show a *trans* configuration of the heteroatoms of DTA. The coordination mode that dithiooxamidato ligand adopts in the herein reported complexes has been elucidated by FTIR and Raman spectroscopy, supported by a computational analysis of the vibration modes using DFT optimized structures of DTA ligand in *cis* and *trans* conformations (Figure S2.6). Due to the poor resolution at low wavenumbers, the focus of the analysis was set on the most intense IR and Raman peaks of the ligand which are located at 1480─1580 cm^{-1} and correspond to C─N stretching modes (Figure 2a).

According to group theory analysis, in an ideal C_{2h} symmetry the *trans* conformation of the ligand give rise to one IR active C–N stretching mode noted as B_u or antisymmetric vibration, and its Raman active symmetric counterpart corresponding to A_g mode. *cis* disposition of the ligand (C_{2v} point symmetry) allows to envisage two IR and Raman active C–N stretching mode identified as A_1 and B_2 characters. In a good agreement with the latter, the simulated IR and Raman spectra show one or two peaks for *trans* and *cis* configurations, respectively, being always the symmetric vibrational mode sited at higher wavenumbers (Figure 2b). Consequently, the presence of a unique C–N stretching peak in the IR and Raman spectra of all the MDTA complexes, allows to postulate a structure consisting of a one-dimensional polymeric chain (Scheme 1) in which the metal centers are sequentially bridged by dithiooxamidato ligands in a μ_2-κ^2N,S:κ^2N',S' coordination mode. The shift of the C–N vibrational peak towards lower frequencies observed for the series PdDTA (1482 cm^{-1}), CuDTA (1490 cm^{-1}) and NiDTA (1497 cm^{-1}) stands for a strengthening of the metal-ligand coordination bond (Pd > Cu > Ni).

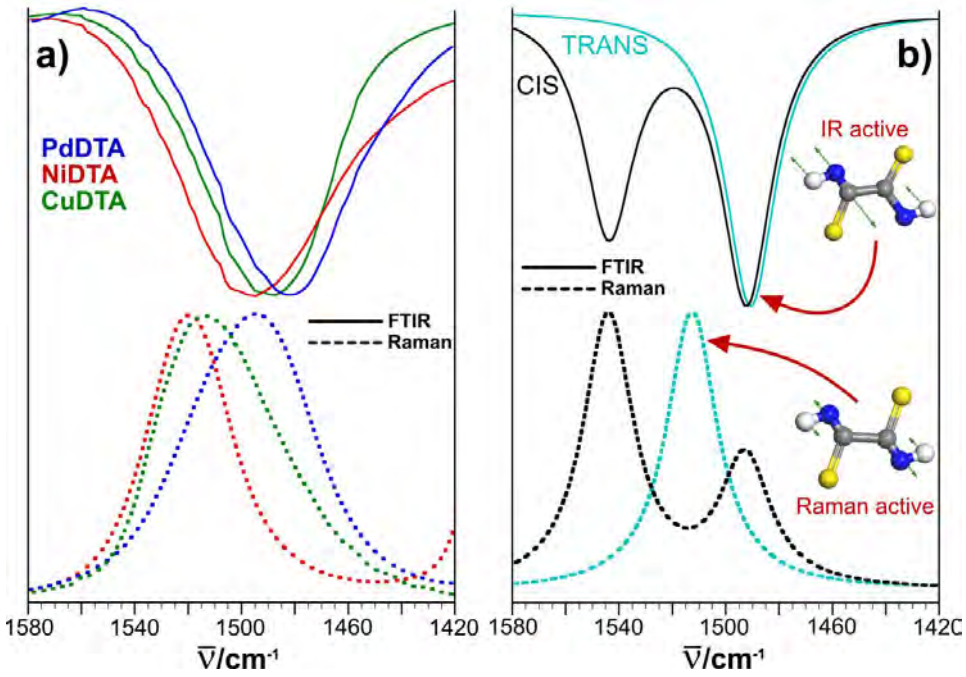

Figure S2.6. a) Experimental and b) simulated FTIR and Raman spectra at 1580−1420 cm^{-1} corresponding to C–N stretching mode. Simulated spectra show the peaks corresponding to the vibration modes of *trans* and *cis* conformers of free DTA molecules.

Simulation of the DMF and metal-DTA interaction

Geometry optimization of a model consisting on 1D–$[Ni(\mu–DTA)]_n$ chain with side-interacting DMF molecules were performed by dispersion-corrected density-functional theory DFT calculations using the code CASTEP, included also in the Accelrys "Materials Studio" package, which employs a plane-wave basis set and pseudopotentials.[1] The calculations employed a plane-wave cutoff of 380 eV and ultrasoft pseudopotentials. The PBE exchange-correlation functional was used in the calculations,[2] together with the "D2" flavor of the dispersion correction scheme proposed by Grimme.[3] Together with the atomic positions cell parameters were also optimized. To save computational time, the calculations were carried out for the primitive, using one k-point located at the Γ-point.

All the intramolecular bond and angles of the optimized structure are similar to the values found in the Cambridge Structural Database (CSD)[4] for crystal structures containing DMF and metal-DTA complexes. Furthermore, hydrogen bonding distances of the optimized structure are consistent with the values found for "N–H···O=C" and "$C_{carbonyl}$–H···S".

[1] S. J. Clark, M. D. Segall, C. J. Pickard, P. J. Hasnip, M. I. J. Probert, K. Refson, M. C. *Z.* Payne, *Kristallogr.***2005**, *220*, 567–570.
[2] J. P. Perdew, K. Burke, M. Ernzerhof, *Phys. Rev. Lett*. **1996**, *77*, 3865–3868.
[3] S. Grimme, *J. Comput. Chem.***2006**, *27*, 1787–1799.
[4] F. H. Allen, *Acta Crystallogr.***2002**, *B58*, 380–388.

The best gelation conditions were obtained using DMF as solvent, which holds adjacent hydrogen bond acceptor/donor groups (aldehyde O and H atoms, respectively) ready to supramolecularly assemble with the dithiooxamidato bridge. According to DFT calculations DMF is capable to establish with the dithiooxamidato a synthon consisting of two donors and two acceptors in a seven-membered ring ($R_2^2(7)$) with relatively short hydrogen bond distances (Figure S2.7). Such interaction, together with steric hindrance that the two methyl groups of the solvent entail, can be considered as a key factor to promote a longitudinal growth of fibers.

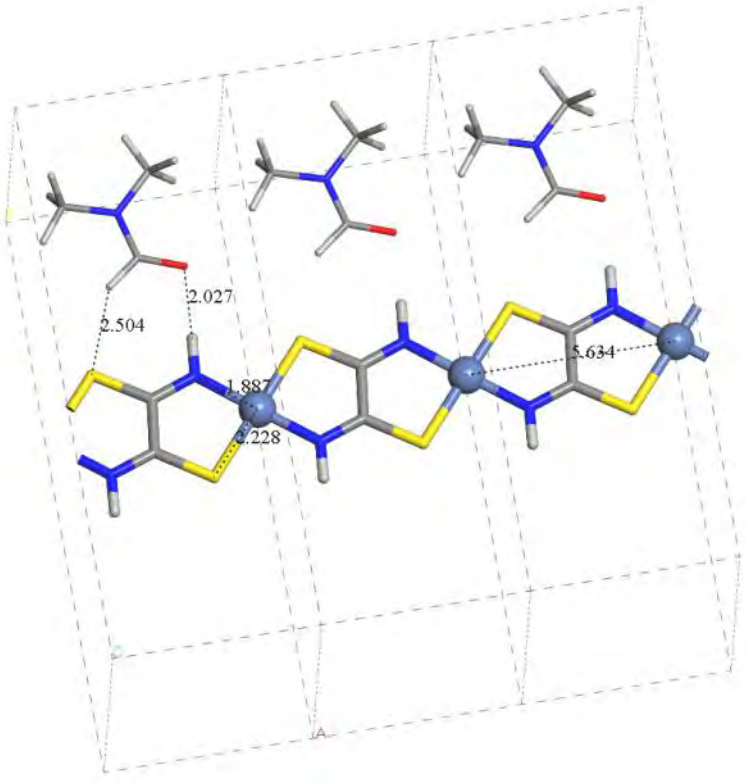

Figure S2.7. Result of DFT geometry optimization on a model consisting of 1D–[Ni(μ–DTA)]$_n$ chain with side-interacting DMF molecules. Distances set in Å units.

S3.TEXTURAL ANALYSIS

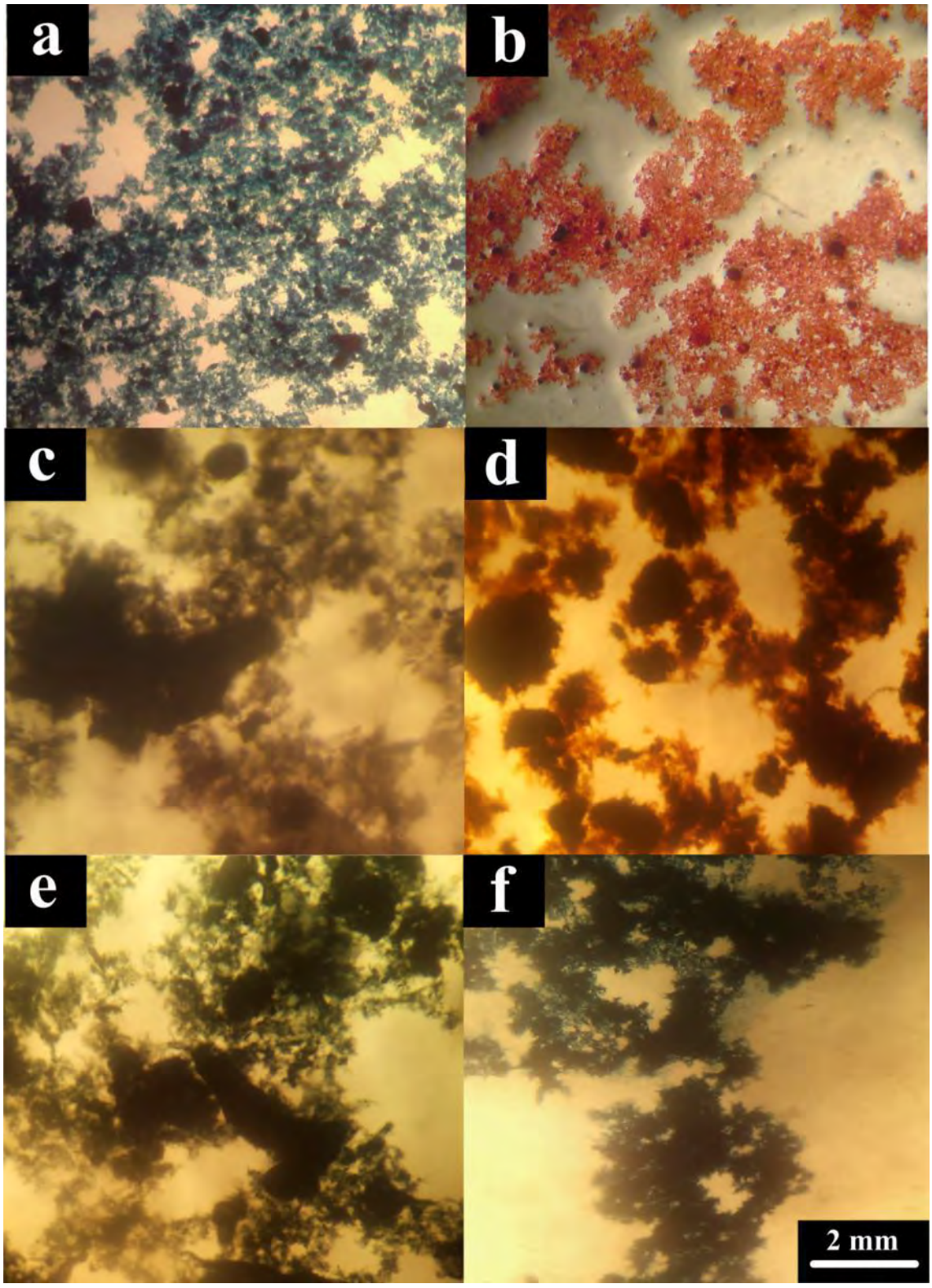

Figure S3.1. Photographs MOGs fragments taken by loupe to 1kX: a) NiDTA. b) PdDTA. c) PdCuDTA. d) NiPdDTA. e) CuDTA. f) NiCuDTA.

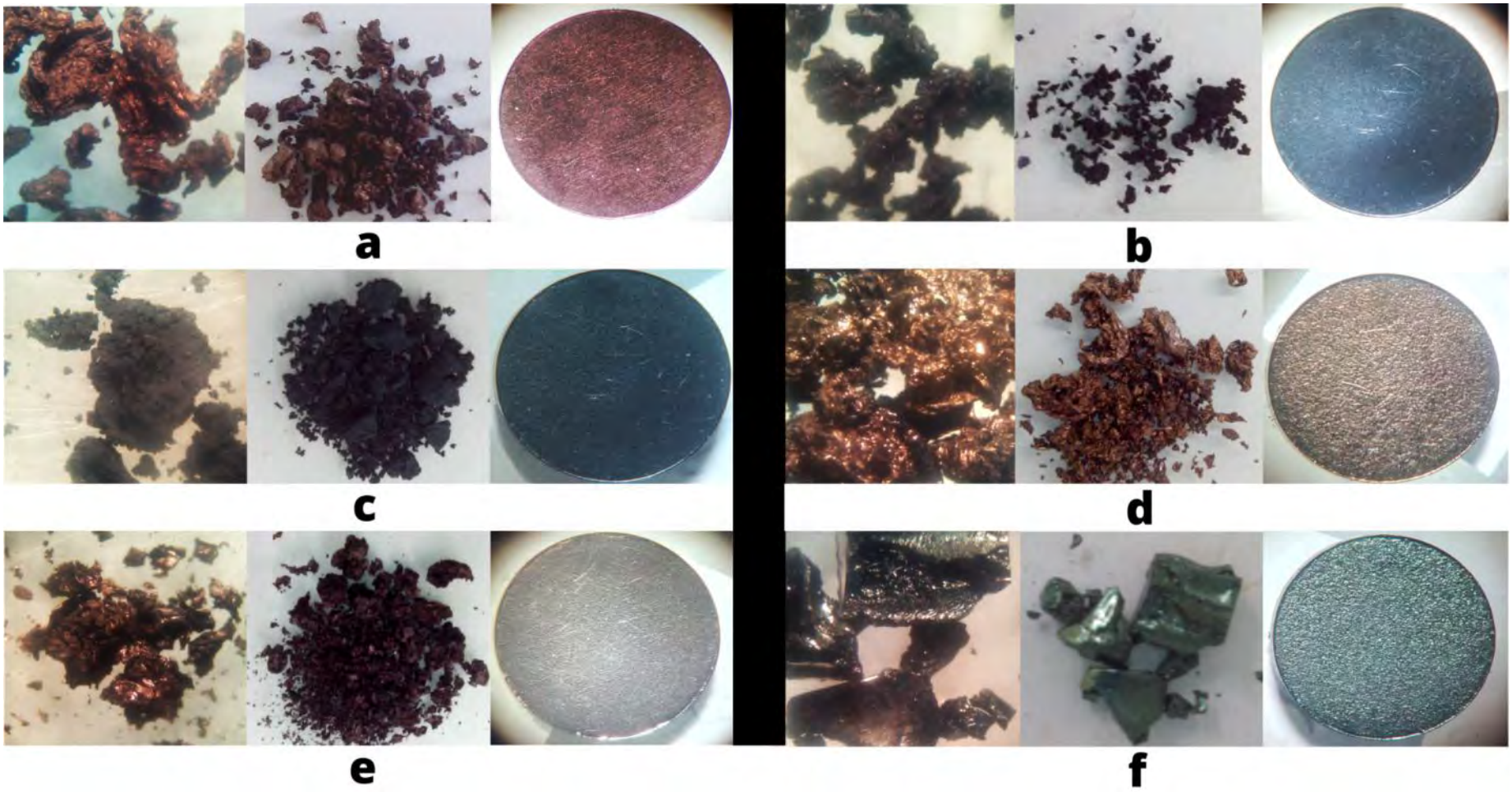

Figure S3.2. Photographs of MOXs (left: taken by loupe to 1 kX magnification, central: no magnification and right: pressed pellets with a pressure of 10^4 kg cm^{-2}: a) NiDTA. b) CuDTA. c) PdCuDTA. d) NiPdDTA. e) NiCuDTA. f) PdDTA.

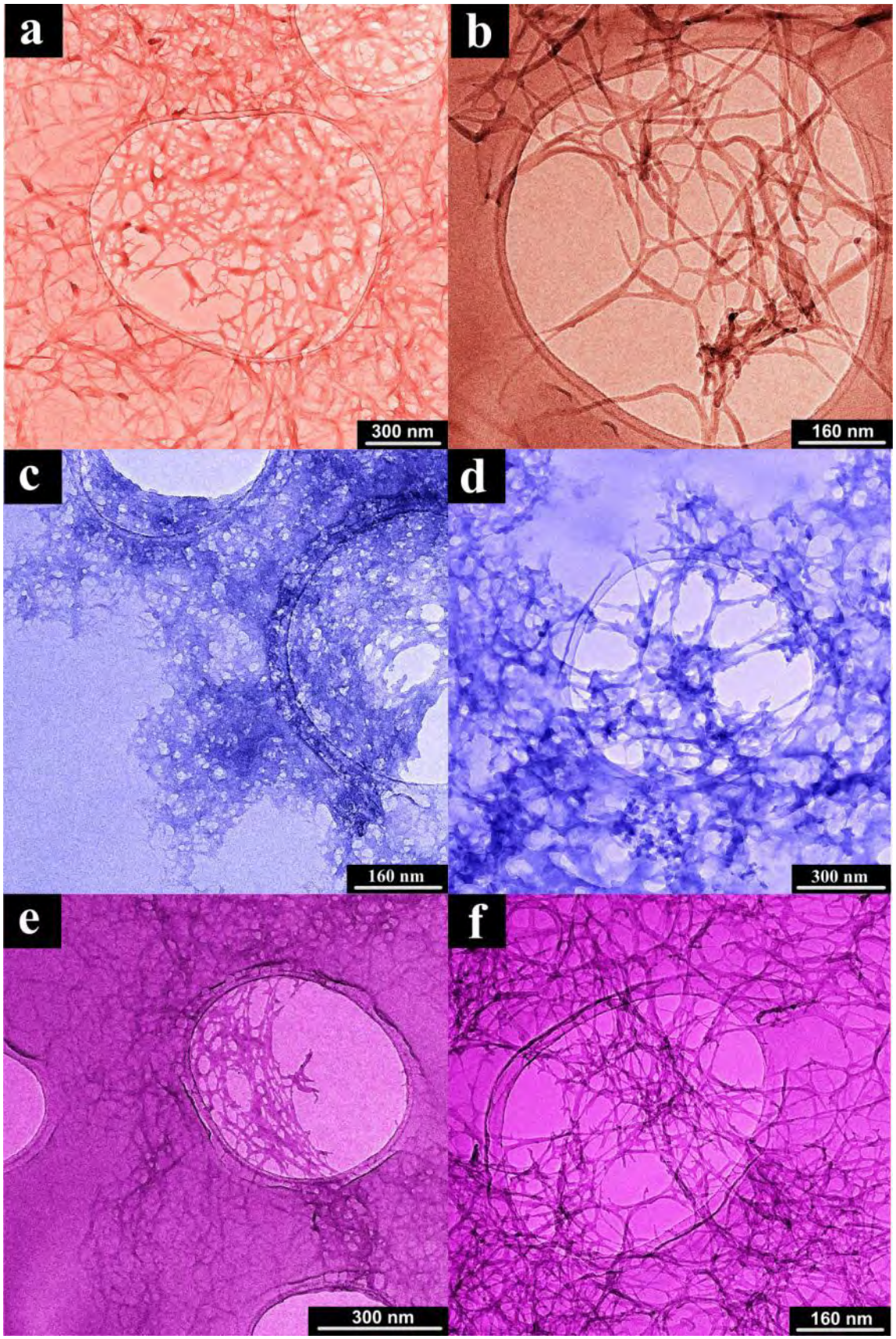

Figure S3.3. TEM images of Ni/Pd based metallogels dispersed in ethanol: a) NiDTA. b) NiDTA + surfactant. c) PdDTA. d) PdDTA + surfactant. e) NiPdDTA. f) NiPdDTA + surfactant. Surfactant: *n*-decylamine.

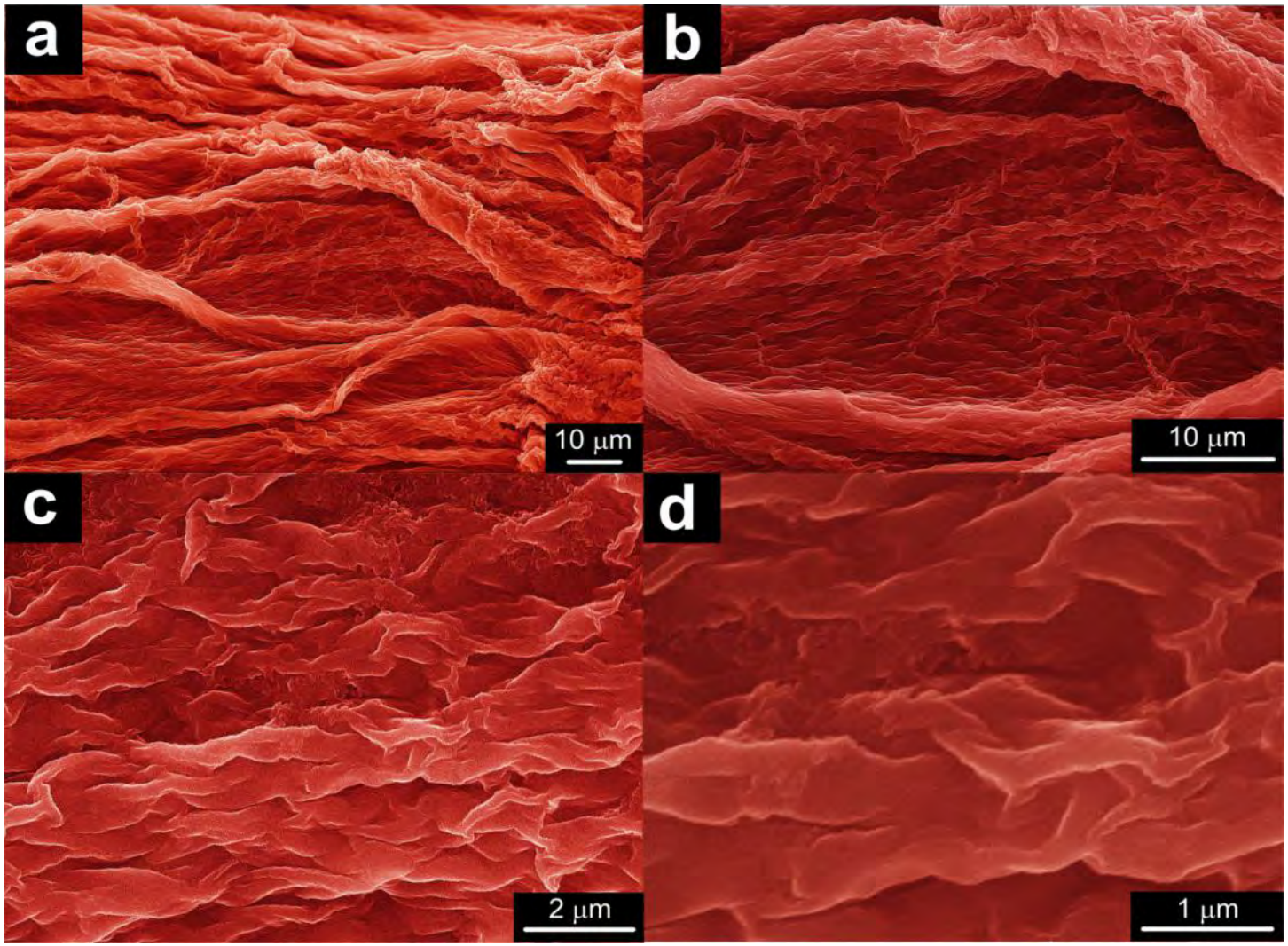

Figure S3.4. SEM images of NiDTA xerogel: a) 1 kX. b) 2.5 kX. c) 10 kX. d) 25 kX.

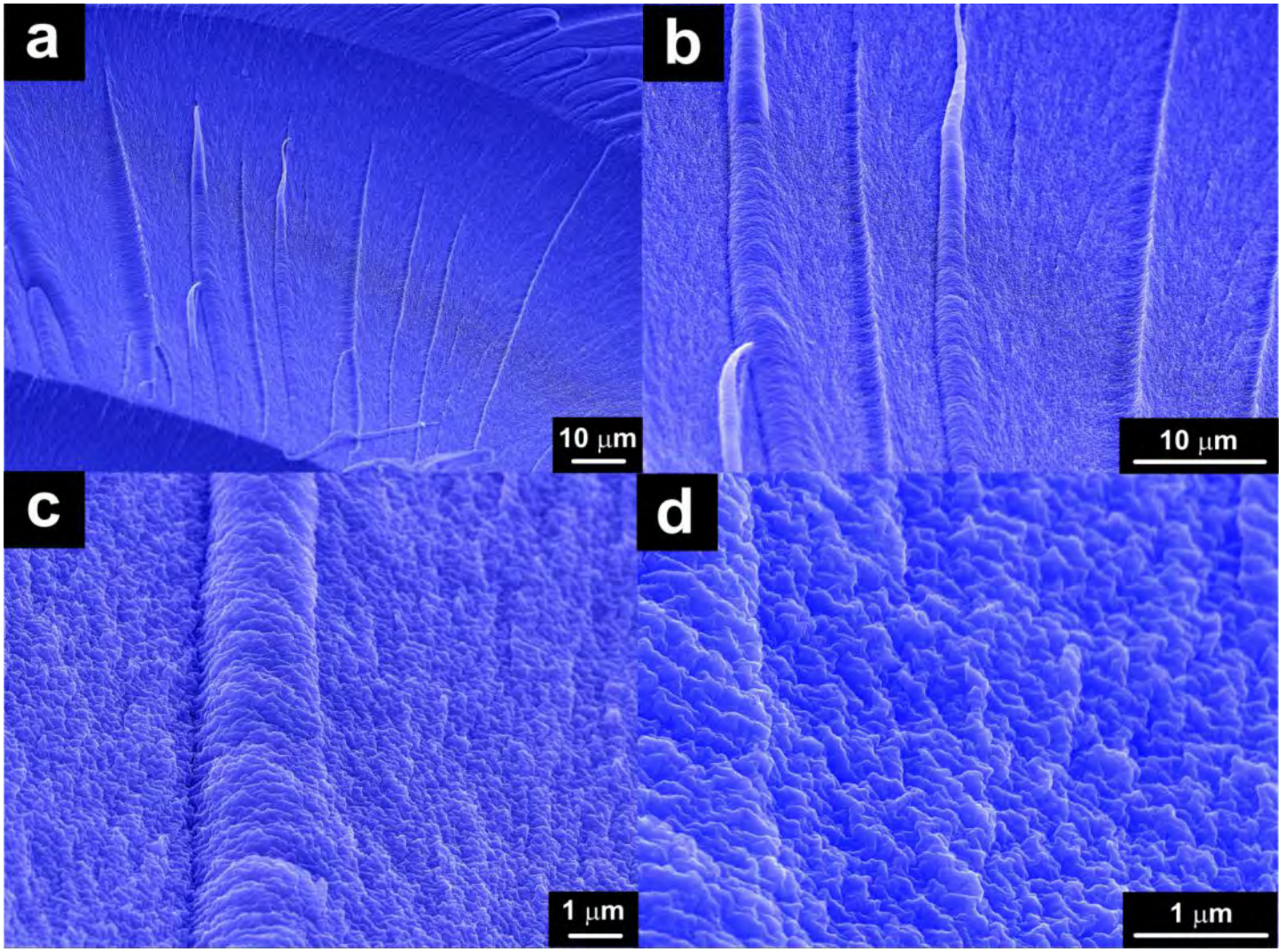

Figure S3.5. SEM images of PdDTA xerogel: a) 1 kX. b) 2.5 kX. c) 10 kX. d) 25 kX.

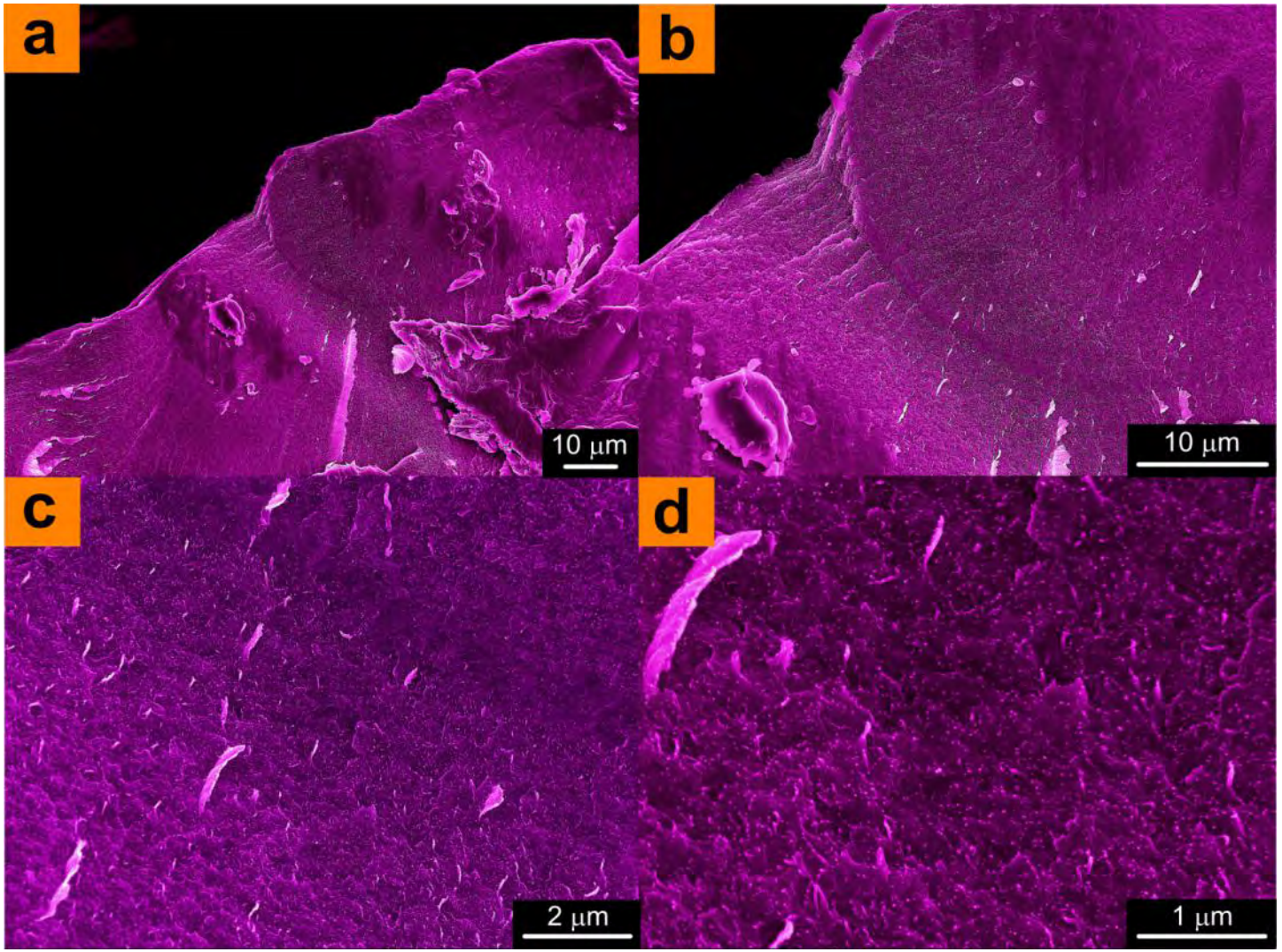

Figure S3.6. SEM images of NiPdDTA xerogel: a) 1 kX. b) 2.5 kX. c) 10 kX. d) 25 kX.

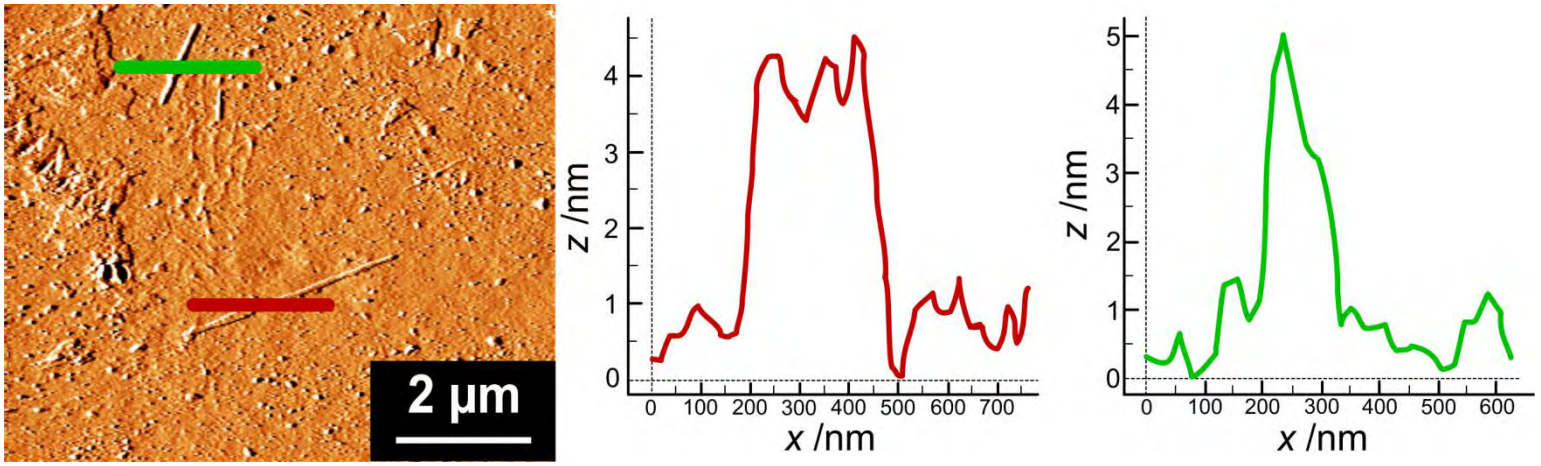

Figure S3.7. AFM topographic image of NiDTA 50 mM aerogel fibers on SiO_2. Heights profiles along the green and red lines.

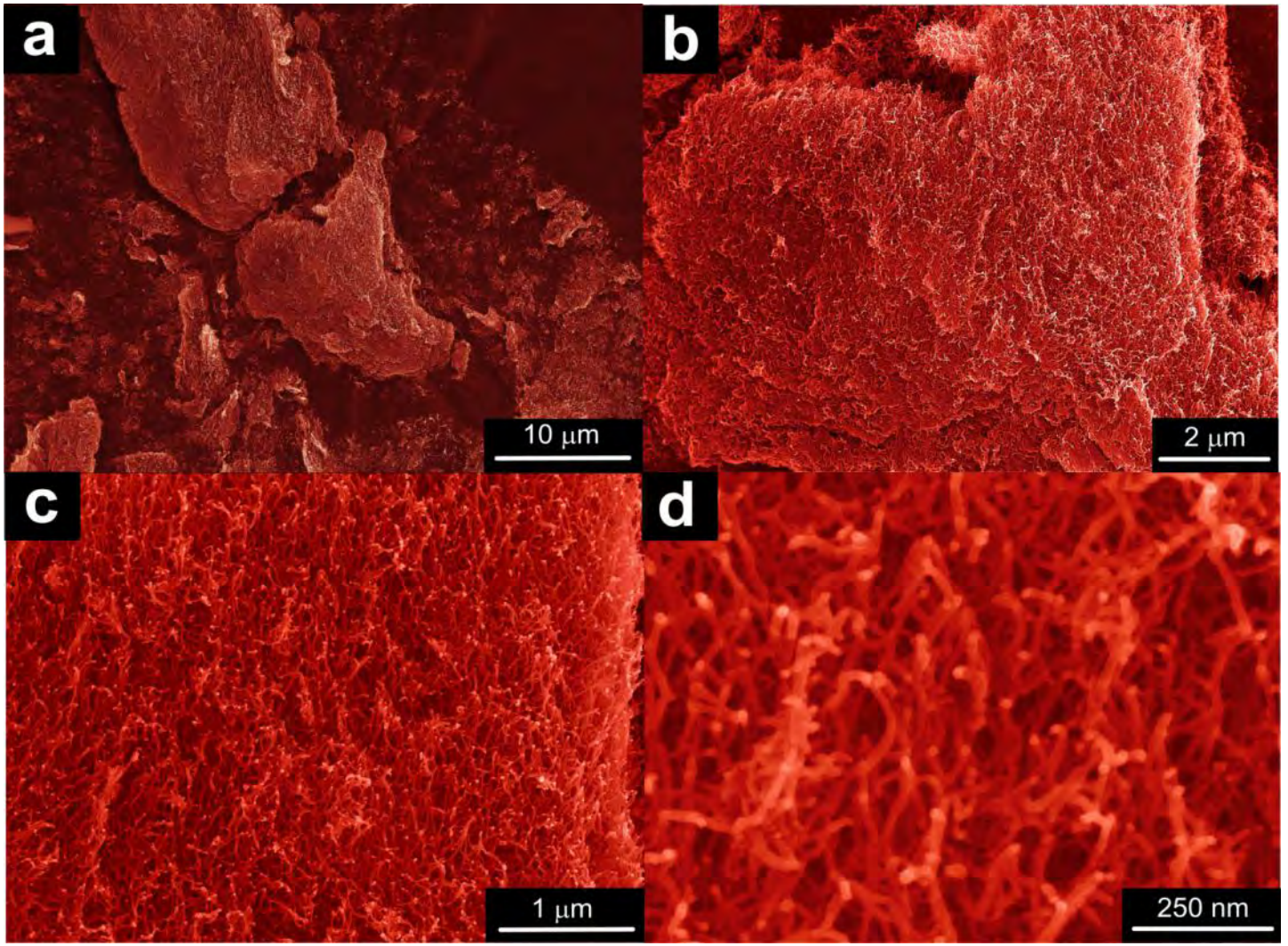

Figure S3.8. SEM images of NiDTA 25 mM aerogel: a) 2.5 kX. b) 10 kX. c) 25 kX. d) 100 kX.

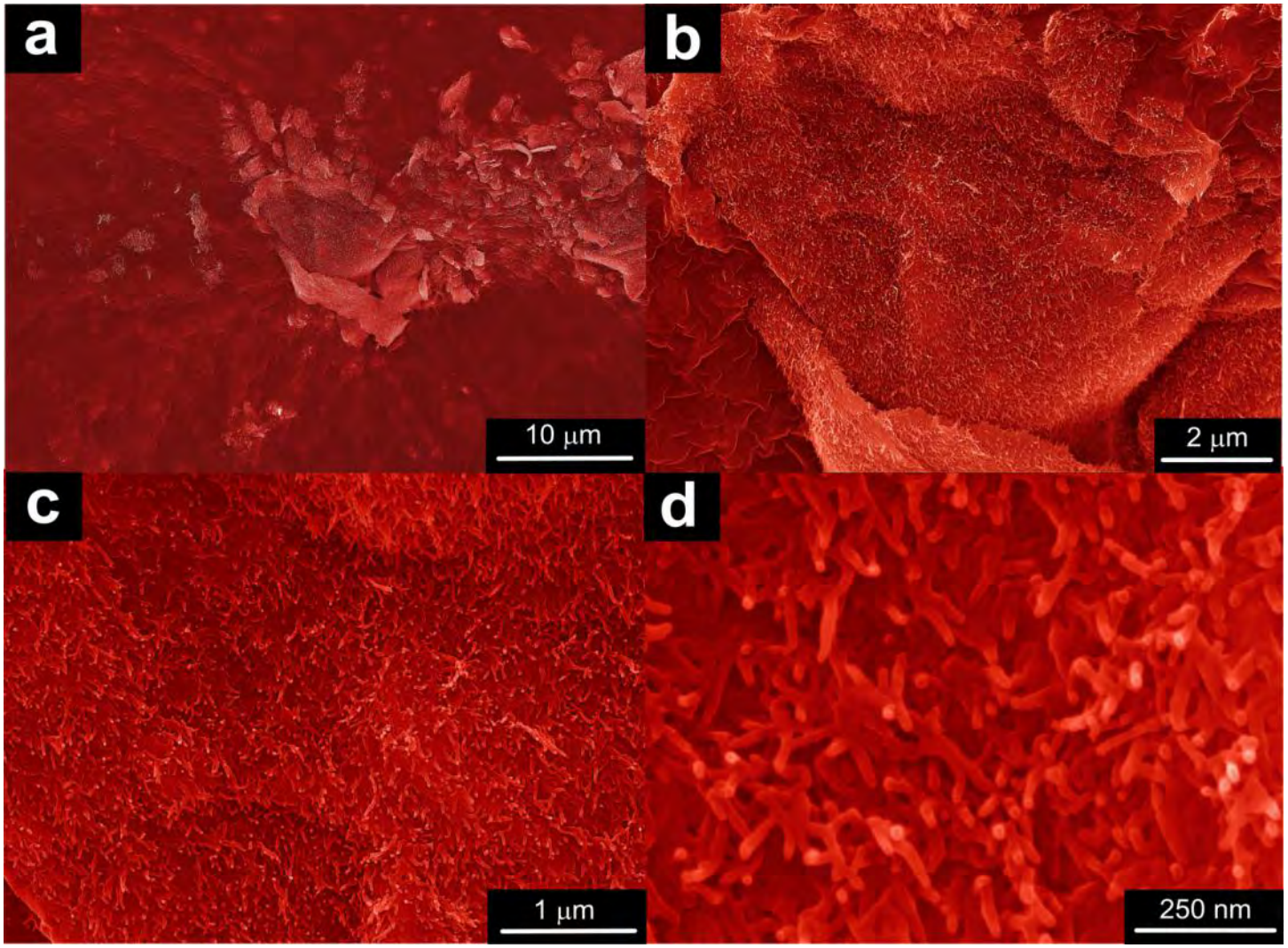

Figure S3.9. SEM images of NiDTA 50 mM aerogel: a) 2.5 kX. b) 10 kX. c) 25 kX. d) 100 kX.

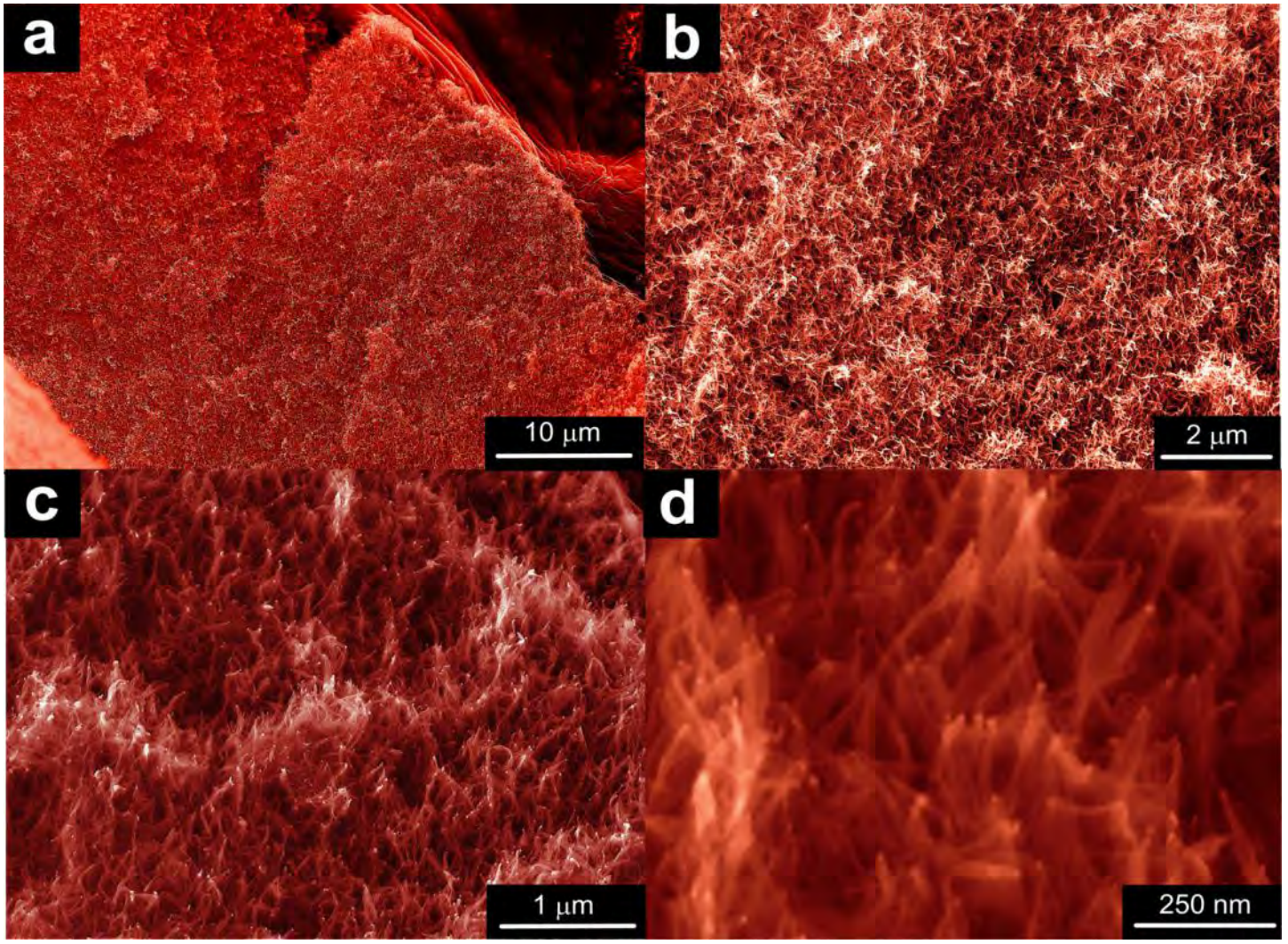

Figure S3.10. SEM images of NiDTA 75 mM aerogel: a) 2.5 kX. b) 10 kX. c) 25 kX. d) 100 kX.

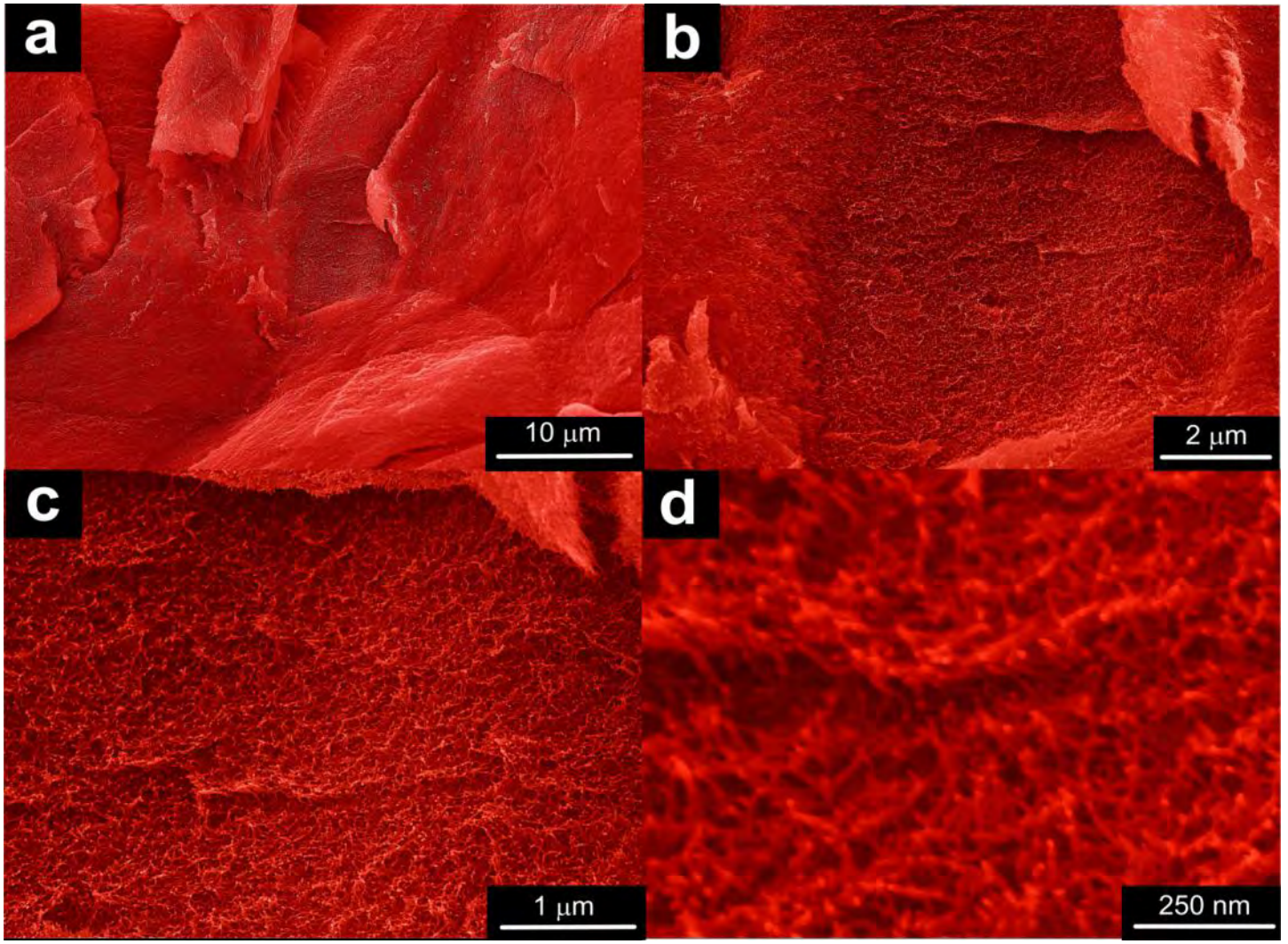

Figure S3.11. SEM images of NiDTA 100 mM aerogel: a) 2.5 kX. b) 10 kX. c) 25 kX. d) 100 kX.

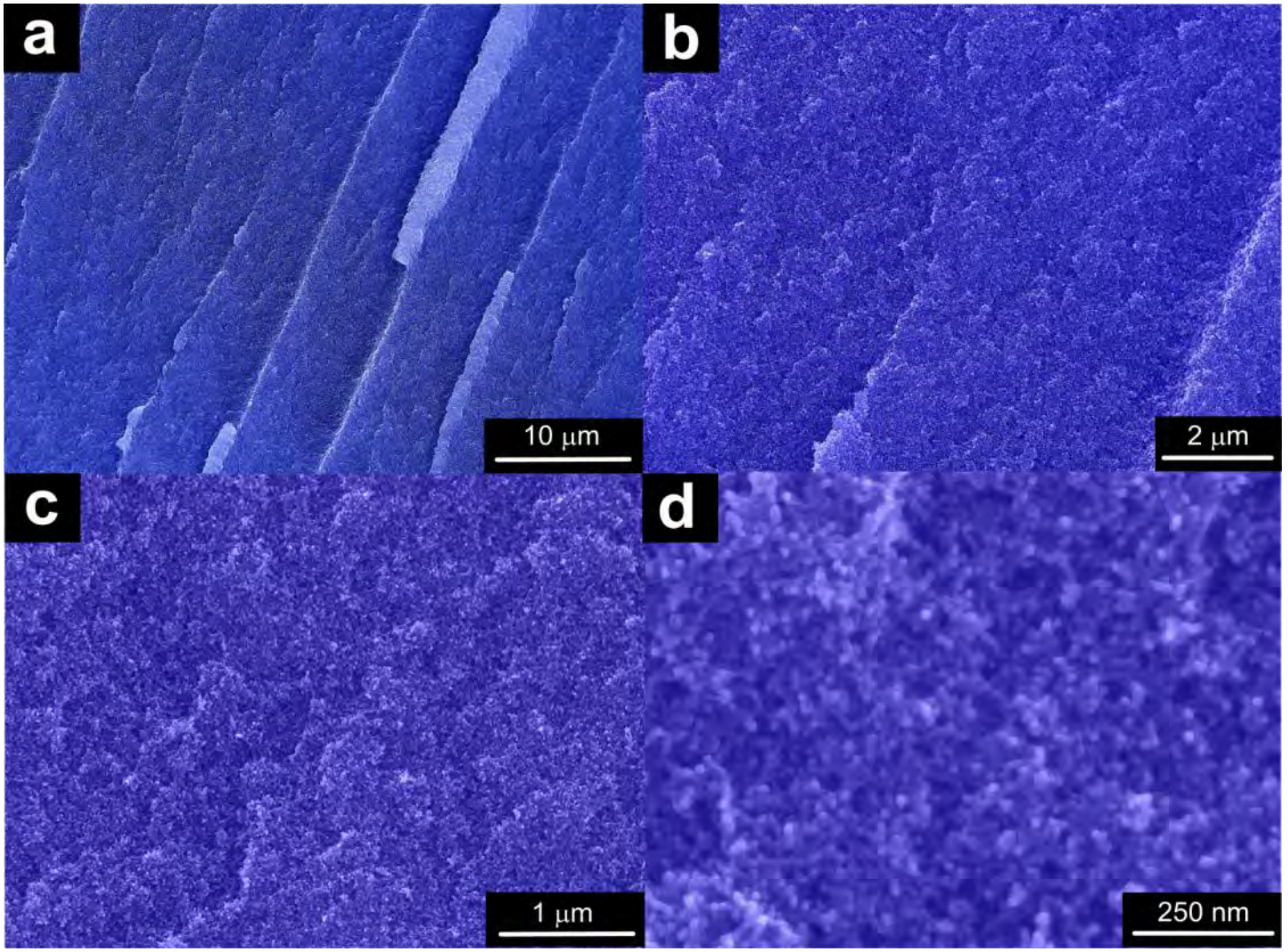

Figure S3.12. SEM images of PdDTA aerogel: a) 2.5 kX. b) 10 kX. c) 25 kX. d) 100 kX.

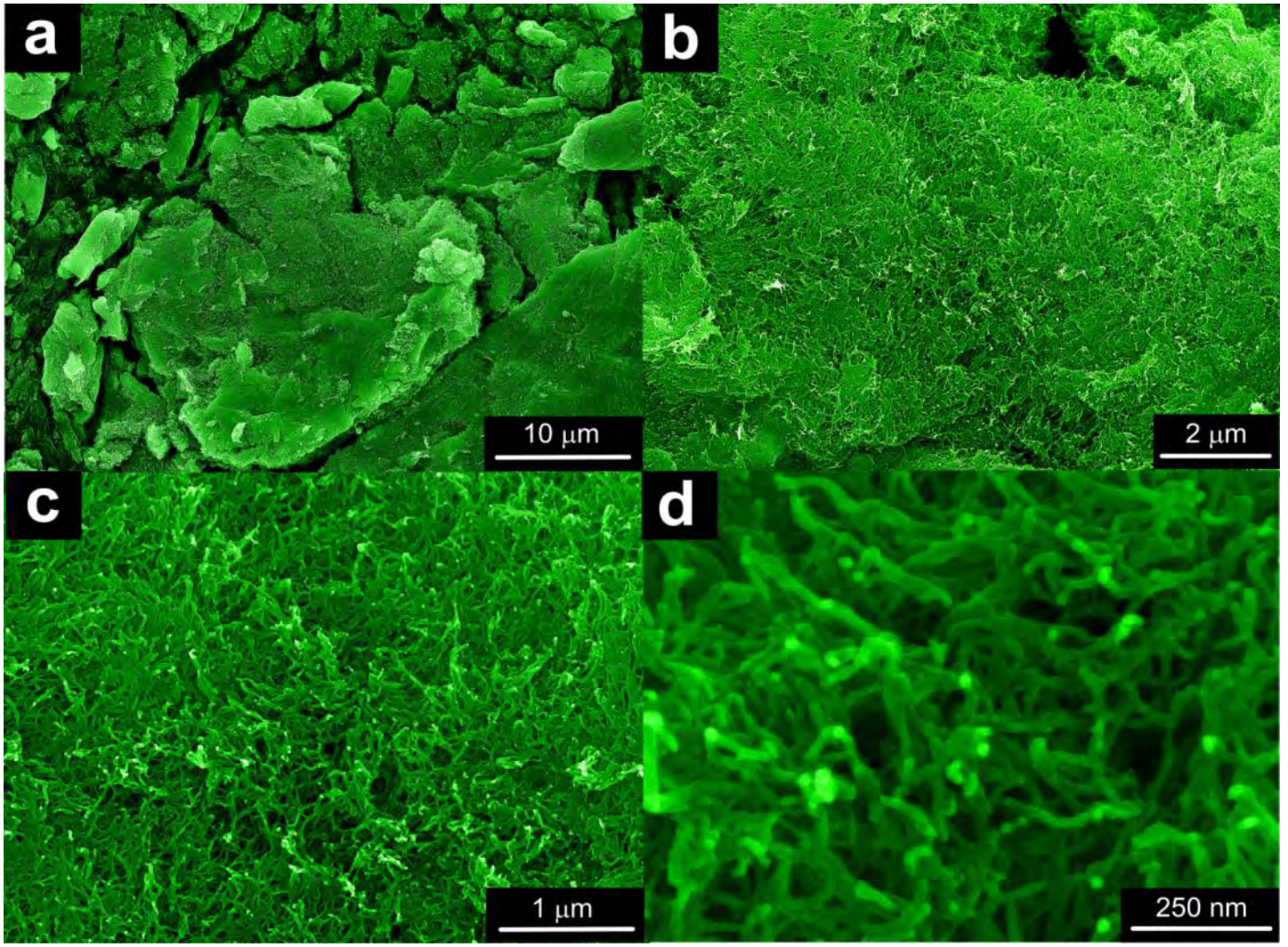

Figure S3.13. SEM images of CuDTA aerogel: a) 2.5 kX. b) 10 kX. c) 25 kX. d) 100 kX.

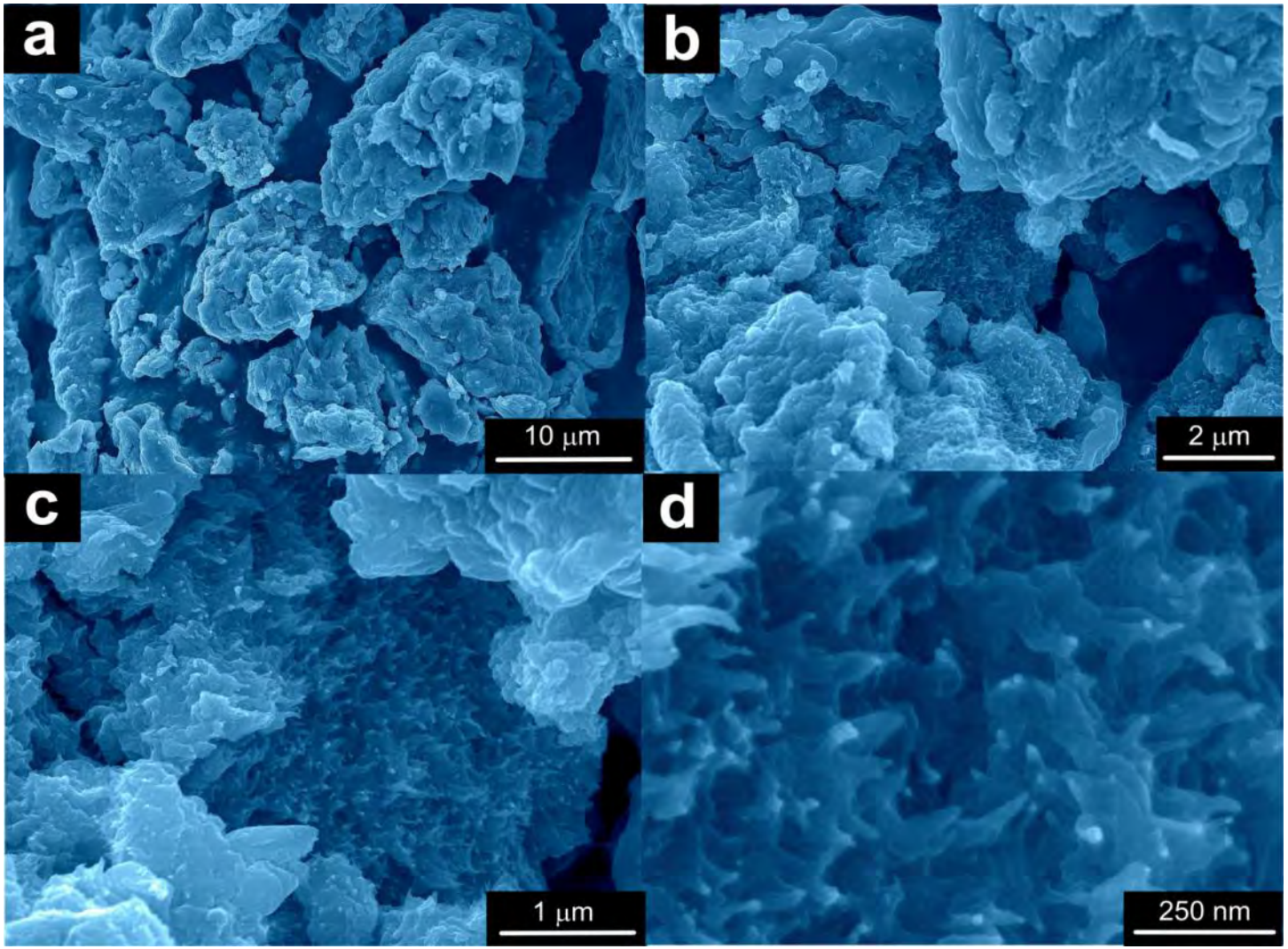

Figure S3.14. SEM images of PdCuDTA aerogel: a) 2.5 kX. b) 10 kX. c) 25 kX. d) 100 kX.

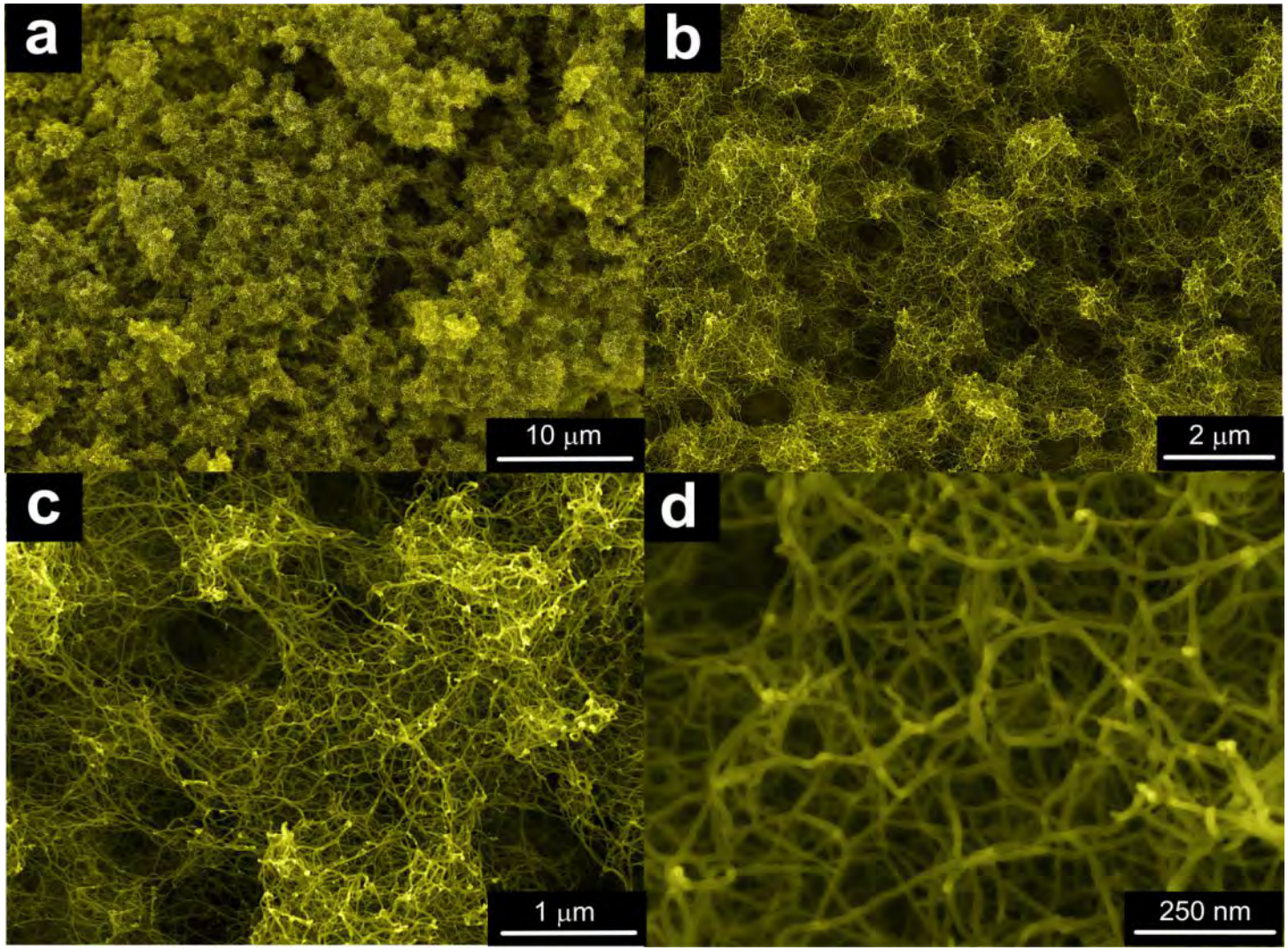

Figure S3.15. SEM images of NiCuDTA aerogel: a) 2.5 kX. b) 10 kX. c) 25 kX. d) 100 kX.

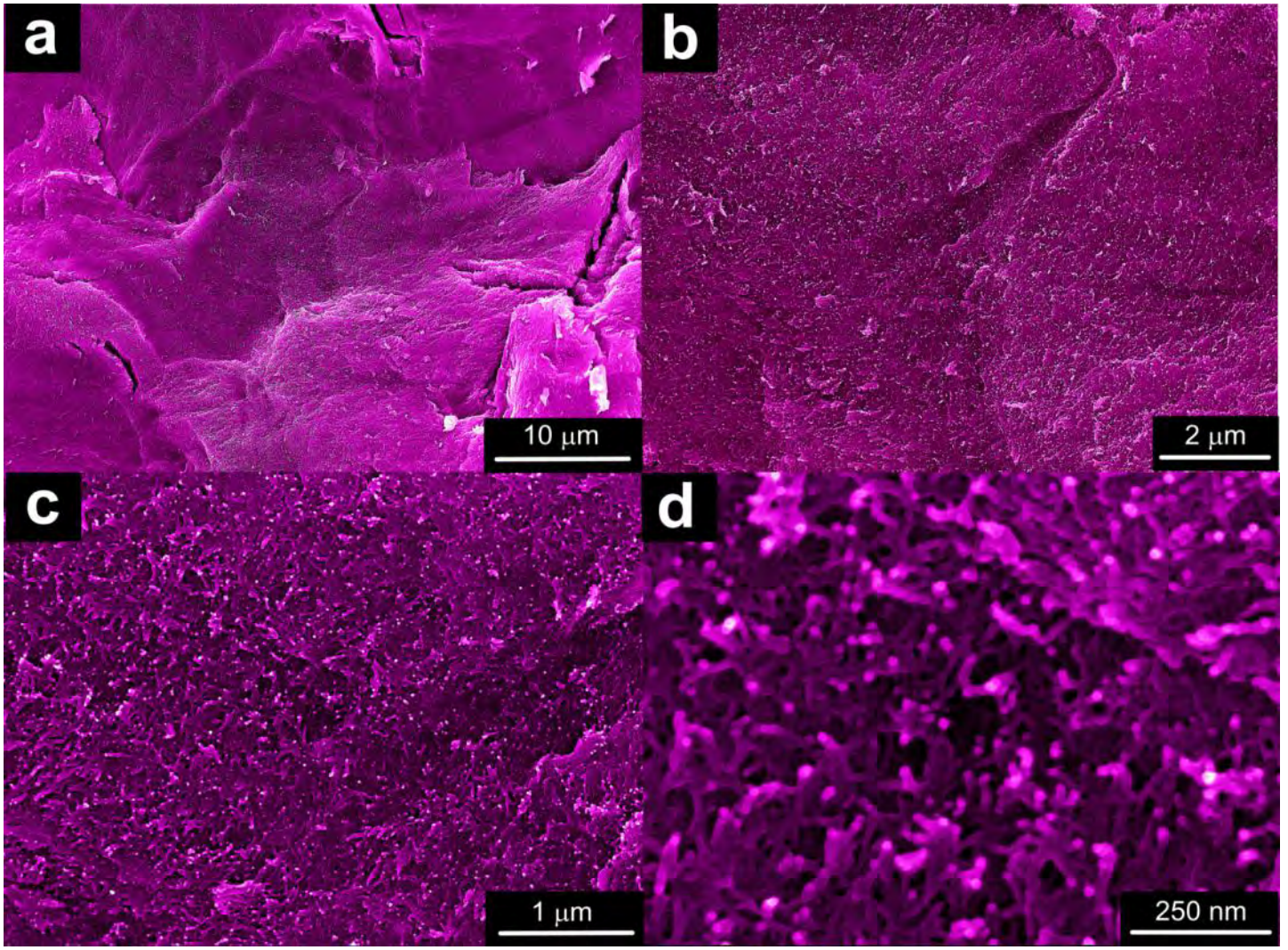

Figure S3.16. SEM images of NiPdDTA aerogel: a) 2.5 kX. b) 10 kX. c) 25 kX. d) 100 kX.

Table S3.1 Main textural parameters of MOAs.

	$D_{F.A}$ [nm][a]	$D_{F.G}$ [nm][b]	Length [nm]	Aspect ratio	c_F [fiber μm^{-2}]
NiDTA-25	7.1 ± 2.9	—	150—410	21—58	420—780
NiDTA-50	11.9 ± 2.0	—	140—180	12—15	400—500
NiDTA-75	2.8 ± 1.6	20.4 ± 6.5[c] 13.4 ± 2.8[d]	150—450	54—161	250—500
NiDTA-100	3.9 ± 1.1	—	80—110	20—28	950—1400
CuDTA	7.5 ± 2.2	—	135—270	18—36	400—700
PdDTA	5.3 ± 1.7	7.9 ± 3.9[c] 14.3 ± 2.7[d]	30— 0	6—11	1400—1900
NiCuDTA	4.7 ± 1.8	—	350—800	75—170	600—750
NiPdDTA	8.2 ± 2.0	13.0 ± 3.3[c] 7.2 ± 1.6[d]	65—120	8—15	600—800
PdCuDTA	4.3 ± 2.2	—	80—150	19—35	80—170

[a)] Mean diameter and standard deviation of aerogel fibers calculated from SEM images and using a population of 20 measurements. [b)] Mean diameter and standard deviation of gel fibers dispersed in ethanol calculated from the TEM images and using a population of 20 measurements: [c)] without surfactant and [d)] adding 200 μL of n-decylamine in 10 mL of ethanol.

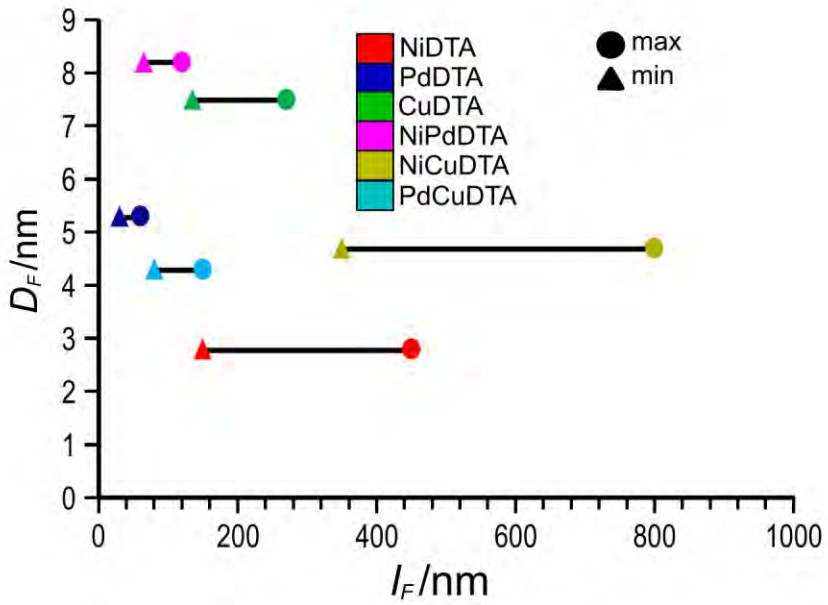

Figure S3.17. Correlation between fiber diameter (D_F) and length (l_F) for MDTA aerogels.

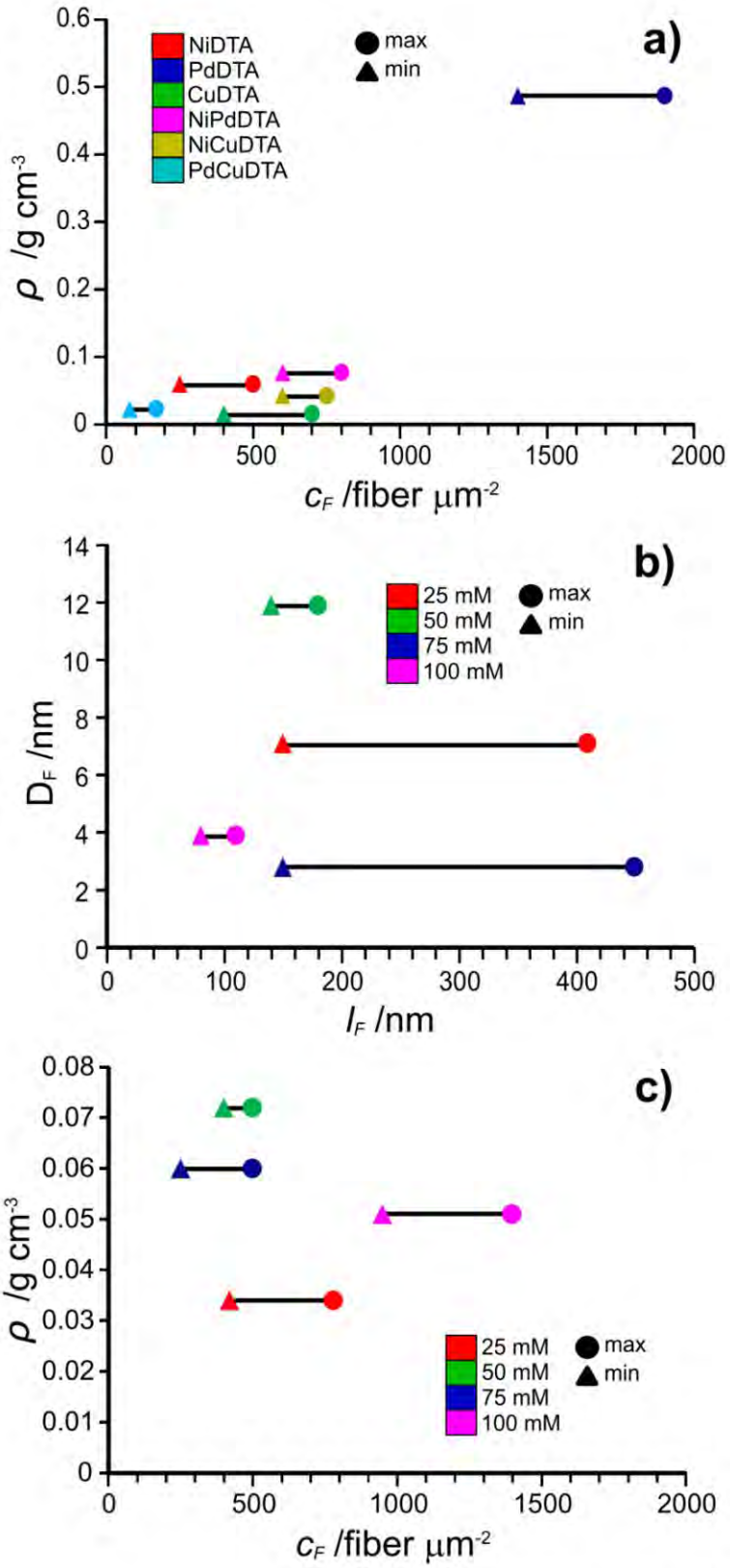

Figure S3.18. Correlation between: a) concentration of fibers and apparent density for MDTA aerogels, b) fiber length and diameter for NiDTA aerogels prepared at different molarities, and c) concentration of fibers and apparent density for NiDTA aerogels prepared at different molarities.

S4. ADSORPTION MEASUREMENTS

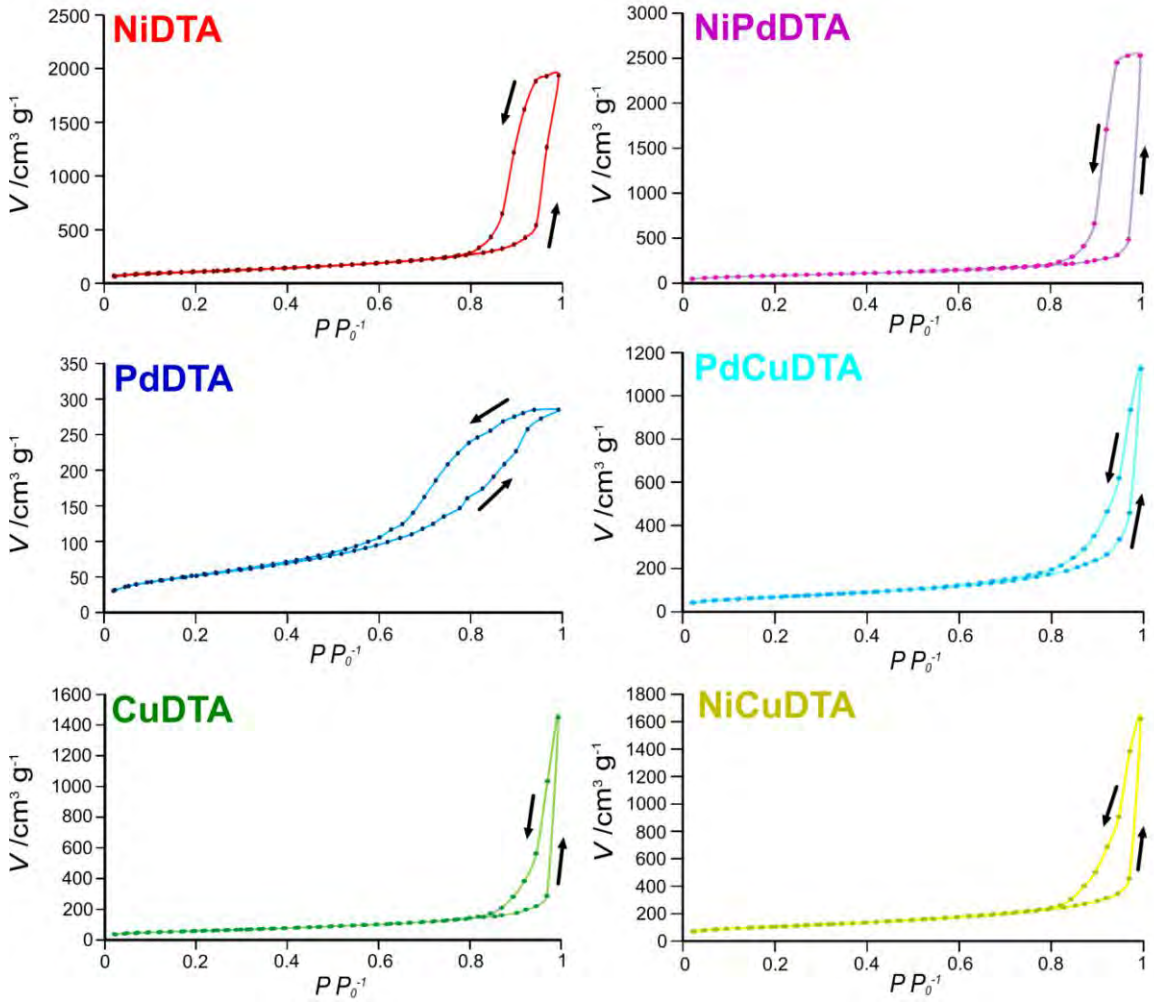

Figure S4.1. N_2 adsorption isotherms at 77 K.

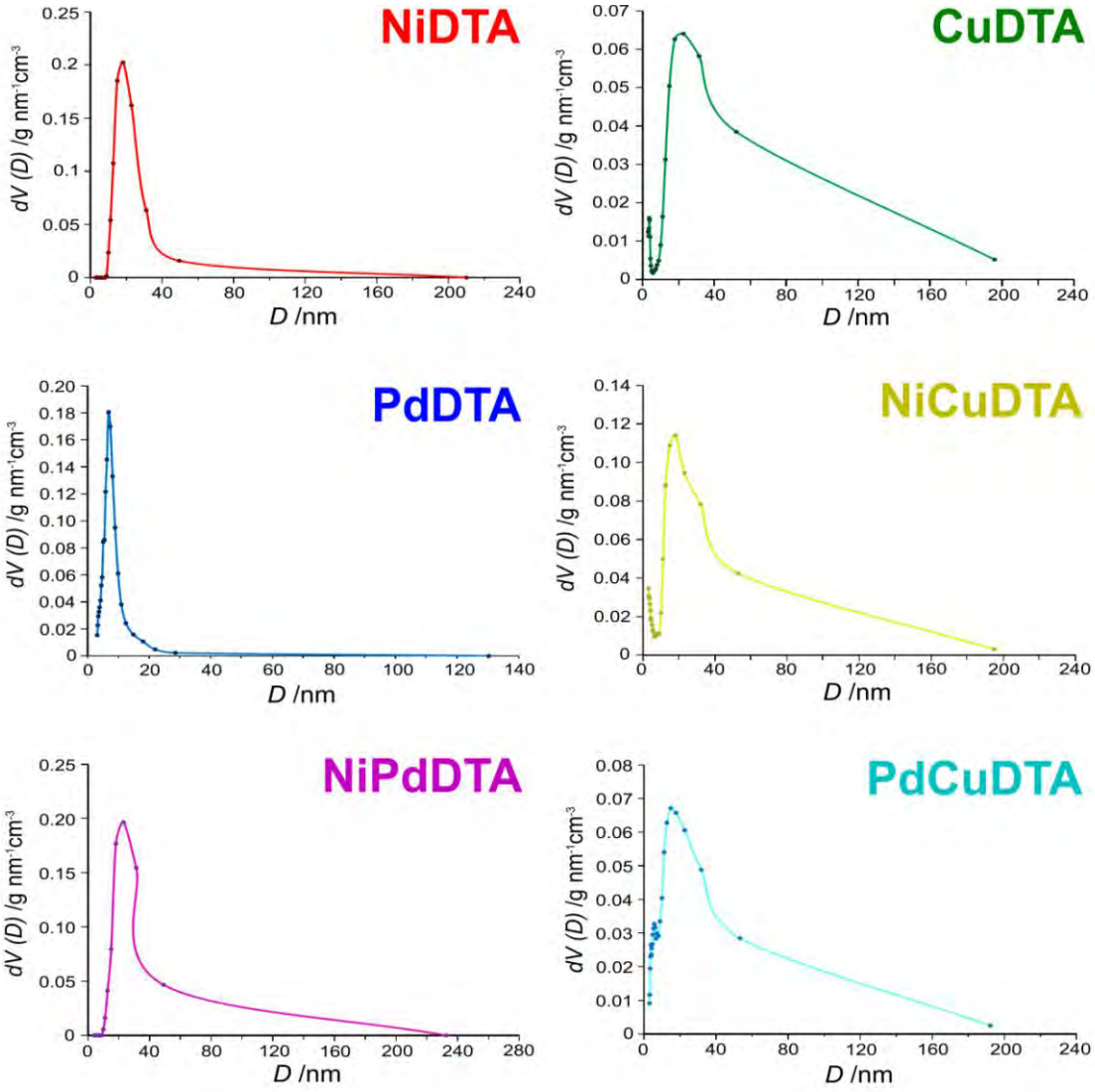

Figure S4.2. Pore size distributions of MOAs determined by BJH method.

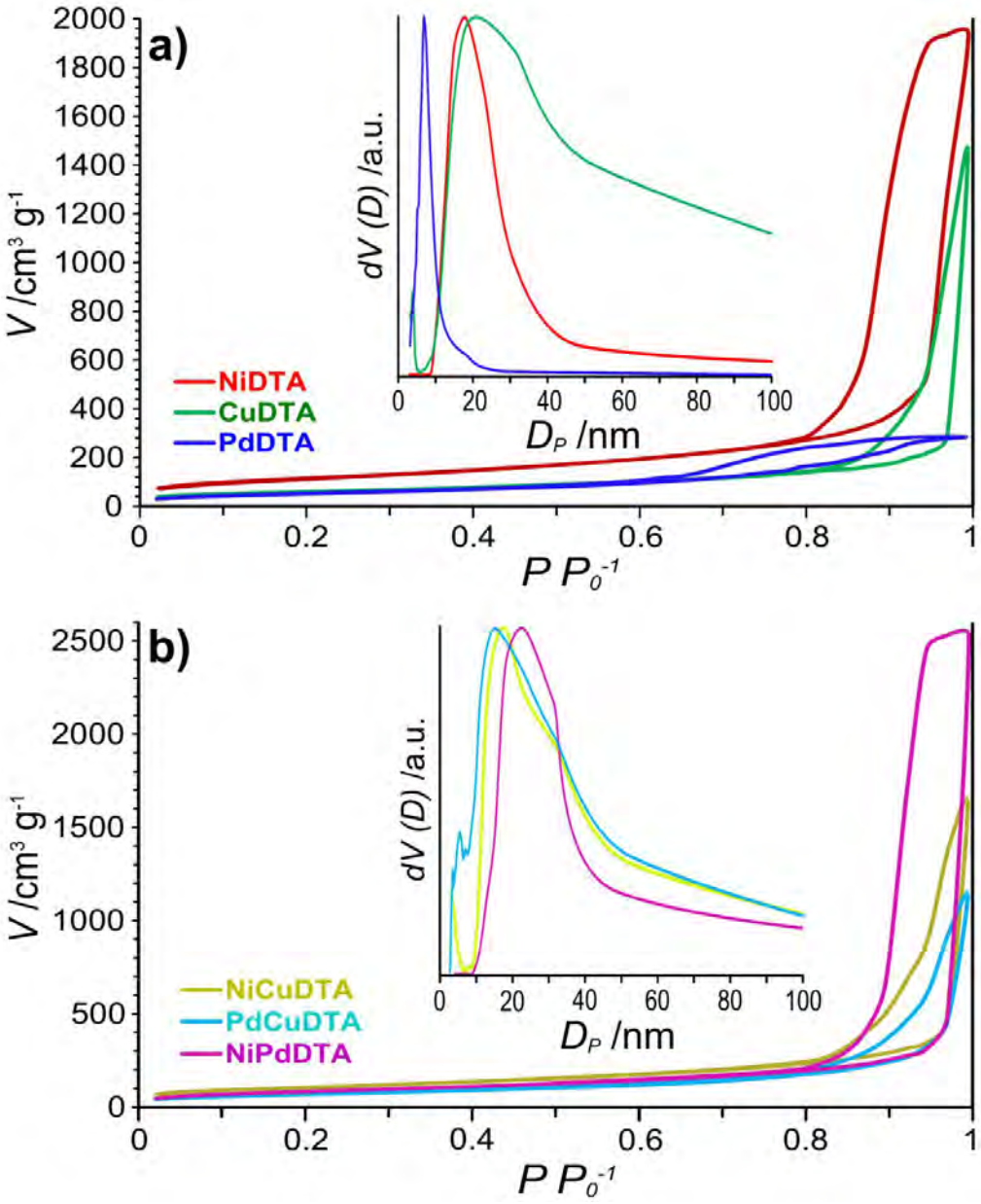

Figure S4.3. N_2 adsorption isotherms at 77 K and pore size distributions (inset graphics) of a) homonuclear and b) heteronuclear MOAs.

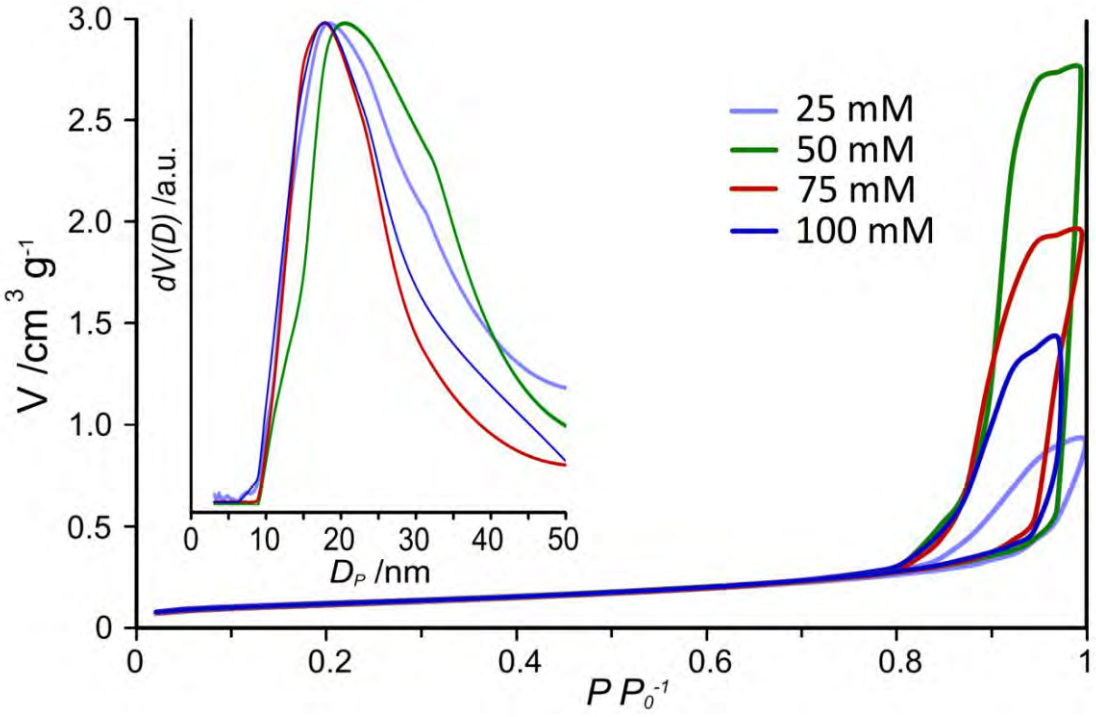

Figure S4.4. N_2 adsorption isotherms at 77 K and pore size distributions of NiDTA MOAs synthesized at different concentrations.

Table S4.1 Most relevant adsorptive parameters of MOAs.

	C	R^2	S_{BET} [$m^2\ g^{-1}$]	$V_{P,77\ K}$ [a] [$cm^3\ g^{-1}$]	q [b] [mmol g^{-1}]	[c] [nm]	D_{med} [d] [nm]	D_{mod} [e] [nm]	S [f] [nm]	C.V [g] [%]
NiDTA-25	131.36	0.9999	407	1.406	–	8.6	13.5	11.1	8.6	20.6
NiDTA-50	149.77	0.9998	427	4.250	–	11.0	18.0	23.2	4.8	43.2
NiDTA-75	156.0	0.9999	406	3.002	515.3 (273 K) 292.3 (298 K)	18.6	15.6	18.2	3.5	37.8
NiDTA-100	246.00	0.9999	418	2.192	–	9.1	15.0	9.0	3.6	39.1
PdDTA	68.69	0.9999	189	0.441	433.1 (273 K) 277.2 (298 K)	6.8	6.4	6.8	1.3	38.3
CuDTA	129.67	0.9999	211	2.243	360.8 (273 K) 241.5 (298 K)	21.0	15.0	22.6	11.6	110.9
NiPdDTA	61.91	0.9999	307	3.917	–	23.4	19.6	23.0	4.6	38.9
NiCuDTA	165.16	0.9999	372	2.508	–	16.0	12.6	18.0	7.8	97.7
PdCuDTA	90.49	0.9999	248	1.742	–	13.4	9.4	15.0	7.2	108.4

[a)] Total pore volume calculated from N_2 isotherm at 77 K at relative pressures of ca. 0.99. [b)] CO_2 uptake at 273 and 298 K. [c)] Mean pore diameter. [d)] Median pore diameter. [e)] Mode pore diameter. [f)] Standard deviation. [g)] Variation coefficient.

Regarding the correlation with the microstructural parameters, it can be concluded that fibers exhibiting a more pronounced longitudinal growth present larger values of surface area and pore size (Figure S4.4). Again, when retaining invariable the metal ion and varying the reagent molarities, materials of similar surface area are obtained (see NiDTA prepared at 25–100 mM in Table 2).

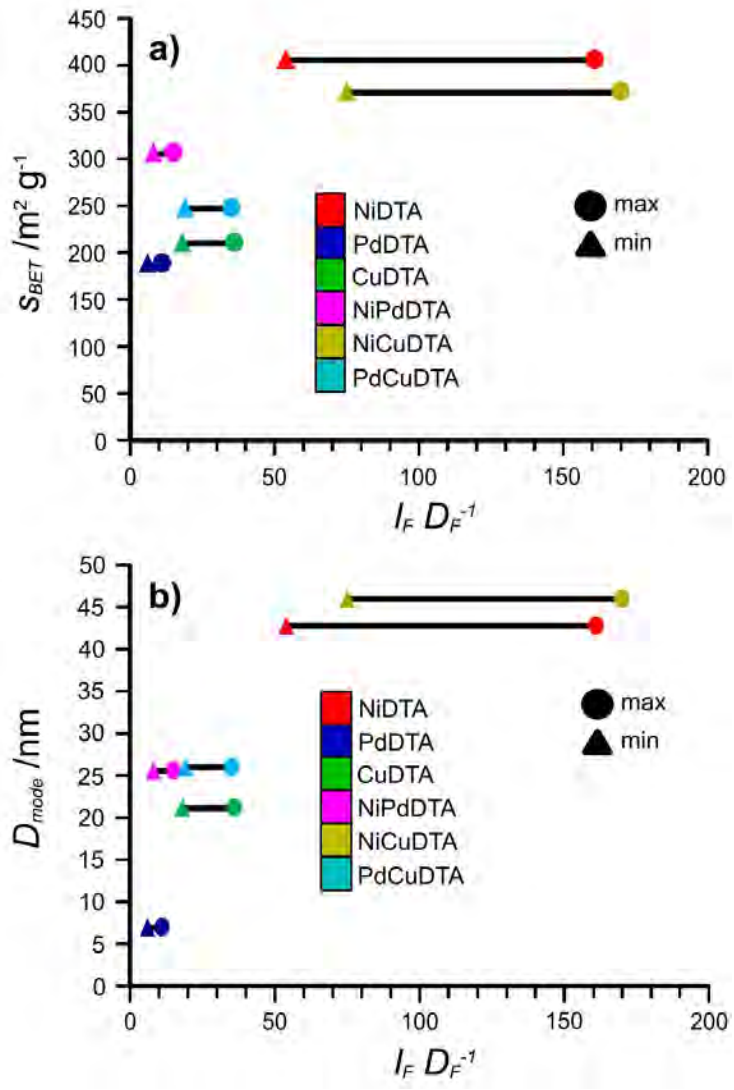

Figure S4.5. Correlation between the aspect ratio and a) surface area, b) pore size.

CO_2 adsorption isotherms

With the aim of completing the characterization of the porosity, CO_2 adsorption isotherms were collected at 273 and 298 K on homonuclear aerogel samples in order to estimate the isosteric heats of adsorption (Qst) that render this kind of materials (Figure S4.6). The Qst values has been calculated using modified Clausius Clapeyron equation,[5,6] which in the limit of zero loading approach to 19.7 kJ mol^{-1}, 24.2 kJ mol^{-1} and 25.0 kJ mol^{-1} for NiDTA, PdDTA, and CuDTA, respectively. These values are lower than those reported for most strongly interacting MOFs such as Cr-MIL-100 (62 kJ mol^{-1}),[7] Cr-MIL-101 (44 kJ mol^{-1}),[7] and Mg-MOF-74 (42 kJ mol^{-1}),[8] but comparable to well-known Al-MIL-53 (35 kJ mol^{-1}),[9] Ni-STA-12 (35 kJ mol^{-1}),[10] Zn2(dobdc) (26 kJ mol^{-1})[11] and Cu-HKUST-1 (29 kJ mol^{-1}).[12] In any case, they can be regarded as relatively high values for a mesoporous material[13] probably due to the availability of the not fully saturated centers that render the square-planar geometries around M(II) centers.

[5] A. L. Myers, P. A. Monson, *Langmuir* **2002**, *18*, 10261–10273.
[6] R. Krishna, *Microporous Mesoporous Mat.* **2012**, *156*, 217–223.
[7] P. L. Llewellyn, S. Bourrelly, C. Serre, A. Vimont, M. Daturi, L. Hamon, G. D. Weireld, J. -S. Chang, D. -Y. Hog, Y. K. Hwang, S. H. Jhung, G. Férey, *Langmuir* **2008**, *24*, 7245–7250.
[8] J. A. Mason, K. Sumida, Z. R. Herm, R. Krishna, J. R. Long, *Energy Environ. Sci.* **2011**, *4*, 3030–3040.
[9] S. Biswas, T. Ahnfeldt, N. Stock, *Inorg. Chem.* **2011**, *50*, 9518–9526.
[10] J. A. Groves, S. R. Miller, S. J. Warrender, C. Mellot-Draznieks, P. Lightfoot, P. A. Wright, *Chem. Commun.* **2006**, 3305–3307.
[11] S. R. Caskey, A. G. Wong-Foy, A. J. Matzger, *J. Am. Chem. Soc.* **2008**, *130*, 10870–10871.
[12] L. Grajciar, A. D. Wiersum, P. L. Llewellyn, J. -S. Chang, P. Nachtigall, *J. Phys. Chem. C* **2011**, *115*, 17925–17933.
[13] J. Zhang, L. Liu, H. Liu, M. Lin, S. Li, G. Ouyang, L. Chen, C. -Y. Su, *J. Mater. Chem. A* **2015**, *3*, 10990–10998.

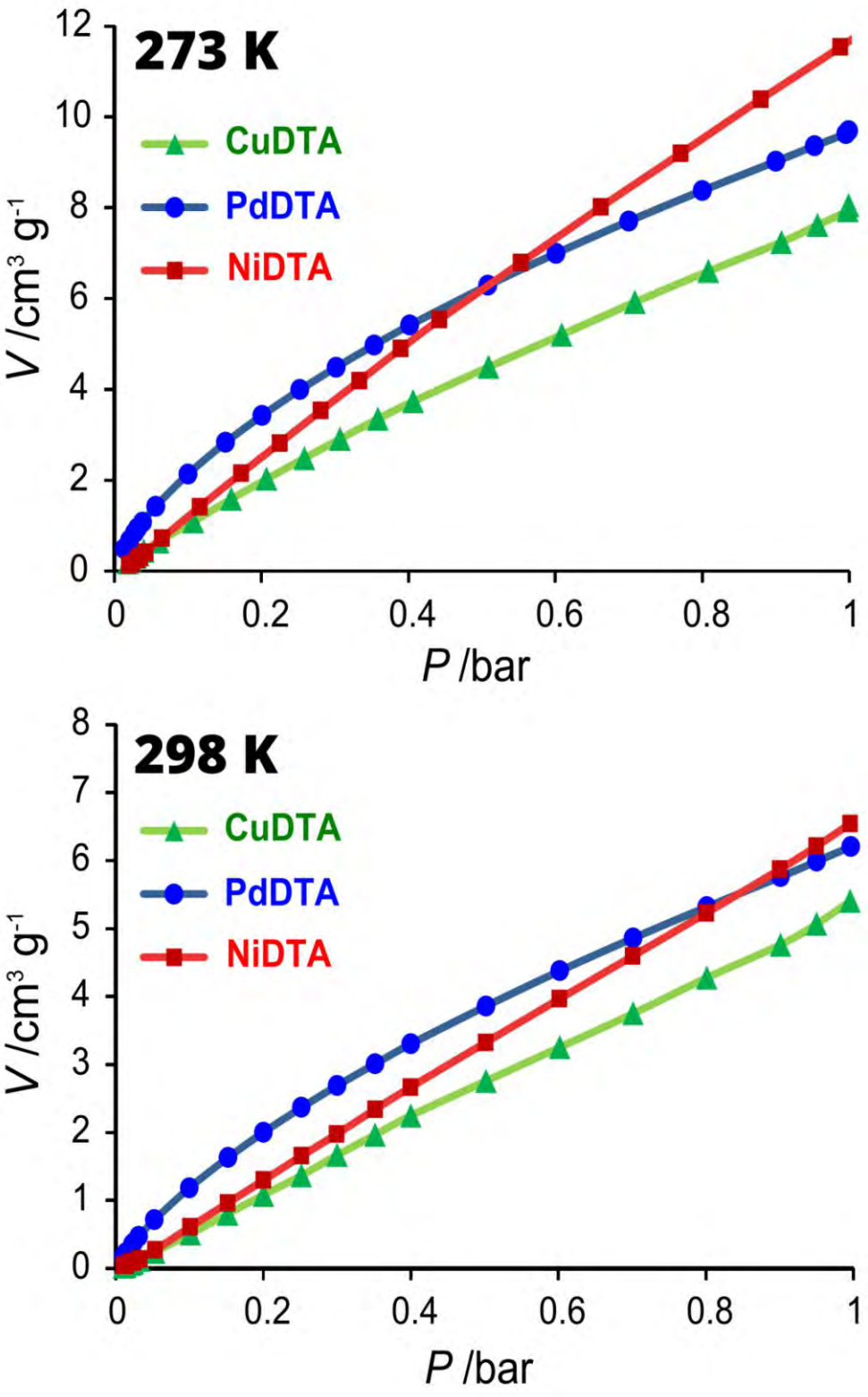

Figure S4.6. Experimental adsorption isotherms of homonuclear MOAs in CO_2 at 273 K.

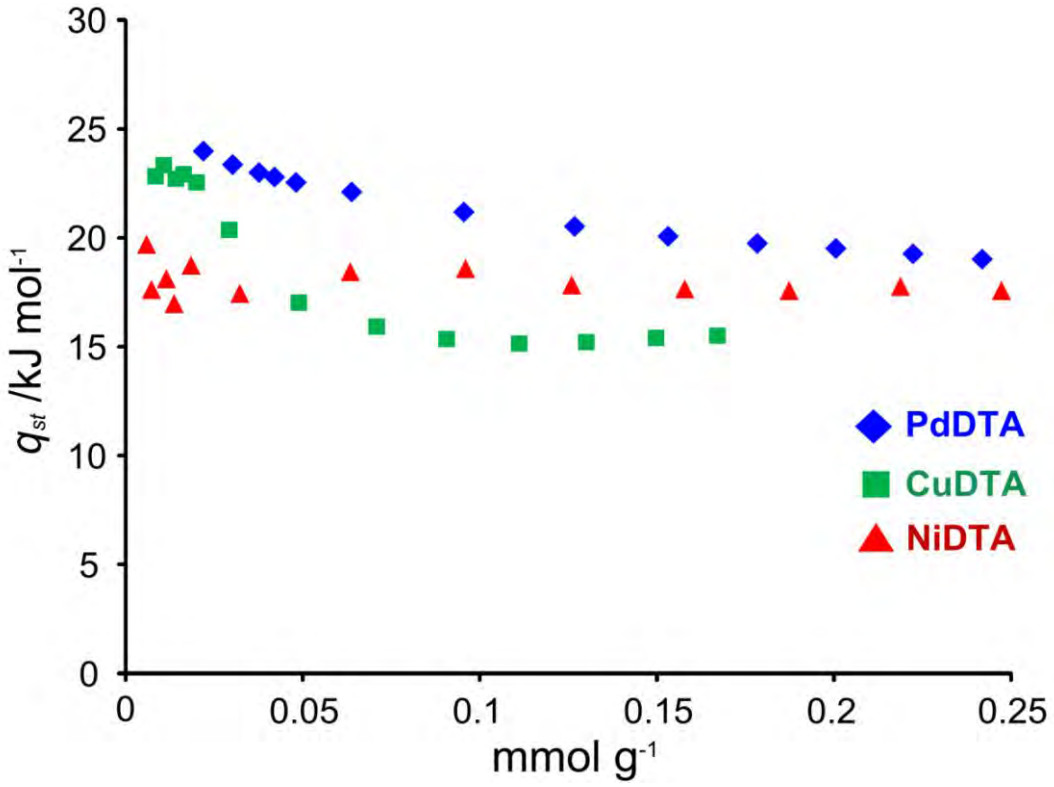

Figure S4.7. Isosteric heats of homonuclear MOAs for CO_2.

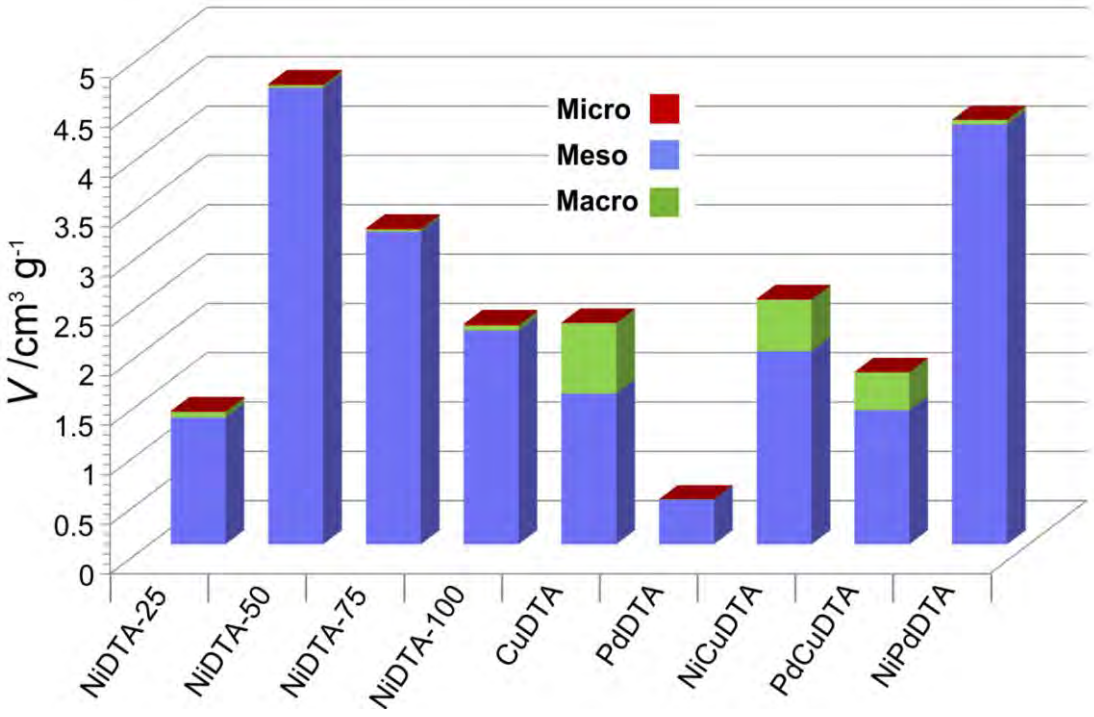

Figure S4.8. Micro-, meso- and macroporosity contribution to pore volume.

S5. CHEMICAL AND MECHANICAL RESISTANCE

Table S5.1. Chemical stability of NiDTA-MOG under different media and conditions. .

ACID/BASE		HYDROTHERMAL CONDITIONS		CONCENTRATED ACIDS/BASES	
293 K, pH = 0–14	Sta.	373 K, pH = 2–12	Sta.	Acetic acid (99 %)	Sta.
		473 K, pH = 2–12	Deg.	HCl (37 %)	Deg.
				HNO_3 (69 %)	Dis.
				H_2SO_4 (96 %)	Dis.
				NH_3 (36%)	Sta.
COORDINATING AGENTS				REDUCTANTS	
Terephthalic acid	Sta.	DEAM	Sta.	Na_2SO_3	Sta.
Trimesic acid	Sta. [c]	EDTA	Sta. [c]	$NaBH_4$	Deg.
2,2'-Bpy	Sta. [c]	TMED	Sta. [c]		
4,4'-Bpy	Sta. [c]	DET	Dis.		
Neocuproine	Sta.				
SOLVENTS				OXIDIZERS	
EtOH	Sta.	$CHCl_3$	Sta.	$KMnO_4$	Dis.
CH_2Cl_2	Sta.	Pyridine	Sta.	H_2O_2	Dis
Pentane	Sta.	CH_3CN	Sta.	HNO_3	Sta.
Toluene	Sta.	Et_2O	Sta.	I_2	Sta.
Acetone	Sta.				
SURFACTANTS AND ELECTROLYTES					
Pluronic-123		Sta.		$LiNO_3$	Sta.
Commercial soap		Sta.		NaCl	Sta.

[a] Sta.: stable, Deg.: degraded, Dis.: dissolved. [b] 2,2'-Bpy: 2,2'-bipyridine, 4,4'-Bpy: 4,4'-bipyridine, DEAM: diethanolamine, EDTA: ethylenediaminetetraacetic acid, TMED: *N,N,N',N'*-tetramethylethylenediamine, DET: diethylenetriamine; Pluronic-123: poly(ethylene glycol)-block-poly(propylene glycol)-block-poly(ethylene glycol) with an average mass of approximately 5800 g mol^{-1}. [c] The gel remains stable but some additional peaks coming from the ligand are observed in the FTIR spectra of the sample.

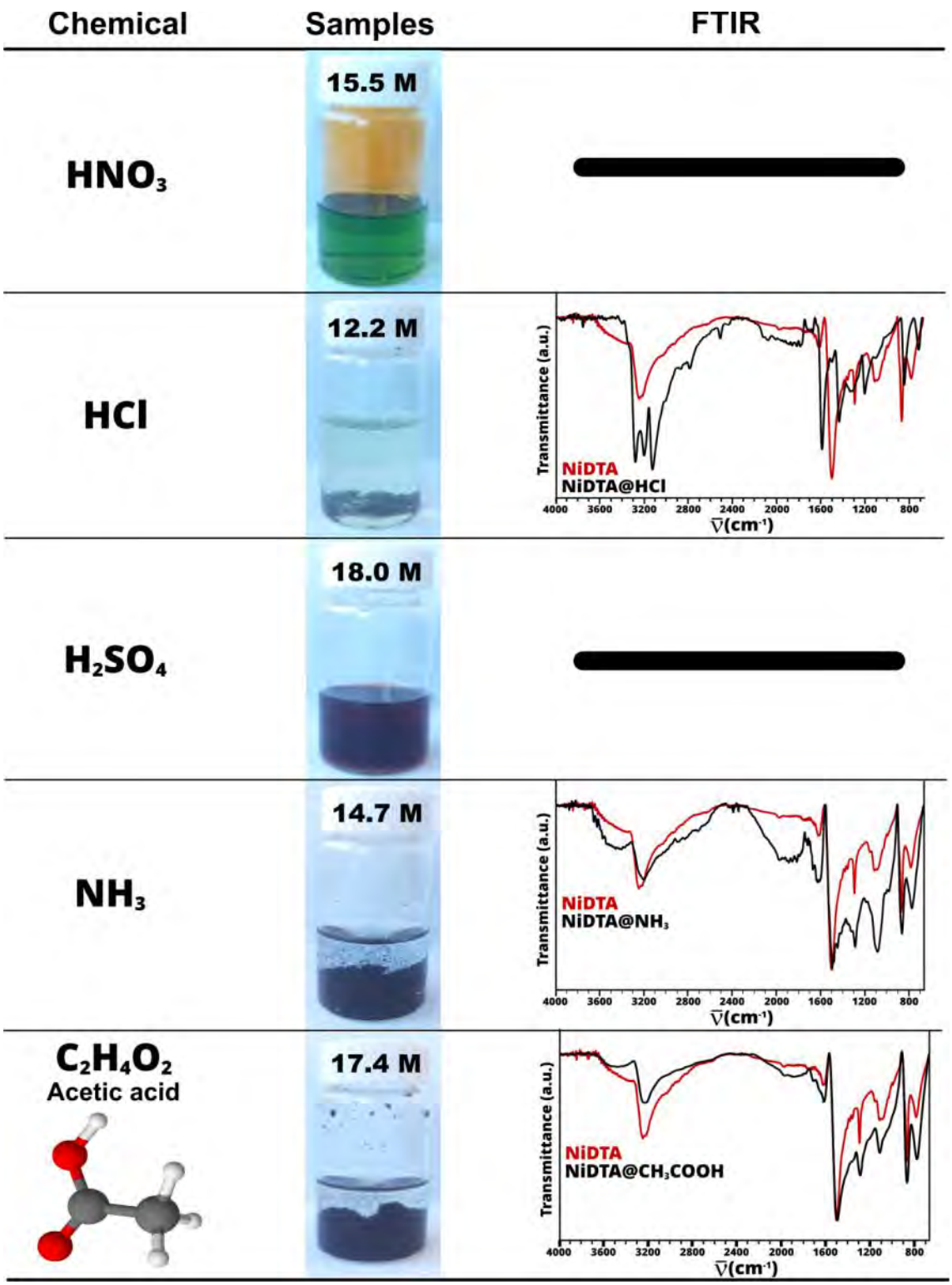

Figure S5.1. Chemical inertness tests carried out over NiDTA gel employing concentrated acids and bases.

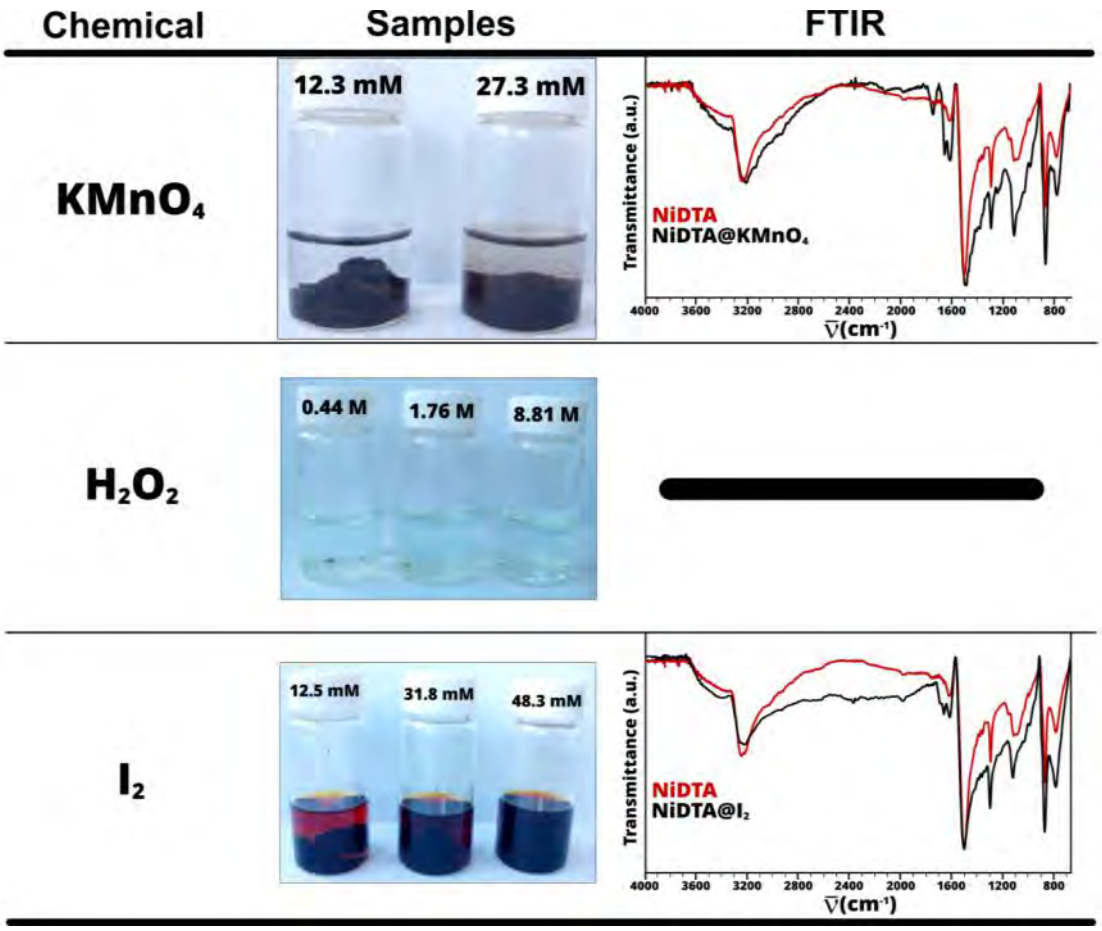

Figure S5.2. Chemical inertness tests carried out over NiDTA gel employing oxidants. Note that $KMnO_4$ dissolves partially the gel since an amount below the stoichiometrically required was used, and thus, the FTIR corresponds to the undissolved gel.

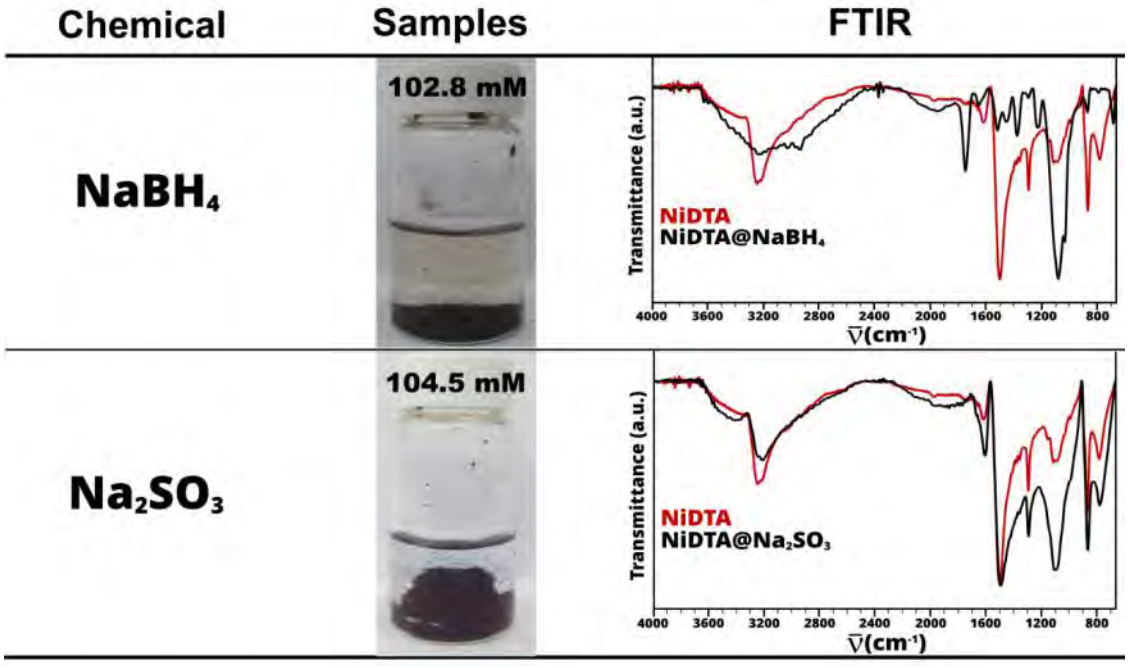

Figure S5.3. Chemical inertness tests carried out over NiDTA gel employing reducing agents.

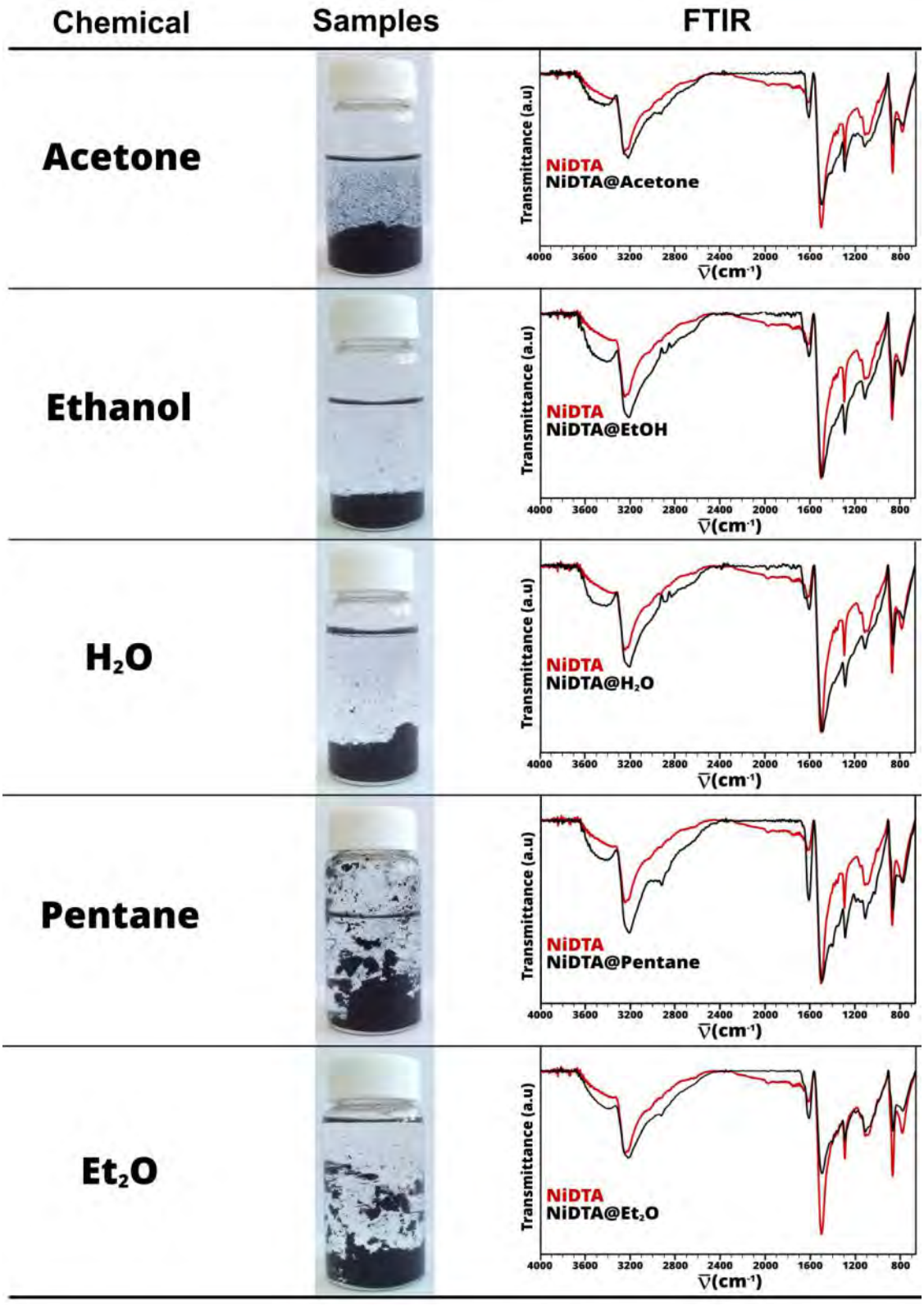

Figure S5.4. Chemical inertness tests carried out over NiDTA gel using several solvents (part 1)

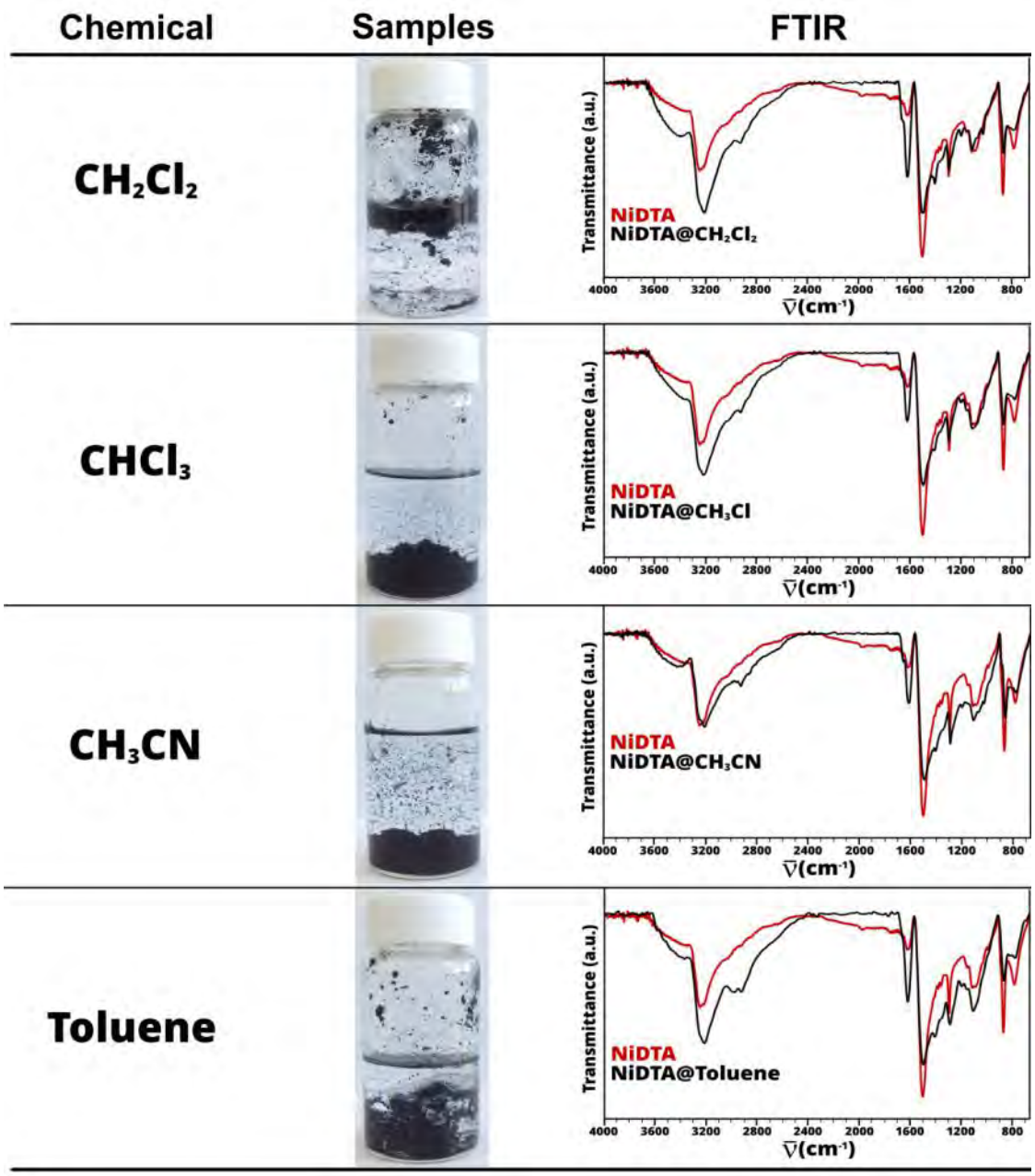

Figure S5.5. Chemical inertness tests carried out over NiDTA gel using several solvents (part 2)

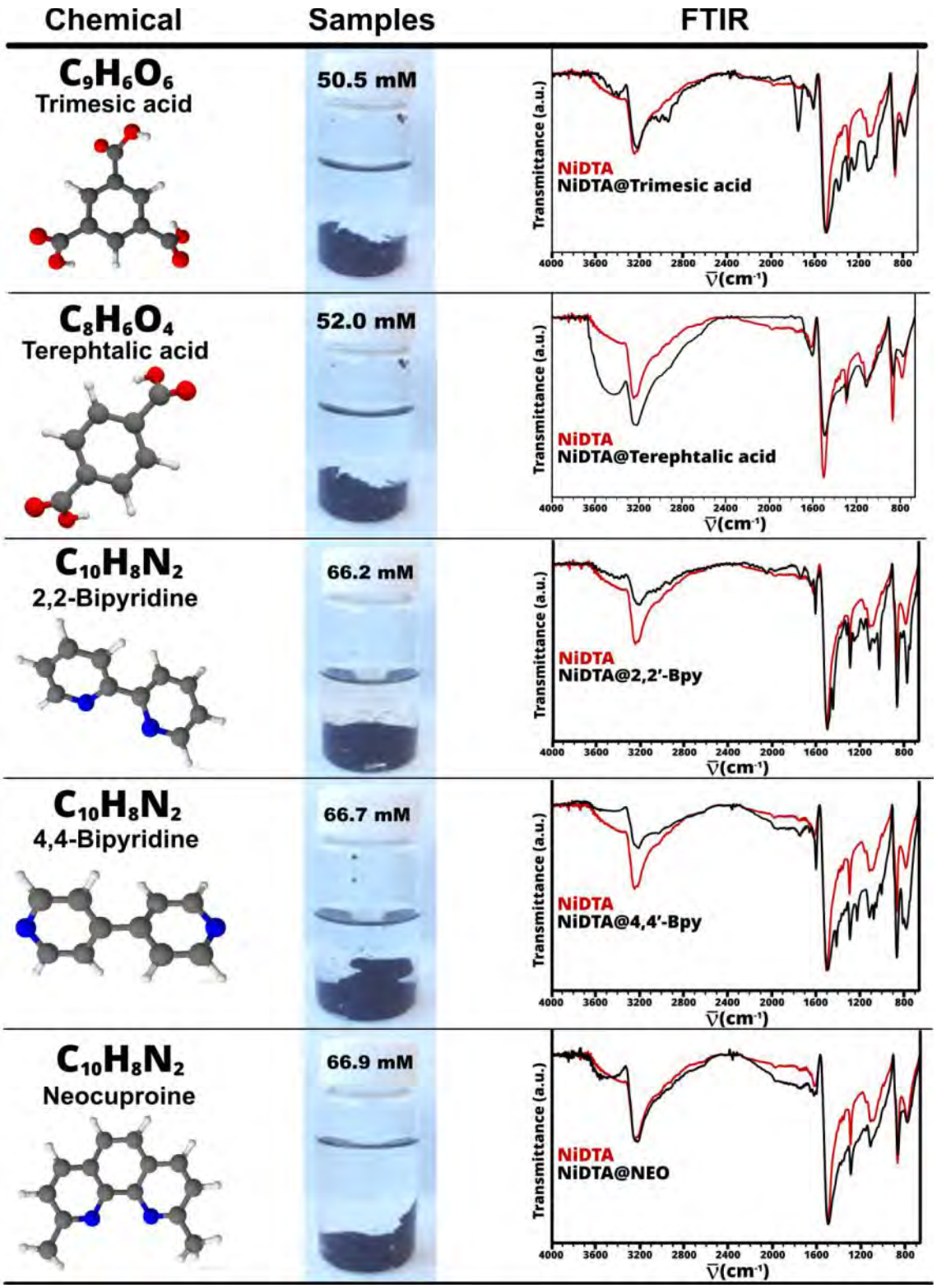

Figure S5.6. Chemical inertness tests carried out over NiDTA gel employing coordinating agents (part 1).

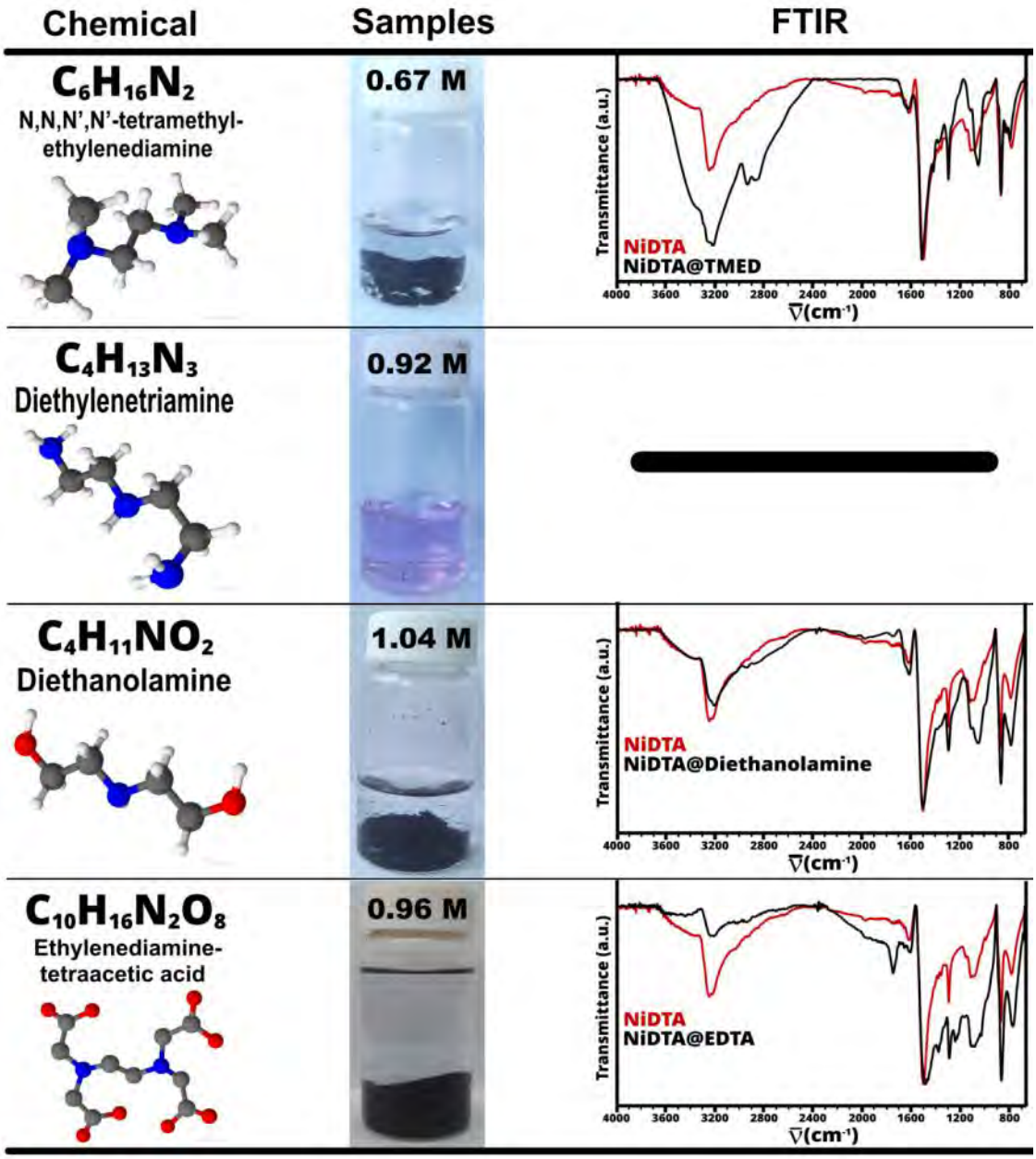

Figure S5.7. Chemical inertness tests carried out over NiDTA gel employing coordinating agents (part 2).

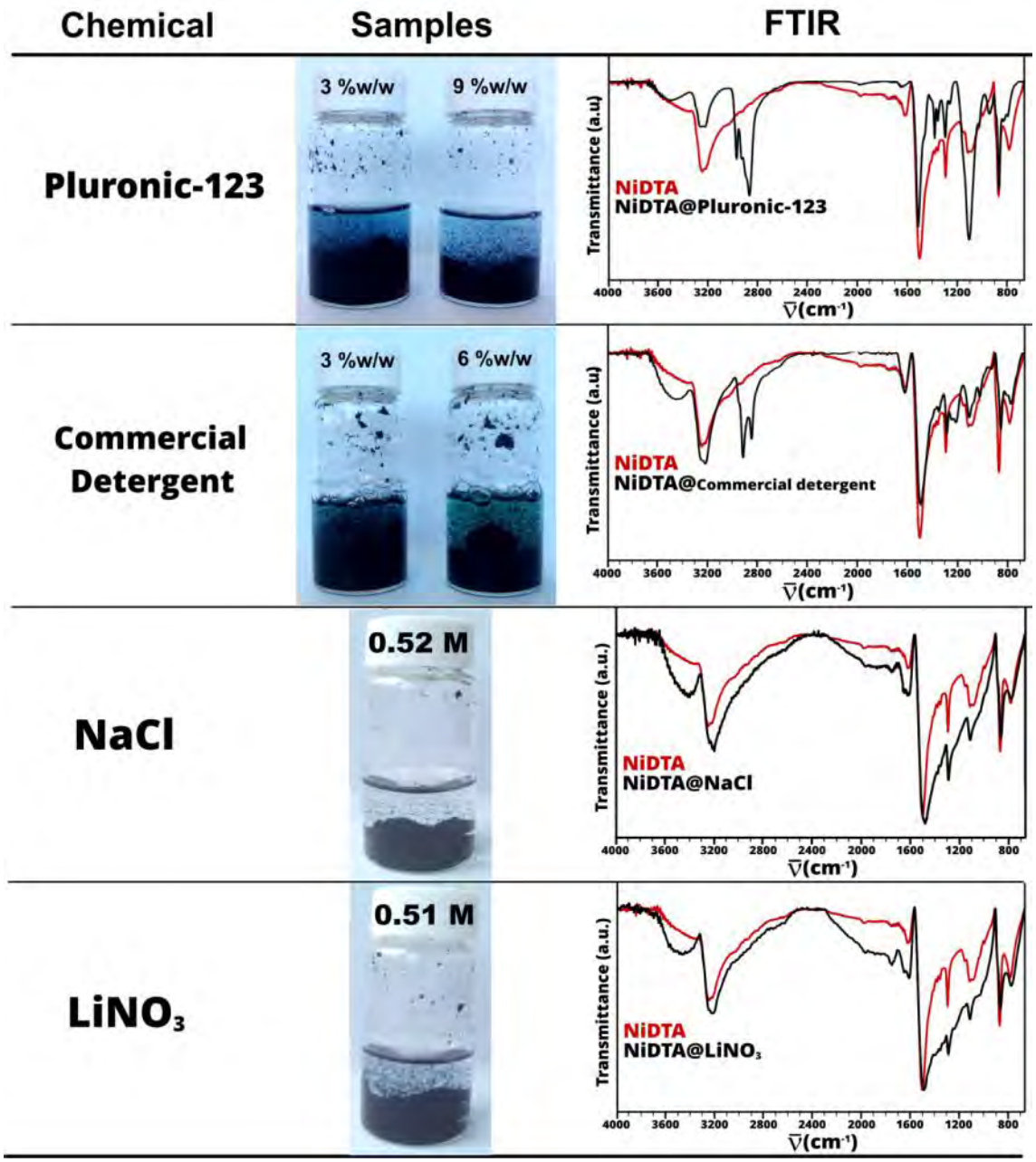

Figure S5.8. Chemical inertness tests carried out over NiDTA gel employing surfactants and saline solutions.

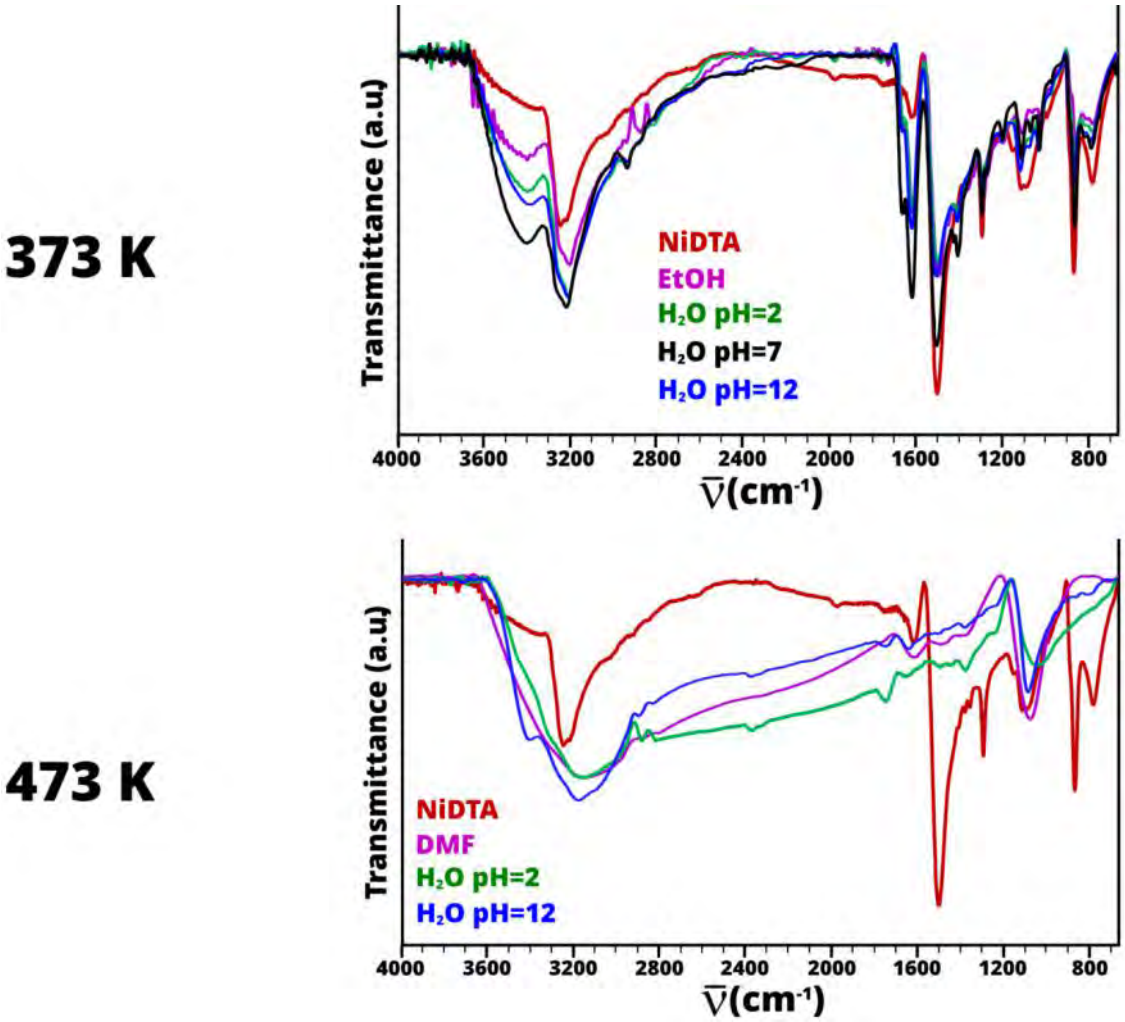

Figure S5.9. Chemical inertness tests carried out over NiDTA gel applying solvothermal conditions.

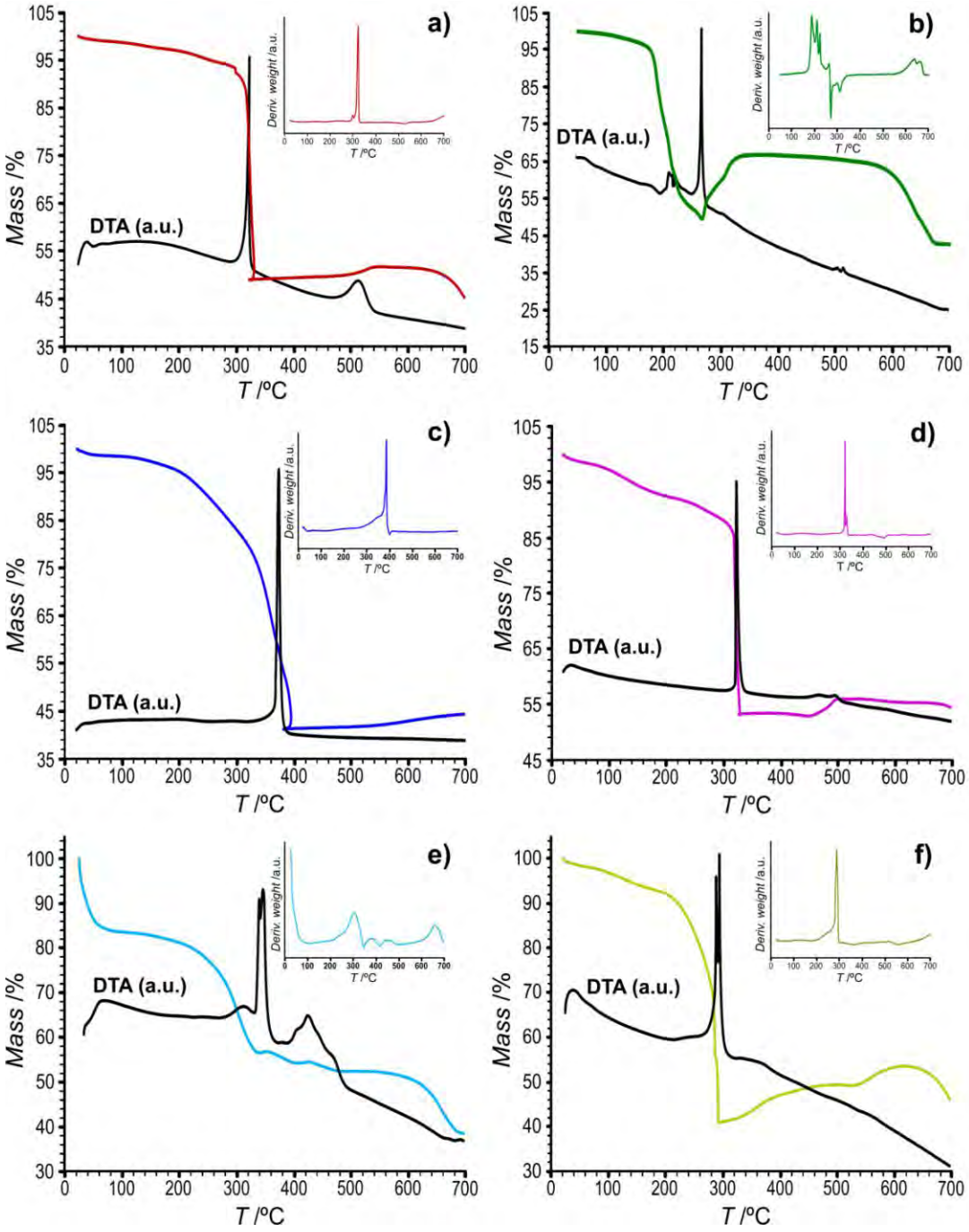

Figure S5.10. Thermogravimetric curves of MOAs in synthetic air: a) NiDTA, b) CuDTA, c) PdDTA, d) NiPdDTA, e) PdCuDTA and f) NiCuDTA. Prior to pyrolisis stage, aerogels lose between 8−20% of its mass due to removal of solvent molecules retained during its preparation (DMF, DMA, EtOH) and the humidity that may have adsorb from the environment.

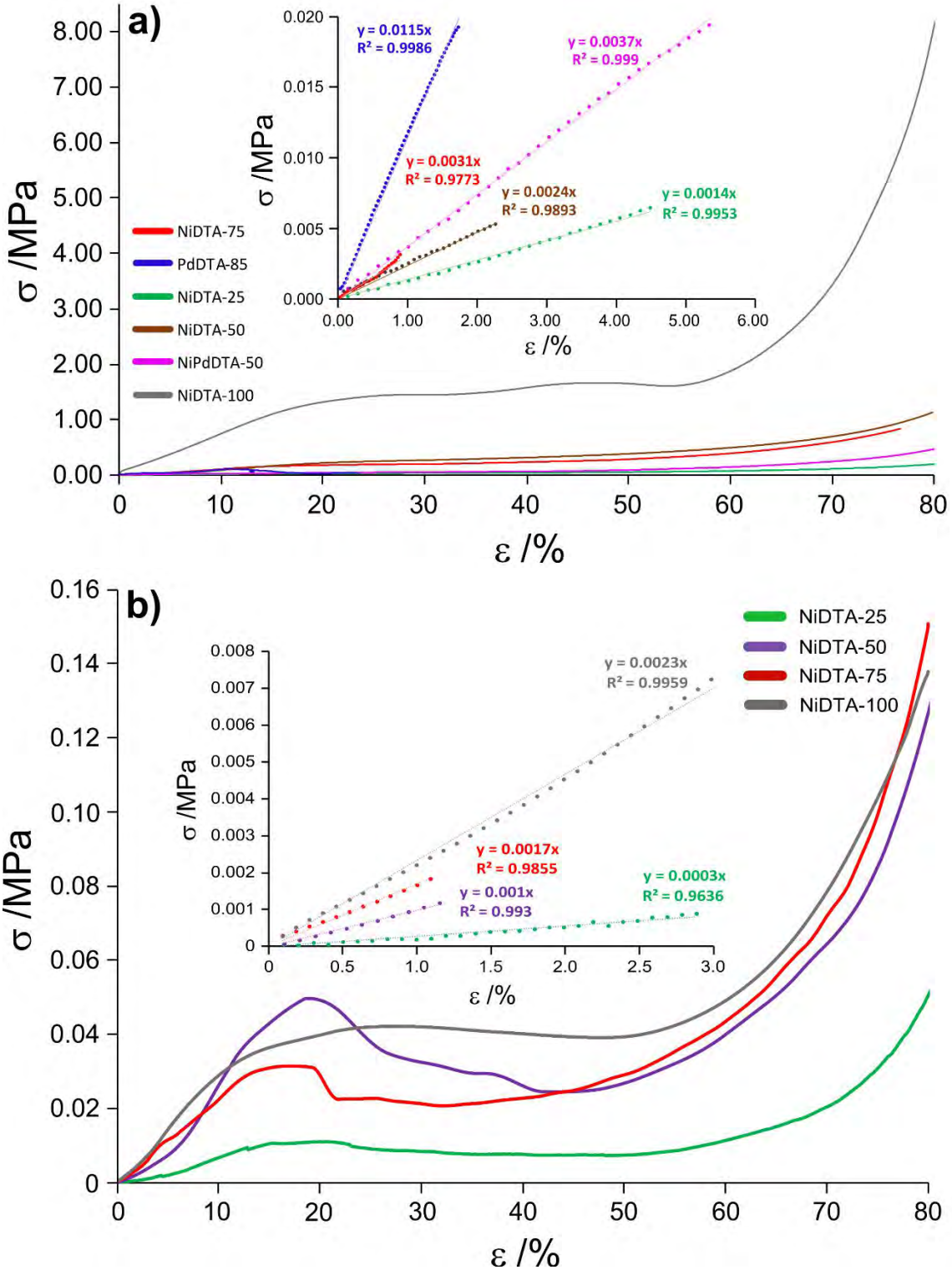

Figure S5.11. Compression-strain curves performed over a) Ni/Pd system based aerogels and b) NiDTA metallogels and their respective linear fits (inset graphics) for determining the Young's modulus.

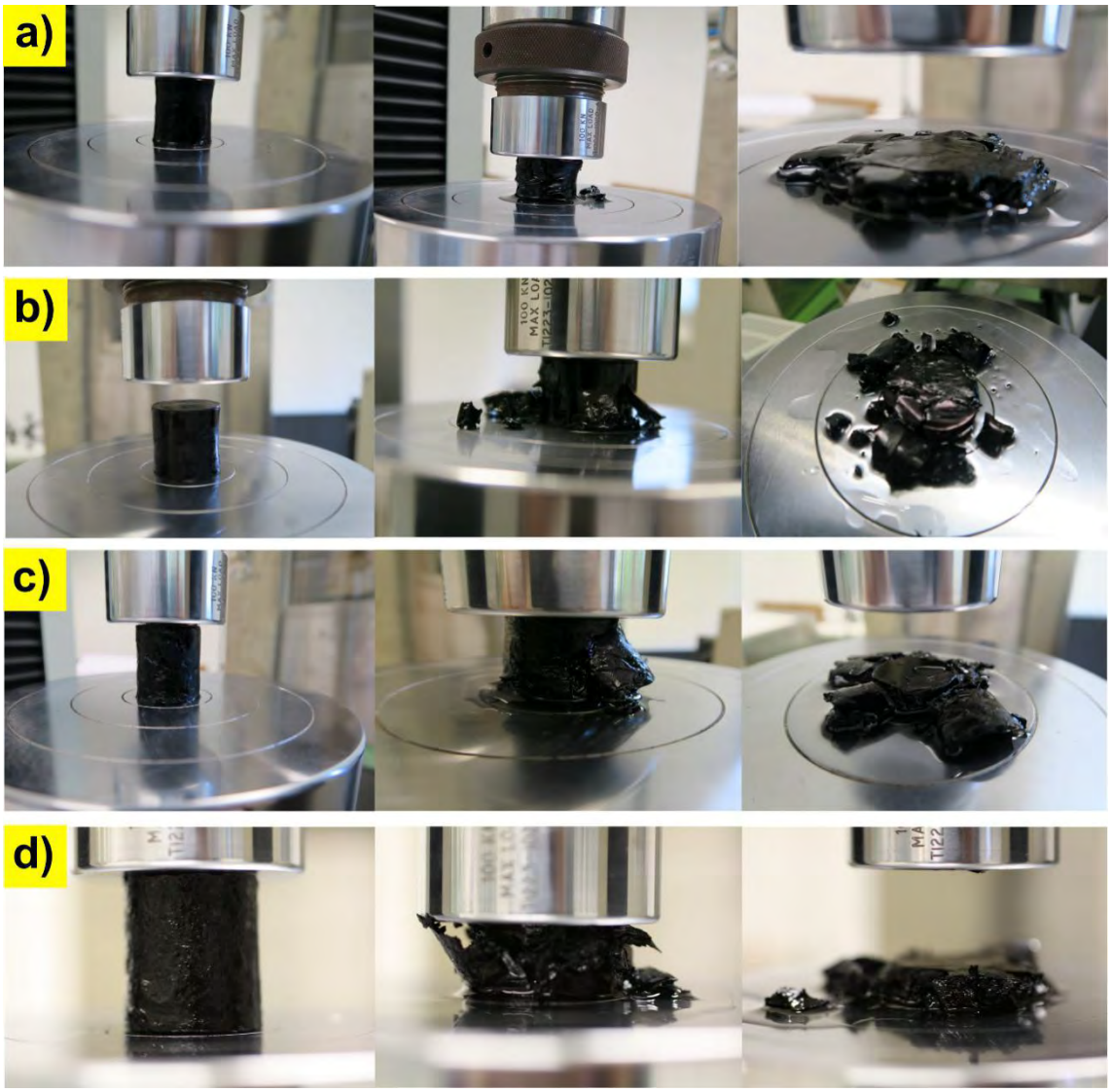

Figure S5.12. Images taken during compression tests for NiDTA metallogels: a) 25 mM. b) 50 mM. c) 75 mM, d) 100 mM.

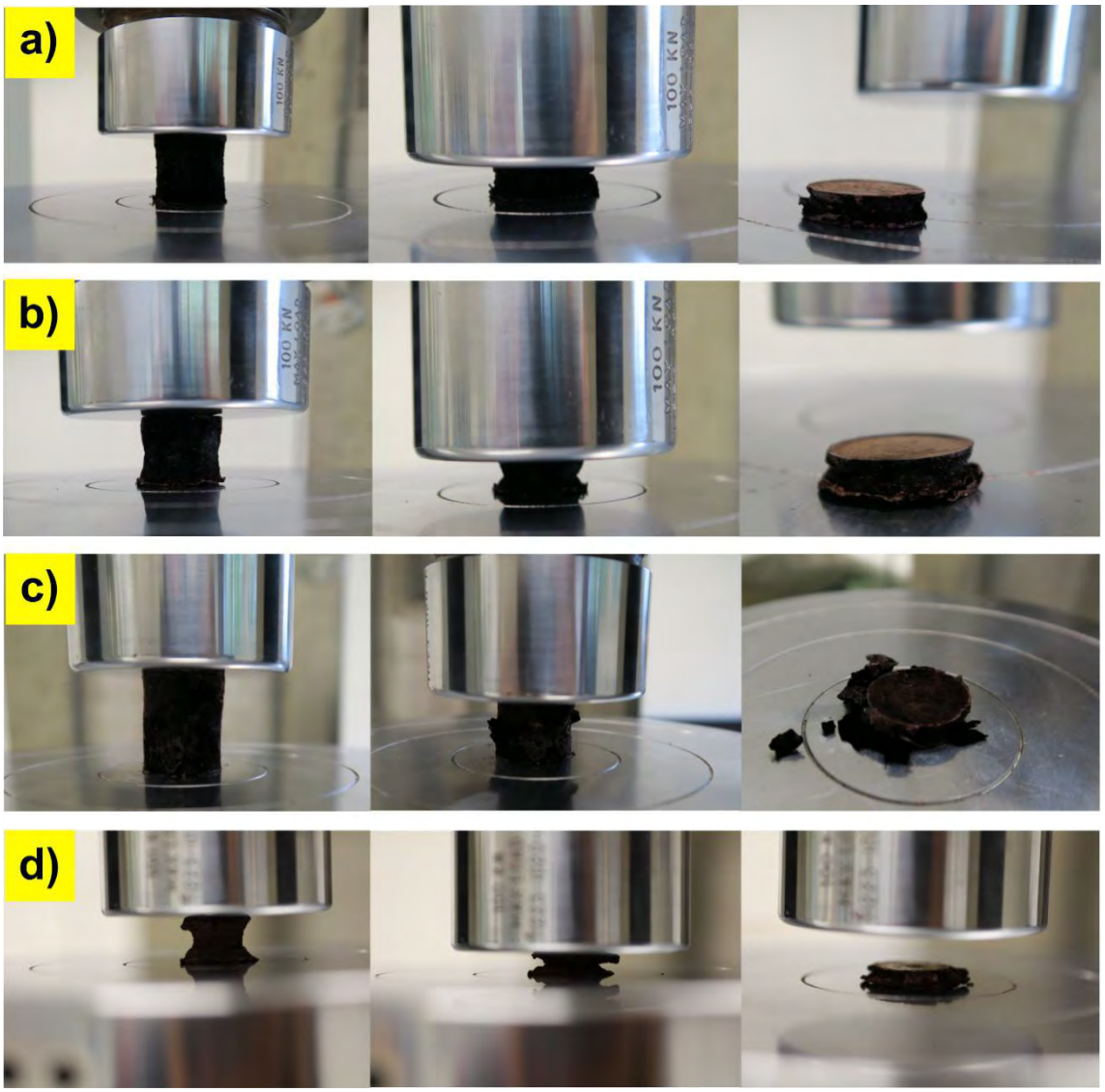

Figure S5.13. Images acquired during compression tests for NiDTA aerogels: a) 25 mM. b) 50 mM. c) 75 mM, d) 100 mM.

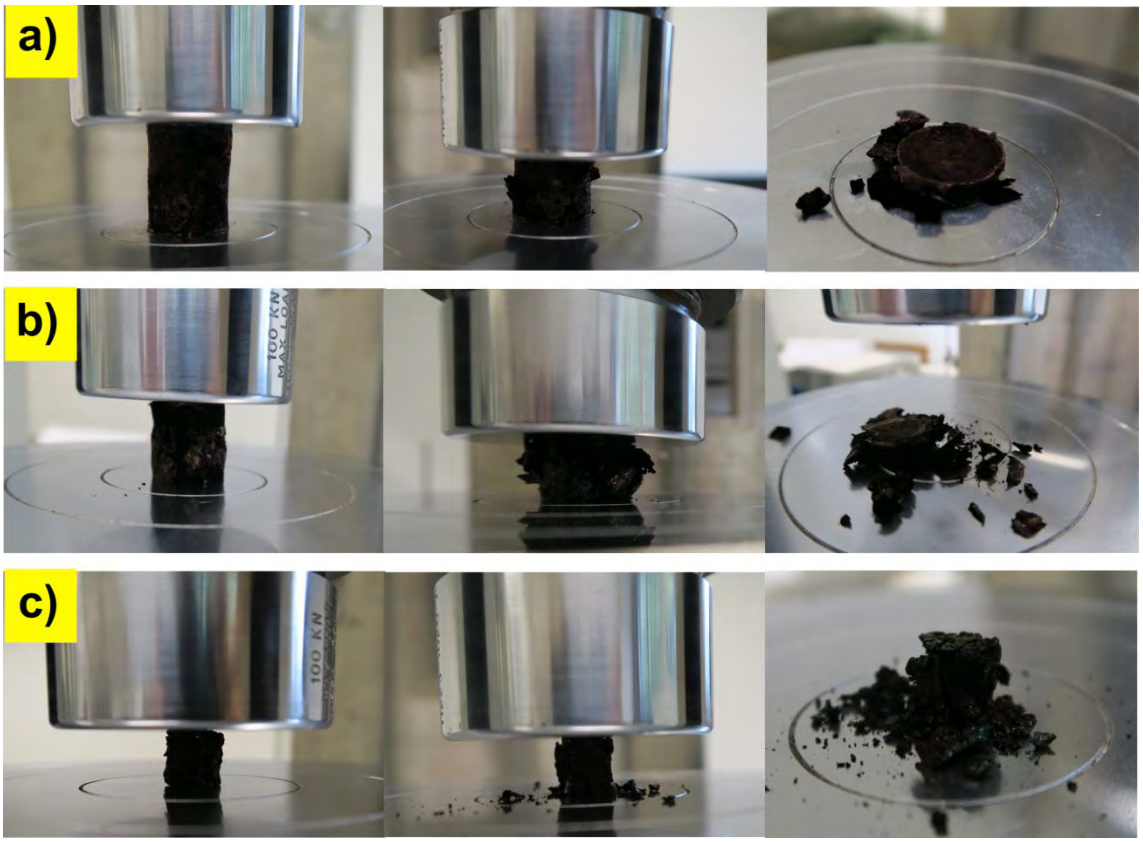

Figure S5.14. Images acquired during compression tests for MDTA aerogels: a) NiDTA. b) NiPdDTA. c) PdDTA.

S6. CONDUCTIVITY MEASUREMENTS

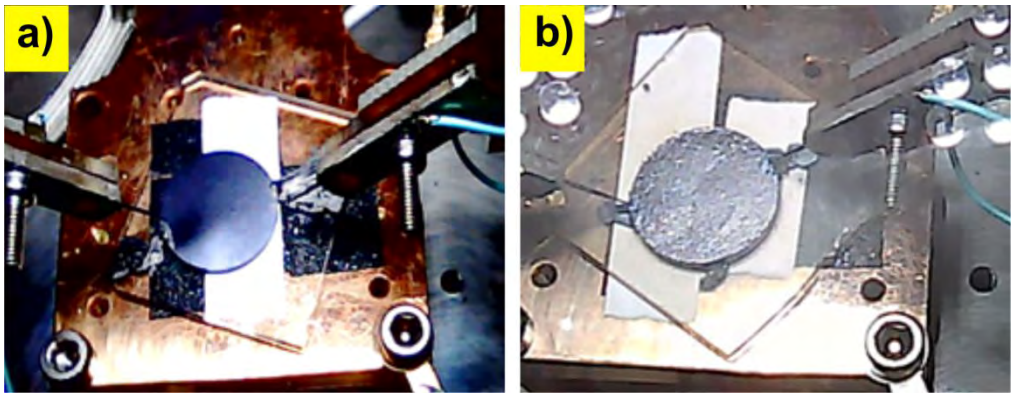

Figure S6.1. Images acquired during DC measurements for a) CuDTA and b) NiCuDTA pellets.

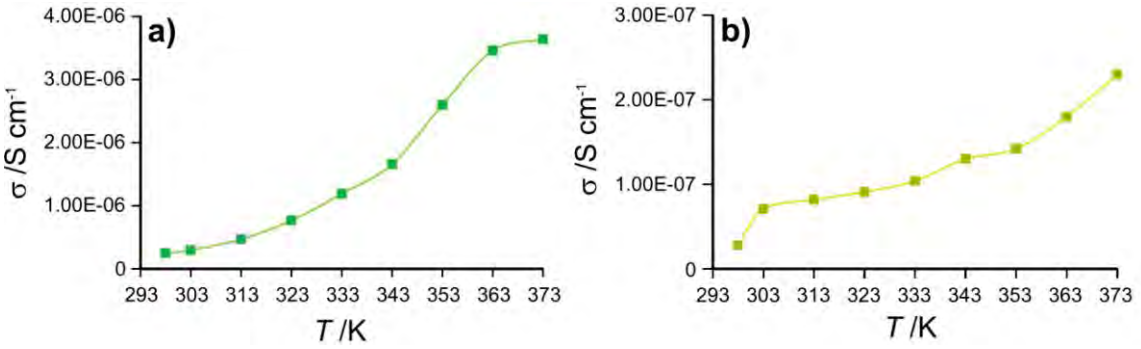

Figure S6.2. Conductivity versus temperature curves for a) CuDTA and b) NiCuDTA pellets.

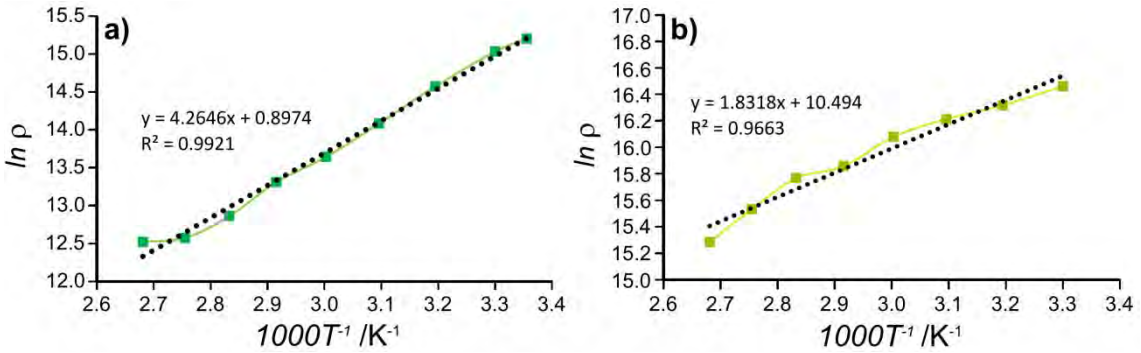

Figure S6.3. Natural logarithm of the resistivity versus the inverse of temperature curves for a) CuDTA and b) NiCuDTA pellets.

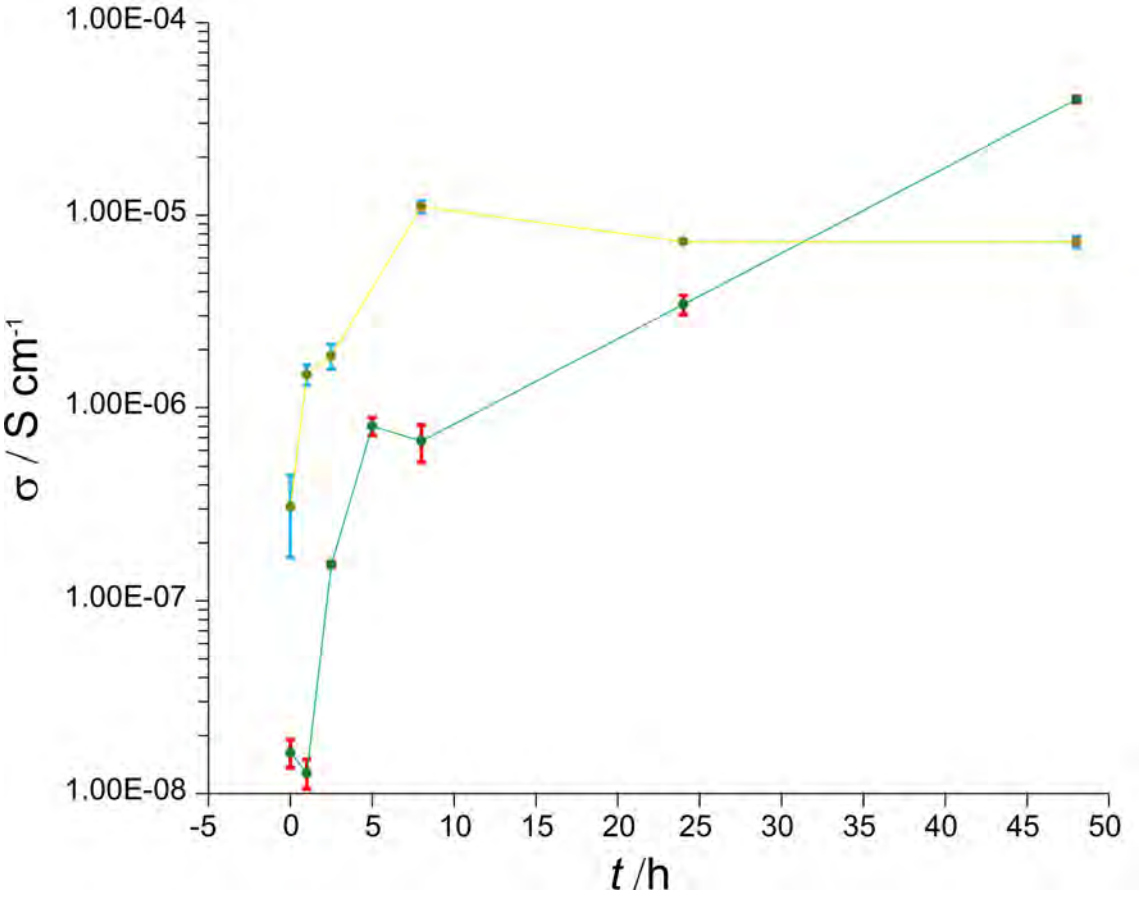

Figure S6.4. Variation of conductivity after different exposure times to AcOH vapors at 298 K for (a) CuDTA and (b) NiCuDTA.

It must be emphasized that in both compounds the greatest conductivity variation occurs at the initial period of exposure, which is an interesting feature for a sensible stimuli-response material. Furthermore, the capacity of these materials to reversibly respond to chemical stimuli provides a chance to explore their application in gas detection.

AC Conductivity measurements**:**

Through plane ionic conductivities of the MOAs materials CuDTA and CuNiDTA were determined by means of complex impedance analysis in the temperature range of 298 K. The two-point technique (through plane) used two stainless steel probes in contact with opposite sides of the measured material. The probes were used to source current and measure the voltage drop. The electrochemical measurements were carried out with an Autolab electrochemical system II PGSTAT30 (Ecochemie, The Netherlands)

impedance analyzer. The frequencies were swept from 1 MHz to 1 Hz against the open circuit potential recording ten points per decade with AC signal amplitude of 10 mV. All the EIS data were fitted employing a ZView 3.1 software (Scribner Association) using equivalent circuit as shown below:

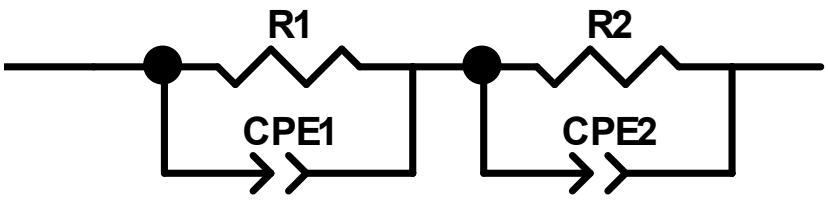

All impedance spectra show two overlapped contributions ascribed to the bulk and the grain boundary. R_1 and CPE_1 are considered the bulk resistance and the constant phase element representing a no ideal capacitance of the pellet and R_2 (Ω) and CPE_2 are resistance and no ideal capacitance typical of materials with capacitive behavior between the mobile ions (that are blocked by the electrode–electrolyte interphase). R_1 (Ω) is used to find the specific conductivity, σ (S cm^{-1}) of the sample according to the equation:

$$\sigma = \frac{l}{R_1 \cdot A}$$

Where A (cm^2) and l (cm) are the area and the thickness of the pellet.

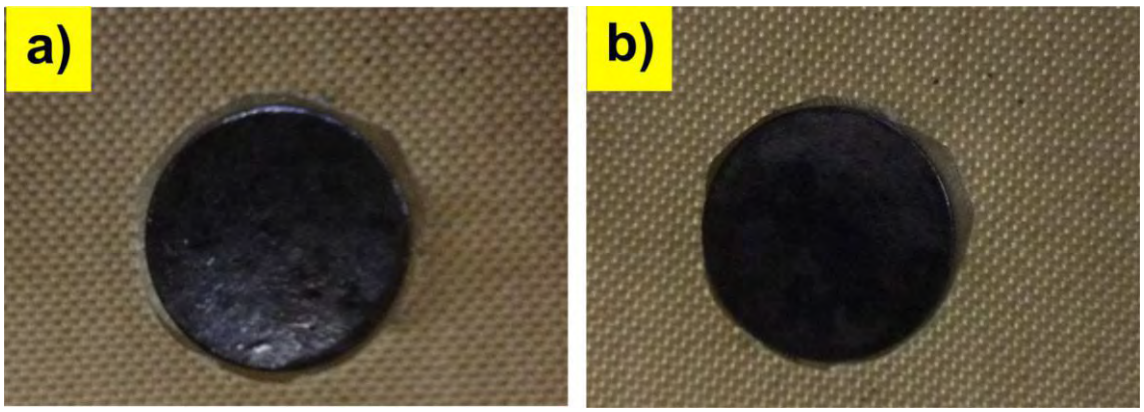

Figure S6.5. Acquired images of CuDTA pellets during AC measurements after having been exposed to acetic acid vapor: a) t = 24 h. b) t = 48 h.

Figure S6.6. Image of MOXs pressed into pellets.

S7. FREEZE-DRIED SAMPLES

Freeze-drying of the gels produced monoliths that retain their shape with a radial shrinkage comparable to that of CO_2 supercritical drying. However, the growth of the water crystals during the cooling with N_2(l) promotes the fusing of the nanofibers into a lamellar structure. As a result the solid is mainly macroporous with an almost negligible surface area (10 m^2/g) and extremely brittle (in fact, it is very difficult to manipulate without fracturing). Optical and SEM images are provided below.

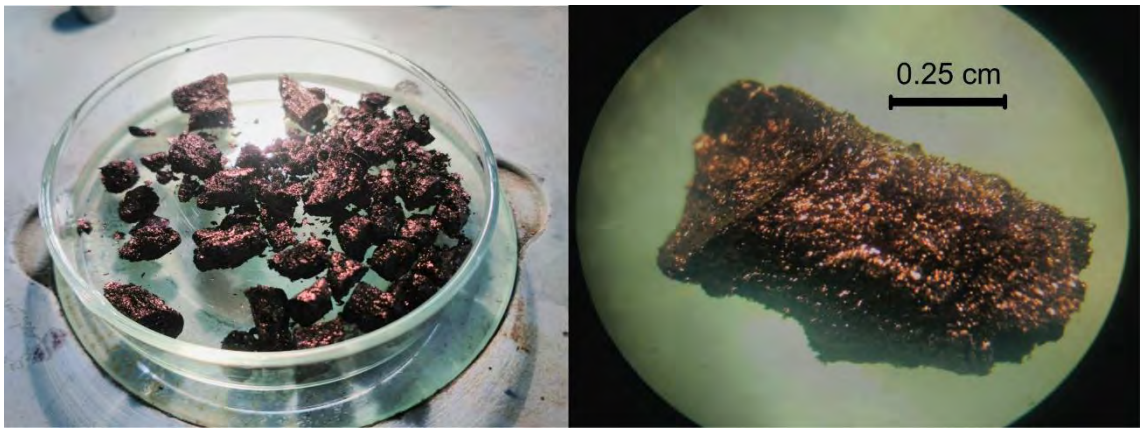

Figure S7.1. Photographs of brittle freeze dried NiDTA samples.

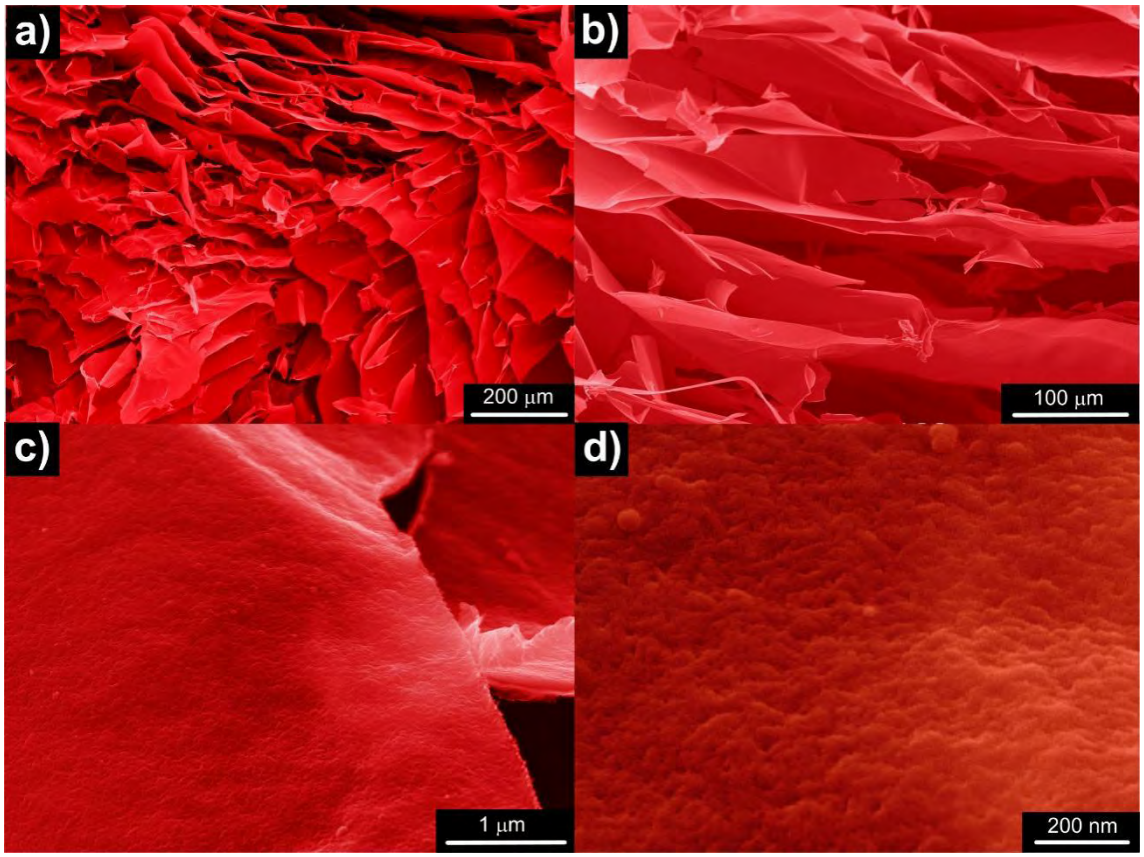

Figure S7.2. SEM images of freeze-dried NiDTA: a) 0.1 kX; b) 0.25 kX; c) 25 kX and d) 100 kX.

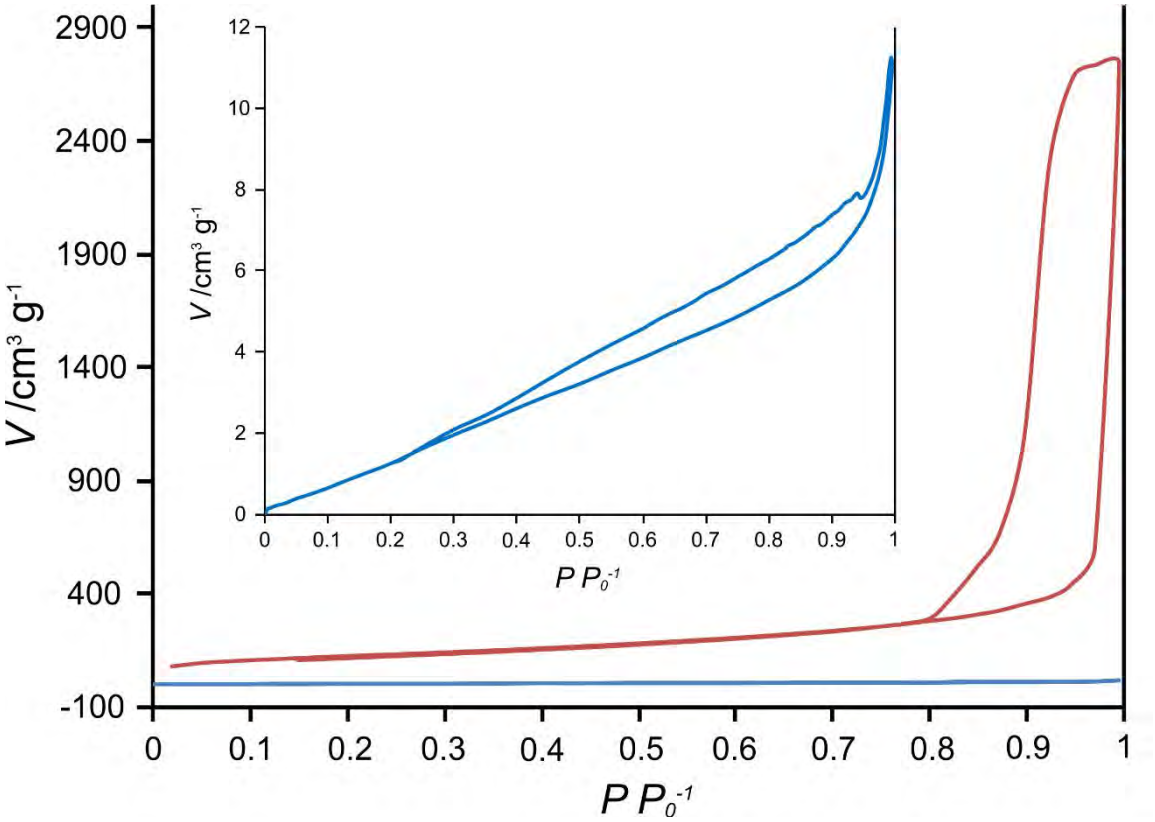

Figure S7.3. N_2 adsorption isotherms at 77 K for freeze-dried (blue) and supercritically dried (red) NiDTA-50 mM.

S8. PHYSICAL MEASUREMENTS

Physical Measurements: True density of samples was determined by an automatic helium microultrapycnometer of Quantachrome Instruments. Elemental analyses (C, H, N) were performed on a Euro EA elemental analyzer, whereas sulfur and metal contents were determined by inductively coupled plasma atomic emission spectrometer (ICP-AES) from Optima 8300. Furthermore, chemical quantitative analysis of the samples was also performed on xerogels using a SPECS X-ray photoemission spectrometer equipped with Phoibos 150 1D-DLD analyzer and employing Al K_α (1486.6 eV) as monochromatic radiation source. The C_{1s} peak was set at 284.6 eV to correct charge effects and the spectrometer was previously calibrated using Ag $3d_{5/2}$ peak (368.28 eV). The spectra were fitted by modeling Gaussian-Lorentzian contributions by CasaXPS 2.3.16 software. Infrared spectra (ATR mode) were recorded at a resolution of 4 cm^{-1} on a FTIR 8400S Shimadzu spectrophotometer for a total of 40 scans in the 4000–650 cm^{-1} spectral region by using a horizontal single-reflection ATR ZnSe prism. Raman spectra were taken with an Invia Reflex Raman Renishaw microscope employing 785 nm as excitation wavelength (Torsana laser) and a working power less than 1 %. Raman signals were collected at an angle of 180° to the incident laser beam in the 150−3500 cm^{-1} frequency range after making 10 accumulations of 30 s. Glass-sustained xerogel pellets were used for X-ray diffraction (XRD) measurements on a Phillips X'PERT powder diffractometer with Cu-Kα radiation (λ = 1.5418 Å) over the range $5 < 2\theta < 70^{o}$ with a step size of 0.02º, a variable automatic divergence slit and an acquisition time of 2.5 s per step at 298 K.

Transmission Electron Microscopy (TEM) images were acquired using a Philips CM200 microscope by depositing a drop of a dilute ethanolic dispersion of the metallogels on a carbon-coated Cu (300 mesh) grid. It deserves to note that a surfactant (*n*-decylamine) was required as dispersing agent, since the fibers composing the gel

showed high predisposition to aggregate as cobwebs-like structures, even at very low concentrations. Atomic Force Microscope (AFM) images were acquired in dynamic mode using a Nanotec Electronica system operating at room temperature in ambient air conditions. Olympus cantilevers with a nominal force constant of 0.75 N m^{-1} and a resonance frequency of about 70 kHz were used. The images were processed using the WSxM software. The substrates employed were SiO_2 (300 nm thickness)/Si (IMS Company). SiO_2 surfaces were sonicated in ultrasound bath at 37 KHz and 380 W, for 15 min in acetone and 15 min in *2*-propanol and then dried under an argon flow. The AFM samples were prepared from a suspension of 3 mg NiDTA in 3 mL of ultrapure EtOH. The mixture was sonicated with a tip during 25 seconds (24 KHz, 80%) to give a bluish suspension. 20 μL of this suspension were deposited on SiO_2 substrates by drop casting and allowed to adsorb for 4 min at room temperature. The remaining suspension was removed blowing with an argon flow. Scanning Electron Microscopy (SEM) studies were carried out on a JEOL JSM-7000F microscope operated at 10–20 kV and coupled with an energy X-Ray spectrometer (EDX). Specimens were mounted on conductive carbon adhesive tabs and imaged after chromium sputter coating of 5 nm to make them conductive. Dinitrogen (77 K) and carbon dioxide (273 and 298 K) physisorption data were measured on activated samples (vacuum at 423 K for 4 h) with a Quantachrome Autosorb-iQ-MP. The specific surface area was calculated from the adsorption branch in the relative pressure interval using the Brunauer–Emmett–Teller (BET) method.[14] Thermal analyses (TG/DTA) were recorded on a TA Instruments SDT 2960 thermal analyzer from room temperature to 973 K in a synthetic air atmosphere (79% N_2 / 21% O_2) with a heating rate of 5 ºC min^{-1} and with an outflow of 150 cm^3 min^{-1}.

[14] S. Brunauer, P. H. Emmett, E. Teller, *J. Am. Chem. Soc.* **1938**, *60*, 309–319

A MTS Insight testing device with a 2.5 kN load cell was used to record compression-strain curves. Cylindrical specimens tested had an approximated diameter of 25–28 mm for gels and 10–18 mm for aerogels. The length of the pieces ranged from 11 to 30 mm. More than 5 repetitions for each material were made in order to ensure the reproducibility and test pieces were distracted to failure or to a maximum deformation of 80 % at a rate of 1 mm min^{-1}.

DC and AC electrical conductivity measurements were performed on sample disks (area: 1.13 cm^2; thickness: 0.025–0.030 cm) pressed at 10^4 kg cm^{-2} (Figure 6.1). Temperature-variable DC measurements (298–373 K) were made under vacuum (10^{-3} hPa). The contacts were made with tungsten wires (25 μm diameter). The samples were measured applying an electrical current with voltages from +10 to -10 V, on a Quantum Design PPMS-9 connected to an external voltage source (Keithley model 2450 source-meter) and an ammeter (Keithley 6514 electrometer model). Iodine doping was achieved by placing the pressed pellets in a closed vessel containing some iodine crystals. Doping occurs by absorption of the iodine vapour. The doping time was 94 hours. To assess the stimuli-response behavior to acetic acid vapours (AcOH), AC measurements were performed using an Autolab electrochemical system II PGSTAT30 (Ecochemie, The Netherlands) electrochemical impedance analyzer over the frequency range from 1 Hz to 1 MHz with an applied voltage of 0.01 V. Vapor exposure times were varied from 1 to 48 h. All measurements were collected at 298 K using a two-probe method. The electrical contact between the sample and the symmetric stainless steel (SS) disk electrodes, for the through plane measurements, was made by applying a pressure of 350 N cm torque with a conductivity cell configuration SS/sample/SS. Each impedance measurement was repeated three times using a fresh pellet.

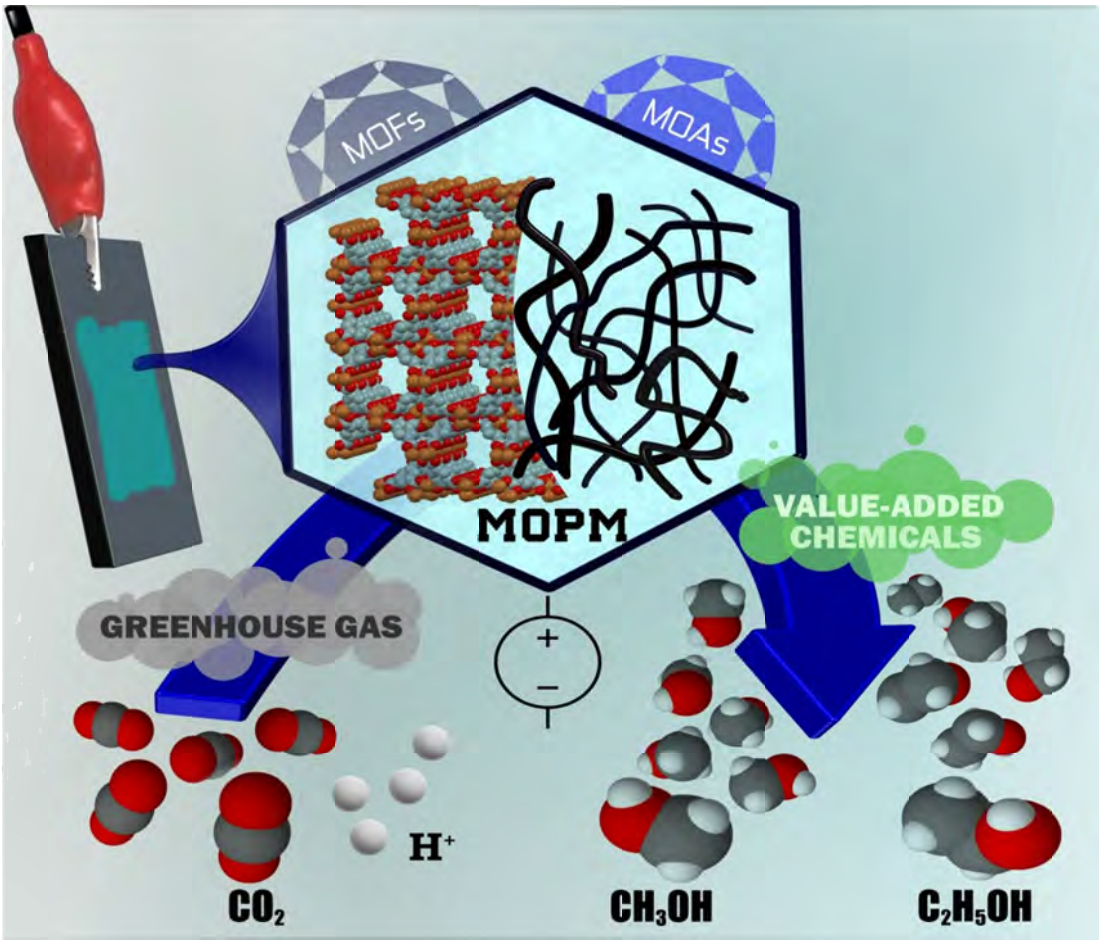

5. Cu-BASED METAL-ORGANIC POROUS MATERIALS FOR CO_2 ELECTROCATALYTIC REDUCTION TO ALCOHOLS

5.1. SUMMARY

After studying in chapter 4 some of the most outstanding physicochemical properties of metal-dithiooxamidato MOGs and MOAs, the following chapter evaluates the redox capacities of different porous metal-organic porous materials (MOPMs) of Cu(II) in the catalytic electroreduction of CO_2: (1) HKUST-1 metal-organic framework (MOF), $[Cu_3(\mu_6\text{-}C_9H_3O_6)_2]_n$; (2) CuAdeAce MOF, $[Cu_3(\mu_3\text{-}C_5H_4N_5)_2]_n$; (3) CuDTA mesoporous metal-organic aerogel (MOA), $[Cu(\mu\text{-}C_2H_2N_2S_2)]_n$; and (4) CuZnDTA MOA, $[Cu_{0.6}Zn_{0.4}(\mu\text{-}C_2H_2N_2S_2)]_n$. MOFs are hybrid materials containing three well-differentiated sites to which the catalytic function can be allocated, namely, the metallic component, the organic linker, and the pore space. MOFs are considered as ideal candidates for CO_2 adsorption, separation, and reduction through catalyzed reactions. This is because of their combined favorable properties of large surface area, high porosity, tunable pore-size, and shape-selective character. Indeed, MOFs are particularly suitable for electrochemical reactions as a result of these features in addition to their high electronic conductivities. On the contrary, examples of metal-organic aerogels (MOAs) are relatively scarce compared with the more conventional MOFs and, to the best of our knowledge; no studies have dealt with their use as electrocatalysts for CO_2 reduction.

In this study, each MOPM was deposited on a gas diffusion layer to form a characteristic gas–solid–liquid three-phase interface, which allows breaking through the mass transfer limitations usually found in electrochemical systems, producing an enhanced CO_2 reduction performance. SEM images recorded at low magnification (5000x) show that homogenous films cover the entire sprayed on the gas diffusion electrodes (GDE) surface. At high magnification (25000x), the microstructures of the HKUST-1 and CuAdeAce GDEs reveal their polycrystalline nature with strongly aggregated sub-micrometric crystals and micrometric octahedral crystals,

respectively. SEM images of CuDTA and CuZnDTA GDEs reveal filamentous structures composed of highly crosslinked fibers with diameters of 5 to 20 nm, comparable to those of the corresponding as-prepared materials. These GDEs were characterized using a set of analytical techniques and cyclic voltammetry analyses and finally, materials were tested in the electrocatalytical reduction of CO_2 using a continuous filter-press electrochemical cell under different operating conditions.

The results indicate the ability of Cu-containing metal-organic porous materials (MOPMs) supported in GDEs to promote the electrocatalytic conversion of CO_2 to alcohols. The electrolysis product analyses show methanol and ethanol to be predominately formed as liquid products from CO_2 reduction. Going to the detail, an enhanced performance for CO_2 conversion was achieved when applying HKUST-1 and CuZnDTA GDEs at j = 10 $mA \cdot cm^{-2}$, Q_e/A = 3 $ml \cdot min \cdot cm^{-2}$ and Q_g/A = 20 $ml \cdot min \cdot cm^{-2}$, where moderate formation rates (HKUST-1, $r_T = 18.58 \times 10^{-6}$ $mol \cdot m^{-2} \cdot s^{-1}$; CuZnDTA, $r_T = 11.57 \times 10^{-6}$ $mol \cdot m^{-2} \cdot s^{-1}$) and Faradaic efficiencies (HKUST-1, FE_T = 15.9%; CuZnDTA, FE_T = 9.9%) can be obtained. These results denoted that MOPMs with unsaturated coordination positions exposed on the pore system are preferred to enhance the performance of the CO_2 electrocatalytic reduction to alcohols. It is also important to note the synergic effect of Cu and Zn in the reduction response, as denoted by the remarkably lower current densities at lower onset potentials for CuZnDTA compared with those of CuDTA.

Finally, the stabilities of the MOPM-GDEs were tested over an extended period. The electrocatalytic activity (FE_T) decays to a plateau after 60 min and remains almost stable during the rest of the run (pseudo-stationary state), except those for the CuDTA GDE, which drops to zero after 120 min, and for CuAdeAce, which is almost negligible since the beginning. This deactivation is attributed to the decrease of their active-site areas or the degradation of the MOPMs owing to their limited stabilities in water, in which they undergo hydrolysis, amorphization, or phase

transformations, even at room temperature. ATR-FTIR spectroscopy on used MOF-GDEs (HKUST-1 and CuAdeAce) show a depletion of the intensity of the main reference signal attributed to the MOF-GDE; this suggests that a degradation of the material occurs during the run. PXRD analysis performed on 30 min used MOF-GDEs (HKUST-1 and CuAdeAce) shows a significant reduction of crystallinity, which is more acute for HKUST-1. It must be pointed out that the performance loss of HKUST-1 is smaller than that expected from the drastic crystallinity loss; thus, the remaining efficiency level can be attributed to the preservation of the local structure, as suggested by the FTIR spectra. In fact, The FTIR analysis also indicates that the loss of intensity for the MOA-GDEs is not so evident; therefore, the initial FE_T decay can be related to a shallow surface degradation/modification of the CuDTA and CuZnDTA nanofibers that is not detectable in the FTIR spectra at this stage, as the bulk of the material remains unaltered. However, in all cases, the FTIR spectra recorded at the end of the run (300 min) reveal a series of emerging peaks that evidence the formation of copper(II) hydroxycarbonate (malachite), which is a plausible degradation path for all Cu-MOPMs and not detectable at the middle of the run. Furthermore, at the end of the run, the decay of the signals corresponding to CuDTA is greater than that observed for CuZnDTA, and this explains the differences in the FE_T trend at the last part of the run. In fact both GDEs containing HKUST-1 and CuZnDTA are able to retain moderate formation rates (HKUST-1, r_T = 18.58 x 10^{-6} mol·m^{-2}·s^{-1}; CuZnDTA, r_T = 11.57 x 10^{-6} mol·m^{-2}·s^{-1}) and Faradaic efficiencies (HKUST-1, FE_T = 15.9%; CuZnDTA, FE_T = 9.9%) for as long as 12 or 17 h, surpassing the previous stability value reached for MOF-GDEs for the electrocatalytic transformation of CO_2.

5.2. PUBLICATION

ChemPubSoc Europe

DOI: 10.1002/cssc.201600693

CHEMSUSCHEM Full Papers

Copper-Based Metal–Organic Porous Materials for CO_2 Electrocatalytic Reduction to Alcohols

Jonathan Albo,*[a] Daniel Vallejo,[b] Garikoitz Beobide,[b] Oscar Castillo,[b] Pedro Castaño,[a] and Angel Irabien[c]

The electrocatalytic reduction of CO_2 has been investigated using four Cu-based metal–organic porous materials supported on gas diffusion electrodes, namely, (1) HKUST-1 metal–organic framework (MOF), $[Cu_3(\mu_6\text{-}C_9H_3O_6)_2]_n$; (2) CuAdeAce MOF, $[Cu_3(\mu_3\text{-}C_5H_4N_5)_2]_n$; (3) CuDTA mesoporous metal–organic aerogel (MOA), $[Cu(\mu\text{-}C_2H_2N_2S_2)]_n$; and (4) CuZnDTA MOA, $[Cu_{0.6}Zn_{0.4}(\mu\text{-}C_2H_2N_2S_2)]_n$. The electrodes show relatively high surface areas, accessibilities, and exposure of the Cu catalytic centers as well as favorable electrocatalytic CO_2 reduction performance, that is, they have a high efficiency for the production of methanol and ethanol in the liquid phase. The maximum cumulative Faradaic efficiencies for CO_2 conversion at HKUST-1-, CuAdeAce-, CuDTA-, and CuZnDTA-based electrodes are 15.9, 1.2, 6, and 9.9%, respectively, at a current density of 10 mA cm^{-2}, an electrolyte-flow/area ratio of 3 mL min cm^{-2}, and a gas-flow/area ratio of 20 mL min cm^{-2}. We can correlate these observations with the structural features of the electrodes. Furthermore, HKUST-1- and CuZnDTA-based electrodes show stable electrocatalytic performance for 17 and 12 h, respectively.

Introduction

The reduction of the CO_2 concentration in the atmosphere has become a critical challenge for sustainable development. There are different approaches to mitigate CO_2 emissions from the use of fossil fuels, including CO_2 capture[1–3] and subsequent storage or its conversion into valuable chemicals.[4–6] CO_2 is considered to be a carbon source for the synthesis of valuable chemicals, as it is abundant in the atmosphere and nontoxic compared with the other C_1 source, CO; therefore, the beneficial reuse of CO_2 is an interesting approach for the future. To this end, several methods have been adopted for the conversion and activation of CO_2 such as chemical, thermochemical, photochemical, biochemical, electrochemical, and hydrothermal methods.[7] Among them, electrocatalytic valorization appears to be a promising strategy owing to its simple procedure and ambient operation conditions. In addition, this technology coupled to a renewable energy source, such as wind or solar energy, could generate carbon-neutral fuels or industrial chemicals that are derived conventionally from petroleum.[8] In recent years, many investigators have studied the electrocatalytic reduction of CO_2 on metallic[9] and modified electrodes in aqueous, nonaqueous, and ionic-liquid media[10] under different operating conditions and system configurations to produce a range of useful products for industrial chemistry (i.e., formic acid, methane, ethane, ethylene, propylene, methanol, and ethanol). In particular, the challenges for the conversion of CO_2 into high-energy-density alcohols, such as methanol (CH_3OH), are great, but the potential rewards are even greater.[8,11,12]

Among the different cathode metals applied, Cu uniquely produces hydrocarbons at high reaction rates over sustained periods of time;[9,13,14] therefore, it is the strongest candidate for CO_2 electrocatalytic reduction. However, Cu generates a range of reaction products, and the selectivity of each product tends to be low.[15] Thus, to improve the selectivity, other catalyst structures should be considered to make the electrocatalytic reduction of CO_2 at Cu-based surfaces technically and economically viable.

In the last decade, metal–organic porous materials (MOPMs) and, particularly, metal–organic frameworks (MOFs), also known as porous coordination polymers or porous coordination networks, have shown many potential applications as new multifunctional materials. MOFs are hybrid materials containing three well-differentiated sites to which the catalytic function can be allocated, namely, the metallic component, the organic linker, and the pore space. MOFs are considered as ideal candidates for CO_2 adsorption, separation,[16] and reduction through catalyzed reactions.[17] This is because of their combined favor-

[a] J. Albo, P. Castaño
Department of Chemical Engineering
University of the Basque Country (UPV/EHU)
PO Box. 644, 48080, Bilbao (Spain)
E-mail: jonathan.albo@ehu.es

[b] D. Vallejo, G. Beobide, O. Castillo
Department of Inorganic Chemistry
University of the Basque Country (UPV/EHU)
PO Box. 644, 48080, Bilbao (Spain)

[c] A. Irabien
Department of Chemical & Biomolecular Engineering
University of Cantabria (UC)
Avda. Los Castros, 39005, Santander (Spain)

Supporting information and the ORCID identification number(s) for the author(s) of this article can be found under http://dx.doi.org/10.1002/cssc.201600693.

This publication is part of a Special Issue around the "1st Carbon Dioxide Conversion Catalysis" (CDCC-1) conference. To view the complete issue, visit: http://dx.doi.org/10.1002/cssc.v10.6.

able properties of large surface area, high porosity, tunable pore-size, and shape-selective character. Indeed, MOFs are particularly suitable for electrochemical reactions as a result of these features in addition to their high electronic conductivities.[18–26] For example, Kumar et al.[19] studied the electrocatalytic reduction of CO_2 on Cu-based MOF (HKUST-1) films with an electrolyte consisting of a DMF solution of tetrabutylammonium tetrafluoroborate saturated with CO_2. Cyclic voltammetry revealed that the electrochemically generated Cu^I species were very selective for CO_2 reduction, although the main product was oxalic acid. In the same year, Hinogami et al.[20] synthesized a copper rubeanate MOF (CR-MOF) supported on carbon films as electrodes. The onset potential for CO_2 reduction at the CR-MOF electrode was approximately 0.20 V higher than that observed on a Cu metal electrode. Hod et al.[23] synthesized iron–porphyrin-based MOFs for the electrocatalytic conversion of CO_2; these materials exhibited high active-site exposure ($\approx 10^{15}$ sites per cm^2) and nearly 100% Faradaic efficiency (FE) for the production of $CO + H_2$ mixtures. Kornienko et al.[24] obtained 76% Faradaic efficiency and high stability for 7 h using Co–porphyrin MOFs. On the contrary, examples of metal–organic aerogels (MOAs) are relatively scarce[27–31] compared with the more conventional MOFs. To the best of our knowledge, no studies have dealt with their use as electrocatalysts for CO_2 reduction.

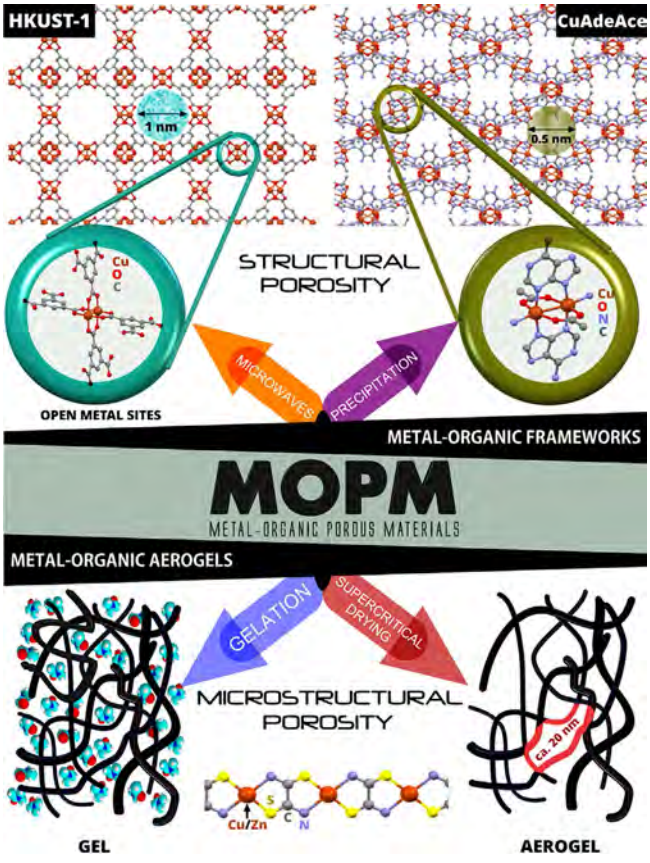

Figure 1. Structural details of the selected metal–organic porous materials (MOPMs).

To face the challenge of synthesizing effective and stable CO_2 reduction electrocatalysts for the continuous production of alcohols, in this work, we have evaluated four MOPMs (two MOFs and two MOAs) containing Cu (Figure 1) as gas diffusion electrodes (GDEs), which are named hereafter MOPM-GDEs: (1) a benchmark MOF with formula $[Cu_3(\mu_6\text{-}C_9H_3O_6)_2(OH_2)_3]_n$ ($C_9H_3O_6$ = benzene-1,3,5-tricarboxylate), commonly known as MOF-199 or HKUST-1,[32] in which the accessible metallic moieties are adsorption sites for CO_2;[33] (2) a microporous copper(II)–adeninate–acetate coordination framework with formula $[Cu_2(\mu_3\text{-adeninate})_2(\mu_2\text{-}OOC(CH_3)_2)]_n$ (CuAdeAce), in which the Watson–Crick faces of the adenine are sites for CO_2 adsorption;[34] (3) a Cu MOA built from successive junctions with bis-bidentate dithiooxamidate (DTA) and named CuDTA; and (4) a MOA with the same synthetic premise as (3) but with oxides of Cu and Zn, named CuZnDTA. The coordination frameworks of MOAs lack intrinsic pore systems; therefore, we have processed the materials as nanofibrous aerogels to increase their surface areas and the accessibility of the catalytic centers. Each MOPM was deposited on a gas diffusion layer to form a characteristic gas–solid–liquid three-phase interface, which allows the mass-transfer limitations usually found in electrochemical systems to be overcome to enhance the CO_2 reduction performance.[4] Then, we characterized the GDEs through a set of analytical techniques and cyclic-voltammetry analyses and finally tested the materials in the electrocatalytic reduction of CO_2 using a continuous filter-press electrochemical cell under different operating conditions.

Results and Discussion

Surface characterization of the GDEs

The MOPM-GDEs were characterized by SEM, attenuated total reflectance (ATR) FTIR spectroscopy, and PXRD to understand their structural and morphological properties in relation to their capability for CO_2 electrocatalytic reduction. In all cases, the SEM images recorded at low magnification (5000×, see Figure S3.1 of the Supporting Information) show that homogenous films cover the entire sprayed GDE surface. At high magnification (25000×), the microstructures of the HKUST-1 and CuAdeAce GDEs reveal their polycrystalline natures (Figure 2a and b) with strongly aggregated sub-micrometric crystals and micrometric octahedral crystals, respectively. The images of the CuDTA and CuZnDTA GDEs (Figure 2c and d) reveal filamentous structures composed of highly crosslinked fibers with diameters of 5 to 20 nm, comparable to those of the corresponding as-prepared materials.

All of the ATR-FTIR spectra feature a set of peaks at $\tilde{\nu} = 1305$, 1210, 1150, 1060, and 975 cm^{-1}, which corresponds to the antisymmetric and symmetric stretching of the sulfonate, perfluorinated, and ether groups of the tetrafluoroethylene copolymer used as the surfactant (Nafion®). Although the MOPMs show less-intense peaks overlapped with those of the surfactant in the low-energy range, the peaks arising from the coordination framework can be distinguished at higher wavenumbers ($\tilde{\nu}$ = 1310–1700 cm^{-1}). The detailed spectroscopy of the MOPM-

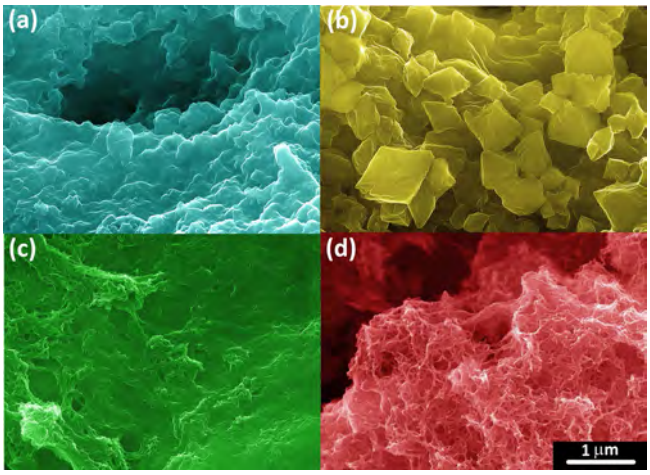

Figure 2. SEM images at 25 000× magnification of (a) HKUST-1, (b) CuAdeAce, (c) CuDTA, and (d) CuZnDTA; not real colors.

GDEs and the analysis of the main vibration modes are provided in the Supporting Information (see Figure S3.3 and Table S3.1).

As the performance of a MOF is closely related to its crystallinity, HKUST-1 and CuAdeAce GDEs were further characterized by PXRD (Figure 3). Both MOF-GDEs show characteristic (002) and (004) reflections of the graphite sites at $2\theta = 26.5$ and 54.6°, respectively. Although, the preferred orientation of graphite gives rise to an outsized peak, the signals corresponding to the MOFs are clearly distinguishable at $2\theta < 22°$. As shown in the inset graphic, all of the observed peaks fit the expected lattice-plane reflections.

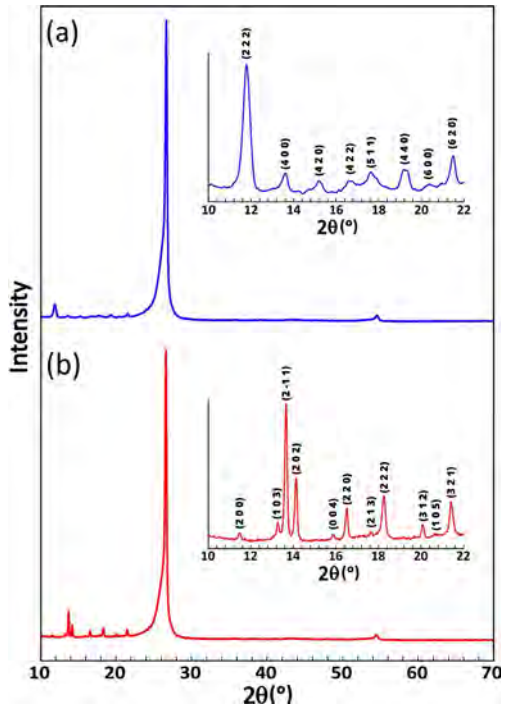

Figure 3. PXRD patterns of HKUST-1 and CuAdeAce GDEs.

Cyclic-voltammetry characterization

To examine the electrocatalytic behavior of the prepared GDEs, cyclic voltammetry was performed for the MOPM-GDEs in CO_2-saturated (0.5 M $KHCO_3$) aqueous solutions; the voltammograms after five scans with the current densities (*j*) normalized to the geometric area of the MOPM-GDEs are shown in Figure 4. The results are compared to the current–voltage response of a Cu plate.

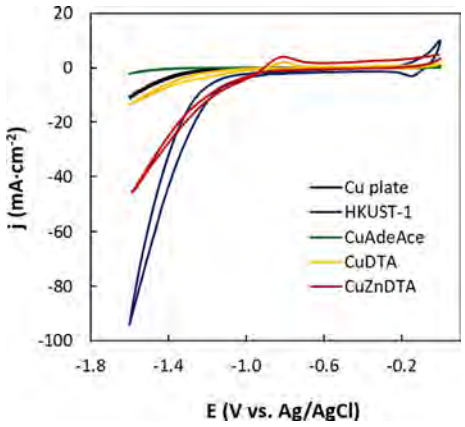

Figure 4. Cyclic voltammograms for the MOPM-GDEs in a CO_2-saturated 0.5 M $KHCO_3$ aqueous solution.

Large differences between the voltammetric profiles of the MOPM-GDEs can be seen in Figure 4, and HKUST-1 and CuZnDTA are the most promising candidates for the electroreduction process. All of the voltammetric profiles show a reduction process that starts at approximately −1 V versus Ag/AgCl and is associated with the reduction of CO_2. On the other hand, for the applied voltage, the CuAdeAce GDE shows almost no response variation, which reveals a low activity for conducting electrons. It is also important to note the synergic effect of Cu and Zn in the reduction response, as denoted by the remarkably lower current densities at lower onset potentials for CuZnDTA compared with those of CuDTA. This result is in agreement with those for Cu_2O/ZnO and Cu_2O GDEs.[5] Furthermore, the oxidative peak at −0.8 V, previously assigned to the transformation of Zn to ZnO,[5] is assigned in this work to the formation of oxidized subproducts from the CO_2 reduction reaction because it is present for both CuDTA and CuZnDTA GDEs, and each voltammetry profile shown in Figure 5 corresponds to the fifth cycle.

To further confirm the reduction of CO_2, the voltammetry profiles of the most promising GDEs (HKUST-1 and CuZnDTA) in the presence and absence of CO_2 (in an Ar-saturated solution) are shown in Figure 5a and 5b. The decrease of the current intensity for both GDEs is an indication that CO_2 is reduced at an onset potential lower than −1 V versus Ag/AgCl. Thus, the intrinsic oxidation–reduction of the GDEs might be neglected, particularly for HKUST-1 GDE, for which the reduction response in the absence of CO_2 is close to the response for a Cu plate in a CO_2-saturated $KHCO_3$ aqueous solution.

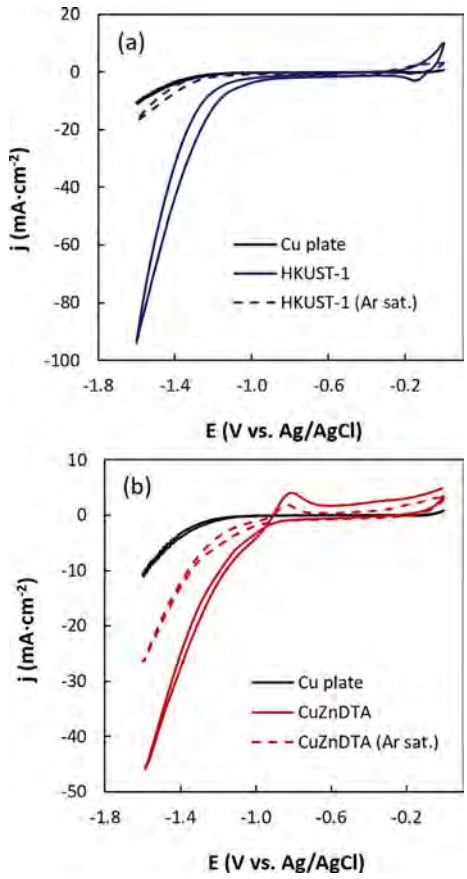

Figure 5. Cyclic-voltammetry responses in medium saturated with CO_2 (0.5 M $KHCO_3$) and Ar of (a) HKUST-1 and (b) CuZnDTA.

Influence of current density on CO_2 reduction performance

The results for the continuous electrocatalytic reduction of CO_2 in a filter-press electrochemical cell are presented hereafter. The quantitative reduction performances (production rate, *r*, and Faradaic efficiency, FE) regarding the liquid-phase product distribution at different current densities ($j = 5$–40 mA cm^{-2}) are shown in Figure 6 for the prepared MOPM-GDEs. The electrocatalytic reduction of CO_2 with the MOPM-GDEs leads to the formation of CH_3OH and C_2H_5OH. It should be noted that the carbon paper without MOPMs did not produce any measurable liquid product. The FEs were calculated for a 6-electron pathway for CO_2 reduction to CH_3OH and a 12-electron pathway to C_2H_5OH. A constant electrolyte-flow/area ratio (Q_e/A) and gas-flow/area ratio (Q_g/A) of 2 and 20 mL min^{-1} cm^{-2}, respectively, were applied. These conditions were found previously to be optimal for the electrocatalytic reduction of CO_2.[4]

As shown in Figure 6, the product distribution and process efficiency are correlated with the current density applied to the system. The HKUST-1 and CuZnDTA GDEs are the most active electrocatalysts for the reduction of CO_2, in agreement with the higher reduction responses observed in the cyclic-voltammetry profiles (Figure 4). This electrocatalytic performance is partially correlated with the surface area of the GDEs, as summarized in Table S2.1 in the Supporting Information: the HKUST-1 GDE exhibits the highest surface area (1710 m^2 g^{-1}) and the highest electrocatalytic performance, whereas CuDTA and CuZnDTA GDEs exhibit much lower surface areas (270 and 260 m^2 g^{-1}, respectively) and significantly poorer electrocatalytic performances. Nevertheless, the surface area is not the only parameter that controls the catalytic performance, as CuAdeAce GDE with an intermediate area (500 m^2 g^{-1}) shows the lowest FE values. The last results could be anticipated from the cyclic-voltammetry profiles displayed in Figure 4, which indicated the lowest electron conductivity for the CuAdeAce GDE. Thus, the electrocatalytic performance should be related to additional features of the GDEs that require additional analysis of the Cu active sites, particularly the accessibility of the pentacoordinate Cu^{II} centers, which are hindered sterically by the surrounding ligands. This leads to the preliminarily conclusion that MOPMs with unsaturated coordination positions exposed in the pore system are preferred for the enhancement of the performance of the electrocatalytic reduction of CO_2 to alcohols.

The maximum CH_3OH and C_2H_5OH production rates for the HKUST-1 GDEs ($r_{CH_3OH} = 5.62\times10^{-6}$ mol m^{-2} s^{-1} and $r_{C_2H_5OH} = 5.28\times10^{-6}$ mol m^{-2} s^{-1}) correspond to product concentrations in the catholyte of 0.54 and 0.73 mg L^{-1} for CH_3OH and C_2H_5OH, respectively. The formation of both alcohols, CH_3OH and C_2H_5OH, has been reported previously,[4,15,35–46] whereas Cu-based GDEs are more selective towards the formation of CH_3OH over C_2H_5OH.[4] The maximum FEs of CH_3OH and C_2H_5OH were 54.8 and 31.4% for Cu_2O and Cu_2O/ZnO GDEs, respectively, at applied potentials of −1.39 and −1.16 V versus Ag/AgCl.[4] Furthermore, the CuO GDE led to a higher selectivi-

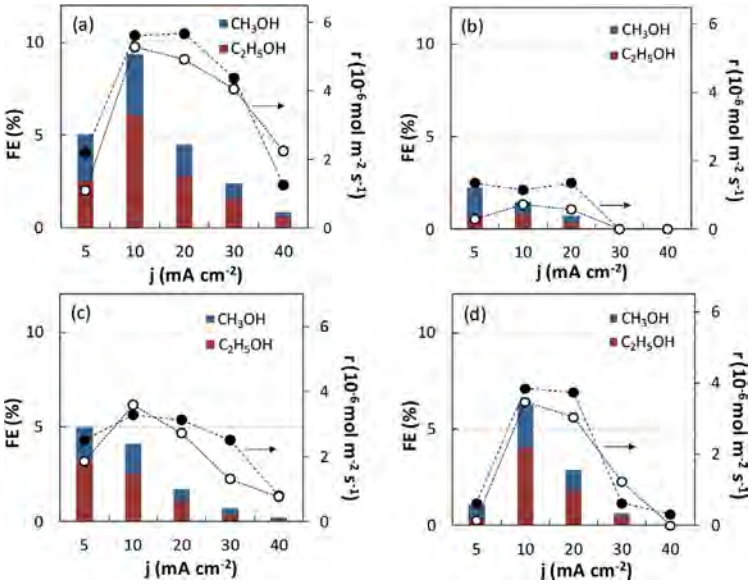

Figure 6. Rates (*r*) for CH_3OH (●) and C_2H_5OH (○) formation and Faradaic efficiencies (FEs) in the electrocatalytic reduction of CO_2 as a function of the current density (*j*) applied with (a) HKUST-1, (b) CuAdeAce, (c) CuDTA, and (d) CuZnDTA; the lines are only guides.

ty for C_2H_5OH (FE = 15.5%) in a 0.2 M $KHCO_3$ solution,[39] and trace amounts of CH_3OH and C_3H_8O were also detected. Another example is the recent study conducted by Gutierrez-Guerra et al.[46] for different Cu-based GDEs, which afforded CH_3OH and C_2H_5OH with selectivities of 80 and 10%, respectively, at an applied current of −30 mA. Kuhl et al.[15] reported a total of 16 different CO_2 reduction products (including CH_3OH and C_2H_5OH) across a range of potentials. They hypothesized that the chemistry involved in the C–C coupling reactions to form C_2–C_3 products occurs through an enol-like surface intermediate, which desorbs to convert to its diol or ketone form. Certainly, the C–C bond formation is one of the most critical factors to be considered in the design of electrocatalysts for the production of alcohols, and further experimental work is needed to fully elucidate the CO_2 reduction steps to form alcohols using Cu-based GDEs.

As shown in Figure 6, the rates for CO_2 reduction to CH_3OH and C_2H_5OH did not improve at $j > 10$ mA cm^{-2}. At this point, the maximum r values can be obtained for all MOPM-GDEs. The total Faradaic efficiency (FE_T, cumulative efficiency for the formation of CH_3OH and C_2H_5OH) drops drastically as the current increases from $j = 10$ to 40 mA cm^{-2}. This result could be explained by the consumption of the additional current by side reactions; hence, the optimal current density is 10 mA cm^{-2} for all MOPM-GDEs. Under these conditions, the FE_T values are 10.9 and 7.3% for the HKUST-1 and CuZnDTA GDEs, respectively. The remaining product is expected to be mainly H_2, which competes with the electrocatalytic reduction of CO_2 to alcohols and affects the GDE stability negatively. The latter observation is caused by the fact that H_2 favors the leaching of the active material from the GDE.[4]

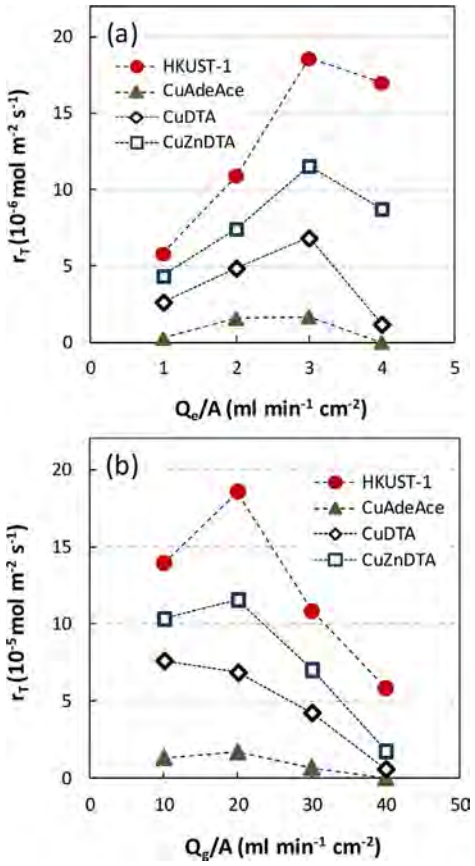

Figure 7. Total rates (r_T) at $j = 10$ mA cm^{-2} for the MOPM-GDE with (a) different electrolyte flow rates (Q_e/A) and (b) CO_2 gas flow rates (Q_g/A); the lines are only guides.

Influence of electrolyte flow rate and gas flow rate

Previous studies demonstrated that variations in Q_e and Q_g could lead to significant mass-transfer differences in the cell and, thus, in the total rate for CO_2 transformation, r_T, and the cumulative FE_T of the process.[4,5] These effects can be observed even for the application of GDEs,[4] for which mass-transfer limitations are expected to be overcome partially.[6,47,48]

In an attempt to improve the CO_2 conversion efficiency, additional experiments were conducted at different Q_e/A and Q_g/A values. The results are presented in Figure 7. The increase in Q_e/A from 1 to 3 mL min^{-1} cm^{-2} led to a significant enhancement in the CO_2 electrocatalytic conversion rate (Figure 7a, e.g., from $r_T = 5.80 \times 10^{-6}$ to 18.57×10^{-6} mol m^{-2} s^{-1} for HKUST-1 GDE). The use of low Q_e/A ratios is preferred as the concentration of alcohols in the liquid would be higher; therefore, for an optimal process operation, a compromise needs to be met between the concentration of alcohols in the product and their formation rate. Further increases in Q_e/A led to a drastic decrease in r_T owing to the leaching of the active material from the GDE.[4] Furthermore, a low Q_e/A allows the infiltration of the catholyte into the GDE structure, which increases the diffusion time and enhances CO_2 electrocatalytic performance.[4,48,49]

Moreover, the increases in Q_g/A from 10 to 20 mL min^{-1} cm^{-2} yields an increase of the CO_2 electrocatalytic conversion rate (Figure 7b, e.g., from $r_T = 13.94 \times 10^{-6}$ to 18.57×10^{-6} mol m^{-2} s^{-1} for HKUST-1 GDE). This observation reveals that the overall kinetics at $Q_g/A = 10$ mL min^{-1} are controlled by the external transport of CO_2 to the GDE actives sites. A further increase of Q_g/A above 20 mL min^{-1} cm^{-2} leads to a drastic decrease in r_T, which is then attributed to the leaching of active material from the GDE, in agreement with previous findings.[4,48,50] Thus, the optimal balance point is at $Q_g/A =$ 20 mL min^{-1} cm^{-2}, at which enough CO_2 gas supply is provided for the reaction well before a massive detachment of active material occurs.

Overall, the optimal conditions for the CO_2 electrocatalytic reduction on MOPM-GDEs is $Q_e/A = 3$ mL min^{-1} cm^{-2} and $Q_g/A = 20$ mL min^{-1} cm^{-2}. The optimal electrocatalytic performances, in terms of r and FE, for the MOPM-GDEs are shown in Table 1. To interpret the electrocatalytic activity further, the total formation rates were normalized to the active Cu surface area of each GDE, $r_{T,a}$. The active Cu area (a) was measured through pulse chemisorption, as described in the Experimental Section. The results were compared to those obtained for a filter-press electrochemical cell equipped with a Cu plate at an applied potential of −1.3 V versus Ag/AgCl ($j =$ 10.83 mA cm^{-2}).

Table 1. r and FE for the electrocatalytic conversion of CO_2 at MOPM-GDEs. j = 10 mA cm^{-2}, Q_e/A = 3 mL min^{-1} cm^{-2}, Q_g/A = 20 mL min^{-1} cm^{-2}.

GDE	E [V]	a_{Cu} [cm^2]	r [10^{-6} mol m^{-2} s^{-1}]				FE [%]		
			r_{CH_3OH}	$r_{C_2H_5OH}$	r_T	$r_{T,a}$	FE_{CH_3OH}	$FE_{C_2H_5OH}$	FE_T
HKUST-1	−0.9	66.48	9.68	8.90	18.58	0.28	5.6	10.3	15.9
CuAdeAce	−1.75	0.13	1.25	0.43	1.68	13.1	0.7	0.5	1.2
CuDTA	−1.41	53.69	3.28	3.58	6.86	0.13	1.9	4.1	6
CuZnDTA	−1.25	1.78	5.93	5.64	11.57	6.52	3.4	6.5	9.9
Cu plate[a]	−1.3	–	8.7	–	8.7	–	4.6	–	4.6

[a] Data from Ref. [5] at j = 10.83 mA cm^{-2} and Q_e/A = 2 mL min^{-1} cm^{-2}.

The alcohol formation rate after 90 min on-stream varied from $r_T = 1.68\times10^{-6}$ to 18.58×10^{-6} mol m^{-2} s^{-1} for CuAdeAce and HKUST-1 GDEs, respectively. The latter GDE also displays the highest FE (≈16%) among the studied electrodes. These values, together with those obtained for CuZnDTA GDE, are remarkably greater than those for a Cu plate and show the great opportunities brought by MOPMs for the electrocatalytic reduction of CO_2. This enhanced performance is related to the demonstrated higher activity for the reduction of protons by CuO_x in comparison with that of Cu^0 for the electrocatalytic reduction of CO_2.[24,35–37,51,52] For example, Lan et al.[37] investigated the electrocatalytic reduction of CO_2 at a Cu/CuO (core–shell) catalyst in 1 M $KHCO_3$ with a flow reactor. This study proved that transformations between Cu, Cu^I, and CuO occurred as a function of applied potential, which at the same time did not affect CH_3OH production severely. Thus, the high yield of CH_3OH obtained at −1.72 V versus Ag/AgCl using a Cu/CuO (core–shell) electrocatalyst was higher than that obtained using Cu foil. Furthermore, the formation rates reached using the HKUST-1 GDEs are in the range of those values reported previously for air-oxidized Cu foil and electrochemically oxidized Cu foil ($r \approx 2\times10^{-5}$ mol m^{-2} s^{-1}) at potentials of −1.2 to −1.5 V versus Ag/AgCl.[53] Nevertheless, the formation rates are still below those reported for Cu_2O GDEs ($r_T = 11.9\times10^{-5}$ mol m^{-2} s^{-1} at −1.05 V versus Ag/AgCl)[54] and also those achieved with Cu_2O/Zn-based GDEs ($r = 4.74\times10^{-5}$ mol m^{-2} s^{-1}).[4] This result is related to the beneficial properties of Cu^I for CO_2 electrocatalytic reduction processes. Previous studies demonstrated that Cu^I presents both intermediate hydrogen overpotentials and CO adsorption properties, which promote CO_2 reduction in aqueous solutions in comparison with Cu^0 or Cu^{II}-based electrocatalysts.[36,51]

Interestingly, if the formation rates are normalized to the active Cu surface available, CuAdeAce shows the highest activity ($r_{T,a} = 13.1\times10^{-6}$ mol m^{-2} s^{-1}). Conversely, the lowest rates were observed for the HKUST-1 GDEs ($r_{T,a} = 0.28\times10^{-6}$ mol m^{-2} s^{-1}). To explain such unexpected behavior, first it must be considered that the idealized crystal structure suggests that the coordination framework of CuAdeAce lacks accessible unsaturated Cu^{II} coordination positions, and this leads to a low Cu active-surface value (0.13 cm^2 g_{Cu}^{-1}), which is probably attributable to the presence of crystal defects that render some Cu^{II} sites unhindered and available for N_2O chemisorption. Therefore, the superior value of the normalized rate found for CuAdeAce implies that the scarce amount of accessible Cu^{II} sites are highly active centers and it provides a clue for the design of more efficient electrocatalysts for CO_2 reduction based on $\{Cu_2(\mu_3\text{-adeninate})_2[\mu_2\text{-OOC}(CH_3)_2]\}_n$ paddlewheel motifs.

On the other hand, the comparison of the normalized rates for CuDTA and CuZnDTA (0.13 and 6.52 mol m^{-2} s^{-1}) supports the previously inferred crucial role that Zn^{II} centers play on the performance of MOF-GDEs.

Long-term stability of MOPM-GDEs

Finally, the stabilities of the MOPM-GDEs were tested over an extended period. The evolution of the cumulative Faradaic efficiency over 5 h on-stream, FE_T, for the observed optimal experimental conditions is shown in Figure 8.

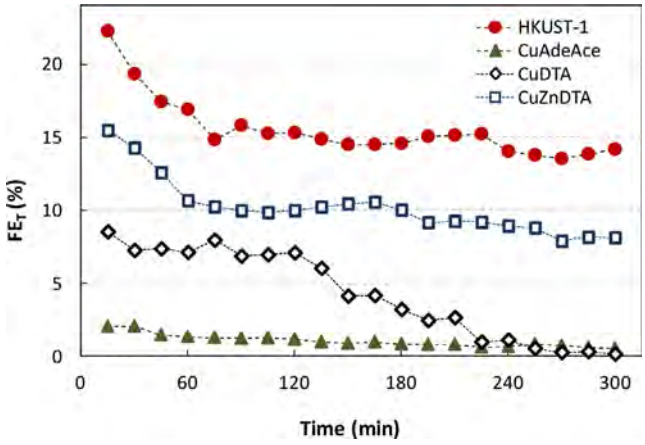

Figure 8. Time-dependence of FE for the MOPM-GDEs under the following conditions: j = 10 mA cm^{-2}, Q_e/A = 3 mL min^{-1} cm^{-2}, and Q_g/A = 20 mL min^{-1} cm^{-2}; the lines are only guides.

As indicated in Figure 8, during the first minutes of the experiment, the electrolyte needs to diffuse through the internal structure of the GDE to form a typical three-phase interface throughout the whole GDE and, thus, enlarge the contact area.[55] The electrocatalytic activity (FE_T) decays to a plateau and remains almost stable during the rest of the run (pseudostationary state), except that for the CuDTA GDE, which drops to zero after 120 min. This deactivation observed for all MOPM-GDEs is attributed to the decrease of their active-site areas[48,49] or the degradation of the MOPMs owing to their limited stabilities in water, in which they undergo hydrolysis, amorphization, or phase transformations, even at room temperature.[56,57] In this sense, the MOPM-GDEs used for 30 min were analyzed further and compared with the as-prepared ones. The ATR-FTIR spectroscopy measurements (Figure 9a and b) of the MOF-GDEs (HKUST-1 and CuAdeAce) show a depletion of the intensity of the main reference signal attributed to the MOF-GDE; this suggests that a degradation of the material occurs during the run.

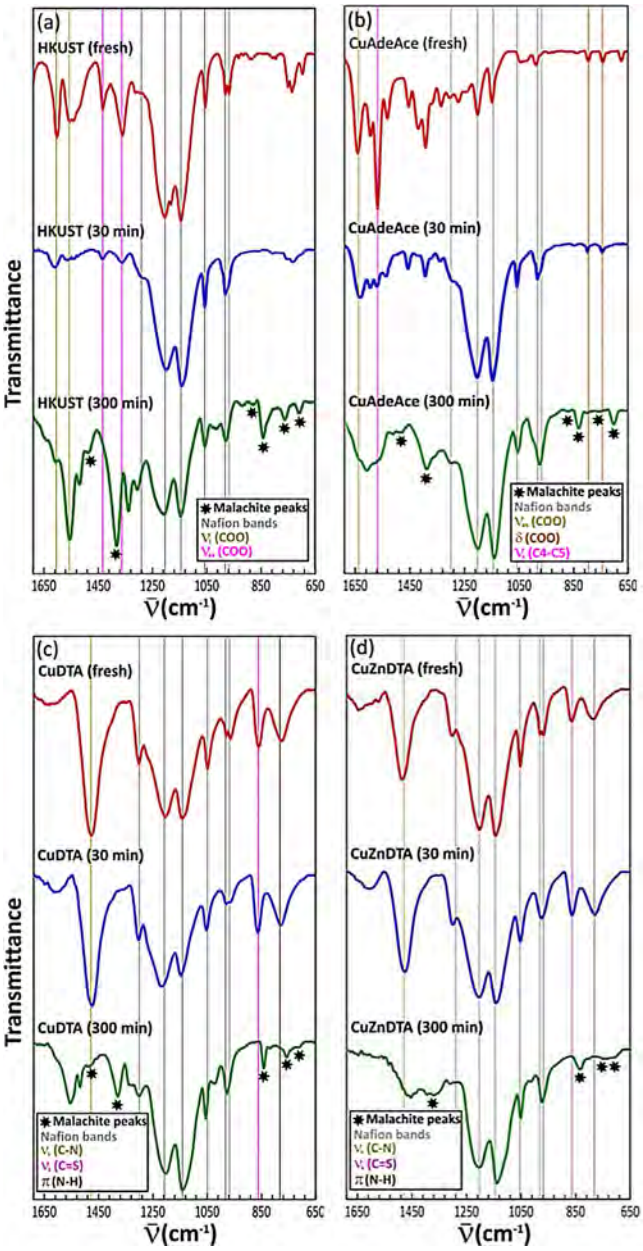

Figure 9. ATR-FTIR spectra for fresh and used (a) HKUST-1, (b) CuAdeAce, (c) CuDTA, and (d) CuZnDTA.

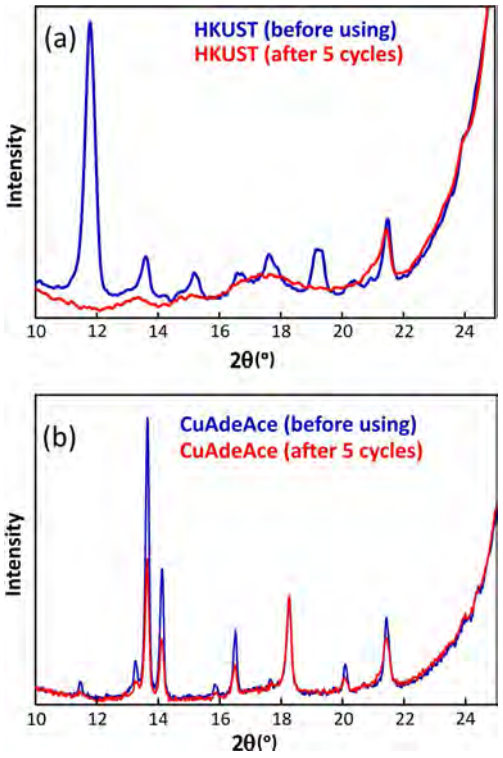

Figure 10. Comparison of the PXRD patterns of fresh and used (a) HKUST-1 and (b) CuAdeAce.

Accordingly, the PXRD analysis of the HKUST-1 and CuAdeAce GDEs (Figure 10) shows a significant reduction of crystallinity, which is more acute for HKUST-1. It must be pointed out that the performance loss of HKUST-1 is smaller than that expected from the drastic crystallinity loss; thus, the remaining efficiency level can be attributed to the preservation of the local structure, as suggested by the FTIR spectra. Coming back to the FTIR analysis (Figure 9), the loss of intensity for the MOA-GDEs (Figure 9c and 9d) is not so evident; therefore, the initial FE_T decay can be related to a shallow surface degradation/modification of the CuDTA and CuZnDTA nanofibers that is not detectable in the FTIR spectra at this stage, as the bulk of the material remains unaltered. However, in all cases, the FTIR spectra recorded at the end of the run (300 min, see Supporting Information) reveal a series of emerging peaks that evidence the formation of copper(II) hydroxycarbonate (malachite), which is a plausible degradation path for all Cu-MOPMs and not detectable at the middle of the run. Furthermore, at the end of the run, the decay of the signals corresponding to CuDTA is greater than that observed for CuZnDTA, and this explains the differences in the FE_T trend at the last part of the run.

The FTIR and PXRD analyses of the fresh and used MOPM-GDEs give a qualitative clue to the activity loss, whereas a quantitative one is obtained from the relative FE_T losses. After 5 h on-stream, the relative FE_T drops are 40, 65, 98, and 51% for HKUST-1, CuAdeAce, CuDTA, and CuZnDTA GDEs, respectively. These relative activity losses indicate that all MOPM-GDEs (except CuDTA) retain an intermediate efficiency despite the cited long-term degradation. In a practical sense, a third reason for the deactivation should be indicated, namely the leaching of the MOPM from the rest of the GDE structure (carbon support).[4] In addition, the probable agglomeration of particles and defects in the catalytic layer during the preparation of the MOPM-GDE would likely assist tunneling and increase the unwanted H_2 formation owing to the easy access of water to catalytic sites.[51] On the contrary, the GDEs containing HKUST-1 and CuZnDTA are able to retain moderate formation rates (KHUST-1, $r_T = 18.58 \times 10^{-6}$ mol m^{-2} s^{-1}; CuZnDTA, $r_T = 11.57 \times 10^{-6}$ mol m^{-2} s^{-1}) and Faradaic efficiencies (KHUST-1, $FE_T = 15.9\%$; CuZnDTA, $FE_T = 9.9\%$) for as long as 12 or 17 h

and surpass the stability value reached recently for MOF-GDEs for the electrocatalytic transformation of CO_2.[19]

These results make the use of MOPMs valuable for the CO_2 electrocatalytic conversion to alcohols in continuous operation, although further work is required to design materials with the same favorable properties and a higher stability for a technoeconomically viable CO_2 valorization process. The outstanding challenges remain in the design of catalyst systems featuring (1) selectivity for CO_2 reduction with minimum H_2 generation, (2) high conversion efficiency at low electrochemical overpotentials, and (3) long-term stability. Furthermore, the detailed mechanisms for the overall catalytic system remain unclear. We hope to elucidate the reactions steps for CO_2 conversion to value-added products on MOPM-GDEs.

Conclusions

This work demonstrates the ability of Cu-containing metal–organic porous materials (MOPMs) supported in gas diffusion electrodes (GDEs) to promote the electrocatalytic conversion of CO_2 to alcohols. We successfully prepared, characterized, and tested four different MOPM-GDEs. Specifically, two metal–organic frameworks, (1) $[Cu_3(\mu_6\text{-}C_9H_3O_6)_2]_n$ (HKUST-1) and (2) $[Cu_3(\mu_3\text{-}C_5H_4N_5)_2]_n$ (CuAdeAce), and two metal–organic aerogels, (3) $[Cu(\mu\text{-}C_2H_2N_2S_2)]_n$ (CuDTA) and (4) $[Cu_{0.6}Zn_{0.4}(\mu\text{-}C_2H_2N_2S_2)]_n$ (CuZnDTA). The characterization involved structural and cyclic-voltammetry analyses, whereas the testing during the electrocatalytic reduction of CO_2 was performed in a continuous setup consisting of a filter-press electrochemical cell under ambient conditions.

The analyses of the electrolysis products showed that methanol and ethanol were formed predominately as the liquid products from CO_2 reduction. An enhanced performance for CO_2 conversion was achieved through the application of HKUST-1 and CuZnDTA GDEs at a current density (j) of 10 mA cm^{-2}, an electrolyte-flow/area ratio (Q_e/A) of 3 mL min^{-1} cm^{-2}, and a gas-flow/area ratio (Q_g/A) of 20 mL min^{-1} cm^{-2}, at which moderate formation rates (KHUST-1, $r_T = 18.58 \times 10^{-6}$ mol m^{-2} s^{-1}; CuZnDTA, $r_T = 11.57 \times 10^{-6}$ mol m^{-2} s^{-1}) and Faradaic efficiencies (KHUST-1, $FE_T = 15.9\%$; CuZnDTA, $FE_T = 9.9\%$) could be obtained. These results denoted that MOPMs with unsaturated coordination positions exposed in the pore system are preferred for the enhancement of the performance of the electrocatalytic reduction of CO_2 to alcohols. Interestingly, if the formation rates were normalized to the active Cu surface available for each MOPM, CuAdeAce showed a superior activity. This gives a clue for the design of more-efficient CO_2 reduction electrocatalysts including paddle-wheel motifs built from N-donor ligands that preserve square-planar coordination geometries around the Cu^{II} atoms and, as a result, produce open metal sites prone to interact strongly with guest molecules throughout the porous network.

Finally, the stability of the HKUST-1 GDE was confirmed for as long as 17 h of operation and can be attributed to the preservation of the local structure, even if a significant reduction in crystallinity occurred during the experimental time. These results make the use of MOPMs valuable for the electrocatalytic conversion of CO_2 to alcohols in continuous operation. The modularity of these systems yields many opportunities for further performance improvements and open new directions in electrocatalysis.

Experimental Section

Preparation of MOPM-GDEs

Synthesis of the MOPMs: HKUST-1 was prepared by a previously described solvent-free synthetic route.[58] In a first step, stoichiometric amounts of benzene-1,3,5-tricarboxylic acid and copper(II) acetate monohydrate were ground together to ensure a homogeneous mixture and placed in the reaction vessel. The reagent mixture was oven-heated for approximately 50 h at a heating rate of 2 °C h^{-1} to a maximum temperature of 120 °C. Polycrystalline CuAdeAce material was prepared by the slow addition of acetic acid to an aqueous solution containing adenine and Cu^{II} salt in equimolar proportions.[59] Both MOFs were washed thoroughly with water to remove unreacted reagents and remaining byproducts. The general procedure to prepare the MOAs (CuDTA and CuZnDTA) proceeded as follows. The corresponding metal acetate (or metal salt mixture) was dissolved in a mixture of *N*,*N*′-dimethylacetamide (DMA) and DMF in a 60:40 volumetric ratio, aided by an ultrasonic tip (Vibra-Cell VCX130 20 kHz and 130 W, Sonics) at 80% of its power for 2 min. Then, dithiooxamide (H_2DTA) ligand, basified with triethylamine, was dissolved in the same solvent mixture and added into the metal-ion-containing solution with the system maintained in an ultrasound bath (ULTRASONS-H, Selecta) at a temperature of 288 K. Once the metal–organic gel reached a certain consistency, it was allowed to age at room temperature for 1 d. Thereafter, the materials were washed first through immersion in pure DMF to remove the unreacted species and then by successive solvent exchanges in DMF/ethanol mixtures and pure ethanol to replace the solvent. In each exchange step, the contact between the solvent and gel was 24 h to ensure an efficient exchange. To prepare the aerogels, an E3100 critical-point dryer from Quorum Technologies equipped with gas-inlet, vent, and purge valves and a thermal bath was employed. Firstly, the gel was immersed in liquid CO_2 at 293 K and 50 bar for 1 h. After this, the exchanged ethanol was removed through the purge valve. This process was repeated five times. Subsequently, the sample was dried under supercritical conditions at a temperature of 311 K and a pressure of 85–95 bar. Finally, under constant temperature (311 K), the chamber was vented slowly to atmospheric pressure. Details on the characterization of the prepared MOPMs are provided in the Supporting Information (S2).

Preparation of the GDEs: The MOPM-GDEs were prepared by the procedure described in a previous study.[4] The GDEs ($A = 10$ cm^2) were prepared by airbrushing a catalytic ink onto a porous carbon paper (type TGP-H-60, Toray Inc.). The catalyst loading in the GDEs was kept at 1 mg cm^{-2}, which is an effective loading for enhanced CO_2 electrocatalytic reduction performance.[5] The catalytic ink was formed by a mixture of the synthesized MOPMs (HKUST-1, CuAdeAce, CuDTA, and CuZnDTA) as electrocatalysts, Nafion® dispersion 5 wt% (Alfa Aesar) as binder, and isopropyl alcohol (IPA, Sigma–Aldrich) as the vehicle with a 70:30 catalyst/Nafion mass ratio and 3% solids (catalyst + Nafion). The mixture was sonicated for 15 min and then airbrushed onto the carbon papers, and the resulting MOPM-GDEs were dried and rinsed with deionized water before use.

Characterization of the prepared MOPM-GDEs

The electrochemical behavior of the materials was evaluated by cyclic voltammetry with a PGSTAT 302N potentiostat (Metrohm, Autolab B.V.) under GPES software control using a conventional three-electrode electrochemical cell. The current–voltage curves were obtained with a scan rate of 50 mV s^{-1} at potentials ranging from 0 to −1.6 V versus Ag/AgCl in a CO_2-saturated 0.5 M $KHCO_3$ (Panreac) aqueous solution as the electrolyte. Portions of the MOPM-based GDEs were used as working electrodes, and glassy carbon and Ag/AgCl (sat. KCl) were used as the counter and reference electrode, respectively. The current density is expressed as the total current divided by the geometric surface area of the electrodes.

Elemental analyses (C, H, N) were performed with a Euro EA elemental analyzer (Eurovector, Milan, Italy), whereas the metal content was determined by inductively coupled plasma atomic emission spectrometry (ICP-AES) with a Horiba Yobin Yvon Activa instrument (Kyoto, Japan). The IR spectra were recorded with an Shimadzu FTIR 8400S spectrometer (Shimadzu, Kyoto, Japan) in the 4000–400 cm^{-1} wavenumber region with a PIKE MIRacle universal ATR sampling accessory equipped with a ZnSe crystal. The PXRD patterns were collected using a Phillips X'PERT powder diffractometer (Panalytical, Eindhoven, The Netherlands) with CuK_α radiation (λ = 1.54060 Å) over the range $5 < 2\theta < 70^\circ$ with a step size of 0.02° and an acquisition time of 2 s per step at 25 °C. The N_2 (77 K) physisorption data of the materials (vacuum at 150 °C for 12 h) was recorded with a Quantachrome Autosorb-iQ-MP instrument (Quantachrome Instruments, Florida, United States). Field-emission scanning electron microscopy (SEM) studies were performed with a JEOL JSM-7000F microscope. Before the analysis, all of the GDEs were coated with 5 nm of chromium.

The Cu exposure (*a*) of the GDEs was determined by N_2O pulse chemisorption with an AutoChem 2920 analyzer (Micromeritics, Georgia, USA) coupled to a Omnistar (Balzers Instruments, New Jersey, USA) mass spectrometer. Part of the N_2O can be reduced to N_2 and otherwise chemisorbed or left unreacted. In particular, we calculated the Cu exposure through the cumulative disappearance of N_2O. The GDEs were first treated at 100 °C in a 50 $cm^3 min^{-1}$ stream of 10 vol% H_2 in Ar (Air Liquide, Madrid, Spain) over 2 h. Then, the GDEs were kept at 35 °C in a 50 $cm^3 min^{-1}$ stream of He, and 20 pulses (0.25 cm^3 each) of 10 vol% N_2O in He (Air Liquide, Madrid, Spain) were applied. The signals of the N_2O and N_2 were recorded in the effluent by the mass spectrometer at m/z = 44 and 28, respectively. Cu was assumed to have a density of 1.63×10^{19} Cu atoms per m^2.

Electrochemical cell and experimental conditions

The prepared MOPM-GDEs were evaluated for the continuous electrocatalytic reduction of CO_2 in a filter-press electrochemical cell (Micro Flow Cell, ElectroCell A/S) under ambient conditions. A Nafion 117 cation-exchange membrane was used to separate the cathode and anode compartments. The MOPM-GDEs were employed together with a platinized titanium electrode as the anode and a Ag/AgCl (sat. KCl) reference electrode assembled close to the cathode. A schematic representation of the experimental plant is shown in Scheme 1. The cathode side of the reactor was fed with CO_2 gas (99.99%) at Q_g/A = 10 to 40 mL min^{-1} cm^{-2}. A 0.5 M $KHCO_3$ (Panreac) aqueous solution was used as both the catholyte and anolyte at Q_e/A = 1–4 mL min^{-1} cm^{-2}. The electrolytes were pumped from the catholyte and anolyte tanks to the cell by two peristaltic pumps (Watson Marlow 320, Watson Marlow Pumps Group). In this study, the filter-press electrochemical system possesses three inputs (catholyte, anolyte, and CO_2 separately) and two outputs (catholyte-CO_2 and anolyte), which make possible the formation of a gas–solid–liquid interface for the electrocatalytic reduction of CO_2 in the gas phase.[4]

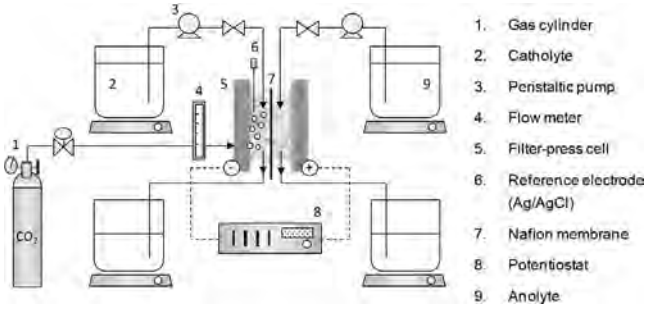

Scheme 1. Schematic representation of the experimental setup.

All of the experiments were performed under galvanostatic conditions (i.e., at a constant current density) with an AutoLab PGSTAT 302N potentiostat (Metrohm, Autolab B.V.). The current density ranged from j = 5 to 40 mA cm^{-2}. The experimental time was 90 min, for which pseudostable conditions are ensured according to our previous analyses.[4,5] Liquid samples were taken every 15 min from the catholyte tank. To quantify the concentration of each product in the liquid phase, the samples were analyzed in duplicate in a headspace gas chromatograph (GC–MS QP2010, Ultra Shimadzu) equipped with a flame ionization detector (FID). The compounds were separated using a DB-Wax 30 m × 0.25 mm × 0.25 μm column with an injection and detector temperature of 250 and 270 °C, respectively. Helium was used as the carrier gas at a flow rate of 50 mL min^{-1}. The identification of the obtained products was further confirmed by a headspace GC–MS instrument (N5975B) equipped with a 60 m × 250 μm × 1.40 μm DB-624 capillary column. The product concentrations were averaged from at least three replicates. The standard deviations of all experiments were below 19.2%.

The performance of the electrochemical processes were evaluated through the rate of product formation, *r* (i.e., the product obtained per unit of cathode area and time), and the Faradaic efficiency, FE (i.e., the selectivity of the reaction for the formation of the different products), according to Equation (1):

$$FE(\%) = (znF)/q \times 100 \quad (1)$$

z is the theoretical number of electrons exchanged to form the desired product, *n* is the number of moles produced, *F* is the Faradaic constant (96485 C mol^{-1}), and *q* is the total charge applied in the process.

Acknowledgements

The authors gratefully acknowledge the financial support from the Spanish Ministry of Economy and Competitiveness (MINECO) under projects CTQ2013-48280-C3-1-R and CTQ2013-48280-C3-3-R and MAT2013-46502-C2-1-P, and the Juan de la Cierva program (JCI-2012-12073).

Keywords: alcohols · copper · electrodes · metal–organic frameworks · reduction

[1] M. E. Boot-Handford, J. C. Abanades, E. J. Anthony, M. J. Blunt, S. Brandani, N. Mac Dowell, J. R. Fernandez, M. C. Ferrari, R. Gross, J. P. Hallet, R. S. Haszeldine, P. Heptonstall, A. Lyngfelt, Z. Makuch, E. Mangano, R. T. J. Porter, M. Pourkashanian, G. T. Rochelle, N. Shah, J. G. Yao, P. S. Fenell, *Energy Environ. Sci.* **2014**, *7*, 130 – 189.
[2] J. Albo, T. Yoshioka, T. Tsuru, *Sep. Purif. Technol.* **2014**, *122*, 440 – 448.
[3] J. Albo, A. Irabien, *J. Chem. Technol. Biotechnol.* **2012**, *87*, 1502 – 1507.
[4] J. Albo, A. Irabien, *J. Catal.* **2015**, DOI: 10.1016/j.jcat.2015.11.014.
[5] J. Albo, A. Sáez, J. Solla-Gullón, A. Irabien, *Appl. Catal. B* **2015**, *176 – 177*, 709 – 717.
[6] A. Del Castillo, M. Alvarez-Guerra, A. Irabien, *AIChE J.* **2014**, *60*, 3557 – 3564.
[7] G. Centi, S. Perathoner, *Catal. Today* **2009**, *148*, 191 – 205.
[8] J. Albo, M. Alvarez-Guerra, P. Castaño, A. Irabien, *Green Chem.* **2015**, *17*, 2304 – 2324.
[9] J. Qiao, Y. Liu, F. Hong, J. Zhang, *Chem. Soc. Rev.* **2014**, *43*, 631 – 675.
[10] M. Alvarez-Guerra, J. Albo, E. Alvarez-Guerra, A. Irabien, *Energy Environ. Sci.* **2015**, *8*, 2574 – 2599.
[11] I. Ganesh, *Renewable Sustainable Energy Rev.* **2014**, *31*, 221 – 257.
[12] A. Goeppert, M. Czaun, J. P. Jones, G. K. Surya Prakash, G. A. Olah, *Chem. Soc. Rev.* **2014**, *43*, 7995 – 8048.
[13] M. Gattrell, N. Gupta, A. Co, *J. Electroanal. Chem.* **2006**, *594*, 1 – 19.
[14] A. A. Peterson, F. Abild-Pedersen, F. Studt, J. Rossmeisl, J. K. Nørskov, *Energy Environ. Sci.* **2010**, *3*, 1311 – 1315.
[15] K. P. Kuhl, E. R. Cave, D. N. Abram, T. F. Jaramillo, *Energy Environ. Sci.* **2012**, *5*, 7050 – 7059.
[16] Y. Liu, Z. U. Wang, H. C. Zhou, *Greenhouse Gases Sci. Technol.* **2012**, *2*, 239 – 259.
[17] J. Gascon, A. Corma, F. Kapteijn, F. X. Llabrés I Xamena, *ACS Catal.* **2014**, *4*, 361 – 378.
[18] A. Doménech, H. García, M. T. Doménech-Carbó, F. Llabrés-i-Xamena, *J. Phys. Chem. C* **2007**, *111*, 13701 – 13711.
[19] R. S. Kumar, S. S. Kumar, M. A. Kulandainathan, *Electrochem. Commun.* **2012**, *25*, 70 – 73.
[20] R. Hinogami, S. Yotsuhashi, M. Deguchi, Y. Zenitani, H. Hashiba, Y. Yamada, *ECS Electrochem. Lett.* **2012**, *1*, H17 – H19.
[21] T. Maihom, S. Wannakao, B. Boekfa, J. Limtrakul, *J. Phys. Chem. C* **2013**, *117*, 17650 – 17658.
[22] I. Hod, P. Deria, W. Bury, J. E. Mondloch, C. W. Kung, M. So, M. D. Sampson, A. W. Peters, C. P. Kubiak, O. K. Farha, J. R. Hupp, *Nat. Commun.* **2015**, *6*, 8304.
[23] I. Hod, M. D. Sampson, P. Deria, C. P. Kubiak, O. K. Farha, J. T. Hupp, *ACS Catal.* **2015**, *5*, 6302 – 6309.
[24] N. Kornienko, Y. Zhao, C. S. Kley, C. Zhu, D. Kim, S. Lin, C. J. Chang, O. M. Yaghi, P. Yang, *J. Am. Chem. Soc.* **2015**, *137*, 14129 – 14135.
[25] W. Xia, A. Mahmood, R. Zou, Q. Xu, *Energy Environ. Sci.* **2015**, *8*, 1837 – 1866.
[26] S. Lin, C. S. Diercks, Y. B. Zhang, N. Kornienko, E. M. Nichols, Y. Zhao, A. R. Paris, D. Kim, P. Yang, O. M. Yaghi, C. J. Chang, *Science* **2015**, *349*, 1208 – 1213.
[27] M. R. Lohe, M. Rose, S. Kaskel, *Chem. Commun.* **2009**, 6056 – 6058.
[28] S. Xiang, L. Li, J. Zhang, X. Tan, H. Cui, J. Shi, Y. Hu, L. Chen, C. Y. Su, S. L. James, *J. Mater. Chem.* **2012**, *22*, 1862 – 1867.
[29] L. Li, S. Xiang, S. Cao, J. Zhang, G. Ouyang, L. Chen, C. Y. Su, *Nat. Commun.* **2013**, *4*, 1174.
[30] Q. Yang, X. Tan, S. Wang, J. Zhang, L. Chen, J. P. Zhang, C. Y. Su, *Microporous Mesoporous Mater.* **2014**, *187*, 108 – 113.
[31] H. Zhu, X. Yang, E. D. Cranston, S. Zhu, *Adv. Mater.* **2016**, DOI: 10.1002/adma.201601351.
[32] S. S. Chui, S. M. Lo, J. P. Charmant, A. G. Orpen, I. D. William, *Science* **1999**, *283*, 1148 – 1150.
[33] K. Sumida, D. L. Rogow, J. A. Mason, T. M. McDonald, E. D. Bloch, Z. R. Herm, T. Bae, J. R. Long, *Chem. Rev.* **2012**, *112*, 724 – 781.
[34] S. Pérez-Yáñez, G. Beobide, O. Castillo, M. Fischer, F. Hoffmann, M. Fröba, J. Cepeda, A. Luque, *Eur. J. Inorg. Chem.* **2012**, 5921 – 5933.
[35] T. Y. Chang, R. M. Liang, P. W. Wu, J. Y. Chen, Y. C. Hsieh, *Mater. Lett.* **2009**, *63*, 1001 – 1003.
[36] M. Le, M. Ren, Z. Zhang, P. T. Sprunger, R. L. Kurtz, J. C. Flake, *J. Electrochem. Soc.* **2011**, *158*, E45 – E49.
[37] Y. Lan, S. Ma, J. Lu, P. J. A. Kenis, *Int. J. Electrochem. Sci.* **2014**, *9*, 7300 – 7308.
[38] F. Jia, X. Yu, L. Zhang, *J. Power Sources* **2014**, *252*, 85 – 89.
[39] D. Chi, H. Yang, Y. Du, T. Lv, G. Sui, H. Wang, J. Lu, *RSC Adv.* **2014**, *4*, 37329 – 37332.
[40] R. Kas, R. Kortlever, A. Milbrat, M. T. M. Koper, G. Mul, J. Baltrusaitis, *Phys. Chem. Chem. Phys.* **2014**, *16*, 12194 – 12201.
[41] C. W. Li, J. Ciston, M. W. Kanan, *Nature* **2014**, *508*, 504 – 507.
[42] D. Ren, Y. Deng, A. D. Handoko, C. S. Chen, S. Malkhandi, B. S. Yeo, *ACS Catal.* **2015**, *5*, 2814 – 2821.
[43] R. Kas, R. Kortlever, H. Yilmaz, T. M. Koper, G. Mul, *ChemElectroChem* **2015**, *2*, 354 – 358.
[44] C. Genovese, C. Ampelli, B. C. Marepally, G. Papanikolaou, S. Perathoner, G. Centi, *Chem. Eng. Trans.* **2015**, *43*, 2281 – 2286.
[45] A. Javier, J. H. Baricuatro, Y. G. Kim, M. P. Soriaga, *Electrocatalysis* **2015**, *6*, 493 – 497.
[46] N. Gutiérrez-Guerra, L. Moreno-López, J. C. Serrano-Ruiz, J. L. Valverde, A. de Lucas-Consuegra, *Appl. Catal. B* **2016**, *188*, 272 – 282.
[47] Q. Wang, H. Dong, H. Yu, *RSC Adv.* **2014**, *4*, 59970 – 59976.
[48] Q. Wang, H. Dong, H. Yu, *J. Power Sources* **2014**, *271*, 278 – 284.
[49] J. Wu, P. P. Sharma, B. H. Harris, X. D. Zhou, *J. Power Sources* **2014**, *258*, 189 – 194.
[50] S. Lee, H. Ju, R. Machunda, S. Uhm, J. Kwang Lee, H. Jin Lee, J. Lee, *J. Mater. Chem. A* **2015**, *3*, 3029 – 3034.
[51] K. W. Frese, *J. Electrochem. Soc.* **1991**, *138*, 3338 – 3344.
[52] L. M. Aeshala, R. G. Uppaluri, A. Verma, *J. CO_2 Util.* **2013**, *3 – 4*, 49 – 55.
[53] E. Andrews, M. Ren, F. Wang, Z. Zhang, P. Sprunger, R. Kurtz, J. Flake, *J. Electrochem. Soc.* **2013**, *160*, H841 – H846.
[54] D. P. Summers, S. Leach, K. W. Frese, *J. Electroanal. Chem.* **1986**, *205*, 219 – 232.
[55] A. Li, H. Wang, J. Han, L. Liu, *Front. Chem. Sci. Eng.* **2012**, *6*, 381 – 388.
[56] L. M. Huang, H. T. Wang, J. X. Chen, Z. B. Wang, J. Y. Sun, D. Y. Zhao, Y. S. Yan, *Microporous Mesoporous Mater.* **2003**, *58*, 105 – 114.
[57] S. Hausdorf, J. Wagler, R. Mossig, F. O. Mertens, *J. Phys. Chem. A* **2008**, *112*, 7567 – 7576.
[58] M. Lanchas, S. Arcediano, A. T. Aguayo, G. Beobide, O. Castillo, J. Cepeda, D. Vallejo-Sánchez, A. Luque, *RSC Adv.* **2014**, *4*, 60409 – 60412.
[59] S. Pérez-Yáñez, G. Beobide, O. Castillo, J. Cepeda, A. Luque, A. T. Aguayo, P. Román, *Inorg. Chem.* **2011**, *50*, 5330 – 5332.

Received: May 24, 2016
Published online on August 25, 2016

5.3. SUPPORTING INFORMATION

CHEMISTRY & SUSTAINABILITY
CHEMSUSCHEM
ENERGY & MATERIALS

Supporting Information

Copper-Based Metal–Organic Porous Materials for CO_2 Electrocatalytic Reduction to Alcohols

Jonathan Albo,*[a] Daniel Vallejo,[b] Garikoitz Beobide,[b] Oscar Castillo,[b] Pedro Castaño,[a] and Angel Irabien[c]

cssc_201600693_sm_miscellaneous_information.pdf

Supplementary Information

Copper-Based Metal-Organic Porous Materials for CO_2 Electrocatalytic Reduction to Alcohols

Jonathan Albo,[a,*] Daniel Vallejo,[b] Garikoitz Beobide,[b] Oscar Castillo,[b] Pedro Castaño,[a] and Angel Irabien [c]

[a]*Department of Chemical Engineering, University of the Basque Country, Apdo. 644, 48080, Bilbao, Spain*

[b]*Inorganic Chemistry Department, University of the Basque Country, Apdo. 644, 48080, Bilbao, Spain*

[c]*Department of Chemical & Biomolecular Engineering, University of Cantabria, Avda. Los Castros s/n, 39005 Santander, Spain*

[*]Corresponding author; e-mail: jonathan.albo@ehu.es

S1. STRUCTURAL FEATURES OF THE SELECTED MOPMS

The structure of HKUST-1 is built up by paddle-wheel type binuclear copper(II) entities linked among them by the tritopic carboxylic ligand (Figure S1.1a). The resulting micropourous network consists of small octahedral cages connected to form two types of large cavities of cubooctahedral symmetry with pores of 9 and 6 Å in diameter. Reported specific surface area values range from 700 to 1900 $m^2 \cdot g^{-1}$. The axially coordinated water molecules at the copper sites can be removed rendering an unsaturated coordination position (so called open-metal site) which enhances ability to interact with guest molecules. It deserves to note that HKUST-1 has been widely studied as CO_2 adsorbent from flue gas. The secondly selected MOF, $[Cu_2(\mu_3\text{-adeninate})_2(\mu_2\text{-}OOC(CH_3)_2]_3 \cdot xH_2O$ (CuAdeAce**)** is built from paddle-wheel shaped copper(II) centrosymmetic dimeric entities (Figure S1.1b). The dinuclear units are cross-linked through the apical coordination of the imidazole N7 atom of the adeninato ligands to four adjacent entities, giving rise to a 3D pore system in which the diameter ranges from ca. 0.4 to 0.6 nm and the surface is decorated by the Watson-Crick faces of the adenine. The latter structural feature renders a highly selective adsorption towards CO_2. CuAdeAce presents specific surface areas ranging from 450-570 $m^2 \cdot g^{-1}$. Regarding the metal-organic aerogels (MOAs), one of the most remarkable advantages arises from the possibility of dispensing of the prerequisites imposed by the reticular design of MOFs, which implies that this approach to prepare porous coordination polymers is in principle extensible to any metal-organic system. In this sense, one must consider that there are many polymers with appealing catalytic, electrical, magnetic or optic properties whose crystal structures lack any porosity arising from the connectivity of the coordination network. Taking this in mind, we have selected a coordination polymer named MDTA (M(II) = Cu, Zn; Figure S1.1c), built from the successive junction a M(II) and bis-bidentate dithiooxamidate (DTA). However, as the coordination framework lacks of any intrinsic pore system, we have processed the material as a nanofibrous aerogel in orther to increase the surface area and the accessibility of the catalytic centers.

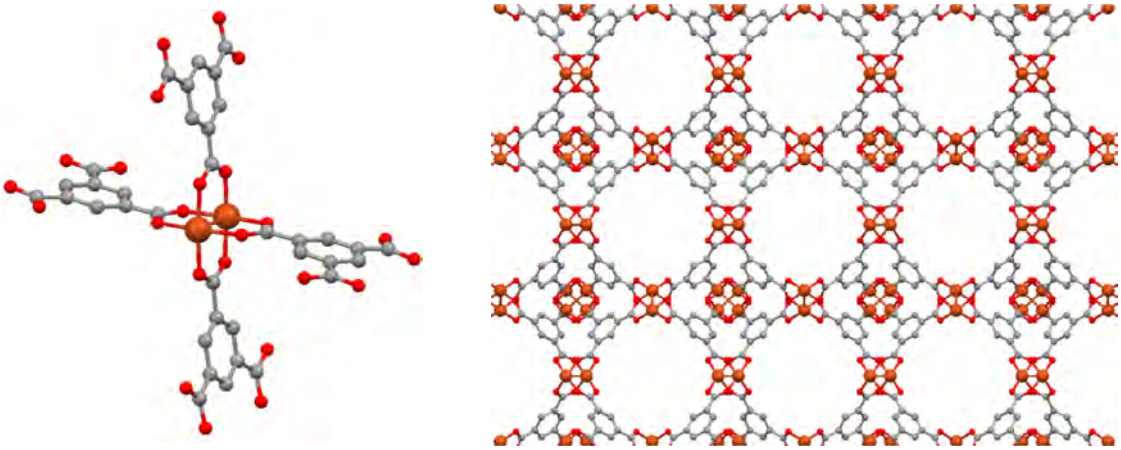

(a)

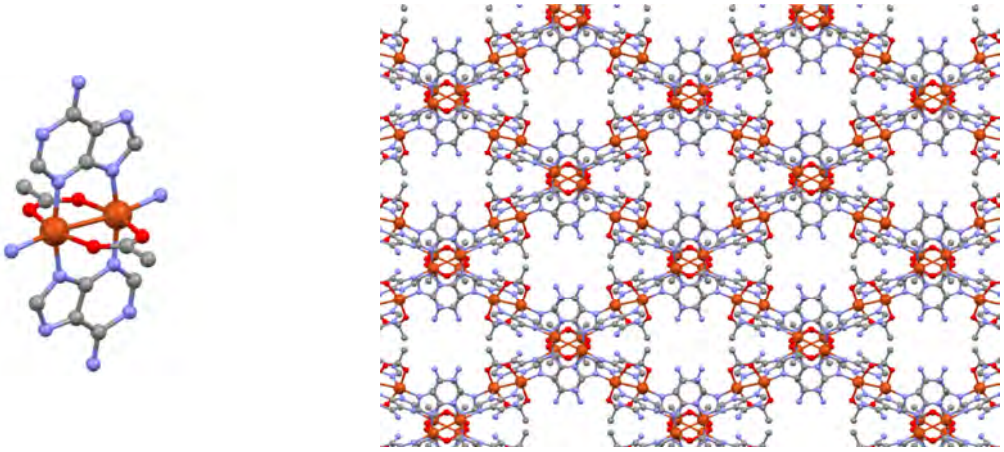

(b)

(c)

Figure S1.1. Molecular building unit and a view of the crystal structure for the microporous MOFs: (a) HKUST-1 and (b) CuAdeAce. (c) Polymeric chain and a sketch of the microstrure for the mesoporous MDTA aerogel. H atoms were omitted for clarity.

S2. CHARACTERIZATION OF THE AS-PREPARED MOPMS

The microtexture all the as-prepared samples was analyzed by scanning electron microscopy (Figure S2.1). The appearance of HKUST-1 and CuAdeAce samples is that of a polycrystalline one, with submicrometric and micrometric crystallite sizes, respectively. The non-crystalline CuDTA and CuZnDTA, are featured by a mesoporous microstructure built by the an intricate network of crosslinked nanofibers (4-15 nm).

ATR-FTIR spectra of as prepared HKUST-1, CuAdeAce, CuDTA and CuZnDTA samples are shown in Figure S2.2. All the bands, fit the expected vibration modes for the ligand and compared to those found on modified electrodes (see Section S3, Table S3.1).

The permanent porosity was studied by means of the measurements of N_2 adsorption isotherms at 77 K (Figure S2.3) using a *Quantachrome* Autosorb-iQ analyser. All samples were dried under vacuum at 140ºC during six hours to eliminate solvent guest molecules prior to measurements. The surface area values were obtained by the fittings of the adsorption data to Braunauer-Emmett-Teller (BET) equation. In order to choose the pressure range appropriate and to avoid ambiguity when reporting the BET surface area of MOFs, we used the three consistency criteria proposed by Walton and Snurr:[1] (1) The pressure range selected should have values of $V(P_0 - P)$ increasing with P/P_0. (2) The points used to calculate the BET surface area must be linear with an upward slope. (3) The line they form must have a positive y-intercept. This procedure is commonly applied for determining the BET surface area values of high/ultrahigh MOFs.[2] Mean pore size for CuDTA and CuZnDTA were calculated from the BJH fitting of the isotherm, while the pore sizes of the microporous HKUST-1 and CuAdeAce correspond to crystallographic values. BET fitting data is gathered in Table S.1, together with other porous features.

PXRD experimental patterns of as prepared samples are shown in Figure S2.4. The simulated patterns were built on the basis of representative crystal structures obtained from the *Cambridge Structural Database* (CSD)[3] for each MOFs (CSD codes: UVIPIZ and DOTSOV01 for HKUST-1 and CuAdeAce, respectively).

[1] K. S. Walton, R. Q. Snurr, *J. Am. Chem. Soc.* **2007**, *127*, 8552.

[2] (a) O. K. Farha, A. O. Yazaydin, I. Eryazici, C. D. Malliakas, B. G. Hauser, M. G. Kanatzidis, S. T. Nguyen, R. Q. Snurr, J. T. Hupp, *Nat. Chem.* **2010**, *2*, 944. (b) H. Furukawa, N. Ko, Y. B. Go, N. Aratani, S. B. Choi, E. Choi, A. O. Yazaydin, R. Q. Snurr, M. O´Keeffe, J. Kim, O. M. Yaghi, *Science* **2010**, *329*, 424. (c) O. K. Farha, I. Eryazici, N. C. Jeong, B. G. Hauser, C. E. Wilmer, A. A. Sarjeant, R. Q. Snurr, S. T. Nguyen, A. O. Yazaydin and J. T. Hupp, *J. Am. Chem. Soc.* **2012**, *134*, 15016.

[3] F. H. Allen, *Acta Crystallogr.* **2002**, *B58*, 380.

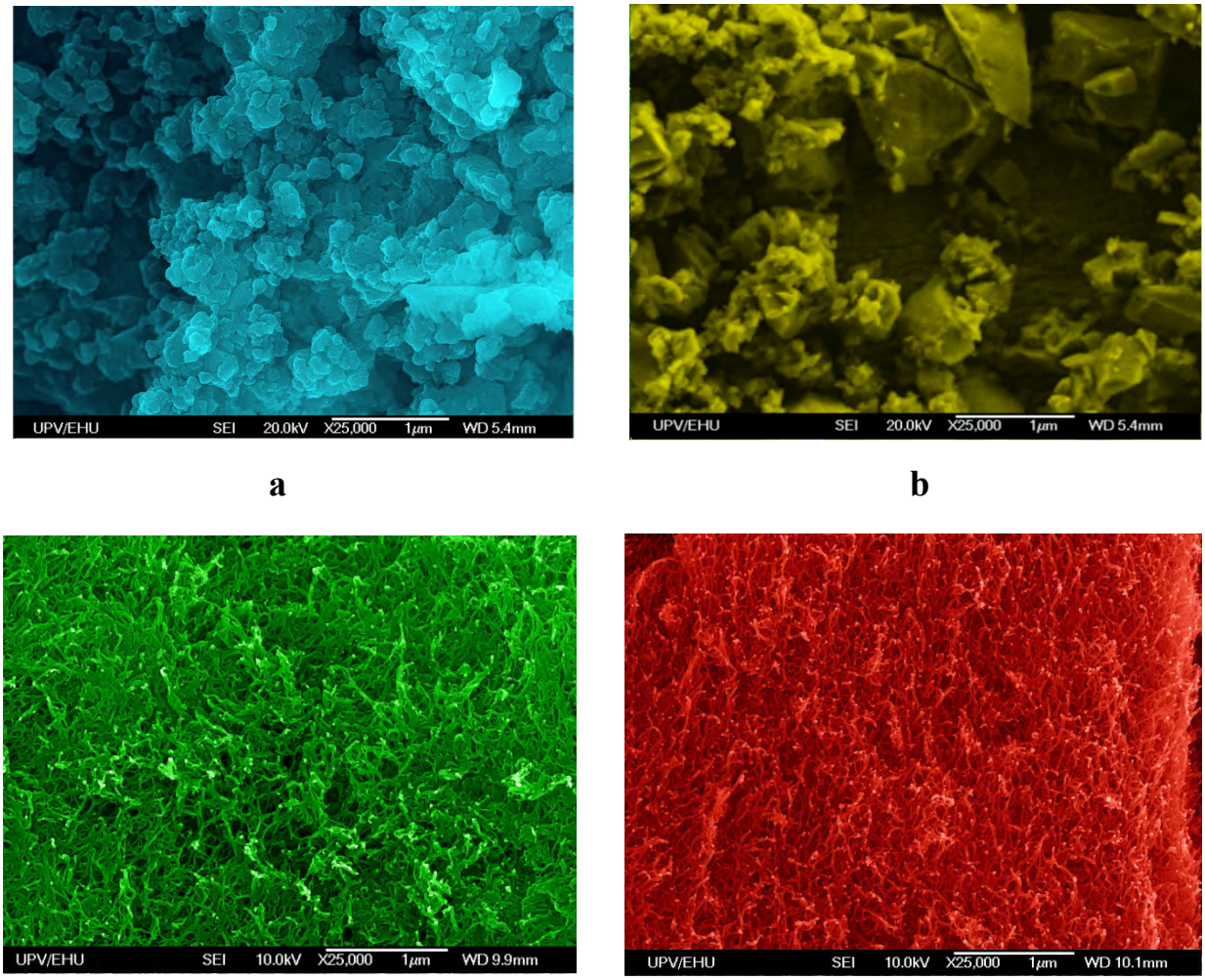

Figure S2.1. SEM images taken on as-prepared MOPM samples: (a) HKUST-1, (b) CuAdeAce, (c) CuDTA y (d) CuZnDTA.

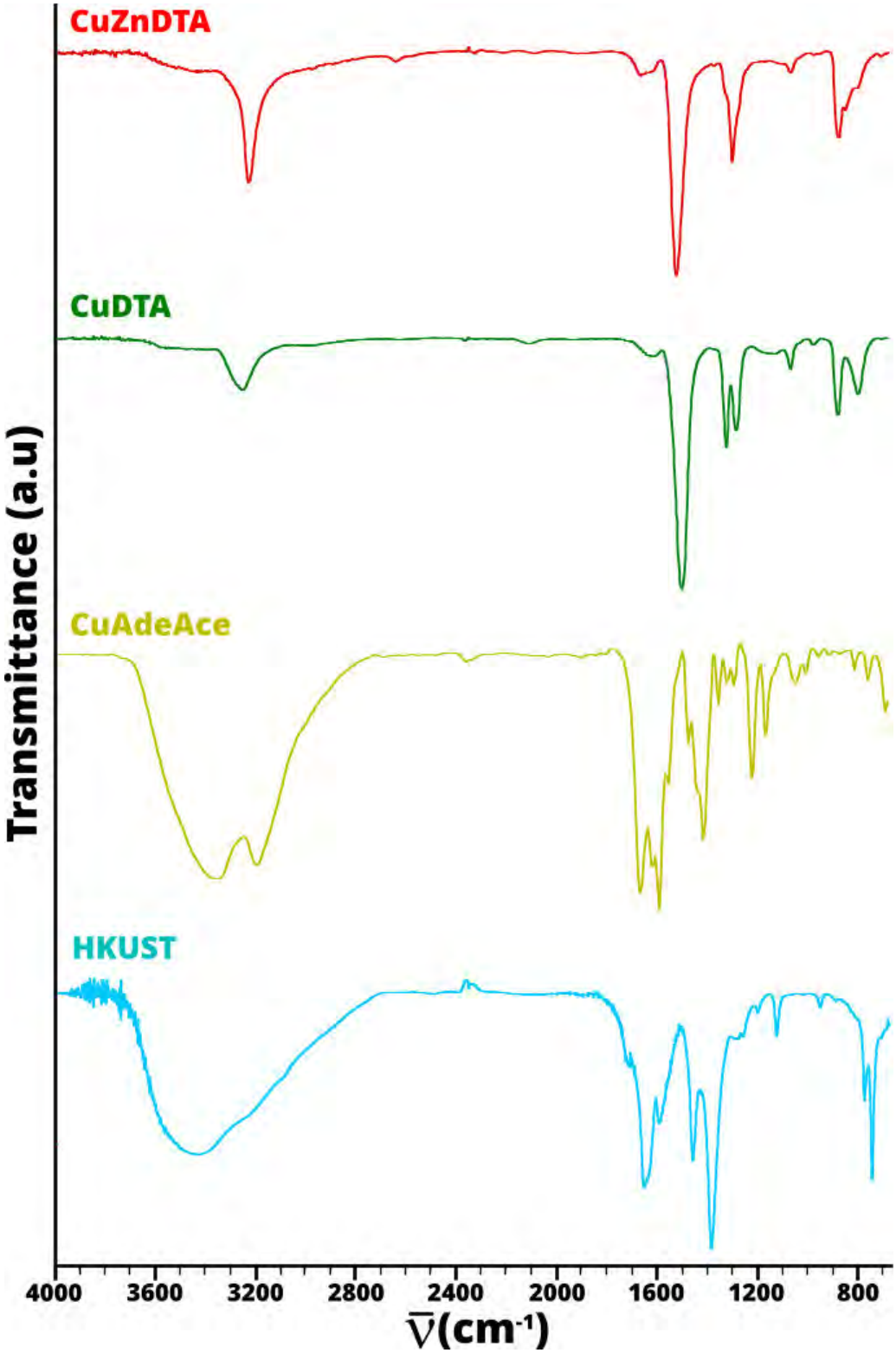

Figure S2.2. FTIR spectra performed upon as-prepared MOPMs samples.

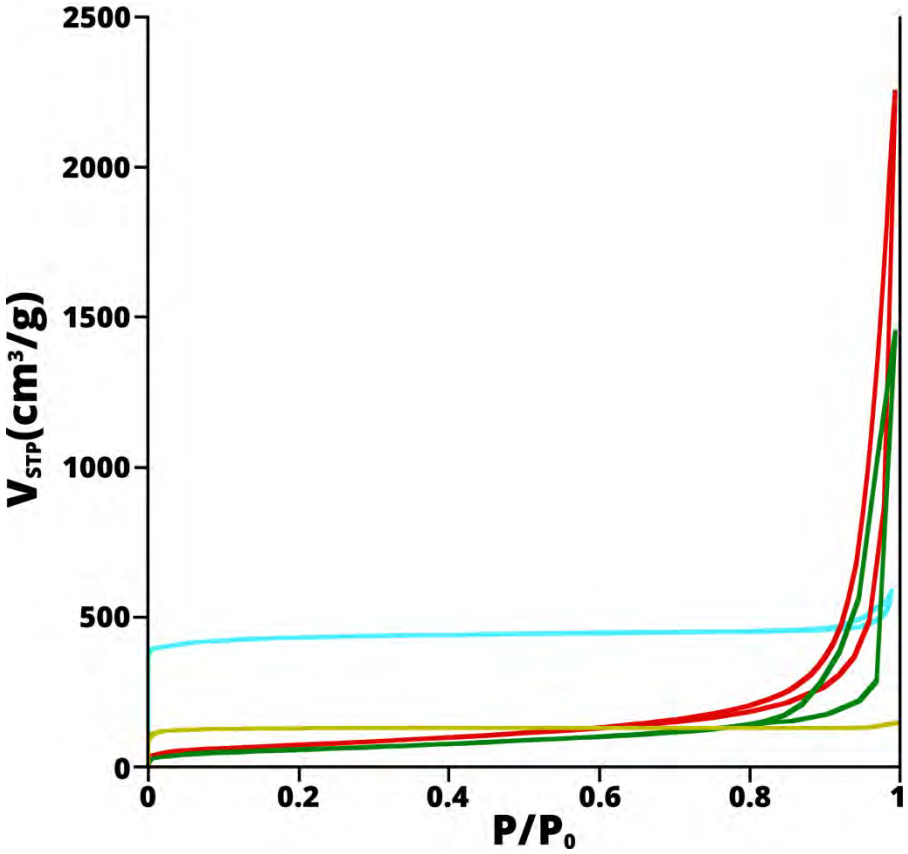

Figure S2.3. Nitrogen adsorption isotherms at 77 K for as prepared MOPM samples.

Table S2.1. BET fitting data, micropore volume and total pore volume.

Sample	**Pressure range**	**R^2**	***c***	**S_{BET} (m^2/g)**	**$V_{micropore}$ (cm^3/g)**	**V_{total} (cm^3/g)** (P/Po < 0.993)
HKUST-1	0.015–0.040	0.9980	28245	1710	0.649	0.908
CuAceAde	0.010–0.030	0.9963	22712	500	0.140	0.212
CuDTA	0.010–0.250	0.9999	130	272	0.004	2.242
CuZnDTA	0.010–0.250	0.9999	104	260	0.001	3.006

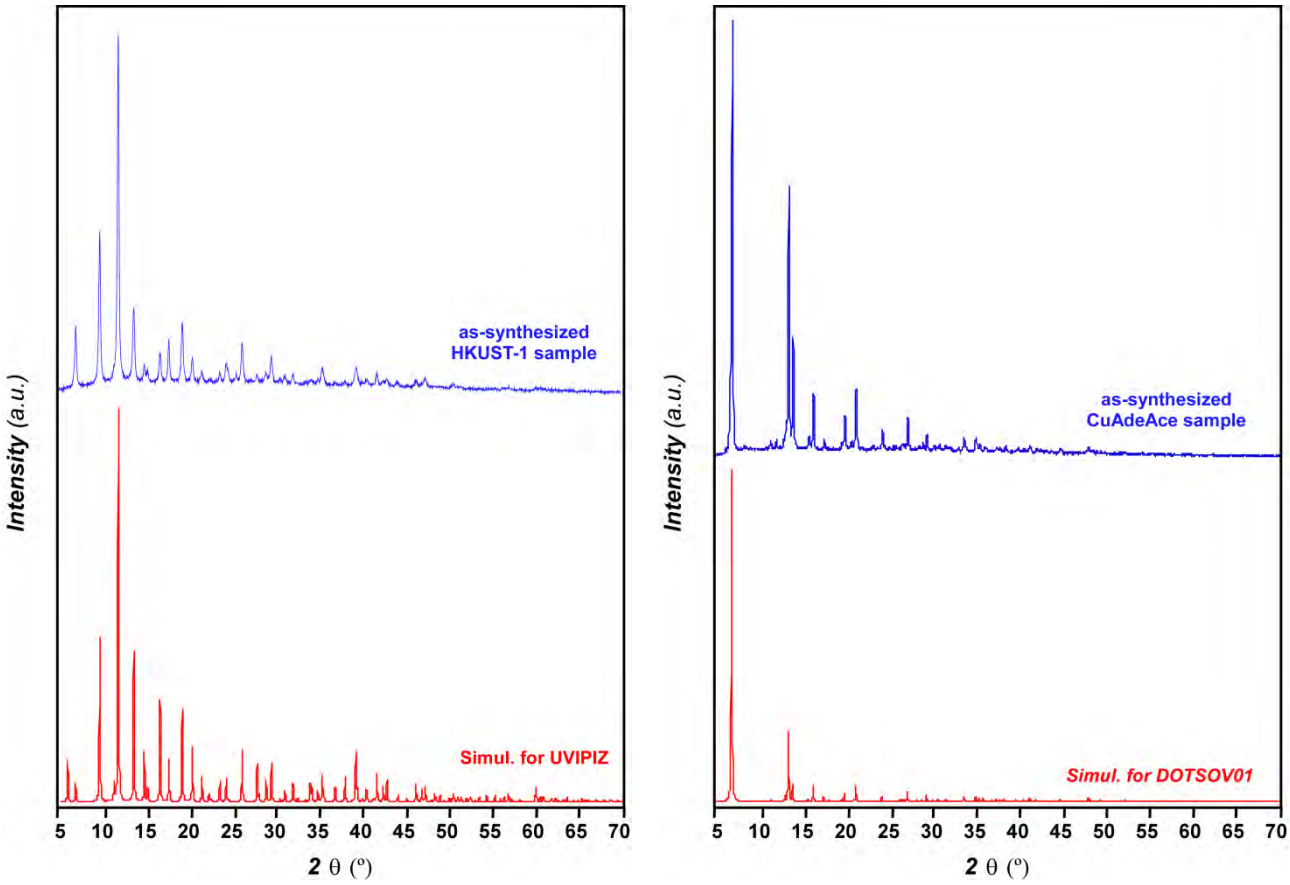

Figure S2.4. Experimental and simulated PXRD patterns for (a) HKUST-1 and (b) CuAdeAce.

S3. CHARACTERIZATION OF THE GDE-MOPMS

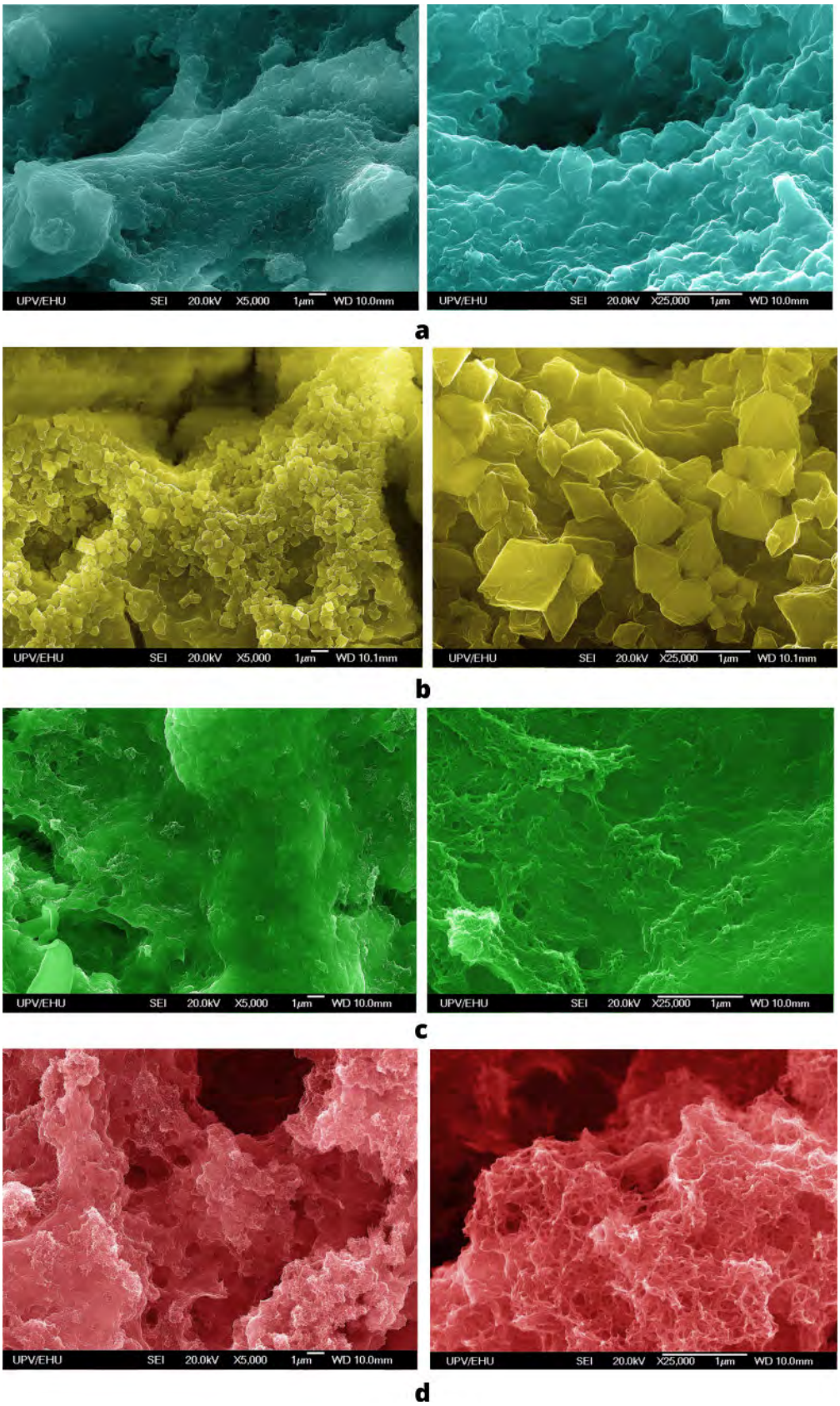

Figure S3.1. SEM images taken at 5 kX (left) and 25 kX (right) for fresh electrodes modified with (a) HKUST-1, (b) CuAdeAce, (c) CuDTA and (d) CuZnDTA.

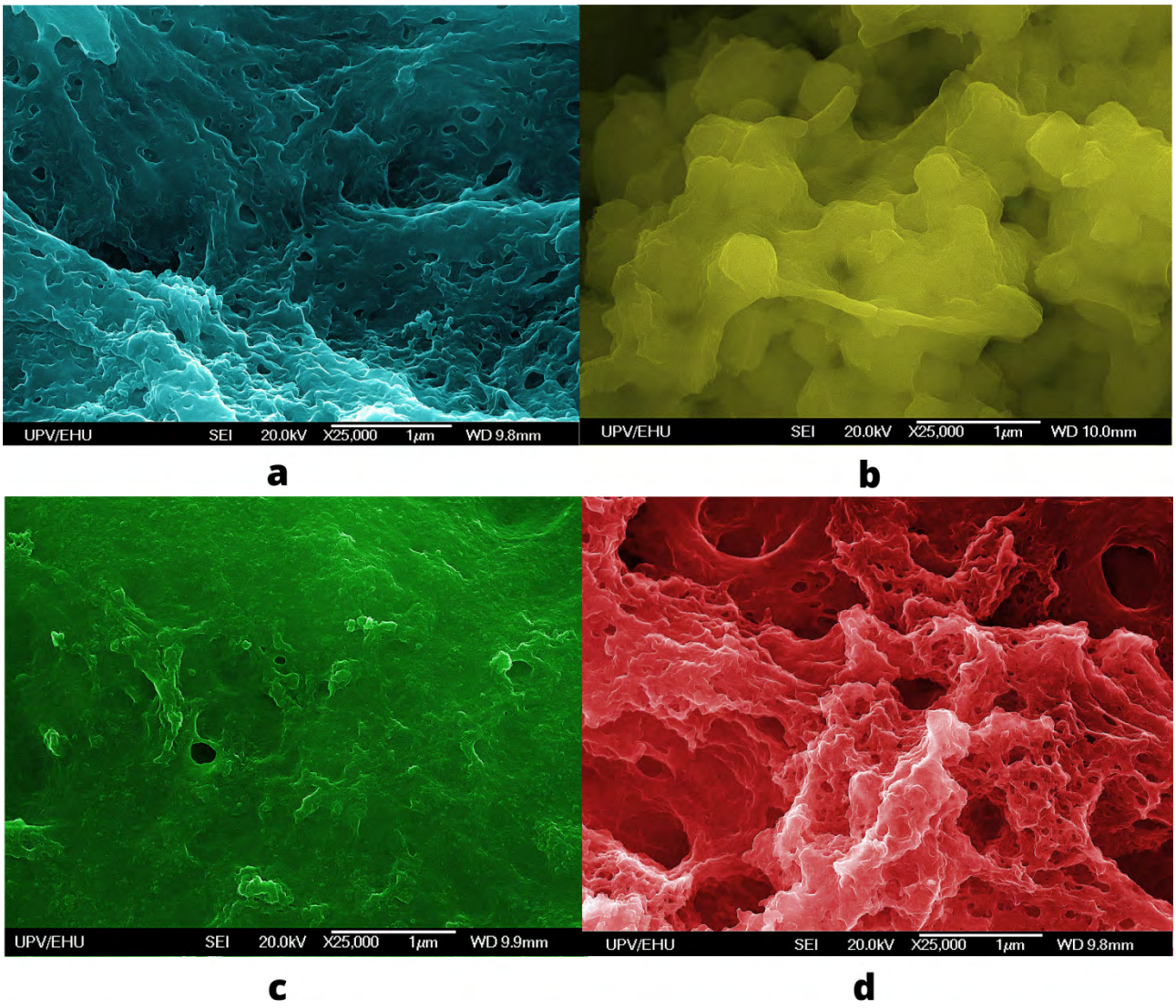

Figure S3.2. SEM images taken at 25 kX (right) for electrodes used during 30 minutes and modified with (a) HKUST-1, (b) CuAdeAce, (c) CuDTA and (d) CuZnDTA.

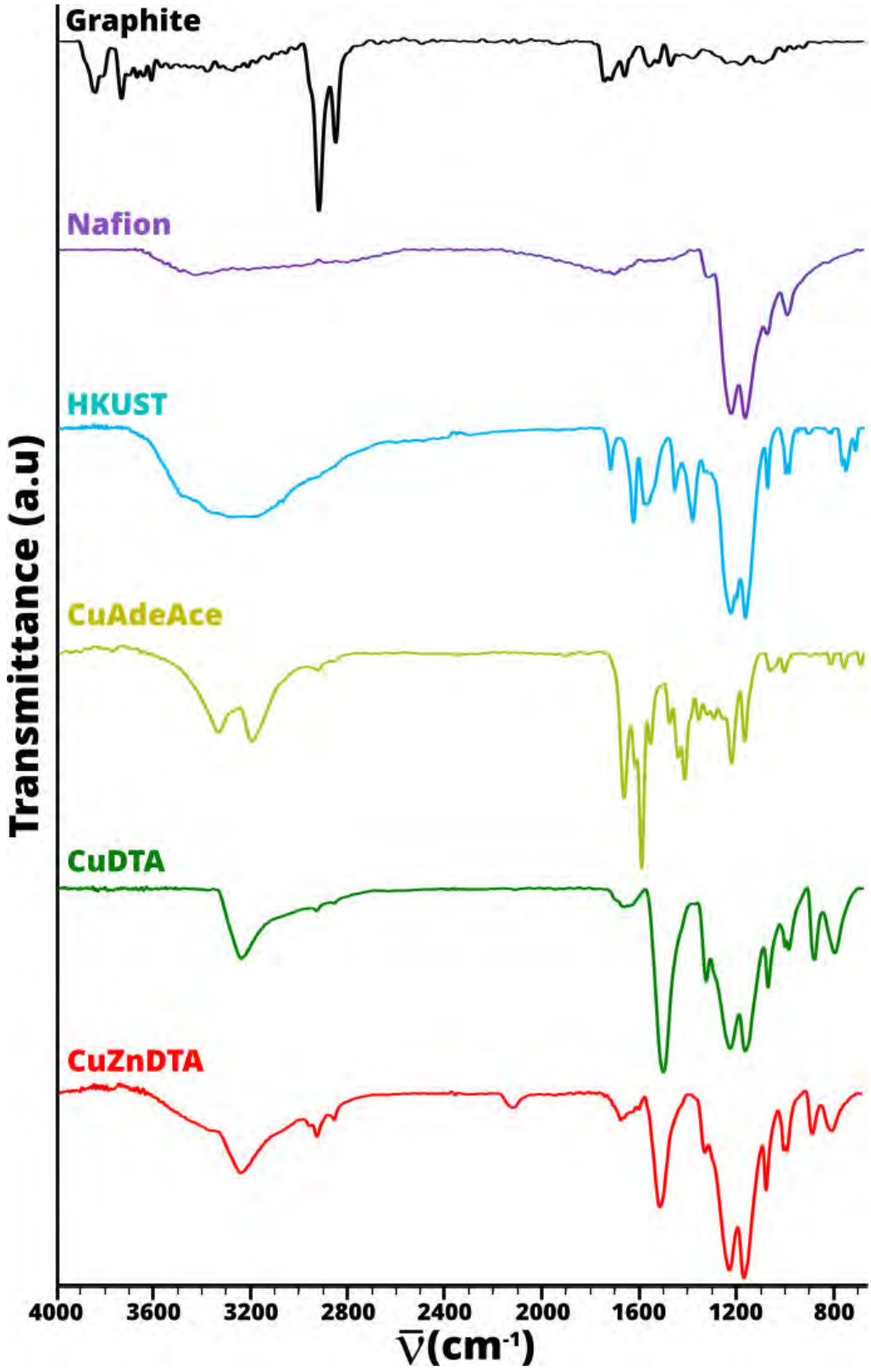

Figure S3.3. ATR-FTIR spectra for pristine graphite electrode and fresh electrodes modified with nafion, HKUST-1, CuAdeAce, CuDTA and CuZnDTA.

Table S3.1. Main IR peaks (cm^{-1}) and corresponding vibration modes for pristine graphite electrode and fresh electrodes modified with nafion, HKUST-1, CuAdeAce, CuDTA and CuZnDTA

GC electrode	Nafion	HKUST-1	CuAdeAce	CuDTA and CuZnDTA
3393 [ν_s(OH)]	1303[ν(C−C)]	3320 [ν_s(OH)]	3348 [ν_s(OH)]	3489 [ν_{as}(NH)]
2923 [ν(C−H)]	1206 [$\nu_{as}(CF_2)$]	2968 [ν(C−H)]	3192 [$\nu_s(NH_2)+\delta(NH_2)$]	3242 [ν_s(NH)]
2850 [ν(C−H)]	1147 [$\nu_s(CF_2)$]	2845 [ν(C−H)]	2962 [ν(C8−H)+ ν(C2−H)]	2958 [ν_s(NH)]
1737 [ν(C=O)]	1059[ν_s(SO)]	1618 [ν_s(C=O)]	2933 [$\nu(NH_2)+ \nu$(C−H)]	2924 [ν(C−H)]
1708 [ν(C=O)]	975 [ν_s(CF)+ ν_s(COC)]	1576 [ν_s(COO)]	2856 [ν(C−H)]	2852 [ν(C−H)]
1652 [ν(C=C)]		1552 [ν_s(COO)]	1643[ν_{as}(O−C−O)]	1662 [ν(CS)]
1559 [ν(C=C)]		1440 [ν_{as}(COO)]	1609 [ν_s(C=C)+ $\delta(NH_2)$]	1627 [ν(CS)]
		1370 [ν_{as}(COO)]	1584[ν_s(C4−C5)]	1485 [ν(CN)]
		1294 [ν(C−C)]	1549 [ν_s(N3−C4−C5)]	1309 [ν(C−C)]
		1202 [$\nu_{as}(CF_2)$]	1468 [δ(C2−H)+δ(C8−N9)]	1224 [$\nu_{as}(CF_2)$]
		1143 [$\nu_s(CF_2)$]	1431[ν_s(C8−H)]	1151 [$\nu_s(CF_2)$]
		1057 [ν_s(SO)]	1400 [δ(N1−C6−H6)]	1053 [ν_s(SO)]
		982[ν_s(CF)]	1379, 1348 [ν(C5−N7−C8)]	982 [ν_s(CF)]
		972 [ν_s(C−O−C)]	1300 [ν(C−C)]	966 [ν_s(C−O−C)]
		752[ν(phenyl)]	1207 [$\nu_{as}(CF_2)$]	860 [ν(CS)]
		729[ν(phenyl)]	1151 [$\nu_s(CF_2)$]	775 [π(NH)]
			1057 [ν_s(SO)]	
			982 [ν_s(CF)]	
			972 [ν_s(C−O−C)]	
			796 [δ(O−C−O)]	
			743[δ(O−C−O)]	

6. CONCLUSIONS AND FUTURE PROSPECTS

6.1. CONCLUSIONS

The most relevant results of the present work are summarized in the following points:

1. A total of 12 new compounds have been synthesized using thiocarboxylate anions as sulfur source (thioacetate and thiobenzoate) and nitrogenous heterocycles with at least two donor atoms as secondary ligands (2,2'-bipyridine, 1,10-phenanthroline, neocuproine, 1,2-bis(4-pyridyl)ethylene and adenine) to complete the coordination sphere of the metal center and to direct the dimensionality of the complexes. All of them have been structurally characterized by single crystal X-ray diffraction.

2. In all compounds, the metal is preferentially bonded to the sulfur atom from the thioacetate group. In some cases, there is a semi-coordination of the oxygen with distances M–O lower than the sum of their respective van der Waals radii. This fact is a common trend in soft metal cations such as those herein used (Cd^{2+}, Zn^{2+} and Pd^{2+}). In all cases, thiocarboxylato ligands behave as terminal ligands, in agreement with the trend found in the literature for these class of coordination complexes.

3. Compounds based on *N,N'*-heterocycles of chelating nature (2,2'-bipyridine, 1,10-phenanthroline, and neocuproine) consist of discrete monomeric entities whereas the compound based on 1,2-bis(4-pyridyl)ethylene polymerize to give rise to zig-zag chains. Despite in the case of adenine a polymeric complex was also expected, it coordinates in a monodentate fashion and a methanol molecule occupies the remaining coordination position to provide a monomeric entity.

4. The viability of metal-thiocarboxylato complexes as direct precursors of nanostructures has been studied through the dry thermolysis method, a variant of the precursor single-source route that eliminates the need for solvents and surfactants. This process is easily scaled to produce large quantities of nanoparticles at a relatively low cost. This work describes a new route towards obtaining metal sulfide nanoparticles under aerobic conditions (in an open atmosphere).

5. It has been analyzed the influence of certain synthetic variables (heating rate, isotherm time, temperature, etc.) and the structural features of the compounds (nature of the ligands and the metal cations, dimensionality of the structure, etc.) on the characteristics of the resulting nanoparticles: purity, crystallinity, polydispersity and mean particle size, polymorphic phase, morphology, degree of sintering, etc.

6. The decomposition temperatures of the synthesized compounds start from 140 to 240°C, although it has been worked at higher temperatures (300–480ºC) to improve the combustion. These moderate temperatures are easily achievable even with the simple furnaces. Compounds based on thioacetato ligand are generally decomposed at lower temperature than those based on thiobenzoato.

7. In general terms, the average diameter of the metal sulfide nanoparticles produced has ranged between 2–20 nm and the size distributions obtained did not present a great dispersion. Pd-thiocarboxylato precursors generate elemental palladium, which according to X-ray diffraction measurements and transmission microscopy images, consists of large nuclei (~ 60–150 nm) mixed together with smaller nanoparticles (1–25 nm) forming a heterogeneous product.

8. Complexes with 2,2'-bipyridyl or 1,2-bis(4-pyridyl)ethylene co-ligands generate practically pure nanoparticles (a content of carbon impurities lower than 5% by weight) because such ligands during decomposition give fragments of a volatile nature. In return, compounds containing 1,10-phenanthroline, neocuproine or adenine as co-ligands produce samples with so much mass percentage of carbon (it could reach up to 50% of the total weight of the sample) that the resulting nanoparticles are actually embedded in a carbonaceous matrix. Therefore, by varying the secondary ligand we can adjust the amount of carbonaceous matrix that embeds the nanoparticles: from carbon free nanoparticles to carbon supported nanoparticles with tunable carbon content.

9. In the case of ZnS and CdS nanoparticles, the nature of the co-ligand plays a key role in the crystalline phase that occurs after decomposition. Some ligands such as adenine favor the thermodynamically stable phase (blende), others such as neocuproine stabilize the metastable wurtzite phase and finally, there are ligands that have no obvious preference for either of the two phases and result in a polymorphic mixture.

10. Metal-organic gels (MOGs) based on M^{II}-dithiooxamidato (MDTA) polymeric systems (M^{II} being Ni, Cu, Pd and their mixtures) have been achieved. Additionally, a detailed analysis of the most important synthetic parameters in the formation of the gels has been done; among which stand out the coordinating capability of solvents, the dissociation constant of the metal salt used as starting reagent, the presence of a basic catalyst and the concentration of the reagents.

11. Metal-dithiooxamidato gels show unusual chemical inertia derived from the strong metal-sulfur bonds. They are insoluble throughout the 1–14 pH range and they withstand all common organic solvents as well as high concentrations of salts or coordinating ligands. They are even kept unaltered under strong reducing conditions, the presence of mild oxidizing agents and hydrothermal conditions.

12. Metal-organic aerogels (MOAs) have been obtained by supercritical drying of their respective metal-dithioxamidato MOGs. Microstructural characterization of MOAs reveals they correspond to meso-/macroporous solids with specific BET areas of 190–430 $m^2\ g^{-1}$, pore volumes up to 4 $cm^3\ g^{-1}$ and monolith densitites as low as 0.02 $g \cdot cm^{-3}$.

13. The microstructure of MOAs is based on the entanglement of nanofibers of metal-dithiooxamidato polymer. These nanofibers present variable aspect ratios depending on the metal cation used. Cu(II) and Ni(II) ions favors to a greater degree the longitudinal growth of the fiber while the Pd(II) limits its growth, creating more nuclei.

14. The microstructure of the resulting aerogels has a considerable influence on the final density and, consequently, on its mechanical and textural properties. Aerogels made from higher aspect ratio nanofibers appear to be lighter and have a greater polydispersion in pore size (greater macroporous contribution). Also, the combination of long fibers with a larger void space translates into a plastic behavior similar to that observed in polymer foams. In contrast, the existence of fibers with low aspect ratios produces denser aerogels with a smaller and less polydisperse pore size. The more compact structure favors the fracture propagation and therefore these latter aerogels behave as brittle materials.

15. NiDTA aerogel has given a maximum value of specific compressive strength of 12725 $J \cdot kg^{-1}$, which is superior to most inorganic, organic and metal aerogels published to date and it is comparable to that of conventional polymeric foams. It is also the first report of a plastic behavior in a metal-organic aerogel.

16. Metal(II)-dithiooxamidate compounds exhibit semiconductor behavior with conductivities ranging from 10^{-7} to 10^{-12} $S \cdot cm^{-1}$ at room temperature. Cu(II) is the metal cation that offers the best conductivity results possibly due to its ability to be reduced. Iodine doping considerably improves the conductivity of the compounds, reaching values of 10^{-5} $S \cdot cm^{-1}$.

17. Both CuDTA and CuNiDTA aerogels respond to chemical stimuli (acetic acid vapors) by varying their proton conductivity in approximately two orders of magnitude. It has been shown that this behavior is totally reversible and that the material does not degrade after acetic acid exposure.

18. The catalytic behavior of certain metal-organic porous materials (MOFs and MOAs) has been studied on the selective electroreduction of carbon dioxide to alcohols. The maximum cumulative Faradaic efficiencies for CO_2 conversion at HKUST-1-, CuAdeAce-, CuDTA-, and CuZnDTA-based electrodes are 15.9, 1.2, 6, and 9.9 %, respectively, at a current density of 10 $mA \cdot cm^{-2}$, an electrolyte-flow/area ratio of 3 $mL \cdot min \cdot cm^{-2}$, and a gas-flow/area ratio of 20 $mL \cdot min \cdot cm^{-2}$. These results denoted that metal-organic porous materials with unsaturated coordination positions

exposed in the pore system are preferred for the enhancement of the performance of the electrocatalytic reduction of CO_2 to alcohols.

19. The results described in chapters 2, 4 and 5 have been published as three research articles in well rated journals in inorganic chemistry and materials science areas (*European Journal of Inorganic*, *Advanced Functional Materials* and *ChemSusChem*). The content of chapter three has been recently submitted for its peer review. In turn, most of the content of the work has been presented in national and international scientific meetings.

20. Some of the research results have also given rise to a national patent (P201630538) that has now been extended to International Patent Cooperation Treaty (PCT). This patent has attracted private capital investors to constitute a new technological company called *Poretune S.L.* of which I am a founding member. Accordingly, the use and exploitation rights of the aforementioned patent have been licensed to *Poretune S.L.*

6.2. FUTURE PROSPECTS

Future research will focus on the optimization of the synthetic processes used trying to adapt routes to new nanostructured systems.

On the one hand, emphasis will be placed on improving dry thermolysis method applying the results obtained to date. The design of precursors will be more oriented towards the desired final product (pure or carbon supported nanoparticles) trying to reduce the decomposition temperatures, the presence of mixtures of polymorphic phases, polydispersion and sintering of the nanoparticles. New mono-and polynuclear metal-thiocarboxylato complexes will be synthesized in order to prepare new high-value industrial metal sulfides. In addition, it will intend to investigate in greater depth the effect of precursor's dimensionality on the final nanostructured product by preparing new 1D, 2D and 3D coordination compounds.

On the other hand, the knowledge acquired in gelation studies of metal(II)-dithiooxamidato compounds will be used to produce other metal-organic gels with relevant physicochemical properties. The mechanics that govern the formation of MOGs and MOAs and their functionalities for high valued applications will be explored. The possibility of growing these materials on different types of substrates to obtain thin films or one-dimensional nanostructures will be investigated. It will be tried to find out what kind of correlations exist between the different synthetic variables and the physical properties of the resulting nanostructures.

Finally, the philosophy of green chemistry will be strengthened by reducing the use of polluting or toxic species as far as possible. New precursors that can be synthesized in aqueous medium will be sought. In addition, new ligands that emit less pollutant byproducts will be chosen.

7. ANNEXES

7.1. REAGENTS AND SOLVENTS

7.2. PUBLICATIONS RESULTING FROM THIS WORK

7.3. PATENT

7.1. REAGENTS AND SOLVENTS

Table A.1.1 and A.1.2. gather the reactants or solvents, formula, commercial supplier (CS), assay (AS), molecular weight (MW), Chemical Abstracts Service number (CAS), and risk (R) and safety (S) statements for their manipulation.

Table A.1.1 Technical information of the reagents and solvents used in the current work.

Name	Formula	CS	AS	MW ($g \cdot mol^{-1}$)	CAS	R	S
Acetic acid	$C_2H_4O_2$	Aldrich	≥99.5%	60.05	64-19-7	10-35	1/2-23-26-45
Acetone	C_3H_6O	Aldrich	≥99%	58.09	67-64-1	11-36-66-67	9-16-26
Acetonitrile	C_2H_3N	Aldrich	99.8%	41.05	75-05-8	11-23/24/25	1/2-16-27-45
Adenine	$C_5H_5N_5$	Aldrich	≥99%	135.13	73-24-5	22	22-26-36
Ammonia	NH_3	Aldrich	25%	35.04	7664-41-7	34-50	26-36/37/39-45-61
2,2'-Bipyridine	$C_{10}H_8N_2$	Aldrich	≥99%	156.19	366-18-7	21-25	22-36/37-45
4,4'-Bipyridine	$C_{10}H_8N_2$	Aldrich	98%	156.18	553-26-4	25	22-24/25-37-45
1,2-Bis(4-pyridil)ethylene	$C_{12}H_{10}N_2$	Aldrich	97%	182.22	13362-78-2	36/37/38	26-37/39
Cadmium(II) acetate dihydrate	$Cd(CH_3COO)_2 \cdot 2H_2O$	Aldrich	≥98%	266.53	5743-04-4	20/21/22-50/53	60-61
Chloroform	$CHCl_3$	Aldrich	≥99%	119.38	67-66-3	22-38-40-48/20/22	2-36/37
Dichloromethane	CH_2Cl_2	Aldrich	≥99.8%	84.93	75-09-2	40	3-36/37
Diethanolamine	$C_4H_{11}NO_2$	Aldrich	≥98%	105.14	111-42-2	22-38-41-48/22-52/53	26-36/37/39-46-61
N,N'-Diethylacetamide	$C_6H_{13}NO$	Aldrich	≥97%	115.17	685-91-6	22	
Diethylenetriamine	$C_4H_{13}N_3$	Aldrich	99%	103.16	111-40-0	21/22-26-34-37-43	9-26-28-36/37/39-45
Diethyl ether	$C_4H_{10}O$	Aldrich	≥99.7%	74.12	60-29-7	12-19-22-66-67	9-16-29-33
N,N'-Dimethylacetamide	C_4H_9NO	Aldrich	≥99.9%	87.12	127-19-5	20/21/61	53-45
N,N'-Dimethylformamide	C_3H_7NO	Aldrich	99.8%	119.16	68-12-2	61-20/21-36	53-45
Dimethylsulfoxide	C_2H_6OS	Aldrich	≥99.7%	78.13	67-68-5	36/37/38	26-37/39
Ethanol	C_2H_5OH	Aldrich	≥95%	46.07	200-578-6	11	2-7-16
Ethylenediaminetetraacetic acid	$C_{10}H_{16}N_2O_8$	Aldrich	≥98%	292.24	60-00-4	36	26
Hydrochloric acid	HCl	Aldrich	37%	36.46	7732-18-5	34-37	1/2-26-36/37/39-45
Hydrogen peroxide	H_2O_2	Aldrich	30%	34.01	7722-84-1	22-41	1/2-26-28-36/37/39-45
Iodine	I_2	Aldrich	≥99.9%	253.81	7553-56-2	20/21-50	23-25-61
Lithium nitrate	$LiNO_3$	Aldrich	≥99%	68.95	7790-69-4	8	17

Table A.1.2 Technical information of the reagents and solvents used in the current work (continuation).

Name	Formula	CS	AS	MW ($g \cdot mol^{-1}$)	CAS	R	S
Methanol	CH_3OH	Aldrich	≥99.8%	32.04	67-56-1	11-23/24/25-39/23/24/25	7-16-36/37-45
Neocuproine	$C_{14}H_{12}N_2$	Aldrich	≥98%	208.26	484-11-7	36/37/38	26
Nitric acid	HNO_3	Aldrich	70%	63.01	7697-37-2	35	26-45-24/25-36/37/39-60
Palladium(II) acetate dihydrate	$Pd(CH_3COO)_2 \cdot 2H_2O$	Aldrich	≥99.9%	224.51	3375-31-3	41	22-26-39
Pentane	C_5H_{12}	Aldrich	≥99%	72.15	109-66-0	11	2-9-16-29-33
1,10-Phenanthroline	$C_{12}H_8N_2$	Aldrich	≥99%	180.21	66-71-7	25-50/53	45-60-61
Potassium permanganate	$KMnO_4$	Aldrich	≥99%	158.03	7722-64-7	8-22-50/53	60-61
Pyridine	C_5H_5N	Aldrich	≥99%	79.10	110-86-1	11-20/21/22	2-26-28
Sodium borohydride	$NaBH_4$	Aldrich	≥96%	37.83	16940-66-2	60-61-25-14/15-34	14-26-36/37/39-43-45-53
Sodium chloride	NaCl	Aldrich	≥99.5%	58.44	7647-14-5		24-25
Sodium sulfite	$NaSO_3$	Aldrich	≥98%	126.04	7757-83-7	22-36/37/38	24/25
Sulfuric acid	H_2SO_4	Aldrich	96%	98.08	7664-93-9	35	26-30-45
Terephthalic acid	$C_8H_6O_4$	Aldrich	98%	166.13	100-21-0	36/37/38	24/25
N,N,N',N'-Tetramethylethylenediamine	$C_6H_{16}N_2$	Aldrich	99%	116.21	110-18-9	11-20/22-34	16-26-36/37/39-45
Thioacetic acid	C_2H_4OS	Aldrich	≥95%	76.09	507-09-5	10-34	9-16-33-36/39
Thiobenzoic acid	C_7H_6OS	Aldrich	≥90%	138.19	98-91-9	36/37/38	26-36/37/39
Toluene	C_7H_8	Aldrich	99.8%	92.14	108-88-3	11-20	16-25-29-33
Trimesic acid	$C_9H_6O_6$	Aldrich	95%	210.14	554-95-0	36/37/38	26/37/38/39
Zinc(II) acetate dihydrate	$Zn(CH_3COO)_2 \cdot 2H_2O$	Aldrich	≥99%	219.51	5970-45-6	22-36-50/53	26-60-61

7.2. PUBLICATIONS RESULTING FROM THIS WORK

7.2. PUBLICATIONS RESULTING FROM THIS WORK

This work has led to the publication of some articles in international scientific journals that are attached below:

1. *Zinc Thiocarboxylate Complexes as Precursors for Zinc Sulfide Nanoparticles under Aerobic Conditions*. D. Vallejo-Sánchez, G. Beobide, O. Castillo, M. Lanchas, *Eur. J. Inorg. Chem.* **2013**, 5592–5602.

2. *Metal-Thiobenzoato Complexes: Synthesis, Structure and Processing as Carbon Supported Nanoparticles*. D. Vallejo-Sánchez, G. Beobide, O. Castillo, M. Lanchas, A. Luque, S. Pérez-Yáñez, P. Román, *Eur. J. Inorg. Chem.* (submitted on May 2017).

3. *Chemically Resistant, Shapeable, and Conducting Metal-Organic Gels and Aerogels Built from Dithiooxamidato Ligand*. D. Vallejo-Sánchez, P. Amo-Ochoa, G. Beobide, O. Castillo, M. Fröba, F. Hoffmann, A. Luque, P. Ocón, S. Pérez-Yáñez, *Adv. Funct. Mater.* **2017**, *27,* 1605448.

4. *Copper-Based Metal–Organic Porous Materials for CO_2 Electrocatalytic Reduction to Alcohols*. J. Albo, D. Vallejo, G. Beobide, O. Castillo, P. Castaño, A. Irabien, *ChemSusChem* **2017**, *10*, 1100–1109.

7.3. PATENT

METAL-ORGANIC GELS AND METAL-ORGANIC AEROGELS MADE FROM COORDINATION POLYMER NANOFIBERS

Field of the Invention

The present invention relates to the field of metal-organic gels (MOGs) and metal-organic aerogels (MOAs) of coordination polymer, method for preparing thereof and their use in the capture of chemical species and/or separation, detection, catalysis, environmental cleanup, metal recovery, passive sampling, among others.

Background of the Invention

Porous coordination polymers, also referred to as MOFs (metal-organic frameworks), are characterized by having unique properties as well as multiple functionalities, therefore they have been the focus of countless papers in recent years in the area of physical chemistry, materials science or similar research areas [Zhou, H.C. *Chem. Soc. Rev*., 2014, 43, 5415-5418].

Despite the existence of commercial activity involving materials of this type, MOF applications are restricted to technologies that are still in the demonstration phase (gaseous fuel storage in vehicles, catalysis, gas treatment, etc.). This is due to a series of limitations that coordination polymers still have to date, such as: limited pore size, material shaping in a post-synthesis step and a high production cost.

Pore size (2-10 nm) depends on the organic ligand length, where increasing said size not only entails a challenge in terms of synthesis, but also may weaken crystalline structure stability or give rise to interpenetrated structures. The small pore size of the MOFs is particularly interesting for the storage and separation of

small molecules that weakly interact with one another, where the narrowness of the gaps strengthens adsorbate-adsorbent interactions. However, in most cases reduced pore sizes entail drawbacks such as prolonged diffusion times or limited accessibility, particularly in applications that are carried out with large molecules, such as non-polymeric macromolecule or biomolecule separation, catalysis or detection, for example [Xuan, W. *et al. Chem. Soc. Rev*., 2012, 41, 1677-1695].

As regards material shaping, MOFs are generally produced in powdery form and the processing thereof as a monolith or tablet involves the use of additives which worsen the porous properties [Bazer-Bachi, D. *et al*., *Power Technology*, 2014, 255, 52-29]. Although there is extensive literature on MOF synthesis, the shaping thereof has not been widely studied, this being one of the points limiting its application at the industrial level.

On the other hand, despite the existence of MOFs that are produced at competitive costs, many of them still have a high cost today, particularly when it comes to MOFs that have high porosity and pore size values.

One proposal for increasing pore size is based on the preparation of metal-organic gels, also known as metallogels. In this aspect, a gel can be defined as a non-fluid polymeric or colloidal network which expands over the entire volume occupied by a liquid. The solid network is characterized by having a low density and a large pore volume which is occupied by the liquid or solvent in the wet state. Porosity is due to the microstructure, i.e., the cross-linking or aggregation of the particles forming same. Metal-organic gels can be defined as a type of gel in which the solid matrix is formed by metal ion and organic ligand coordination complexes.

The metal-organic gel can be used in wet form (with solvent) or in dry form (aerogel, xerogel or cryogel). By

subjecting the gel to a drying process (air, lyophilization, supercritical drying, etc.), solvent molecules are removed thereby creating empty pores. This method allows producing very porous structures, with pore sizes greater than 20 nm and also having a high specific surface area, as well as a markedly low density (generally less than 0.5 g/cm^3).

Furthermore, the possibility of producing them directly in monolithic form without requiring subsequent processing is another noteworthy difference of metal-organic gels and metal-organic aerogels. All this contributes to overcoming the drawbacks mentioned for MOFs.

Some examples of MOFs which are processed as gels and/or aerogels prepared with different transition metal ions (Fe^{3+}, Ni^{2+}, Cu^{2+}, Cr^{3+}) and ligands such as trimesate (benzene-1,3,5-tricarboxylate), oxalate, 4-aminopyridine or acetylacetonate, have been described in the prior art. Lohe, M.R. *et al*. (*Chem. Commun*., 2009, 6056-6058) describe an Fe(III) and benzene-1,3,5-tricarboxylate aerogel (MIL-100(Fe) aerogel) that is proposed as a new route for the application of MOFs as catalysts or catalytic supports due to being microporous/mesoporous or macroporous. Xiang, S. *et al* (*J. Mat. Chem*., 2012, 22, 1862-1867) refer to Cr^{3+}/Fe^{3+}- and carboxylic ligand-based metal-organic aerogels. These compounds are made from carboxylic ligands for producing structures inspired, once again, in the known MIL compounds. Yang, Q. *et al*. (*Micropor. Mesopor. Mater*., 2014, 187, 108-113) show the formation process dependency of the Al^{3+}/Cr^{3+} and acetylacetonate aerogel with various synthesis parameters.

Aerogels have also been prepared from non-porous coordination polymers (Angulo-Ibañez, A. *et al*., *Polymers*, 2016, 8, 16), where a one-dimensional polymer of general formula $[M(oxalate)(4\text{-aminopyridine})_2]_n$ in a mesoporous/macroporous monolithic form (pores > 20 nm) is processed.

However, the examples listed in the literature lack any stability comparable to that of conventional porous materials such as zeolites, mesoporous silica or activated carbon. This is because the coordination polymers used in metal-organic gels are based on readily reversible coordination bonds.

Another prior art example is a Cu(II)-oxalate coordination complex-based metal-organic gel (Saha, S., *et. al*., *Chem. Eur. J.* 2013, 19, 9562–9568) the polymer of which adopts the form of nanometric fibers having a size comprised between 20 and 45 nm. However, given the acid-base equilibria of the ligand and the strength of the metal-oxalate bond, this metal-organic gel has reduced acid/base stability.

Other examples in the prior art describe coordination polymers based on different transition metals and the DTO ligand (DTO: dithiooxamidate, also known as rubeanate and by its IUPAC name, ethanedithioamidate), but in no case are a gel (be it metallogel, xerogel, aerogel, cryogel…) or nanometric fibers produced from same. In Japanese and United States patents of reference JP5074458 and US2013/0306488, respectively, the Cu-DTO coordination complex is produced in the form of micrometric particles which, once isolated, are used in cathode manufacturing for electrochemical purposes. In the method used, the reaction is performed by mixing rubeanic acid and copper sulfate in an aqueous-ethanolic solution, without adding a base, which gives rise to the production of micrometer-sized particles. Patent GB1006120 discloses information about an electrolyte containing a polymer formed by the DTO ligand and a transition metal which can be Fe(II), Cu(II), Ni(II) or Co(II). Once again, no reference is made to the produced product being similar to a gel, or to it being made up of nanometric fibers. According to the paper by Kitagawa H. *et al*., published in *Synthetic Metals*, 119 (2001) 485-486, a copper coordination polymer-based formulation with a DTO derivative forms a two-dimensional structure but not in

the form of nanometric fibers.

Brief Description of the Invention

The authors of the present invention have developed a gel based on a metal-organic matrix formed by a framework of coordination polymer nanometric fibers, where said metal-organic matrix has a high pore volume and a high specific surface area. Furthermore, unlike other metal-organic gels, this material is characterized by withstanding well reducing environments and by being stable in a wide pH range (1-14) and in organic and aqueous solvents.

The metal-organic gel of the present invention is one that can be easily produced, chemically and thermally stable and insoluble in most solvents. The key factor for producing these resistant materials with improved properties is the use of the dithiooxamidate ligand which forms particularly strong coordination bonds with metal ions that are soft or have an intermediate hardness and confers a high chemical stability to the material.

On the other hand, controlling metal-organic gel synthesis allows the growth of the coordination polymer in the form of cross-linked nanometric fibers, giving rise to a three-dimensional structure characterized by having, as mentioned above, high pore volumes and a high specific surface area. Furthermore, said synthesis process leads to the formation of gels enclosing a large amount of solvent and allows producing the material with the shape of the container in which it has been prepared without requiring subsequent processing, so the shape of the end product can be controlled. This, along with their high porosity, confers unique properties to said gels as alternative candidate to porous coordination polymers or MOFs.

Therefore, a first aspect of the present invention relates to a metal-organic gel comprising a metal-organic

matrix of cross-linked nanometric fibers, wherein said nanometric fibers comprise coordination polymer chains of general formula $(M\text{-}DTO)_n$, where M is a transition metal or a mixture of at least two transition metals; DTO is dithiooxamidate; and n is the number of M-DTO repeating units forming the coordination polymer, n being a number greater than or equal to 10.

In a second aspect, the present invention relates to a method (hereinafter method of the invention) for preparing a metal-organic gel, wherein said method comprises:

a) dissolving or dispersing a transition metal salt or a mixture thereof, in an organic solvent or a mixture of at least two organic solvents;

b) dissolving dithiooxamide and a base in an organic solvent;

c) mixing the solution or dispersion produced in step a) with the solution produced in step b); and

d) allowing the resulting mixture to stand until formation of the metal-organic gel.

An additional aspect of the present invention consists of a metal-organic gel obtainable by the method of the preceding inventive aspect.

In a particular embodiment, the method of the invention further comprises, after step d), a drying step for drying at room pressure and temperature. This process leads to solvent removal at a speed such that it allows microstructural reorganization of the polymer network, thus giving rise to a xerogel.

Accordingly, an additional aspect relates to a xerogel obtainable by the method of the preceding paragraph.

In another particular embodiment, the method of the

invention further comprises, after step d), a supercritical drying step for drying in the presence of a supercritical fluid. This step involves exchanging the synthesis solvent with a solvent which is soluble in the supercritical fluid and then removing same.

During this process, the liquid that is inside the gel is extracted, which leads to the formation of an aerogel which maintains the three-dimensional structure of cross-linked nanometric fibers of the metal-organic gel.

Accordingly, an additional aspect relates to an aerogel obtainable by the method of the preceding paragraph.

The metal-organic gel and aerogel, produced as described above, are characterized by having a large pore size and volume along with a high accessible surface area. Specifically, the large pore size makes them excellent candidates for applications such as chemical species capture and separation or catalysis, given that the species of interest can more easily access the active zones of the polymer, unlike what is observed in the so-called MOFs where the small pores generally complicate diffusion processes.

Furthermore, in any of the forms thereof (gel or aerogel), the thiol groups which the metal-organic matrix contains on its surface cause the matrix to be highly selective to soft metals such as Hg and Ag, this capture furthermore being irreversible. This feature is particularly interesting because it makes them viable as passive samplers when determining mercury or its derivatives (methyl-mercury) in rivers, lakes, etc.

Therefore, a final aspect of the invention relates to the use of the gel and aerogel as defined in the preceding paragraph, in chemical species capture, separation and/or catalytic processes, contaminated water cleanup or metal recovery processes and in analytical passive sampling

applications.

Brief Description of the Drawings

Figure 1 shows a photograph of the metal-organic gel.

Figure 2 shows the stability of the metal-organic gels in different conditions. a) Polydentate carboxylic acids (1 M): 1. Terephthalic acid; 2. 2,3-pyrazinedicarboxylate acid; 3. Trimesic acid; 4. Isophthalic acid; 5. Oxalic acid. b) Amines (1 M): 1. Pentylamine; 2. Diethanoldiamine; 3. Pyridine; 4. N,N,N',N'-tetramethylethylenediamine; 5. Diethylenetriamine. c) Conventional solvents: 1. Dichloromethane; 2. DMSO; 3. Toluene; 4. Acetonitrile; 5. Chloroform; 6. Diethyl ether; 7. Pentane; 8. Acetone. d) pH: from 14 to 1, referring to the pH value adjusted with NaOH or H_2SO_4. The vial numbered with 0 is a concentrated 96% H_2SO_4 solution. e) Others: 1. 69% HNO_3; 2. 37% HCl; 3. pure CH_3COOH; 4. 25% NH_3; 5. 30% H_2O_2; 6. 0.2 M I_2; 7. 2.8 M $NaBH_4$; 8. 1 M KNO_3; 9. 1 M NaCl.

Figure 3 shows the transmission electron microscopy image (TEM) of a metal-organic gel fragment.

Figure 4 shows optical images (left) and transmission electron microscopy (TEM) images (right) for the metal-organic gel (a), metal-organic xerogel (b) and metal-organic aerogel (c).

Figure 5 shows TEM images of several metal-dithiooxamidate gels: a) CoDTO, b) FeDTO, c) PdDTO, d) RhDTO, e) NiPdDTO and f) NiCoDTO.

Figure 6 shows an image showing the metal capture (in percentage) in metal-organic gels by means of immersing the gel in an aqueous solution with different metal concentrations for 24 hours.

Detailed Description of the Invention

The first aspect of the invention consists of a metal-organic gel comprising a metal-organic matrix of cross-linked nanometric fibers, wherein said nanometric fibers comprise coordination polymer chains of general formula $(M\text{-}DTO)_n$, where M is a transition metal or a mixture of at least two transition metals; DTO is dithiooxamidate; and n is the number of M-DTO repeating units forming the coordination polymer, n being a number equal to or greater than 10.

Throughout this specification and in the attached claims, the term “metal-organic gel” must be understood as a structure comprising a metal-organic matrix dispersed in an organic liquid. In the context of the present invention, the metal-organic matrix corresponds with a structure formed by a framework of cross-linked nanometric fibers, wherein said nanometric fibers comprise a one-dimensional coordination polymer based on repeating units of a transition metal and an organic ligand bound by coordinate covalent bonds.

The term “nanometric fibers” must be understood as structures consisting of continuous polymeric filaments the diameter of which is equal to or less than 100 nm.

In a preferred embodiment, the nanofibers have a diameter comprised between 2 and 300 nm, preferably between 2 and 200 nm, more preferably between 2 and 100 nm, even more preferably between 2 and 50 nm, more preferably between 5 and 40 nm, and even more preferably between 5 and 20 nm.

In another preferred embodiment, the nanofibers have a length comprised between 0.1 and 30 μm, preferably between 0.1 and 20 μm, more preferably between 0.1 and 10 μm, even more preferably between 0.1 and 8 μm, more preferably between 0.1 and 5 μm, even more preferably between 0.2 and 2 μm.

In the present invention, the organic ligand of the coordination polymer, i.e., dithiooxamidate, is the conjugate base of dithiooxamide (H_2DTO; CAS: 79-40-3), a compound which

is also known as rubeanic acid or ethanedithioamide and has the chemical formula $C_2H_4N_2S_2$:

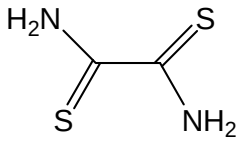

Said organic ligand is coordinated in a bis-bidentate manner to two transition metals, forming a μ-κ^2N,S:κ^2N´,S´ bridge. The molecular structure of the coordination polymer can therefore be described according to the following formula (I):

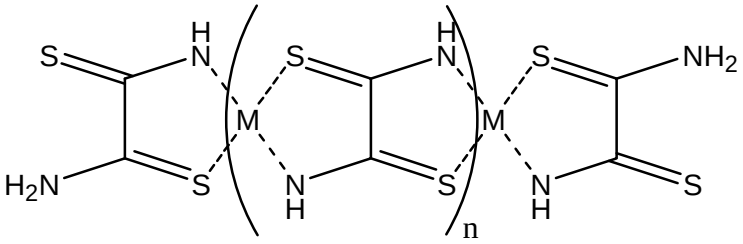

(I)

where M is the transition metal or a mixture of at least two transition metals and n are the M-DTO repeating units forming the coordination polymer.

In a particular embodiment, the transition metal is selected from Cr, Rh, Ru, Mn, Fe, Co, Ni, Cu, Zn, Pd, Ag, Au, Cd, Pt and mixtures thereof. Preferably, the transition metal is selected from Ni, Cu, Co, Fe, Rh, Pt, Ru, Pd and mixtures thereof, more preferably Pd, Ni and Cu.

Said transition metals are in the coordination polymer in the form of metal ions, such as Cr^{3+}, Mn^{3+}, Mn^{2+}, Fe^{2+}, Co^{3+}, Co^{2+}, Ni^{2+}, Cu^{2+}, Cu^{+}, Zn^{2+}, Pd^{2+}, Ag^{+}, Au^{+}, Cd^{2+}, Pt^{2+}, Rh^{2+}, Ru^{2+}, Ru^{3+}.

In a particular embodiment, n is a number such that the molecular weight of the coordination polymer is between 1,769 and 235,245 kDa, more preferably between 29,361 and 117,976

kDa.

Figure 1 shows a photograph of a metal-organic gel representative of the present invention.

The metal-organic gel of the present invention is characterized by having improved chemical stability, particularly against acidic pHs, organic solvents and reducing conditions, due to the strength of the coordination bond the DTO ligand establishes with the transition metals. Figure 2 shows the stability of the metal-organic gels in different conditions such as in coordinating environments, organic solvents, pH, weak oxidizing environments, reducing environments and saline solutions.

Furthermore, compared to MOFs, they have the advantages mentioned for metal-organic gels given that the metal-organic gel of the invention is obtained with large pore volumes and sizes (> 15 nm), can be prepared in monolithic form without a post-synthesis processing, and is synthesized using a simple and commercially accessible ligand, the dithiooxamide.

Therefore, in a particular embodiment the metal-organic matrix has a pore volume comprised between 0.5 and 10 cm^3/g, preferably between 1 and 10 cm^3/g. In another particular embodiment, the metal-organic matrix has an average pore size comprised between 2 and 300 nm, preferably between 2 and 100 nm, more preferably between 2 and 50 nm, even more preferably between 2 and 30 nm.

In another particular embodiment, the metal-organic matrix making up the metal-organic gel has a high specific surface area, more particularly said specific surface area is comprised between 100 and 800 m^2/g.

“Specific surface area” must be understood as the surface area of the metal-organic matrix divided by its mass (expressed in m^2/g).

In a particular embodiment, the metal-organic gel comprises between 60 and 99% by weight of solvent in which the metal-organic matrix comprising the network of cross-linked nanometric fibers is dispersed.

Said solvent fills the pores formed during the assembly of the metal-organic matrix made by the framework of cross-linked nanofibers, as can be seen in Figure 3.

In a second aspect, the invention relates to a method for preparing a metal-organic gel. Said method comprises:

a) dissolving or dispersing a transition metal salt or a mixture thereof, in an organic solvent or a mixture of at least two organic solvents;

b) dissolving dithiooxamide and a base in an organic solvent;

c) mixing the solution or dispersion produced in step a) with the solution produced in step b); and

d) allowing the resulting mixture to stand until formation of the metal-organic gel.

A solution or dispersion of a transition metal salt or a mixture thereof, in an organic solvent or a mixture of at least two organic solvents, is prepared in step a) of the method of the invention.

In a particular embodiment, the transition metal salt is selected from nitrate, chloride, perchlorate, bromide, sulfate, acetate and other organic carboxylates, preferably acetate and other organic carboxylates, more preferably acetate. The degree of hydration (water molecules) of the salt should not be relevant, provided that the purity of the reagent is taken into account when preparing the solution.

In another particular embodiment, the salt of the metal used is based on transition metals selected from Cr, Mn, Fe,

Co, Ni, Cu, Zn, Pd, Rh, Ru, Ag, Au, Cd, Pt and mixtures thereof, more preferably Ni, Cu, Pd, Co, Fe, Pt, Rh, Ru or a mixture thereof, and particularly Pd, Ni and Cu.

The transition metal salt solution or dispersion is prepared in an organic medium, without adding water. The organic solvent is selected based on the best fiber formation and gelling conditions. In a particular embodiment, the organic solvent is selected from N,N-dimethylformamide (DMF); N,N-diethylformamide (DEF); dimethylsulfoxide (DMSO); N,N-dimethylacetamide (DMA); alcohols such as methanol, ethanol, iso- or n-propanol, butanol; tetrahydrofuran and a mixture thereof.

The amount of organic solvent will depend on the desired concentration. Therefore, in another particular embodiment the concentration of transition metal salt in the organic solvent is comprised between 0.5 and 500 mM, preferably between 25 and 100 mM. Nevertheless, optimal concentrations differ depending on the metal. Therefore, 85 mM are more preferably used for Pd-DTO, 25 mM for Cu-DTO, 75 mM for Ni-DTO and 100 mM for heterometallic compounds such as NiPd-DTO, NiCu-DTO and PdCu-DTO, for example. In another preferred embodiment, 50 mM are used for heterometallic compounds such as NiPd-DTO, NiCu-DTO and PdCu-DTO, for example.

In a preferred embodiment, the transition metal salt is a Ni, Cu or Pd acetate and the solvent is DMF. In another preferred embodiment, the transition metal salt is a Ni, Cu or Pd acetate and the solvent is DMSO.

In step b) of the method of the invention, the dithiooxamide ligand (H_2DTO) is added to an organic solution further comprising a base.

In a particular embodiment, the base is selected from sodium hydroxide, potassium hydroxide, sodium methoxide, ammonia and alkylamines such as diethylamine and

triethylamine, more preferably alkylamines such as diethylamine and triethylamine and even more preferably triethylamine is used. The base is used to promote ligand deprotonation.

In another particular embodiment, the solvent is selected from N,N-dimethylformamide (DMF); N,N-diethylformamide (DEF); dimethylsulfoxide (DMSO); N,N-dimethylacetamide (DMA); alcohols such as methanol, ethanol, iso- or n-propanol, butanol; tetrahydrofuran and a mixture thereof. Preferably, the organic solvent is DMF. More preferably, the organic solvent is DMSO.

Even more preferably, the organic solvent used in step b) is the same as the organic solvent used in step a) of the process of the invention.

Given that the nanometric fibers in the end product comprise repeating units with a stoichiometric ratio of 1:1 (metal-ligand), the ligand concentration must be the same as that obtained in step a) for the metal solution. Therefore, in a particular embodiment the ligand concentration in the organic solution is comprised between 0.5 and 500 mM, preferably between 25 and 100 mM, and even more preferably 85 mM for Pd-DTO, 25 mM for Cu-DTO, 75 mM for Ni-DTO and 100 mM for heterometallic nuclear compounds such as NiPd-DTO, NiCu-DTO and PdCu-DTO, for example. In another preferred embodiment, the ligand concentration in the organic solution is 50 mM for heterometallic compounds such as NiPd-DTO, NiCu-DTO and PdCu-DTO, for example.

If the metal salt used is not soluble in the organic solvent, a dispersion will be obtained instead of a solution. Nevertheless, this detail is not significant for obtaining the desired product.

In step c), the two solutions a) and b) are mixed, or the dispersion a) plus the solution b) are mixed if the

transition metal salt is not soluble in the organic solvent.

In a preferred embodiment, the solution containing the DTO ligand is added continuously and in a single step to the transition metal solution or dispersion.

Preferably, the resulting mixture is subjected to stirring or sonication. If stirring is used, a preferable embodiment is to stir the mixture between 100 and 2000 rpm, more preferably at 800 rpm. In the case of mixing by sonication, a preferable embodiment is to use a frequency comprised between 5 and 40 kHz, more preferably 16 kHz. The mixing of a) and b) is preferably done in a temperature range comprised between 0 and 50°C, more preferably between 10 and 30°C.

In step d) of the method of the invention, the produced mixture is allowed to stand until formation of the metal-organic gel. Depending on the starting reagents and on the reaction and mixing conditions, the metal-organic gel can be formed almost immediately, for example, within less than one minute after the mixing process of step c), or it may require more time. In a particular embodiment, the mixture is allowed to stand between 1 and 48 hours, more preferably for 24 hours.

The synthesis process of the invention leads to the formation of a metal-organic gel enclosing a large amount of solvent, particularly between 60 and 99% by weight with respect to the total weight of the metal-organic gel. Furthermore, it allows the metal-organic gel to acquire the shape of the container in which it has been prepared, so the shape of the end product can be controlled, designing it for example, in monolithic form, and therefore without requiring a post-synthesis shaping process.

The metal-organic gel thus produced is characterized by withstanding reducing conditions well and by being stable in a wide pH range (1-14) and in organic and aqueous solvents.

Furthermore, it has a high porosity.

Accordingly, an additional aspect of the present invention consists of a metal-organic gel that can be produced according to the process of the invention described above.

In a preferred embodiment, the metal-organic gel produced according to the process of the invention is subjected to a first step of washing with organic solvents leading to the removal of the remaining reagents and synthesis solvents. Preferably, a solvent in which the reagents and the by-products are soluble, more preferably, the synthesis solvent is used.

In a second step, the metal-organic gel free of unreacted species is washed. For this step, the use of solvents that are soluble in CO_2 is preferred, for example alcohols, such as methanol, ethanol or propanol, more preferably ethanol.

Additionally, the organic solvent initially incorporated in the polymeric matrix can be exchanged with another solvent without requiring said solvent to be an organic solvent. In a particular embodiment, said exchange solvent can be water.

In another preferred embodiment, the metal-organic gel produced according to the method of the invention is subjected to a drying process for the purpose of producing a metal-organic xerogel. Said drying method can be performed at room temperature and pressure conditions. In this case, drying can be performed at ambient temperature at a pressure of about 1 bar or, to speed up the process, at higher temperatures (50-150ºC) which are provided by an external source, such as an oven, for example.

Preferably, the temperature ranges between 100 and 120ºC, whereas the pressure is usually about 1 bar.

Alternatively, or in a combined manner, said drying

method can be performed by applying a vacuum.

Even more preferably, this drying method is performed on a metal-organic gel containing a volatile organic solvent such as an alcohol, for example, as the organic solvent. Said solvent can be the one that was used for preparing precursor solutions leading to the production of the metal-organic gel or the one that is used in a subsequent washing step such as the one described above.

This drying process, at ambient pressure and temperatures or by means of providing external heat and/or by applying a vacuum, allows removing the organic solvent, or where appropriate the exchange solvent, and leads to the production of a xerogel. By means of this process, the solvent present in the metal-organic gel is removed at a rate such that it allows reorganizing the microstructure formed by the nanofibers, causing them to collapse and stack to give rise to a framework that virtually lacks porosity but is chemically identical to the metal-organic gel and aerogel.

In another preferred embodiment, the metallogel produced according to the method of the invention is subjected to a supercritical drying process.

Supercritical drying must be understood as a process of removing the solvent contained in the metal-organic gel above its critical point, or by means of a process of exchanging said solvent with a supercritical fluid followed by evaporating said fluid at a temperature greater than its critical temperature.

If the solvent contained in the metal-organic gel is not soluble in the supercritical fluid, said solvent is firstly exchanged with a solvent soluble in said supercritical fluid.

After exchanging the initial solvent (the synthesis solvent of the gel), the new solvent is exchanged with a fluid

in subcritical conditions. The temperature of the gel immersed in the fluid (all the gel being inside an airtight container equipped with valves required for correct operation) is then raised until exceeding the critical point of the chosen fluid. Finally, the pressure is gradually reduced to its ambient value in isothermal conditions.

In a preferred embodiment, the supercritical fluid is CO_2. In this case, supercritical drying is performed by first immersing the metal-organic gel in liquid CO_2 at a temperature comprised between 15 and 30ºC and a pressure between 35 and 60 bar. The resulting material is then dried in supercritical conditions, i.e., increasing the temperature above the critical temperature of CO_2 (above 31ºC) and a pressure between 60 and 150 bar. Finally, the pressure is reduced in isothermal conditions until reaching ambient pressure.

If the solvent contained in the metal-organic gel is not soluble in CO_2, said solvent is first exchanged with a solvent soluble in CO_2, such as an alcohol or an alkane, for example. Said solvent is exchanged afterward by CO_2in conditions close to 20ºC and 50 bar. Supercritical drying is then performed in the same conditions described above, i.e., if CO_2 is used as a supercritical fluid, the system is brought to a temperature above the critical temperature of CO_2 (31ºC) and to a pressure between 60 and 150 bar, and the pressure is then reduced in isothermal conditions until reaching ambient pressure.

This supercritical drying process allows removing the solvent contained in the metal-organic gel, giving rise to the production of a metal-organic aerogel.

Furthermore, it has been observed that supercritical drying of the metal-organic gel allows said gel to retain its initial shape, i.e., to keep the three-dimensional structure of the metal-organic matrix formed by the network of cross-linked nanometric fibers, therefore resulting in a highly

porous material.

Therefore, an additional aspect of the present invention consists of an aerogel that can be produced according to the method described above.

In the context of the present invention, the term “metal-organic aerogel” must therefore be understood as a porous network of a structure that is identical or similar to that of the metal-organic gel from which it originated, but without the solvent.

In a preferred embodiment, the aerogel is characterized by having pore volumes comprised between 0.5 and 10 cm^3/g, preferably between 1 and 10 cm^3/g. This allows producing a material with a high specific surface area, particularly the specific surface area of the aerogel can have values ranging between 100 and 800 m^2/g. The surface area values can be calculated by means of the BET model [Brunauer, S. *et. al*. J. Am. Chem. Soc. 1938, 60, 309].

As a result of this drying, a material with very low apparent densities, preferably between 0.5 and 0.01 g/cm^3, with respect to its actual density (between 2.0 and 3.5 g/cm^3) is produced.

By means of N_2 adsorption isotherm measurements at 77 K, it is found that aerogels have a significant meso- and macroporous contribution, although the average pore size is comprised between 2 and 300 nm, preferably between 2 and 100 nm, more preferably between 2 and 50 nm, even more preferably between 2 and 30 nm.

In a particular embodiment, the nanometric fibers comprised in the aerogel have a diameter equal to or less than 100 nm, preferably comprised between 2 and 100 nm, preferably between 2 and 50 nm, more preferably between 5 and 40 nm, and even more preferably between 5 and 20 nm.

In another particular embodiment, the nanometric fibers comprised in the aerogel have a length comprised between 0.1 and 10 μm, preferably between 0.1 and 8 μm, more preferably between 0.1 and 5 μm, even more preferably between 0.2 and 2 μm.

Due to the chemical stability of the gels and aerogels of the invention, derived fundamentally from the strength of the bonds between the transition metal and the DTO ligand, and their large pore size and high specific surface area, gels and aerogels are excellent candidates for applications in chemical species capture, separation and/or catalytic processes, contaminated water cleanup or metal recovery processes and in analytical passive sampling applications.

The application thereof for the selective capture of soft metals is also particularly relevant. The thiol groups which the aerogel contains on its surface cause the aerogel to be highly selective to soft metals such as Hg and Ag, this capture furthermore being irreversible. This feature is particularly interesting because it makes them viable as passive samplers when determining mercury or its derivatives (methyl-mercury) in rivers, lakes, etc.

Accordingly, the aerogel of the present invention can be used in processes requiring easy permeability of chemical species due to the high specific surface area and mesoporous character. In this context, as particular embodiments of the present invention, the aerogel that can be produced according to the method described above can be used in chemical species capture, separation and/or chemical catalysis, contaminated water cleanup or metal recovery processes and in analytical applications such as passive sampling.

Throughout this specification and in the attached claims, “chemical species capture” must be understood as the irreversible immobilization of chemical species which may

include, and are not limited to, free molecules in solution or in gaseous phase, solvates and/or salts, cationic or anionic species and chemical elements. In this context, “contaminated water cleanup processes” must be understood as those processes which allows capturing chemical species in water that belong to the chemical contaminant group, i.e., any organic/inorganic substance in an amount which causes an irritating, corrosive, suffocating or toxic effect in animals or plants. Likewise, “metal recovery” must be understood as the capture of chemical species that belong to the metal and metalloid group.

In this specification and in the attached claims, the “passive sampling” technique must be understood as the collection of chemical species controlled by a physical process such as diffusion, or permeability through the metal-organic framework.

Example 1. Preparation of a Ni-DTO metal-organic gel

0.933 g of $Ni(OAc)_2$ were dissolved in 48 mL of DMF/DMA (60:40 vol:vol) with the help of a sonic tip at 80% its power for 2 minutes. The ligand solution was prepared by dissolving 0.451 g of dithiooxamide in 2 mL of DMF/DMA (60:40 vol:vol) together with 523 µL of triethylamine. The dithiooxamidate ligand solution was added at once to the metal dispersion. This addition process was performed in an ultrasonic bath (ULTRASONS-H, Selecta) at a temperature of 15ºC until a change in the viscosity of the samples was visually observed (5 minutes). Once the metal-organic gel acquired the suitable consistency, it was left at room temperature for a day.

The sample was washed according to the following method: first the metal-organic gel was immersed in DMF to remove unreacted species (24 h) and washes with DMF/ethanol mixtures were then performed (every 24 h). Finally, exchange with pure ethanol was performed (24 h).

Figure 4a (left) corresponds to a photograph of the

metal-organic gel in which it is observed that the metal-organic gel keeps the shape of the container where it has been synthesized. Figure 4a (right) shows an image of a fragment of the metal-organic gel obtained by transmission electron microscopy (TEM) taken in a Philips CM200 microscope.

Example 2. Preparation of a Ni-DTO metal-organic xerogel

The corresponding xerogel was prepared by leaving the metallogel produced in Example 1 to dry at room temperature and pressure. The results are shown in Figure 4b.

Example 3. Preparation of a Ni-DTO metal-organic aerogel

The corresponding aerogel was prepared using a Quorum Technologies® E3100 supercritical drying equipment equipped with gas inlet valves, venting valves and purge valves, and a thermal bath. The metal-organic gel produced following the method of Example 1 was first immersed in liquid CO_2 at 20ºC and 50 bar for one hour. After that, ethanol was removed through the purge valve. This process was repeated five times. The sample was then dried in supercritical conditions by increasing the temperature and pressure to 38ºC and 85-95 bar, respectively. Finally, the chamber was slowly vented to atmospheric pressure, keeping it at a constant temperature (38ºC).

Figure 4c shows the optical image and the electron microscopy image corresponding to a Ni-DTO aerogel synthesized according to the method described in this example.

From the images shown in Figure 4, a highly porous structure consistent with the high pore volume value (3.0 cm^3/g) and specific surface area value (406 m^2/g) can be seen in the case of the gel and aerogel.

Example 4. Stability tests of the metal-organic gel

Different samples of a metal-organic gel produced

following the method described in Example 1 were subjected to different conditions:

1) Polydentate carboxylic acid solutions (1 M):
Terephthalic acid; 2,3-pyrazinedicarboxylic acid; Trimesic acid; Isophthalic acid; Oxalic acid.

2) Amine solutions (1 M):
Pentylamine; Diethanoldiamine; Pyridine; N,N,N',N'-tetramethylethylenediamine; Diethylenetriamine.

3) Conventional solvents:
Dichloromethane; DMSO; Toluene; Acetonitrile; Chloroform; Diethyl ether; Pentane; Acetone.

4) Solutions at different pH (1-14) adjusted with NaOH or H_2SO_4.

5) Others:
69% HNO_3; 37% HCl; pure CH_3COOH; 25% NH_3; 30% H_2O_2; 0.2 M I_2; 2.8 M $NaBH_4$; 1 M KNO_3; 1 M NaCl.

Figure 2 shows how the metal-organic gel is stable in any of the conditions to which it has been subjected, without the structure thereof being altered. Particularly, the remarkable stability presented at different pH values, both acidic and basic should be highlighted.

These tests have clearly demonstrated the stability shown by the metal-organic gel of the invention at different pH values, which broadens its range of actuation as metal capturing agents. It must be added that other metal-organic gels lack stability at a low pH, which makes them unsuitable for use thereof in applications imposing extremely acidic conditions.

Example 5. Preparation of other homometallic and bimetallic M-DTO metal-organic gels

Following a method similar to that of Example 1, but changing the metal cation, M-DTO type gels where the metal centers used were Cu(II), Co(II), Fe(II), Pd(II) and Rh(II),

were produced. Figure 5 shows electron microscopy images for M-DTO gels with M = Co(II), Fe(II), Pd(II) and Rh(II). Bimetallic compounds were prepared in a similar manner using combinations of Fe/Co, Fe/Pd, Fe/Cu, Fe/Ni, Co/Ni, Co/Cu, Co/Pd, Ni/Cu, Ni/Pd and Pd/Cu. The atomic content for each metal is shown in Table 1. Figure 5 shows electron microscopy images for M-DTO gels with M = Co(II), Fe(II), Pd(II), Rh(II), Ni(II)/Pd(II) and Ni(II)/Co(II).

Table 1

	M_1 (atomic %)	M_2 (atomic %)
FeCoDTO	46	54
FePdDTO	72	28
FeCuDTO	44	56
FeNiDTO	47	53
CoNiDTO	47	53
CoCuDTO	50	50
CoPdDTO	67	33
NiCuDTO	55	45
NiPdDTO	62	38
PdCuDTO	43	57

Example 6. Selective metal capture tests

Different tests were conducted by immersing 1 g of metal-organic gel produced following the method of Example 1 for 24 h in aqueous solutions containing different concentrations of the following metals: Cu, Ag, Hg, Pb, Zn, Cd

and Co. All the solutions were adjusted to low pH values (1-3); nevertheless, as clearly demonstrated in the preceding example, the metal-organic gel continued to remain stable even at such extreme conditions. The concentrations of each metal species were determined by ICP-AES (Inductively Coupled Plasma Atomic Emission Spectroscopy) before and after exposure to the metal-organic gel.

Figure 6 shows the results of the performed capture, being particularly effective in the case of Cd^{2+}, Pb^{2+}, Cu^{2+}, Hg^{2+} and Ag^{+}. The x-axis represents the initial concentration of the metal ion in the solution, whereas the y-axis shows the percentage of recovery or removal of the metal ion relative to its initial concentration. By way of example, if the percentage is 90%, it would indicate that the content of a 10 ppm metal ion solution is reduced to 1 ppm.

CLAIMS

1. A metal-organic gel comprising a metal-organic matrix of cross-linked nanometric fibers, characterized in that said nanometric fibers comprise coordination polymer chains of general formula $(M\text{-}DTO)_n$, where M is a transition metal or a mixture of at least two transition metals; DTO is dithiooxamidate; and n is the number of M-DTO repeating units forming the coordination polymer, n being a number greater than or equal to 10.

2. The metal-organic gel according to claim 1, characterized in that the nanometric fibers have a diameter between 2 and 300 nanometers.

3. The metal-organic gel according to claim 1 or 2, characterized in that the nanometric fibers have a length comprised between 0.1 and 30 μm.

4. The metal-organic gel according to any one of claims 1 to 3, characterized in that M is a transition metal selected from Cr, Rh, Ru, Mn, Zn, Fe, Co, Ni, Cu, Pd, Ag, Au, Cd, Pt and a mixture thereof.

5. The metal-organic gel according to any of claims 1 to 4, characterized in that it further comprises between 60 and 99% by weight of a solvent with respect to the total weight of the metal-organic gel.

6. A method for preparing a metal-organic gel as defined in claims 1 to 5, characterized in that said method comprises:

a) dissolving or dispersing a transition metal salt or a mixture thereof, in an organic solvent or a mixture of at least two organic solvents;

b) dissolving dithiooxamide and a base in an organic solvent;

c) mixing the solution or dispersion produced in step a) with the solution produced in step b); and

d) allowing the resulting mixture to stand until formation of the metal-organic gel.

7. The method according to claim 6, characterized in that the transition metal salt is selected from nitrate, chloride, perchlorate, bromide, sulfate, acetate and other organic carboxylates.

8. The method according to claim 6 or 7, characterized in that the transition metal salt is selected from a Cr, Mn, Fe, Co, Ni, Cu, Zn, Pd, Rh, Ru, Ag, Au, Cd, Pt salt, and a mixture thereof.

9. The method according to any one of claims 6 to 8, characterized in that the organic solvent used in step a) and the organic solvent used in step b) are independently selected from N,N-dimethylformamide (DMF); N,N-diethylformamide (DEF); dimethylsulfoxide (DMSO); N,N-dimethylacetamide (DMA); alcohols such as methanol, ethanol, iso- or n-propanol, butanol; tetrahydrofuran and a mixture thereof.

10. The method according to any one of claims 6 to 9, characterized in that the base used in step b) is selected from sodium hydroxide, potassium hydroxide, sodium methoxide, ammonia and alkylamine.

11. A metal-organic gel obtainable by the method defined in any of claims 6 to 10.

12. The method according to any of claims 6 to 10, characterized in that it further comprises at least one washing step for washing the metal-organic gel.

13. The method according to claim 12, characterized in that at least one washing step is performed in the presence of an alcohol.

14. The method according to any one of claims 6 to 10 and 12 to 13, characterized in that it further comprises a drying step for drying the metal-organic gel at room temperature and pressure conditions or by means of providing external heat and/or by applying a vacuum.

15. A metal-organic xerogel obtainable by the method defined in claim 14.

16. The method according to any one of claims 6 to 10 and 12 to 13, characterized in that it further comprises a supercritical drying step for drying the metal-organic gel.

17. The method according to claim 16, characterized in that the supercritical drying is performed by first immersing the metal-organic gel in liquid CO_2, and then imposing supercritical conditions for drying at a temperature greater than 31ºC and a pressure between 60 and 150 bar.

18. A metal-organic aerogel obtainable by the method defined in any of claims 16 to 17.

19. The metal-organic aerogel according to claim 18, characterized in that it has a specific surface area between 100 and 800 m^2/g.

20. The metal-organic aerogel according to claim 18 or 19, characterized in that it has pore volumes comprised between 0.5 and 10 cm^3/g.

21. The metal-organic aerogel according to any one of claims 18 to 20, characterized in that it has an average pore size between 2 and 300 nm.

22. Use of a gel as defined in any one of claims 1 to 5 and 11, or of a metal-organic aerogel as defined in any of claims 18 to 21, in chemical species capture, separation and/or catalytic processes, contaminated water cleanup or metal recovery processes, and in analytical applications such

as passive sampling.

ABSTRACT

The present invention relates to metal-organic gels and metal-organic aerogels made of dithiooxamidate (DTO) or rubeanate ligand-based coordination polymers, method for preparing thereof and use in chemical species capture, separation and/or catalysis, environmental cleanup, metal recovery, passive sampling, among others.

Figure 1

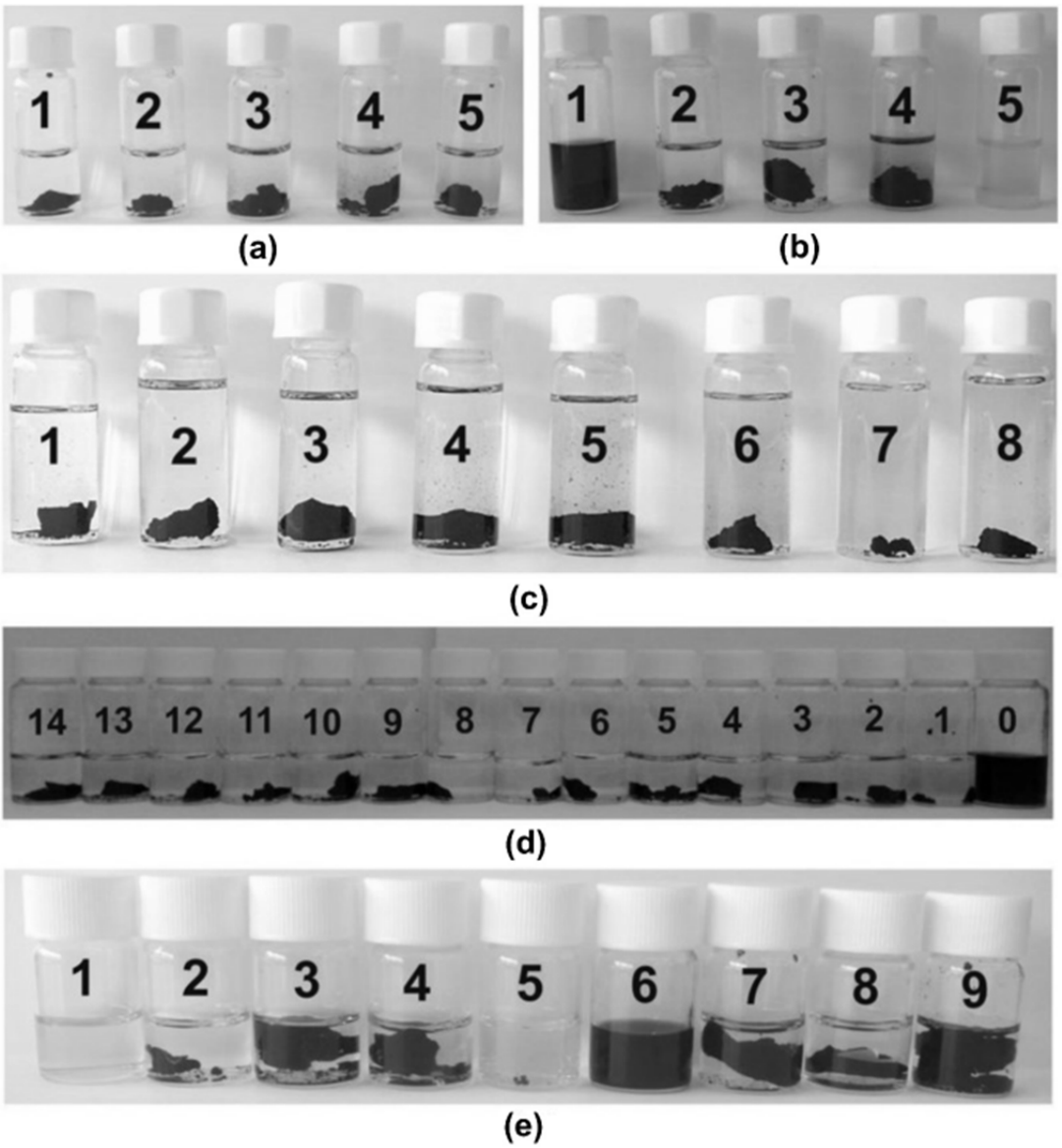
1 2 3 4 5
(a)
1 2 3 4 5
(b)
1 2 3 4 5 6 7 8
(c)
14 13 12 11 10 9 8 7 6 5 4 3 2 1 0
(d)
1 2 3 4 5 6 7 8 9
(e)

Figure 2

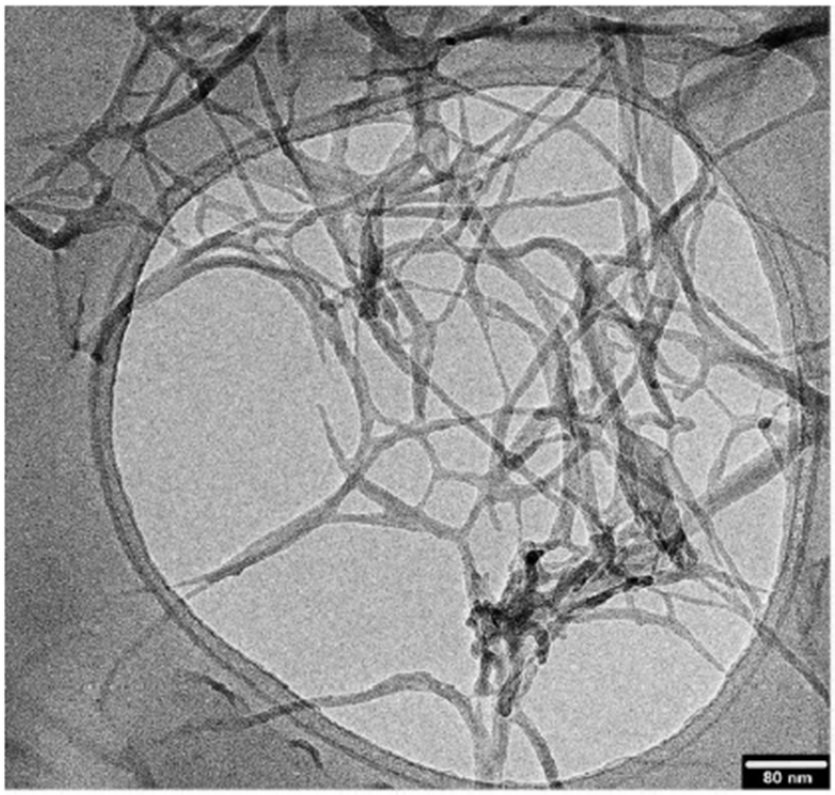

Figure 3

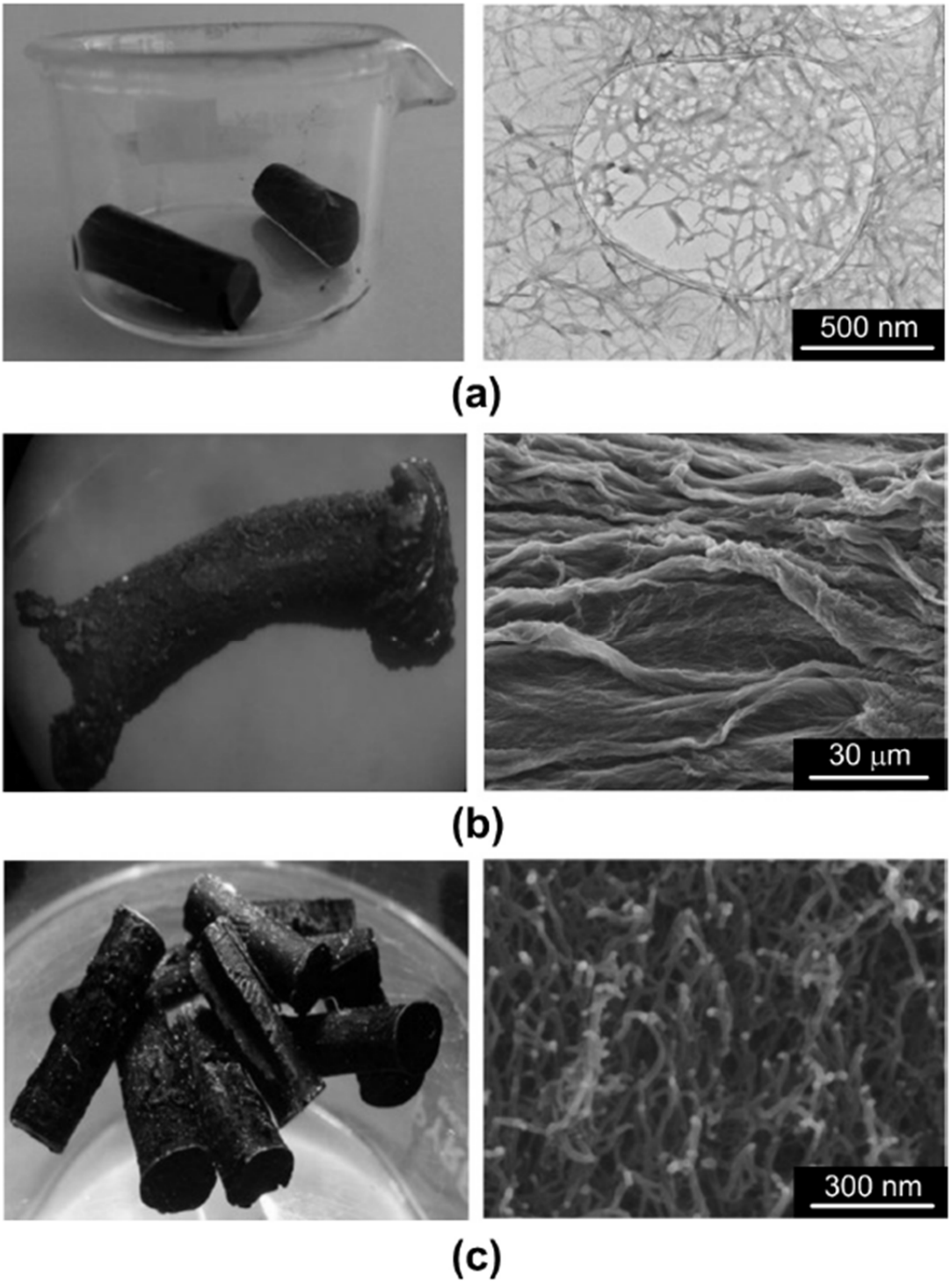

Figure 4

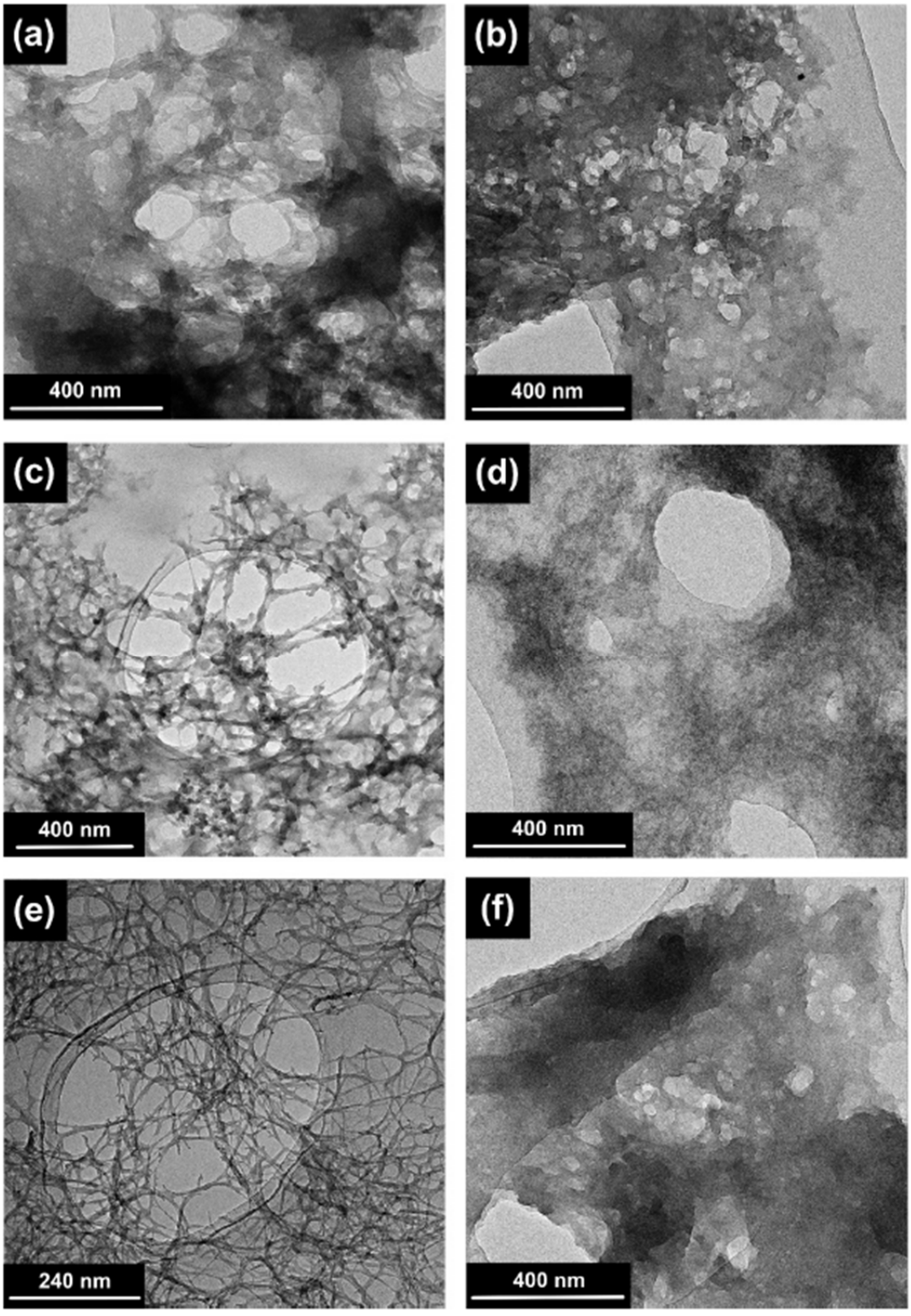

Figure 5

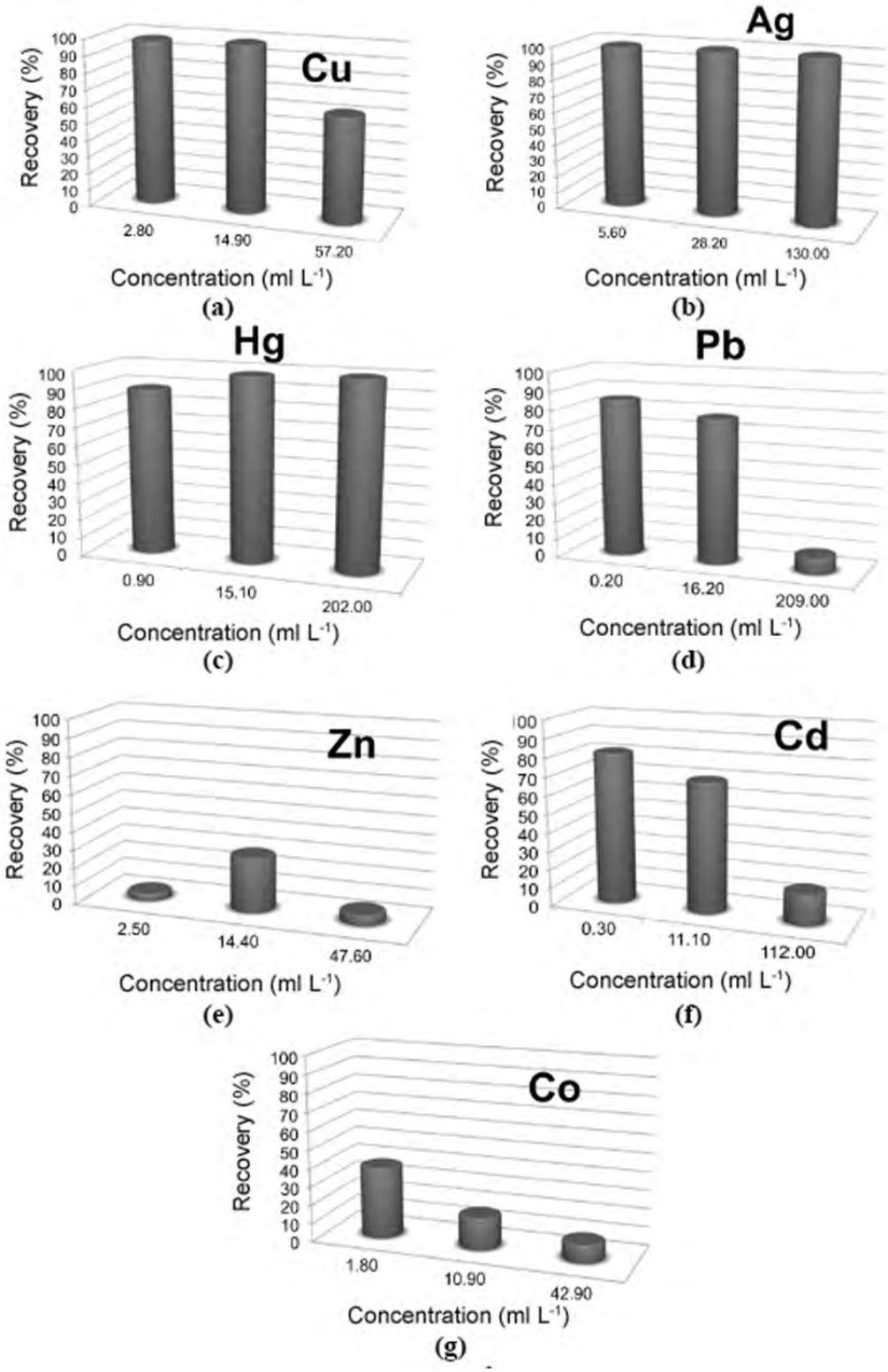
Cu
Recovery (%)
100
90
80
70
60
50
40
30
20
10
0
2.80
14.90
57.20
Concentration (ml L-1)
(a)
Ag
Recovery (%)
5.60
28.20
130.00
Concentration (ml L-1)
(b)
Hg
Recovery (%)
0.90
15.10
202.00
Concentration (ml L-1)
(c)
Pb
Recovery (%)
0.20
16.20
209.00
Concentration (ml L-1)
(d)
Zn
Recovery (%)
2.50
14.40
47.60
Concentration (ml L-1)
(e)
Cd
Recovery (%)
0.30
11.10
112.00
Concentration (ml L-1)
(f)
Co
Recovery (%)
1.80
10.90
42.90
Concentration (ml L-1)
(g)

Figure 6

This work presents the synthesis and characterization of a series of coordination compounds based on metal(II)-organosulfur complexes as precursors of zero- and three-dimensional nanomaterials.

On the one hand, thiocarboxylato ligands have been used for the preparation of metal(II) sulfide nanoparticles both in pure form and as homogeneous dispersion within a carbonaceous matrix. Dry thermolysis, the synthetic method chosen to achieve this goal, is a simple, controllable and economical route that allows the scaling of these materials, a requirement that the industrial sector demands.

Moreover, 3D nanoporous structures have been obtained by gelation of coordination polymers based on dithiooxamidato ligand. The entrapped solvent can be extracted from the gels through a supercritical treatment, consolidating the structure in the form of aerogels: ultralight mesoporous solids in which more than 80% of their volume is made up of air. Throughout the text the reader will have the opportunity to discover the surprising physicochemical properties exhibited by this emerging class of metal-organic materials.

ZTF-FCT
Zientzia eta Teknologia Fakultatea
Facultad de Ciencia y Tecnología

eman ta zabal zazu
Universidad del País Vasco
Euskal Herriko Unibertsitatea